Ryszard S. Choraś

Editor

Image Processing and Communications Challenges 5

Springer

Advances in Intelligent Systems and Computing

Volume 233

Series Editor

Janusz Kacprzyk, Warsaw, Poland

Ryszard S. Choraś
Editor

Image Processing
and Communications
Challenges 5

Springer

Editor
Ryszard S. Choraś
Institute of Telecommunications
University of Technology Life Sciences
Bydgoszcz
Poland

Printed on acid-free paper

Springer is part of Springer Science+Business Media (www.springer.com)

Preface

It gives us great pleasure to present the book/proceedings of the 5th International Conference in Image Processing & Communications IP&C 2013, held in Bydgoszcz, Poland, in September 2013. The 2013 International Conference on Image Processing and Communications (IP&C 2013) placed emphasis on efficient and effective image processing and communications technologies and systems.

The key objective of the book/proceedings is to provide a collection of comprehensive references on some recent theoretical development as well as novel applications in image processing and communications.

The book is divided into two parts. Part I deals with image processing. A comprehensive survey of different methods of image processing, computer vision is also presented. Part II deals with the telecommunications networks and computer networks. Applications in these areas are considered.

In conclusion, the edited book comprises papers on diverse aspects of image processing and communications systems. There are theoretical aspects as well as application papers.

Contents

Real-Time Recognition of Selected Karate Techniques Using GDL Approach

2DKLT-Based Color Image Watermarking

Knowledge Transformations Applied in Image Classification Task

Local Eigen Background Substraction

Polarization Imaging in 3D Shape Reconstrucion

Background Subtraction and Movement Detection
Algorithms in Dynamic Environments – An Evaluation for
Automated Threat Recognition Systems

Part I

Image Processing

Adaptive Windowed Threshold for Box Counting Algorithm in Cytoscreening Applications

Dorota Oszutowska-Mazurek[1], Przemysław Mazurek[2],
Kinga Sycz[3], and Grażyna Waker-Wójciuk[3]

[1] Gryfice Hospital Medicam, Department of Pathomorphology
   Niechorska 27 Str., 72300 Gryfice, Poland
   adorotta@op.pl
[2] West–Pomeranian University of Technology, Szczecin,
   Department of Signal Processing and Multimedia Engineering,
   26. Kwietnia 10 Str., 71126 Szczecin, Poland
   przemyslaw.mazurek@zut.edu.pl
[3] Independent Public Voivodeship United Hospital,
   Department of Pathomorphology, Arkońska 4 Str., 71455 Szczecin, Poland
   grazynka@blue.net.pl

Summary. Two threshold techniques are compared in this paper for the application of the box–counting algorithm. The single threshold is sensitive on the selection of the threshold value. Application of the proposed, adaptive windowed threshold allows selection of the threshold values using standard deviation and mean value. The application of the windowed threshold allows preclassification of cell nuclei.

1 Introduction

Automatic or computer assisted preclassification of the cell nuclei for two classes: atypical (precancerous and cancerous) and correct is important diagnostic tool. There are many available techniques for analysis of such objects and fractal based techniques are very promising.

Fractal dimension (FD) estimators could be applied for the cell nucleus boundary analysis using stick method [1, 2]. It allows estimation of the FD for shapes, so detection of irregularities is possible.

The main problem of the cell nuclei analysis is the segmentation of the cell nuclei. Image artifacts, related to the biological sample, influence greatly the segmentation. Poor quality images should be processed also, if it is possible. Precise segmentation of cell nuclei by humans is not possible in many cases. The analysis of the cell nuclei should be based on the boundary of cell nuclei analysis if it is possible, but more important is the texture analysis.
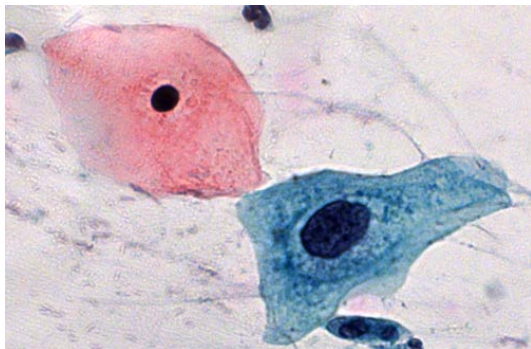
Fig. 1. Example microscopic image of cell nuclei (Papanicolaou smear)

The observed texture of cell nucleus (Fig. 1) is the optical density of microscopic object.

The optical density consists of optical effects related to small objects. The cell nucleus has a specific transparency, so front surface of the object is not observed, but all properties and optical effects related to the volumetric properties of the object. The texture is considered during the cytoscreening, so it is important factor in medical diagnostics. Higher granularity of the object could be a symptom of atypical cell nucleus.

The segmentation problem is common in many kinds of cytological images. Breast cytology images are considered in many papers, and some algorithms are valuable for cervical cytology analysis. Different techniques are used together, like the shape of the cell, e.g. area, perimeter, convexity, eccentricity and simple texture measure, based on the average value of red channel [3]. The segmentation of cells nuclei is possible using many algorithms [4, 5]: watershed algorithm, active contours, cellular automata, grow–cut technique, fuzzy sets of I and II type, sonar–like method, [6, 7]: Hough transform and (1+1) search strategy. Advanced PCA techniques for color images are promising [8] and generalized shape estimation [9] also. The shape of the cell could be processed using AM-FM algorithm [10].

There are many techniques of the texture analysis. One proposed technique is the texture analysis, based on multiresolutional image representation [11]. Fractal analysis is a kind of the mulitresolutional analysis especially. There are many fractal analysis techniques for textures. The box–counting [1, 2] could be applied for binary images after thresholding. The number of boxes that are completely filled by specific values (0's or 1's) is plotted against the width of the box side. The slope of regression curve on double logarithmic plot (Richardson's plot) corresponds to the FD. Another technique is based on the Minkowski-ŰBouligand dimension [12, 13].

Application of the threshold technique simplifies processing, but the selection of proper value of the threshold level is not trivial. The binary representation of the image is lossy and useful information could be lost. Another image representation, based on the DEM (Digital Elevation Map), is more convenient. There are few techniques for the estimation of the FD using DEM. The 3D extension of the box–counting is the straightforward technique [14]. Another techniques are the TPM (Triangular Prism Method) [15] and TPM derivatives [16]. TPM analysis is based on the surface area interpolation for different scales. Analysis of Papanicolaou smears using TPM is proposed in [17, 18]. Variogram is very important technique for FD estimation, especially for non–regular sampling points of the surface [19, 20]. There are many other techniques also: Isarithm [21], Variation Estimator [22], Probability Estimator [23].

The object of interest is not square. Many FD estimation techniques require that the side of square should fulfill specific requirements. Typical requirement is the side length of the square: $(2^p + 1)$ or 2^p, where p corresponding to the scale. The most important is the resolution of the analyzed area. The limited area of the object could be analyzed using clipping of the inner part of cell nucleus to the square, so quality of the FD estimation is reduced.

Irregular objects like cell nuclei could be processed using variogram that utilizes all available pixels of the object. Variogram is proposed for the analysis of cell nuclei in [24]. Another techniques could be applied using tiled method [18], that is better in comparison to the clipping. The image of the object is divided into a set of the non–overlapped squares. The selected FD estimation technique is applied for all squares.

The size of the square limits maximal scale of analysis. This limitation is not significant disadvantage, because large scales are noised usually. It is a result of the estimation based on the single or a few large squares. Smaller scales are important for the analysis, so tiled method is an important solution.

2   Threshold Based Box–Counting

The application of threshold is important for the reduction of computational requirements. It is important for the processing of large resolution microscopic images at high magnification (e.g. 400x), especially. The selection of the proper value of the threshold for specific cell nucleus, allows application fast algorithm dedicated to binary image representations.

The selection of the threshold should be based on the histogram of the cell nucleus image. The absolute threshold cannot be applied due to high variability of the brightness of the cell nuclei in acquired images. The variable exposure time is the optimal technique for the optimal utilization of dynamic range of camera sensor. The image of the cell nucleus is normalized after segmentation.

Two types of normalizations are possible. The first one is based on two side normalization, where the black and white points are normalized using histogram. The first method is the contrast normalization and maximal contrast is obtained.

The second one is based on the one side normalization, where the white point is normalized only. The second method is the brightness normalization. Both of them stretches the histogram and emphasizes visibility of details of the cell nuclei texture.

Normalized images are processed by the texture analysis techniques. The box–counting algorithm needs the selection of the threshold for binary image. It could be arbitrary value from $0 - 1$ range, depending on the knowledge, but adaptive techniques is better.

The fixed threshold for normalized images is not a proper solution. The black and white points depend on artifacts. The segmentation of the cell nucleus could be not efficient and some pixels of the cytoplasm could be assigned to the cell nucleus. The area of the cell nucleus is dark, but the cytoplasm is highly transparent and bright. Such assignment disturbs histogram and forces white point.

More robust selection of the threshold should be applied. The mean value based threshold is not the correct one. Black point could be related to the significant part of the cell nucleus area due to low exposure so mean value is shifted toward black level. The typical histogram of cell nuclei is Gaussian approximately, with well visible maximum.

Inappropriate selection of the black level during the acquisition adds additional peak for zero value and the mean value does not correspond to the expected peak. This effect of the image values clipping due to too low exposure. The minimal value $X_{m}in$ of the cell nuclei for the image X should be calculated:

$$X_{min} = \min(X) \tag{1}$$

Every cell nucleus image has corresponding image mask M that is defined as:

$$M_{x,y} = \begin{cases} 1 : cell\_nucleus\_pixel \\ 0 : otherwise \end{cases} \tag{2}$$

where x,y are pixel coordinates. New mask, without minimal value is computed:

$$M_{x,y}^* = M_{x,y} > X_{min} \tag{3}$$

The threshold value is the mean value of the cell nuclei for mask area:

$$\overline{m} = \frac{1}{\sum_{x,y} M^*} \sum_{M_{x,y}^*=1} X_{x,y} \tag{4}$$

Obtained mean value could be used directly as a threshold $T = \overline{m}$ or as a basis of another techniques additive or multiplicative:

$$T = a \cdot \overline{m} \tag{5}$$

$$T = \overline{m} + b \tag{6}$$

or more generally:

$$T = a \cdot \overline{m} + b \tag{7}$$

where the a, b are constant values. The selection and constant values is an opened problem. After random testing of different variants (a few hundreds of test) we have not found solution that gives good separation for our database and has low sensitivity on selected constants.

3   Adaptive Windowed Thresholding

An alternative thresholding is possible. Two threshold values could be applied instead single one. The motivation of this technique is the human vision is especially sensitive in high contrast. The mean and surrounding values have small difference in comparison to the darkest and lightest pixels. The single threshold around mean value (near the maximum of distribution) introduces differences between similar values, so such thresholding is not well motivated.

Window threshold uses two values of threshold T_1 and T_2. The proposed technique uses placement around mean value:

$$T_1 < \overline{m} < T_2 \tag{8}$$

The selection of the both threshold should be adaptive, because standard deviation of the distribution is not fixed. The proposed formula uses symmetrical threshold:

$$X_{x,y}^B = \begin{cases} 1 : |\overline{m} - X_{(x,y)}| < T_S \\ 0 : otherwise \end{cases} \tag{9}$$

where T_S is threshold value adaptively computed for every cell nucleus using standard deviation:

$$T_S = k \cdot std(X_{(x,y)}^*) \tag{10}$$

for image pixels inside modified mask X^*. The selection of constant k is the subject of the search. The value $k \in (1.1 - 1.2)$ range gives good separation of atypical and correct cell nuclei as it is shown in next section.

Few example images of correct and atypical cell nuclei using single and proposed windowed threshold are shown in Fig. 2 and Fig. 3.
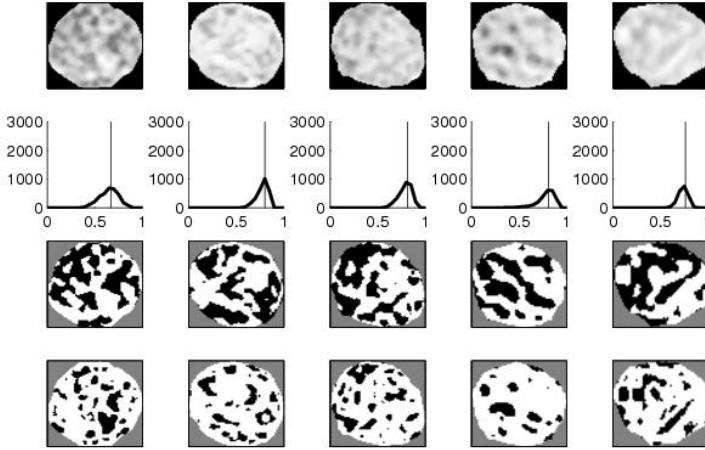
Fig. 2. Examples of correct cell nuclei (top row, scale not preserved, negative image), histogram (second row, with emphasized mean value), segmentation based on the mean (third row), segmentation based on the windowed threshold (fourth row)
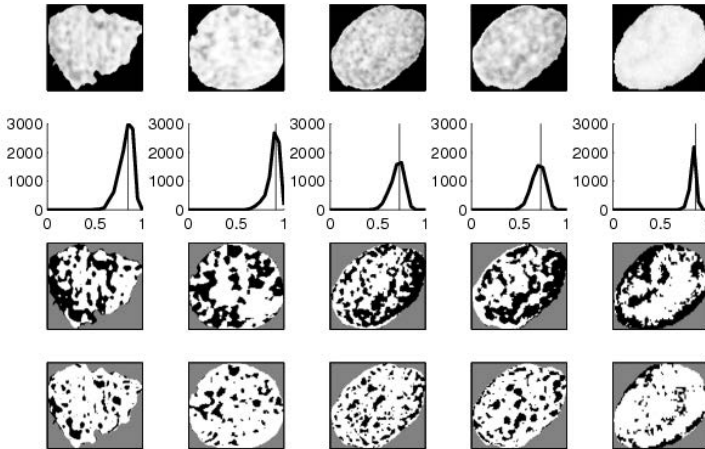
Fig. 3. Examples of atypical cell nuclei (top row, scale not preserved, negative image), histogram (second row, with emphasized mean value), segmentation based on the mean (third row), segmentation based on the windowed threshold (fourth row)

4   Example Results

We use the database of the separate cells nuclei classified as correct and atypical (there are many types of atypical cells nuclei types). There are 91 correct and 59 atypical cells nuclei from single pathomorphology laboratory in our database. Images have been acquired using AxioCamMRc5 color camera, that supports 2584x1936 resolution (about 5M pixels).

Separation of both classes of cell nuclei is not possible using FD only. Very good estimator is the cell nucleus size (area). Atypical cell nuclei have higher area in most cases.

The difference between numbers of pixels for two scales is used instead of the calculation of the FD using regression curve. The results are normalized by the area of cell nucleus (modified mask size):

$$\frac{(N(1) - N(3))}{M^*} \tag{11}$$

The most important is the small group (7 cases) of atypical cells that cannot be distinguished from correct cells nuclei using area only. The separation between small group and correct cell nuclei is desired.
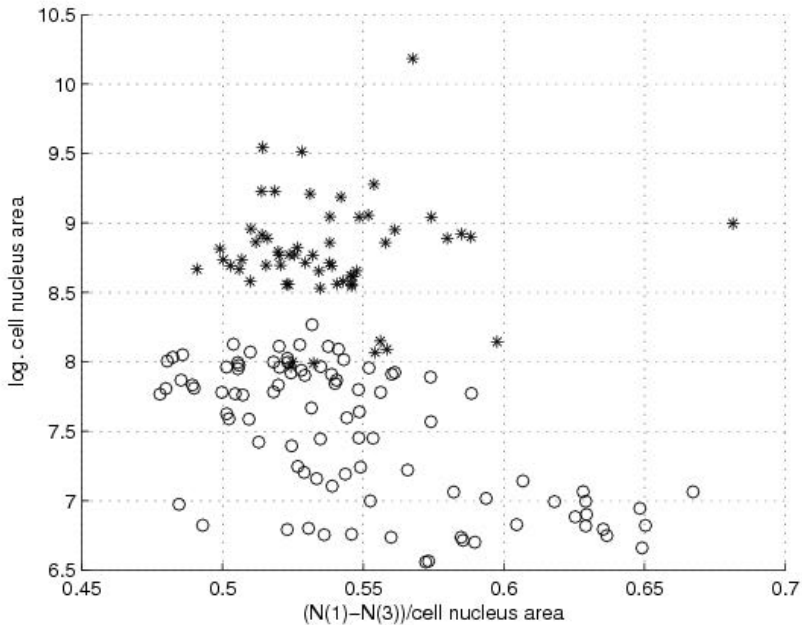
Fig. 4. Separation of correct (circles) and atypical (stars) cell nuclei using single threshold method
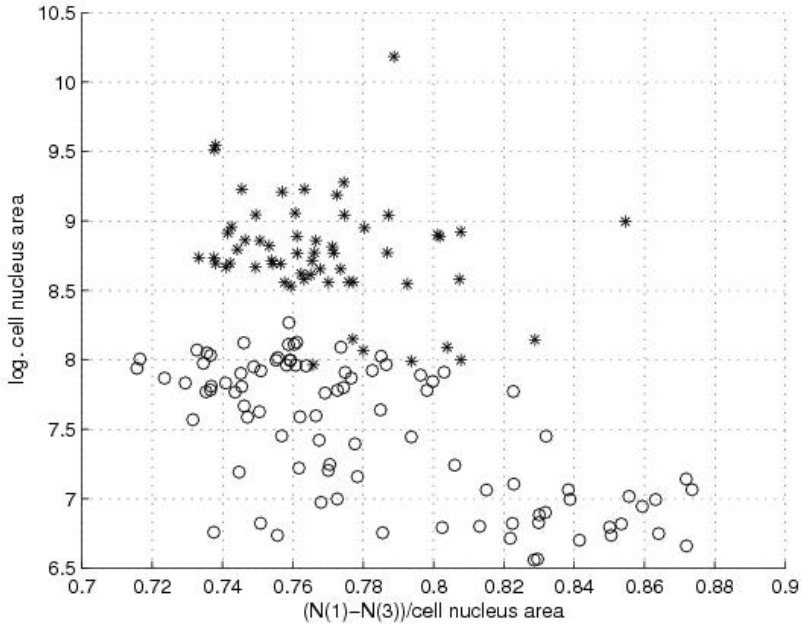
Fig. 5. Separation of correct (circles) and atypical (stars) cell nuclei using windowed threshold method

5 Discussion and Conclusions

The single threshold is sensitive in the selection of value around mean value. The mean value is located near to the maximum of the distribution. The peak of the distribution is related to the large number of pixels, so small changes in the selection of threshold (mean value with fixed additive value) give significant changes in output image.

The application of the two threshold values, located symmetrically around mean value, moves threshold values toward area of distribution with smaller number of pixels. It reduces mentioned effect. The additional motivation is the texture that is characterized for human mostly by the high values changes. The walleyes and peaks of texture are emphasized using windowed threshold.

Adaptive threshold is necessary, because the normalization of such images is problematic. The tails of the distributions are related to the discrete number of pixels and they are random variable. Adaptive thresholding does not use tails of the distributions that are related to the black and white points. This is more robust approach.

The selection of the constant multiplier of the standard deviation is provided using random search, but it is quite simple to find using iterative search. The selection of the value is less sensitive in comparison to the other techniques.

The preclassification is not ideal, what is typical for biological objects, but the number of atypical cells nuclei in area of the correct cells is reduced.

References

1. Mandelbrot, B.B.: The Fractal Geometry of the Nature. W.H. Freeman and Company (1983)
2. Peitgen, H.O., Jürgens, H., Saupe, D.: Fractals for the Classrooms, vol. 1. Springer (1991)
3. Jeleń, L., Fevens, T., Krzyzak, A.: Classification of breast cancer malignancy using cytological images of fine needle aspiration biopsies. International Journal of Applied Mathematics and Computer Science 18(1), 75–83 (2008)
4. Obuchowicz, A., Hrebień, M., Nieczkowski, T., Marciniak, A.: Computational intelligence techniques in image segmentation for cytopathology. In: Smolinski, T.G., Milanova, M.G., Hassanien, A.-E. (eds.) Computational Intelligence in Biomedicine and Bioinformatics. SCI, vol. 151, pp. 169–199. Springer, Heidelberg (2008)
5. Hrebień, M., Stec, P., Nieczkowski, T., Obuchowicz, A.: Segmentation of breast cancer fine needle biopsy cytological images. International Journal of Applied Mathematics and Computer Science 18(2), 159–170 (2008)
6. Filipczuk, P., Wojtak, W., Obuchowicz, A.: Automatic nuclei detection on cytological images using the firefly optimization algorithm. In: Piętka, E., Kawa, J. (eds.) ITIB 2012. LNCS, vol. 7339, pp. 85–92. Springer, Heidelberg (2012)
7. Hrebień, M., Korbicz, J., Obuchowicz, A.: Hough transform (1+1) search strategy and watershed algorithm in segmentation of cytological images. In: Kurzynski, M., et al. (eds.) Computer Recognition Systems 2. ASC, vol. 45, pp. 550–557. Springer, Heidelberg (2007)
8. Forczmański, P.: Comparison of Tensor Unfolding Variants for 2DPCA-Based Color Facial Portraits Recognition. In: Bolc, L., Tadeusiewicz, R., Chmielewski, L.J., Wojciechowski, K. (eds.) ICCVG 2012. LNCS, vol. 7594, pp. 345–353. Springer, Heidelberg (2012)
9. Frejlichowski, D., Forczmański, P.: General Shape Analysis Applied to Stamps Retrieval from Scanned Documents. In: Dicheva, D., Dochev, D. (eds.) AIMSA 2010. LNCS (LNAI), vol. 6304, pp. 251–260. Springer, Heidelberg (2010)
10. Piórkowski, A.: An Algorithm for Objects Straightening in M-Mode Echocardiography Images. In: Choraś, R.S. (ed.) Image Processing and Communications Challenges 4. AISC, vol. 184, pp. 33–38. Springer, Heidelberg (2013)
11. Metze, K.: Fractal dimension of chromatin and cancer prognosis. Epigenomics 2(5), 601–604 (2010)

12. Adam, R.L., Silva, R.C., Pereira, F.G., Leite, N.J., Lorand-Metze, I., Metze, K.: The fractal dimension of nuclear chromatin as a prognostic factor in acute precursor B lymphoblastic leukemia. Cellular Oncology 28, 55–59 (2006)
13. Ferro, D.P., Falconi, M.A., Adam, R.L., Ortega, M.M., Lima, C.P., de Souza, C.A., Lorand-Metze, I., Metze, K.: Fractal characteristics of Grünwald-Giemsa stained chromatin are independent prognostic factors for survival in multiple myeloma. PLoS One 6(6), 1–8 (2011)
14. Bedin, V., Adam, R.L., de Sa, B., Landman, G., Metze, K.: Fractal dimension of chromatin is an independent prognostic factor for survival in melanoma. BMC Cancer 10(260), 1–6 (2010)
15. Clarke, K.C.: Computation of the fractal dimension of topographic surfaces using the triangular prism surface area method. Computer and Geoscience 12(5), 713–722 (1986)
16. Sun, W.: Three new implementations of the triangular prism method for computing the fractal dimension of remote sensing images. Photogrammetric Engineering & Remote Sensing 72(4), 372–382 (2006)
17. Oszutowska-Mazurek, D., Mazurek, P., Sycz, K., Waker-Wójciuk, G.: Estimation of fractal dimension according to optical density of cell nuclei in Papanicolaou smears. In: Piętka, E., Kawa, J. (eds.) ITIB 2012. LNCS, vol. 7339, pp. 456–463. Springer, Heidelberg (2012)
18. Oszutowska, D., Purczyński, J.: Estimation of the fractal dimension using tiled triangular prism method for biological non-rectangular objects. Electrical Review R.88(10b), 261–263 (2012)
19. Atkinson, P.A.: Spatial Statistics. In: Spatial Statistics and Remote Sensing, pp. 57–82. Kluwer Academic Publishers (2002)
20. Kaye, B.H.: A Random Walk Through Fractal Dimensions. VCH (1994)
21. Goodchild, M.F.: Fractals and the accuracy of geographical measures. Mathematical Geology 12, 85–98 (1980)
22. Parker, J.R.: Algorithms for Image Processing and Computer Vision. Wiley (1997)
23. Voss, R.F.: Fractals in nature: From characterization to simulation. In: The Science of Fractal Images, pp. 21–70. Springer (1998)
24. Oszutowska–Mazurek, D., Mazurek, P., Sycz, K., Waker–Wójciuk, G.: Variogram Based Estimator of Fractal Dimension for the Analysis of Cell Nuclei from the Papanicolaou Smears. In: Choraś, R.S. (ed.) Image Processing and Communications Challenges 4. AISC, vol. 184, pp. 47–54. Springer, Heidelberg (2013)

Corneal Endothelial Grid Structure Factor Based on Coefficient of Variation of the Cell Sides Lengths

Jolanta Gronkowska-Serafin[1] and Adam Piórkowski[2]

[1] Departament of Ophthalmology
Pomeranian Medical University, Szczecin, Poland
[2] Department of Geoinfomatics and Applied Computer Science
AGH University of Science and Technology, Cracow, Poland
`pioro@agh.edu.pl`

Summary. Description of the corneal endothelial cell grid is a valuable diagnostic pointer, used in Ophthalmology. Until now, two quality factors were used: hexagonality (H) and the relative standard deviation of the cell surface (CV). Both the factors do not take into account the length measure of the grid cells, which has been presented in an article on the sample images. The authors propose an additional factor, the average relative standard deviation of the cell sides lengths (CVSL), which takes the cells non-uniformity into account.

1 Introduction

Cornea is the anterior translucent layer of the eye. To maintain corneal transparency stable hydratation level is obligatory. Water from the anterior chamber fluid goes into corneal structure with the free diffusion rule and needs to be actively removed. Cell responsible for the water removal are called corneal endothelium and lay on the Descemet membrane. Corneal endothelium is a monolayer of mainly hexagonal cells and in humans and other Primates in contrary to other species it has almost none mitotic activity [1, 2, 3]. Corneal cell number decreases with ageing and disrupting the anterior chamber integrity (i.e. cataract surgery, corneal transplant, filtration surgery) enhance the decrease. When the cell density is below 300-500 cells/mm^2, irreversible corneal edema appears. In the '70 corneal endothelial specular photography performed in vivo gained the clinical meaning, and shortly after three main parameters were described to assess indirectly endothelium function: CD (cell density; number of cells per square mm), H (hexagonality, % of hexagonal cells) and CV (coefficient of cell area variation, i.e. standard deviation/mean cell area, %). Neither H nor CV is corneal regularity cell measure; irregularity occurs after corneal trauma and slowly decreases, that may be a good

prognostic factor for assessing the number of cells and ratio of their density decrease in a long time period. The authors propose a new quality factor that takes into account difference in cells sides length.

2 Shape Factors Used for Describing Corneal Endothelial

In the research using specular microscopy pictures of corneal endothelial cells encounter existing quality measure factors are hexagonality and CV. Index of H determines the percentage share of hexagonal cells among all cells in the image (1).

$$H = \frac{N_6}{N_T} * 100\%$$ (1)

where N_6 is the number of six-side cells, and N_T is the total number of cells in the image.

CV is a factor of relative variance cell sizes. In the following part of the work will be marked as CVofS. Its value can be calculated from the formula (2).

$$CVofS = \frac{\sqrt{\frac{\sum_{i=1}^{N}(c_i^2 - \mu_c)^2}{N}}}{\mu_c}$$ (2)

where c_i is area of i-th cell, μ_c is a mean of size of all cells in the image.

2.1 Average Coefficient of Variation of the Cell Sides Lengths

Looking over a lot of pictures corneal endothelial authors proposed its own factor, which is sensitive to deformation of cells. For each cell is calculated average length of the sides (3),

$$\mu_{SL} = \frac{\sum_{i=1}^{NL} l_i}{N}$$ (3)

where l_i is lenght of i-th side, and NL is the number of sides. Next the Coefficient of Variation of the Cell Sides Lengths is given by the formula (4).

$$CVofSL = \frac{\sqrt{\frac{\sum_{i=1}^{NL}(l_i^2 - \mu_{SL})^2}{NL}}}{\mu_{SL}}$$ (4)

To refer to the entire image, the average value $AvCVofSL$ (shortly: CVSL) of factor $CVofSL$ for all cells is calculated (5).

$$CVSL = \overline{CVofSL} = \frac{\sum_{i=1}^{N} CVofSL_i}{N}$$ (5)

3   The Method of Determining Cells Sides Lengths

The initial question is to determine the length of the sides of the cell. The sides can be approximated by a variety of lines, forming segments of the cell borders of the cells (Fig. 1).
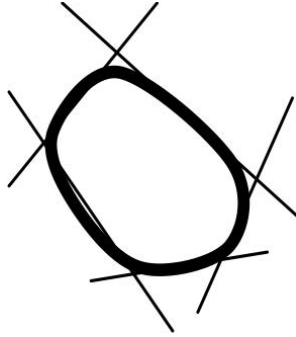
Fig. 1. The approximation of cell sides by lines

Unfortunately, there are many possibilities of lines' placement. Leaving the user to their choice, objective measurement is lost.

Triple points use allows for some simplification [4, 5] resulting in segmentation and determining them as endpoints of sections approximating cells' sides (Fig. 2).
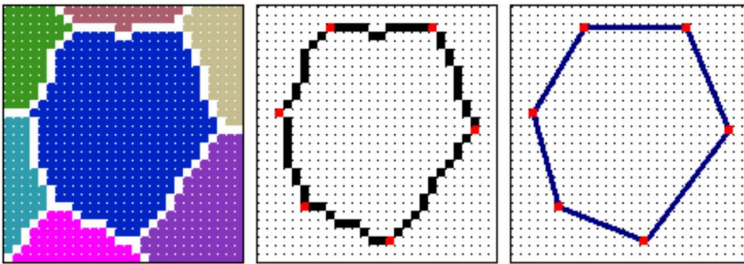
Fig. 2. A sample of cell segmentation, the border, triple points and approximation by sections

The segmented image of cells grid contains triple points adjacent to a selected cell. Assuming that the figure is convex, the designation of the order of points making up the subsequent sides is done by sorting the points according to the angle formed by the horizontal axis running through the center section of cells and cells from the center point to the triple point (Fig. 3).
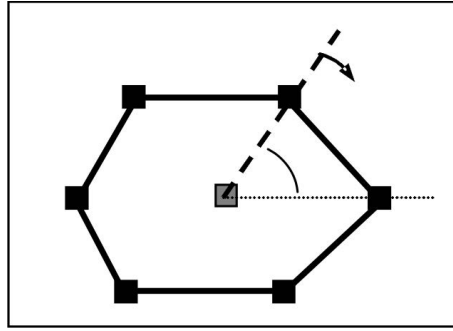
Fig. 3. A method of selecting subsequent triple points

4   Assessment of CVSL Factor Application for Synthetic Models

To justify the need for further pre-research on the use of factor, there are pointed the synthetic examples, which show the model situations. The example (Fig. 4) contains two mesh cells. The first one (A) contains a uniform square cells with sides of lengths a, the second (B) - homogeneous rectangular, with sides of lengths a and $2a$.
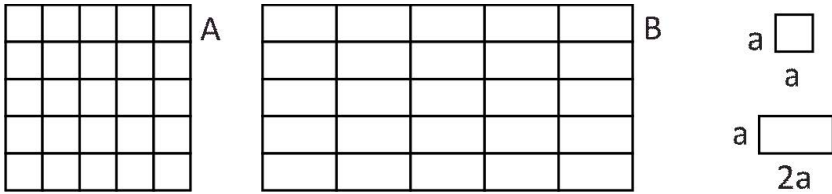
Fig. 4. A sample mesh with square and rectangular cells

Hexagonality for both grids (A and B) is 0%.

$$H(A) = 0 \tag{6}$$

$$H(B) = 0 \tag{7}$$

Calculating $CVofS$ for these cases (CVofS(A) i CVofS(B)):

$$\mu_S(A) = a^2 \tag{8}$$

$$CVofS(A) = \frac{\sqrt{\frac{25*(a^2-\mu_S)^2}{25}}}{\mu_S} = \frac{\sqrt{\frac{25*(a^2-a^2)^2}{25}}}{\mu_S} = 0 \tag{9}$$

$$\mu_S(B) = 2a^2 \tag{10}$$

$$CVofS(B) = \frac{\sqrt{\frac{25*(2a^2-\mu_S)^2}{25}}}{\mu_S} = \frac{\sqrt{\frac{25*(2a^2-2a^2)^2}{25}}}{\mu_S} = 0 \tag{11}$$

Calculating the $CVSL$ factor for these cases (A and B) we get the following values of $CVofSL(A)$ i $CVofSL(B)$:

$$\mu_{SL}(A) = \frac{a+a+a+a}{4} = a \tag{12}$$

$$CVofSL(A) = \frac{\sqrt{\frac{(a-\mu_{SL})^2+(a-\mu_{SL})^2+(a-\mu_{SL})^2+(a-\mu_{SL})^2}{4}}}{\mu_{SL}} = \frac{\sqrt{\frac{4*(a-a)^2}{4}}}{\mu_{SL}} = 0 \tag{13}$$

$$CVSL(A) = \overline{CVofSL} = \frac{25*0}{25} = 0 \tag{14}$$

$$\mu_{SL}(B) = \frac{2a+a+2a+a}{4} = 1.5a \tag{15}$$

$$CVofSL(B) = \frac{\sqrt{\frac{(2a-\mu_{SL})^2+(a-\mu_{SL})^2+(2a-\mu_{SL})^2+(a-\mu_{SL})^2}{4}}}{\mu_{SL}} =$$
$$\frac{\sqrt{\frac{(2a-1.5a)^2+(a-1.5a)^2+(2a-1.5a)^2+(a-1.5a)^2}{4}}}{1.5a} =$$
$$\frac{\sqrt{\frac{4*(0.5a)^2}{4}}}{1.5a} = \frac{0.5}{1.5} = \frac{1}{3} \approx 0.33 \tag{16}$$

$$CVSL(B) = \overline{CVofSL} = \frac{25*1}{25*3} = \frac{1}{3} \approx 0.33 \tag{17}$$

All values of factors are collected in Tab. 1. The data indicate that the provided factors H and $CVofS$ do not change, but the proposed factor $CVSL$ varies significantly. Similar behavior applies to other models of networks. The Fig. 5 shows hexagonal grid (C) and the second, stretched in the horizontal axis (D).

This image, as a bitmap, was processed in the test application, performing operations according to the methods described in this article. The results are presented in Table 2. As in the previous case, the value of H and $CVofS$ not

Table 1. Values of the factors for the first example of mesh

Picture	Hex	CVofS	CVSL
A	0	0	0
B	0	0	0.33
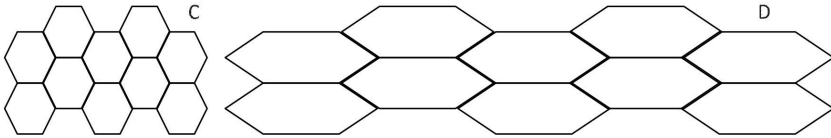
Fig. 5. A sample mesh with hexagonal cells

Table 2. Values of the factors for the second example of mesh

Picture	Hex	CVofS	CVSL
C	100	0.011	0.0112
D	100	0.013	0.3560

have changed or have changed insignificantly, while the value of the proposed pointer $CVSL$ has changed significantly. Thus, the Authors can conclude that if $CVofS$ rate is not sensitive to even stretch the cells, a factor of $CVSL$ is able to demonstrate it. It is therefore important for further research into the use of this factor in scientific research.

5 Conclusion

This paper presents proposals for a new pointer based on coefficient of variation of the cell sides lengths ($CVSL$). In tests based on synthetic examples sensitivity of the proposed factor was pointed, while the standard factors used showed no significant difference. Further research on the use of the proposed pointer should be on data from actual examinations. The next work involves also the research on the shape of cells [6, 7, 8] and the application of factors in diagnostics. Possibilities of cells shape recognition by using the methods described in [9, 10, 11] are studied and are planned to be the topic of the next papers. It should also be mentioned that the problem of medical pictures preprocessing is crucial in automatic medical image analysis [12] and will be also studied in the context of microscopy pictures of corneal endothelial cells.

References

1. Szostek, K., Gronkowska-Serafin, J., Piorkowski, A.: Problems of corneal endothelial image binarization. Schedae Informaticae 20, 211–218 (2011)
2. Piorkowski, A., Gronkowska-Serafin, J.: Selected issues of corneal endothelial image segmentation. Journal of Medical Informatics and Technologies 17, 239–245 (2011)
3. Piorkowski, A., Gronkowska-Serafin, J.: Analysis of corneal endothelial image using classic image processing methods. The computer-aided scientific research. XVIII, The Works of Wroclaw Scientific Society (217), 283–290 (2011)
4. Marques, F.: Multiresolution Image Segmentation Based on Compound Random Fields: Application to Image Coding. THD Dpto. TSC-UPC (1992)
5. Apprato, D., Gout, C., Vieira-Teste, S.: In: Proceedings of IEEE International Conference Geoscience and Remote Sensing Symposium (2000)
6. Ogiela, M.R., Tadeusiewicz, R.: Artificial intelligence methods in shape feature analysis of selected organs in medical images. International Journal: Image Processing and Communications 6(1-2), 3–11 (2000)
7. Oszutowska–Mazurek, D., Mazurek, P., Sycz, K., Waker–Wójciuk, G.: Variogram Based Estimator of Fractal Dimension for the Analysis of Cell Nuclei from the Papanicolaou Smears. In: Choraś, R.S. (ed.) Image Processing and Communications Challenges 4. AISC, vol. 184, pp. 47–54. Springer, Heidelberg (2013)
8. Oszutowska-Mazurek, D., Mazurek, P., Sycz, K., Waker-Wójciuk, G.: Estimation of Fractal Dimension According to Optical Density of Cell Nuclei in Papanicolaou Smears. In: Piętka, E., Kawa, J. (eds.) ITIB 2012. LNCS, vol. 7339, pp. 456–463. Springer, Heidelberg (2012)
9. Bielecka, M., Bielecki, A., Korkosz, M., Skomorowski, M., Wojciechowski, W., Zieliński, B.: Application of shape description methodology to hand radiographs interpretation. In: Bolc, L., Tadeusiewicz, R., Chmielewski, L.J., Wojciechowski, K. (eds.) ICCVG 2010, Part I. LNCS, vol. 6374, pp. 11–18. Springer, Heidelberg (2010)
10. Bielecka, M., Bielecki, A., Korkosz, M., Skomorowski, M., Wojciechowski, W., Zieliński, B.: Modified jakubowski shape transducer for detecting osteophytes and erosions in finger joints. In: Dobnikar, A., Lotrič, U., Šter, B. (eds.) ICANNGA 2011, Part II. LNCS, vol. 6594, pp. 147–155. Springer, Heidelberg (2011)
11. Bielecka, M., Skomorowski, M., Zieliński, B.: A fuzzy shape descriptor and inference by fuzzy relaxation with application to description of bones contours at hand radiographs. In: Kolehmainen, M., Toivanen, P., Beliczynski, B. (eds.) ICANNGA 2009. LNCS, vol. 5495, pp. 469–478. Springer, Heidelberg (2009)
12. Korkosz, M., Bielecka, M., Bielecki, A., Skomorowski, M., Wojciechowski, W., Wójtowicz, T.: Improved fuzzy entropy algorithm for X-ray pictures preprocessing. In: Rutkowski, L., Korytkowski, M., Scherer, R., Tadeusiewicz, R., Zadeh, L.A., Zurada, J.M. (eds.) ICAISC 2012, Part II. LNCS, vol. 7268, pp. 268–275. Springer, Heidelberg (2012)

A Distributed Approach for Development of Deformable Model-Based Segmentation Methods

Daniel Reska, Cezary Boldak, and Marek Kretowski

Faculty of Computer Science
Bialystok University of Technology, Bialystok, Poland
`{d.reska,c.boldak,m.kretowski}@pb.edu.pl`

Summary. This paper presents a distributed solution for the development of deformable model-based medical image segmentation methods. The design and implementation stages of the segmentation methods usually require a lot of time and resources, since the variations of the tested algorithms have to be constantly evaluated on many different data sets. To address this problem, we extended our web platform for development of deformable model-based methods with an ability to distribute the computational workload. The solution was implemented on a computing cluster of multi-core nodes with the use of the Java Parallel Processing Framework. The experimental results show significant speedup of the computations, especially in the case of resource-demanding three-dimensional methods.

1 Introduction

Medical imaging methods provide a non-invasive insight into the human body and are an invaluable source of information in clinical and research practice. The constant progress of the imaging techniques calls for the development of more accurate and efficient image analysis algorithms. One of the most important task is segmentation, i.e. partitioning of the image into distinct regions in order to extract, for example, specific tissues, pathological changes or entire organs.

The usefulness of the segmentation methods is determined by their ability to provide fast, accurate and reproducible results, while dealing with the increasing size of the analyzed data. Image sets obtained with magnetic resonance imaging (MRI) or computed tomography (CT) can contain hundreds of hi-resolution images, which poses a performance challenge to the image processing and analysis algorithms. The time and resource-consuming computations are especially evident in the development stage of the segmentation methods, since the designed algorithms have to be fully tested on different

data sets and parameter values. Such a computational overhead urges for the use of parallelization tools that will utilize the power of the modern computers. The ubiquity of powerful, multi-core desktop machines encourages the usage of commodity hardware for the parallelization and distribution of the computations.

In this paper we present a distributed platform for development of the deformable model-based methods - a group of algorithms suitable for medical image segmentation [1], which use a deforming shape to match and extract an interesting object from the image. We used our extensible Java-based segmentation platform [2], originally build in a client-server architecture, and employed the Java Parallel Processing Framework (JPPF) [3] to distribute of computations over a cluster of commodity machines. The distribution scheme also makes use of parallelization within one process with the help of Java 7 Fork/Join Framework [4]. This solution aims for the simplicity of the computational model, reusability of the existing code and low deployment and maintenance cost. The framework was tested on different data sets and segmentation methods of various complexity and showed a significant performance speedup.

The paper is organized as follows. Section 2 outlines the deformable models background and the work in distributed image analysis. Section 3 presents our web platform for the development of segmentation methods. Section 4 describes the distribution method integrated in the platform. Experimental results are presented in Section 5. Conclusions and plans for future research are sketched in the last section.

2   Background and Related Work

Deformable models are a class of segmentation methods based on a deforming shape that tries to adapt to a specific image region. The shape is usually represented as a 2D contour or a 3D surface and undergoes a deformation process under the influences of external and internal forces. The external forces attract the shape to the segmented image features, while the internal forces control its smoothness and continuity. The classical forms of the deformable models, like the influential 2D "snake" algorithm [5] and a 3D active surface [6], were modified and extended, e.g., with adaptive topology mechanisms [7] or robust expansion forces [8]. The distinctive features of deformable models, like their continuous nature and noise insensitivity, make them well suited for medical image segmentation [1].

Recently, many tools for distributed computing have been used in general and medical image analysis. Apache Hadoop [9], an open-source implementation of MapReduce paradigm, was successfully used for the task of image processing, proving to be particularly effective in analysis of large volumes of data [10]. Notably, a distributed active contour [11] was implemented using the Globus Toolkit [12] - a powerful tool for building grid systems. JPPF [3]
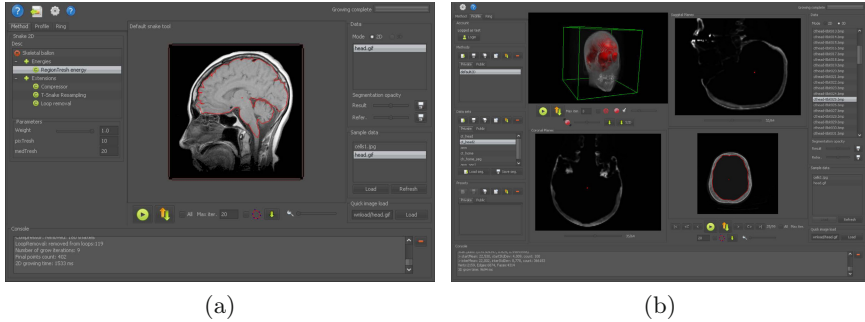
Fig. 1. Client interface of the segmentation application in 2D contour (a) and 3D surface mode (b)

is an another distributed computing framework, written in the Java language, that exhibited usefulness in medical image analysis [13].

3 Web-Based Segmentation Framework

We have developed a web-based platform [2] for the task of design and evaluation of deformable model-based biomedical image segmentation methods. The system is built in a server-client architecture, offering client applications in a form of Java applets, while the computations and data storage are performed on the server. The clients are provided with a set of tools for development, evaluation and visualization (2D planar reconstruction and 3D volume rendering) of the methods, a remote image data repository (with planned DICOM support) and a system of user profiles. The segmentation framework is based on an extensible template system for constructing two and three-dimensional methods. Each segmentation method can be composed from a set of existing components, like deformation models, internal and external energies, constraints or custom extensions. The users can also create their own components with a build-in scripting language and store them in the profile system. This decomposition scheme enforced the creation of a unified method interface for computation, visualization and comparison of the results. Currently, the platform support the 2D active contour, working on a set of images, and a 3D active surface, working on a volumetric data set (see Fig. 1).

The deformable models computations are performed in a request-response manner. The client request contains a user-defined script with the method definition and its parameters, an address of the segmented data (stored in the repository) and, optionally, a location of a reference segmentation, essential for the evaluation of the results. Furthermore, the client can submit a batch job of many requests with the same image data, but different method

parameters. This case is a typical development scenario for finding the optimal set of parameter values and is the most time and resource consuming. After the computation, a response with the segmentation and evaluation results is returned to the client.

4 Distributed Solution

Our segmentation system was extended with the ability to parallelize the computational workload using a JPPF cluster of desktop machines. The service-oriented architecture of our framework allowed the distribution of the existing computing requests, making this process opaque from the client perspective. To fully utilize the hardware potential, the task are not only divided into many processes and distributed among the cluster worker nodes, but also parallelized on the single node level.

4.1 Task Distribution

The distribution of the requests among different machines was achieved with the JPPF Framework. The framework turned out to be a powerful tool with a very low integration cost.

The system structure was extended by the addition of the JPPF cluster (see Fig. 2). Previously, the system consisted of an Axis2/Java [14] web service server that was performing the computations, a data repository and an LDAP server for user authentication and profile storage. The cluster is composed of a single master server (called the Driver) and a set of worker desktop machines (nodes), contained in a private network. After the integration, the Axis2 server is only a facade for the computational requests, hiding the cluster from the public access. Requests passed to the Driver are distributed and performed independently on the nodes. After the computations, the results are send to the Driver, gathered and returned to the Axis2 server, that transmits them to the client using the original protocol.

Each node is directly connected to the data repository and loads the images required by the executed request. To avoid the unnecessary overhead of reloading of the recurring data, the nodes are equipped with an in-memory cache for the recent images. The cache is implemented with the Google Guava library [15], that provides lightweight and thread-safe caching utilities.

One of the most useful features of JPPF is the dynamical deployment of the services: the framework automatically copies and distributes the client code among the cluster nodes. This process relieves the developer from the maintenance overhead and provides a way for rapid prototyping on the distributed level, which is especially beneficial during the development stage. However, the auto-deployment can open a possibility of abuse, therefore, in our system, the cluster is hidden behind the Axis2 web service facade.
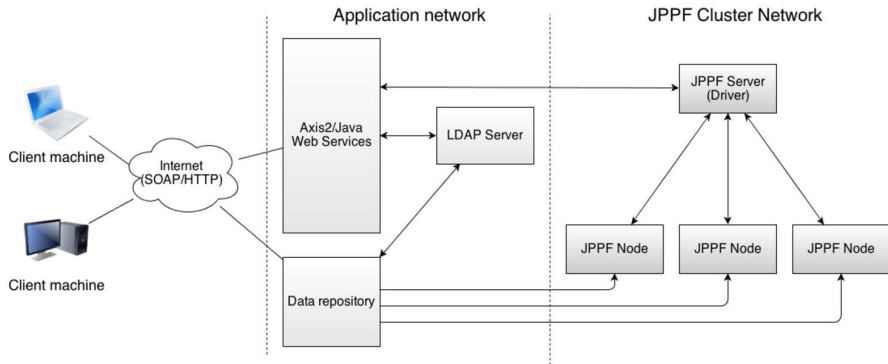
Fig. 2. Diagram of the application network system

The programming model of the framework is also very simple and encourages the reusability of the existing code. There is no need for adaptation of a specific programming model (like MapReduce in Apache Hadoop) and no labor-intensive creation and configuration process (like in Globus Toolkit).

4.2 Single Task Parallelization

Apart from the distribution of the workload among different machines, much of the computations could be also parallelized within the single node process. This hybrid approach was used to fully utilize the power of multi-core worker machines and reduce the communication overhead.

The implemented algorithms make an extensive use of Java Fork/Join Framework [4], introduced in Java SE 7. The framework helps to recursively divide the work among many threads and uses a work-stealing algorithm to uniformly distribute the computations. This approach was used in two cases: to parallelize the execution of multi-image 2D request and to speed up the 3D active surface. In the first case, multiple active contours are uniformly split over the cores of a single node and executed in parallel. The active surface evolution time benefited from the parallelization of the polygon mesh voxelization algorithm [16]. This method is used to find the internal region of the surface, necessary for the calculation of its statistics [17] and during the generation of the segmentation results.

5 Experimental Evaluation

The distributed system was evaluated on a cluster of 16 worker machines. The experiments were performed with deformable model methods of various computational complexity and data demand.

(a)   (b)
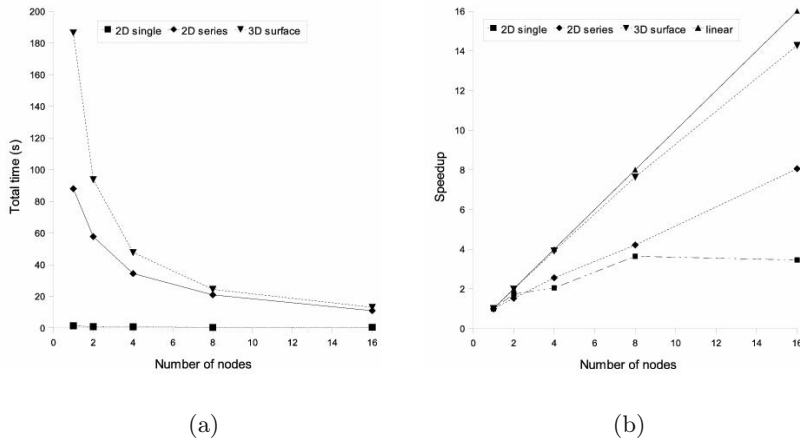
Fig. 3. Results of the experiments: total processing time (a) and speedup (b)

The cluster consisted of 16 desktop computers with Intel Xeon CPU E31270 4 core processors and 8 GB of RAM, each running a single instance of JPPF node on Linux 2.6 and connected by Gigabit Ethernet network. The JPPF Driver was deployed on a rack server with 6 core Intel Xeon E5645 CPU with 16 GB RAM. The Axis2 server configuration was similar to the Driver. The cluster was built using the 3.2 version of JPPF.

The system performance was tested on a 3 real-life segmentations tasks. Each task used a single deformable method, but was divided into a number of request with different sets of method parameters. The experiments consisted of:

- **2D single**: a brain segmentation on a single 512x512 MRI image with the adaptive 2D active contour [18] (20 sets of parameters);
- **2D series**: a segmentation of human cranium on a set of 90 256x256 CT images with the mentioned 2D active contour (16 sets of parameters);
- **3D surface**: a segmentation of human cranium with 3D deformable surface [17] (100 256x256 CT images, 16 sets of parameters).

Figure 3a presents the total calculation time of the tasks and the speedup is shown in Fig. 3b. Sample results of the segmentations are presented in Fig. 4.

The performance gain is clearly visible for the last two cases (2D series and 3D surface), while the speedup benefit of the first case is less impressive. The 2D single contour was not computationally intensive enough to overcome the framework overhead (i.e. network communication, data retrieval) and even demonstrated a slight decrease of the speedup between 8 and 16 cluster nodes. The two other, more demanding tasks showed a significantly better scalability, where the 3D surface speedup was the closest to the ideal linear reference.
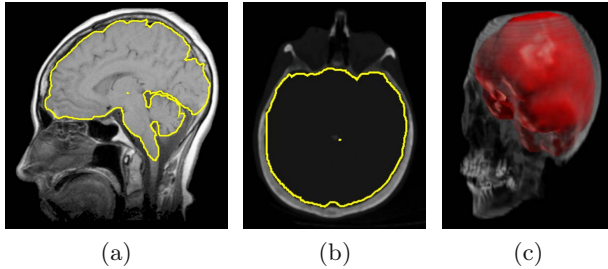
Fig. 4. Sample results from the experiments: brain segmentation with a 2D active contour (a), segmentation of the cranium with a 2D snake (b) and with a 3D active surface (c)

The 2D series case achieved a steady performance gain, but the overall speedup was less impressive. All the requests of the 3D surface exhibited a roughly constant time, while the execution time of the 2D active contour was more dependent on the value of the parameters. This time variation leads to the decrease of the scalability, because the optimal distribution of the tasks would require an advance-knowledge of the tasks execution time, or an employment of a more advanced, work-stealing load balancing algorithm.

It should be noted that the single node performance is dependent on the retrieval of the image data from the repository. Fortunately, the usage of the cache mechanism makes the data loading overhead present only during the execution of the first request from the group.

6 Conclusion

In this paper a distributed framework for deformable model-based medical image segmentation is presented. The solution makes use of a workload distribution on a JPPF cluster and shared-memory parallelization with the Java Fork/Join framework. This approach was seamlessly integrated in the existing, centralized client-server architecture of our segmentation framework and demonstrated a significant performance improvement during the experimental validation.

The presented solution is still in its development stage. Before the eventual integration with the production version of the segmentation platform, we will investigate the usage of custom load-balancing algorithms, incorporation of heterogeneous cluster hardware and utilization of general-purpose computing on graphics processing units.

References

1. Tsechpenakis, G.: Deformable model-based medical image segmentation. In: Multi Modality State-of-the-Art Medical Image Segmentation and Registration Methodologies, vol. 1. Springer Publishing (2011)
2. MESA - a web platform for deformable model-based segmentation method development, `http://mesa.wi.pb.edu.pl`
3. JPPF – an open-source, Java-based, framework for parallel computing, `http://www.jppf.org`
4. Lea, D.: A Java fork/join framework. In: Proceedings of the ACM 2000 Conference on Java Grande JAVA 2000, pp. 36–43 (2000)
5. Kass, M., Witkin, A., Terzopoulos, D.: Snakes: Active contour models. International Journal of Computer Vision 1(4), 321–331 (1988)
6. Miller, J., Breen, D., Lorensen, W., O'Bara, R., Wozny, M.: Geometrically deformed models: a method for extracting closed geometric models form volume data. SIGGRAPH Comput. Graph. 25(4), 217–226 (1991)
7. McInerney, T., Terzopoulos, D.: Topology adaptive deformable surfaces for medical image volume segmentation. IEEE Transactions on Medical Imaging 18(10), 840–850 (1999)
8. Xu, C., Prince, J.: Snakes, shapes, and gradient vector flow. IEEE Transactions on Image Processing 7(3), 359–369 (1998)
9. Apache Hadoop, `http://hadoop.apache.org`
10. Huang, F., Zhao, H., et al.: Watermarking Massive Remote Sensor Images in Parallel. In: International Conference on Computational Intelligence and Software Engineering, CiSE 2010, pp. 26–29 (2010)
11. Cannataro, M., Guzzi, P.H., Lobosco, M., Dos Santos, R.W.: GridSnake: A Grid-based implementation of the Snake segmentation algorithm. In: 2009 22nd IEEE International Symposium on Computer Based Medical Systems, pp. 2–7 (2009)
12. Globus Toolkit, `http://www.globus.org/toolkit`
13. Zerbe, N., Hufnagl, P., Schlüns, K.: Distributed computing in image analysis using open source frameworks and application to image sharpness assessment of histological whole slide images. Diagnostic Pathology 6(Suppl. 1), S16 (2011)
14. Apache Axis2 - Apache Axis2/Java - Next Generation Web Services, `http://axis.apache.org/axis2/java/core`
15. Guava: Google Core Libraries for Java 1.6+, `http://code.google.com/p/guava-libraries`
16. Thon, S., Gesquière, G., Raffin, R.: A Low Cost Antialiased Space Filled Voxelization of Polygonal Objects. In: GraphiCon 2004, pp. 71–78 (2004)
17. Reska, D., Boldak, C., Kretowski, M.: Fast 3D segmentation of hepatic images combining region and boundary criteria. Image Processing & Communications 17(4), 31–38 (2012)
18. Reska, D., Kretowski, M.: HIST - an application for segmentation of hepatic images. Zeszyty Naukowe Politechniki Bialostockiej. Informatyka 17(8), 71–93 (2011)

Enhancement of Low-Dose CT Brain Scans Using Graph-Based Anisotropic Interpolation

Tomasz Węgliński and Anna Fabijańska

Institute of Applied Computer Science, Lodz University of Technology
18/22 Stefanowskiego Str., Lodz, Poland
{tweglinski,an_fab}@kis.p.lodz.pl

Summary. This paper considers the problem of enhancement of low-dose CT images. These images are usually distorted by the artifact similar to 'film grain', which affects image quality and hinders image segmentation. The method introduced in this paper reduces influence of the distortion by retrieval of pixel intensities under the 'grains' using graph-based anisotropic interpolation. Results of applying the introduced method to low-dose CT scans of hydrocephalic brains are presented and discussed. The influence of the introduced method on the accuracy of image segmentation is analysed.

1 Introduction

Medical imaging procedures plays important role in modern radiologic diagnosis. Recently, one of the most preferred radiological studies is computed tomography (CT). It's application is increasing over the last years. CT produces volumetric scans of specific regions of the human body in a brief time, what is a significant advantage over other existing imaging procedures (e.g. MRI or PET)[1]. However, computed tomography requires the highest radiation doses over other procedures. Additionally, the collective dose is still rising due to wide availability and increasing resolution of multislice CT scanners. As a result, the radioactive exposure that some patients are receiving is recently so high, that causes definitive risks to health. One of the steps to minimize this risk is using low-dose protocols for CT imaging. In particular, more and more often ALARA principle (i.e. *As Low As Reasonably Achievable*) is applied.

Low-dose CT imaging is now becoming a standard in diagnosis in children which often undergo multiple follow-up scanning at short time intervals. Therefore, in order to minimize the potential risk of malignancies later in life, low-dose protocols for head CT are being developed [2, 3, 4]. They aim at

bringing down the radiation dose to the lowest level, which would provide effective diagnostic information.

Although clinicians find low-dose head CT images diagnostically acceptable, the dose reduction significantly deteriorates image quality. This in turn affects the performance of known algorithms for an automatic and a semiautomatic assessment brain diseases. These algorithms are mainly dedicated to high quality standard-dose CT scans and fail when applied to noisy and low contrast low-dose datasets.

Having in mind the abovementioned, this paper proposes the algorithm, dedicated to enhancement of low-dose CT images of hydrocephalic brains in children. The introduced method compensates intensity distribution within intracranial region using graph-based intensity interpolation.

2   Problem Definition

In automatic assessment of brain diseases the main step is lesion segmentation from the CT dataset. It separates information connected with the lesion from the entire information contained within CT scan. Binary image after segmentation is next used to determine important parameters of the lesion (e.g. dimensions, area or volume)[5, 6]. Therefore the accuracy of image segmentation is crucial for the precise diagnosis.

Extraction of the diseased region can be effectively performed in the case of normal-dose CT scans. These are usually high contrast images where the lesion can be easily distinguished. However, in the case of low-dose CT images, the segmentation algorithms fail, due to high level of noise and film grain artifacts. This effect is presented in Fig. 1, which shows the result of cerebrospinal fluid segmentation from low-dose (Fig. 1a) and normal-dose (see Fig. 1b) CT scans of a hydrocephalic brain.
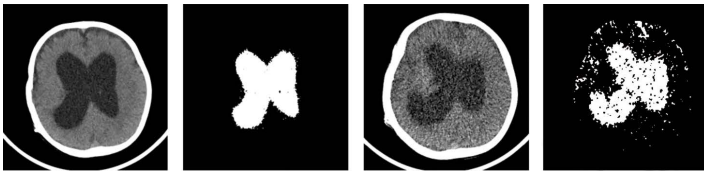
Fig. 1. Exemplary CT slices of hydrocephalic brain and the corresponding image segmentation results; normal-dose CT (on left) and low-dose CT (on right)

To ensure a uniform processing of normal and low-dose CT scans, it is desirable to develop the specialized image enhancement algorithms dedicated to preprocessing of low-dose CT brain scans. Image preprocessing algorithm introduced in this paper is a step forward into solving this problem.

3 Graph-Based Image Intensity Interpolation

The introduced image enhancement algorithm retrieves intensities of pixels distorted by low-dose artifact using graph interpolation approach proposed in [7]. The method uses graph based image representation (where nodes represent pixels and edge weights describe relations between pixels) and then interpolates the missing nodal values (i.e. interior nodes) using known intensities from undistorted boundary nodes.

Having the pixel adjacency graph $G = (V, E)$ with vertices $v \in V$ and edges $e \in E \subseteq V \times V$ with cardinalities $n = |V|$ and $m = |E|$, the problem of graph interpolation is equivalent with finding combinatorial harmonic function u which minimizes Dirichlet integral given as follows:

$$D[u] = \frac{1}{2} u^T L u \tag{1}$$

where L is $n \times n$ Laplacian matrix indexed by vertices v_i and v_j in accordance with Equation 2, $d_{v_i} = \sum w_{ij}$ stands for degree of node and $w_{ij} > 0$ is weight assigned to edge e_{ij} connecting nodes v_j and v_j.

$$L_{v_i v_j} = \begin{cases} d_{v_i} & \text{if } i = j \\ -w_{ij} & \text{if } v_i \text{ and } v_j \text{ are adjacent} \\ 0 & \text{otherwise} \end{cases} \tag{2}$$

Assuming, that nodes in L are ordered, such that the boundary (known) nodes are first and the interior (unknown) nodes are the second, Equation 1 may be rewritten into:

$$D[u_i] = \frac{1}{2} [u_b^T u_i^T] \begin{bmatrix} L_b & R \\ R & L_i \end{bmatrix} \begin{bmatrix} u_b \\ u_i \end{bmatrix} \tag{3}$$

where u_b and u_i corresponds to the intensities (potentials) of the boundary and interior nodes respectively. After differentiating $D[u_i]$ with respect to u_i yelds the following system of linear equations with $|u_i|$ unknows:

$$L_i u_i = -R^T u_b \tag{4}$$

The solution contaned in u_i are the interpolated values of pixel intensities.

According to results in [7] the highest resemblance between the original and the restored pixel intensities is ensured when anisotropic interpolation is performed. It is when the image information is encoded into edge weights w_{ij}. Therefore in the introduced approach we employed a Gaussian weighting function given by the following equation:

$$w_{ij} = \exp(-\beta |I_i - I_j|) \tag{5}$$

where I_i is image intensity of pixel represented by node v_i and β is parameter that controls the severity of anisotropy induced by image intensity.

4 The Proposed Approach

The main idea behind the introduced method is to retrieve intensity information in regions distorted by low-dose artifact using graph based intensity interpolation. Intensity retrieval is performed iteratively where each iteration detects faulty regions and interpolates image information within them.

Detection of faulty regions incorporates two steps. Firstly, the traditional Otsu thresholding is applied [8]. It produces binary image which exhibits pixels of intensities significantly different than their neighbors. These may be regarded as the boundary objects (parents) and their children (single objects completely enclosed by the parents) as explained in Figure 2. Child objects indicate regions to be corrected based on intensities of parent objects. In the second step, the algorithm traces all the child objects (which are easy to find as they are isolated regions seen on the contrasting background) and labels them as *interior pixels*.
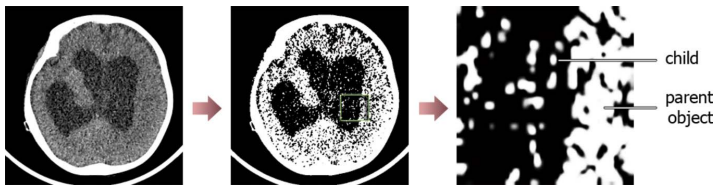
Fig. 2. The outer objects (parents) and their children in exemplary image after thresholding

The search of *interior pixels* considers both: *white* child objects surrounded by *black* parents as well as *black* child objects surrounded by *white* parents. In the case of CT scans of hydrocephalic brains, the first ones correspond to distortions found within region of cerebrospinal fluid, while the last ones are distortions appearing in the surrounding brain tissue. Child objects found within both these regions in two consecutive iterations are shown in red color in Figure 3.

In the next step interpolation is performed. It finds values of the *interior pixels* that interpolate between the intensities of the neighboring *boundary pixels*. In particular weighted undirected graph $G(V, E)$ is built for an input
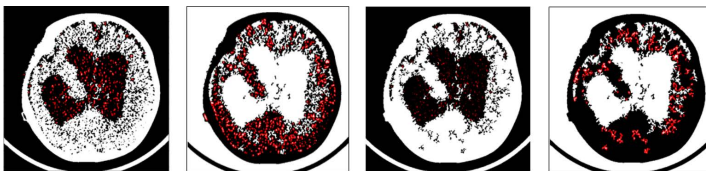
Fig. 3. Child objects found within intracranial region in two consecutive iterations

(grayscale) image as described in Section 3. Weights are assigned to edges in accordance with Equation 5. Nodes which intensities are interpolated correspond with pixels located within child regions. The output (retrieved) image is then used for the next iteration. The pseudocode of the method is sketched in Algorithm 1.

Input: *img*, *iter*
Output: *img*
1: $sw := 1$
2: **while** $iter > 0$ **do**
3:     **threshold** image *img* to find *interior pixels*
4:     **build graph** $G\{V, E\}$ where weights incorporate intensity information
5:     **interpolate** *interior pixels* on $G\{V, E\}$ with Dirichlet function
6:     **replace** *img* with the output of interpolation
7:     $iter := iter - 1$
8:     $sw := -1 * sw$
9: **end while**

Algorithm 1. The proposed image enhancement algorithm; *img* - input image, *iter* - number of iterations

The number of iterations is set manually. The optimal number of iterations depends on the quality and degree of image degradation. However for low-dose CT images used in the described research, the number of iterations varied between 2 and 4.

5 Results and Discussion

Visual results of applying the introduced approach to exemplary low-dose CT images are presented in Figure 4. In particular, top panel presents the original image, while the corresponding results of image enhancement using the introduced approach are shown in the bottom panel.

Results presented in Figure 4 clearly show that the introduced approach diminishes level of 'grain' distortions within the image. Distribution of image intensity within the intracranial brain region was visibly equalized while the edge information was preserved.

Due to lack of the original (undistorted) CT images, it was impossible to assess the accuracy of image reconstruction using the traditional image quality measures (PSNR, SSIM Index, etc.). Therefore, the accuracy of the introduced approach was determined based on the results of image segmentation. In particular results of segmentation of cerberospinal fluid (CSF) performed on the original and the retrieved image were compared with results of manual segmentation performed by the specialist. The assessment was
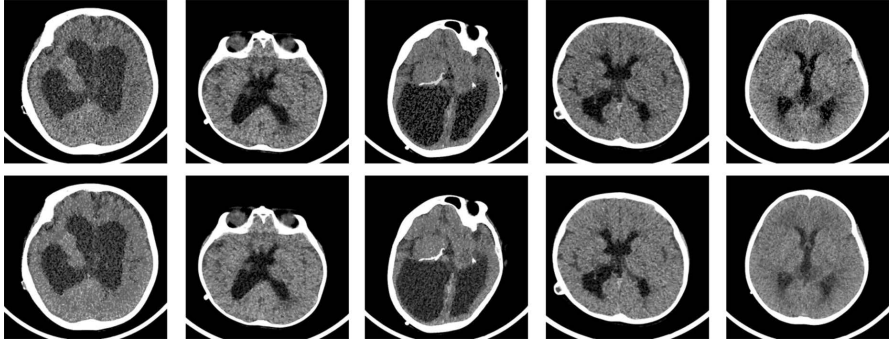
Fig. 4. Results of image enhancement using the introduced method; top panel - original low-dose CT images; bottom panel - images after enhancement

performed by means of precision P, recall R, accuracy A and F-Score FS given by Equations 6-9 respectively.

$$P = \frac{tp}{tp + fp} \tag{6}$$

$$R = \frac{tp}{tp + fn} \tag{7}$$

$$A = \frac{tp + tn}{tp + tn + fp + fn} \tag{8}$$

$$FS = \frac{PR}{P + R} \tag{9}$$

where tp is a number of true positives, tn is a number of true negatives, fp is a number of false positives and fn is a number of false negatives. For a perfect segmentation, all these measures should be equal 1. Low precision P indicates over-segmentation, low recall R means under-segmentation and a significant object data loss. F-Score is an indicator of total segmentation quality.

Visual results of image segmentation applied to the original (low-dose) and the enhanced CT images are presented in Figure 5. In particular, the first row presents the referential results of manual CSF segmentation compared to the input image (series: *ground truth*). This is followed by the results of image segmentation applied to the original low-dose CT images (series: *low*). Finally, the last row presents results of CSF segmentation from the enhanced images (series: *enhanced*). For image segmentation, the min-cut/max-flow approach was applied, as described in our previous work [5].

The corresponding results of the numerical assessment of image segmentation accuracy are given in Table 1. The case ID (corresponding with Fig. 5) is indicated in the first column. The second column contains the name
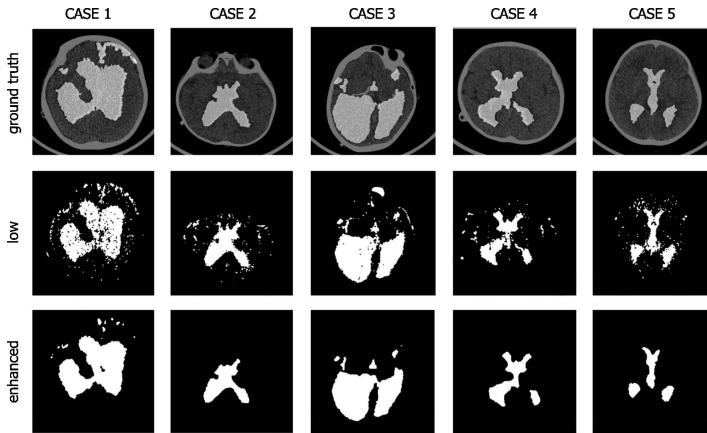
Fig. 5. Comparison of image segmentation results

of the regarded series of images (i.e. *low* and *enhanced*). This is followed by the values of precision, recall, accuracy and F-Score determined for image segmentation performed on the original and the enhanced images.

Table 1. Numerical assessment of image segmentation quality

Case ID	Quality	Precision	Recall	Accuracy	F-score
1	low	0.55	0.63	0.85	0.59
	enhanced	0.74	0.83	0.92	0.78
2	low	0.69	0.44	0.92	0.56
	enhanced	0.72	0.65	0.95	0.68
3	low	0.79	0.74	0.92	0.77
	enhanced	0.84	0.78	0.93	0.81
4	low	0.57	0.52	0.92	0.54
	enhanced	0.60	0.67	0.95	0.63
5	low	0.54	0.51	0.91	0.52
	enhanced	0.84	0.78	0.93	0.80

The numerical results presented in Table 1 clearly shows, that the introduced image enhancement algorithm improves the quality of image segmentation using min-cut/max-flow approach. In all regarded cases, measures of image segmentation quality obtained for the enhanced images are higher than those calculated for the original low-dose CT images. The improvement is observed especially in cases 1 and 5 where the level of distortion is subjectively the highest.

6   Conclusions

In this paper the algorithm for reduction of the artifact similar to 'film grain' was introduced. This kind of distortion often appears in the low-dose CT brain images. The method is an iterative approach which detects 'grains' and restores pixel intensities within these regions using graph based intensity interpolation.

The algorithm was tested on CT scans of hydrocephalic brains. The obtained results proved the algorithm efficiency. The usefulness of the introduced image enhancement algorithm increases together with the increasing level of distortions arising from low doses used for CT imaging.

Although the algorithm was developed for enhancement of images of hydrocephalic brains, it can be easily extended to other applications where low-dose CT images are used.

References

1. Shrimpton, P.C., Hillier, M.C., Lewis, M.A., Dunn, M.: National survey of doses from CT in the UK. Br. J. Radiol. 79, 968–980 (2006)
2. Jończyk-Potoczna, K., Frankiewicz, M., Warzywoda, M., Strzyzewski, K., Pawlak, B.: Pol. J. Radiol. 77(1), 7–11 (2012)
3. Kuriakose, G., Deb, R.: A low radiation computed tomography protocol for monitoring shunted hydrocephalus. Surg. Neurol. Int. 3, 103 (2012)
4. Rybka, K., Staniszewska, A., Biegański, T.: Low-dose protocol for head CT in monitoring hydrocephalus in children 13, 147–151 (2007)
5. Węgliński, T., Fabijańska, A.: Min-cut/max-flow segmentation of hydrocephalus in children from CT datasets. In: Proc. IEEE Int. Conf. Signals and Electronic Systems, pp. 1–6 (2012)
6. Halberstadt, W., Douglas, T.S.: Fuzzy clustering of CT images for the measurement of hydrocephalus associated with tuberculous meningitis. In: Proc. IEEE Int. Conf. Engineering in Medicine and Biology, pp. 4014–4016 (2005)
7. Grady, L., Schwartz, E.L.: Anisotropic interpolation in graphs: the combinatorial Dirichlet problem. CAS/CNS Technical Report, Boston University (2003)
8. Otsu, N.: A threshold selection method from gray level histograms. IEEE Trans. Syst. Man Cybern. 9(1), 62–66 (1979)

Using of EM Algorithm to Image Reconstruction Problem with Tomography Noises

Piotr Dobosz and Robert Cierniak

Institute of Computational Intelligence, Czestochowa University of Technology,
Armii Krajowej 36, 42-200 Czestochowa, Poland
{piotr.dobosz,robert.cierniak}@iisi.pcz.pl

Summary. This paper describes an analytical iterative approach to the problem of image reconstruction from parallel projections using Expectation Minimization algorithm. The experiments with noisy measurements have shown that EM algorithm can deblur the reconstructed image. The achieved results confirm that designed reconstruction procedure is able to reconstruct an image with better quality than image obtained using the traditional back-projection algorithm.

1 Introduction

The image recostruction problem is a popular research thread mainly met in the medical imaging techniques e.g. computed tomography (CT). The obtained images are often blurred because real measurements of x-ray intensity, which are used to perform the reconstruction process, are distorted by physical noise. One of the possible solution to resist the mentioned problem is to increase the intensity of x-rays. Unfortunately, this approach has undoubtedly negative effect for health of the patient and causes conflicts with current safety requirements for radiation protection. This creates a new fields of research for many scientists who are working on the problem of image reconstruction. The most popular reconstruction algorithms are those using filtered back-projection methodology (FBP) and the algebraic reconstruction technique (ART) [1]. Beside those methods, there exist iterative reconstruction techniques which can be exploited to reduce influence of the measurement noise on the quality of reconstructed image [2]. Statistical algorithms are strongly based on the statistical model of a given medical imaging system, e.g. the maximum a posteriori probability (MAP) approach (see e.g. [3]). The MAP model is a part of the design of the iterative coordinate descent (ICD) reconstruction method [3][4]. An analytical approach (see e.g. [5], [6], [7], [8]) would eliminate the most of

problems involved with the algerbraic background of that approach, including the computational complexity of the method. The performed experiments have shown that good convergence result can be achieved after only a few thousand iteration.

2   Image Reconstruction Algorithm

An analytical statistical reconstruction algorithm was described in [9]. In this paper this idea is developed taking into considerations the time of reconstruction process and calculation complexity of the algorithm. The scheme of the proposed reconstruction method using the Expected Maximization algorithm is shown in Fig. 1, where the parallel-beam geometry of collected projections is used.
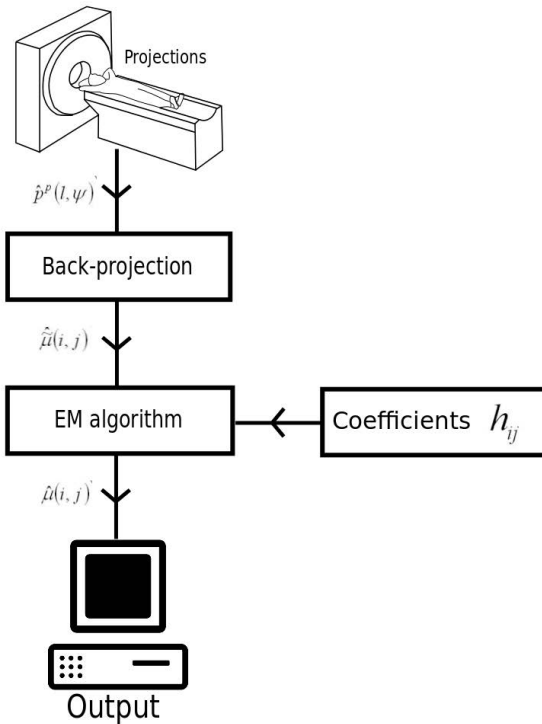
Fig. 1. A image reconstruction algorithm with parallel-beam geometry of the scanner

2.1   The Back-Projection Operation

The first step of the explored reconstruction algorithm is a back-projection operation. A defined function as $\mu(x, y)$ describes a distribution of the attenuation coefficient of x-rays in investigated cross-section of the human body. This operation is carried out according to the following relation:

$$\tilde{\mu}(x, y) = \int_0^\pi \dot{p}(s, \alpha) \, d\alpha. \tag{1}$$

During this operation, measurements $p(s, \alpha)$ are used, which are obtained in physical way by scanner. It is highly possible that for a given projection any ray will not pass through a certain point (x, y) of the reconstructed image. To evaluate a projection value for a virtual ray passing through on this point it can be applied interpolation, as follows

$$\dot{p}(\dot{s}, \alpha) = \int_{-\infty}^{+\infty} p(s, \alpha) \cdot int(\dot{s} - s) \, ds, \tag{2}$$

where $int(\Delta s)$ is an interpolation function, and $s = x \cos \alpha + y \sin \alpha$. After the back-projection operation we obtain a strongly blurred image $\tilde{\mu}(x, y)$.

   In literature (see e.g. [8]) is shown that this image $\tilde{\mu}(x, y)$ can be expressed by the following relation:

$$\hat{\tilde{\mu}}(i, j) \cong \sum_k \sum_l \hat{\mu}(l, k) \cdot h(i - k, j - l), \tag{3}$$

where

$$h(\Delta i, \Delta j) = \Delta_\alpha (\Delta_s)^2 \cdot \sum_{\psi=0}^{\Psi-1} int(i\Delta_s \cos \psi \Delta_\alpha + j\Delta_s \sin \psi \Delta_\alpha), \tag{4}$$

and $i, k = 0, 1, \ldots, I$; $j, l = 0, 1, \ldots, J$, where I and J are numbers of pixels in horizontal and vertical directions.

   From equation (3) can be deduced that the image obtained after back-projection operation is a convolution of the original image and the geometrical distortion element given by (4). The coefficients $h(\Delta i, \Delta j)$ can be precalculated in numerical way, before the reconstruction procedure is started.

2.2   The Reconstruction Process Using EM-Type Algorithm

According to the considerations of Snyder et al. [10], the deconvolution problem (deblurring problem) can be presented in the following scheme

$$\int\limits_{\mathbf{x}\in\mathbf{X}} h\left(\mathbf{y}|\mathbf{x}\right) c\left(\mathbf{x}\right) d\mathbf{x} = a\left(\mathbf{y}\right), \tag{5}$$

where $a\left(\mathbf{y}\right)$; $\mathbf{y} \in \mathbf{Y}$ is an observed function, $h\left(\mathbf{y}|\mathbf{x}\right)$ is a kernel, $c\left(\mathbf{x}\right)$ is a function which has to be reconstructed.

An iterative reconstruction algorithm was proposed in [10] which minimizes monotonically Csiszár I-divergence (it is worth to note that this divergence is a generalization of the Kullback-Leibler divergence). That divergence is observed between a reconstructed function $c\left(\mathbf{x}\right)$ and a based on measurement function $a\left(\mathbf{y}\right)$. The original iterative deblurring algorithm was written in the following way

$$c_{t+1}\left(\mathbf{x}\right) = c_t\left(\mathbf{x}\right) \frac{1}{H\left(\mathbf{x}\right)} \cdot \int\limits_{\mathbf{y}\in\mathbf{Y}} \frac{h\left(\mathbf{y}|\mathbf{x}\right)}{\int\limits_{\mathbf{x}\in\mathbf{X}} h\left(\mathbf{y}|\mathbf{x}\right) c_t\left(\mathbf{x}\right)} a\left(\mathbf{y}\right) d\mathbf{y}, \tag{6}$$

where

$$H\left(\mathbf{x}\right) = \int\limits_{\mathbf{y}\in\mathbf{Y}} h\left(\mathbf{y}|\mathbf{x}\right) d\mathbf{y}, \tag{7}$$

and $c_{t+1}\left(\mathbf{x}\right)$; $c_t\left(\mathbf{x}\right)$ are current and updated versions of the functions $c\left(\mathbf{x}\right)$, respectively.

Taking into account the form of the invariant system (3) and basing on the scheme (6), we can formulate an iterative EM-type reconstruction algorithm as follows

$$\hat{\mu}_{t+1}\left(i,j\right) = \hat{\mu}_t\left(i,j\right) \frac{\hat{\bar{\mu}}\left(i,j\right)}{\sum_k \sum_l \hat{\mu}_t\left(l,k\right) \cdot h\left(i-k,j-l\right)}. \tag{8}$$

Above iterative expression is fundamental for our new concept of image reconstruction procedure.

3   Experimental Results

A mathematical model of the projected object, a so-called phantom, is used to obtain projections during simulations. The most common matematical phantom of head was proposed by Kak (see eg. [11]).

A measurement noise can be modeled by Poisson distribution. A generic probability function for this distribution can be described as:

$$f(x;\lambda) = P(X = x) = \frac{\lambda^x e^{-\lambda}}{x!} \tag{9}$$

where λ is a nonnegative real number which is expectation number of events in a given period of time and x is a random variable.

$P(X = x)$ is a probability mass function. It gives probability for any real number x such that a discrete random variable takes the value x

$$\sum_x P(X = x) = 1 \tag{10}$$

At start the values of the projections $\dot{p}(s, \alpha)$ are calculated in the similar way as it is performed in the Shepp-logan phantom. Then values of radiation I^* intensity were established according to the following relation:

$$\ln(I^*(U)) = \ln(I(0)) - \dot{p}(s, \alpha) \tag{11}$$

where $I(0)$ is the same initial x-ray intensity for all projections. Afterwards, the statistical value of the intensity $I(U)$ are generated with expected value $I^*(U)$. After all this value are applied to back-calculated the projections.

In presented experiment the size of the image was fixed at $I \times J = 128 \times 128$ pixels.

The discret approximation of the interpolation operation expressed by equation (2) takes the form

$$\dot{p}(s, \alpha) = \sum_{l=-L/2}^{L/2-1} \hat{p}(l, \alpha) \cdot int\,(s - l\Delta_\alpha). \tag{12}$$

The interpolation function $Int\,(\Delta s)$ can be defined for example as linear interpolation function

$$int_L(\Delta s) = \begin{cases} \frac{1}{\Delta_s}\left(1 - \frac{|\Delta s|}{\Delta_s}\right) & if\,|\Delta s| \geq \Delta_s \\ 0, & if\,|\Delta s| > \Delta_s \end{cases}, \tag{13}$$

where $\Delta s = (i\cos\alpha + j\sin\alpha)$.

The obtained after back-projection operation image was next subject to a process of reconstruction using iterative reconstruction process described by (8).

The differences between reconstructed images obtained using: the standart convolution/back-projection method using Shep-Logan kernel and presented originally in this paper algorithm are depicted in Fig. 2. For better quality of reconstructed image the initial values of inner pixels of head were changed to 1.02.

The quality of the reconstructed image has been evaluated in this case by error measure defined as follows

$$MSE = \frac{1}{I \cdot J} \sum_{i=1}^{I} \sum_{j=1}^{J} [\mu(i, j) - \hat{\mu}(i, j)]^2, \tag{14}$$

where discrete function $\mu(i, j)$ describes an original image of reconstructed cross-section.

These images are obtained using window described in [12]. In this case we used the following parameters of the window $C = 1.02$, $W = 0.2$.

Image	a	b	c
MSE	1	1.17363e-06	0.82444e-06

Fig. 2. View of the results image: mathematical model image (a); standard reconstruction method (back-projection with Shepp-Logan filter) (b); EM-type reconstruction algorithm described in this paper (c)

4 Conclusions

This paper presents EM algorithm whose implementation gives some benefits in comparison to the standard back-projection method. It achieves convergence very fast, i.e. it takes less than 3000 iterations. The results from Fig. 2 show that using the proposed solution one can achieve much better quality of the reconstructed image with the same number of iterations in comparison with traditional recostruction algorithms.

References

1. Cierniak, R.: Tomografia komputerowa. Akademicka Oficyna Wydawnicza EXIT, Warsaw (2005)
2. Cierniak, R.: X-ray computed tomography in biomedical engineering. Springer, London (2011)
3. Thibault, J.B., Sauer, K.D., Bouman, C.A., Hsieh, J.: A three-dimensional statistical approach to improved image quality for multislice helical CT. Medical Physics 34, 4526–4544 (2007)
4. Bouman, C.A., Sauer, K.: A unified approach to statistical tomography using coordinate descent optimization. IEEE Trans. on Image Processing 5(3), 480–492 (1996)
5. Cierniak, R.: A 2D approach to tomographic image reconstruction using a Hopfield-type neural network. Elsevier Science: International Journal Artificial Intelligence in Medicine 43, 113–125 (2008)
6. Cierniak, R.: A new approach to image reconstruction from projections problem using a recurrent neural network. Applied Mathematics and Computer Science 18, 147–157 (2008)

7. Cierniak, R.: A Novel Approach to Image Reconstruction Problem from Fan-Beam Projections Using Recurrent Neural Network. In: Rutkowski, L., Tadeusiewicz, R., Zadeh, L.A., Zurada, J.M. (eds.) ICAISC 2008. LNCS (LNAI), vol. 5097, pp. 752–761. Springer, Heidelberg (2008)
8. Cierniak, R.: New neural network algorithm for image reconstruction from fan-beam projections. Elsevier Science: Neurocomputing 72, 3238–3244 (2009)
9. Cierniak, R., Lorent, A.: A Neuronal Approach to the Statistical Image Reconstruction From Projections Problem. In: Nguyen, N.-T., Hoang, K., Jędrzejowicz, P. (eds.) ICCCI 2012, Part I. LNCS (LNAI), vol. 7653, pp. 344–353. Springer, Heidelberg (2012)
10. Snyder, D.L., Schulz, T.J., O'Sullivan, J.A.: Deblurring subject to nonnegativity constraints. IEEE Trans. on Signal Processing 40, 1143–1150 (1992)
11. Jain, A.K.: Fundamentals of Digital Image Processing. Prentice Hall, New Jersey (1989)
12. Kak, A.C., Slanley, M.: Principles of Computerized Tomographic Imaging. IEEE Press, New York (1988)

Preprocessing Using Maximal Autocovariance for Spatio–Temporal Track–Before–Detect Algorithm

Przemysław Mazurek

West–Pomeranian University of Technology, Szczecin,
Department of Signal Processing and Multimedia Engineering,
26. Kwietnia 10 Str., 71126 Szczecin, Poland
przemyslaw.mazurek@zut.edu.pl

Summary. The detection of local regular patterns and dependent values in heavy noised signal is proposed in this paper. The moving window approach allows computation of the maximal autocovariance of signal. The differences are emphasized using Spatio–Temporal Track–Before–Detect algorithm so tracking such objects is possible. The possibilities of this technique are shown in a few illustrative examples and discussed. The detection of weak signals hidden in the background noise is emphasized.

1 Introduction

Tracking systems are very important in military and civil applications [1, 2]. The most well recognized systems are related to the surveillance. Such systems are applied in the air, space, water surface and underwater surveillance applications. There are many tracking algorithms that are proposed for general or specific applications. Almost all tracking algorithms use conventional processing approach, that is based on the detection and tracking scheme [1, 2]. Tracking systems could be characterized by the number of tracked objects (single or multiple objects) and the number of sensors (single or multiple sensors). The simplest case is related to the single object and single sensor scenario. Larger number of objects needs assignment algorithm that is responsible for the track maintenance. Increased number of sensors needs the proper data fusion.

The position is estimated using the detection algorithm. The detection algorithm is based on the fixed or adaptive threshold. Numerous filtering algorithms are applied for improvement of the detection. Obtained position is processed by the tracking algorithm, so the trajectory is obtained. The tracking algorithm could be very simple if SNR (Signal–to–Noise Ratio) is high. Lower SNR case should be processed by more advanced tracking algorithm, that support motion model of the object. Lower SNR case is characterized by

the multiple detections, so position of the object cannot be estimated using single observation. Multiple observations and processing of them by tracking algorithm allows estimation of the object position for such case. The additional detections (false detections) are suppressed by the gate technique. The gate is assigned to the predicted position of the object. It is possible to estimate (predict) position even if the object detection is not achieved in some measurements due to noise. There are many tracking algorithms like the Benedict–Bordner, Kalman, EKF, Bayes filters [1, 2, 3, 4]. The scheme of conventional approach is shown in Fig. 1.
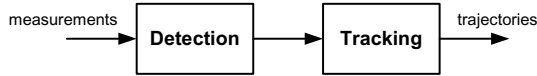
Fig. 1. Detection and Tracking Scheme

The application of the tracking algorithm and the gate technique improves SNR of overall system [1, 5]. SNR could be also very small, e.g. $SNR < 1$. The signal of object is hidden in the noise background in such case. The detection is not possible using conventional techniques at all. The threshold value cannot be correctly selected, and giant amount of false observation may occur, so conventional tracking approach is useless [1, 6, 7].

Low SNR case could be processed using alternative tracking approach that is based on the Track–Before–Detect (TBD) scheme. This approach is based on the opposite processing. All possible trajectories are processed using tracking algorithm. There are many tracking algorithms processed in parallel. There are 100M of tracking filters assuming 1000×1000 image resolution (measurement data) and 100 motion vectors for example. Such processing requirements are fixed and independent on the number of tracked object. The processing cost is fixed even if no one object is in the range. Multiple objects could be processed at the same cost. Most TBD algorithms are multiple object tracking algorithms. The detection of the object is possible after the tracking. The tracking is based on spatial and temporal filtering of signal. It is possible using multidimensional filtering algorithms in some cases. The motion model is related to the motion vectors that define trajectories and cooperation between neighborhood motion vectors. The scheme of TBD approach is shown in Fig. 2.
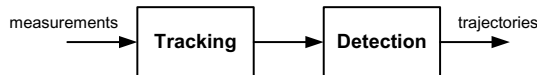
Fig. 2. Track–Before–Detect Scheme

2   Spatio–Temporal Track–Before–Detect Algorithm

The Spatio–Temporal Track–Before–Detect algorithm (ST TBD) is the kind of the multidimensional recursive filter [8]. The following pseudocode shows ST TBD details:

Start
// Initial:

$$P(k = 0, s) = 0 \tag{1}$$

For $k \geq 1$ and $s \in S$
// Motion Update:

$$P^-(k, s) = \int_S q_k(s|s_{k-1})P(k - 1, s_{k-1})ds_{k-1} \tag{2}$$

// Information Update:

$$P(k, s) = \alpha P^-(k, s) + (1 - \alpha)X(k) \tag{3}$$

EndFor
End
where:

S	– state space: e.g. 2D position and motion vectors,
s	– state (spatial and velocity components),
k	– time moment,
α	– smoothing coefficient $\alpha \in (0, 1)$,
$X(k)$	– measurements,
$P(k, s)$	– estimated value of objects,
$P^-(k, s)$	– predicted value of objects,
$q_k(s|s_{k-1})$	– state transitions (Markov matrix).

There are two formulas in ST TBD. Incoming measurements are processed using the information update formula. It is a kind of the exponential filter with the weight coefficient α. The motion update formula is the predictor. The predicted values of the state space are mixed with incoming measurements using the information update formula. There are two processes that occur in ST TBD. The state space blurring occurs in the motion update, and the state space sharpening occurs in information update formulas. The balance between them is obtained by the selection of the smoothing coefficient.

The state space could be defined using numerous ways. The simplest case occurs for the direct application of the measurement space to the state space. The state space is multidimensional. The ST TBD works as low pass filter so it is well destined to the processing of the positive signals that are disturbed by the zero mean value noise.

The ST TBD have efficient implementations, using for example GPG-PUs [9, 10, 11, 12, 13].

3   Preprocessing of Measurement Space Using Maximal Autocovariance

The processing of the positive signal of the object is very important in numerous applications. Weak signals are emphasized by ST TBD and the detection is possible together with the trajectory estimation.

The amplitude modulated signals could be processed using demodulation techniques that are a part of the modified ST TBD [14].

Another kind of the object could be processed after preprocessing. The noise object is characterized using comparison of distribution or distribution parameters. Local variance [15] could be applied for the noise object. Another possibility is direct comparison of distribution histograms. The chi–square statistics [16] could be used for the computation of differences between two distributions [17, 18, 19].

Such approach changes raw signal to the appropriate measurement space [20, 21, 22, 23]. Direct application of ST TBD is not possible, because noise signal has zero mean value, so output of ST TBD for the background and object will be similar.

Autocovariance allows comparison of the original and delayed signal [24]. The signal X is delayed, and the lag is defined as n. The total length of the signal is defined as N.

$$C_{XX}(n) = \frac{1}{N-n} \sum_{i=1+n}^{N} X_i X_{i-n} - (\overline{X}|_{1+n}^{N})(\overline{X}|_{1}^{N-n}) \tag{4}$$

Application of the autocovariance allows testing regularities (e.g. periodicity) of signal [24]. The signal could be any kind. The typical application of the autocovariance is the testing of random generators.

The window approach is applied for the comparison of signals locally. The lag $n = 0$ is omitted, so only positive lags $n > 0$ are considered. The lag $n = 0$ is adequate to the variance computation. The signal is compared with own direct copy, so the output value is positive and high. It is signal variance that is biased. Lack of the relation between signal and specific lag gives zero value, but it is noised value due to small sample size. Periodic signal give high values. Different noise distributions or filtered noise signal also give changes. The object position is not always determined by the highest value and the opposite output is possible. High dependence in the background signal gives high value. The object could be based on low dependence in the own signal, so lower value of autocovariance is obtained. The window approach allows computation of the new measurement for the information update formula (1b).

4   Example Results

4.1   Example: Random Signal – Different Distributions

This example shows results of the Gaussian background noise and the uniform noise related to the object. The result of this example is shown in Fig. 3.
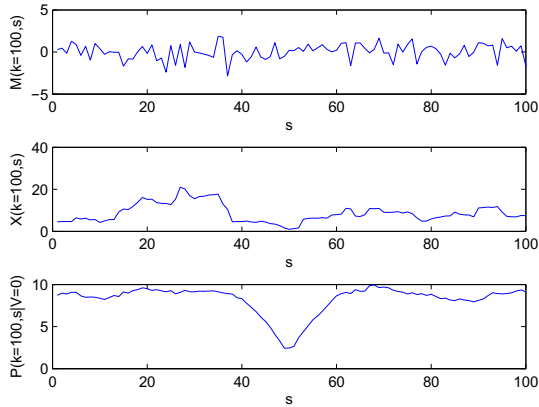
Fig. 3. Output of ST TBD for different noise distributions
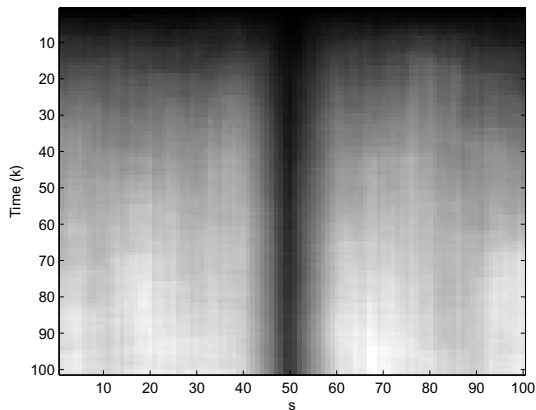
Fig. 4. Example signals after 100 steps: input signal, maximal autocovariance, ST TBD output

This is an example of the case where lower value of maximal autocovariance has lower value (Fig. 4) for the object in comparison to the background. The difference is quite quickly emphasized and is visible after less then 20 step (Fig. 4).

4.2   Example: Periodic Pattern Inside Gaussian Noise

This example shows results of the Gaussian background noise and pattern:
(-0.5, 0.5, -0.5, 0.5, -0.5, 0.5, -0.5, 0.5, -0.5). The result of this example is
shown in Fig. 5.
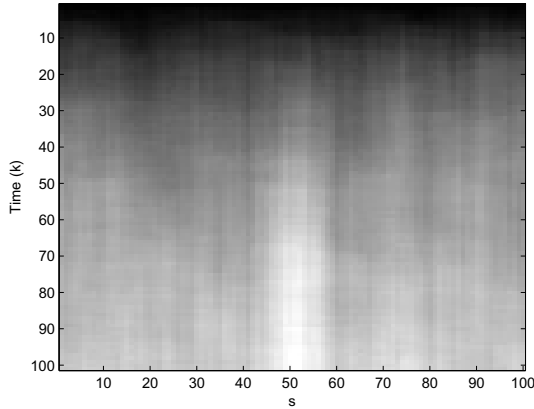
Fig. 5. Output of ST TBD for periodic pattern
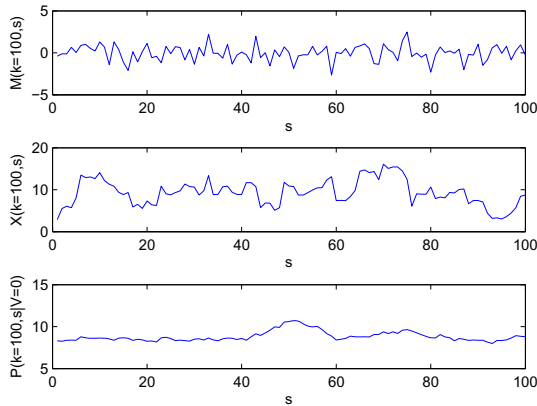
Fig. 6. Example signals after 100 steps: input signal, maximal autocovariance, ST
TBD output

This pattern is hidden in the additive background noise, but it is possible
to find it. The width of area of detection is extended and blurred due to
possibility of the detection even if not all patterns are observed (Fig. 5).

4.3   Example: Filtered Random Signal

This example shows results of the Gaussian background noise and the filtered random signal related to the object. The result of this example is shown in Fig. 7. The signal where, the object is located, is obtained by summation of the Gaussian noise (multiplied by 0.5) and filtered Gaussian noise (also multiplied by 0.5). The signal is filtered using the moving average filter (MA1).
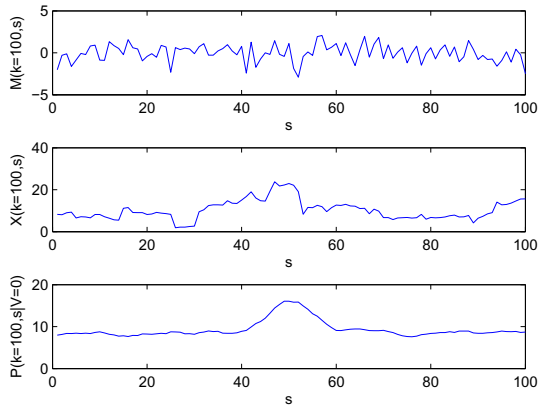
Fig. 7. Output of ST TBD for filtered random signal

This example shows the detection based on the different distributions and samples dependency in the object area. The detection is possible after about 20 processing steps. The detection area is blurred due to partial dependency when the moving window overlaps partially area of the object.
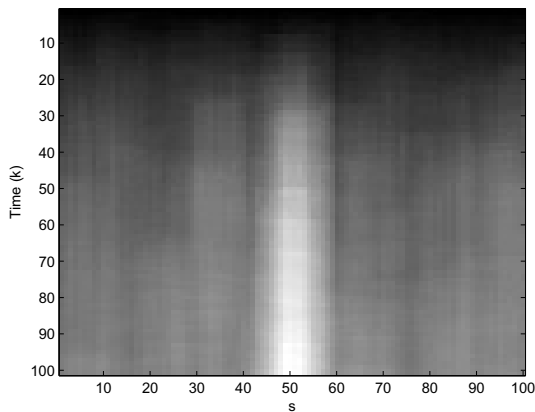
Fig. 8. Example signals after 100 steps: input signal, maximal autocovariance, ST TBD output

5   Discussion and Conclusions

The window size consist of 10 samples, only. Autocovariance is computed for $N - 1 = 9$ lags. It is extremely small data set for the application of the autocovariance.

The obtained results for specific time moment cannot be used for the detection (Fig. 3, Fig. 5, Fig. 7 middle). The detection is possible after/during tracking by filtering of many differences between the background and object signals (Fig. 4, Fig. 6, Fig. 8).

Application of ST TBD allows filtering (e.g. accumulation of the results) so it is possible to distinguish signals after some time steps (Fig. 4, Fig. 6, Fig. 8). The difference is visible after about 20 steps.

ST TBD state space is initialized by zeros, so steady state is achieved after some iterations. It is visible as dark (low value) strip at the beginning of processing (Fig. 4, Fig. 6, Fig. 8).

The state space is multidimensional so it is assumed that object is not moving and the appropriate subspace is shown. The position of the object is fixed around the position 50. The 1D signal is processed but images (2D signals) could be processed also.

The maximal value of autocovariance is processed by ST TBD algorithm. The computation cost of the preprocessing is very small in comparison to ST TBD algorithm. This is important advantage of the proposed algorithm. Efficient implementations using pipeline processing of autocovariance are possible.

The detection of dim objects is important. There is limitation of the proposed algorithm related to the size of the object, that should be large - a few samples (pixels) is the minimum. It is kind of the extended target. Smaller object that occupy single sample cannot be processed using the proposed solution.

The smoothing weight $\alpha = 0.98$ is assumed in all examples. The optimization of this value is possible [16] for improving time response of ST TBD. The delay related to this behavior (similar to delay of the exponential filter) limits application possibilities, where a new object is in the measurement range.

The proposed preprocessing is a valuable tool for the detection specific from the autocovariance point of view differences between the background and noise object signals.

References

1. Blackman, S.S., Popoli, R.: Design and Analysis of Modern Tracking Systems. Artech House (1999)
2. Bar–Shalom, Y.: Multitarget–Multisensor Tracking: Applications and Advances, vol. II. Artech House (1992)

3. Brookner, E.: Tracking and Kalman Filtering Made Easy. Willey–Interscience (1998)
4. Kalman, R.E.: A New Approach to Linear Filtering and Prediction Problems. Transactions of the ASME–Journal of Basic Engineering 82(D), 35–46 (1960)
5. Blackman, S.: Multiple–Target Tracking with Radar Applications. Artech House (1986)
6. Stone, L.D., Barlow, C.A., Corwin, T.L.: Bayesian Multiple Target Tracking. Artech House (1999)
7. Boers, Y., Ehlers, F., Koch, W., Luginbuhl, T., Stone, L.D., Streit, R.L. (eds.): Track Before Detect Algorithm. EURASIP Journal on Advances in Signal Processing (2008)
8. Mazurek, P.: Direct visualization methods for Track–Before–Detect algorithms. Poznan University of Technology Academic Journals–Electrical Engineering 59, 25–34 (2009)
9. Mazurek, P.: Implementation of spatio–temporal Track–Before–Detect algorithm using GPU. Pomiary Automatyka Kontrola 55(8), 657–659 (2009)
10. Mazurek, P.: Optimization of Track–Before–Detect Systems with Decimation for GPGPU. Pomiary Automatyka Kontrola 56(12), 1523–1525 (2010)
11. Mazurek, P.: Optimization of bayesian Track–Before–Detect algorithms for GPGPUs implementations. Electrical Review R 86(7), 187–189 (2010)
12. Mazurek, P.: Optimization of Track-Before-Detect systems for GPGPU. Pomiary Automatyka Kontrola 56(7), 665–667 (2010)
13. Mazurek, P.: Code reordering using local random extraction and insertion (LREI) operator for GPGPU–based track–before–detect systems. Soft Computing (2012), 10.1007/s00500-012-0956-8
14. Mazurek, P.: Hierarchical Track–Before–Detect Algorithm for Tracking of Amplitude Modulated Signals. In: Choraś, R.S. (ed.) Image Processing and Communications Challenges 3. AISC, vol. 102, pp. 511–518. Springer, Heidelberg (2011)
15. Mazurek, P.: Track–Before–Detect Algorithm for Noise Objects. Pomiary Automatyka Kontrola 56(10), 1183–1185 (2010)
16. Aczel, A.D.: Complete Business Statistics. Wohl Publishing (2012)
17. Mazurek, P.: Chi–square statistic for noise objects tracking in Track–Before–Detect systems. Poznan University of Technology Academic Journals - Electrical Engineering 71, 177–184 (2012)
18. Mazurek, P.: GPGPU–based implementation of chi–square spatio–temporal track–before–detect algorithm. Pomiary Automatyka Kontrola 58(7), 590–592 (2012)
19. Mazurek, P.: Background noise distribution for noise object tracking. Computer Applications in Electrical Engineering, Poznan 10, 431–441 (2012)
20. Mazurek, P.: Comparison of Different Measurement Spaces for Spatio–Temporal Recurrent Track–Before–Detect Algorithm. In: Choraś, R.S. (ed.) Image Processing and Communications Challenges 3. AISC, vol. 102, pp. 157–164. Springer, Heidelberg (2011)
21. Okarma, K., Mazurek, P.: Vehicle tracking using the high dynamic range technology. In: Mikulski, J. (ed.) TST 2011. CCIS, vol. 239, pp. 172–179. Springer, Heidelberg (2011)

22. Mazurek, P., Okarma, K.: Vehicle tracking using a multi–scale Bayesian algorithm for a perspective image of a road. In: Mikulski, J. (ed.) TST 2011. CCIS, vol. 239, pp. 346–353. Springer, Heidelberg (2011)
23. Mazurek, P., Okarma, K.: Background suppression for video vehicle tracking systems with moving cameras using camera motion estimation. In: Mikulski, J. (ed.) TST 2012. CCIS, vol. 329, pp. 372–379. Springer, Heidelberg (2012)
24. Glover, D.M., Jenkins, W.J., Doney, S.C.: Modeling Methods for Marine Science. Cambridge University Press (2011)

Which Color Space Should Be Chosen for Robust Color Image Retrieval Based on Mixture Modeling

Maria Łuszczkiewicz-Piątek

University of Lodz, Faculty of Mathematics and Computer Science,
Department of Applied Computer Science, Banacha 22, 90-238 Lodz, Poland
mluszczkiewicz@math.uni.lodz.pl

Summary. As the amount of multimedia data captured and published in Internet constantly grows, it is essential to develop efficient tools for modeling the visual data similarity for browsing and searching in voluminous image databases. Among these methods are those based on compact image representation, such as mixture modeling of the color information conveyed by the images. These methods could be efficient and robust to possible distortions of color information caused by lossy coding. Moreover, they produce a compact image representation in form of a vector of model parameters. Thus, they are well suited for task of a color image retrieval in large, heterogenous databases. This paper focuses on the proper choice of the color space in which the modeling of lossy coded color image information, based on the mixture approximation of chromaticity histogram, is evaluated. Retrieval results obtained when RGB, $I1I2I3$, YUV, $CIE\ XYZ$, $CIE\ L^*a^*b^*$, HSx, $LSLM$ and TSL color spaces were employed are presented and discussed.

1 Introduction

As the amount of multimedia data captured and published in Internet constantly grows in latest years, it is essential to develop tools for managing this enormous amount of information, to be suited for everyday use to growing number of users [1]. This huge amount of visual information is so far the largest and the most heterogenous image database, thus there is a question which features meaningfully describe its content. Color is a useful characteristic of our surrounding world, giving clue for the recognition, indexing and retrieval of the images presenting the visual similarity. However, the image representation in various color spaces can possibly yield different retrieval results due to the fact that employed color spaces can present different characteristics and thus they are suitable for different image processing tasks [2].

The presented paper is organized as follows. Firstly the color space set, which was used for retrieval efficiency evaluation, is discussed. Then the retrieval methodology is presented and along with the discussion on the experimental results. Finally, conclusions are presented.

2 Analyzed Color Spaces

The color is uniquely defined in specified color space. The RGB color space is considered as fundamental and commonly used space, which is a base for many others obtained by it linear or nonlinear transformations. The color spaces evaluated by linear transformation of RGB (e.g. YUV, YIQ) are commonly associated with hardware color displays. On contrary, the color spaces obtained via nonlinear transformation of the RGB (e.g. HSV or $L^*a^*b^*$) are considered as reflection the characteristic of the human visual systems. Let us note that different color spaces derived from RGB by either group of linear or nonlinear transformation can reveal various performance. Thus it is important to determine which of the color spaces is the most desirable for image retrieval task. The most common RGB color space enables to describe each color in terms of red, green and blue components. Other color spaces can be derived from this space using linear or nonlinear transformations. This first group of spaces are obtained by using the specified transformation matrix.

First of the analyzed color spaces is the XYZ color space. It was derived by the International Commission on Illumination (CIE) in 1931 as a result of set of experiments on the human perception, [4]. The second analyzed color space $I_1I_2I_3$ is the result of the decorrelation of the RGB components using the $K - L$ transform performed by Ohta 1980, [5]. The next color space is the YUV color space used by color video standards. It consists of luminance (Y) component and chrominance components (U and V).

The $LSLM$ is a color space based on the opposite responses of the cones, i.e. black-white, red-green and yellow-blue. The following transformation matrix defines the $LMLS$ color space, [6]:

$$\begin{bmatrix} L \\ S \\ LM \end{bmatrix} = \begin{bmatrix} 0.209 & 0.715 & 0.76 \\ 0.209 & 0.715 & -0.924 \\ 3.148 & -2.799 & -0.349 \end{bmatrix} \begin{bmatrix} R \\ G \\ B \end{bmatrix} \tag{1}$$

The nonlinear transformation of RGB color spaces are, among the others, HSV, TSL and $CIE\ L^*a^*b^*$. The TSL (Tint, Saturation, and Luminance) color space is widely used in face detection research field,[7, 8]. The transformation is based on the formulae:

$$T = \begin{cases} \frac{1}{2\pi} \arctan \frac{r'}{g'} + \frac{1}{4}, & \text{if } g' > 0 \\ \frac{1}{2\pi} \arctan \frac{r'}{g'} + \frac{3}{4}, & \text{if } g' < 0 \\ 0, & \text{if } g' = 0 \end{cases} \tag{2}$$

$$S = \sqrt{\frac{9}{5}\left(r'^2 + g'^2\right)}, \qquad L = 0.299R + 0.587G + 0.114B \qquad (3)$$

$CIE\ L^*a^*b^*$ color space is a color-opponent space with dimension L for lightness and a and b for the color-opponent dimensions, [9]. The HSV (Hue, Saturation, Value) color space is related with the phenomenon of the human eye vision. This model assumes that all colors can be extracted from the white color, when some parts of the spectrum are absorbed by the illuminated object and other parts can be reflected.

3   Image Retrieval Scheme

The parametric color image description is used in many image analysis solutions. Although several proposed image retrieval techniques utilize the *Gaussian Mixture Model* (GMM) [10, 11] as color distribution descriptor [12, 13, 14], the aspect of the distortions caused by the lossy compression was not taken into account. These methods simply index all images in the database by fitting GMM to the data, according to some predefined rules. The *mixture* based retrieval scheme applied in this work is robust to distortions introduced by lossy compression and noise, [15, 17, 18, 19, 16], thus it is important to test whether the use of various color spaces in information modelling process will alternate the retrieval results, influencing the retrieval accuracy.

The first step in applying the applied methodology is to construct the histogram $H(x,y)$ in the chosen chromaticity space defined as $H(x,y) = N^{-1}\sharp\{r_{i,j} = x, g_{i,j} = y\}$, where $H(x,y)$ denotes a specified bin of a two-dimensional histogram with first component equal to x and second component equal to y, the symbol $\sharp$ denotes the number of samples in a bin and N is the number of color image pixels. As the pairs of the components representing analyzed color spaces the following pairs were chosen: $r - g$ (RGB), $I2I3$ (I1I2I3), $U - V$ (YUV), $T - S$ (TSL), $a - b$ ($L^*a^*b^*$), $H - S$ (HSV), and $S - LM$ (LSLM.)

The next stage of the presented technique is the modeling of the color histogram using the Gaussian Mixture Models (GMM) and utilizing the Expectation-Maximization (EM) algorithm for the model parameters estimation as described in details in [15, 16]. Let us assume the following probabilistic model: $p(x|\Theta) = \sum_{m=1}^{M}\alpha_m p_m(x|\theta_m)$, which is composed of M components and its parameters are defined as: $\Theta = (\alpha_1, \ldots \alpha_M, \theta_1, \ldots, \theta_M)$, with $\sum_{m=1}^{M}\alpha_m = 1$. Moreover, each p_m is a function of the probability density function which is parameterized by θ_m. Thus, the analyzed model consists of M components with M weighting coefficients α_m.

Finally after derivations shown in [11] the model parameters are defined as:

$$\alpha_m^{k+1} = N^{-1}\sum_{i=1}^{N}p(m|x_i, \Theta^k),\quad \mu_m^{k+1} = \frac{\sum_{i=1}^{N}x_i \cdot p(m|x_i, \Theta^k)}{\sum_{i=1}^{N}p(m|x_i, \Theta^k)}, \qquad (4)$$

$$v_m^{k+1} = \frac{\sum_{i=1}^{N} p(m|x_i, \Theta^k)(x_i - \mu_m^{k+1})(x_i - \mu_m^{k+1})^T}{\sum_{i=1}^{N} p(m|x_i, \Theta^k)} \quad , \tag{5}$$

where μ and v denote the mean and variance, m is the index of the model component and k is the iteration number. The E (Expectation) and M (Maximization) steps are performed simultaneously, according to (4) and (5) and in each iteration, as the input data we use parameters obtained in the previous one.

The main idea of the application of the GMM technique lies in the highly desirable properties of this approach. The inherent feature of the GMM enables to approximate the distorted color histogram of the color image subjected to lossy compression, which is obtained through limited model complexity (7 components) and number of iterations (75) of E-M algorithm, as shown in [15, 17, 18, 19, 16]. Thus, this approach does not reflect exactly the corrupted (by e.g. lossy coding) data, but rather approximates it toward the chromaticity histogram of the original image. The lossy compression significantly corrupts the color distribution of an image and a lack of the application of any refinement techniques may lead to the high rate of false negative results, as images stored in lossy formats are considered as dissimilar on the basis of their corrupted color palette. In details, in the used method the GMM is used as a descriptor of the image color distribution. However, the very important aspect is the fact that the used method, based on weighted two-dimensional Gaussians is robust to distortions introduced by lossy compression techniques and therefore it can be used for the retrieval of images contained in the Web based databases, which very often store images in lossy compression formats, like JPEG and noise can be present. Due to this highly desirable properties of the GMM retrieval method it is important to support it efficiency by the proper choice of the color space, which describes accurately the color composition of the analyzed image without influencing the similarity of the GMM models for the visually related images. Having image indexed using the GMM signatures, it is important to choose the accurate similarity measure to compare the indexes associated with each of the images with that of the given query. In general, the Minkowski metrics can be used to compare point to point the color histograms. However, these measures are very susceptible to bin shifts, thus even highly similar images can be considered as dissimilar when corresponding bins of their chromaticity histograms are shifted and therefore, this group of similarity measures is not taken into account in further analysis. However, it is more suitable to generalize this concept toward distribution to distribution similarity. For that purpose the Kullback-Leibler based similarity measures as (D_G) [20] and that taking into account the correlation of components within each of the both mixture models, representing the analyzed images, as (D_V) [21], are employed.

Let us note that the first approach are designed to measure image similarity for image retrieval tasks whereas the second approach was initially designed for acoustic models used for speech recognition. The following

formulae describe the distances as follows: $D_{KL}(G_i, G_j) = (\mu_i - \mu_j)^T \Sigma^{-1}(\mu_i - \mu_j) + TR(\Sigma_i \Sigma_j^{-1} + \Sigma_i^{-1} \Sigma_j)$ where G_i and G_j denotes normal distributions with mean values μ_i and μ_j, and covariance matrices Σ_i and Σ_j respectively. $D_G(G^a, G^b) = \sum_{i=1}^{k} \alpha_i^a (D_{KL}(G_i^a, G_{\pi(i)}^b) + \log \frac{\alpha_i^a}{\alpha_{\pi(i)}^b})$ where $\pi(i) = \arg\min_j (D_{KL}(G_i^a, G_j^b) - \log \alpha_j^b)$ is the matching function between components i and j of the Gaussian Mixture Models G^a and G^b and α_i^b denotes the weighting parameter α for i^{th} component of model G^a. The second similarity measure is defined as: $D_V(G^a, G^b) = \sum_{i=1}^{k} \alpha_i^a \frac{\sum_{i'=1}^{k} \alpha_{i'}^a e^{-D_{KL}(G_i^a, G_{i'}^b)}}{\sum_{j=1}^{k} \alpha_j^b e^{-D_{KL}(G_i^a, G_j^b)}}$.

The second group of analyzed similarity measures are the adaptive approaches such as *Earth Movers Distance* [22] (*EMD*), which is based on the assumption that one of the histograms reflects hills and the second represents holes in the ground of a histogram. The measured distance is defined as a minimum amount of work needed to transform one histogram into the other using a soil of the first histogram. As a measure of the distance between two distributions in EMD framework the Kullback-Leibler divergence was used, which is a measure of the dissimilarity between two probability distributions.

4   Experimental Results

In order to choose the most accurate color space for purpose of color image retrieval, the set of eight color spaces (RGB, $CIE\ XYZ$, YUV, $I1I2I3$, $LSLM$, $CIE\ L^*a^*b^*$, HSx and TSL) were analyzed. Firstly, the color images of database of Wang[3] (1000 color images categorized into 10 thematically consistent categories), were compressed to 25% of their file size and rescaled to 10% of their size, using IrfanView software (`www.irfanview.com/`). These images produced distorted histograms in comparison to the histograms of the original, uncompressed images. Next step was to model the color chromaticity histograms using the GMM methodology obtaining image signatures, according to formulae presented in previous Section. These image signatures were compared by the D_V ,D_G and EMD similarity measures due to the reasoning given in previous Section. However, to generalize retrieval observations, the *Precision* and *Recall* measures are employed. In more details, *Precision* is the fraction of retrieved images that are relevant, while Recall is the fraction of relevant instances that are retrieved. Fig. 1 illustrates the *Precision − Recall* plots evaluated for the entire analyzed Wang database, i.e. each of the database image was used as a query. The evaluated *Precision* values for each of 1000 queries were averaged (for each corresponding *Recall* value) producing the plots shown on Fig. 1 The criterion of the image similarity was the membership of the image to one of the 10 categories of this database. This Figure illustrates the comparison of the retrieval efficiency for the set of color spaces obtained by the linear (left) transformations of the RGB color space for EMD similarity meaures. The best performance
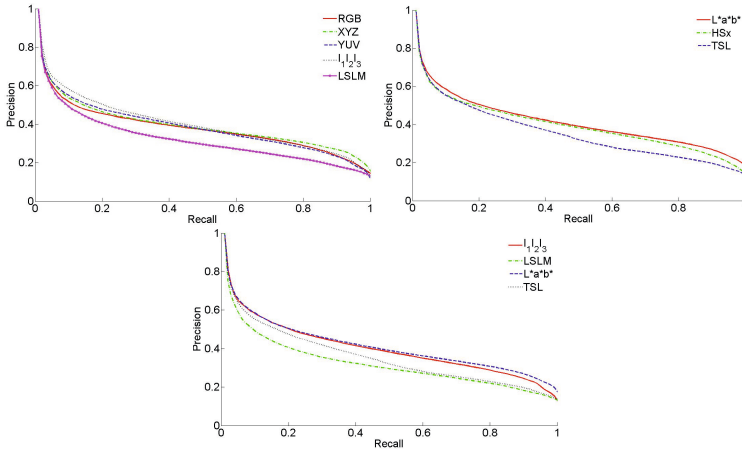
Fig. 1. The $Precision - Recall$ plots of the retrieval results evaluated using GMM methodology for set of color spaces obtained by linear (left upper row) and non-linear (right upper row) transformations of the RGB color space. The comparison between best performing color space retrieval results is shown in bottom row. The comparisons of retrieval efficiency was evaluated using the EMD similarity measure. Plots were evaluated over all the images of the database of Wang [3].

presents the $I1I2I3$ color space, which is the result of the decorrelation of the RGB components, while the worst efficiency is associated with $LSLM$ color space. Then the nonlinear transformations of RGB are analyzed in (center), showing that the $CIE\ L^*a^*b^*$ color space provides the highest accuracy of retrieval results. The comparison of the retrieval performance of the color spaces related to the best and the worst results in terms of effectiveness shows that $CIE\ L^*a^*b^*$ (nonlinear) and $I1I2I3$ (linear) presents the comparable efficiency, however, the latter needs much simpler computation during transformation from RGB. As the D_G and D_V similarity measures seems to be not well suited for GMM based image retrieval scheme (as shown in Table 1), their efficiency was not shown on $Precision - Recall$ plots. The comparison between best performing linear and nonlinear color spaces is depicted on 1(bottom row) Let us note, that $Precision$ and $Recall$ tend to ignore the ranking of retrieved images, e.g. $Precision$ of 0.5 indicates that half of the retrieved images is relevant to the given query but without any further information if relevant images are the first half of the retrieved set or are the second half. In order to counteract this, it is advised to measure $Precision$ and $Recall$ at the specified points e.g. at the answer set of 1, 5, 10, and 25 images. These measurements are assumed to give the better idea of the behavior of the analyzed retrieval scheme for applied color spaces. This results show that D_G and D_V are not well suited color spaces when GMM based retrieval is considered, presenting much lower retrieval efficiency than retrieval based

on EMD similarity measure. Thus, D_G and D_V similarity measures should not be used for mixture based retrieval techniques.

The used technique was also tested in order to evaluate it robustness to noise for various color spaces. Fig. 2 illustrates the $Precision - Recall$ plots (EMD similarity measure was used) for the set of 150 color images divided into 14 categories. Each category consist of original image, from the $LIVE$ database - without added noise (http://live.ece.utexas.edu/research/quality/) and its 9 versions. Original images were subjected to 9 noise distortions: "salt & pepper" where noise density is 2%, 10% and 20% of total image pixels affected; poisson noise; gaussian white noise of variance: 0.01, 0.03, 0.05, multiplicative noise of image values governed by I = I + I n where n is uniformly distributed random noise with (mean,variance): (0,0.04) and (0,0.2). The retrieval experiment was evaluated using the same scheme as for database of Wang. It can be noticed that the $CIE\ L^*a^*b^b$ (nonlinear), RGB and $I1I2I3$ (linear) color spaces offer the best retrieval efficiency. One must be aware that the retrieval efficiency is not only related with the retrieval method, but also with the content of the analyzed database and the used ground truth. In the case of the Wang database some of the categories share not only the semantic relation between images within the category but also the arrangement of the colors present on the images (e.g. "Beaches", "Horses"), but some do not as "Buses" and "Flowers", what influences the retrieval efficiency of applied technique. It is important to underline that this work does not test the effectiveness of the GMM based retrieval scheme, as it effieciency was elaborated and tested in other Author's work [15, 17, 18, 19, 16] as well as the comparison with other widely used retrieval schemes as $MPEG - 7$ descriptors, correlograms and others. The previous work clearly show the usefullness of the GMM based retrieval technique, especially when lossy compressed images are analyzed. However there is an open question which color space is best suited for this kind of retrieval scheme. Presented paper addresses this problem.

The overall behavior of the proposed retrieval method can be specified by *average recall* $(\hat{R})$ and *average precision* $(\hat{P})$. The *average precision* is defined as a sum of $\frac{1}{rank(O_i)}$ divided by number of queries q:$\hat{P} = \frac{1}{q} \sum_{i=1}^{q} \frac{1}{rank(O_i)}$. In this approach only the *average precision* $\hat{P}$ is analyzed.

Table 1 summarizes the average precision for the entire database of Wang at the points of 1, 5, 10 and 25 retrieved images for D_G, D_V and EMD similarity measures. It can be observed that $L^*a^*b^b$ and $I1I2I3$ color spaces provide comparable results for small set of retrieved candidate images. The average precision values at the points related to 1, 5, 10 and 25 retrieved images should be chosen to examine the retrieval efficiency as user is usually more interested in relevance of the highly ranked candidate images than the overall success rate of the retrieval system.
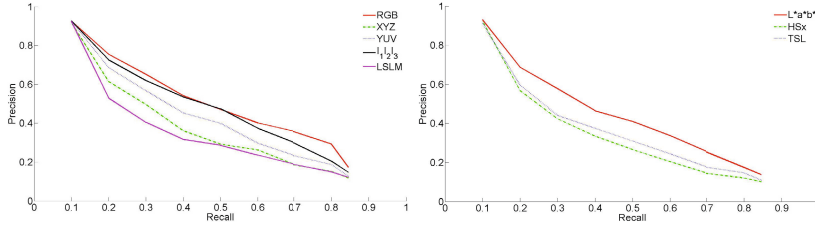
Fig. 2. The $Precision - Recall$ plots of the retrieval results evaluated using GMM methodology for set of color spaces obtained by linear (left) and nonlinear (right) transformations of the RGB color space, evaluated over all the images of the $LIVE$ database and their noisy versions.

Table 1. The Average precision ($\hat{P}$) values of the retrieval results evaluated using GMM methodology for set of color spaces. Average precision values at specified points related to 1, 5, 10 and 25 retrieved images were obtained over all the images of the database of Wang.

Color space	$\hat{P}_1$	$\hat{P}_5$	$\hat{P}_{10}$	$\hat{P}_{25}$	$\hat{P}_1$	$\hat{P}_5$	$\hat{P}_{10}$	$\hat{P}_{25}$	$\hat{P}_1$	$\hat{P}_5$	$\hat{P}_{10}$	$\hat{P}_{25}$
	EMD				D_G				D_V			
RGB	1	0.6052	0.5176	0.4368	0.3384	0.1659	0.1522	0.1174	0.1724	0.1077	0.1039	0.1250
XYZ	1	0.6225	0.5365	0.4429	0.3630	0.1963	0.1765	0.1757	0.1918	0.1207	0.1232	0.1371
YUV	1	0.6240	0.5505	0.4587	0.3929	0.2021	0.1826	0.1786	0.1923	0.1130	0.1079	0.1101
I1I2I3	1	0.6491	0.5833	0.4750	0.3440	0.1944	0.1798	0.1784	0.1526	0.0989	0.1012	0.1122
LSLM	1	0.5908	0.4925	0.3781	0.3984	0.1923	0.1674	0.1745	0.1584	0.1039	0.1063	0.1179
$L^*a^*b^*$	1	0.6491	0.5833	0.4750	0.3958	0.1848	0.1757	0.1528	0.1485	0.0956	0.0995	0.1086
HSx	1	0.6283	0.5559	0.4722	0.3766	0.1360	0.1204	0.1198	0.1845	0.1123	0.1143	0.1239
TSL	1	0.6374	0.5524	0.4462	0.3696	0.13675	0.1285	0.1193	0.1066	0.1254	0.1252	0.1323

5 Conclusions

In this work the problem of the choice of the most accurate color space for the GMM based retrieval scheme was analyzed. The conducted experiments shown that this decision plays a crucial role in the efficiency of the retrieval system. Thus, the best performance of the GMM based scheme is associated with CIE $L^*a^*b^*$ and $I1I2I3$ color spaces using the EMD similarity measure. As CIE $L^*a^*b^*$ slightly outperforms the $I1I2I3$ it should be taken into account that when image color information is given using RGB values, the linear transformation to $I1I2I3$ is less complicated than for CIE $L^*a^*b^*$ Due to the fact that user is, in general, interested in relatively small set of top ranked images, it is important to examine the system efficiency (in terms of $Precision$ and $Recall$) at points of e.g. 1, 5 and 10 retrieved images. This comparison (see Table 1) also indicates that CIE $L^*a^*b^*$ and $I1I2I3$ color spaces are the most accurate choice.

References

1. Datta, R., Joshi, D., Li, J., Wang, J.Z.: Image Retrieval: Ideas, Influences, and Trends of the New Age. ACM Computing Surveys 40(2), 1–60 (2008)
2. Stokman, H., Gevers, T.: Selection and Fusion of Color Models for Image Feature Detection. IEEE Trans. on Pattern Analysis and Machine Intelligence 29(3), 371–381 (2007)
3. Wang, J.Z., Li, J., Wiederhold, G.: SIMPLIcity: Semantics-Sensitive Integrated Matching for Picture Libraries. IEEE Trans. Patt. Anal. Mach. Intel. 9, 947–963 (2001)
4. Weeks, A.R.: Fundamentals of Electronic Image Processing. SPIE Optical Engineering Press, IEEEPress, Washington (1996)
5. Ohta, Y., Kanade, T., Sakai, T.: Color Information for Region Segmentation. Computer Graphics and Image Processing 13(3), 22–241 (1980)
6. Colantoni, P.: Color space transformations, http://www.couleur.org
7. Terrillon, J.-C., Akamatsu, S.: Comparative Performance of Different Chrominance Spaces for Color Segmentation. In: Internat. Conf. on Face and Gesture Recognition, pp. 54–61 (2000)
8. Hsu, R.-L., Abdel-Mottaleb, M., Jain, A.K.: Face Detection in Color Images. IEEE Trans. Pattern Anal. Mach. Intell. 24(5), 696–706 (2002)
9. Fairchild, M.D.: Color and Image Appearance Models, Color Appearance Models. John Wiley and Sons (2005)
10. McLachlan, G., Peel, D.: Finite Mixtures Models. John Wiley & Sons (2000)
11. Bilmes, J.: A Gentle Tutorial on the EM Algorithm and its Application to Parameter Estimation for Gaussian Mixture and Hidden Markov Models. University of Berkeley, ICSI-TR-97-021 (1997)
12. Jeong, S., Won, C.S., Gray, R.M.: Image Retrieval Using Color Histograms Generated by Gauss Mixture Vector Quantization. Comp. Vis. Image Underst. 94(1-3), 44–66 (2004)
13. Xing, X., Zhang, Y.: Bo Gong: Mixture Model Based Contextual Image Retrieval. In: CIVR 2010, pp. 251–258 (2010)
14. Beecks, C., Ivanescu, A.M., Kirchhoff, S., Seidl, T.: Modeling Image Similarity by Gaussian Mixture Models and the Signature Quadratic Form Distance. In: ICCV, pp. 1754–1761 (2011)
15. Luszczkiewicz, M., Smolka, B.: Gaussian Mixture Model Based Retrieval Technique for Lossy Compressed Color Images. In: Kamel, M.S., Campilho, A. (eds.) ICIAR 2007. LNCS, vol. 4633, pp. 662–673. Springer, Heidelberg (2007)
16. Luszczkiewicz, M., Smolka, B.: A Robust Indexing and Retrieval Method for Lossy Compressed Color Images. In: Proc. of IEEE International Symposium on Image and Signal, Processing and Analysis, pp. 304–309 (2007)
17. Luszczkiewicz-Piatek, M., Smolka, B.: Effective color image retrieval based on the Gaussian mixture model. In: Schettini, R., Tominaga, S., Trémeau, A. (eds.) CCIW 2011. LNCS, vol. 6626, pp. 199–213. Springer, Heidelberg (2011)
18. Luszczkiewicz, M., Smolka, B.: Application of bilateral filtering and Gaussian mixture modeling for the retrieval of paintings. In: Proc. of 16th IEEE International Conference on Image Processing (ICIP), pp. 77–80 (2009)

19. Luszczkiewicz-Piatek, M., Smolka, B.: Selective color image retrieval based on the Gaussian mixture model. In: Blanc-Talon, J., Philips, W., Popescu, D., Scheunders, P., Zemčík, P. (eds.) ACIVS 2012. LNCS, vol. 7517, pp. 431–443. Springer, Heidelberg (2012)
20. Goldberger, J., Gordon, S., Greenspan, H.: An Efficient Image Similarity Measure Based on Approximation of KL Divergence Between Two Gaussian Mixtures. In: ICCV, pp. 487–493 (2003)
21. Harshey, J., Olsen, P.: Approximating the Kullback-Leibler Divergence Between Gaussian Mixure Models. In: Proc. IEEE ICASSP, vol. 4, pp. 317–320 (2007)
22. Rubner, Y., Tomasi, C., Guibas, L.J.: The Earth Movers Distance as a Metric for Image Retrieval. International Journal of Computer Vision 40(2), 99–121 (2000)

The Perception of Humanoid Robot by Human

Rafał Stęgierski and Karol Kuczyński

Institute of Computer Science,
Maria Curie-Sklodowska University in Lublin, Poland
`{rafal.stegierski,karol.kuczynski}@umcs.pl`

Summary. The article presents results of experiments which test acceptance level of a humanoid robot. We stated that in most cases people have tendencies to anthropomorphize machines, especially humanoid ones. Acting like this is a result of a social bias, so characteristic for our specie. We conducted two experiments in which participants during a poll were in a room with a robot observer, with active face and sound tracking implemented. By analyse of post review questionnaire and time parameters from video recording, we could point out that in some cases participants observed robot's behaviours which had not taken place, but are quite natural for a human.

1 Introduction

Human is a social specie. We cooperate, interact, are empathic, polite, build up society. Thousands years of evolution shaped our brains and encoded specific behaviour. Correct and fast reaction, possibility to read intentions, often non verbal ones, helps us to survive. This bias of our kind experiences gives us ability in everyday life to make proper decisions. Advanced machines, especially robots, are in our surroundings from just few dozens of years, if not less. Our behaviour code is not ready for that change and we have tendencies to deal with machines as with humans. We want to see in a robot, especially a humanoid one, an equal partner. This anthropomorphizing takes place not only on rational level but, if not more, on irrational. We just want to think about machines as members of our society.

2 Background

Creating of sociable robot has to take place on many different levels. From mechanical, where limbs have similar number, degrees of freedom and functionality as human joints, face which could express emotions, voice system which verbalizes expectations and even artificial feelings, to, least but not

last, motivation system associated tightly with behaviour [1]. The last part should correspond to general purpose and appearance of a robot. We expect different actions and reactions from a child than from an adult [5].

In most cases, dyadic interaction between a human and a robot were studied [3]. There are few works where triadic interaction takes place and is analysed in direction of humanoid acceptance by autistic children [6] or a responder during an interview [4]. In both cases robot is steered with WOZ (Wizard Of Oz) method with human operator, who decides how the machine should react.

In case when interaction takes place between a human and a robot, eye contact, response to sound and proper limbs movements are necessary to create illusion of full participation of the machine in the communication [2]. It is hard, or even impossible at this moment, to build a solution where a robot not only understands verbal statement, but also information hidden in the non-verbal level. To express our feelings, we use a lot of different additional signals, from gesture to face expression, and often spoken words do not correspond with them.

3   Assumption

We assume that our perception of a robot is biased by our expectations how a machine should act. In case of a triadic interaction, where humans are active participants and a humanoid is only an observer, we state that its presence is enough to build up a sense of an equal partnership. For an outside responder taking part in a review process, behaviour of a robot is interpreted as understanding, even if it is only a simple reaction on a stimulus. In an average person case, vision of humanoid as a reasoning entity is so strong that even knowledge how in reality such a system acts does not alter the perception.

4   Humanoid Platform

In the presented experiments Nao programmable humanoid robot, created by Aldebaran Robotics for scientists, as a hardware platform for research in robotics, was used. Our version, H25 v. 4, has 25 degrees of freedom, a range of sensors, an audio system and LED lights. Main controller is build around ATOM CPU.

5   Software Controller

The software is based on NAOqi standard API for access to all capabilities offered by the robot. In our case, information from four microphones and camera is used as an input. A person that the humanoid should look at,
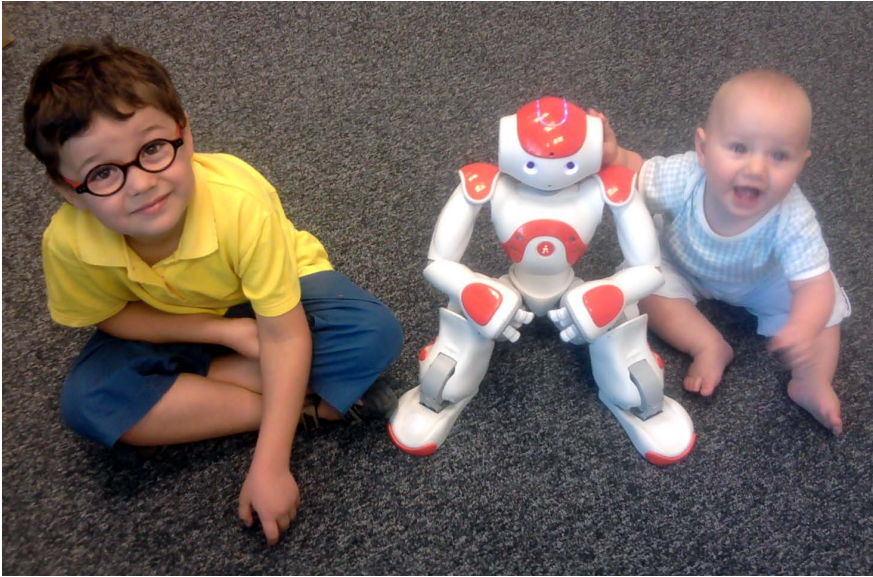
Fig. 1. Aldebaran Nao H25 v. 4. Humanoid robot about 57 centimetres tall

is found with a fuzzy logic controller, making decision according to sound direction, time from beginning of saying, and current head position. When the decision is made, direction of the robot head is set according to the cached face position, nearest to the position of the sound source. If the new face position is detected during the head movement, the cache is updated and the head movement is corrected. Position correction takes place every five seconds and LEDs around eyes of the robot change color for half a second, from lightblue to green. The last operation mimics blinking. At the beginning of every interview, the robot looks around and precaches the position of each face. Head is moved with tenth of full servo speed in pitch and yaw direction, to minimize noisy sound typical for mechanical motors. Probably it would be the best solution to use pneumatic actuators which are almost silent as in [4], but in our experiment we want to present anthropomorphising of a humanoid robot which only resembles a human in its shape and behaviour, but is not an android.

6 Experiments

Two experiments were conducted. In both cases, in the first part a responder took part in an interview and answered eleven general questions about his or her studies, most and least favourite lectures, future plans and students life. Before this part, the interviewee was introduced to the robot observer.

The review was performed in simple environment in which participants were not distracted. The configuration was different for each experiment, but generally, a table was in the center of the room with two chairs in the first case, and three chairs in the second case, the humanoid robot, a laptop of the reviewer and a camera. Every interview was registered to obtain data of the robot head position and eye focusing of the participant.

The reviewer during all interviews had no eye contact with the robot and tried to focus on the interviewee. The robot observed all the participant according to rules described in the previous section.

In the first case, the robot was placed next to the reviewer on a chair and directed almost front to the interviewee. This situation helps to catch an eye contact between the participant and the humanoid, without large head movement.

In the second case, the robot was placed on the table. This time the reviewer and the interviewee were closer to each other. Sides of the humanoid were set to the both persons. The interviewee had not only to focus eyes but also turn his or her head to look at the robot.

Fig. 2 graphically presents arrangement of the room during both experiments.

The second part of the experiment was a paper questionnaire with twelve questions, filed out independently by every participant. Question asking about general impressions, atmosphere, eye contact of the reviewer and the interviewee with the robot and annoyance of this form of interviewing. All questions are presented in table 1. The interviewee could check one out of five answers for each question: "definitely no", "no", "neither yes or no", "yes", "definitely yes". Each answer is valued from 0 to 10 with 2.5 step.

Twenty three students participated in the first experiment, all males with one exception. Fifteen participants, including three females, participated in the second experiment. The groups did not come in contact with each other.

7   Results

During the experiments we could obtain to kinds of data. The first one are answers from the questionnaire with values assigned to each item. The second are statistics from the video recordings analysed towards eye contact between the interviewee and the robot and glazing of the interviewee with single frame precision (1/25 second).

As we can see, in both experiment the results of questionnaire are very similar. Change of the robot's position to interviewee did not alter good impression and average 8.26 in the first experiment and 7.86 points in the second one. Generally, the humanoid was accepted and presence of the robot was noticeable (7.17 and 7.15), non distractable (2.17 and 2.68) and not annoyed (1.96 and 2.50) by most of the participants. We could not say if it was result of positive relationship during poll with 9.13 points in the first
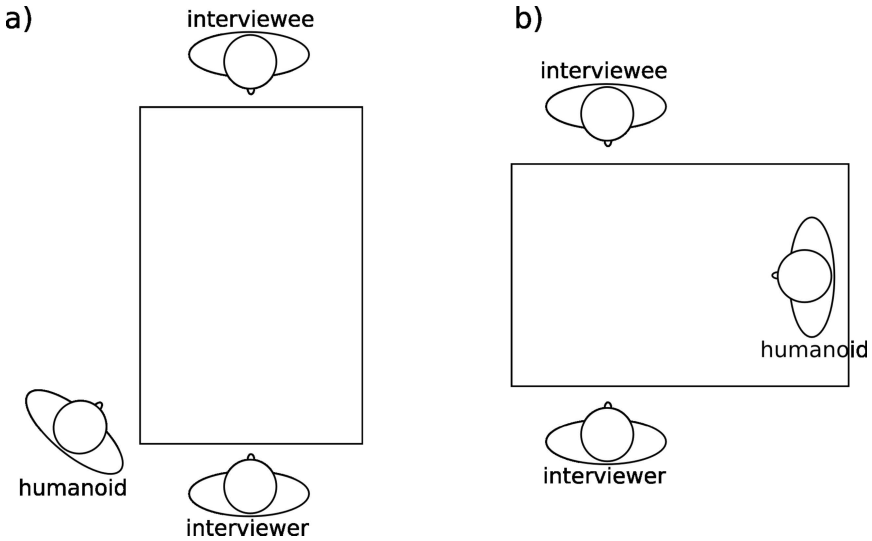
Fig. 2. Setup during the experiments. In the first one (a) the interviewee could easier catch eye contact with the robot. In second the case (b) the humanoid is higher on the table and closer to the interviewee, but sideways, so an eye contact impossible without a head movement.

experiment and 7.50 in the second one. According to the participants, the interviewer was positively disposed toward an interviewee (respectively 9.35 and 8.57). One possible way to extend the experiment is to add a situation where the interviewer acts to favoured neutral or even negative relationship by for eg. acting upset or irritated.

In the second case, when possibility of eye contact is limited, less participants (6.43 versus 7.28 points) saw robot's tries to find this kind of contact.

Half of the interviewees observed that the interviewer pointed out the robot and the same amount of participant saw reaction of the robot to their answers.

Average total time of the review is very similar in both experiments. Poll takes about two and half minutes. Maximum review time recorded in experiment was 305.8 and 347.12 seconds respectively. Minimum was 108.72 and 100.88 seconds.

Average total eye contact time was 1.33 seconds in the first experiment, when the interviewee could easier look toward the humanoid. In the second experiment it was only 0.71 seconds. In both cases it is interesting that it was less than one percent of all the poll time. Similar situation and very similar time values are in the case of when the participant glance at the robot (1.53 and 0.70 seconds).

We could also see that glances where more often than eye contacts but are shorter.

Table 1. Statistics for each question in both experiments. Answers "definitely no", "no", "neither yes or no", "yes", "definitely yes" counted from 0 to 10 with 2.5 step.

Question	1st experiment		2nd experiment		Diff.
	Mean	Std. Dev.	Mean	Std. Dev.	
1. Has the atmosphere during the poll been favoured a positive relationship?	9.13	2.19	7.50	1.80	1.63
2. Has the interviewer been positively disposed towards you?	9.35	2.24	8.57	2.06	0.78
3. Have the questions been clear and understandable?	9.24	2.22	7.68	1.70	1.56
4. Has the presence of the robot been noticeable?	7.17	1.29	7.14	1.43	0.03
5. Has the interviewer been pointed out the robot?	5.22	1.08	4.82	0.59	0.40
6. Has the robot caused a positive impression?	8.26	1.81	7.86	1.53	0.40
7. Has the interviewer been positively disposed towards robot?	7.50	1.45	7.32	1.61	0.18
8. Has the robot tried to find eye contact with You?	7.28	1.36	6.43	1.26	0.85
9. Have You been annoyed by the presence of the robot?	1.96	0.47	2.50	0.40	-0.54
10. Have You observed robot's reaction to Your answers?	5.22	1.02	5.00	1.10	0.22
11. Have You been distracted by presence of the robot?	2.17	0.48	2.68	0.64	-0.50
12. Has the robot behaved appropriately (eg. has not performed uncoordinated movements)?	7.17	1.51	5.89	1.41	1.28

Table 2. Time results of experiments

	Exp. no. 1	Exp. no. 2
Average total review time in seconds	150.7	147.63
Std. Dev. of total time	34.91	46.82
Eye contact time in seconds	1.33	0.71
Respondent observe time in seconds	1.53	0.70
Average number of eye contacts	1.08	0.5
Average number of responders glances	1.42	0.67
Minimum cont. eye contact time in seconds	0.4	0.68
Maximum cont. eye contact time in seconds	4.36	3.72

8 Conclusions

Half of the participants of both experiments did observe actions that had not taken place. These were robot's reaction to interviewee's answers. The humanoid did not have any algorithms which interpreted any human behaviours or voice recognition. There was only simple sound–vision tracking. It seems that the participants wanted the robot to behave like a human observer, who understands the conversation. It is also the fact that the reviewer omitted any eye contact with the machine and concentrated all the time on a participant. We could state that in normal situation ignoring of an observer is a cultural misbehave, and the interviewee tried to compensate such reviewer's acting.

The robot caused a positive impression but have minimal affect on a interviewee. In most cases the humanoid was not annoying.

Most of the participants observed eye contact catching by the robot but statistical data shows that robot was less than two percent in first experiment and less than one percent in second experiment of time under active gaze of. There is of course a small probability that peripheral vision helped an interviewee to see if the robot kept its head toward a participant.

The interviewee had eye contact with a reviewer most of time.

References

1. Breazeal, C.: Designing Sociable Robots. A Bradford Book, The MIT Press, Cambridge (2002)
2. Cassell, J.: Nudge nudge wink wink: Elements of face-to-face conversation for embodied conversational agents. In: Embodied Conversational Agents, pp. 1–27. The MIT Press, Cambridge (1999)
3. Robins, B., Dautenhahn, K., Te Boekhorst, R., Billard, A.: Robotic assistants in therapy and education of children with autism: can a small humanoid robot help encourage social interaction skills? Uernivsal Access in the Information Society 4(2), 105–120 (2005)

4. Shimada, M., Yoshikawa, Y., Asada, M., Saiwaki, N., Ishiguro, H.: Effects of Observing Eye Contact between a Robot and Another Person. International Journal of Social Robotics 3(2), 143–154 (2011)
5. Yoshikawa, Y., Noda, T., Ikemoto, S., Ishiguro, H., Asada, M.: CB2: A child robot with biomimetic body for cognitive developmental robotics. In: Humanoid Robots 2007 7th IEEE-RAS International Conference on Humanoid Robots, Pittsburg, pp. 557–562 (2007)
6. Colton, M., Ricks, D., Goodrich, M., Dariush, B., Fujimura, K., Fujiki, M.: Toward Therapist-in-the-Loop Assistive Robotics for Children with Autism and Specific Language Impairment. In: AISB 2009 Symposium on New Frontiers in Human-Robot Interaction, Edinburgh (2009)

A Fast Histogram Estimation Based on the Monte Carlo Method for Image Binarization

Piotr Lech, Krzysztof Okarma, and Mateusz Tecław

West Pomeranian University of Technology, Szczecin
Faculty of Electrical Engineering, Department of Signal Processing
and Multimedia Engineering
26. Kwietnia 10, 71-126 Szczecin, Poland
{piotr.lech,krzysztof.okarma,mateusz.teclaw}@zut.edu.pl

Summary. In the paper the idea of fast histogram estimation is proposed which is based on the application of the Monte Carlo method. Presented method can be useful for fast image binarization especially for low computational efficiency solutions e.g. autonomous mobile robots. Proposed method has been compared with full image analysis and the obtained estimates have been used for threshold determination and binarization using well-known Otsu method.

1 Introduction

One of the most relevant advantages of the application of the Monte Carlo method for image and video analysis is the reduction of the number of analysed pixels, which can be desired especially in reduced memory systems with low computational power e.g. embedded systems or autonomous mobile robots. Possible applications of the Monte Carlo based image analysis can be related to fast image quality estimation [1], line following robots [2] or fast preliminary video analysis [3]. On the other hand, calculations of the image histograms can be considered as the starting point of many image processing algorithms e.g. segmentation, contrast enhancement, compression and encryption [4], Content-Based Image Retrieval (CBIR) [5] or preprocessing of images for face recognition purposes [6].

Distribution of luminance levels in each digital image, typically presented as the histogram, can be determined using the full image analysis counting the number of pixels at each level. Such approach is time consuming, therefore a fast estimation of the histogram may be applied. Unfortunately, the loss of information corresponding to the reduction the number of analysed pixels often causes some concerns related to the precision of obtained results. Nevertheless, in some applications the precise knowledge of the histogram

in not necessary, so some estimation methods may be successfully applied, assuming their lower computational cost. For this reason, the application of the Monte Carlo method is proposed in order to gather the estimated distribution of luminance levels which can be used for binarization e.g. using classical Otsu algorithm [7].

2   Proposed Method

The main assumption of the Monte Carlo method is using the pseudo-random generator of numbers with uniform distribution for drawing the coordinates of analysed pixels. For simplification of theoretical analysis a convenient approach is reshaping the image into one-dimensional vector so a single generator may be used for determining a random position of each pixel in this vector.

Assuming the reshaped vector X representing the image, the analysis of the Monte Carlo method for a single luminance level is presented below. For the vector X and specified luminance level a constant value may be defined which is directly related to the number (or percentage) of pixels belonging to this level. The membership to the specified level can be considered as a specified logical condition.

The estimator of the number of pixels at each level $\hat{Lum}$ given as:

$$\hat{Lum} = m \, , \tag{1}$$

where m denotes the total number of pixels fulfilling the logical condition i.e. belonging to the specified level.

Increase of the algorithm's speed by reduction of the number of analysed samples is possible by the application of a statistical experiment using the Monte Carlo method. The number of analysed pixels (n) is equal to the number of independent draws (with returns) for the vector X using the pseudo-random generator with uniform distribution. Assuming k drawn pixels fulfilling the logical condition, estimated number of pixels at the specified luminance level is equal to

$$\hat{Lum}_{MC} = \frac{k}{n} \cdot N \, , \tag{2}$$

where N - the total number of samples in the vector X.

The error of estimation is equal to:

$$\varepsilon_\alpha = \frac{u_\alpha}{\sqrt{n}} \cdot \sqrt{\frac{K}{N} \cdot \left(1 - \frac{K}{N}\right)} \, , \tag{3}$$

where: u_α - the value denoting two-sided critical range, K - total number of pixels at the specified luminance level in the entire image.

The considerations presented above for a single luminance level are correct for the generator with uniform distribution. Relatively small values of the
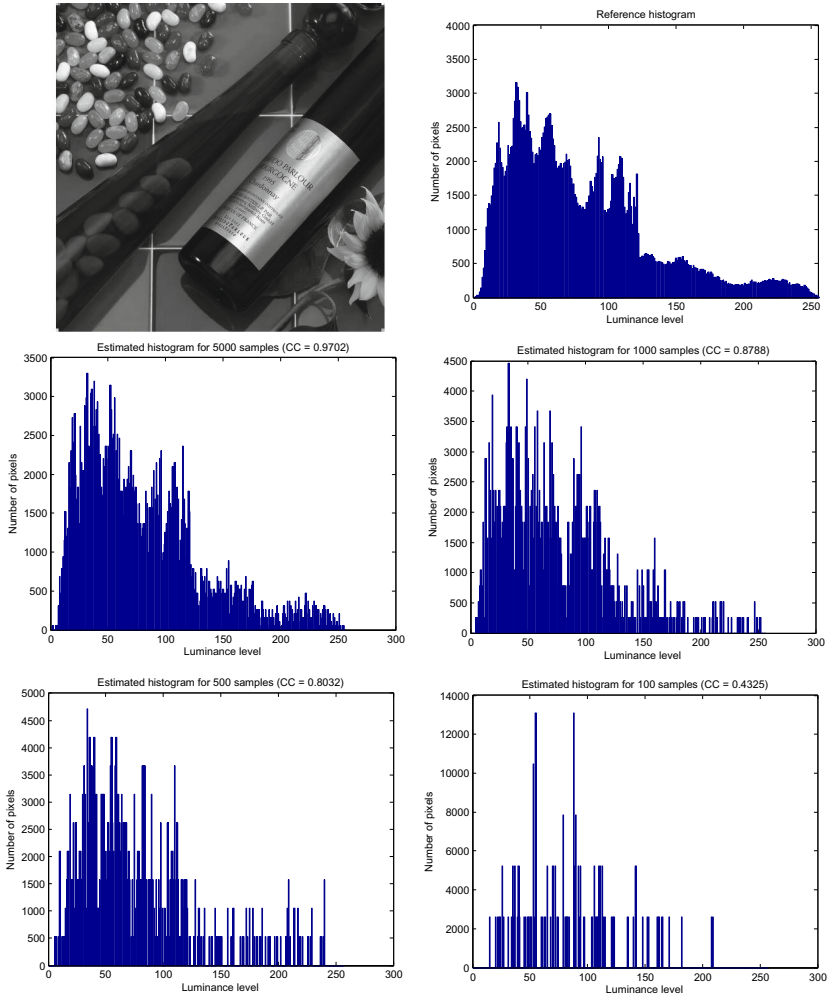
Fig. 1. Illustration of changes of the histogram shape using the proposed method for exemplary image using 5000, 1000, 500 and 100 draws

estimation error are conditioned by good statistical properties of the pseudo-random generator.

Such analysis can be conducted independently for each luminance level (typical 256 in the 8-bit greyscale images). Nevertheless, in practical applications the number of pixels for all luminance levels are estimated in a single drawing pass, leading directly to the estimation of the image histogram.

3   Discussion of Experimental Results

The verification of the properties of the proposed method has been conducted using the database delivered by Computer Vision Group at University of Granada available at `http://decsai.ugr.es/cvg/dbimagenes` containing 96 greyscale images of 512×512 pixels resolution. Our experiments have covered the estimation of histograms using the Monte Carlo method with various number of drawn pixels as well as the threshold estimation for Otsu binarization.

3.1   Results of Fast Histogram Estimation

The first experiment is related to the verification of the correctness of the obtained results of the histogram estimation depending on the number of samples. According to the theoretical background, the reduction of the number of draws causes the increase of the estimation error of the shape of the histogram. The changes of the histograms' curves for an exemplary representative image from the database together with the Pearson's linear correlation coefficients (CC) between the "ground truth" calculated for all $N = 262144$ pixels and the estimated histograms are shown in Fig. 1.

As the experiments have been conducted using 96 images, the obtained correlation results for the whole dataset are presented in Table 1.

Table 1. Pearson's linear correlation coefficients between the estimated histograms and the reference one for various number of samples used in the Monte Carlo method

Number of samples	CC_{min}	CC_{avg}	CC_{med}	CC_{max}
$n = 5000$	0.9271	0.9832	0.9902	0.9999
$n = 1000$	0.6952	0.9295	0.9523	0.9998
$n = 500$	0.6107	0.8788	0.9135	0.9998
$n = 100$	0.2964	0.6717	0.6581	0.9997
$n = 50$	0.1633	0.5825	0.5829	0.9993
$n = 10$	0.0438	0.3597	0.2865	0.9924

3.2   Comparison of Binarization Results

Preliminary experiments conducted using the considered dataset have led to the conclusion that a variety of greyscale images included in the database indicates its universal character. Since the dataset has not been designed for the binarization or segmentation purposes, even classical and well established algorithms not always lead to satisfactory results for each of the images. An illustration of such variety is shown in Fig. 2, where two different images and results of their classical binarization are presented. The left one is extremely easy for binarization but the right image seems to be difficult. This problem
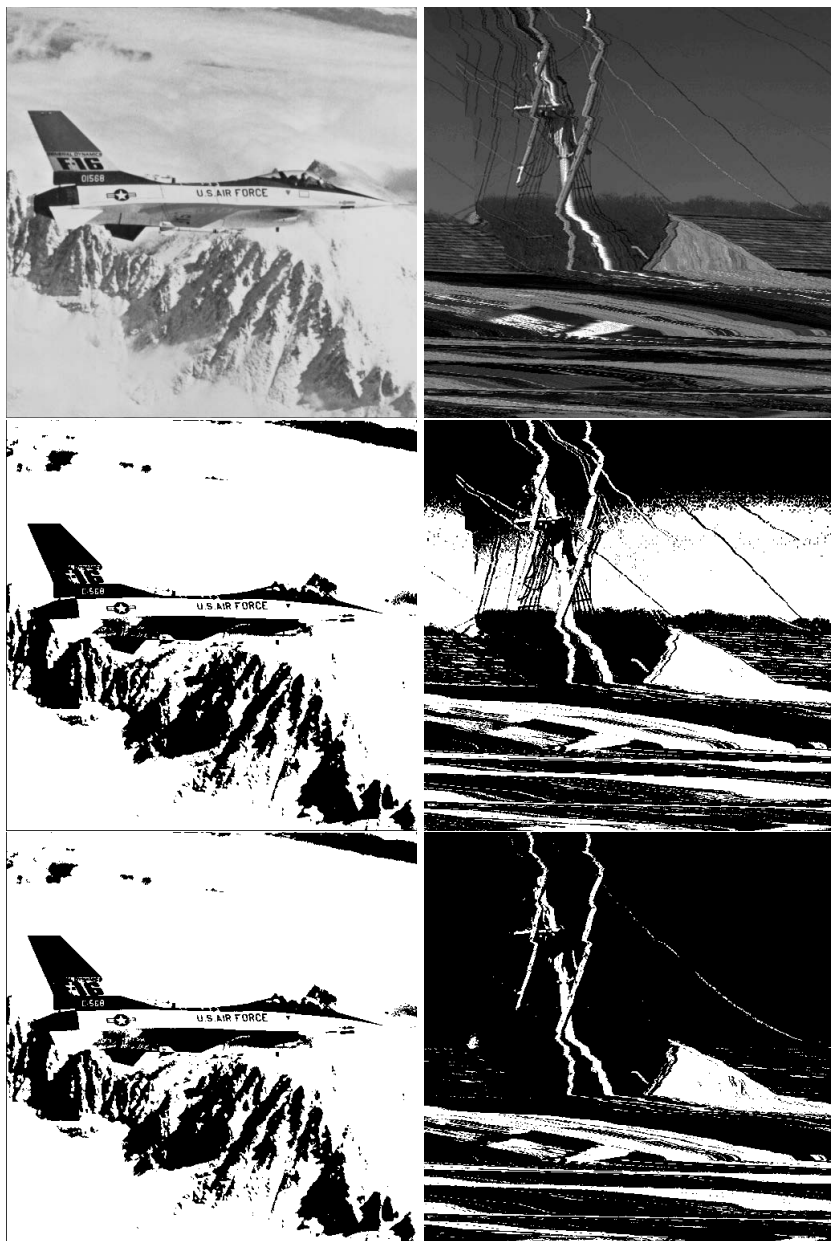
Fig. 2. Illustration of the results of binarization of exemplary images from the considered dataset using Otsu method (middle row) and Monte Carlo method for 1000 samples (bottom row)

Table 2. Average absolute differences between the normalised threshold values for binarization using Otsu method calculated using the reference histograms and Monte Carlo based estimation

Number of samples	Error$_{min}$	Error$_{avg}$	Error$_{med}$	Error$_{max}$
$n = 5000$	0.0000	0.0025	0.0000	0.0176
$n = 1000$	0.0000	0.0072	0.0039	0.0529
$n = 500$	0.0000	0.0128	0.0059	0.2255
$n = 100$	0.0000	0.0223	0.0167	0.2255
$n = 50$	0.0000	0.0385	0.0275	0.2373
$n = 10$	0.0000	0.0920	0.0588	0.4451

Table 3. Sum of absolute differences for the binary images obtained using Otsu method using the reference histograms and Monte Carlo based estimation

Number of samples	NSAD$_{min}$	NSAD$_{avg}$	NSAD$_{med}$	NSAD$_{max}$
$n = 5000$	0.0000	0.0014	0.0000	0.0098
$n = 1000$	0.0000	0.0102	0.0000	0.3804
$n = 500$	0.0000	0.0047	0.0000	0.0779
$n = 100$	0.0000	0.0156	0.0000	0.1839
$n = 50$	0.0000	0.0288	0.0000	0.4333
$n = 10$	0.0000	0.0656	0.0000	0.6150

results also in different values of obtained errors so in further analysis the minimum, maximum, average and median values will be presented, similarly as for correlation coefficients.

In order to verify the influence of the estimated shape of the histogram on the binarization results the absolute differences of the thresholds normalised to the range $\langle 0; 1 \rangle$ have been calculated for all considered images. The obtained results are presented in Table 2.

The comparison of the binarization results has been made using the normalised SAD (Sum of Absolute Differences) measure – the normalisation has been conducted by division by the total number of pixels in the image. The results obtained for the whole dataset are presented in Table 3.

4　Conclusions and Future Work

Presented method leads to satisfactory binarization results even for very small number of samples (e.g. 100) assuming the use of Otsu binarization. Such satisfactory may be obtained although the shape of the histogram changes noticeably for small number of drawn samples. Low values of the correlation coefficients between the reference histogram and the estimated one are not directly related to the thresholding error and the results of binarization using Otsu algorithm.

Fig. 3. Binarization results for an exemplary image using the proposed method for exemplary image using the reference histogram and its estimates for 5000 and 1000 draws (top row) and 500, 100 and 10 draws (bottom row)

Presented results, especially for the normalised SAD measure, are often equal to 0. Such phenomenon is related to the variety of images resulting on the same effect of binarization using Otsu algorithm and proposed one. It takes place for some of the images which contain easily separable objects on homogeneous background – easy for binarization using any of well known methods. Zero median values of the normalised SAD measure indicate the dominance of such images within the whole dataset. The presence of the outliers is easily noticeable analysing the minimum and maximum values of correlation with the reference histograms, threshold errors and the normalised SAD measure.

Our future work should concentrate on the application of some more suitable binary image quality assessment method for the verification of obtained results as well as the possible application of the proposed approach for segmentation purposes. An interesting direction of research, utilising some databases designed specifically for segmentation and binarization purposes, may be related to determining the optimal number of drawn samples for images of different resolution.

References

1. Okarma, K., Lech, P.: A statistical reduced-reference approach to digital image quality assessment. In: Bolc, L., Kulikowski, J.L., Wojciechowski, K. (eds.) ICCVG 2008. LNCS, vol. 5337, pp. 43–54. Springer, Heidelberg (2009)
2. Okarma, K., Lech, P.: A fast image analysis technique for the line tracking robots. In: Rutkowski, L., Scherer, R., Tadeusiewicz, R., Zadeh, L.A., Zurada, J.M. (eds.) ICAISC 2010, Part II. LNCS (LNAI), vol. 6114, pp. 329–336. Springer, Heidelberg (2010)
3. Okarma, K., Lech, P.: Monte Carlo based algorithm for fast preliminary video analysis. In: Bubak, M., van Albada, G.D., Dongarra, J., Sloot, P.M.A. (eds.) ICCS 2008, Part I. LNCS, vol. 5101, pp. 790–799. Springer, Heidelberg (2008)
4. Lima, J.B., Campello de Souza, R.M.: Histogram uniformization for digital image encryption. In: Proc. 25th SIBGRAPI Conf. Graphics, Patterns and Images, pp. 55–62 (2012)
5. Imamura, K., Kuroda, H., Fujimura, M.: Image content detection method using correlation coefficient between pixel value histograms. In: Kim, T.-H., Adeli, H., Ramos, C., Kang, B.-H. (eds.) SIP 2011. CCIS, vol. 260, pp. 1–9. Springer, Heidelberg (2011)
6. Forczmański, P., Kukharev, G., Shchegoleva, N.: An algorithm of face recognition under difficult lighting conditions. Electrical Review 88(10b), 201–204 (2012)
7. Otsu, A.: Threshold selection method from gray-level histograms. IEEE Trans. Systems, Man, and Cybernetics 9(1), 62–66 (1979)

Adaptation of the Combined Image Similarity Index for Video Sequences

Krzysztof Okarma

West Pomeranian University of Technology, Szczecin
Faculty of Electrical Engineering,
Department of Signal Processing and Multimedia Engineering
26. Kwietnia 10, 71-126 Szczecin, Poland
okarma@zut.edu.pl

Summary. One of the most relevant areas of research in the image analysis domain is the development of automatic image quality assessment methods which should be consistent with human perception of various distortions. During last years several metrics have been proposed as well as their combinations which lead to highly linear correlation with subjective opinions. One of the recently proposed ideas is the Combined Image Similarity Index which is the nonlinear combination of three metrics outperforming most of currently known ones for major image datasets. In this paper the applicability and extension of this metric for video quality assessment purposes is analysed and the obtained performance results are compared with some other metrics using the video quality assessment database recently developed at École Polytechnique Fédérale de Lausanne and Politecnico di Milano for quality monitoring over IP networks, known as EPFL-PoliMI dataset.

1 Introduction

The necessity of using automatic image and video quality assessment methods is unquestionable and is related to their usefulness as the optimisation criterions for new image and video lossy compression schemes of filtration algorithms. On the other hand, a reliable video quality assessment is also important e.g. for video streaming and transmission over IP networks, especially wireless ones.

The disadvantages of the classical image quality assessment methods, such as MSE or PSNR, are widely known, therefore many new metrics have been proposed starting from 2002 when the Universal Image Quality Index [1] have been developed, further extended into Structural Similarity (SSIM) metric [2]. The SSIM metric, sensitive to luminance, contrast and structure distortions, has become probably the most popular modern image quality metric, also in its multi-scale (MS-SSIM) version [3]. All those methods belong to the

most universal group of objective full-reference metrics based on the comparison with an undistorted reference image. Another group of metrics utilising only partial information about the reference image is known as the reduced-reference approach, while metrics which do not use the reference data at all are called no-reference or "blind" ones. Although no-reference metrics seem to be the most desired ones, their universality is lower as they are sensitive only to specific types of distortions. Nevertheless, the usage of automatic image quality assessment methods resulting in scalar values is the only reasonable possibility for the optimisation purposes.

2 Recently Proposed Image Quality Metrics Well Correlated with Subjective Assessment

In recent years, some new metrics well correlated with subjective scores have been proposed and two of them, briefly described above, lead to especially interesting results for the most relevant image quality assessment datasets. The first one originates from the information theory and is known as Visual Image Fidelity (VIF) [12, 13] and is based on the information that vision extracts from the reference and distorted images according to the formula

$$VIF = \frac{\sum_{j=0}^{S} \sum_{i=1}^{M_j} I(c_{i,j}; f_{i,j})}{\sum_{j=0}^{S} \sum_{i=1}^{M_j} I(c_{i,j}; e_{i,j})} \; , \tag{1}$$

where S stands for the number of sub-bands (or scales for the pixel domain version of the metric - VIFp), M_j denotes the number of blocks at j-th sub-band (scale), $I(x; y)$ and is the mutual information between x and y with the assumptions that c is a block vector at a specified location in the reference image, e is the perception of block c by a human viewer with additive noise n, and f is the perception of distorted block c.

Another interesting idea is recently proposed Feature Similarity (FSIM) metric [14] based on the comparison of the phase congruency (PC) and gradient magnitude (G) for calculation of the local similarity index $S(x, y)$ as

$$S(x,y) = \left(\frac{2 \cdot PC_1(x,y) \cdot PC_2(x,y) + T_{PC}}{PC_1^2(x,y) + PC_2^2(x,y) + T_{PC}} \right) \cdot \left(\frac{2 \cdot G_1(x,y) \cdot G_2(x,y) + T_G}{G_1^2(x,y) + G_2^2(x,y) + T_G} \right) \tag{2}$$

where T_{PC} and T_G are small stabilising constants.

The overall quality index is defined as

$$FSIM = \frac{\sum_x \sum_y S(x,y) \cdot PC_m(x,y)}{\sum_x \sum_y PC_m(x,y)} \tag{3}$$

where $PC_m(x,y) = max(PC_1(x,y), PC_2(x,y))$ denotes the highest of the two local phase congruency values (for original and distorted image). Gradient values can be obtained using Scharr convolution filter (Prewitt or Sobel masks can also be applied for this purpose).

The colour version of the metric (FSIMc) can be calculated in YIQ colour space and requires a small modification of the local similarity value in the equation (3) according to

$$S_c(x,y) = S(x,y) \cdot \left[\frac{2 \cdot I_1(x,y) \cdot I_2(x,y) + T_{IQ}}{I_1^2(x,y) + I_2^2(x,y) + T_{IQ}} \cdot \frac{2 \cdot Q_1(x,y) \cdot Q_2(x,y) + T_{IQ}}{Q_1^2(x,y) + Q_2^2(x,y) + T_{IQ}} \right]^\gamma \quad (4)$$

where the recommended value of the parameter γ is 0.03.

3 Motivation

Development of any new objective image or video quality metric is dependent on the availability of the "ground truth" assessment results. They can be obtained using perceptual experiments delivering some datasets containing a number of images or video files corrupted by various distortions. Nevertheless, the datasets used for image and video quality assessment purposes are different than some widely known ones utilised e.g. for the verification of face recognition accuracy [4] or some other purposes, as they have to contain the values of subjective quality evaluations of images or video sequences subjected to various types of distortions.

The performance evaluation of proposed metrics should be conducted by computing the values of the correlation coefficients with Mean Opinion Score (MOS) or Differential MOS (DMOS) values available as an integral part of each dataset. For this purpose well-known Pearson's Linear Correlation Coefficient (PCC) may be used as corresponding to the prediction accuracy, as well as Spearman Rank Order Correlation Coefficient (SROCC) or Kendall Rank Order Correlation Coefficient (KROCC) for the evaluation of the prediction monotonicity. Rank order coefficients are based on the analysis of the differences between two probabilities related to the same and inverse order of image lists sorted by subjective and objective scores.

Nevertheless, many researchers apply the additional regression using the polynomial or logistic function before calculating the PCC values as the relation between the objective metric raw scores and MOS or DMOS values is nonlinear. Unfortunately, the parameters of the nonlinear mapping function are obtained as the optimisation result and are different for each dataset. To override this problem one should define a metric characterised by highly linear correlation of its raw values with subjective evaluations without the necessity of any further nonlinear mapping. One of the possible solutions is the application of the combined metric, introducing the nonlinearity into the metric, with the weighting coefficients obtained by optimisation using the subjective scores from the most important image or video quality assessment databases.

4   Image and Video Quality Assessment Datasets

The most relevant image quality assessment database is known as Tampere Image Database (TID2008) and contains 1700 colour images corrupted by 17 types of distortions assessed by over 800 observers from three countries [5]. Some other, less important ones, such as Categorical Subjective Image Quality (CSIQ) database [6] with 866 images and LIVE Image Quality Database [7] containing 779 distorted images, are strongly limited by the number of distortions. There are also some other less significant image datasets available, but typically they contain only a few reference images with reduced number of distortion types assessed by much less number of observers.

Nevertheless, considering the problem of video quality assessment, the availability of such video datasets is much lower, since only a few reasonable databases have been delivered by various research groups. Two of them are available thanks to the Laboratory for Image and Video Engineering (LIVE) from the University of Texas at Austin. The first one is LIVE Video Quality Database [8] containing 150 distorted videos created from 10 reference video files using four types of distortions: MPEG-2 and H.264 compression and simulated transmission of H.264 compressed bitstreams through error-prone IP and wireless networks. The second one, published in 2012, is known as LIVE Mobile Video Quality Database [9, 10] consisting of 200 distorted videos created from 10 reference files, each of resolution 1280×720 at a frame rate of 30 fps lasting 15 seconds, which have been assessed by 34 students. Apart from compression and wireless packet-loss distortions some dynamically varying distortions changing in time e.g. frame-freezes and temporally varying compression rates have also been applied.

An interesting dataset, namely EPFL-PoliMI [11], has also been developed by researchers from two European universities: École Polytechnique Fédérale de Lausanne and Politecnico di Milano. It contains two sets of video streams (78 files based on 6 reference files in each set) at CIF (360×288 pixels) and 4CIF (720×576 pixels) resolutions which have been encoded with H.264/AVC and corrupted by packet losses over simulated error-prone network, together with the subjective evaluations by 40 naive subjects.

Since there is still a need of an automatic image and video quality assessment methods which should be linearly correlated with subjective scores, some previously proposed combined image quality metrics may be applied for video files with some modifications discussed in the paper.

Considering the availability of two different resolutions as well as higher number of human subjects involved in the subjective tests at two universities, the EPFL-PoliMI has been chosen for the conducted experiments discussed in the paper.

5 The Idea of Combined Quality Metrics and the Proposed Metric

Since the PCC values for the raw scores of most metrics, even recently proposed, and MOS/DMOS values are not always high and the nonlinear fitting is often used to achieve better correlation, a new approach based on the nonlinear combination of some metrics has been proposed. The preliminary idea of the combined metric [15] has been the combination of the MS-SSIM, VIF and R-SVD metrics (the latter one is based on the application of the Singular Value Decomposition) leading to PCC=0.86 for TID2008 dataset.

The modification of this metric for the video sequences, denoted as Combined Video Quality Metric (CVQM) has been defined [16] assuming using the frame-by-frame approach as the combination of SSIM, MS-SSIM and VIF metrics. Nevertheless, the optimisation of the weighting coefficients has been conducted using the LIVE Wireless Video Quality Assessment Database, which is not available any more due to the development of LIVE Mobile Video Quality Database [9, 10].

Recently, the proposed approach has been further extended resulting in the idea of Combined Image Similarity Index (CISI) [17] being the combination of the MS-SSIM, VIF anf FSIMc metrics, leading to PCC=0.8752 for TID2008 database.

The experimental verification of the CVQM and CISI metrics for the newly developed EFPL-PoliMI video database has led to better correlation values than for single metrics, as shown in Table 1, which are quite similar to each other. Nevertheless, the PCC results are quite unstatisfactory as illustrated on the scatter plots in Figs. 1 and 2.

As both combined metrics consist of different combinations of previously proposed ones, the nonlinear combination of their four elements is proposed in the paper in order to achieve even more linear correlation with subjective scores. The proposed Combined Video Similarity metric can be defined as

$$\text{CVS} = \left(\sum_i \text{SSIM}\right)^a \cdot \left(\sum_i \text{MS-SSIM}\right)^b \cdot \left(\sum_i \text{VIF}\right)^c \cdot \left(\sum_i \text{FSIM}\right)^d . \quad (5)$$

Since the EFPL-PoliMI database is divided into two parts the optimisation of the exponents has been conducted independently for each resolution leading to higher PCC values for the 4CIF files. The obtained values of parameters are: $a = -49.908$, $b = 46.206$, $c = 5.216$ and $d = 32.544$ for CIF, and $a = -16.617$, $b = 16.786$, $c = 1.664$, and $d = 27.4811$ for 4CIF files. Obtained PCC values are presented in Table 1 together with rank order correlations and the scatter plot for the proposed metric versus MOS values is shown in Fig. 3, where the high linearity of the relation between them is clearly visible.

Table 1. Obtained results of correlation coefficients with MOS values for EPFL-PoliMI database

Metric	Pearson (PCC)		Spearman (SROCC)		Kendall (KROCC)	
	CIF	4CIF	CIF	4CIF	CIF	4CIF
SSIM	0.7966	0.8433	0.9392	0.9556	0.7817	0.8263
MS-SSIM	0.8705	0.8760	0.9667	0.9781	0.8451	0.8740
VIF	0.9061	0.9214	0.9512	0.9604	0.8067	0.8318
FSIM	0.8624	0.9023	0.9495	0.9796	0.8005	0.8850
CVQM	0.9287	0.9473	**0.9720**	**0.9818**	0.8584	0.8850
CISI	0.9016	0.9350	0.9516	0.9787	0.8059	0.8772
Proposed	**0.9685**	**0.9785**	**0.9717**	**0.9809**	**0.8670**	**0.8889**
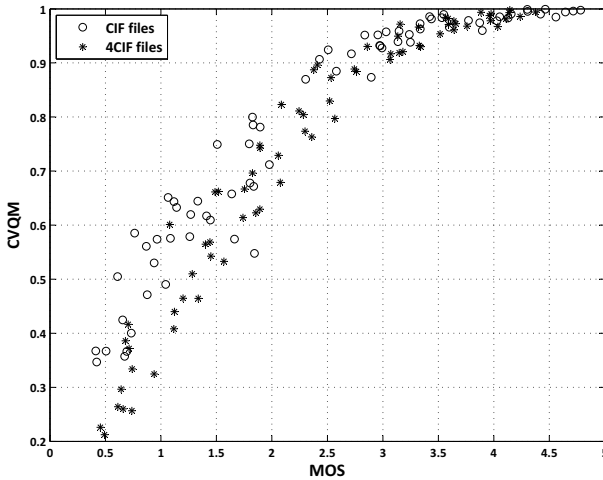
Fig. 1. Scatter plot of the CVQM metric versus subjective scores for CIF and 4CIF files from the EFPL-PoliMI dataset

The cross-validation of the parameters obtained for both resolutions has led to PCC=0.9616, SROCC=0.9691 and KROCC=0.8505 for the 4CIF files assessed using the metric with exponents optimised for CIF files. Application of the exponents obtained using 4CIF files to the assessment of CIF files has allowed to achieve slightly better results (PCC=0.9698, SROCC=0.9753 and KROCC=0.8662).
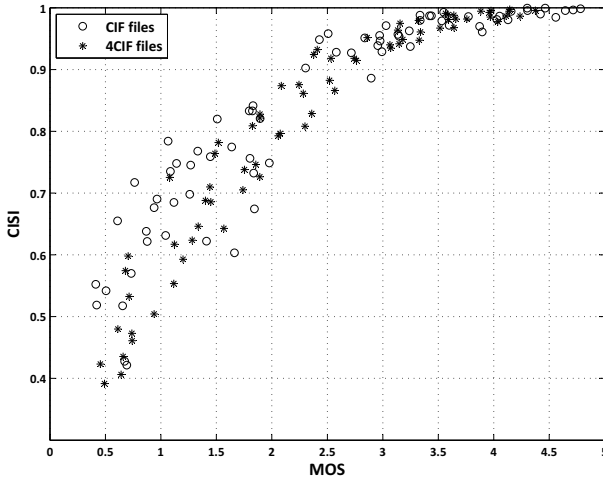
Fig. 2. Scatter plot of the CISI metric versus subjective scores for CIF and 4CIF files from the EFPL-PoliMI dataset
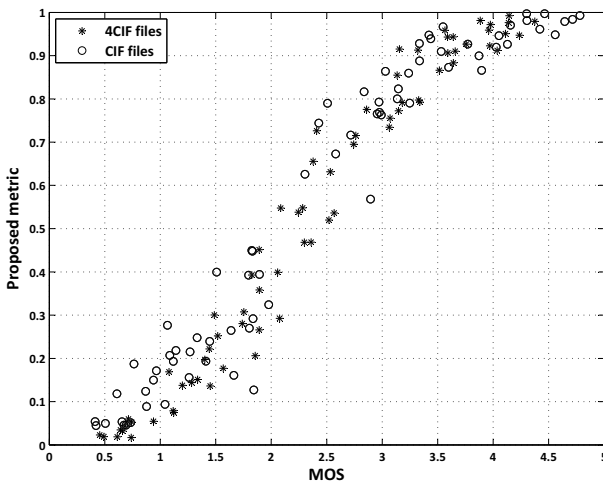
Fig. 3. Scatter plot of the proposed metric versus subjective scores for CIF and 4CIF files from the EFPL-PoliMI dataset

6   Conclusions

Proposed Combined Video Similarity metric leads to very high values of the linear correlation with subjective scores with only slight dependence on the video resolution. It may also be applied in a simplified form using nearly optimal values of the exponents but the values closer to the results of the

optimisation for 4CIF files are recommended due to observed better performance of all metrics for this resolution. Since the quality assessment of low resolution video is not an easy task and the importance of such sequences decreases, further verification and possible modifications of the proposed metric should be conducted using High-Definition video files e.g. using the LIVE Mobile Video Quality Database.

References

1. Wang, Z., Bovik, A.: A universal image quality index. IEEE Signal Proc. Letters 9(3), 81–84 (2002)
2. Wang, Z., Bovik, A., Sheikh, H., Simoncelli, E.: Image quality assessment: From error measurement to Structural Similarity. IEEE Trans. Image Proc. 13(4), 600–612 (2004)
3. Wang, Z., Simoncelli, E., Bovik, A.: Multi-Scale Structural Similarity for image quality assessment. In: Proc. 37th IEEE Asilomar Conf. on Signals, Systems and Computers (2003)
4. Forczmański, P., Furman, M.: Comparative Analysis of Benchmark Datasets for Face Recognition Algorithms Verification. In: Bolc, L., Tadeusiewicz, R., Chmielewski, L.J., Wojciechowski, K. (eds.) ICCVG 2012. LNCS, vol. 7594, pp. 354–362. Springer, Heidelberg (2012)
5. Ponomarenko, N., Lukin, V., Zelensky, A., Egiazarian, K., Carli, M., Battisti, F.: TID2008 – a database for evaluation of full-reference visual quality assessment metrics. Advances of Modern Radioelectronics 10, 30–45 (2009)
6. Larson, E., Chandler, D.: Most apparent distortion: full-reference image quality assessment and the role of strategy. Journal of Electronic Imaging 19(1), 011006 (2010)
7. Sheikh, H., Wang, Z., Cormack, L., Bovik, A.: LIVE image quality assessment database release 2 (2005), `http://live.ece.utexas.edu/research/quality`
8. Seshadrinathan, K., Soundararajan, R., Bovik, A., Cormack, L.: Study of Subjective and Objective Quality Assessment of Video. IEEE Trans. Image Proc. 19(6), 1427–1441 (2010)
9. Moorthy, A., Choi, L., de Veciana, G., Bovik, A.: Mobile Video Quality Assessment Database. In: Proc. IEEE ICC Workshop on Realizing Advanced Video Optimized Wireless Networks (2012)
10. Moorthy, A., Choi, L., Bovik, A., de Veciana, G.: Video Quality Assessment on Mobile Devices: Subjective, Behavioral and Objective Studies. IEEE J. Selected Topics in Signal Proc. 6(6), 652–671 (2012)
11. De Simone, F., Tagliasacchi, M., Naccari, M., Tubaro, S., Ebrahimi, T.: A H.264/AVC video database for the evaluation of quality metrics. In: Proc. IEEE Int. Conf. Acoustics Speech Signal Processing, pp. 2430–2433 (2010)
12. Sheikh, H., Bovik, A., de Veciana, G.: An information fidelity criterion for image quality assessment using natural scene statistics. IEEE Trans. Image Proc. 14(12), 2117–2128 (2005)
13. Sheikh, H., Bovik, A.: Image information and visual quality. IEEE Trans. Image Proc. 15(2), 430–444 (2006)

14. Zhang, L., Zhang, L., Mou, X., Zhang, D.: FSIM: A Feature Similarity index for image quality assessment. IEEE Trans. Image Proc. 20(8), 2378–2386 (2011)
15. Okarma, K.: Combined full-reference image quality metric linearly correlated with subjective assessment. In: Rutkowski, L., Scherer, R., Tadeusiewicz, R., Zadeh, L.A., Zurada, J.M. (eds.) ICAISC 2010, Part I. LNCS (LNAI), vol. 6113, pp. 539–546. Springer, Heidelberg (2010)
16. Okarma, K.: Video quality assessment using the combined full-reference approach. In: Choraś, R.S. (ed.) Image Processing and Communications Challenges 2. AISC, vol. 84, pp. 51–58. Springer, Heidelberg (2010)
17. Okarma, K.: Combined Image Similarity Index. Optical Review 19(5), 349–354 (2009)

Time-Frequency Analysis of Image Based on Stockwell Transform

Ryszard S. Choraś

Department of Telecommunications, Computer Science & Electrical Engineering
University of Technology & Life Sciences
85-796 Bydgoszcz, S. Kaliskiego 7
Poland
`choras@utp.edu.pl`

Summary. The time-frequency representation (TFR) provides a powerful method for identification of the non-stationary of the signals. The paper describes the basic principle of Stockwell Transform and approach to texture image feature extraction based on 2D discrete orthonormal Stockwell transform.

1 Introduction

Conventional Fourier Transform is a linear operator that maps the signal into a set of frequency component but not show where in time these components occur. It is good representation for stationary signal since the frequency components of the stationary signal do not change with time. In many applications the signals are non-stationary and conventional Fourier Transform might not be suitable to analyze these real signals. In this case signal have time dependent for their frequency and phase information. Such signals are best described by a time-frequency representation (TFR) which show haw the energy of the signal is distributed over 2D time-frequency (time and frequency) space.

Dennis Gabor [3] proposed expansion, that any signal could be expressed as a summation of mutually orthogonal time-shift and frequency-shift Gaussian function. Gabor expansion is one kind of sampled Short Time Fourier Transform ($STFT$). $STFT$ uses sliding window to get the local signal and then transform this signal into frequency domain (Fig. 1). The $STFT$ has a disadvantage because the window is frequency-independent with its width being determined by the user defined parameter σ. Solutions of this problem is modifying the window using frequency-dependent Gaussian time windows.

The ST-transform, introduced by Stockwell et al. [1, 2], which combines the separate strengths of the $STFT$ and the continuous wavelet transforms CWT, has provided an alternative approach to process the non-stationary
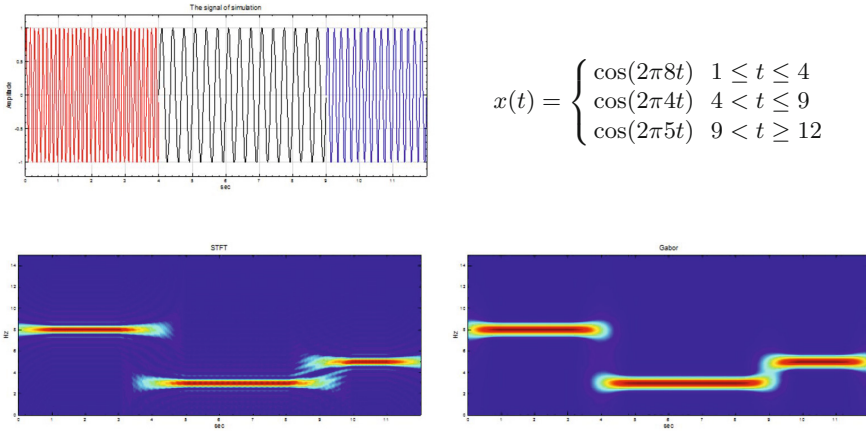
$$x(t) = \begin{cases} \cos(2\pi 8t) & 1 \le t \le 4 \\ \cos(2\pi 4t) & 4 < t \le 9 \\ \cos(2\pi 5t) & 9 < t \ge 12 \end{cases}$$

Fig. 1. *STFT* and Gabor transform as a special case of *STFT* of the signal $x(t)$

signals. The *ST* decomposes a signal into temporal (τ) and frequency (f) components. It employs a variable window length. The frequency-dependent window function produces higher frequency resolution at lower frequencies, while at higher frequencies, sharper time localization can be achieved.

2 *ST*-Transform

2.1 Continuous *ST*-Transform

The S-transform of a time signal $x(t)$ is:

$$S(\tau, f) = \int_{-\infty}^{\infty} x(t) \frac{|f|}{2\pi} e^{\left(\frac{(t-\tau)^2}{2\sigma^2}\right)} e^{-i2\pi ft} dt = A(\tau, f) e^{i\theta(\tau, f)} \qquad (1)$$

where f is the frequency and t and τ are time variables, σ is scale factor and $\sigma = \frac{1}{|f|}$; A is an amplitude factor and $A = (\tau, f)$; $e^{i\theta(\tau, f)}$ is a phase factor. The *ST* decomposes a signal into temporal (τ) and frequency (f) components. The normalizing factor $\frac{|f|}{\sqrt{2}}$, in eq.(1) ensures that, when integrated over all τ, $S(\tau, f)$ converges to $X(f)$, the Fourier transform of $x(t)$:

$$\int_{-\infty}^{\infty} S(\tau, f) d\tau = \int_{-\infty}^{\infty} x(t) e^{-i2\pi ft} dt = X(f) \qquad (2)$$
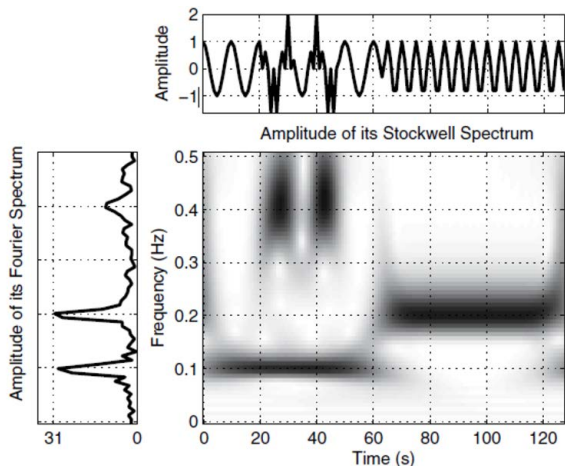
Fig. 2. Time-frequency representation of the Stockwell transform

2.2   The Discrete ST-Transform

The discrete version of ST-transform for $n \neq 0$, where $X[.]$ is the DFT of $x[.]$ is given as follows:

$$S[k,n] = \sum_{m=0}^{N-1} X[m+n] e^{\frac{2\pi^2 m^2}{n^2}} e^{\frac{i2\pi mk}{N}} = A[k,n] e^{(-k,\frac{n}{N})} \tag{3}$$

where:

$x[k], \;\; k = 0, 1, , N-1$ denote a discrete time series,
$f \to \frac{n}{N}$ and $\tau \to k$,
$A(k, \frac{n}{N})$ is magnitude factor of discrete ST-transform and $e^{(-k,\frac{n}{N})}$ is phase factor of discrete ST-transform.
For the $n = 0$, $S[k,0] = \frac{1}{N} \sum_{m=0}^{N-1} x[m]$ analogous to the DC value of the FT. From eq.(3), it is obvious that the ST is an overcomplete representation. For a signal of length N, there are N^2 Stockwell coefficients, and each one takes $\mathcal{O}(N)$ to compute. Hence, computing all N^2 coefficients of the ST has computational complexity $\mathcal{O}(N^3)$.

2.3   Two-Dimensional ST-Transform

Stockwell Transform (ST) is a new linear time-frequency representation method, time-frequency resolution of which changes with frequency. For a two-dimensional image $f(x,y)$ the transformation formula of two-dimensional DST is as follows:

$$S(u, v, f_u, f_v) = \int\limits_{-\infty}^{\infty} \int\limits_{-\infty}^{\infty} f(x, y) \frac{|f_u||f_v|}{2\pi} \cdot \exp\left[\frac{(u-x)^2 f_u^2 + (v-y)^2 f_v^2}{2}\right] \cdot$$

$$\cdot \exp[-i2\pi(f_u x + f_v y)] dx dy \quad (4)$$

where u and v are the shift parameters controlling the center position of Gaussian windows on the x-axis and y-axis, respectively, while f_u and f_v ($f_u \neq 0; f_v \neq 0$) are frequencies related to the scale parameters in two directions, which respectively control the spatial extension of the window in x and y directions.

Integrates $S(u, v, f_u, f_v)$ over the u and v gives 2D Fourier transform (2D-FT)

$$F(f_u, f_v) = \int_{-\infty}^{\infty} \int_{-\infty}^{\infty} S(u, v, f_u, f_v) du dv \quad (5)$$

and computed 2D inverse Fourier transform (2D-IFT) of eq. (5) is obtained original signal.

The output of the ST-Transform is a matrix whose rows is concerning to time and whose columns is concerning to frequency. This matrix called the ST-matrix contains all the values of the complex valued ST-Transform output. The computation of the ST-Transform is efficiently implemented using the convolution theorem and FFT.

$S(u, v, f_u, f_v)$ is a four dimensional S-matrix. For any point (u, v) in image, its 2-DST coefficients obtained by eq. (4) are a two dimensional S-matrix expressed as $S_{u,v}(f_u, f_v)$.

2.4 2D Discrete Orthonormal ST-Transform (DOST)

One main drawback of the ST is the amount of information redundancy in its resulting time-frequency representation. To improve its computational efficiency, the discrete orthonormal Stockwell transform ($DOST$) is proposed [4, 6]. The discrete, orthonormal ST ($DOST$) provides a spatial frequency representation similar to the DWT [6].

The 2D-$DOST$ of a $N \times N$ image $f(x, y)$ is defined as

$$S(u, v, f_u, f_v) = \frac{1}{\sqrt{2^{p_x + p_y - 2}}} \cdot$$

$$\cdot \sum_{m=-2^{p_x-2}}^{2^{p_x-2}-1} \sum_{n=-2^{p_y-2}}^{2^{p_y-2}} F(m + v_x, n + v_y) e^{2\pi i \left(\frac{mu}{2^{p_x-1}} + \frac{nv}{2^{p_y-1}}\right)}$$

$$(6)$$

where:

- $v_x = 2^{p_x-1} + 2^{p_x-2}$; $v_y = 2^{p_y-1} + 2^{p_y-2}$ are the horizontal and vertical frequency;
- p_x and $p_y = 0, 1, \ldots, \log(N-1)$
- $F(m, n)$ - the Fourier transform of the image $f(x, y)$.

Inverse transform for 2D-$DOST$ is defined using following equations:

$$F(m, n) = \sqrt{2^{p_x + p_y - 2}} \sum_{m=-2^{p_x-2}}^{2^{p_x-2}-1} \sum_{n=-2^{p_y-2}}^{2^{p_y-2}} S(m-v_x, n-v_y) e^{-2\pi i \left(\frac{mu}{2^{p_x-1}} + \frac{nv}{2^{p_y-1}} \right)}$$

(7)

$$f(x, y) = \frac{1}{N^2} \sum_{m=-\frac{N}{2}}^{\frac{N}{2}-1} \sum_{n=-\frac{N}{2}}^{\frac{N}{2}-1} F(m, n) e^{\frac{2\pi i (mx+ny)}{N}}$$

(7a)

The total number of points in the $DOST$ result, and in the input image, are the same.

By integrating over all values p_x, p_y, a local spatial frequency domain consists of the positive and negative frequency components from $(f_u, f_v) = 0$ (DC component) to the $(f_u, f_v) = (\frac{N}{2}, \frac{N}{2})$ can be built.

The $DOST$ gives the information about the frequencies (f_u, f_v) in bandwidth of $2^{p_x-1} \times 2^{p_y-1}$ frequencies.

3 Feature Extraction

The $DOST$ matrix is divided on blocks of the size $k \times l$. For each block the statistical measures such as mean, variance, skewness, kurtosis and energy are computed as follow

$$mean = \frac{1}{k \times l} \sum_{x=1}^{k} \sum_{y=1}^{l} |S(x, y, p_x, p_y)|$$

(8)

$$std = \frac{1}{k \times l} \sum_{x=1}^{k} \sum_{y=l}^{N} \sqrt{(|S(x, y, p_x, p_y)| - mean)^2}$$

(9)

$$skewness = \frac{1}{k \times l} \sum_{x=1}^{k} \sum_{y=1}^{l} \left(\frac{S(x, y, p_x, p_y) - mean}{std} \right)^3$$

(10)
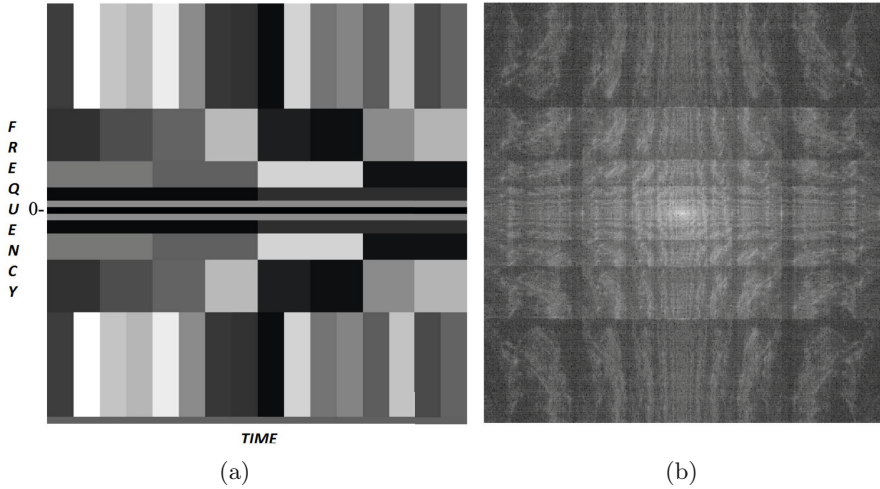
Fig. 3. 2-D visualization of the *DOST* coefficients (a) and the logarithm of the magnitude of the 2-D *DOST* coefficients for a image *Lena* (b)

$$energy = \frac{1}{k \times l} \sum_{x=1}^{k} \sum_{y=1}^{l} \left(|S(x, y, p_x, p_y)| \right)^2 \tag{11}$$

where $S(x, y, p_x, p_y)$ is magnitude of *DOST* for frequency (p_x, p_y) in image point (x, y).

Then, feature vector $FV(p_x, p_y)$ is

$$FV(p_x, p_y) = \{mean_1, \ldots, mean_T, std_1, \ldots, std_T,$$
$$skewness_1, \ldots, skewness_T, energy_1, \ldots, energy_T\} \tag{12}$$

where T is the block number.

The feature vector presents the statistical parameters of the spectral frequency pattern of the image in the various bandwidths.

4   Conclusion

The 2D-*ST*-Transform is more convenient to measure of image texture than other time-frequency transforms, such as the Gabor transform. The *ST*-Transform provides good frequency localization, better time and frequency resolution at low frequencies and higher time resolution at high frequencies. The *ST*-Transform properties make it a good choice for medical image texture analysis.

References

1. Stockwell, R.G., Mansinha, L., Lowe, R.L.: Localization of the Complex Spectrum: the S-transform. IEEE Transactions on Signal Processing 17(4), 998–1001 (1996)
2. Stockwell, R.G.: S-transform Analysis of Gravity Wave Activity from a Small Scale Network of Airglow Imagers. Ph.D. Thesis, Western Ontario University, Ontario, Canada (1999)
3. Gabor, D.: Theory of communication. J. Inst. Elect. Eng. 93, 429–459 (1946)
4. Stockwell, R.G.: A basis for efficient representation of the S-Transform. Digital Signal Processsing 17, 371–393 (2007)
5. Wang, Y., Orchard, J.: Fast Discrete Orthonormal Stockwell Transform. SIAM J. Science Computation 31(5), 4000–4012 (2009)
6. Drabycz, S., Stockwell, R.G., Mitchell, J.R.: Image Texture Characterization Using the Discrete Orthonormal S-Transform. Journal of Digital Imaging 22(6), 696–708 (2009)
7. Badrinath, G.S., Gupta, P.: Stockwell transform based palm-print recognition. Applied Soft Computing 11, 4267–4281 (2011)
8. Djurovic, I., Sejdic, E., Jiang, J.: Frequency-based window width optimization for S-transform. Int. J. Electron. Commun. 62, 245–250 (2008)
9. Goodyear, B.G., Zhu, H., Brown, R.A., Mitchell, R.: Removal of phase artifacts from fMRI data using a Stockwell transform filter improves brain activity detection. Magn. Resonance Med. 51, 16–21 (2004)

Real-Time Recognition of Selected Karate Techniques Using GDL Approach

Tomasz Hachaj[1], Marek R. Ogiela[2], and Marcin Piekarczyk[1]

[1] Pedagogical University of Krakow,
  2 Podchorazych Ave, 30-084 Krakow, Poland
  `tomekhachaj@o2.pl, marp@ap.krakow.pl`
[2] AGH University of Science and Technology,
  30 Mickiewicza Ave, 30-059 Krakow, Poland
  `mogiela@agh.edu.pl`

Summary. In this paper will be presented a new approach for recognition and interpretation of several karate techniques used specially defined Gesture description language (GDL). The novel contribution of this paper is validation of our new semantic Gesture Description Language classifier on several basic Karate techniques recorded with set of Kinect devices. We also present the calibration procedure that enables integration of skeleton data from set of tracking devices into one skeleton what eliminates many segmentation and tracking errors. The data set for our research contains 350 recorded sequences of qualifies professional sport (black belt) instructor, and master of Okinawa Shorin-ryu Karate. 83% of recordings were correctly classified. The whole solution runs in real-time and enables online and offline classification.

1 Introduction

Real-time recognition of complex body gestures is a difficult task. Each gesture might be consisted of subtle motions of many body muscles. In case of real Karate techniques the additional difficulty is the fact that skilled sportsmen performs his movements very fast. Because of movement speed and complexity many typical methods that are based on analysis of trajectories like random forest approach [1], fuzzy neural networks [2], Bayesian network [3] or Full Body Interaction Framework [4] might be ineffective without large training data set and expensive motion-capture hardware [5]. Lately in [6] a solution aims at automatically recognizing sequences of complex karate movements and giving a measure of the quality of the movements performed has been proposed. The proposed system is constituted by four different modules: skeleton representation (real-time tracking of automatically segmented body key points with OpenNI software), pose classification (prior k-means

clustering on test data set, then with a multi-class Support Vector Machine), temporal alignment (Dynamic Time Warping - DTW), and scoring (score is obtained by regression among human judgments and the normalized DTW distances). The proposed system was tested on a set of different punch, kick and defense karate moves executed starting from the simplest up to sequences in which the starting stances is different from the ending one. The dataset has been recorded using a single Microsoft Kinect.

The novel contribution of this paper is validation of our new semantic classifier on various traditional Karate techniques recorded with set of Kinect devices (with frame capture frequency 30Hz). The proposed classifier uses significantly different approach than previously reported methods. We also present the calibration procedure that enables integration of skeleton data from set of tracking devices into one skeleton what eliminates many segmentation and tracking errors. The whole solution runs in real-time and enables online and offline classification. None of results presented in this paper has been previously published.

2   Materials and Methods

In this paragraph we will describe the classifier, hardware and software of data acquisition system and data set itself.

2.1   GDL and GDL Script

GDL (Gesture Description Language) is classifier that uses semantic description of particular body position and movements. The general GDL's methodology was introduced in our previous papers [7], [8]. In this approach human body is partitioned into twenty so-called body joints (Fig. 1) that together create so-called skeleton. Body positions can be ordered in sequences and sequences builds body gestures. The body position is described as relative or absolute position of selected joints. Descriptions are organized in rules and rules are created in LALR-1 grammar called GDL script. The set of rules builds knowledge base that is used by inference engine that runs forward-chaining inference schema.

2.2   Hardware Set-Up and Calibration

The single Kinect device is capable to measure distance between camera lean and object that is in the field of view. The standard software (Kinect SDK 1.6) can be used for real-time tracking of set o body joints on user body (Figure 1). The body joints are automatically segmented and no markers placed on ones body are required. If one joint is covered by another body part that joint cannot be directly tracked and its position is estimated. However
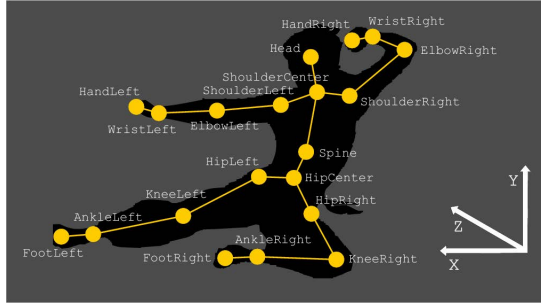
Fig. 1. Body joints in Microsoft Kinect SDK 1.6 used by GDL script. The SDK returns coordinates of body joint in three-dimensional space using right-handed coordinate system.

estimation rarely predicts the correct position of missing body part. In order to overcome this problem we propose our novel architecture of data acquisition system.

The data acquisition was performed by system consisted of three Kinect controllers connected to two standard PC computers - Figure 2. We had to use more than one PC because of USB bandwidth limitation. Recording was made with our software that records incoming skeleton data (positions of body joints). The acquisitions made on different machines were synchronized by synchronization server.
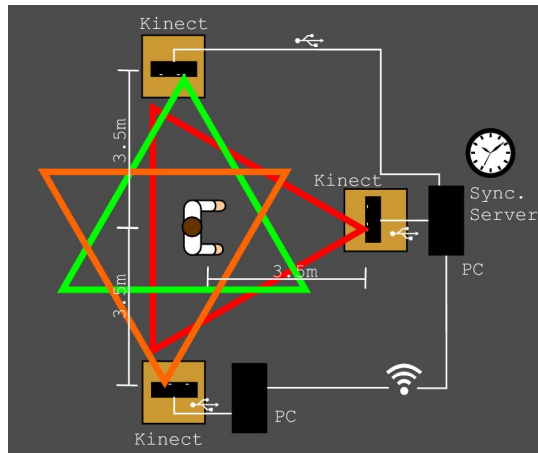
Fig. 2. Hardware set up for karate session recording

Each Kinect measure distance to observed point in its own right-handed Cartesian frame situated relatively to sensor orientation. Because of that same point V has different coordinates (1) and (2) relatively to each pair of devices.

$$\overline{v'} = [x', y', z', 1] \tag{1}$$

$$\overline{v} = [x, y, z, 1] \tag{2}$$

Our task now is to map all of those points to the same coordinate system. Let us assume that a Cartesian frame that represents orientation of each Kinect was translated and rotated around y (vertical) axis relatively to each other frame. That means there are four degrees of freedom (three for translation, one for rotation). Knowing that the linear transform that map coordinates of a point represented by vector $\overline{v'}$ in one coordinate system to coordinates in another has form of following matrix:

$$\overline{v'} \cdot \begin{bmatrix} cos(\beta) & 0 & -sin(\beta) & 0 \\ 0 & 1 & 0 & 0 \\ sin(\beta) & 0 & cos(\beta) & 0 \\ t_x & t_y & t_z & 1 \end{bmatrix} = \overline{v} \tag{3}$$

After multiplication the vector $\overline{v'}$ by matrix we get:

$$y' + t_y = y \tag{4}$$

$$x' \cdot cos(\beta) + z' \cdot sin(\beta) + t_x = x \tag{5}$$

$$-x' \cdot sin(\beta) + z' \cdot cos(\beta) + t_z = z \tag{6}$$

As can be seen in (4) translation along y-axis (t_y) can be found when we know coordinates of single point in both frames. To find next four unknown coefficients in (5) and (6) we need to know coordinates of two points in both frames, but one can be the same point as we used in (4). The following linear system has to be solved:

$$A \cdot \overline{b}^T = \overline{x}^T \tag{7}$$

$$\overline{b} = [cos(\beta), sin(\beta), t_x, t_z]; A = \begin{bmatrix} x'_1 & z'_1 & 1 & 0 \\ z'_1 & -x'_1 & 0 & 1 \\ x'_2 & z'_2 & 1 & 0 \\ z'_2 & -x'_2 & 0 & 1 \end{bmatrix}; \overline{x} = [x_1, z_1, x_2, z_2] \tag{8}$$

Where indexes 1 and 2 marks known coordinates of the first and the second point.

To calibrate the three sensors of our system we solved (7) for two pairs of Kinects recalculating coordinates to the frame of device situated in front of observed sportsmen. Because depth sensor of devices generates distortions that make calculation of distance unstable between incoming frames (fluctuation has amplitude of several centimeters) we decided not to correct any additional potential distortions.

If front Kinect does not "see" particular body joint, system checks if this joint is visible by another device. If yes our software takes coordinates measured by that adjective device. If more than two devices have detected same joint, coordinates are taken from camera that is closest to observed point.

2.3   Data Set and Classifier Fitting

The data set for our research are recordings of black belt instructor (sensei) in Okinawa Shorin-ryu Karate, 3 dan (sandan) that performs seven different basic techniques: four static positions (Moto-dachi, Zenkutsu-dachi, Shiko-dachi and Naihanchi-dachi), two blocks (Gedan-barai and Age-uke) and one kick (Mae-geri). The instructor has indicated essential aspects of each technique (starting and ending position of limbs and movement trajectory). That information was consisted in GDL script that we created for recognition. Each gesture was partitioned into key-frames (Figure 3) that was later verified and accepted by instructor. Also instructor was present during final validation of method.

Fig. 3. Example karate key-frames for GDL script. Movements are separated into stages, each stage is a key-frame used in semantic description. In this picture Mae-geri begins with Moto-dachi but in our experimental recordings set it started from different, "neutral" position.

Because of space limitation of this paper we cannot show all rules of GDL script that was created to fulfill the classification tasks. Set of rules that recognize Mae-geri is presented in Appendix.

3 Results

Table 1 summarizes the classification results obtained from our experiments. The description in first column is the actual technique (or group of techniques) that is present in particular recording. Each technique (or group of techniques) was repeated 50 times. Symbol + means that particular recording consisted of more than one technique. Description in first row is classification results. Last row sums up percentage of correct classifications of particular technique.

Table 1. The classification results of our experiment

	Moto -dachi	Zenkutsu -dachi	Shiko -dachi	Naihanchi -dachi	Gedan -barai	Age -uke	Mae -geri	Not classified
Moto -dachi	50	1	0	0	6	0	0	0
Zenkutsu -dachi	1	37	0	0	1	0	0	12
Shiko-dachi +gedan-barai	0	0	37	0	29	0	0	13+21=34
Naihanchi -dachi	0	0	0	50	0	0	0	0
Gedan-barai Zenkutsu + -dachi	0	49	0	0	36	0	0	1+14=15
Age-uke +Moto-dachi	50	0	0	0	0	43	0	0+7=7
Mae-geri	4	0	0	0	0	0	34	16
%	100.0%	86.0%	74.0%	100.0%	65.0%	86.0%	68.0%	16.8%

Because several karate techniques can be present in same movement sequence we investigated if actual technique/techniques was/were classified. If yes that case was called *correct classification*. If technique was not classified and was not mistaken with similar one (like Moto-dachi which is similar to Zenkutsu-dachi) that case was called *not classified*. If technique was mistaken with similar one that case was called *misclassified*. Those three sums up to 100%. If technique was correctly classified but additional - actually not present - behavior was classified that case was called *excessive misclassification*. According to this terminology 83% of recordings was correctly classified, 16.8% was not classified and 0.2% was misclassified. Excessive misclassification was at the level of 2.4%.

4   Discussion

Classification errors in our test set were cased by inaccuracies of joints segmentation done by Kinect SDK software. If particular part of body is covered by another one it is probable that the covered joint position would be wrongly estimated what affect final classification. The integration of recordings from three Kinects situated on different angles to karateka limits number of body positions from that particular body parts are invisible. The low value of *excessive misclassification* and *misclassified* relatively to *not classified* shows that GDL-based classification rather does not classify sequence that is too deformed to fit script description to another class. This is extremely important in case of classifiers that are capable to recognise many classes in the same time in one recording like GDL can.

5   Conclusion

As we have proved the proposed methodology is capable to classify in real time complex movement sequences that are performed faster than typical common-life gestures. What is more important those type of gestures were recorded by relatively cheap, off-the-shelf multimedia devices. Our approach has many advantages over state of the art methods: the GDL classifier does not require any training data set - GDL scripts can be easily thought and written for any movement sequence that can be separated into set of key frames. Also GDL classifier can recognize all scripted gestures sequences that are consisted in one recording in the same time. In order to add new technique to be recognized it is not necessary to retrain the whole classifier but just to add another set of rules to GDL script. The drawback of GDL is that the description is time constrained (unlike DTW). Also proper selection of key frames and body joints relation might require the consultation with expert. However it should be remembered that even "full automatic" methods of classification require the expert knowledge about relevant features that are consisted in data. Our future plan is to expand GDL classfier on other Karate techniques and to validate that method on recordings of sportsmen and sportswomen with different age, body proportions and abilities.

References

1. Vinayak, S., Murugappan, H.R., Ramani, L.K.: Shape-It-Up: Hand gesture based creative expression of 3D shapes using intelligent generalized cylinders. Computer-Aided Design 45, 277–287 (2013)

2. Elakkiya, R., Selvamai, K., Velumadhava Rao, R., Kannan, A.: Fuzzy Hand Gesture Recognition Based Human Computer Interface Intelligent System. UACEE International Journal of Advances in Computer Networks and its Security 2(1), 29–33 (2012)
3. Du, Y., Chen, F., Xu, W., Zhang, W.: Activity recognition through multi-scale motion detail analysis. Neurocomputing 71, 3561–3574 (2008)
4. Kistler, F., Endrass, B., Damian, I., Dang, C.T., André, E.: Natural interaction with culturally adaptive virtual characters. Journal on Multimodal User Interfaces 6(1-2), 39–47 (2012)
5. Ntouskos, V., Papadakis, P., Pirri, F.: A Comprehensive Analysis of Human Motion Capture Data for Action Recognition. In: Proc. VISAPP (1), pp. 647–652 (2012)
6. Bianco, S., Tisato, F.: Karate moves recognition from skeletal motion. In: Proc. SPIE 8650, Three-Dimensional Image Processing (3DIP) and Applications (2013)
7. Hachaj, T., Ogiela, M.R.: Recognition of human body poses and gesture sequences with gesture description language. Journal of Medical Informatics and Technology 20, 129–135 (2012) ISSN 1642-6037
8. Hachaj, T., Ogiela, M.R.: Semantic description and recognition of human body poses and movement sequences with Gesture Description Language. In: Kim, T.-h., Kang, J.-J., Grosky, W.I., Arslan, T., Pissinou, N. (eds.) MulGraB, BSBT and IUrC 2012. CCIS, vol. 353, pp. 1–8. Springer, Heidelberg (2012)

Appendix

```
//GDL script for Mae-geri recognition
//Both legs are in the same level above the ground
//Figure 3 Mae-geri stage 1
RULE ABS(AnkleRight.y[0] - AnkleLeft.y[0]) < 50 THEN MaeStart
//Right knee in the line with right hip, bended right knee
//Figure 3 Mae-geri stage 2
RULE (HipRight.y[0] - KneeRight.y[0]) < 100 & ABS(KneeRight.a[0] - 90)
< 30 THEN MaeMiddleRight
//Kick with right foot - Figure 3 Mae-geri stage 3
RULE (HipRight.y[0] - KneeRight.y[0]) < 200 & KneeRight.a[0] > 150 THEN
MaeEndRight
//Left knee in the line with left hip, bended left knee
//Figure 3 Mae-geri stage 2
RULE (HipLeft.y[0] - KneeLeft.y[0]) < 100 & ABS(KneeLeft.a[0] - 90) < 30
THEN MaeMiddleLeft
//Kick with left foot - Figure 3 Mae-geri stage 3
RULE (HipLeft.y[0] - KneeLeft.y[0]) < 200 & KneeLeft.a[0] > 150 THEN
MaeEndLeft
//Proper sequence of Mae-geri stages
RULE (sequenceexists("[MaeMiddleRight,1][MaeStart,1]") & MaeEndRight)
| (sequenceexists("[MaeMiddleLeft,1][MaeStart,1]") & MaeEndLeft) THEN
Mae-geri
```

2DKLT-Based Color Image Watermarking

Paweł Forczmański

West Pomeranian University of Technology, Szczecin,
Faculty of Computer Science and Information Technology,
Żołnierska Str. 52, 71–210 Szczecin, Poland
`pforczmanski@wi.zut.edu.pl`

Summary. The paper presents a digital image watermarking algorithm realized by means of two-dimensional Karhunen-Loeve Transform (2DKLT). The information embedding is performed in the two-dimensional specturm of KLT. Employed two-dimensional approach is superior to standard, one-dimensional KLT, since it represents images respecting their spatial properties, resulting in a lower noise and better adaptation to the image characteristics. The principles of 2DKLT are presented as well as sample implementations and experiments, which were performed on benchmark images. We propose a measure to evaluate the quality and robustness of the watermarking process. Finally, we present a set of experiments related to the color-space, embedding variants and their parameters.The results show that the 2DKLT employed in the above application gives obvious advantages in comparison to certain standard algorithms, such as DCT, FFT and wavelets.

1 Introduction

The problem of hiding certain content into some other data is called *steganography* and its modern applications include embedding watermarks and copyright information into music, images and videos (so called digital rights management – DRM), hiding secret messages in order to transfer them over the Internet, protect data against alteration, etc.[1, 2]. Many algorithms have been developed so far, however, not all all of them are usable and robust enough in practical applications. The main issue is if the carrier (cover object) is altered, the watermark should be preserved. This problem often exists in cases when data have to be protected against unauthorized usage or modification. In literature there are many general approaches aimed at still image steganography and watermarking [1, 2, 3, 4, 5, 6]. Almost all such methods work in either space domain [4] or in certain spectrum domain (FFT, DFT, DCT, Wavelets [3]).

One of the most popular yet not very effective method is a least significant bit (LSB) insertion [2], which alters the least important part of the cover object. The main problem with LSB and other methods is the low robustness to typical visual manipulations, e.g. changes of intensity, contrast and focus as well as lossy re-compression and framing. On the other hand, typical transformation-based methods introduce high level of distortions into the cover image and are sensitive to lossy compression. It means we need a compromise between high robustness to attacks and low visibility.

The natural solution to above stated problems is the usage of transformation that adapts to the characteristics of input data. Many transformation methods have been proposed in the literature, most of them based on operations such as Karhunen-Loeve Transform (KLT), Discrete Cosine Transform (DCT), Discrete Fourier Transform (DFT), Linear Discriminant Analysis (LDA), Discrete Wavelet Transform (DWT), etc. The literature survey shows that in case of images presenting real scenes one of the most promising is KLT since it uses basis functions optimally adjusted to actual data characteristic. The KLT also known as Principal Components Analysis (PCA) is a technique widely used to reduce multidimensional data sets to lower dimensions for analysis, compression or classification [7]. The PCA/KLT involves the computation of eigenvalue decomposition or singular value decomposition of a data set, usually after mean centering [8]. However, it should be noted that using PCA/KLT for tasks such as pattern recognition or image processing can be challenging because it treats data as one-dimensional, when in fact they are two-dimensional. That is why almost all developed algorithms employ some sort of dimensionality pre-reduction discarding, in many cases, the spatial relations between pixels. One of the possible solutions is using two-dimensional transformation based on PCA (and KLT). The first algorithm from this group was presented in [9], where a novel, two-dimensional version of KLT for face recognition task was developed. An extension of this method (known as PCArc - for row and column representation) was presented in [10, 11]. Many current publications show that two-dimensional KLT (2DKLT) can be directly applied for high-dimensional data [10, 11] because it does not require any preliminary processing or additional reduction of dimensionality of input images. There are several works related to watermarking in the KLT domain, however they deal with one-dimensional representation [6, 12, 13] or process gray-scale images only [6].

In the further parts of the paper we show the main principles of 2DKLT together with the discussed application area - information embedding (watermarking). The experiments performed on the standard benchmark images gave satisfactory results, comparable to the other known approaches [1, 6, 12, 13].

2   Algorithm Description

2.1   Processing Scheme

Developed algorithm uses a two-dimensional version of Karhunen-Loeve Transform and redundant pattern encoding [4]. It consists of the following steps: 1. preparation of data – input image is being decomposed into blocks of equal size, a message is expanded into bit-wise sequence, 2. calculation of two-dimensional basis functions by means of PCA row/column, 3. transformation of blocks (2DKLT), 4. inserting a binary representation of a message according to the specified key, 5. inverse 2DKLT transformation, 6. joining blocks into a single image. The reverse algorithm used for extracting the message is based on the same general rules. In the beginning, the carrier image is being decomposed into blocks, which are transformed by means of known eigenvectors (calculated previously). Then the message fragments are being extracted from specific blocks' elements according to the known key. Finally, the bit-wise extended message is compacted into graphical form for a convenient readout.

In order to unnoticeably embed a message into the cover image, it should be modified in a way that it will contain small differences similar to the original object. That is why we operate in KLT spectrum, in order to spread the change in several pixels. Thus, the watermark is being expanded into a longer sequence of small values e.g. binary ones. Then we have to generate a key which will determine where in the transformed blocks the elements of expanded watermark have to be placed. The key is a sequence of offsets from the origin of each block. It is important to place the watermark into the "middle-frequency" part of each block as a compromise between output image quality and robustness to intentional manipulations (see first matrix in the Fig. 1). This rule is especially significant in a case of images containing large number of small details, which helps keeping all the changes imperceptible. The only noticeable difference can be observed in the areas of uniform color.

2.2   2DKLT Principles

Let us assume that the image I being processed is stored in a structure of $P \times Q \times R$ elements, containing R channels of $P \times Q$ matrices. We decompose each r-th channel into a set of K subimages (blocks) X_k with equal, constant dimensions $M \times N$, where $(M << P, N << Q)$. These blocks do not have common parts and do not overlap each other. They cover the whole image area. This approach is similar to JPEG/JFIF, where $M = N = 8$, which is a compromise between compression ratio and performance [14]. In a case being discussed here it is possible to use block of any size, even not square [11]. The algorithm uses PCA for row/column representation (PCArc) in order to calculate the eigenvectors and KLT in order to transform them [10]. In the

first step, for all blocks in the dataset we calculate mean block $\bar{X}$ and remove it from each individual block $\hat{X}_k = X_k - \bar{X}$.

In the next step we calculate two covariance matrices for both row and column representations of input blocks, which correspond to the variation of blocks in the set [9]: $\Sigma^{(r)} = \sum_k \hat{X}_k \hat{X}_k^T$ and $\Sigma^{(c)} = \sum_k \hat{X}_k^T \hat{X}_k$.

After solving the following equations $\Lambda^{(r)} = (V^{(r)})^T \Sigma^{(r)} V^{(r)}$ and $\Lambda^{(c)} = (V^{(c)})^T \Sigma^{(c)} V^{(c)}$ we get eigenvectors V and eigenvalues Λ matrices which will further serve as the transformation basis. Usually, this step requires a computer-based algorithm for computing eigenvectors and eigenvalues. Finally, for each block X_k in order to get its transformation Y_k the following operation is performed [10]: $Y_k = V^{(r)}(X_k - \bar{X})V^{(c)}$.

It should be noted that we do not perform any kind of dimensionality reduction here, hence the KLT coefficients preserve total information of blocks X_k. The transformation on blocks is the main operation for further steps described in the following sections.

2.3   Watermark Embedding/Recovering

The maximal size of a watermark is directly linked to the number of blocks (K), which are calculated from the proportion of image dimensions and block size. If we assume to have binary watermark, then one bit is embedded in one image subblock. So the size of the watermark is equal to the number of blocks. If the watermark is smaller than the number of blocks then it can be inserted in the cover image repeatedly. This approach is called redundant pattern encoding [4] and increases the robustness of the watermark to the intentional manipulations like compressing of filtering. There is also a possibility of inserting more than one bit in each block, however it decreases the robustness of the method.

The recovery algorithm, in a comparison to the embedding phase, is performed in the following order. In the first step we decompose the cover image into sub-blocks, which are further transformed using known eigenvectors (2DKLT) and finally, the appropriate part of a watermark is being extracted from KLT spectrum of each block. It is important to know the right eigenvectors as well as the key used to extract the exact watermark. If we do not know the key we still are able to extract the watermark (with the help of eigenvectors calculated straight form the cover image), but its exact content will be hard to guess.

As it was already written, there are several variants of information embedding. We investigated three variants, namely:

1. **Direct Bit Once** - one bit put in each block according to the key;
2. **Direct Bit Twice** - one bit put twice in each block according to the key;
3. **Direct Two Bits** - two bits put in each block according to the key;

The areas of alternation in each block are presented in Fig.1. The first block presents an area of middle frequencies which are especially suitable for

alternation, since they are responsible for least noticeable changes in the image. The second block in Fig.1 represents a variant of the embedding called Direct Bit Once, which changes single element in the chosen area according to the key. The change is done by substitution of original element $X(i,j)$ with a value equal to:

$$\tilde{X}(i,j) = \begin{cases} SX(i,j) & \text{if} \quad X(i,j) = 1 \\ -SX(i,j) & \text{if} \quad X(i,j) = 0 \end{cases} \tag{1}$$

The extraction of the watermark is done by checking the sign of the element in the KLT spectrum. If the extracted element is more (or equal) than zero, then the extracted bit of watermark is set to one. Otherwise, it is set to zero.

The third block in Fig. 1 represents a variant of the embedding called Direct Bit Twice, that changes two elements in the chosen area according to two independent keys. It was developed in order to increase the robustness of the embedding. The change is done by substitution of original elements $X(i_1, j_1)$ and $X(i_2, j_2)$ with a value calculated according to the Eq.1. The extraction of the watermark is done in the following manner. Both elements are extracted (according to the keys) and then added. If the sum is more (or equal) than zero, than the extracted bit is set to one. Otherwise it is set to zero.

The method called Direct Two Bits is similar to the above one. The main difference is the fact of coding two independent bits of the watermark in each block. Instead of doubling the embedded information, in each block, we put there two successive bits of the watermark. The extraction algorithm is also similar.
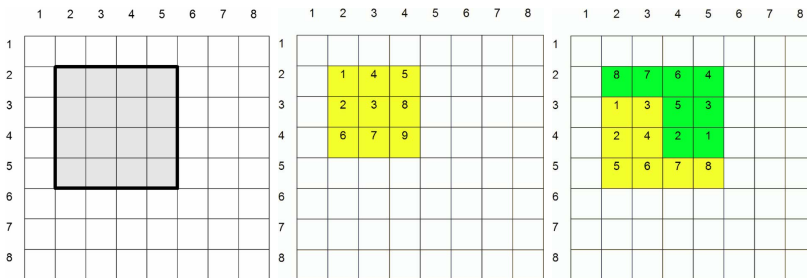
Fig. 1. KLT spectrum area being altered (left), Subarea chosen in Direct Bit Once (middle) and in Direct Bit Twice (right), respectively

2.4 Watermarking Quality/Robustness Evaluation

Three are two main measures of evaluating the quality and robustness of watermarking. They include Peak Signal-to-Noise Ratio and Cross-Correlation. Both are used in an independent manner [6, 12, 13] and can not give an

unequivocal answer. In order to evaluate the influence of parameters of presented process on image quality as well as the robustness of the watermarking procedure simultaneously we introduce the combined metrics. It employs cross-correlation coefficient calculated for original W and extracted watermark image $\tilde{W}$ and the Peak Signal-to-Noise Ratio of modified image $\tilde{I}$ vs. original one I:

$$D = PSNR(I, \tilde{I}) * log_{10}(Corr(W, \tilde{W})). \tag{2}$$

Such measure is capable of capturing both characteristics of watermarking process and help finding its practically useful parameters. In future, some more advanced image quality metrics (like [15]) may be used in order to reproduce the subjective characteristic of quality estimation.

3 Experiments

Developed algorithm and its prototype implementation have been investigated on sample color images of different origin and characteristic (see Fig. 2). To prove the robustness of the algorithm, several tests, according to the *de facto* standards, have been performed [1, 2]. They included 13 operations: geometrical transforms (scaling and rotation), lossy JPEG compression, noising (Gaussian, Poisson), changing the brightness and contrast of an image and finally convolution filtering with different masks.

Fig. 2. Images used for experiments: *Lena, Griffin, Ladybug* and the watermark

We investigated two aspects of the method:

1. selection of color space (single color channel) in which the watermark is embedded: RGB, HSB, YCbCr;
2. selection of watermark power $S \in 10, 25, 50, 75$;

The combined results of the experiments (mean results for all 13 attack types) are shown in Fig. 3. The lower row of the figure represents the normalized quality values for 4 different watermarking powers (S). As it can be seen, the best results were obtained for Y, G and V channels. However, when we consider the robustness to attacks, the results are quite different. The first row of the figure presents the combined metric D in dB. The higher the
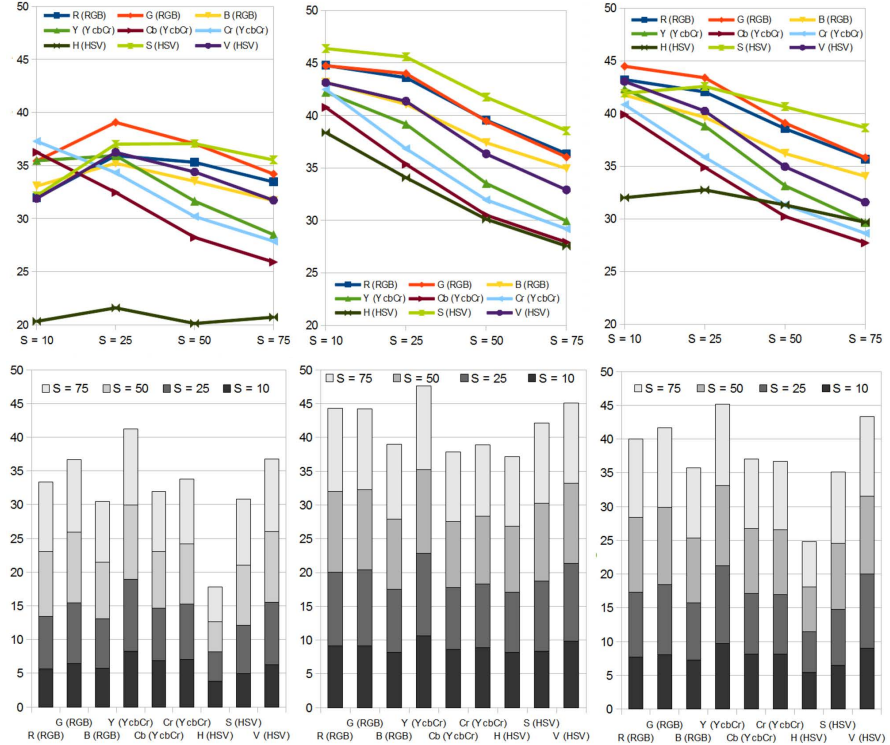
Fig. 3. The combined quality/robustness metric (upper row) and detailed color-space comparision in terms of joint PSNR (lower row) for *Lena, Griffin, Ladybug,* respectively

value, the better quality and the higher robustness to attacks, thus the best results give *Green* and *Saturation* channels (depending on the characteristics of images).

4 Summary

Algorithm presented here and its application area showed that the 2DKLT method can be a valuable basis for efficient color image watermarking. This approach makes it possible to hide a watermark in the so called cover image with high resistance to image distortions by using optimal representation in the eigenvectors space. During the experiments high robustness of 2DKLT-based algorithm to typical steganographic attacks has been proved. The quality and strength is similar to the ones presented in [6, 12, 13], however the proposed approach is more flexible in the aspect of color-space and quality

settings. The bottom line is that during investigations the hidden message was not detected by one of the most popular steganalysis tools - stegdetect v0.4 [2], which makes the proposed method highly promising.

References

1. Podilchuk, C.I., Delp, E.J.: Digital Watermarking Algorithms and Applications. Proc. IEEE Signal Processing Magazine 18(4), 33–46 (2001)
2. Provos, N., Honetman, P.: Hide and Seek: An Introduction to Stegangography. IEEE Security & Privacy Magazine (May/June 2003)
3. Kaarna, A., Toivanen, P.: Digital Watermarking of Spectral Images in PCA/Wavelet Transform Domain. In: Proc. IGARSS, vol. 6, pp. 3564–3567 (2003)
4. Cheung, W.N.: Digital Image Watermarking in Spatial and Transform Domains. In: Proc. TENCON, vol. 3, pp. 374–378 (2000)
5. Artz, D.: Digital Steganography, Hiding Data within Data. In: Proc. IEEE Internet Computing, vol. 5(3), pp. 75–80 (2001)
6. Dafas, P., Stathaki, T.: Digital image watermarking using block-based Karhunen-Loeve transform. In: Proceedings of the 3rd International Symposium on Image and Signal Processing and Analysis, ISPA 2003, vol. 2, pp. 1072–1075 (2003)
7. Jolliffe, I.T.: Principal Component Analysis. Springer, NY (1986)
8. Fukunaga, K.: Introduction to Statistical Pattern Recognition, 2nd edn. Academic Press, New York (1990)
9. Tsapatsoulis, N., Alexopoulos, V., Kollias, S.: A Vector Based Approximation of KLT and Its Application to Face Recognition. In: Proc. of the IX European Signal Processing Conference, EUSIPCO 1998, Island of Rhodes (1998)
10. Kukharev, G., Forczmański, P.: Data Dimensionality Reduction for Face Recognition. Machine Graphics and Vision 13(1/2) (2004)
11. Kukharev, G., Forczmański, P.: Facial images dimensionality reduction and recognition by means of 2DKLT. Machine Graphics and Vision 16(3/4), 401–425 (2007)
12. Stanescu, D., Stratulat, M., Ciubotaru, B., Chiciudean, D., Cioarga, R., Borca, D.: Digital Watermarking using Karhunen-Loeve transform. In: 4th International Symposium on Applied Computational Intelligence and Informatics, SACI 2007, pp. 187–190 (2007)
13. Botta, M., Cavagnino, D., Pomponiu, V.: KL-F: Karhunen-Loeve based fragile watermarking. In: 2011 5th International Conference on Network and System Security, NSS 2011, September 6-8, pp. 65–72 (2011)
14. Wallace, G.K.: The JPEG Still Picture Compression Standard. Communications of the ACM 34(4) (April 1991)
15. Okarma, K.: Combined image similarity index. Optical Review 19(5), 349–354 (2012)

Knowledge Transformations Applied in Image Classification Task

Krzysztof Wójcik

Pedagogical University of Cracow, Institute of Computer Science
ul.Podchorążych 2, 30-084 Kraków, Poland
`krzywg@gmail.com`

Summary. The main goal of the article is a presentation of the usage of knowledge transformation methods in an iterative scheme of ontology building. The presented approach tries to overcome vital problems of automatic ontology building. They concern especially initial assumptions and problems of the learning. The article concentrate on the knowledge joining operation. The details of this operation are illustrated by example of building of the knowledge structure applied in a simple image recognition system. The proposed scheme is compared with other well-known approaches. The article points to conditions of a successful usage of the described methodology, i.e. developing effective search algorithms of a suitable concept structure and the efficient methods of distributing the main task of knowledge building.

1 Paper Objectives and Bibliography Remarks

The task of image classification and understanding often requires the usage of the knowledge about images [6]. This approach, having many advantages (e.g. flexibility), suffers from several difficulties. One of them is assumption that a useful model of reality (i.e. ontology) is available. The term "ontology" may be simply defined as a 3-tuple: a set of concepts, a set of relationships and a set of instances [2]. However, its automatic creation is a complex problem. The literature provides many frameworks of the ontology building, especially concerning the Semantic Web methods [2, 3]. Among them, the OWL (Web Ontology Language) is the most known. The OWL is a knowledge representation language which makes it possible to describe features of classes, relationships, and allows to define basic operations on the classes [4]. Analogous operations concern also described in the paper simplified ontology structure (next sections illustrate the usage of a fundamental operation of knowledge joining). The proposed methodology favors the automatic ontology creation, and satisfies the assumption that knowledge updating should be based on the observation of direct relations between objects.

We can articulate now the main two goals of the article:

1. The presentation of the most important features of iterative scheme of the knowledge building, which applies the knowledge joining operations.
2. Establishing conditions of a profitable usage of this scheme in relatively simple image classification tasks.

2   Knowledge Representation and Learning Scheme

At first some theoretical background concerning the knowledge representation and an architecture of the whole system should be provided. This introduction will be based on the works [7] and (especially) [8]. According to them, we assume that the phenomena from the given reality consist of elementary parts, which are called primitive objects. The objects correspond to "concepts", also called "types". Additionally, we assume that the objects are connected by relationships. We assume also the possibility of creating the new concepts, objects and relations. The work [8] provides details of the concept definition. The starting point is here a set of objects that are "strongly" connected by the relations. This set allows to create an abstract arrangement (pattern) of the relations. Let us denote this pattern by $\mathbf{S}_p$. Basing on this, we can define the concept as a triple of elements:

$$(\mathbf{S}_p, \mathbf{FR}, \mathbf{FA}) \tag{1}$$

where: $\mathbf{FR}$ - process of defining new relationships, $\mathbf{FA}$ - process of defining new object attributes (for details see [7]).

According to the newly constructed pattern $\mathbf{S}_p$, we can create new objects (as a combination of several sub-objects). The procedures of concept and object creating may be operated repetitively. This leads to the construction of hierarchical structure of concepts and hierarchical structure of objects. The concept structure includes the general knowledge, while the object structure contains knowledge about the particular scene. The presence of the objects of the specific types in that structure may be considered as a response of the system.

However, we should be aware of two important problems. The first is the problem of knowledge evaluation (see [7]). We will notice here only a few possible approaches to solve it: evaluation by the practical action, by the directly defined performance function and evaluation by the usage of an arbiter (supervised learning).

The second vital problem is connected with methods of finding a useful concept structure. There are many possible ways of creating the pattern $\mathbf{S}_p$, thus the solution is a point of a huge search space. Some proposals to solve this crucial problem are provided by the paper [7]. For example: evolutionary algorithms and variants of local-search techniques.

The complex process of creating the new concepts may be described in more consistent way by introduction a uniform scheme called an OTO

(Observation-Transformation-Operation) [8]. The main steps of OTO scheme are as follows:

A. The observation. In this process the relationships between objects are identified.
B. The transformation. This process refers to the transformation of the knowledge, in order to better describe the observed phenomena.
C. The operation. This stage consist in the object creation or removal.

The transformations phase may refer to the particular relationships in the $\mathbf{S}_p$ sets, its types of arguments as well as whole interior structure of $\mathbf{S}_p$. A brief study of main kinds of these transformation is provided by [8]. Let us shortly itemize them:

Creating an alternative concept definition (two, or more patterns define the same concept).

Creating a recursive concept.

Let us assume that some pattern $\mathbf{S}_p$ defines concept denoted by c. By changing types of relations arguments in $\mathbf{S}_p$ into c we obtain a recursive type.

Modifications of the relation definition.

Let us consider a binary relationship r. We can define the new unary relation r_e, which is satisfied by particular object $\mathbf{x}$ if there does not exist other object $\mathbf{y}$ which satisfies r relation ($r(\mathbf{x}, \mathbf{y})$). This kind of modification will be called "excluding transformation".

Let us focus on the consequence of the simple modification of relationship arguments types. Let us assume, that a $\mathbf{S}_p$ set defines a c_1 concept. In $\mathbf{S}_p$ we change the type of a particular argument of an individual relation into c_2. In this way the concept c_2 is used in the definition of the concept c_1. More generally, we may interpret such a modification of relation arguments as joining of one knowledge structure to another one. The usage of this transformation is the main topic of next sections.

3   Examples of Knowledge Structure Joining

3.1   *Partial Knowledge Building*

Before we will illustrate the idea of knowledge joining we should demonstrate some abstract example of OTO scheme usage. This example was presented in the paper [8], here only a brief outline will be given. Let us assume that we want to build knowledge about operations on integer numbers. First, we must provide the description of the concept "number". It may be defined on the basis of an elementary concept of "equinumerosity of sets". We want to define this concept with minimal assumptions (we will not use its well-known definition that utilizes a bijection transformation).

As a primitive concept we consider a class of vectors, which have only one essential feature called *color* (with two values: 0 and 1 or *blue* and *red*). Thus, all the primitive objects can be divided into two sets. There are also defined primitive binary relationship: *equality* and *inequation* of the *color* and two unary relations: *having_blue_color* and *having_red_color*.

The execution of the searching process has been carried out in the environment of a test program. The program has generated many proper solutions, one of them (drawn according to the program output window) is as follows:

typ 20 q1 pat:
typ 21 q1 pat: 13: 20 20
typ 22 q1 pat: 15: 21 21
typ 22 q1 pat: 15: 22 21
typ 24 q4 pat: neg 13: 22 20   15: 22 20   15: 22 21

Let us interpret that definition.

typ 20 q1 pat:

typ 20 - a header of the definition of concept (type) no. 20, this is the concept of primitive objects, q1 - a performance value of this concept, (not significant), pat: - relation definitions (empty here);

typ 21 q1 pat: 13: 20 20

typ 21 - the header of the definition of concept 21 (headers will be omitted in further descriptions),

13: 20 20 - relation 13 (*inequation*) held between two objects of type 20; the object of concept 21 is a pair of primitive objects (type 20) having different colors, such a pair will be called a "different pair"; the color of this compound object is always 0 (*blue*) as a result of calculating the average color of components using integer values; the first argument of this binary relation (and all next ones) will be called a "central object" (definition of the central object is provided by [8]);

typ 22 q1 pat: 15: 21 21

15: 21 21 - relation 15 (*equality*) held between two objects of type 21; the object of type 22 contains two objects of type 21 (different pairs); all objects of type 21 have *blue* color, so relation 15 expresses here an existence of another object of type 21;

typ 22 q1 pat: 15: 22 21

15: 22 21 - relation 15 (*equality*) held between objects of type 22 and 21, this is a transformation of the previous concept, type 22 becomes the "recursive type"; the object of extended concept 22 may be a set of different pairs (type 21);

typ 24 q4 pat: neg 13: 22 20   15: 22 20   15: 22 21

this is the excluding transformation (denoted by "neg") of relations:

13: 22 20   15: 22 20   15: 22 21;

object of type 24 may be interpreted as a set of different pairs (type 22) for which:

13:22 20 - another object (type 20) having a different color does not exist,

15:22 20 - another object (type 20) having the equal color does not exist,

15:22 21 - another pair does not exist (all pairs have *blue* color).

The last conditions mean that an object of type 24 includes all different pairs, and there exists no other object (type 20) that is not a component of

them. Thus, the possibility of creating the object of type 24 indicates that two sets have the same cardinality.

We will omit a further description of this solution, concentrating on its practical usage in the classification task.

3.2 Image Classification Task

We will deal with a simplified version of pattern recognition problem in which the objects' membership to one class only will be considered.

Our example concerns a mineralogy problem of the proper classification (identification) of the granite stones. Figure 1 is a photo of several stones that include different amounts of specific minerals (e.g. quartz, mica). We assume that some of these stones, which are marked by the expert (black circle) belong to one particular class.
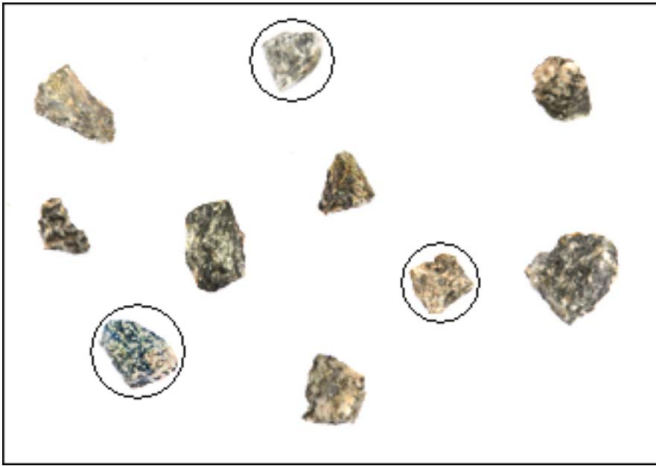
Fig. 1. The example of objects which include different amounts of some minerals

Leaving the discussion about the structure of the pictures of stones, let us assume that they are consisted directly from pixels. Let each pixel be represented by a vector: *(x_ coordinate, y_ coordinate, brightness)*, which will be regarded as a primitive object of OTO process. Assuming that the inborn knowledge may be imprecise, we can simplify the object properties and relationships between them. We will consider the 8-degree *brightness* of pixels only. Accordingly, we will define eight very simple unary relationships that assesses the object brightness (*having_ brightness_ 0, having_ brightness_ 1, ...*). Moreover, we will use two binary relationships (*equality* and *inequation*) for a comparison of brightness of two objects. Finally, we assume that a concept structure which is able to check the cardinality of sets is available.

As a result of the searching process we obtain a structure:

typ 20 q1 pat:
typ 21 q1 pat: 13: 29 29
typ 22 q1 pat: 15: 21 21
typ 22 q1 pat: 15: 22 21
typ 24 q4 pat: neg 13: 22 29   15: 22 29   15: 22 21
typ 25 q1 pat:
typ 26 q1 pat: 15: 25 25   15: 25 25   4: 25
typ 26 q1 pat: 15: 25 25   6:25
typ 28 q1 pat: 15: 26 26
typ 29 q1 pat: 15: 28 28

A part of it, containing concepts from 20 to 24, is the transformed structure from the first example, we will return to this soon. The concept number 25 represents primitive objects (see above). Let us consider next concepts:

typ 26 q1 pat: 15: 25 25   15: 25 25   4: 25

15: 25 25 - relation 15 (*equality*) held between central objects (type 25) and another object of type 25,

15: 25 25 - the same relation between central object and just another one,

4: 25 - the relation having_brightness_4 satisfied object of type 25 (central object); the object of type 26 contains three primitive objects (25) which have brightness 4;

typ 26 q1 pat: 15: 25 25   6:25

the arrangement of this relation is analogous to the previous one; the object of this concept is a pair of primitive objects having brightness 6; this is the alternative definition of the previous concept (both concept have number type 26);

typ 28 q1 pat: 15: 26 26

15: 26 26 - relation 15 (*equality*) held between central objects (type 26) and another object of type 26; the object of type 28 is a pair of objects of the same brightness;

typ 29 q1 pat: 15: 28 28

like above; the object of concept 29 is a pair of objects of type 28, which have the same brightness; the object of concept 29 is a quartet of objects of type 26.

In the process of creating the last concept the operation of knowledge joining is executed. All types of relations in the partial knowledge structure (concepts 20-24) which equal 20 are changed to 29. This transformation joins two "piece" of knowledge (concept 25-29 and 20-24).

Let us try to understand how the whole structure works. The object of concept 26 may be a triple of primitive objects having brightness 4 or a pair of them having brightness 6 (alternative definition). The number of objects of this type which have the brightness 4 can be expressed by:

$n_{(26,4)} = n_{(25,4)} \; div \; 3$,   where: $n_{(25,4)}$ - the number of primitive objects (25) having brightness 4, div - division operation in integer domain (objects can be used in the creation of the other object only once).

Similarly, the number of objects of type 26 which have brightness 6 is:

$n_{(26,6)} = n_{(25,6)} \; div \; 2$.

Let us assume, that using the concept structure 20-24 we want to compare the cardinality of two sets of objects (type 26) having brightness 4 and 6.

If these sets have the same cardinality, the ratio of the number of primitive objects having brightness 4 to those of brightness 6 is $3/2$. This value, describing components of the stones, may be used in classification task. However, an acceptance of all positive examples of the learning sequence needs some tolerance of this value. The rough calculation may come from taking into account remainders of the division operations ($n_{(25,4)}$ div 3 and $n_{(25,6)}$ div 2). Let us look at concept 29. The number of all objects of type 29 is:

$n_{(29)} = n_{(26)}$ div 4,   where: $n_{(26)}$ is the number of all objects of type 26. Taking into consideration the last division operation, we can notice that the equinumerosity of sets of objects of type 29 infers an approximate equinumerosity of corresponding sets of objects of type 26.

3.3 Main Features of OTO Method in Comparison with Other Approaches

The problem of the objects classification has many typical solutions [5]. One of them (let it briefly denote by "classical") utilizes a distance function between objects (minimum distance algorithm). The main problem is the suitable selection of the objects properties. Omitting detailed discussion we may propose to use features of histogram of images (e.g. position of the histogram maximum or parameters of Normal or Poission's distribution that estimate the histogram function). In a more approximate method, relationships between average histogram values in chosen ranges might be considered.

The classification tasks are also commonly solved be the usage of artificial Neural Networks (NN) [1]. In the general case, when the network structure is unknown, the task of generating the network is NP-complete. Practically, making some assumption about the network architecture we can make this process simpler. For example, we can imagine that each pixel of the picture is connected to one node of the input layer of NN. In classification task we can use a three or four-layer feed forward NN, with nodes applying a sigmoidal activation function [1].

Let us look now at the ability of OTO method to generate the proper solution. The intervals of the brightness, in which the pixel numbers are calculated, have the same width. It relates to the "rough" (8 levels) quantization of pixel brightness. We can see however, that the usage of the more accurate quantization and the operation of the alternative concept definition allows to create intervals of any arbitrary width (the method becomes similar to the variant of classical one, see above).

By the creation of triples and pairs of objects the method is able to identify the quotient of the pixel numbers equals $3/2$. Nevertheless, be the combination of the pairs, triples, quartets, etc., the method can detect any value of the quotient (with limitation that it must be a rational number).

The comparison of the object number with the established tolerance is done by 4-fold decreasing the cardinality of object sets. However, a more complex structure may be able to compare the set cardinality with any given tolerance.

Summarizing, OTO process, using the combination of elements defined before (pairs and triples of objects, partial knowledge structures, etc.) can produce a method which substitutes the "classical" method developed by the human. Moreover, the method is generated online, depending on specific circumstances. This feature is similar to features of NN. Neural Network, in the form describe above, can solve any task of classification. Unfortunately, the solution is difficult to interpreted and applied into other systems.

4 Conclusions

By the presentation of features of OTO scheme in image classification task , we can conclude that OTO methodology has properties halfway between features of the Neural Network techniques and classical approaches (based on the distance function). Its main advantage is possibility to build the knowledge automatically, what is similar to NN. Additionally, the knowledge may by interpreted by a human, modified and easily adapted to other systems, what makes it similar to the classical methodology.

Nevertheless, the main difficulty is an exponential growth of a searching space with the growth of the step number of OTO process. This growth limits the created knowledge structure to few concepts only. In this connection, we can point to conditions of successful usage of presented methodology in building the more complex structure:

- Developing efficient methods of local-search for best $\mathbf{S}_p$ pattern.
- The proper distribution of the main task of knowledge building to subtasks.

References

1. Bishop, C.M.: Neural Networks for Pattern Recognition. Oxford University Press, New York (1995)
2. Davies, J., Studer, R., Warren, P. (eds.): Semantic Web Technologies Trends and Research in Ontology-based Systems. John Wiley & Sons Ltd. (2006)
3. Fortuna, B., Mladenič, D., Grobelnik, M.: Semi-automatic construction of topic ontologies. In: Ackermann, M., et al. (eds.) EWMF 2005 and KDO 2005. LNCS (LNAI), vol. 4289, pp. 121–131. Springer, Heidelberg (2006)
4. McGuinness, D.L., van Harmelen, F. (eds.): OWL Web Ontology Language (2009),
   http://www.w3.org/TR/2004/REC-owl-features-20040210/
5. Russell, S., Norvig, P.: Artificial Intelligence: A Modern Approach, 3rd edn. Prentice Hall, Englewood Cliffs (2010)

6. Tadeusiewicz, R., Ogiela, M.R.: Medical Image Understanding Technology. STUDFUZZ, vol. 156. Springer, Heidelberg (2004)
7. Wójcik, K.: Hierarchical Knowledge Structure Applied to Image Analyzing System - Possibilities of Practical Usage. In: Tjoa, A.M., Quirchmayr, G., You, I., Xu, L. (eds.) ARES 2011. LNCS, vol. 6908, pp. 149–163. Springer, Heidelberg (2011)
8. Wójcik, K.: OTO Model of Building of Structural Knowledge - Areas of Usage and Problems. In: Choraś, R.S. (ed.) Image Processing and Communications Challenges 4. AISC, vol. 184, pp. 215–222. Springer, Heidelberg (2013)

Problems of Infrared and Visible-Light Images Automatic Registration

Karol Kuczyński and Rafał Stęgierski

Maria Curie-Skłodowska University,
Institute of Computer Science
ul. Akademicka 9, 20-033 Lublin, Poland
`karol.kuczynski@umcs.pl`

Summary. In this paper the problem of infrared and visible-light images registration is analysed. The authors propose a registration procedure that could be used for a wide range of applications. It is based on B-spline transformation and mutual information similarity measure.

1 Introduction

Infrared thermography is a modern imaging technique. It has quite a long history. Infrared cameras are still expensive, but their availability has significantly increased in the recent years. Thermography has numerous applications in science (including medicine), technique, industry, military, rescue services, etc. New potentially useful applications are proposed every year.

Digital infrared images are often processed and analysed for various purposes. For this task it is often either useful or necessary to have also visible-light photographs. Many infrared cameras offer such functionality.
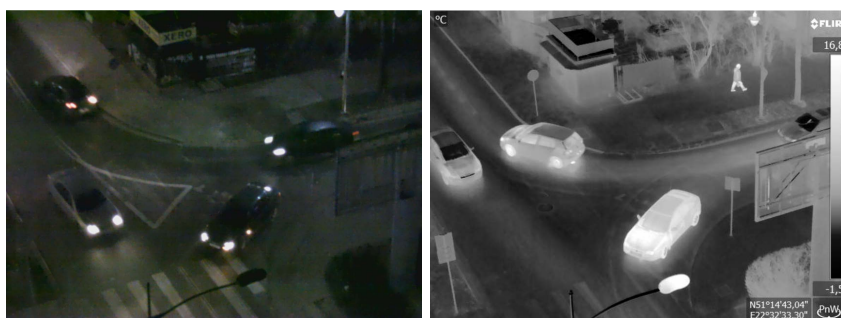
Fig. 1. Potentially problematic images (left – visible light, right – infrared) due to time delay between acquisitions
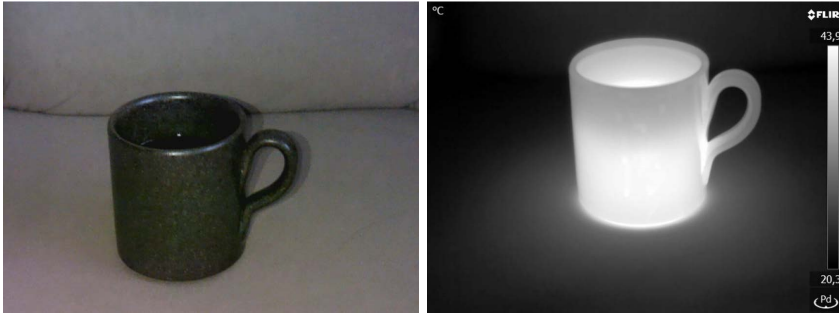
Fig. 2. Illustration of parallax phenomenon

Both infrared and visible-light images are then acquired at the same time
(actually, there is usually a delay between acquisition of both images that
can be significant in some situations - Fig. 1). Having them it is easier for
example to spatially localise interesting temperature abnormalities. Unfortu-
nately, these images are usually not perfectly aligned and it is not possible to
easily find all corresponding points in both images. It results from two factors.
Infrared and visible-light lenses have different properties and introduce differ-
ent kinds of distortions. The other phenomenon is parallax, because infrared
and visible-light lenses are located in two different places, a few centimetres
from each other. The displacement is especially severe when photographed
objects are located within a small distance from the camera (Fig. 2).

Image registration (fusion) techniques provide solutions of this problem.
Typical software provided by infrared equipment manufacturers requires an
user to select a few corresponding points in the two images and then performs
appropriate transformation [4]. Sometimes special markers are attached to
photographed objects. The purpose of the presented study is to design a
registration procedure able to register images automatically, without prepro-
cessing and user interaction.

Unfortunately, it seems impossible to create a fully automatic image regis-
tration procedure that could be applied for any kind of images. For successful
automatic registration it is necessary to have enough objects that are visible
in both infrared and visible light. Images presented in Fig. 3 do not meet
this condition. Such images can be registered manually (by selection of cor-
responding points) or additional markers (visible in both spectra) should be
attached to the objects.

2   Materials and Methods

Each image registration procedure consists of similar main building blocks: ge-
ometrical transformation, interpolation method, similarity measure (registra-
tion criterion), optimisation scheme, interpolation method and visualisation
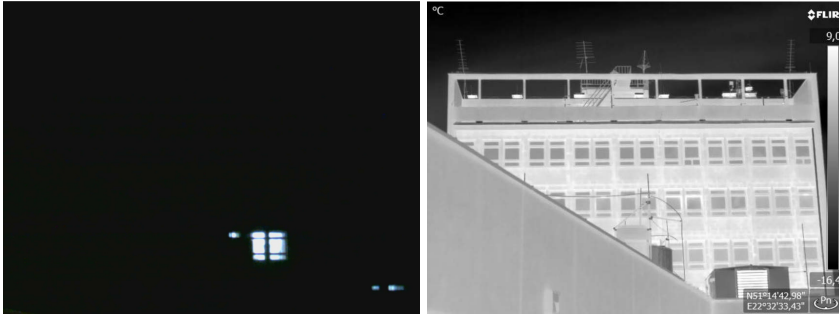
Fig. 3. Example of images that probably cannot be registered automatically because visible-light photo shows not enough objects (both photos were taken in the night, left – visible light, right – infrared)
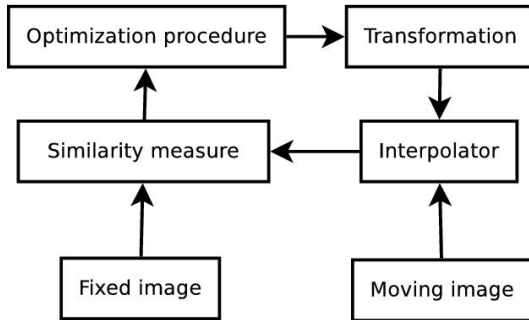
Fig. 4. General structure of the registration framework

method (for registered images) – Fig. 4. All these elements should be carefully selected according to the given registration problem.

As it has been already mentioned, it is impossible to create an all-purpose registration procedure. We need to make some initial assumptions regarding the problem to be solved here. We will operate on images for which there is a chance to perform successful automatic registration. Selection of such images is an another problem that is not discussed here in detail. We also assume that view area of both images is similar and we have to correct only relatively small distortions resulting from different properties of infrared and visible-light optics, rather than large-scale translations, rotations and scaling. This situation is typical if visible-light images are acquired by infrared camera together with infrared ones.

The registration engine has been implemented using ITK library (Insight Segmentation & Registration Toolkit, `http://http://www.itk.org/`). An infrared image is treated as a fixed one and a visible-light image is a moving one.

B-spline transformation [1] is known to be a good choice for correction of the expected kind of distortions introduced by optical systems. It is important to set a reasonable number of B-spline grid nodes for the transformation (discussed later). Linear interpolation is used do evaluate pixel intensities at mapped positions.

In multi-modal registration (where correspondence between greylevels in both images is not evident) various variants of mutual information are commonly employed as similarity measure. Here we use implementation proposed by Mattes et. al [2]. All available pixels are used for calculations and 50 histogram bins are created.

Regular step gradient descent optimizer [3] is a well known optimiser, expected to perform well with this kind of cost function.

3   Results

Fig. 5 presents exemplary images used for the experiments and the final result. This situation is quite typical. Both visible-light and infrared images show approximately the same area. However, the checkerboard test (Fig. 6) displays some displacements between corresponding objects, significantly corrected using the presented procedure.

The grid size for the B-spline transformation was 2 by 2 nodes, on image. Using splines of order 3 (cubic B-spline), it is necessary to use additional 3 nodes for each dimension. Thus, 50 transformation parameters (translation along x and y axis for each node) need to be found during the optimisation process.

The registration time strongly depends on given images' properties and required accuracy that can be tuned by setting optimiser's parameters. In the example presented above, minimum step length of the regular step gradient descent optimiser was 0.01 (the stop condition). The optimal transformation was found after 1085 iterations, within about 30 minutes, on a standard modern PC (Intel® Core™ i7-3930K CPU 3.20GHz).

The same images were registered using FLIR Reporter software. The result is presented in Fig. 7. The transformation calculation was based on three reference points, manually selected in both images by the program operator (Fig. 8).

4   Discussion

It is known that the more general transformation (described by more parameters), the more accurate registration might be potentially obtained. However, in this case situation is slightly more complicated. For pixel-based image registration all (or most of) pixels are used for similarity measure calculation. Some image region may include no information useful for registration (for example a complex thermal pattern on a plain, uniformly painted wall;

Fig. 5. Infrared image, visible-light image, transformed visible-light image

complex visible structures and uniform thermal image or no correlation between both images). Too general transformation will likely introduce unwanted distortions in such areas. Registration time will be long and it will be difficult to find the correct, optimal solution.

The transformation should be as accurately as possible matched to the kind of expected image deformations. Here we would like to correct global distortions introduced by optical systems rather than local discrepancies. According to the experiments, B-spline transformation with 2 by 2 grid nodes on image (5 by 5 nodes including additional, necessary ones) can be used
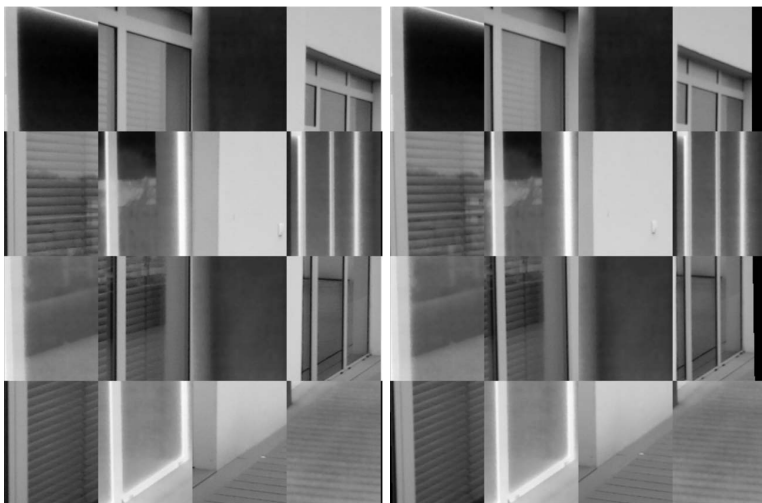
Fig. 6. A checkerboard test for the original (left) and registered images (right)
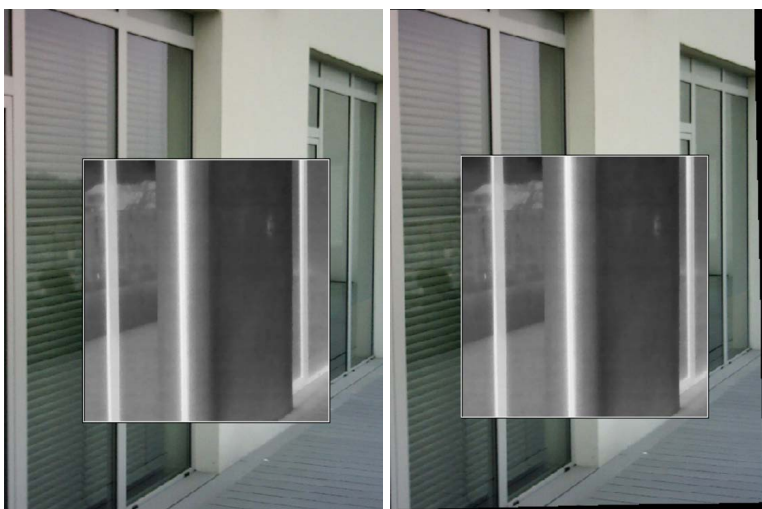
Fig. 7. Image fusion performed with commercial software (FLIR Reporter), original images (left) and registered images (right)
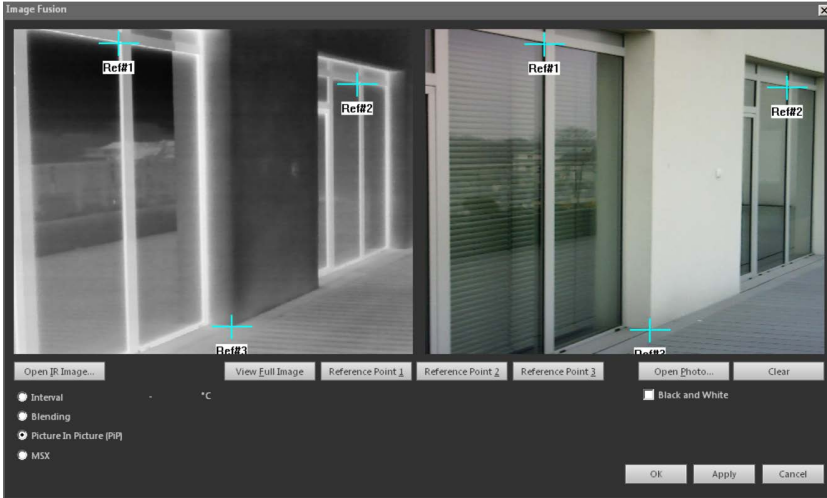
Fig. 8. Manual reference points selection for image registration (FLIR Reporter software)

to successfully model such distortions. Increasing the number of nodes did not significantly improve registration quality and in some images introduced additional distortions as mentioned above. Registration accuracy (and processing time) can be still altered by changing number of iterations during optimisation (directly or by modifying the stop criterion).

Automatic image registration procedures are usually designed for specific applications. No general-purpose commercial program for automatic registration of infrared and visible-light images is currently known to the authors. Typically, such programs offer image fusion feature, but image registration is based on corresponding points, selected manually by an user (Fig. 8 – FLIR Reporter software). Thus, direct comparison of accuracy and processing time for the presented solution and the commercial application is meaningless, because in the second case they are determined by user's actions.

5   Conclusion

A great variety of automatic image registration algorithms is currently known [5]. Despite this fact, algorithms that require user interaction (for example selection of corresponding points in both images) are still commonly applied, because of practical problems with automatic registration. The registration procedure has to be carefully tuned for a given application. The solution presented here can be used for a wide class of thermal and visible-light images,

but still has serious limitation. It is desirable to improve its performance. Selection of images that could be successfully registered using this procedure is also an open issue.

References

1. Unser, M.: Splines: A Perfect Fit for Signal and Image Processing. IEEE Signal Processing Magazine 16(6), 22–38 (1999)
2. Mattes, D., Haynor, D.R., Vesselle, H., Lewellen, T.K., Eubank, W.: PET-CT image registration in the chest using free-form deformations. IEEE Trans. on Medical Imaging 22(1), 120–128 (2003)
3. Ibanez, L., Schroeder, W., Ng, L., Cates, J.: The ITK Software Guide, 2nd edn. Updated for ITK version 2.4 (2005), `http://www.itk.org`
4. Flir Systems, FLIR Reporter Professional User's manual (March 2012)
5. Zitova, B., Flusser, J.: Image registration methods: a survey. Image and Vision Computing 21, 977–1000 (2003)

Computational Complexity Analysis of Adaptive Arithmetic Coding in HEVC Video Compression Standard

Damian Karwowski

Poznan University of Technology,
Chair of Multimedia Telecomunications and Microelectronics, Poznań, Poland
`dkarwow@multimedia.edu.pl`

Summary. This paper presents computational complexity analysis of adaptive arithmetic coding (CABAC) in the emerging HEVC video compression technology. In particular, computational complexity of individual parts of CABAC (and the whole CABAC entropy codec in the HEVC video decoder) was measured from the point of view of video decoder side. Experiments were done using publically available HM reference software of the HEVC video codec and a set of test video sequences. The range of bitrates that can be processed in real time by CABAC entropy decoder were also evaluated for the considered in the paper implementation of CABAC.

1 Introduction

Contemporary techniques of video compression have been dominated by hybrid coding scheme of images with intra-frame prediction, inter-frame prediction and lossy transform coding of residual data [1, 2, 3]. The well-known and commonly used examples of technologies that use hybrid coding scheme are MPEG-2 [1, 2], H.263 [1, 2] and MPEG-4 AVC/H.264 [1, 2, 3, 5]. The essential part of each hybrid video codec is a block of entropy coding that is used to extra reduce redundancy that exists within residual data in order to further improve the compression performance of a video encoder. Works on entropy coding of a video data resulted in the development of a very efficient Context-based Adaptive Binary Arithmetic Coding (CABAC) algorithm [3, 4, 5, 6]. CABAC technique represents the state-of-the-art solution and has become a part of the MPEG-4 AVC/H.264 video compression technology. The impact of CABAC algorithm on compression performance and computational complexity of a video codec has been already tested well and presented in the literature [3, 4, 5, 6, 7]. What is very important, such works have been only done in the context of the MPEG-4 AVC/H.264 video compression standard.

In the last years intensive works have been carried out aimed at further improving the techniques of hybrid video coding. The works were mainly done in the context of high definition television. As a result of these works the new High Efficiency Video Coding (HEVC) international standard has been announced this year [8]. In the course of work on the new standard, modified version of CABAC algorithm has been elaborated and chosen to be a part of the HEVC video compression technology. It was experimentally proved that the two versions of CABAC (original and modified) have similar compression performance, but complexity of the modified version (used in HEVC) is lower relative to the original one (used in MPEG-4 AVC/H.264). Additionally, compared to previously known solutions for video coding, the new HEVC technology includes many improvements and new coding tools that affect both the compression performance and complexity of a video codec [8]. These changes come down to a more flexible way of splitting the image into coding units, more sophisticated mechanisms of intra- and inter-frame prediction, more advanced techniques of transform coding of residual data and the application of in-loop image filters.

These improvements (made in the parts of a video codec that calculate the residual data and that perform entropy coding of the data) influences the amount of computations that are needed in individual parts of contemporary video codec. Computational complexity analysis and results obtained in the context of older video compression technologies (such as MPEG-4 AVC/H.264) may not be appropriate for the emerging HEVC technology.

At this point the question arises on computational complexity of modified CABAC entropy codec in the framework of the new HEVC video codec. This paper strictly addresses this subject. Additionally, the paper presents detailed computational complexity analysis of individual functional blocks of CABAC entropy codec using representative set of test video sequences. The rest of the paper is organized as follows. Section 2 presents the general concepts of CABAC entropy coding that is used in the HEVC standard. Section 3 describes methodology of experiments on computational complexity analysis of CABAC in HEVC. Section 4 presents obtained results and the last section 5 concludes the paper.

2 HEVC Video Compression – CABAC Entropy Coding

Proper evaluation of results presented in this paper requires the knowledge of CABAC entropy codec structure. In this section only the most important elements of CABAC algorithm are presented.

The general structure of the version of CABAC used in HEVC is the same as compared to that used in MPEG-4 AVC/H.264 video codec. The block diagram of CABAC encoder was presented in Fig. 1.
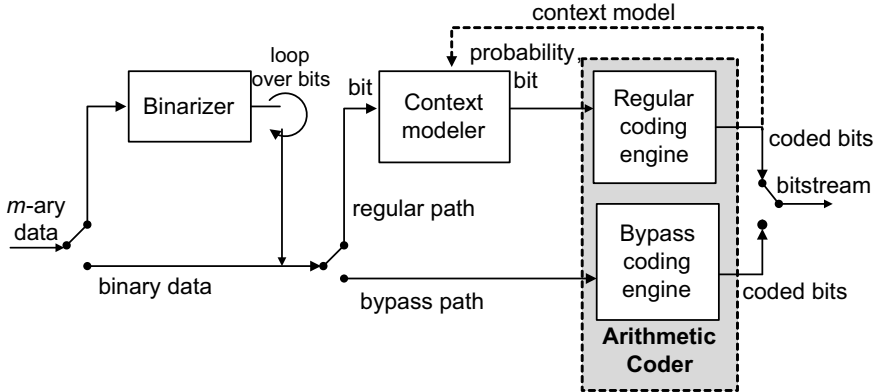
Fig. 1. Block diagram of CABAC entropy encoder

Characteristic feature of an algorithm is using the binary arithmetic encoder core (instead of m-ary core), the so-called M-encoder, which was highly optimized toward speed [4, 5, 6, 7]. The binary encoder core is able to process symbols from alphabet A={0, 1} - in notation of CABAC the symbols are considered as least probable symbol (LPS) or most probable symbol (MPS).

Due to application in CABAC of the binary arithmetic encoder core, all m-ary symbols must be mapped into string of binary symbols at the first stage of CABAC encoding. This operation is realized in the binarizer. It must be stated, that the way in which binarizer works strongly affects the number of resulted binary symbols, which in turn translates into performance and complexity of the entropy encoder. It was the motivation to use several different binarization schemes in CABAC in order to account different statistics of individual syntax element coded in the HEVC encoder. In general, binarization techniques are used that are based on unary coding, Exp-Golomb coding and Golomb-Rice coding [4, 5, 6, 9]. In this way, this part of CABAC encoder is very similar to adaptive variable-length coding, but data statistics modeling together with arithmetic coding of binary symbols is additionally realized in order to increase compression performance of entropy encoder.

Data within string of binary symbols (data at the output of a binarizer block) still exhibit some statistical redundancy. This redundancy is additionally reduced in CABAC by the use of data statistics modeling and arithmetic encoding of symbols. From compression performance point of view these are also important parts of entropy encoder. It is known, that the 'quality' of data statistics estimation (accuracy of probabilities of symbols that are estimated in the context modeler block) strongly affects compression efficiency of arithmetic encoding. Experiments proved different character of data associated with individual syntax elements and even varied nature of binary data

within bit planes of binarized words for a given syntax element. Therefore, estimation of probabilities should be realized independently not only on the level of individual syntax elements, but also independently on the level of bit planes in a binarized word. It was the motivation to split the input stream of binary symbols into a big number of individual binary sub-streams, for which the probabilities of symbols are calculated independently. This refers to sub-streams of data that are coded in the so-called regular coding mode (see Fig. 1). In relation to solution used in CABAC of MPEG-4 AVC/H.264 standard, in CABAC of HEVC the number of regular sub-streams was highly reduced in order to simplify the mechanism of data statistics estimation. Total number of 205[1] regular sub-streams was introduced in CABAC of HEVC (in contrast to 460 regular sub-streams used in CABAC of MPEG-4 AVC/H.264). The way in which binary symbols are assigned to individual regular sub-streams determines the efficiency of entropy encoder. In CABAC it is done based on context information (i.e. values of neighboring binary symbols that have been coded previously), wherein actual context pattern (the location of neighboring symbols that are taken into account) is different for individual syntax elements. For some binary symbols uniform probability distribution is assumed and no conditional probabilities are calculated for such symbols. It refers to the so-called bypass coding mode and bypass sub-stream of symbols (see Fig. 1). Relative to the CABAC of MPEG-4 AVC/H.264 greater percentage of symbols is classified as bypass symbols in the CABAC of HEVC.

In general the process of probabilities estimation makes a bulk of computations in adaptive entropy codec. Therefore, CABAC calculates probabilities in a simplified way using pre-defined Finite State Machines (FSMs). The number of FSMs corresponds to the number of regular sub-streams defined in CABAC - it means that a given FSM calculates probabilities of symbols that come from individual sub-stream. Each FSM consists of 64 states which correspond to particular 64 values of probabilities for LPS symbol and 64 values of probabilities for MPS symbol. Probability of a symbol is finally used by the arithmetic encoder core.

3 Complexity Analysis of CABAC in HEVC – Methodology

Main goal of the paper was to perform detailed complexity analysis of individual functional blocks of CABAC entropy codec when operating in the framework of HEVC video codec. The starting point to research was the publicly available reference software of the HEVC video codec, known as HM software [10]. In particular, version 3.2 (HM 3.2) of the software was used. As a matter of fact the newer versions of HM software are available now (HM 10.0 at time of writing this paper), nevertheless the general structure

---

[1] This is the number of regular sub-streams used in the HM 10.0 version of the HEVC reference software.

of CABAC algorithm has not been changed (since HM 3.2 software version) and results obtained with older version of the software may be regarded as reliable.

Experiments were done from the point of view of HEVC video decoder. It is known that the most computationally complex blocks of CABAC are data statistics modeling and arithmetic encoding [7]. These parts are the same in both the encoder and the decoder. Therefore, complexity results of CABAC decoder correspond well to that of the CABAC encoder side.

The HM software was modified by the author in order to be able to capture the execution time of the following parts of CABAC: (1) binary arithmetic decoder core operating in the regular mode (regular mode of the M-decoder), (2) binary arithmetic decoder core operating in the bypass mode (bypass mode of the M-decoder), (3) de-binarization of data and context modeling for binary symbols. Additionally, the execution time of the whole CABAC entropy decoder was tested in the HEVC decoder. Execution times of mentioned parts of CABAC (and the whole CABAC entropy decoder) were measured using RDTSC Pentium processor instruction. This instruction counts the number of processor cycles that elapsed during execution of considered fragment of a program code. Finally, the frequency of use the bypass mode in CABAC codec was explored for a wide range of target bitrates. All experiment were done using the following scenario:

- HD and full HD test video sequences were used: *Station* (1920×1080, 25Hz), *RiverBed* (1920×1080, 25Hz), *PoznańStreet* (1920×1088, 25Hz), *Balloons* (1024×768, 30Hz), *ChinaSpeed* (1024×768, 30Hz), *SliceEditing* (1280×720, 30Hz);
- The IBBPBBPBBPĚ structure of group of pictures (GOP) was used;
- Experiments were done for different values of quantization parameter (QP): QP=22, 27, 32, 37, that correspond to quality of reconstructed video from excellent (QP=22) to poor (QP=37).

All tests were done on Intel Core i7 950 platform (3.07GHz clock frequency, 8MB cache memory) equipped with 12GB of RAM and working under Microsoft Windows 7 system.

4   Complexity of CABAC in HEVC – Results

In the course of experiments complexity of individual parts of CABAC decoder was measured, as clearly pointed out in the previous section. Detailed results achieved for different test video sequences and wide range of bitrates (250-31000 kbps) were presented in Table 1.

Results revealed that de-binarization of syntax elements and context modeling of binary symbols make a bulk of computations in CABAC. Depending on the bitrate of encoded bitstream it is 50% to 70% of the total computations in entropy codec (it was 62% in average). Such a large amount of computations for this part of entropy codec results from main features of

applied algorithms. And so, de-binarization of syntax elements is very similar to traditional Huffman decoding with necessity of bit-by-bit processing of data. Binary symbols are finally arithmetically decoded taking into account the statistics of symbols. The algorithm of context modeling is very irregular in CABAC and large amount of computations must be done to calculate probabilities of symbols. In particular, calculation of context information is the most time consuming part of the context modeler block. All this affects complexity of CABAC codec to a large extent.

The core of binary arithmetic coding has been greatly accelerated due to application of the M-codec core. Additionally, some of symbols are coded using bypass coding mode where the computationally complex stage of symbols' probabilities estimation is skipped. All mentioned simplifications of the core have reduced its complexity significantly - the M-decoder core makes 27% to 47% of the total computations in CABAC (it was 37% in average).

Share of computations in different parts of CABAC strongly depends on the target bitrate. As achieved in experiments, the higher the bitrate the higher amount of computations are associated with arithmetic decoder core. Such an observation has been noticed for each of test video sequences (see Table 1). In author's opinion, the answer lies in the number of symbols coded in bypass mode. Lower values of QP parameter (that correspond to higher bitrate and better quality of reconstructed video) increases the number of symbols that are coded in the bypass mode. For this coding mode there is no context modeling of symbols, which increases percentage contribution of arithmetic decoder core in the whole CABAC noticeably.

The solution in CABAC of HEVC that reduces complexity of the entropy codec substantially (relative to CABAC of MPEG-4 AVC) is increasing the frequency of using the bypass mode (in average, 21% of symbols are coded in this mode in HEVC - see Table 2). Table 2 presents details for the percentage of bypass bins in the encoded stream and comparison of complexity of arithmetic decoder (AD) core when operating in the regular and bypass mode. In average, complexity of the bypass AD core is 80% of the complexity of the regular AD core. This comparison concerns arithmetic decoder cores only (bypass and regular cores) and does not take into account the computationally complex stage of context modeling that must be additionally done in the case of regular mode. Additionally, other complexity differences were noticed for the lower and the higher bitrates (see Table 2). It may be a result of different actions in re-normalization part of AD core for cases of uniform (bypass mode) and non-uniform (regular mode) probability distributions of symbols.

The optimized CABAC decoder is 8% of computations in the whole HEVC decoder (see Table 1). Table 3 presents the averaged (over test sequences) results of complexity of CABAC codec per one binary symbol.

CABAC decodes a binary symbol in almost 190 processor cycles, with 120 processor cycles needed for de-binarization and context modeling part of CABAC. For a processor operating with 3GHz clock frequency it gives a

Table 1. Percentage contribution of arithmetic decoder (AD) core (M-decoder) and de-binarization (de-bin) and context modeling in CABAC decoder. Contribution of CABAC decoding in the whole HEVC decoding time.

Test sequence	HEVC decoder time (**original HEVC**)		
	% of AD core in CABAC	% of de-bin and context modeling in CABAC	% of CABAC in HEVC
Station2			
QP=22 (3781 kbps)	38.91	61.09	7.36
QP=27 (1430 kbps)	35.14	64.86	3.93
QP=32 (707 kbps)	31.66	68.34	2.46
QP=37 (361 kbps)	27.86	72.14	1.68
River Bed			
QP=22 (30874 kbps)	41.93	58.07	24.91
QP=27 (15880 kbps)	40.47	59.53	15.07
QP=32 (8041 kbps)	38.71	61.29	9.69
QP=37 (3858 kbps)	36.91	63.09	6.18
Poznań Street			
QP=22 (3050 kbps)	38.99	61.01	7.69
QP=27 (1574 kbps)	36.13	63.87	4.77
QP=32 (808 kbps)	32.66	67.34	3.44
QP=37 (425 kbps)	28.71	71.29	2.51
Balloons			
QP=22 (1742 kbps)	37.58	62.42	6.64
QP=27 (807 kbps)	35.25	64.75	4.40
QP=32 (433 kbps)	32.76	67.24	3.02
QP=37 (251 kbps)	29.93	70.07	2.26
China Speed			
QP=22 (7007 kbps)	42.88	57.12	20.06
QP=27 (3675 kbps)	41.07	58.93	14.32
QP=32 (1827 kbps)	39.01	60.99	9.48
QP=37 (926 kbps)	36.79	63.21	6.09
Slice Editing			
QP=22 (2153 kbps)	47.17	52.83	14.59
QP=27 (1577 kbps)	45.11	54.89	11.32
QP=32 (1154 kbps)	42.49	57.51	8.55
QP=37 (844 kbps)	39.54	60.46	6.37
Average	**37.402**	**62.598**	**8.200**

Table 2. Computational complexity of bypass coding engine (relative to regular coding engine) in binary arithmetic decoder core of CABAC. Percentage contribution of bins coded in bypass mode in the HEVC video decoder.

Test sequence	HEVC decoder time (**original HEVC**)	
	% Complexity of AD bypass core (relative to AD regular core)	% of bypass bins
Station2		
QP=22 (3781 kbps)	80.774	15.336
QP=27 (1430 kbps)	75.597	16.806
QP=32 (707 kbps)	69.769	16.711
QP=37 (361 kbps)	64.408	16.539
River Bed		
QP=22 (30874 kbps)	91.694	20.566
QP=27 (15880 kbps)	87.792	21.127
QP=32 (8041 kbps)	84.424	19.978
QP=37 (3858 kbps)	82.225	19.157
Poznań Street		
QP=22 (3050 kbps)	81.265	21.402
QP=27 (1574 kbps)	77.541	19.241
QP=32 (808 kbps)	73.560	17.383
QP=37 (425 kbps)	68.388	16.395
Balloons		
QP=22 (1742 kbps)	80.579	19.739
QP=27 (807 kbps)	76.816	20.384
QP=32 (433 kbps)	72.447	20.008
QP=37 (251 kbps)	68.287	19.267
China Speed		
QP=22 (7007 kbps)	83.085	24.641
QP=27 (3675 kbps)	79.820	22.582
QP=32 (1827 kbps)	76.554	20.552
QP=37 (926 kbps)	73.441	18.621
Slice Editing		
QP=22 (2153 kbps)	95.150	37.816
QP=27 (1577 kbps)	91.981	32.573
QP=32 (1154 kbps)	85.671	27.123
QP=37 (844 kbps)	78.258	21.901
Average	**79.147**	**21.077**

Table 3. Complexity of CABAC (in processor cycles) for one binary symbol. Average over 6 test sequences

	Complexity of CABAC in HEVC **(per 1 binary symbol)**			
	whole CABAC decoder time **[processor ticks]**	de-bin and context modeling time **[processor ticks]**	AD regular core time **[processor ticks]**	AD bypass core time **[processor ticks]**
Average over test sequences	188	119	72	57

possibility of real-time CABAC decoding of streams with bitrate up to 16Gbps. It should be keep in mind that this result applies only to algorithmically optimized sequential version of the software CABAC decoder. Additional opportunities exist to parallelize computations in CABAC in the case of hardware implementation [7].

5 Conclusions

CABAC entropy decoding makes significant part of total computations in the process of HEVC video decoding. For the considered in the paper implementation of the HEVC decoder it is 8% (in average) of total decoding time, but this value strongly depends on the value of bitrate and increases with the increase of the bitrate. The content of the video sequence also affects exact percentage contribution of entropy decoding in the whole video decoder.

Results revealed that de-binarization of data and context modeling of binary symbols make a bulk of computations in CABAC. Depending on the bitrate of encoded bitstream it is 50% to 70% of the total computations performed in entropy decoder (it was 62% in average). The core of binary arithmetic decoder makes 37% of total computations in CABAC in average.

Using of bypass coding mode for selected binary symbols reduces complexity of CABAC entropy decoder significantly (see section 4 for detailed discussion). Depending on the bitrate and content of a video sequence, 15%-37% of binary symbols are processed in this coding mode (21% in average). In the bypass mode, complexity of arithmetic decoder core is about 80% of complexity of the core operating in the regular mode.

In experiments, almost 190 processor cycles were needed to process one binary symbol with CABAC. It allows to process in real-time encoded streams with bitrates up to 16Mbps.

References

1. Domański, M.: Obraz cyfrowy, Wydawnictwa Komunikacji i Lacznosci (2011)
2. Woods, J.W.: Multidimensional Signal, Image, and Video Processing and Coding. Academic Press (2012)
3. Richardson, I.E.G.: The H.264 Advanced Video Compression Standard, 2nd edn. Wiley (2010)
4. Marpe, D., Schwarz, H., Wiegand, T.: Context-Based Adaptive Binary Arithmetic Coding in the H.264/AVC Video Compression Standard. IEEE Transactions on Circuits and Systems for Video Technology 13(7), 620–636 (2003)
5. Special issue on H.264/AVC video coding standard. IEEE Trans. Circuits and Systems for Video Technology 13 (2003)
6. Tian, X., Le, T.M., Lian, Y.: Entropy Coders of the H.264/AVC Standard. Springer (2011)
7. Karwowski, D.: Advanced Adaptation Algorithms of Arithmetic Coding in Hybrid Video Compression. Doctoral Dissertation, Poznañ University of Technology (2008)
8. Sullivan, G.J., Ohm, J.R., Han, W.J., Wiegand, T.: Overview of the High Efficiency Video Coding (HEVC) standard. IEEE Transactions on Circuits and Systems for Video Technology 22(12), 1649–1668 (2012)
9. Nguyen, T., Winken, M., Marpe, D., Schwarz, H., Wiegand, T.: Reduced-complexity entropy coding of transform coefficient levels using a combination of VLC and PIPE, JCTVC- D336. In: JCT-VC Meeting, Daegu (2011)
10. HEVC Test Model, HM 3.2, `http://hevc.hhi.fraunhofer.de`

Object Detection and Segmentation Using Adaptive MeanShift Blob Tracking Algorithm and Graph Cuts Theory

Boudhane Mohcine and Nsiri Benayad

LIAD. Faculty of Sciences, Hassan II University,
Km 8 Route d'El Jadida B.P 5366 Maarif, Casablanca 20100 Morocoo
MrBoudhane@gmail.com, benayad.nsiri@enst-bretagne.fr

Summary. In this paper, we present method of detection, segmentation and tracking to different objects in video sequence in real-time. We propose new approach based on Blob tracking, the technique, we find a hybrid combination between tracking-detection, in blob tracking use detection model based on two pieces of information; brightness and color. Our approach adds new properties in these blobs based on shape features extractions, where we define several properties for efficient detection. These blobs, present objects detected, the motion is estimated by non-parametric Kernel density estimation by using MeanShift algorithm to track this blobs. Segmentation is performed by GraphCuts approach; it generates and updates a set of Blobs in the sequence. Experimental results demonstrate that our method is robust for challenging data and present many advantages inside other approaches.

1 Introduction

This is a new automated approach that can be applied in many areas of computer vision. The goal is to allow a machine to understand what it sees when it is connected to one or more cameras. Segmentation and detection are very important problems in computer vision. We applied this method in video-surveillance, we go to track and detect multiple objects on different resolutions. However, the cases of multiple target localization, detection in non-lucid medium and tracking in multiple overlapping objects makes it difficult in many computer vision domain and video analysis applications. It has critical effect in image sequence result.

By that analysis and design of mechanisms for managing real-time vision is still an open problem. In this paper, we conduct an experiment to achieve a reliable monitoring of all objects in video sequences. This paper presents efficient method for solving these problems. In this paper we use blob tracking that defines the objects detected by adding more characteristics of these

objects. This algorithm has recently been adopted as an efficient technique based on blob tracking [1, 2, 3], but it does not have enough parameters for a reliable extraction of the characteristics of objects detected.

The mean-shift algorithm is an efficient technique for tracking 2D blobs in an image sequence although the scale is a crucial parameter. In [2] they showed that the difference of Gaussian (DOG) average displacement of the core allows effective monitoring of blobs in the scale space. One of the drawbacks of the methods of background difference for the detection Movement is the length of processing time. Therefore, the motion detection in real time in some cases is very difficult, rather impossible with this type of method. Because Object tracking should deal with some challenges like occlusion, target appearance changes, cluttering, etc., In [3] new approach based on Blob tracking using histogram filtering, is based on meanShift theory, This algorithm needs less computational complexity compared with methods performed in the whole image. In the traditional mean-shift algorithm, the target model is unchanged during the tracking and belongs to the first frame, so this algorithm is not robust in the case of large changes of appearance, size and direction of the target. Mean-shift is a non-parametric kernel estimation, which gives good results, especially in image segmentation [4]. However, the size of the kernel must be defined beforehand. Several techniques are defined in [5, 6] and [7]. We are based on one of these methods to solve this problem of scale. We will also incorporate a notion to track-segmentation simultaneously [9] with the introduction of the theory of Graphcut [8]. That will guarantee fast in terms of performance and cost calculations weakness.

In the first section we have defined all the theoretical concepts used of this solution, we recall the principles of the method Meanshift, the blob tracking, and the theory of Graphcuts. Then in the second section, we describe the algorithm proposed. And in the third section we present the experimental results of the algorithm, followed by a conclusion.

2 Architecture

The approach is typically able to react according to the content of the captured scene. In which we deal with a lot of problems namely: lighting problem and luminance change issues such as movement changes the background and changes in small claims for this we proceed by a able to make simultaneous segmentation and tracking based on storing blobs for each iteration. For this reason the system must predict the existence of the blob based on a list of blobs comparing their histograms, which is going to reduce the processing time. After this step it may have new birth of blobs. Blobs if the list is updated (correction step).

It is a method to identify and trace the movements of objects; it allows determining the positions in successive frames. Before pursuing a blob, you must first identify and located. So the first step we must do is detecting blobs.

The process is performed by grouping pixels of similar brightness (contrast) and of the same color (texture). A tolerance threshold indicates the difference between the values that can appear in a blob. The difficulty is that the shape and values of blobs may change as they move. Then we should detect the blob in the following frames by establishing a significant correlation between the different blobs in each frame (Fig. 1).
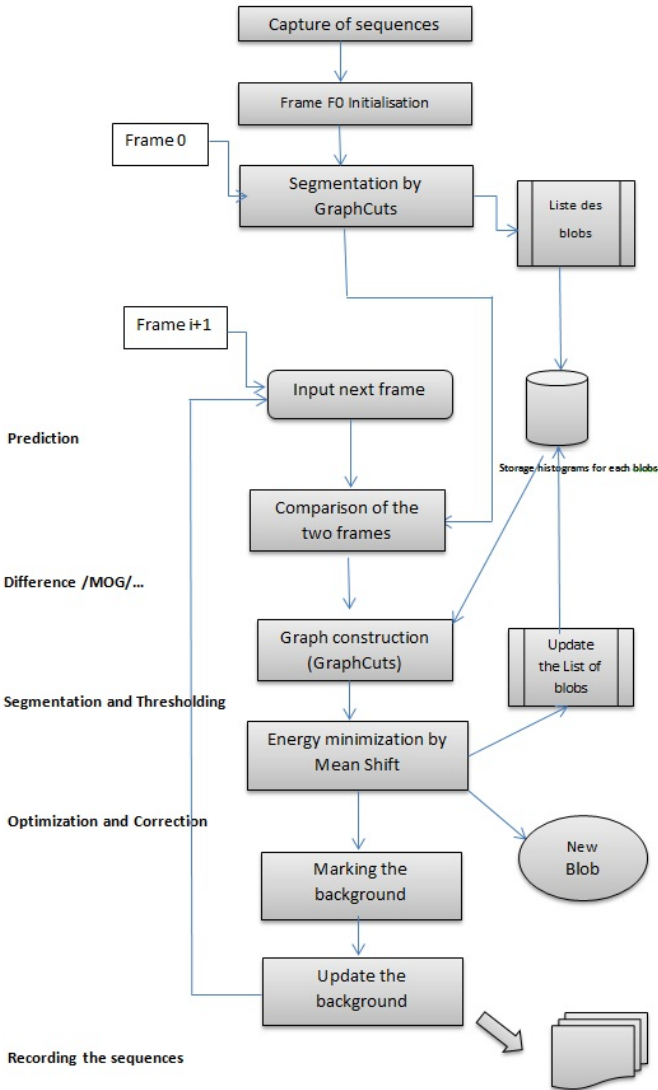
Fig. 1. Architecture of our approach

3   Theories Concept

In this section we will show all the theoretical tools used in our approach. First, we will make a simultaneous detection monitoring way which gives us a high speed (Fig. 2). We know that rapid detection generally leads to a loss of data; this method is based on several theoretical principles for accurate detection of high quality.
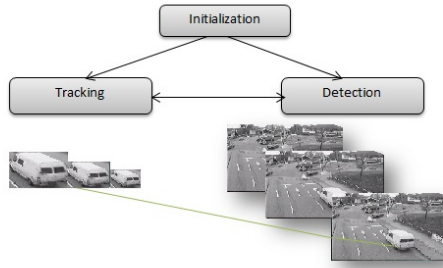
Fig. 2. process of detection-tracking

The first step is initializing, it allows the observation and preparation of new frames for the detection-monitoring. For this we are based on several techniques like Meanshift (motion estimation) algorithm, GraphCuts (segmentation) under Blob tracking. We can decompose the initialization phase in two phases: preprocessing and prediction (Fig. 3).
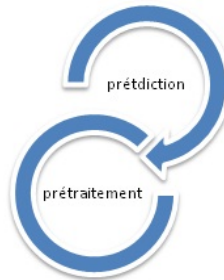
Fig. 3. initialization phase

The first frame initialization is based on a simple background subtraction, which we will use Gaussian mixture MoG. In this phase we will make two classifications of pixels: objects (blobs) pixels and others pixels. When the blob is detected for the first time, it stores its histograms in a list of blobs; this list will be to update each suspension or detection of objects. From the second

frame, the initialization phase is to predict objects (blobs), it functions using energy minimization algorithm in which GraphCuts warranty segmentation at a modest cost, blobs obtained segmentation by this, we will compare the histogram with that of previous frame, by updating a list of blobs.

- **Blob tracking and Shape Feature extraction:** In the traditional blob tracking feature two are taken to model an object by contour modeling and by color modeling. In this article we will add more features while getting a reliable and accurate detection.
  - *Moment:* The statistical concept of the moment is defined by the following formula:

  $$m_{pq} = \sum_{(u,v)\in R} I(u,v).u^p v^q \tag{1}$$

  It describes the moment of the order p,q for a discrete (image) function $I(u,v) \in R$. All the following definitions are also generally applicable to regions in grayscale images. This moment is used by central moment.
  - *Central moments:* To compute position-independent (translation-invariant) region features, the region's centroid,which can be determined precisely in any situation, can be used as a reference point. In other words, we can shift the origin of the coordinate system to the region's centroid $\bar{x} = (\bar{x}, \bar{y})$ to obtain the central moments of order p,q:

  $$u_{pq}(R) = \sum_{(u,v)\in R} I(u,v).(u - \bar{x})^p (v - \bar{y})^q \tag{2}$$

  For a binary image $I(u,v) = 1$.
  - *Eccentricity:* Similar to the region orientation, moments can also be used to determine the "elongatedness" or eccentricity of a region. We adopt the following definition because of its simple geometrical interpretation:

  $$E_{cc}(R) = \frac{a_1}{a_2} = \frac{\mu_{20}+\mu_{02}+\sqrt{(\mu_{20}-\mu_{02})^2+4.\mu_{11}^2}}{\mu_{20}+\mu_{02}-\sqrt{(\mu_{20}-\mu_{02})^2+4.\mu_{11}^2}} \tag{3}$$

  where $a_1 = 2\lambda_1, a_2 = 2\lambda_2$ are multiples of the eigenvalues λ_1, λ_2 of the symmetric 2×2 matrix :

  $$A = \begin{pmatrix} \mu_{20} & \mu_{11} \\ \mu_{11} & \mu_{02} \end{pmatrix}$$

  formed by the central moments μ_{pq} of the region R.
- **GraphCuts:** In practice, there are several methods of segmentation interactive of foreground/background classical tools of image segmentation that use either texture (color) or edge (contrast). In [7] an approach based on optimization by graph cut has been successfully developed, which combined the two types of information. Which shows that the graph Cuts is the best tool for making a good discrete optimization. In cases where finding a global minimum is not possible, we have seen there exist many efficient algorithms based on Graph Cuts [9, 10].

- **MeanShift:** The Meanshift method proposed by Fukanaga [4] defined an algorithm non parametric density estimation, which converges quickly to the local maximum of the probability density function through iterations. Meanshift is an effective technique for tracking 2D blobs in year image sequence although the scale is a crucial parameter. In [2] they showed as the difference of Gaussian (DOG) average displacement of the core allows effective monitoring of blobs in the scale space. We will try to make a choice (and updates) scale while blobs following that exchange in size.

4 Algorithm and Theory

The approach is typically able to react according to the content of the captured scene. In which we deal with a lot of problems namely: lighting problem and luminance change issues such as movement changes the background and changes in small claims. For this we proceed by a able to make a simultaneous segmentation and tracking based on storing blobs for each iteration. For this reason the system must predict the existence of the blob based on a list of blobs where comparing their histograms, this is going to reduce the processing time. After this step it may have new birth of blobs, blobs if the list is updates (correction step).Input sequences are in the form of segmented images (by GraphCuts), each blob is identified by a unique number that is identical in all sequences of images on this number will be displayed above each detected blob. At first we select the image that contains the pixel values objects that were used to define the blobs (removal of objects from the background).When the blob is detected, you must check that the blob is already featured in the previous images, why we do what we call: verification of similarity which is checked: The location (pixel coordinates), the size, color (texture), orientation (time computation of second-order) form (we calculate the eccentricity) and histogram (color distribution in the blob) with other blobs in the previous frames. This criterion of similarity varies in functions of all the properties mentioned above by representing a percentage. As the percentage is large it is more likely to have a similar blob. If we found a similar blob is recovered easily from a list of already detected blobs, if the blob is considered new and not connected to a previous blob.In this case it creates the new blob that must Identify (associate an id) and extract its features which will store the list of blobs. When detected blobs disappear in an image sequence, they may reappear in the following images in the hope of preserving the id. For this we define a threshold which is the minimum number of images for that we should start tracking this blob. To avoid small movements that does not correspond to the target object. We also define another threshold: the minimum number of pixels containing a blob for it to be considered a blob active, to avoid false detections dedicated noise.

The Proposed Algorithm


```
Begin
Input sequences
Initialization of the first frame (Frame) img0
General adaptations thresholds th1, th2, th.
Segmentation (img0) // GraphCuts
Feature extraction
For all images of the sequence do
Binarization (img (i))
Thresholding th
Segmentation (img (i))
Detection-Prediction (img (i)) // MeanShift
Verification of similarity (location, shape, size, color, orientation, histogram)
Treating blobs (creation or Updates)
Update (list of blobs (Idblob, features, histogram)))
End for
SequenceResultat display;
End
```

Fig. 4. Algorithm of our approach

5   Experimental Result

In this section we will show the practical results of all that we have done in
the screen. We have developed a system for real-time monitoring based on
smart algorithms presented. The system is implemented on a standard PC
(Core2Duo, 2 MBRAM). The size of the video image is 320×240 (24 bits per
pixel). The system is tested in two environments, one artificial and one real.
Image sequences in these examples are captured by a built-in camera (2MP).
We are going to compare our approach with other existing, and we will show
you that it obtains good results compared to others. The following presents
the results (frames: 12, 49, 86 and 112).
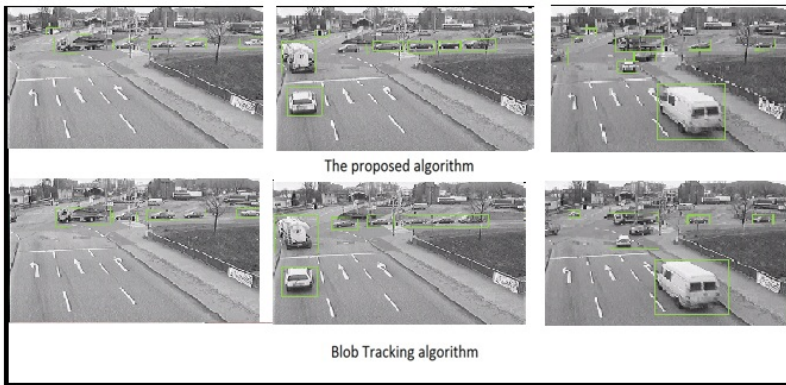
Fig. 5. Sequences result

In the other method, the detection and tracking are sensitive to small movements (it ignores objects smaller movements), very sensitive in the overlaps between objects (it's considered as a single object), and the effects of light in the sequences. Against by our approach is very effective and less susceptible to these effects. As you may notice that our application provides a high accuracy in detecting vehicle over other methods. Precision and reliable detection is guaranteed in a reduced time with minimal resources. Below is a comparison of our method with the other two numbers side of blobs generated.
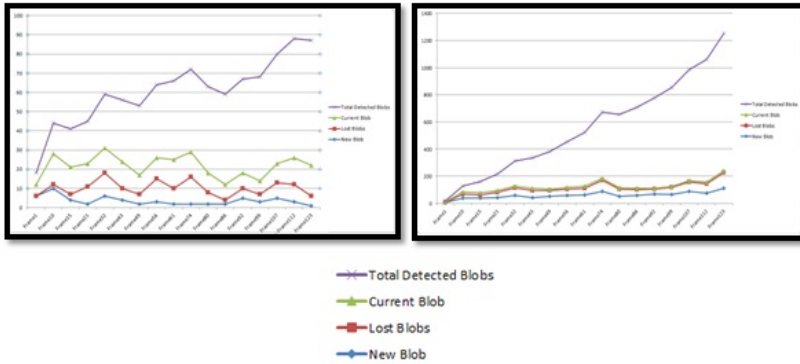
Fig. 6. Number of blobs generated by traditional blob tracking method(left) and by our approach (right)

The two graphs representing the generation of blocks in the sequence of frames, we took some samples of the frames on which we will make a comparison between the traditional blob tracking and our approach. Hollowing it is that our method limits the generation of blobs, since the first dice until the last frame is generating only 66 blobs (diced 1st frame to 123th frame), against the blob tracking traditional generates 1013 blobs. This is due to the fact that traditional tracking blob generated each frame of new blobs. It is also a fact that the blob tracking in traditional lacks the precision criterion, because it's based solely on two things: color, brightness and tolerance, against our approach by adding several characteristics that we obtain a precise detection, fast detection and tracking and good performance.

6   Conclusion

In this article we presented a new approach that combines several principles and methods to achieve the goal of ensuring a better detection and monitoring of vehicle in video sequences, on which we are based at the beginning of the first modeling approach background. In an initialization step, we invoked blobs to identify patterns of body parts through a contour analysis

and segmentation region (Mean-shift). After initialization, based on a cost minimization (GraphCuts) approach is used for matching patterns of several related components and monitoring.This minimization of energy is applied to an area of the image containing parts of the body. The results showed very good performance in terms of computational cost and quality of precision in the detection-monitoring. This method is not limited only to the detection of vehicles, it can be also applied in other utility such as video surveillance.

References

1. Comaniciu, D., Ramesh, V., Meer, P.: Real Time Tracking of Non-Rigid Objects using Mean Shift. In: IEEE Computer Vision and Pattern Recognition II, pp. 142–149 (2000)
2. Collins, R.T.: Mean-shift Blob Tracking through Scale Space. In: IEEE, pp. 234–240 (2003)
3. Liang, D., Huang, Q., Jiang, S., Yao, H., Gao, H.: Mean shift blob tracking with kernel histogram filtering and hypothesis testing, pp. 605–614 (2005)
4. Fukunaga, K., Hostetler, L.: The estimation of the gradient of a density function, with applications in pattern recognition. IEEE Trans. on Information Theory 21(1), 32–40 (1975)
5. Comaniciu, D., Ramesh, V., Meer, P.: Real-time tracking of non-rigid objects using mean shift. In: Proceedings of IEEE Conference on Computer Vision and Pattern Recognition, vol. II, pp. 142–149 (2000)
6. Liang, D., Huang, Q., Jiang, S., Yao, H., Gao, W.: Mean-Shift Blob Tracking with Adaptive Feature Selection and Scale Adaptation. In: IEEE International Conference on Image Processing, ICIP 2007, vol. 13(3), pp. 369–372 (2007)
7. Zhao, L., An, G., Zhang, F., Wang, H., Dai, G.: Scale Adaptation of Mean Shift Based on Graph Cuts Theory. In: 12th International Conference on Computer-Aided Design and Computer Graphics, pp. 202–205. Chinese Academy of Sciences (September 2011)
8. Bugeau, A., Pérez, P.: Track and Cut: Simultaneous Tracking and Segmentation of Multiple Objects with Graph Cuts. EURASIP Journal on Image and Video Processing, Ref: 2008:317278 (2008)
9. Boykov, Y., Veksler, O., Zabih, R.: Fast approximate energy minimization via graph cuts. IEEE Transactions Pattern Analysis and Machine Intelligence 123, 1222–1239 (2001)
10. Boykov, Y., Funka-Lea, G.: Graph Cuts and Efficient N-D Image Segmentation. International Journal of Computer Vision 70(2), 109–131 (2006)

Semantics Driven Table Understanding in Born-Digital Documents

Jacek Siciarek

Faculty of Electronics, Telecommunications and Informatics,
Gdansk University of Technology, Narutowicza 11/12, 80-233 Gdansk, Poland
`siciarek@gmail.com`

Summary. This paper presents a new approach to table understanding, suitable for born-digital PDF documents. Advance beyond the current state of the art in table understanding is provided by the proposed reverse MVC method, which takes advantage of only partial logic structure loss (degradation) in born-digital PDF documents, as opposed to unrecoverable loss (deterioration) taking place in scan based PDF documents.

1 Introduction

Every day people worldwide produce millions of new documents, using different word processors, stylesheets (e.g. MS Word, MS Excel, Open Office Write) and typesetting tools. Some of these tools are commercial, many others are for free; usually they are compatible but, especially on mobile devices not every document can be opened. The solution is exporting documents to Portable Document Format - practically any modern word processor enables that. PDF documents look the same everywhere, can be read by anybody, and at the same time may be protected against unauthorized modifications. Edited and then exported PDF documents are called *born-digital*, and as such should be distinguished from documents created from images of scanned paper pages or other binary images.

PDF is a very popular format for document archives — from technical instructions to literature. Plenty of documents contain data which could be used for further processing, e.g. cost reports, summary data, or simply present in other context, e.g. as a chart. The problem is that a *born-digital* PDF document loses loses its original logical structure during the generation process. PDF is a typographically oriented document format and preserves no information about the document structure, as it is designed for human readers.

Recovering information from PDF archives is a new challenge for computer science, and a growing concern for the document engineering community. The *Executable Paper Grand Challenge* launched by Elsevier [2] attracted

scientists from around the world presenting their solutions for data and information recovery, rather then extraction, from digital documents published in the electronic form. Executable paper (document) should offer much more than a plain paper or digital document – namely straight access to meaningful data contained in it.
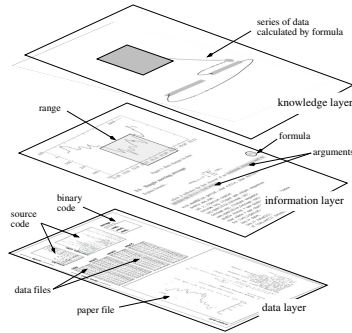
Fig. 1. Layers of the IODA executable paper

One of the proposals to the Elsevier challenge has been *IODA* [6], a lightweight document architecture enabling document executability despite of its particular representation format. It is very important to have data separated from the rest of document. Executable IODA document assumes three layers shown schematically in Fig. 1: *data layer*, which stores data in a raw form (data and document files in any format, executable code), *information layer*, which presents data to the user with the use of human interpretable patterns (text, tables, charts, formulas), and a *knowledge layer*, which allows users to process document data with embedded (data layer scripts), local (user specific tools) or external (third party services) functionality.

Data elements are extracted from the document content during its acquisition process to the repository, archive or a digital library. Some data may be extracted automatically (e.g. images and other known binary streams) or on user request (e.g highlighted parts of text, parts of images or tables). Especially tables are important, because they provide specific interpretation patterns for the data, indented by the document author. So according to IODA, table is a semantic unit of *information layer*, while the content of its individual cells constitutes a data resource of the *data layer*.

As far as the PDF documents are concerned, their elements like tables, equations and charts are most interesting to be retrieved as meaningful data sources. These data and their interpretation patterns, if properly retrieved, can be processed further at the *knowledge layer* level. This paper focus is on recovering table data from *born-digital* PDF documents.

2   Table Structure

Extracting data and recovering base document structure is a tremendous challenge to document engineering, especially when using search engines become basic way of knowledge search. As far as tables are concerned there is a popular approach to table understanding which consists of the three following steps [3]:

- table detection – finding parts of document with data in tabular structures
- table structure recognition – retrieving data structure from detected parts
- table interpretation – detecting of table cell roles, which includes: *cell functional analysis* and *semantic interpretation*

2.1   Table Model

Table model refers to the way one may to retrieve the data from a tabular structure. On the one hand we have *structural models* like those proposed by *Hu* [4] or *Hurst* [5], where tables are modelled as Directed Acyclic Graph with table regions represented by leaf nodes and collections of such nodes as composite nodes, relationships are modeled as edges (Hu) or mapping table into geometric model that identifies the relative location of cells and captures their textual content (Hurst), while on the other hand we have a *conceptual models*, which goal is abstraction of content from presentation, like the one propsed by [8], probably the best known and exhaustive work in the table understanding idea, including layout model specification, data types used in tables, editing and formatting problems as well. *Wang* defined two main table cell types: *data cell* containing data an *access cell* containing table labels.

3   Logical Structure of PDF Document Content

Loss of a logical document structure is a common problem in PDF documents. Reverse engineering is usually the only way to proceed to extract it, but in most cases we are not able to perform this process automatically. Information loss in PDF can take two forms:

- *distortion* – format is unchanged but its logical structure is unrecoverably lost
- *degradation* – visual document format is unchanged, but its logical structure is only partially deformed

PDF stores data as (limited length) string objects, or as (arbitrary length) stream objects [1].

Fig. 2 illustrates how tabular data are represented in scan based documents, where tabular data are unrecoverably lost (a), and in a born-digital document (b), where many data elements are clearly visible, e.g., the table header part `name`.

(a)

name	amount
Oranges	4
Apples	12
Plums	31
Pears	7

(b)

```
00000000  ffd8 ffe0 0010 4a46 4946 0001 0101 0048 .X.'..JFIF.....H
00000010  0048 0000 ffdb 0043 0003 0202 0202 0203 .H...[.C........
00000020  0202 0203 0303 0304 0604 0404 0404 0806 ...............
00000030  0605 0609 080a 0a09 0809 090a 0c0f 0c0a ...............
```

(c)

```
/F2 12 Tf
1 0 0 1 70.584 731.26 Tm
[(na)4(me)] TJ
ET
Q
q
68.064 722.26 66.24 19.8 re
```

Fig. 2. Tabular part of PDF document in human readable format (a), preview of scan based stream (b) and born-digital stream (c)

3.1 Content Structure Distortion

Document created from images of scanned pages loses not only its logical structure but textual context as well. One cannot get text without using OCR applications. Only printing is allowed, but high quality is often hard to achieve. However, some advantages exist, e.g. there is no problem with text misformatting or unexpected font change — scans look like original every time.

3.2 Content Structure Degradation

Exporting documents to PDF format causes some loss of its logical structure in general. However, document parts, like chapters, a table of content, footnotes, references, etc., differ from the body only with typography. Tables are turned into boxes with textual content. This is common for PDF readers, e.g. Adobe Acrobat Reader or KDE Okular, to allow copying of text, so if tabular data are stored as the plain text, upon removing typographical data, it should be possible to restore tabular data, most often without any loss. Therefore, in order to extract a table content it must be found first how the

original document generation application has encoded tabular data into a PDF document; fortunately the vendor information is specified in PDF, as values of the *Producer* and *Creator* variables.

Throughout the rest of the paper we argue that digital-born PDF document structure degradation does not prevent partial recovery of table semantics, and will show that thus recovered table structure suffices in terms of accessing and manipulating table data.

4 Table Semantics

Tables are used when we want to compare some results, to present data in a specific order, e.g. chronologically, or to emphasize special relations. In fact almost any textual data can be presented as a table. For example a simple sentence:

<div align="center">
Tables are commonly
used in documents.
</div>

can be presented as a table:

Tables	are	commonly
used	in	documents.

Although the data above are constitute a table, nothing has changed in their semantics. Both plain text and tabular representation has exactly the same value of information.

Popular word processors, like MS Word or Open Office Writer provides a *convert text to table* functionality. But there is no meaning in such a conversion – neither order nor relation emphasized whatsoever. It shows that for useful table application, special kind of data is needed.
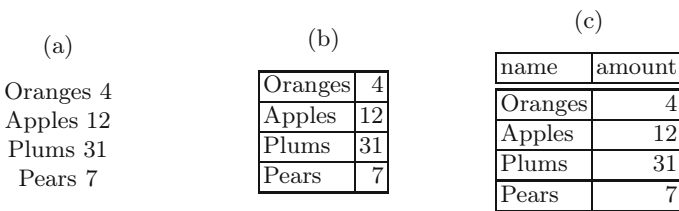
Fig. 3. Tabular data in three different formats

Consider the next example in Fig. 3, information contained in the plain text (a) becomes more apparent if organized as a table (b) and yet more apparent with column headers in place (c).

Examples above show that for valuable tabular data presentation, data should have strong relations in rows, while columns should contain similar data types.

Let us introduces ome basic notions before proceeding further to the major development of this paper:

- *cell* – an atomic part of a table, container with indivisible data,
- *column* – a vertical set of cells with similar type of data and the same context,
- *row* – a horizontal set of related cells,
- *label* – a distinguished cell that contains a name of set of cells, e.g. a column header, usually emphasized visually. In a typical table the number of labels is much lower than the number of regular cells.

Based on the example tables shown in Fig. 3 we distinguish *plain* and *labeled* tables:

- *plain table* – a table which contains at least one row and one column (one cell)
- *labeled table* – a plain table in which at least one cell is a *label*

We say that a table is in a normalized form if its each cell has at most one neighbor at every edge (see Fig. 5).

In our further considerations we focus on *labeled tables*.

4.1   Reverse MVC method

The method for recovering tables proposed in this paper combines the general idea of a table as a *data interpretation pattern* described above with a software design pattern called *Model-View-Controller* (MVC) – especially useful for programming Web applications, because of separating representation of information from the user's interaction with it [7].

```
[
    { "name": "Oranges", "amount": 4 },
    { "name": "Apples", "amount": 12 },
    { "name": "Plums",  "amount": 31 },
    { "name": "Pears",  "amount": 7 }
]
```

Fig. 4. Raw table data from previous examples in JSON

MVC distinguishes three components, namely a Model, a View and a Controller. The Model component contains data and notifies its associated View component on any change of their state. It does not know details of the View, so no data are transmitted with the notification. Upon receiving notification the View component retrieves the necessary data from the Model and produces updated output. The Controller component is responsible for intercepting user generated events and can send requests to both: the View,

to change presentation of the Model data, and the Model, to update the state of its data.

A table in a PDF document can be mapped to the respective MVC components in a straightforward way. One important difference, however, is that for born-digital PDF documents it should be done in a reverse way - in fact only the View component data are available, whereas we want to reconstruct the Model component data. So in the *reverse* MVC approach the View component must get PDF file as an input and:

1. parse the file structure,
2. separate data streams,
3. decode data streams and chooses textual ones,
4. separate meta data to obtain the document creator info, and
5. transfer streams and creator info to the Controller component.

The Controller component gets the textual streams and creator info as an input and:

1. based on the creator info chooses the appropriate table parser algorithm,
2. analyses streams and extracts parts containing tabular data,
3. processes cells by separating labels and regular cells,
4. normalizes data by splitting cells spanning more than one row or column into a set of adjacent cells,
5. creates data structure and transfers is to the Model component.

city	gender	03/2013	04/2013
Warsaw	male	134	44
Warsaw	female	34	24
Berlin	male	0	522
Berlin	female	10	412
Dublin	male	310	22
London	female	741	40

city	gender	2013	
		03	04
Warsaw	male	134	44
	female	34	24
Berlin	male	0	522
	female	10	412
Dublin	male	310	22
London	female	741	40

Fig. 5. Normalized and unnormalized table

Model component is responsible for raw data management. It provides data in application native or required format, e.g. XML or JSON (shown in Fig. 4). Model can be implemented as a ORM and store data in repositories (e.g. databases).

5   Conclusions

In this paper we have presented a reverse MVC method for retrieving data from tables in born-digital PDF documents, enabling creation of executable

papers based on the IODA architecture [6]. Compared to methods cited earlier in p.3.1 it takes advantage of the fact that born-digital PDF documents preserve to some extent the logical structure of information units contained in their source counterparts. Therefore attempting reconstruction of that structure, scattered over the analyzed PDF document, seems to be more effective in the case of born-digital documents than complex analysis methods developed for scanned documents [4].

Working on textual data streams and other PDF objects does not go beyond simple parsing, since rules for table elements are strictly enforced by the PDF format. Also information of the document generating tool helps a lot, since each particular PDF generator produces output document files in a specific way. The first prototype version of the logical structure extractor implemented by the author can analyze digital PDF documents generated by MS Word and Open Office Write.

It is planned soon to embed that prototype as one of the standard services of the IODA data layer. Besides tables, the reverse MVC method will be expanded during the project to other semantic objects of born-digital PDF documents, such as charts, block-diagrams, BPMN schemas and musical scores.

References

1. Adobe Systems Inc., Document management – Portable document format – Part 1: PDF 1.7 (2008)
2. Elsevier. Grand Paper Challenge Webpage, `http://www.executablepapers.com`
3. Gbel, M., Hassan, T., Oro, E., Orsi, G.: A Methodology for Evaluating Algorithms for Table Understanding in PDF Documents (2013)
4. Hu, J., Nagy, G., Kashi, R., Wilfong, G., Lopresti, D.: Why table ground-truthing is hard (2011)
5. Hurst, M.: A constraint-based approach to table structure derivation (2003)
6. Siciarek, J., Wiszniewski, B.: IODA - an Interactive Open Document Architecture. Procedia Computer Science 4, 668–677 (2011)
7. Veit, M., Herrmann, S.: Model-View-Controller and Object Teams: A Perfect Match of Paradigms. In: AOSD 2003, pp. 140–149. ACM Press (2003)
8. Wang, X.: Tabular Abstraction, Editing and Formatting. PhD thesis, University of Waterloo (1996)

Contextual Possibilistic Knowledge Diffusion for Images Classification

B. Alsahwa[1,2], S. Almouahed[1], D. Guériot[1,2], and B. Solaiman[1,2]

[1] Image & Information Processing Dept., Télécom Bretagne,
   Institut Mines-Télécom, Brest, France
   `bassem.alsahwa@telecom-bretagne.eu`
[2] Lab-STICC UMR CNRS 3192, Brest, France

Summary. In this study, an iterative contextual approach for images classification is proposed. This approach is based on the use of possibilistic reasoning in order to diffuse the possibilistic knowledge. The use of possibilistic concepts enables an important flexibility for the integration of a context-based additional semantic knowledge source formed by pixels belonging with high certainty to different semantic classes (called possibilistic seeds), into the available knowledge encoded by possibility distributions. The possibilistic seeds extraction and classification process is conducted through the application of a possibilistic contextual rule using the confidence index used as an uncertainty measure. Once possibilistic seeds are extracted and classified, possibility distributions are updated and refined in order to diffuse the possibilistic knowledge. Synthetic and real images are used in order to evaluate the performances of the proposed approach.

1 Introduction

An accurate and reliable image classification is a complex and crucial task in many applications such as medical and remote-sensing image analysis. An important difficulty related to this task stems from the higher spectral variability of local areas of the image, which becomes apparent as the sensor spatial resolution power becomes finer. Using such sensors may not necessarily generate improved classifications when per-pixel images classification systems are used [1]. The addition of information from neighboring pixels seems to be a more powerful way of characterizing the classes of interest and may increase classification accuracy. This information is generally referred to as spatial contextual information and the suitable use of this contextual information allows the elimination of possible ambiguities, the recovery of missing information and the correction of errors [2]. Many contextual classification system have been developed to cope with the problem of intra-class spectral variations such as smoothing techniques, Markov random fields, spatial statistics,

fuzzy logic, segmentation, or neural networks [3]. Markov random field (MRF) classifiers such as Iterative Conditional Mode (ICM) [5] are the most widely used for characterising contextual information and image segmentation [4]. However, all encountered approaches have some limitations: *(a)* computational complexity; *(b)* sensitivity of the results to the classifier parameters. In order to overcome the limitations of the above mentioned approaches, an iterative and contextual possibilistic knowledge diffusion approach for image classification context is proposed in this study. In this approach, per-pixel images classification systems are considered under the closed world assumption. Based on prior knowledge, M class probability density functions are, first, estimated using the KDE (*Kernel Density Estimation*) approach [6] and, then, transformed into M initial possibility distributions encoding the "expressed" expert knowledge in a possibilistic framework. The application of the M class possibility distributions on the considered image I will lead to M possibilistic maps PM_{I,C_m}, m = 1, ..., M where (PM_{I,C_m} encodes the possibility degree of different image pixels to belong to the thematic class C_m). The application of possibilistic reasoning concepts on the M possibilistic maps will lead to enrich the prior knowledge by extracting and classifying new learning samples (possibilistic seeds) and hence, updating the estimation of the M possibility distributions. This updating in possibility distributions is projected on possibilistic maps by the attribution of new possibility values to the selected seeds which, in turns, results in possibilistic knowledge diffusion. Based on the use of a degree of confidence (measuring the extent of certainty for each sample to belong to these different classes), the extraction of new learning samples is conducted using possibilistic spatial contextual information, *i.e.* applied on different possibilistic maps. This extraction process is thus strongly inspired from region growing approaches used for image segmentation. The extraction of seeds and thus the possibilistic knowledge diffusion process is then iteratively repeated until no more seeds can be added to the knowledge diffusion process. This paper is organized as follows. In the next section, a brief review of basic concepts of possibility theory is introduced. The proposed approach of possibilistic knowledge diffusion will be detailed in the 3 and 4 sections. Section 5 is devoted to the experimental results obtained when the proposed approach is applied using synthetic as well as real images.

2 Possibility Theory

Possibility theory was first introduced by Zadeh in 1978 as an extension of fuzzy sets and fuzzy logic theory to express the intrinsic fuzziness of natural languages as well as uncertain information [7]. In the case where the available knowledge is ambiguous and encoded as a membership function into a fuzzy set defined over the decision set, the possibility theory transforms each membership value into a possibilistic interval of possibility and necessity measures. The use of these two dual measures in possibility theory makes

the main difference from the probability theory. Besides, possibility theory is not additive in terms of beliefs combination and makes sense on ordinal structures [8].

2.1 Possibility Distribution

Let us consider an exclusive and exhaustive universe of discourse $\Omega = \{C_1, C_2, ..., C_M\}$ formed by M elements C_m, $m = 1, ..., M$ (*e.g.* thematic classes, hypothesis, elementary decisions, etc). A key feature of possibility theory is the concept of a *possibility distribution*, denoted by π, assigning to each element $C_m \in \Omega$ a value from a bounded set [0,1] (or a set of graded values). This value $\pi(C_m)$ encodes our state of knowledge, or belief, about the real world representing the possibility degree for C_m to be the unique occurring element.

   As we consider, in this study, that the available expert's knowledge is expressed through the definition of learning areas representing different thematic classes, *i.e.* statistical data, we will use the probability (Pr)-possibility(π) transformations proposed by Dubois et al. [9].

$$\pi(C_m) = \Pi(\{C_m\}) = \sum_{j=1}^{M} \min\left[\Pr(\{C_j\}), \Pr(\{C_m\})\right] \tag{1}$$

   In our study, this transformation is considered for the good results that it provides in pattern recognition and classification [10].

2.2 Maximum Confidence Index Decision Rule

A few possibilistic decision rules using uncertainty measures are developed. The most frequently encountered rule (proposed by S. Kikuchi et al. [11]) is based on the maximization of the confidence index *Ind* defined as a combination of the possibility $\Pi(A) = \max_{C_m \in A} (\pi(C_m))$ and necessity $N(A) = 1 - \Pi(A^C) = \min_{C_m \notin A} \{1 - \pi(C_m)\}$ measures for each event $A \subseteq \Omega$:

$$\begin{aligned} Ind : 2^\Omega &\to [-1, +1] \\ A &\to Ind(A) = \Pi(A) + N(A) - 1, \forall A \subseteq \Omega \end{aligned} \tag{2}$$

where 2^Ω denotes the power set of Ω, *i.e.* the set of all subsets from Ω. Notice that: Restricting the application of this measure to events having only one element $A_m = \{C_m\}$ results in the following interesting property:

$$\begin{aligned} Ind(A_m) &= \Pi(A_m) + N(A_m) - 1 \\ &= \pi(C_m) - \max_{m \neq n} \pi(C_n) \end{aligned} \tag{3}$$

   This means that $Ind(A_m)$ measures the difference between the possibility measure of the event A_m (which is identical to the possibility degree of the

element C_m) and the highest possibility degree of all elements contained in Ω/A_m (*i.e.* the complement of A_m). If $A_{m_0} = \{C_{m_0}\}$ is the only event having the highest possibilistic value then, A_{m_0} will be the unique event having a positive confidence index value, whereas all other events will have negative values (Fig. 1).
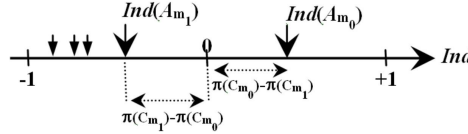
Fig. 1. Confidence indices associated with different decisions (A_{m_0}: event having the highest possibility degree, A_{m_1}: event with the second highest possibility degree)

The decision rule associated with this index can be formulated by:
Decision = A_{m_0} iff

$$Ind(A_{m_0}) = \max[Ind(A_m)], m = 1, ..., M \tag{4}$$

This decision rule can be more severe by accepting the decision making only when the index value $Ind(A)$ exceeds a predefined threshold S (called *possibilistic confidence threshold*):
Decision = A_{m_0} iff

$$\begin{cases} Ind(A_{m_0}) = \max[Ind(A_m)], m = 1, ..., M \\ Ind(A_{m_0}) \geq S \end{cases} \tag{5}$$

Decision= Rejection iff $Ind(A_m) < S$

3 Possibilistic Seeds Extraction Rules

A seeds extraction rule tackles the issue of determining the set of pixels, from the analyzed image I that can be considered as belonging, with a high degree of certainty, to different thematic classes. In this study, the following contextual possibilistic extraction rule is proposed. This seeds extraction associates each pixel P0 with the contextual-based possibility distribution $\overline{\pi_{P_0}} = [\overline{\pi_{P_0}}(C_1), \overline{\pi_{P_0}}(C_2), ..., \overline{\pi_{P_0}}(C_M)]$ instead of the pixel-based possibility distribution $\pi_{P_0} = [\pi_{P_0}(C_1), \pi_{P_0}(C_2), ..., \pi_{P_0}(C_M)]$ where $\overline{\pi_{P_0}}(C_m), m = 1, 2, ..., M$ is extracted from the mth possibilistic maps by the application of a smoothing filter. In this study, the Nogao filter [12] is used in the possibilistic space to control, first, the homogeneity and, second, to insure that selected seeds do not belong to edges. In this filter, 9 cliques $f_h, h = 1, 2, ..., 9$ in a 5×5 window surrounding each pixel in each possibilistic map are defined (Fig. 2):

This leads to have for each pixel $\overline{\pi_{P_0}}(C_m) = [\overline{\pi_{P_0}}(C_m, f_1), \overline{\pi_{P_0}}(C_m, f_2), ..., \overline{\pi_{P_0}}(C_m, f_9)]$ where:
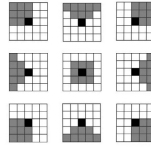
Fig. 2. Nagao filter diagonal, vertical and horizontal cliques

$$\overline{\pi_{P_0}}(C_m, f_h) = \frac{1}{9} \sum_{P \in f_h} PM_{I,C_m}(P) \tag{6}$$

The wining clique $\overline{\pi_{P_0}}(C_m, f_w)$ in each possibilistic map is chosen by the clique having the maximum value of the distribution $\overline{\pi_{P_0}}(C_m) = [\overline{\pi_{P_0}}(C_m, f_1), \overline{\pi_{P_0}}(C_m, f_2), ..., \overline{\pi_{P_0}}(C_m, f_9)]$. Hence, a pixel $P_0 \in I$ is considered as a possibilistic seed if its wining clique have a possibility value exceeds the threshold S:

$$P_0 \in I \text{ is a possibilistic seed if } \exists C_{m_0} \in \Omega/$$

$$\overline{Ind}(A_{m_0}) = \overline{\pi_{P_0}}(C_{m_0}, f_w) - \max_{m \neq m_0} \overline{\pi_{P_0}}(C_m, f_w) \geq S \tag{7}$$

4   Iterative Possibilistic Knowledge Diffusion

As previously detailed, the samples initial set B_0, is used in order to estimate the probability distribution functions of different thematic classes using (KDE) approach, which in turns are transformed into possibility distributions through the application of the $Pr - \pi$ Dubois-Prade's transformation. At iteration "n", the application of the possibilistic seeds extraction rule produces the additional set of seeds B_{n+1}. This seeds set is then used to enrich the samples set $B = \bigcup_{k=0}^{n+1} B_k$ and hence, updating the M possibility distributions (Fig. 2). This updating in possibility distributions is projected at on possibilistic maps by the attribution of new possibility values to the selected seeds in this iteration, which in turns results in possibilistic knowledge diffusion. The possibilistic knowledge diffusion is then iteratively repeated until the no more seeds are added. The possibilistic confidence threshold S associated with a decision in the proposed approach is considered as a decreasing function of the iteration n.

5   Experimental Results

In this section, the behaviour of the possibilistic knowledge diffusion and classification quality is evaluated. For this purpose, the Markov random field
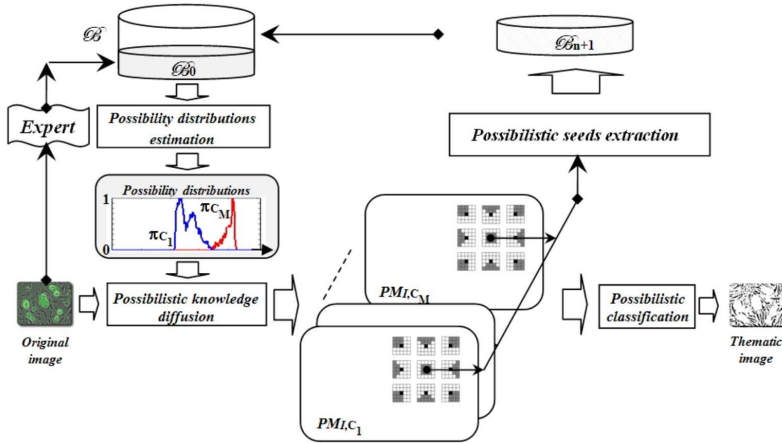
Fig. 3. Iterative possibilistic knowledge diffusion approach

(MRF) classifier Iterative Conditional Mode (ICM) and the proposed approach are applied on synthetic and real images. Iterative Conditional Mode works with the clustering segmentation K-means algorithm [13] for performing initial labeling.

5.1 Simulated Data

For the experimental evaluation purpose, a $96{\times}128$ pixel synthetic image, given in (Fig. 4), is generated. This synthetic image is composed of two meaningful thematic classes $\{C_1, C_2\}$. Pixels from C_1 and C_2 are generated as two Gaussian distributions $G(m_1, \sigma_1)$ and $G(m_2, \sigma_2)$ with means $m_1 = 130$ and $m_2 = 100$ and different standard deviations $\sigma_1 = 15$ and $\sigma_2 = 20$. $10{\times}10$ pixel learning zones positioned by the expert are also illustrated on the generated image. The initial possibility distributions are illustrated on the same figure (Fig. 4).

The obtained results of classification, after 15 iterations for the MRF and 5 iterations for the proposed approach, are also illustrated in Fig. 4. It is apparent that the results from MRF show small patch sizes in the class 2 compared to the results from the proposed approach. In other words the sensitivity of the MRF classifier to the initialization parameters becomes more apparent in the noisy image context (class 2).
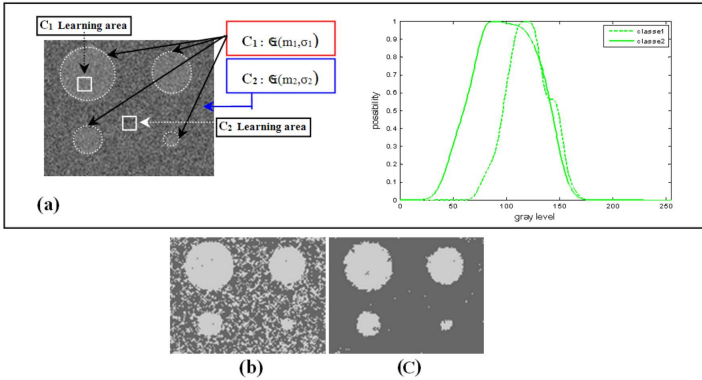
Fig. 4. (a) Synthetic image with learning zones and initial possibility distributions (two Gaussian generated thematic classes) (b) Classified Image using MRF and (c)Classified Image using the proposed approach

5.2   Medical Application

The Markov random field (MRF) and the proposed approach are applied on a set of two mammographic images composed of two classes (Fig. 5) tumor and normal tissue. This set is extracted from the MIAS image database provided by the British learned society (Mammographic Image Analysis Society). In order to show the performance of the Markov random field (MRF) and the proposed approach, Fig. 5 shows the contour of homogeneous regions of tumor resulting from the the Markov random field (MRF)after 15 iterations and 5 iterations for the proposed approach.
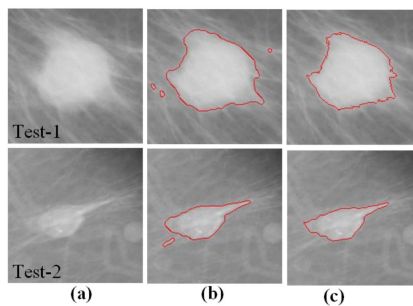
Fig. 5. (a) Set of two mammographic images composed of two classes, (b) Contour extracted after MRF classification, (c) Contour extracted after the proposed approach classification

A visual analysis of the obtained results shows that the performance of the proposed approach is very similar to that of Markov random field (MRF) in terms of countour localisation. Indeed, the proposed approach allows to eliminate small regions (false alarm), which are labeled as object of interest,in other words, the proposed approach allows to obtain good results by exploiting the flexibility of possibilistic reasoning for the integration of the contextual information and, thus the diffusion of possiblistic knowledge.

6   Conclusion

The proposed approach consists on the use of an initial knowledge expressed by the expert, transforming this knowledge into an initial probability density functions, and then using Dubois-Prade's transformation to obtain possibility distributions. The application of contextual possibilistic reasoning using Nagao princible allows the possiblistic knowledge diffusion. The obtained results using Markov random field (MRF) and the proposed approach show similarity and even superiority of the proposed approach by reducing the computational complexity and less dependence on parameters which reduce to delimitation of the initial samples learning set.

References

1. Mather, P.M.: Computer Processing of Remotely-Sensed Images: An introduction, 3rd edn. John Wiley & Sons, Chichester (2004)
2. Tso, B., Mather, P.M.: Classification methods for remotely sensed data. Taylor & Francis Group (2009)
3. Lu, D., Wang, Q.: A survey of image classification methods and techniques for improving classification performance. Int. Journal of Remote Sensing 28, 823–870 (2007)
4. Magnussen, S., Boudewyn, P., Wulder, M.: Contextual classification of Landsat TM images to forest inventory cover types. International Journal of Remote Sensing 25, 2421–2440 (2004)
5. Besag, J.: On the statistical analysis of dirty pictures. Journal of the Royal Statistical Society 48, 259–302 (1986)
6. Epanechnikov, V.A.: Non-parametric estimation of a multivariate probability density. Theory of Probability and its Applications 14, 153–158 (1969)
7. Zadeh, L.A.: Fuzzy Sets as a Basis for a Theory of possibility. Fuzzy Sets Syst. 1, 3–28 (1978)
8. Dubois, D., Prade, H.: When upper probabilities are possibility measures. Fuzzy Sets and Systems 49, 65–74 (1992)
9. Dubois, D., Prade, H.: Unfair Coins and Necessity Measures: towards a possibilistic Interpretation of Histograms. Fuzzy Sets and Syst. 10, 15–20 (1983)
10. Mouchaweh, S.: Semi-supervised classification method for dynamic applications. Fuzzy Sets and Systems 161, 544–563 (2010)

11. Kikuchi, S., Perincherry, V.: Handling Uncertainty in Large Scale Systems with Certainty and Integrity. In: MIT Engineering Systems Symposium, Cambridge (2004)
12. Nagao, M., Matsuyama, T.: Edge Preserving Smoothing. Computer Graphics and Image Processing 9, 394–407 (1979)
13. MacQueen, J.B.: Some Methods for classification and Analysis of Multivariate Observations. In: Proceedings of 5th Berkeley Symposium on Mathematical Statistics and Probability, pp. 281–297 (1967)

An Efficient 2-D Recursive Inverse Algorithm for Image De-noising

Mohammad Shukri Salman and Alaa Eleyan

Electrical & Electronic Engineering Department
Mevlana University, Yeni Istanbul Cad. No: 235 42003
Selçuklu, Konya, Turkey
{mssalman,aeleyan}@mevlana.edu.tr

Summary. In this paper, we propose a revised version of the recently proposed two-dimensional Recursive Inverse (2-D RI) adaptive algorithm. Instead of updating the filter coefficients both along the horizontal and vertical directions on the 2-D plane, as in the old 2-D RI algorithm, our new revised algorithm performs the update process simultaneously for every element in the 2-D plane. Simulation results show that the proposed 2-D RI algorithm leads to an improved performance compared to that of the 2-D RLS algorithm and similar performance compared to 2-D RI algorithm with reduced computational complexity.

1 Introduction

Digital signal processing has been the main actor in most recent technical advancements where the adaptive filtering techniques are very efficient in many classical problems such as noise filtering, system identification, and voice prediction. Due to the revolutionary increase in the multimedia devices from mobile phones to PDAs and Tablets, new or revised adaptive filtering techniques are evolving and 2-D adaptive filtering algorithms started to replace the old 1-D adaptive filtering algorithms.

First introduction of 2-D adaptive filtering algorithms was introduced by [1] and [2]. However, these algorithms updated the filter coefficients only along the horizontal direction on a 2-D plane. Consequently, these algorithms result in degradations and could not sufficiently exploit the 2-D signals' information [3]. Later on, various types of 2-D LMS adaptive algorithms, which can update the filter coefficients both along the horizontal and the vertical directions on a 2-D plane were developed, and applied to reduce noise of the image signals [3].

One of the most and efficient algorithms that have shown great performance in image noise removal and image degradation is the 2-D RLS algorithm [4]. Torres et al. [5] developed an adaptive scene-based nonuniformity

correction methodology for infrared image sequences. The method estimates
detector parameters and carry out the non-uniformity correction based on
the adaptive RLS algorithm. Sanubari & Tokuda [6] proposed a novel 2-D
adaptive filter based on assumption that the error signal has a t-distribution
probability distribution. Their system helps to suppress the effect of the large
amplitude error signal to the obtained adaptive parameter. The parameter of
the adaptive system is solved using an RLS-like adaptive algorithm. A 2-D
projection algorithm proposed in [7] by which filter coefficients can be up-
dated both along the horizontal and the vertical directions on a 2-D plane. Re-
searchers claim that the results of 2-D Modified Projection Algorithm (MPA)
outperform results of [2] and [3].

In this paper we propose a revised version of 2-D Recursive Inverse (RI)
[8] adaptive filtering technique which provides a better performance than the
2-D RLS algorithm [6] in terms of image quality and a less computational
complexity than 2-D RI [8] algorithm with similar performance. Moreover, it
does not require inversion of the autocorrelation matrix which in turn leads
to a stable performance.

This paper is organized as follows: In Section 2 the proposed algorithm is
introduced. In Section 3 simulation results that show the performance of the
proposed algorithm compared to those of the 2-D RI and RLS algorithms are
given. Finally, conclusions are drawn.

2   Proposed Algorithm

The filter weight update equation of the RI algorithm [9] can be generalized
into its 2-D form as:

$$\mathbf{w}_k(m_1, m_2) = [\mathbf{I} - \mu_k \mathbf{R}_k]\mathbf{w}_{k-1}(m_1, m_2) + \mu_k \mathbf{p}_k, \qquad (1)$$

where $\mathbf{w}_k(m_1, m_2)$ is the 2-D tap-weight vector with dimensions $N \times N$,
where $m_1 = 0, 1, \ldots, N - 1$ and $m_2 = 0, 1, \ldots, N - 1$, μ_k is the variable
step-size defined in [9], $\mathbf{R}_k$ and $\mathbf{p}_k$ are the instantaneous autocorrelation and
crosscorrelation matrices, respectively. They are estimated recursively as:

$$\mathbf{R}_k = \beta \mathbf{R}_{k-1} + \mathbf{x}(n_1, n_2)\mathbf{x}^T(n_1, n_2), \qquad (2)$$

and

$$\mathbf{p}_k = \beta \mathbf{p}_{k-1} + d(n_1, n_2)\mathbf{x}(n_1, n_2). \qquad (3)$$

where $\mathbf{x}(n_1, n_2)$ is the filter input and $d(n_1, n_2)$ is the desired output.

For 2-D applications, there can be a number of ways that data can be
reused. One possible way is shown in Fig. 1 [10]. In this scheme, as shown
in Fig. 1(b), we consider a mask of 3×3 pixels which move horizontally to
the right by one column at a time until the end of each row. Afterward, the
same process is repeated with the next row below until the last 9 pixels of

the image are reached. At the end of each process of the mask, the data are reshaped as shown in Fig. 1(a), starting from the last pixel in the lower right corner. This method usually provides significance performance. However, the computational complexity of this algorithm is very high. Another way of implementing the 2-D RI [8] could be done by directly estimating the correlations without reshaping data by the method explained in Fig. 1(a).

The filter output is given by the following 2-D convolution:

$$y(n_1, n_2) = \sum_{m_1=0}^{N-1} \sum_{m_2=0}^{N-1} w(m_1, m_2)x(n_1 - m_1, n_2 - m_2). \tag{4}$$

(a)   (b)
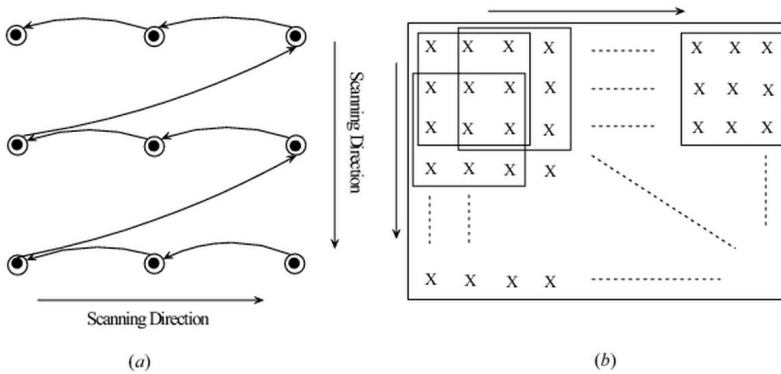
Fig. 1. Rectangular configuration of data-reusing in 2-D
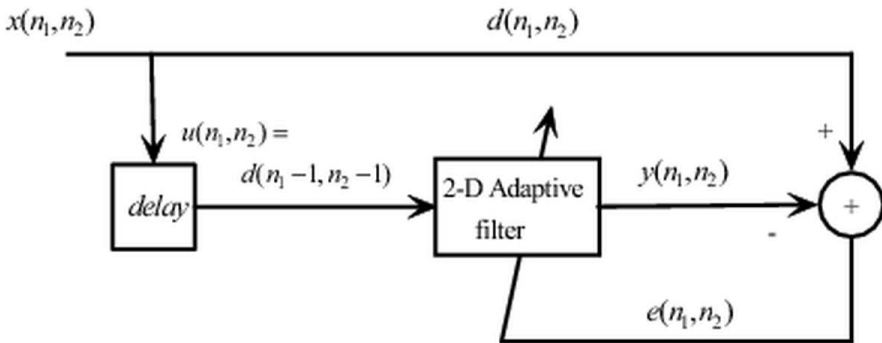
Fig. 2. The block diagram of a 2-D adaptive line enhancer (ALE)

3   Simulation Results

In order to see the performance of the proposed algorithm, it is applied to a 2-D ALE shown in Fig. 2 [10] with different noise types. During all of the simulations, the proposed algorithm is implemented with a forgetting factor ($\beta = 0.999$) and an initial step-size ($\mu_0 = 0.0005$). The image is selected to be a binary (i.e., checkerboard) because the performance of the proposed algorithm would be very significant.

In the first experiment, the noise is selected to be additive white Gaussian noise (AWGN) with zero mean and normalized variance ($\sigma^2 = 0.8$). Fig. 3(a) shows the original image, Fig. 3(b) shows the image with noise and Fig. 3(c) shows the image recovered by the proposed algorithm. In the second experiment, a salt & pepper noise is added to the image with normalized density ($D = 0.3$). Fig. 3(d) shows the image with noise and Fig. 3(e) shows the recovered image by the proposed algorithm. From the previous two experiments, it is clearly noted that the proposed algorithm is always capable of estimating the original image from the one buried in noise.

In the third experiment, the noise added to the image is assumed to be a multiplicative noise using (5),

$$I_{noise} = I_{orig} + \nu I_{orig}. \qquad (5)$$

where I_{noise} is the image with noise, I_{orig} is the original image and ν is the multiplicative noise with zero mean and variance ($\sigma^2 = 13$).
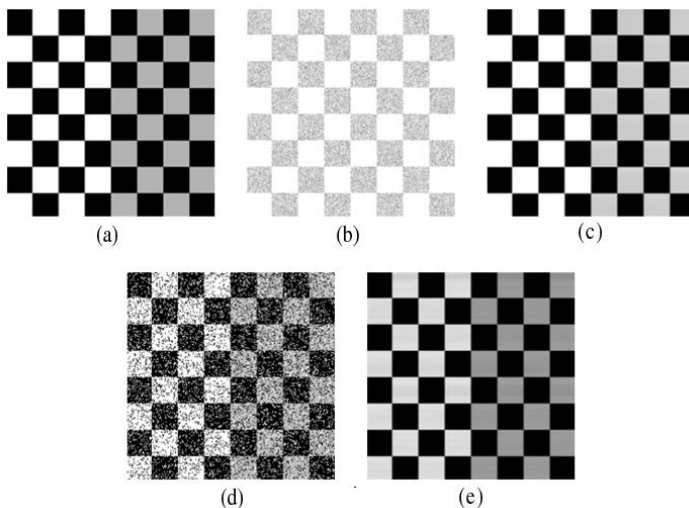
Fig. 3. (a) original image, (b) noisy image (AWGN with $\sigma^2 = 0.8$), (c) de-noised image using proposed algorithm, (d) noisy image (Salt & Pepper with density $D = 0.3$), (d) de-noised image using proposed algorithm ($\beta = 0.999$)

Fig. 3(a) shows the original image and Fig. 3(b) shows the image with noise ('Speckle' with $\sigma^2 = 13$). Fig. 3(c) shows the image recovered by the RLS algorithm, Fig. 3(d) shows the image recovered by the 2-D RI algorithm and Fig. 3(e) shows the image recovered by the proposed algorithm. It is noted that, the proposed algorithm outperforms the RLS algorithm and performs the same as the 2-D RI algorithm with significant reduction in the computational complexity.

(a)   (b)   (c)

(d)   (e)
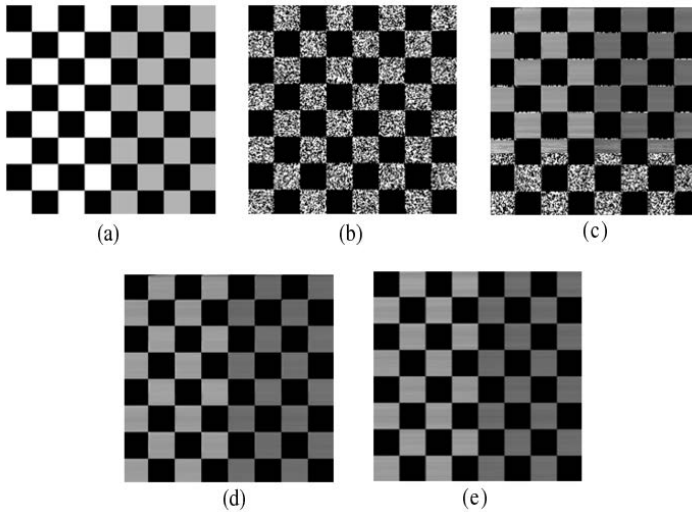
Fig. 4. (a) original image, (b) noisy image (Speckle noise with $\sigma^2 = 13$), (c) de-noised image using RLS algorithm ($\beta = 0.999$), (d) de-noised image using 2-D RI algorithm ($\beta = 0.999$), (d) de-noised image using proposed algorithm ($\beta = 0.999$)

4   Conclusion

In this paper, a new 2-D version of the recently proposed RI algorithm is introduced. The proposed approach avoids the use of data reshaping. Instead, it performs the update process simultaneously for every element in the 2-D plane. Simulation results have shown that the proposed 2-D RI algorithm leads to an improved performance compared to that of the 2-D RLS algorithm and similar performance compared to 2-D RI algorithm with reduced computational complexity.

References

1. Hadhoud, M.M., Thomas, D.W.: The two-dimensional adaptive LMS (TDLMS) algorithm. IEEE Trans. on Circ. Sys. CAS 35(5), 485–494 (1998)
2. Jenkins, W.K., Faust, R.P.: A constrained two-dimensional adaptive digital filter with reduced computational complexity. In: Proc. of IEEE Int. Symp. on Circ. Sys., pp. 2655–2658 (1988)
3. Ohki, M., Hashiguchi, S.: Two-dimensional LMS adaptive filters. In: Tech. Digest of Korea-Japan Joint Symp. on Infor. Disp., pp. 46–51 (1990)
4. Muneyasu, M., Uemoto, E., Hinamoto, T.: A novel 2-D adaptive filter based on the 1-D RLS algorithm. Proc. of IEEE Int. Symp. on Circ. Sys. 4, 2317–2320 (1997)
5. Torres, F., Torres, S.N., Martín, C.S.: A recursive least square adaptive filter for nonuniformity correction of infrared image sequences. In: Sanfeliu, A., Cortés, M.L. (eds.) CIARP 2005. LNCS, vol. 3773, pp. 540–546. Springer, Heidelberg (2005)
6. Sanubari, J., Tokuda, K.: RLS-type two-dimensional adaptive filter with a t-distribution assumption. Jour. of Sig. Proc. 80(12), 2483–2495 (2000)
7. Fan, H., Wen, C.: Two-dimensional ddaptive filtering based on projection algorithm. IEEE Trans. on Sig. Proc. 52(3), 832–838 (2004)
8. Ahmad, M.S., Kukrer, O., Hocanin, A.: A 2-D Recursive Inverse Adaptive Algorithm. Sig. Image and Vid. Proc. 7(2), 221–226 (2013)
9. Ahmad, M.S., Kukrer, O., Hocanin, A.: Recursive Inverse adaptive filtering algorithm. Dig. Sig. Proc. 21(4), 491–496 (2011)
10. Soni, R.A., Jenkins, W.K.: Projection algorithms for two-dimensional adaptive filtering applications. In: Thirty-First Asilomar Conference on Signals, Systems & Computers, vol. 1, pp. 333–337 (1977)

Image Feature Extraction Using Compressive Sensing

Alaa Eleyan[1], Kivanc Kose[2], and A. Enis Cetin[2]

[1] Mevlana University
Electrical and Electronics Engineering Dept., Konya, Turkey
aeleyan@mevlana.edu.tr
[2] Bilkent University
Electrical and Electronics Engineering Dept., Ankara, Turkey
cetin@bilkent.edu.tr, kkivanc@ee.bilkent.edu.tr

Summary. In this paper a new approach for image feature extraction is presented. We used the Compressive Sensing (CS) concept to generate the measurement matrix. The new measurement matrix is different from the measurement matrices in literature as it was constructed using both zero mean and nonzero mean rows. The image is simply projected into a new space using the measurement matrix to obtain the feature vector. Another proposed measurement matrix is a random matrix constructed from binary entries. Face recognition problem was used as an example for testing the feature extraction capability of the proposed matrices. Experiments were carried out using two well-known face databases, namely, ORL and FERET databases. System performance is very promising and comparable with the classical baseline feature extraction algorithms.

1 Introduction

Reliable automated face recognition is useful in several applications such as security and access control systems. There are many other possible uses for facial recognition that are currently being developed. For example, the technology could be used as a security measure at ATMs and airports in order to intensify security. The same concept could also be applied to computers where facial images would replace passwords in the login process. Given still or video images of a scene, the system should identify or verify one or more persons in the scene using a stored database of faces. The face representation falls into two categories[1]. The first category is global approach or appearance-based, which uses holistic texture features and is applied to the face or specific region of it. Many applied well-known algorithms falls in this category such as principal components analysis (PCA) [2, 3], which is also called eigenfaces [4, 5], linear discriminant analysis (LDA) [6, 7], Gabor wavelet transform[8, 9], and Discrete cosine transform[10]. The second

category is feature-based or component-based, which uses the geometric relationship among the facial features like mouth, nose, and eyes. Wiskott et al. [11] implemented feature-based approach by a geometrical model of a face by 2-D elastic graph. Another example of feature-based was done by independently matching templates of three facial regions (eyes, mouth and nose) and the configuration of the features was unconstrained because the system did not include any geometrical model [12]. In this paper we used the concept of compressive sensing (CS) to generate a random measurement matrix. The CS is based on the fact that we can represent images and signals with a small number of coefficients which, in turn, makes CS powerful as a feature extractor [13] [14]. In our proposed approach, the measurement matrix is different from the random measurement matrices used in most CS problems. We used a matrix containing both zero-mean and nonzero-mean rows. We also compared this matrix with another measurement matrix which is constructed using random binary entries. The measurement matrix will serve as a projection matrix to project image vectors to a new space resulting in feature vector with much shorter length. The matrix with both zero-mean and non-zero mean rows showed superior results using both face databases with various feature vector lengths.

The paper is organized as follows: Section 2 discusses the compressive sensing concept; Section 3 explains the proposed approach. The experimental results and discussions are in Section 4 and then results are concluded at the end of this paper.

2   Compressive Sensing

The Nyquist-Shannon sampling theorem [15] is one of the fundamental theorems in signal processing literature. It specifies the conditions for perfect reconstruction of a continuous signal from its samples. If a signal is sampled with a sampling frequency that is at least two times larger than its bandwidth, it can be perfectly reconstructed from its samples. This approach is very simple to implement however, it is not very efficient in terms of data rates. Sampling the signal according to the Nyquist criteria will end up in large amount of samples, most of which may be thrown away in the later parts of the processing e.g. compression. For example in JPEG compression, first the sampled image is transformed into the DCT domain and then most of the negligible valued (small amplitude) DCT coefficients are thrown away.

Compressed sensing (CS) overcomes this problem by taking compressed measurements [16, 18, 20] from the signal. In a compressive sensing framework, the signal is assumed to be K-Sparse in a transformation domain, such as the wavelet domain or the DCT domain. A signal with length N is K-Sparse if it has at most K non-zero and $(N - K)$ zero coefficients in a transform domain. The case of interest in CS problems is when $K << N$, i.e., sparse in the transform domain.

In CS instead of taking individual, regularly spaced samples from the signal, a composition of the values of the signal at some instances is taken. These new samples are called compressed measurements $\mathbf{y}$, and they are collected as follows

$$\mathbf{y} = \phi\mathbf{x} = \phi.\psi.\mathbf{s} = \theta.\mathbf{s}, \qquad (1)$$

where ϕ is the $M \times N$ measurement matrix, $M << N$, and $\mathbf{s}$ is the $K-$sparse transform domain representation of the signal $\mathbf{x}$ in the transform domain represented by ψ. The reconstruction of the original signal $\mathbf{x}$ from its compressed measurements $\mathbf{y}$ cannot be achieved by simple matrix inversion or inverse transformation techniques. A sparse solution can be obtained by solving the following optimization problem:

$$\mathbf{s}_p = argmin||\mathbf{s}||_1 \quad such \; that \;\; \theta.\mathbf{s} = \mathbf{y} \qquad (2)$$

One important characteristic of the measurement matrix ϕ is that it does not need to have a specific structure like transformation matrices or sampling matrices. In fact, in [16, 17, 18], the authors states that the measurement matrix should satisfy the *restricted isometry property (RIP)* for a given number of measurements. They also prove that a random matrix with entries that are i.i.d Gaussian random variables, satisfies the RIP property. Measurement matrix can even be constructed from binary entries [19].

Reconstruction of the original signal from these compressed measurements is another active research field in signal processing and mathematics. Different optimization techniques are frequently used for this purpose. However, for the proposed classification method, we are only interested in the sampling part of the CS framework. Therefore, we will not get into the details of these techniques since the proposed method is related to only the sampling part of the CS framework.

As the perfect reconstruction of the original signal from these compressed measurements is possible, it is also possible to state that, these compressed measurements have descriptive information about the original signal. Therefore, they can used as features in a classification process. In the proposed framework, we are taking compressed measurements from face images using gaussian and binary random measurement matrices and use the measurements as features in the classification. The details of the algorithm is presented in Section 3.

3   Proposed Approach

An illustration of the proposed approach is shown in Fig. 1. The face database is divided into two sets; training set and testing set. Each image in both sets are projected into new space using one of the proposed measurement matrices. After generating the feature vectors of both training set and testing sets, an appropriate classifier is used for classifying each test image to its
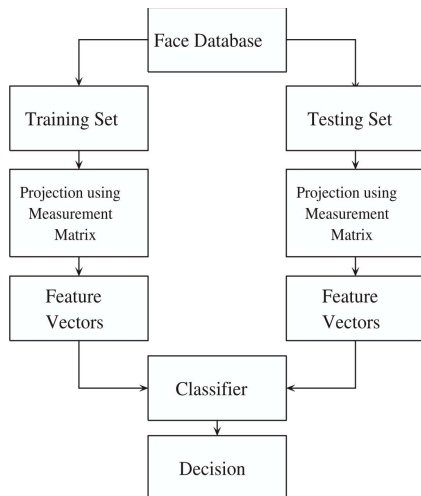
Fig. 1. Flowchart of the proposed approach

corresponding class by comparing its feature vector with the feature vectors of the training set.

The similarity measures used in our experiments to evaluate the efficiency of different representation and recognition methods include ℓ_1 distance measure, δ_{ℓ_1}, ℓ_2 distance measure, δ_{ℓ_2}, and cosine similarity measure, δ_{cos}. The measures for n dimensional vectors are defined as follows

$$\delta_{\ell_1}(x, y) = |x - y| \tag{3}$$

$$\delta_{\ell_2}(x, y) = ||x - y||^2 \tag{4}$$

$$\delta_{cos}(x, y) = \frac{xy}{||x||||y||} \tag{5}$$

Experiments were conducted on two commonly used face databases: FERET database [21] and ORL database [22]. For FERET database, 600 frontal face images from 200 subjects are selected. The 600 face images were acquired under varying illumination conditions and facial expressions. Each subject has three images of size 256×384 with 256 gray levels. Each face image is resized to 128×128. Fig. 2(a) shows sample images from the FERET database. The first two rows are the training images while the third row shows the test images. It can be noticed from this figure that the test images all display variations in illumination and facial expression. To test the algorithms, two images of each subject are randomly chosen for training, while remaining one is used for testing.

The ORL database consists of 400 face images acquired from 40 subjects (i.e., ten images per subject) with variations in facial expression and facial

<center>(a)</center> <center>(b)</center>

Fig. 2. Example images from the face databases: (a) Example images from the FERET database. (b) Example images from the ORL database.

details. All images are grey scale with a 92×112 pixels resolution. All images in the database are resized to 128×128 pixels. Fig. 2(b) shows sample images from the ORL database.

4 Comparative Results and Discussions

Preliminary experiments were conducted on both FERET and ORL databases to study the performance of the proposed algorithm for the face recognition problem. Leave-one-out strategy is used in the preparation of the results in Table 1 and 2. Taking p as the number of poses for each person in the database, p-1 poses will be used for training while remaining one pose for testing. In this strategy, test pose is changed at every run of the program and the rest p-1 is used for training making a total of $(\frac{p!}{p-1!} = p)$ runs. At the end, averaging the results from all these runs will give the final recognition rate.

Both in Table 1 and 2 results of using 3 different measurement matrices were recorded; measurement matrix with zero mean rows, measurement matrix with nonzero mean rows and measurement matrix with mixed zero mean and nonzero mean rows. The measurement matrix size is $M \times N$, where $N = 128 \times 128$ and M can take an arbitrary value which will later represent the resulting feature vector length.

In Table 1, the best performance obtained by using measurement matrix on FERET database with zero mean rows was 81.5%, while it reached 80% by using measurement matrix with nonzero mean rows. Using measurement matrix with zero and nonzero mean rows gave a better performance reached 84.5%. In Table 2, the max performance obtained by using measurement matrix on ORL database with zero mean rows was 96.25%, while it reached 96.5% by using measurement matrix with nonzero mean rows. Using measurement matrix with zero and nonzero mean rows gave a better performance reached 96.75%. It is clear from these results that using a measurement

matrix with both zero and nonzero mean rows helped to slightly improve the performance for both ORL and FERET databases.

Table 3 has the same scenario as in Table 1 and 2. The difference is in the used random measurement matrix. In Table 3 a random measurement matrix with binary entries is used. Normalization of the feature vectors obtained by measurement matrix before the classification stage dropped the performance in Table 1 and 2 by nearly 1 to 2%. On the other hand, normalizing the feature vectors obtained using the binary random measurement matrix helped to improve the performance of the ℓ_1 and ℓ_2 classifiers drastically while it had almost no effect on Cosine distance results. For example, with ORL database, using normalized feature vector of length 1000 gives 96.29% using ℓ_1 distance(Table 3) while it gives 47.5% without feature vector normalization. So, Table 1 and 2 were prepared without normalization of the feature vectors, while Table 3 was prepared using normalized feature vectors.

Even though the results for FERET database show that by using a measurement matrix with both zero and nonzero mean rows (reached 84.5%) can give better performance than using a matrix with binary entries(reached 81%). This improvement was not very clear in ORL database results, as it

Table 1. Face recognition rates on FERET database obtained using different number of features taken using different Measurement Matrices. The rates are given in 3 different metrics defined in (3)-(5).

	zero mean rows			nonzero mean rows			mixed mean rows		
M	δ_{ℓ_1}	δ_{ℓ_2}	δ_{cos}	δ_{ℓ_1}	δ_{ℓ_2}	δ_{cos}	δ_{ℓ_1}	δ_{ℓ_2}	δ_{cos}
50	70.50	70.50	70.00	70.50	70.00	70.00	72.00	71.75	71.50
100	73.00	75.00	72.00	75.00	74.50	75.00	76.00	78.50	75.00
200	78.00	79.50	78.50	79.00	80.50	77.50	80.00	82.00	79.75
300	79.50	79.50	80.00	79.50	80.00	80.00	82.50	82.00	81.50
500	79.00	79.50	79.00	79.75	80.50	81.00	84.50	84.00	81.50
1000	80.50	81.00	81.50	81.00	81.00	80.00	83.00	83.50	82.50

Table 2. Face recognition rates on ORL database obtained using different number of features taken using different Measurement Matrices. The rates are given in 3 different metrics defined in (3)-(5).

	zero mean rows			nonzero mean rows			mixed mean rows		
M	δ_{ℓ_1}	δ_{ℓ_2}	δ_{cos}	δ_{ℓ_1}	δ_{ℓ_2}	δ_{cos}	δ_{ℓ_1}	δ_{ℓ_2}	δ_{cos}
50	89.25	90.25	90.25	91.50	91.50	90.75	90.00	92.75	92.00
100	93.75	93.75	94.00	92.75	93.50	92.75	93.75	94.00	93.75
200	94.50	94.75	93.50	94.75	94.75	94.00	95.00	94.25	94.50
300	95.75	95.00	95.25	95.25	95.00	95.00	95.25	95.75	95.75
500	95.25	96.00	95.50	94.75	95.50	93.50	96.25	96.25	95.00
1000	96.00	96.25	94.50	96.50	95.75	94.50	96.75	96.50	94.75

Table 3. Face recognition rates on FERET and ORL database obtained using different number of features taken using Measurement Matrices with binary entries. The rates are given in 3 different metrics defined in (3)-(5).

	FERET			ORL		
M	δ_{ℓ_1}	δ_{ℓ_2}	δ_{cos}	δ_{ℓ_1}	δ_{ℓ_2}	δ_{cos}
50	69.50	68.25	69.75	90.50	91.00	90.25
100	77.50	76.50	76.75	94.00	95.00	93.00
200	80.50	80.25	80.51	94.75	95.75	94.25
300	80.00	79.75	80.25	94.50	94.25	95.00
500	79.50	78.75	79.25	95.50	95.75	94.25
1000	80.75	80.00	81.00	95.50	96.50	95.25

reached 96.75% by using a measurement matrix with both zero and nonzero mean rows and 96.5% by using a matrix with binary entries, which is a very close performance.

5 Conclusion

In this paper the compressive sensing concept is used to prepare a Gaussian or binary random measurement matrix. Measurement matrix is used as a projection matrix for the image feature extraction. The proposed approach were tested on the face recognition problem. It is experimentally observed that measurement matrices with nonzero mean rows improve results compared to ordinary measurement matrices. This is due to the fact that multiplying an image with a zero mean row is somewhat equivalent to bandpass or highpass filtering. By including nonzero mean rows we also introduce lowpass energy to the measurement process. The preliminary results of the experiments conducted on both FERET and ORL databases indicate that the proposed approach is able to extract the salient features from the face images effectively and provides a high recognition performance . In our future work, more extensive experiments will be carried out on various pattern classification problems to evaluate the performance of the proposed approach under different conditions.

References

1. Chellappa, R., Wilson, C.L., Sirohey, S.: Human and machine recognition of faces: a survey. Proceedings of the IEEE 83(5), 705–741 (1995)
2. Sirovich, L., Kirby, M.: Low-dimensional procedure for the characterization of human faces. Journal of the Optical Society of America A 4(3), 519–524 (1987)
3. Kirby, M., Sirovich, L.: Application of the Karhunen-Loeve procedure for the characterization of human faces. IEEE Transactions on Pattern Analysis and Machine Intelligence 12(1), 103–108 (1990)

 4. Turk, M., Pentland, A.: Eigenfaces for recognition. Journal of Cognitive Neuroscience 3, 0898-929X, 71–86 (1991)
 5. Pentland, A., Moghaddam, B., Starner, T.: Viewbased and modular eigenspaces for face recognition. In: Proceedings of Computer Vision and Pattern Recognition, pp. 84–91 (1994)
 6. Belhumeur, P., Hespanha, J., Kriegman, D.: Eigenfaces vs. fisherfaces: recognition using class specific linear projection. IEEE Transactions on Pattern Analysis and Machine Intelligence 19(7), 711–720 (1997)
 7. Zhao, W., Chellappa, R., Nandhakumarm, N.: Empirical performance analysis of linear discriminant classfiers. In: Proceedings of Computer Vision and Pattern Recognition, pp. 164–169 (1998)
 8. Shen, L., Bai, L.: A review on Gabor wavelets for face recognition. Pattern Analysis and Applications 9(2), 273–292 (2006)
 9. Eleyan, A., Ozkaramanli, H., Demirel, H.: Complex wavelet transform-based face recognition. EURASIP Journal on Advances in Signal Processing, Article ID 185281, 13 pages (2008)
10. Hafed, Z.M., Levine, M.D.: Face recognition using the discrete cosine transform. International Journal of Computer Vision 43(3), 167–188 (2001)
11. Wiskott, L., Fellous, J., Kruger, N., Malsburg, V.: Face recognition by elastic brunch graph matching. IEEE Transactions on Pattern Analysis and Machine Intelligence 19(7), 775–779 (1997)
12. Brunelli, R., Poggio, T.: Face recognition: features versus templates. IEEE Transactions on Pattern Analysis and Machine Intelligence 15(10), 1042–1052 (1993)
13. Eleyan, A., Kose, K., Cetin, A.E.: New face representation using compressive sensing. In: IEEE Conference on Signal Processing and Communications Applications, pp. 558–561 (2011)
14. Liu, L., Fieguth, P., Kuang, G.: Compressed sensing for robust texture classification. In: Kimmel, R., Klette, R., Sugimoto, A. (eds.) ACCV 2010, Part I. LNCS, vol. 6492, pp. 383–396. Springer, Heidelberg (2011)
15. Shannon, C.E.: Communication in the presence of noise. In: Proceedings of Institute of Radio Engineers, vol. 37(1), pp. 10–21 (1949)
16. Baraniuk, R.G.: Compressed sensing (Lecture Notes). IEEE Signal Processing Magazine 24(4), 118–124 (2007)
17. Candes, E., Romberg, J., Tao, T.: Robust uncertainty principles: exact signal reconstruction from highly incomplete frequency information. IEEE Transactions on Information Theory 52(2), 489–509 (2006)
18. Candes, E.: Compressive sampling. International Congress of Mathematics 3, 1433–1452 (2006)
19. Candes, E., Tao, T.: Near optimal signal recovery from random projections: Universal encoding strategies. IEEE Transactions on Information Theory 52(12), 5406–5425 (2006)
20. Donoho, D.: Compressed sensing. IEEE Transactions on Information Theory 52(4), 1289–1306 (2006)
21. Philipps, P.J., Moon, H., Rivzi, S., Ross, P.: The Feret evaluation methodology for face-recognition algorithms. IEEE Transaction on Pattern Analysis and Machine Intelligence 22(10), 1090–1100 (2000)
22. Samaria, F., Harter, A.: Parameterization of a stochastic model for human face identification. In: Proceedings of the 2nd IEEE Workshop on Applications of Computer Vision, pp. 138–142 (1994)

A Modification of the Parallel Spline Interpolation Algorithms

Michał Knas and Robert Cierniak

Institute of Computational Intelligence,
Armii Krajowej 36, 42-200 Czestochowa, Poland
{michal.knas,robert.cierniak}@iisi.pcz.pl

Summary. An extension of standard interpolation algorithm for image zooming is proposed. The presented method of the spline function arguments are modified, what makes the images more sharper. Implementation on Compute Unified Device Architecture is made what makes this re-sampling very fast.

1 Introduction

Image zooming will always be useful, because even with increase of resolution of digital sensors there always will be situations, when we would like to enlarge some detail of image or rotate it, etc. A lot of interpolation algorithms can come with help in this problem which allow us to do this. There are some types of these zooming methods, e.g. the non-adaptive such as nearest-neighbor, linear, spline and adaptive methods, for example, edge-adaptive zooming, Genuine Fractals. Big advantage of these algorithms is that they can be used not only for images, but also for the other kind of matrixes, including three-dimensional, such as those in the computed tomography [1].

Simple in design, but also giving good results are those algorithms based on spline interpolation, like Bicubic or Catmull-Rom [2, 3]. They have own kernels which results with different visual effects. The arguments for these functions are always calculated in the same way by evaluation of the distance between the new point and nodes that surrounds him. Development of this idea could be very profitable, especially based on parallel programming in CUDA [4].

2 Proposed Algorithm

In the standard algorithms, the arguments of interpolated function are limited to the range [0,1) and it is a decimal part of number of the created pixels multiplied by resolution ratio of old and new width (or height) of the

processed image. If we enlarge the picture eight times, then between each pair of pixels, seven additional nodes are created. They are apart from each other by the same distance. We decided to create a function that will move them in the direction of pixels. It intuitive should sharpen the image as well as filtering or convolution, but at the stage of the interpolation operation.

We create two functions, both with parameter $K \in [0,1]$ that determines how strongly nodes are shifted.

Our first modified function is designed on the basis of Hanning equation (1). Listing 1 describes how nodes are moved (recalculated) and Fig. 1 shows how it looks for different K.

$$h(x) = 0.5(1 - \cos(2\pi x)) \tag{1}$$

Listing 1. Modified function based on Hanning equation

```
h = 0.5f * ( 1.0f - GMath.Cos((2.0f * GMath.PI * x)));
if (x <= 0.5f)
 xprim = x - h * K * x;
else (x > 0.5f)
 xprim = x + h * K * (1 - x);
```
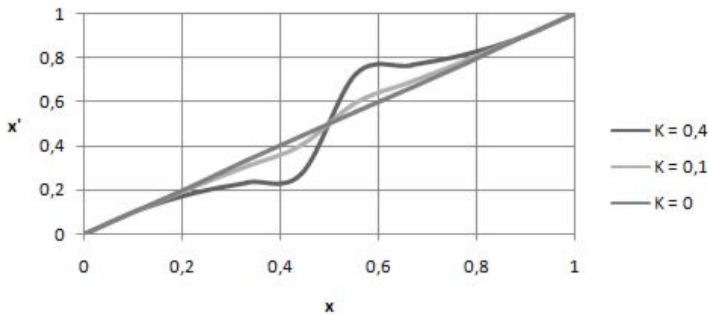

Fig. 1. Modifying function based on Hanning equation with different K

The second modified function is based on square function. Listing 2 describes how arguments are modified and Fig. 2 shows how it looks for different K.

Listing 2. Modified function based on square equation

```
if (x <= 0.5f)
 xprim = K * 2 * x * x;
else (x > 0.5f)
 xprim = 1 - K * 2 * (1 - x) * (1 - x);
```
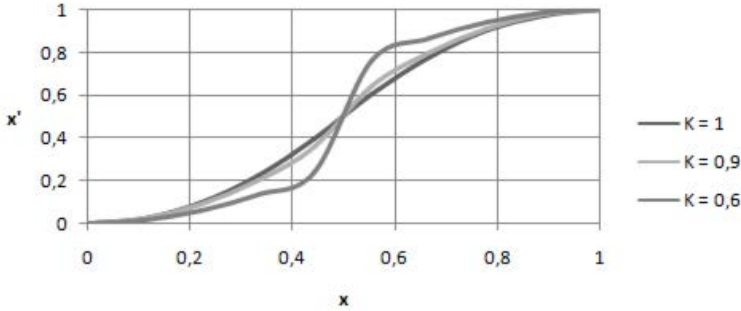
Fig. 2. Modifying function based on Hanning equation with different K

Use of the computing power of GPU becomes more and more popular and simpler thanks to high-level programming languages. In particular, it is very convenient to implement re-sampling, because there are plenty of operations that can be performed parallelly. Thus, creation of the modified functions is moved to the graphic card with BiCubic and Catmull-Rom interpolation. To implement that, we just have to treat each new pixel as a separate thread to execute. Thus, we need to write a simple function, i.e. kernel, that will interpolate and will calculate the value of pixel in new image. This function will be carried out on multiple processors on GPU at the same time. With number of over thousand kernels we should be able to work even with video streams in high definition.

The only problem which is not resolved yet is data transmission. The simulations shows that it frequently takes a proportionally much more time in comparison with the time of calculations. Even small data transfer from computer memory to video memory can take more than millions of operations. But even in this case the profit of using SIMD - Single Instruction Multiple Data - architecture is undoubtedly very appealing.

Due to the vast computational power of GPU, we also decide to check what results will give the algorithms when we use multiple small zooming instead of the single re-sampling.

3   Experimental Results

We carried out some computer simulations to verify whether our modifications will give better results than the standard approach.

To create experimental environment we used Microsoft Visual Studio 2008 with CUDAfy library and NVIDIA CUDA Toolkit 5.0. Tests were performed on NVIDIA GTX 680 and also on Intel Core2Quad Q8400. The testing platform was Windows 8.

We prepared two identical images in gray scale: first with resolution of 128x128 and next with 2048×2048 for comparison, and to measure the mean square error. Thus the magnification was sixteen or also double four times when we used GPU.

First of all, we checked difference of re-sampling time between CPU and GPU what shows the Table 1 .

Table 1. Re-sampling time on CPU and GPU(ms)

CPUx16	GPUx16	GPUx2x4	GPUx2x3
1374.74	3.55	60.48	17.49

Further, we measured mean square error. We checked it for both modified functions where coefficient K was set from 0 to 1 with 0.1 step. Tests were made with single and multiple magnification for BiCubic and Catmull-Rom interpolation, where τ was set at $\{0, 0.5, 1\}$. Fig. 3 depicts best results for standard zooming and Fig. 4 for multiple zooming.
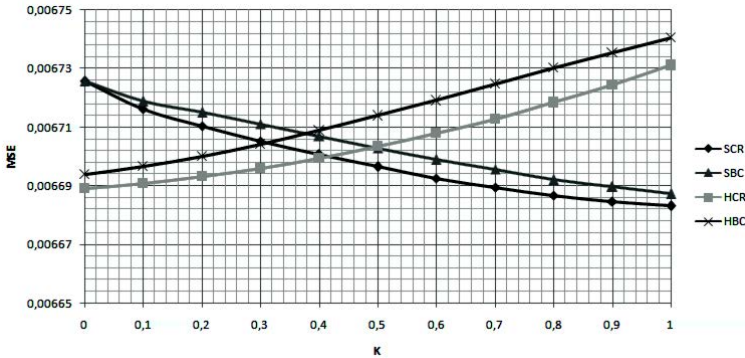
Fig. 3. MSE for standard re-sampling, SCR - Catmull-Rom with square-based modified function, SBC - BiCubic, HCR - Catmull-Rom with hanning-based modified function, HBC - BiCubic

Next, we prepared images for these minimal errors to confirm visual effect. Fig. 5 shows crops of results.
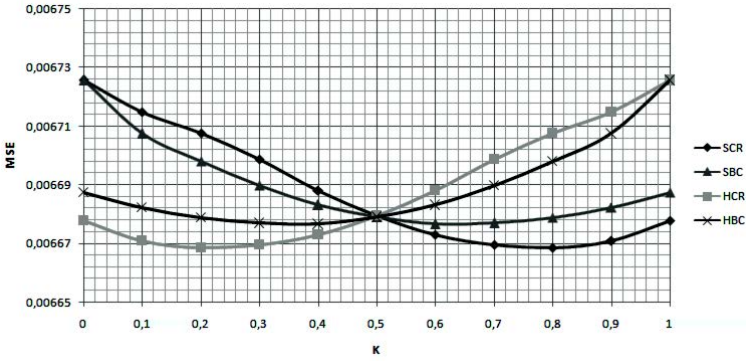
Fig. 4. MSE for multiple re-sampling, SCR - Catmull-Rom with square-based modified function, SBC - BiCubic, HCR - Catmull-Rom with hanning-based modified function, HBC - BiCubic
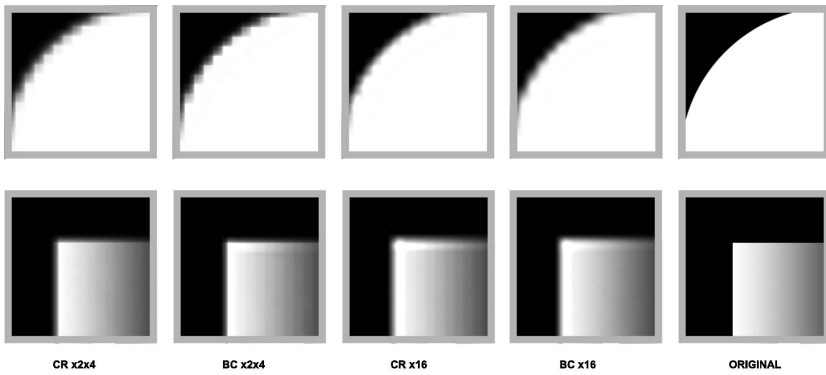
Fig. 5. Visual results of magnification for minimal MSE, CR x2x4 - Catmull-Rom multiple re-sampling, BC x2x4 - BiCubic multiple re-sampling, CR x16 - Catmull-Rom standard re-sampling, BC x16 - Bicubic standard re-sampling
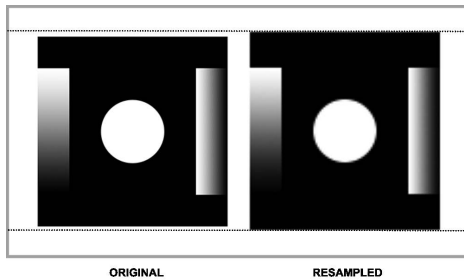
Fig. 6. Distortion of objects on re-sampling

4   Conclusion

Tests performed by us have shown that proposed modified function and multiple magnification can improve standard BiCubic and Catmull-Rom interpolations. Algorithms based on GPU are very fast and they can be used for realtime zooming. However, for both kind of enlarging images, if we ignore errors at the edges of objects, there can be seen a distortion problem (Fig. 6) which is very undesired. Very nice visual effect gives our algorithm with small K and multiple re-sampling.

References

1. Cierniak, R.: X-Ray Computed Tomography in Biomedical Engineering. Springer, London (2011)
2. Zhang, R.-J., Ma, W.: An efficient scheme for curve and surface construction based on a set of interpolatory basis functions. ACM Transactions on Graphics (TOG) 30(2), Art. No. 10 (2011)
3. Yuksel, C., Schaefer, S., Keyser, J.: Parameterization and applications of Catmull Rom curves. Computer-Aided Design 43(7), 747–755 (2011)
4. Song, G., Biao, G., Qinkun, X., Haiyun, W.: Research on Multi-GPUs Image Processing Acceleration Based CUDA. In: 2012 International Conference on Industrial Control and Electronics Engineering (ICICEE), pp. 196–199 (2012)

Multi-object Tracking System

Jacek Zawistowski[2], Piotr Garbat[1], and Paweł Ziubiński[2]

[1] Institute of Microelectronics and Optoelectronics,
   Warsaw Univeristy of Technology,
   Warsaw, Poland
   `p.garbat@elka.pw.edu.pl`
[2] LINGARO Sp. z o.o.,
   Warsaw, Poland
   `{jacek.zawistowski,pawel.ziubinski}@lingaro.com`

Summary. The article describes the multi-object tracking system based on new approach to object management after preprocessing and background modeling. Object manager determine correlation between objects in previous and current frame by matching features. For matching features algorithm use color histogram with a small number of bins. Each moving object extracted from the scene is assigned to an individual and independent Kalman filter. System stores information about real position of the objects extracted directly from image processing and keep information about centroids predicted by Kalman filter.

1 Introduction

Computer vision is one of the most popular issue in recent years. A lot of efficient and reliable algorithms for general image processing and visual systems including objects detection, classification and objects tracking has been yielded in computer vision research. However, reliable visual tracking algorithms is still one of the most important problem in real-time video processing systems due to the complexity of the problems. It is well known that multi-object tracking algorithms need to resolve key problems such as rotation, scaling, affine distortion, quick movement, similarity and occlusion of objects.

Object tracking is important application in computer vision and image processing because it provides the basics to intelligent video analysis. Tracking gives information about motion in the scene and stores it into a motion path. Hence, there is a ability to use advanced algorithms and achieved information about object behavior on the scene.

In most cases, previous work present single-camera objects tracking algorithms, which can track mostly only one object. In [1] is presented on of the most popular algorithm for tracking objects Kalman filter, which use several

equations such as equation of time update and equation of measurements update to correct current state of the object and predict next position.

Saira Saleem Pathan et al. in [4] describes using Kalman filter as solution for multi-object tracking. Their system create Kalman filter for every moving object entering in the video sequence.

Another solution for objects tracking is to use species based particle swarm optimization which is describe in [5].

More similar previous work on multi-objects tracking is presented in [4, 3, 5]. However, if they use a multi-camera system, most of them analyze only one scene (the same scene for each camera). These solutions allow to partial solve occlusion problem.

Paek, Park et al. in [3] describes solution for multiple-view tracking problem by using metadata. They use background substraction for static object extraction and optical flow-based motion segmentation for moving objects, then they compute information about motion, shape, color and etc. for comparing objects and finally matching.

2 Algorithm

In this paper we introduce new approach to tracking multiple-objects in multi-camera scene. This approach focus on analyze wide area, which can not be able to observe by single-camera system. The two fundamental issues are: first, define occlusion as more than one case or event; second, finding the correlation between objects in previous and current frame by matching features - objects management.

2.1 *Preprocessing and Background Modeling*

The acquired image has noise coming from fluctuations of the light in indoor spaces. In first step we used median filter for smoothing pixels value to become independent from minor light changes. After that we separate foreground and background for extracting foreground objects from the scene. We propose use static background model, which based on simple Gaussian model. To improve the effectiveness of segmentation after background modeling we use morphological operation. Erosion and dilation operations were applied. Erosion remove single pixels incorrectly classified as foreground pixels. Dilation improves consistency of foreground objects.

2.2 *Objects and Feature Extraction*

The proposed multi-camera system extract a moving objects from the binary image after background modeling. For objects extraction we use finding contours algorithm, which is described in [6]. Algorithm looking for contours and
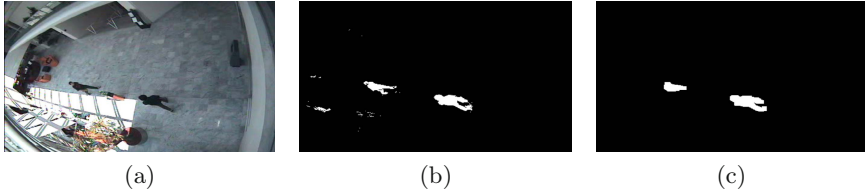
Fig. 1. An example of object segmentation. (a) Input video. (b) Subtraction Image. (c) Morphology filtering result.

store only extreme outer contours. Further we check the contours area and reject contours which can't be desirable objects. After this step we have information about all found objects in current frame. Also we have information about bounding rectangle, center of the object and area.

The next step is obtaining more features for future objects matching. Our proposed algorithm compute three dimensional color histogram with a small number of bins (to accelerate object computing and compassion).

2.3 Objects Management and Occlusion

In proposed approach, a background subtraction method to detect and extract moving objects was used. The detection results allows to determine occlusion or split between multiple object. The realized OT (Object Tracking) module includes two main steps: (1) tracking management, and (2) splitting analysis. The tracking management process attempts to associate the foreground regions with one of the existing tracks. Let $K(t), K1(t), K2(t), ...,$
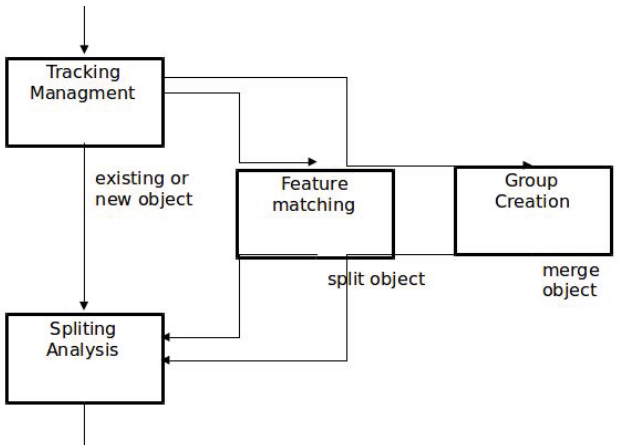
Fig. 2. Object Tracking module diagram

$Km(t)$ denote the existing tracks and $T(t), T1(t), T2(t), ..., Tn(t)$ denote the detected objects at time t. Based on distance between center position of detected and tracking objects the best alignment was found. The distant D_t is based on the Euclidean distance. If the distance is larger than a threshold, they will not be analyze in the next step. Five possible results are possible:

- a tracking object is not associated to any detected object
  (ex. object out of scene)
- a detected object is not associated to any tracking object
  (ex. new object in scene)
- a detected object is associated to tracking object
  (ex. continues tracking)
- a tracking object is associated to more then one detected object
  (merging case)
- a detected object is associated to more then one tracking object
  (splitting case)

When the first case are detected the existing object is moved to long term tracking buffer. If object return to scene in time of quarantine it will be recovered, in other case after this time object will be deleted. In next tracking management case, the new object is added to tracking buffer and feature vectors are calculated. When multiple object region are connected together, the object's region is merged and tracked as a whole one object. After merging, a new feature vectors for object matching are calculated and the information about group is added as a feature for this object. The last case started the second step of OT module. In the splitting analysis part, similarity between analyzed objects is measurement based on the color feature. The occluded objects in merged group are described by the color distribution Poi. In the same way the color distribution in RGB space PSi for the split objects from group is calculated. The color histograms are calculated for contour area. The color distance is measured using Mahalanobis distance.

$$D_t^S(i,j) = \sqrt{\sum_{p=1}^{N} \sum_{ch=1}^{\xi} \left(\frac{P_{Oi} - P_{Sj}}{\sigma(p, ch)} \right)^2}$$

When a group object merge occurred before contains two or more moving object split into independent moving objects, splitting analysis module matching the split objects with objects feature before splitting. If the similar objects not exist, new features will be established and new tracking object will be assigned for moving objects tracking.

2.4   Objects Tracking

For tracking objects we use a proven and versatile approach âĂŞ Kalman filter. Each moving object extracted from the scene is assigned to an individual and independent Kalman filter which receives information from object

manager about central position and velocity of the tracking object. We use two vectors to store informations about movement. First container has information about real position of the objects extracted directly from images, whereas second keep information about centroids predicted by Kalman filter. Several cases can be distinguished according to object status on the scene. The whole process of a Kalman filter is explained in the algorithm:

Kalman filtration algorithm

  Initialization **do**
    Initialize X_0, A, H, P, Q and R
    $\widehat{\overline{X}}_t = A\widehat{X}_{t-1}$
    $\overline{P}_t = AP_{t-1}A^T + Q$
  end

  foreach *frame time t* **do**
    foreach *Kalman measurement update* **do**
      $K_t = P_t H (HP_t H + R)^{-1}$
      $\widehat{X}_t = \widehat{\overline{X}}_t + K_t \left(Z_t - H_k \widehat{\overline{X}}_t \right)$
      $P_t = \overline{P}_t - K_t H \overline{P}_t$
    end
    foreach *Kalman update and prediction* **do**
      $\widehat{\overline{X}}_{t+1} = A\widehat{X}_t$
           $\overline{P}_t = AP_{t-1}A^T + Q$
    end
  end

In proposed implementation, parameters P and Q are fixed and all other variables are calculated dynamically. The parameter R_t can be given any value, because it is automatically updated after each frame. The matrix's , which we use in our system are:

$$A = \begin{bmatrix} 1 & \Delta t & 0 & 0 \\ 0 & 1 & 0 & 0 \\ 0 & 0 & 1 & \Delta t \\ 0 & 0 & 0 & 1 \end{bmatrix}, h = \begin{bmatrix} 1 & 0 & 0 & 0 \\ 0 & 0 & 1 & 0 \end{bmatrix}, Q = \begin{bmatrix} 1 & 0 & 0 & 0 \\ 0 & 0.5 & 0 & 0 \\ 0 & 0 & 1 & 0 \\ 0 & 0 & 0 & 0.5 \end{bmatrix}, Q = \begin{bmatrix} 0.5 & 0 & 0 & 0 \\ 0 & 0.5 & 0 & 0 \\ 0 & 0 & 0.5 & 0 \\ 0 & 0 & 0 & 0.5 \end{bmatrix},$$

2.5 Motion Path and Further Analytics

Tracking objects in scene gives us a informations about movement. We have entire movement history for all of objects on the scene. This type of information formulate the basics for the further analysis. Based on these results we can try to define and analyze objects specific behavior. This will be the subject of further work.

3   Experimental Results

The system is implemented on standard PC hardware (Intel i7 at 1.5GHz)
and works at 25 fps. The video image size is 640×480. The system is tested
in typical environments. In the system we use color histogram in RGB color
space witch 30×30×30 bins for feature correspondence.

   We exam system for selected clips taken under difficult conditions. The
following presents the results. Fig. 3 shows an example of tracking two inter-
acting persons in an indoor environment. The blue ROI's shows the position
of the person without occlusion. Yellow selection shows the position of the
objects after group creation (people are occluded with each other).

   In this sequence, the person Nr.1 and No.2 are moving in the opposite di-
rections. (Fig. 3, frame #214, red and green line). At frame #1202, occlusion
happens and after that the two persons are tracked as a whole group until
frame #2185. During this process, the target No.2 is partially occluded by
target No.1 for several frames. Next group is split (Fig. 3, frame #2522) and
objects No.1 and No.2 tracked separately. This sequence is difficult to track
moving human bodies because their shape change and consist occlusions and
split. Moreover, proposed solution working properly and can track multiple
objects with partially and complete occlusion and split group to separate
objects.

   We report results of the system on the most recent dataset of EC Funded
CAVIAR project [7]. In the CAVIAR dataset (Fig. 4, two people walk, meet,
and walk away. The system correctly tracks each person before, during and
after meet.

(a)   (b)   (c)
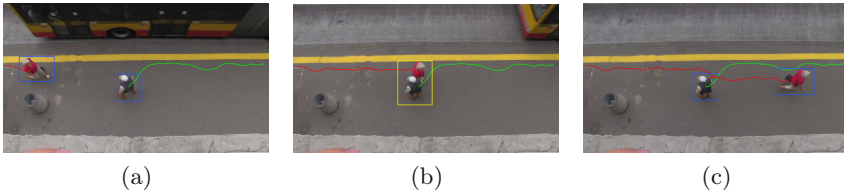
Fig. 3. Example of tracking two person interaction. (a) frame #214 (b) frame
#1202 (c)frame #2185.
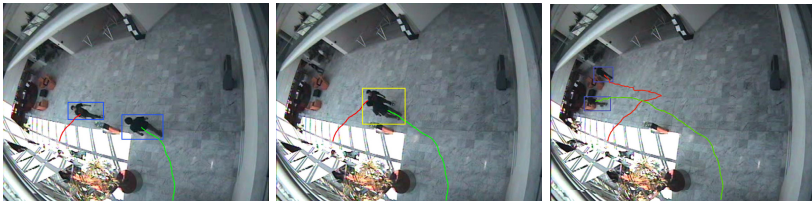
Fig. 4. Tracking results of CAVIAR sequence

4   Conclusions

A real-time multiple objects tracking system is presented. We researched multi-target tracking algorithm based on Kalman filter and color feature matching. Experiments on complex indoor environments show that the system allow to tracking multiple objects in difficult sequence. Moreover, here also we have been able to track multiple persons correctly after they merge and separate.

The system is computationally cost effective, and in the future allows to developing a real-time human actions recognition system.

References

1. Kalman, R.E.: A New Approach to Linear Filtering and Prediction Problems. Transaction of the ASME - Journal of Basic Engineering, 35–45 (1960)
2. Welch, G., Bishop, G.: An Introduction to the Kalman Filter. UNC-Chapel Hill, TR95-041 (2006)
3. Paek, I., Park, C., Ki, M., Park, K., Paik, J.: Multiple-view object tracking using metadata. In: International Conference on Wavelet Analysis and Pattern Recognition, Beijing, China, pp. 2–4 (2007)
4. Pathan, S.S., Al-Hamadi, A., Michaelis, B.: Intelligent Feature-guided Multi-object Tracking Using Kalman Filter, In: Signal Processing and Communications (IESK), Institute for Electronics, Otto-von-Guericke-University Magdeburg, Germany
5. Zhang, X., Hu, W., Li, W., Qu, W., Maybank, S.: Multi-Object Tracking via Species Based Particle Swarm Optimization. In: IEEE 12th International Conference on Computer Vision Workshops, ICCV Workshops (2009)
6. Suzuki, S., Abe, K.: Topological Structural Analysis of Digitized Binary Images by Border Following. CVGIP 30(1), 32–46 (1985)
7. http://homepages.inf.ed.ac.uk/rbf/CAVIARDATA1

Local Eigen Background Substraction

Paweł Ziubiński[2], Piotr Garbat[1], and Jacek Zawistowski[2]

[1] Institute of Microelectronics and Optoelectronics,
   Warsaw Univeristy of Technology, Warsaw, Poland
   `p.garbat@elka.pw.edu.pl`
[2] LINGARO Sp. z o.o.,
   Warsaw, Poland
   `{jacek.zawistowski,pawel.ziubinski}@lingaro.com`

Summary. The article describes the extended background modeling based on the well-known Eigenbackground method. The idea presented in the article expands the Eigenbackground method, breaking the scene into many smaller ones, modeling the background separately for each of its sections. This approach allows for better separation of the foreground objects, and better modeling of spots in which the light changes. Furthermore, it also ensures efficient implementation of the algorithm for CUDA graphics cards, separating particular local models into threads. In the future the approach shall also enable users to update models more efficiently when locally there occurs no movement in a given section.

1 Introduction

The detection of foreground objects is one of the standard image processing and identification operations, often carried out via modeling the background of the image. Knowing the correct background model, we can easily remove the background from the existing frame. The remaining elements are the foreground objects. The key assumption behind this approach is the cameraŠs static field of view.

In most cases the intensity of light changes during the light exposure (the setting sun, or changing shadow thrown by a building). Also the shadow cast by passersby can be considered a change of lighting. Hence, in order to effectively model the background, more robust algorithms need to be employed. At first, Eigenbackground-based background modeling has been presented in [1]. Afterwards was presented several algorithms with different methods [2], and adaptive algorithms [3] and [4]. In most cases, the basic methods such as Temporal Median Estimator, Temporal Median or Motion Based Background Estimator are not robust to changing light conditions, in contrast to the present method.

The document has been organized according to the following order: Chapter 2 describes the Eigenbackground algorithm, Chapter 3 presents the method of dividing the background model into smaller regions, Chapter 4 introduces the methods of thresholding obtained results, Chapter 5 presents the experimental results of the method, and Chapter 6 summaries the entire article.

2 Eigenbackground Method

In the following paper the following notations shall be utilised: $i^{n,m}$, where the right-hand superscripts describe the size of a matrix or a vector, and $i_{1,...,N}$, where right-hand subscripts refer to the number of the box (frame) of the image.

Image i is transformed by combining the lines into a vertical vector according to the following formula:

$$i^{h,w} \rightarrow I^n \tag{1}$$

where h and w are the height and width of the input image respectively, while n is the length of the vector, where $n = hw$. The sequence of subsequent N images I_i in the vector form (1) can be recorded as the matrix $I^{n,N}$:

$$I = [I_1, I_2, ..., I_N] \tag{2}$$

If μb is the vector of mean values for the sequence of the N length of the $\mu_b^{n,1}$. If from each image vector I_i for $i = 1, ..., N$ the mean value of μ_b is deducted, then the obtained vector shall have zero mean value and shall represent the variation of a given vector from the mean (equation 3):

$$X_i = I_i - \mu_b \tag{3}$$

where $i = 1, ..., N$, and recording the subsequent X_i vectors by means of the following matrix:

$$X = [X_1, X_2, ..., X_N] \tag{4}$$
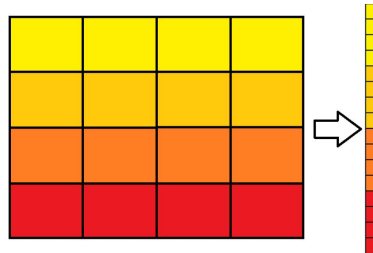
Fig. 1. Imgage to vector transformation

Then the matrix (4) can be utilized to calculate the covariance matrix:

$$C_b = E\{X_i X_i^T\} \tag{5}$$

which can be recorded as:

$$C_b = \frac{XX^T}{N} \tag{6}$$

where X is given in the following equation (4), whereas the size of the matrix is $C_b^{n,n}$.

The SVD distribution for such a large matrix is costly calculation-wise, hence in order to accelerate this step, the following transformations are applied:

$$D_b = \frac{X^T X}{N} \tag{7}$$

where the size of the matrix is $D_b^{N,N}$. The size of the N model is usually far smaller than the size of the C_b one.

The distribution of the D_b matrix for eigenvalues exists and looks as follows:

$$D_b V = V \Delta \tag{8}$$

these matrices have the following sizes: $D_b^{N,N}$, $V^{N,N}$, $\Delta^{N,N}$, and δ_i is i-th value of Δ, for eigenvalues ranked from the highest one.

The V matrix is utilised to calculate the P matrix for series $i = 1, ..., N$ frames, where the size of the P matrix is $P^{n,N}$:

$$P_i = X V_i \tag{9}$$

which is used to calculate:

$$U_i = P_i / \sqrt{\delta_i} \tag{10}$$

where the size of the U matrix is $U^{n,N}$ and $i = 1, ..., N$. Based on the above calculations we can recreate the space of N images from the obtained model.

For calculations in the Matlab software we can use the following command:

$$[V_b, \Delta] = svds(D_b, N', L')$$

where V_b to . . . eigenvectors, Δ is the diagonal matrix for eigenvalues . . . and the $svds$ command calculates N for the highest eigenvalues of the D_b matrix.

3   The Division of the Model into Local Sections

The matrix of the input image presented in the form of: $i^{h,w}$, can be recorded as matrices of smaller images:

$$i = \begin{bmatrix} i_{11} & i_{12} & \ldots & i_{1m} \\ i_{21} & i_{22} & \ldots & i_{2m} \\ \vdots & \vdots & \vdots & \vdots \\ i_{n1} & i_{n2} & \ldots & i_{nm} \end{bmatrix}$$

where n and m are the number of fields the i image has been divided into, whereas local images include $i_{11}, i_{12}, ..., i_{nm}$. For the diagram of such a transformation see (Fig. 2). For an image divided in such a fashion we obtain nm for smaller images and just as many separate background models - one background model per one image respectively. The background model is made of nm number of matrices U^{nm}, Δ^{nm} and μ_b^{nm}, and they are sufficient to calculate the background model.
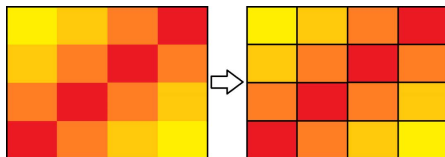
Fig. 2. Division of the image into smaller matrices

4   Local Background Substraction

The presented approach allows for utilizing other methods of separating the background from the foreground, thanks to which the model can be updated with a larger amount of information more frequently. The model features U, Δ and μ_b, matrices, whereas the dimension of the model is N which - for the sake of simplification - is equal to (or smaller than) the number of frames that the model has been created from. The reconstruction of the image from the background model is conducted according to the following sequence. The subsequent frame from the i video sequence is transformed to a vector according to equation 1:

$$R = (I - \mu_b)^T U \tag{11}$$

where: $R^{1,N}$, $I^{n,1}$, $\mu_b^{n,1}$, $U^{n,N}$. Moreover, for subsequent elements of the matrix R_i and subsequent δ_i values, where $i = 1, ..., N$, the following condition has to be applied:

$$Rp_i = \begin{cases} 3\delta_i & \text{if } R_i > 3\delta_i \\ R_i & \text{if } -3\delta_i < R_i < 3\delta_i \\ -3\delta_i & \text{if } R_i < 3\delta_i \end{cases}$$

The recreated image from the model assumes the following form:

$$\hat{I} = URp^T + \mu_b \tag{12}$$

The comparison of the $\hat{I}$ recreated image and the current I one:

$$Dif = \left| \hat{I} - I \right| \tag{13}$$

Based on the Dif matrix we can interpret the results and conduct threshold-ing. If the variance and the mean value of a given Dif matrix are low, then we know that no movement has taken place, and the only thing that could have possibly changed is the lighting in a given section of the image. Initial thresholding:

$$dv = \begin{cases} 1 & \text{if } var(Dif) > \alpha \\ 0 & \text{if } var(Dif) < \alpha \text{ and } mean(Dif) < \beta \end{cases}$$

where α, β are the thresholds. The value of the α threshold is of a given order, e.g. 10^{-3}. If the difference variance between the model and the image is insignificant, and additionally the mean value is below the β threshold, then the only element that changed is the lighting. If we took into account only the change of the variance, for example, then thresholding would also work for monochromatic objects.

Then for the fields for which the truth value is $dv = 1$ the thresholds is calculated, based on the mean and standard variation. We assume constant $\eta_{\min}$, $\eta_{\max}$, κ:

$$\eta = \max\left(\eta_{\min}, \min(\eta_{\max}, mean(Dif) + \kappa std(Dif))\right) \tag{14}$$

In the case of RGB images we can additionally assess the extent to which a given image recreated from the model differs from the processed one in particular channels.

5   Experimental Results

This chapter shall present the results for the proposed method for test se-quences.

First video "ThreePastShop1cor" is from well-known Caviar Data Set, have size 384×288 pixels. For this video Eigenbackground methods (Fig. 3.2, 3.3) we have better object substraction, than in (Fig. 3.4, 3.5). In MOG2 (Fig. 3.5) gray values - it is the shadow. Second test video is from underground station in Warsow. Size of this video is 1280×720 pixels. When light is from back side, we have shadow in front. Depending on thresholding to be executed, different results will be obtained. In case of the comparison of different sizes of models recived from the Eigenbackground method (Fig. 4.2, 4.3, 4.4), we can observe a better shadow modelling for smaller size of models.

Fig. 3. Comparison - from left - 1. Original picture, 2. Original eigenbackground, 3. Eigenbackground 16×16 frames, 5. MOG, 6. MOG2
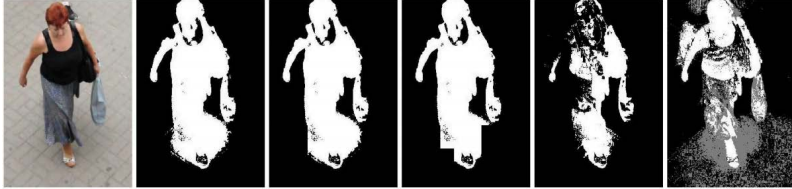
Fig. 4. Comparison - from left - 1. Original picture, 2. Original eigenbackground, 3. Eigenbackground 20×20 frames, 4. Eigenbackground 40×40 frames, 5. MOG, 6

6 Conclusions

The article presents the background modeling method for local image fields. The modeling results using this method resemble the standard Eigenbackground method. However, by setting the thresholds properly, we get the information about the location of the movement and shadow. This way, the model is better matches the object, and the shadow from the frame can be added to the adaptive model. The key argument in favor of the method with division into smaller frames is the fact that the algorithm can be adapted to multiple thread CUDA cards, which is one of directions for further development.

References

1. Oliver, N.M., Rosario, B., Pentland, A.P.: A Bayesian computer vision system for modeling human interactions. IEEE Transactions (2000)
2. Gritti, T.: Robust Background Subtraction with Incremental Eigen Models. Philips Research (2008)
3. Parks, D.H., Fels, S.S.: Evaluation of Background Subtraction Algorithms with Post-Processing. In: IEEE Fifth International Conference on Advanced Video and Signal Based Surveillance, AVSS 2008 (2008)
4. Renno, J., Greenhill, D., Orwell, J., Jones, G.A.: Adaptive eigenbackgrounds for object detection. In: 2004 International Conference on Image Processing, ICIP 2004 (2004)

Polarization Imaging in 3D Shape Reconstrucion

Piotr Garbat and Jerzy Woźnicki

Institute of Microelectronics and Optoelectronics,
Warsaw Univeristy of Technology, Warsaw, Poland
`p.garbat@elka.pw.edu.pl`

Summary. We report a new polarimetric imaging setup based on tunable liquid crystal components and its application in computer vision. The analysis of polarization parameters (polarimetric imaging) has been used in photometric 3D shape reconstruction. This research describes a novel approach for 3D shape measurement system supported by polarization image analysis. Enhancement of fringe image quality is realized using the detector unit with special liquid crystal filter.

1 Introduction

The polarization is very important feature of light that isn't perceive by human eye. Some of insects and sea animals can see this feature. Recent research in this topic allow to bring closer this phenomenon. This research are base for new polarization vision systems and methods. Current polarization imaging systems can be divided on two groups [1, 6]:

- temporal phase analysis [2, 3],
- spatial phasr analysis, including beam splitting [3, 4].

State of technique in image acquisition system domain, as also fast liquid crystal device technology allow to realize polarization imaging systems for video signal. One of he most important application video polarimetric imaging could be high eficient and quality 3D shape or depth map aquisition system. This requires gathering real data about dynamic 3D objects and scenes. One common way of approaching this problem is the shape measurement based on structer light approach [1, 2]. In this case the information about shape are determined based on the analysis of fringe deformation of structural light projected onto the measured object. Three-dimensional image measurement technique based on color pattern projection have characteristics such as activeness, high-speed measurement and potentially high accuracy . The main problem of the measurement process using this method in real conditions is the significant influence of hardware applied in the

set-up, objects surface properties, and properties of medium on the achieved accuracy. The influence of the measurement environment is a big problem in industrial applications. The analysis of polarization parameters (polarimetric imaging) has been used in numerous imaging applications, including removal of scattering effects eg.underwater [3, 4]. Method of imaging through scattering media using Polarization Difference Imaging (PDI) or active polarization was presented in many publications [3, 4]. The analysis of photometric stereo and light stripe range scanning in the scattering media was presented by S.G.Narasimhan [5]. Laser light stripe scanner supported by polarization analysis for removal reflection effect was presented by [6]. The polarization-difference imaging can be used for eliminate subsurface scattering effects in traditional optical 3D scanning techniques, such as structured light. In this paper polarization image analysis for 3D shape registration is used.

2 Aquisition Setup

The poarization imaging system consists of the camera-filter (C-F) units, the processing unit and the measurement volume witch controled light source.The C-F unit includes monochrome camera and with polarization analysis device. The detection units works witch controlled light.

The measurement volume, in which the object is located, is isolated from sun light. For the first component, image acquisition, a fast camera model Basler Scout is used. This is an monochrome camera, capable of capturing up to 60fps, with VGA (640×480) resolution, and GigE interface. The camera is synchronized by signal from liquid crystal filters divice. Experimental device consists fast liquid crystal variable retarders, fixed polarizer and camera

Fig. 1. Prototype of polarization camera

(Fig.3). Variable retaders based on special liquid crystal mixture for dual frequency switching. Suggested solution allows polarization boost of efficiency of appointment of largeness describing state and definition of direction of orthogonal pivot for real vision system. Proposed filter contain inseries a pair of liquid crystal retarder cells with 45° between their principal axes and a linear polarizer.
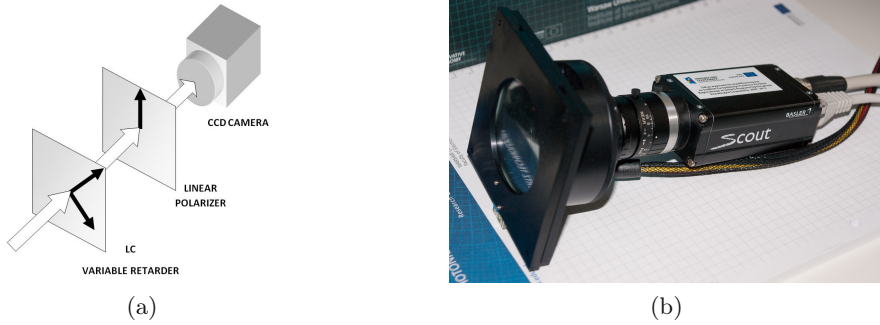
Fig. 2. LC polarization analyzer: (a) scheme, (b) real photo

2.1 Polarization Analysis

Several experimental methods can be used to determine the polarization state of an incoming light or the depolarizing effect of an object.

Polarization of a light wave can be fully described by four parameters known as the Stokes polarization parameters or Stokes vector. The first parameter S_0 is the total intensity of the optical field and the other three parameters S_1, S_2, S_3 describe the polarization state.

$$S = \begin{bmatrix} S_0 \\ S_1 \\ S_2 \\ S_3 \end{bmatrix} = \begin{bmatrix} m_x^2 + m_y^2 \\ m_x^2 - m_y^2 \\ 2m_x m_y \cos\delta \\ 2m_x m_y \sin\delta \end{bmatrix} = (1-\rho) \begin{bmatrix} S_0 \\ 0 \\ 0 \\ 0 \end{bmatrix} + \rho \begin{bmatrix} S_0 \\ S_1 \\ S_2 \\ S_3 \end{bmatrix}, \qquad (1)$$

Based on the Stokes polarization parameters we can obtain four parameters of polarized light: - intensity

$$I = S_0 \,, \qquad (2)$$

- degree of polarization

$$\rho = \frac{\sqrt{S_1^2 + S_2^2 + S_3^2}}{S_0} \,, \qquad (3)$$

- angle of polarization

$$\tan 2\alpha = \frac{S_2}{S_1} \,, \qquad (4)$$

- ellipticity

$$\sin 2\nu = \frac{S_3}{\sqrt{S_1^2 + S_2^2 + S_3^2}} \, , \tag{5}$$

In practical machine vision implementations analysis of first three paramters are very usefull. Propossed, experimental system of polarization vision takes advantage temporal analysis of state of polarization for assignment of basic three parameter polarization enlightened.

In proposed 3D shape measurement system The information about polarization is used for identification of gathered fringes. Using polarizing analysis we can separate the part of illumination of the projecting mode source from constant illumination. The proposed LC filter can be described based on Mueller matrix:

$$s_r = M_{pola} M_{ret}(\delta, 45°) M_{ret}(\gamma, 0°) s_{in} \tag{6}$$

Thus, the measured intensity I_r is:

$$I_r(\delta) = \frac{1}{2}(s_0 + s_1 cos\delta + s_2 sin\delta) = \frac{I}{2}(1 + \rho cos(\delta - 2\varphi)) \, , \tag{7}$$

2.2 3D Shape Acquisition

In proposed 3D shape measurement system The information about polarization is used for identification of gathered fringes. Using polarizing analysis we can separate the part of illumination of the projecting mode source from constant illumination.

The goal aim of proposed method is reconstruction of real model 3D shape. The first stage of this process is normal vectors determining. The normal vectors could be represented in polar coordinate system (θ, φ) where θ, and φ - represented normal vector. ($0 < \theta < 90°, 0 < \varphi < 360°$).

The θ angle is calculated based on value of degree of polarization DOP. The value equal 1 mean polarized light, and value 0 unpolarized light:

$$\rho = \frac{F_\perp - F_\parallel}{F_\perp + F_\parallel} \, , \tag{8}$$

From the Fresnel formulae, we know that $F_\perp$ and $F_\parallel$ depend of $\theta_i and \theta_r$ And from the Snell-Descartes' law, one can write:

$$\theta_r = arcsin(\frac{1}{n} sin\theta_i) \tag{9}$$
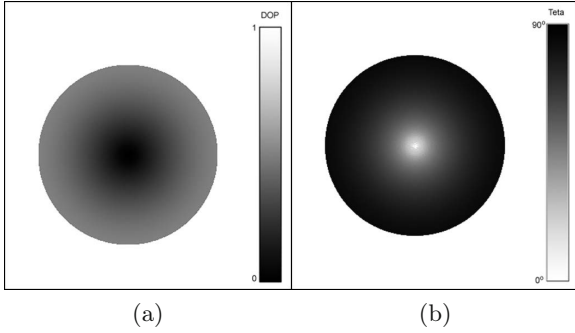
Fig. 3. Degree of polarization (a) and $\theta angel$ (b) for n=1.7

Therefore, since $\theta_i = \theta_r$ we can deduce that $F_\perp$ and $F_\parallel$ depend of θ_r and n If the object refractive index n is known we have $\rho(\theta_r)$

$$\rho = \frac{(n - 1/n)^2 sin^2\theta}{2 + 2n^2 - (n + 1/n)^2 sin^2\theta + 4cos\theta\sqrt{n^2 - sin^2\theta}} \, , \qquad (10)$$

where $\rho=$ degre of polarization , n birefringence of material.

Based on (8) and (10)we can calculate first part of normal vector.

Fig. 4. Angel of polarization ϕ (a) and φ angel (b) for synthetic data

In next step the phase image is determined. This representation show values of azimuthal angel. Becouse characteristic of polarisation filter is periodic we can obserw value repetition. The final value of continius phase is calculated:

The second parameter φ angle can be calculated based on value of angle of polarization.

$$\varphi = \phi \pm \frac{\pi}{2} \, , \qquad (11)$$

In that way the coordinates of normal vector in polar system are calculated. The normal vector is calculated for all points of surface. On 5 the needle maps is presented. In last step normals vector are used to determine depth maps based on Frankott-Chellapp alghoritm.

<div align="center">(a)   (b)</div>
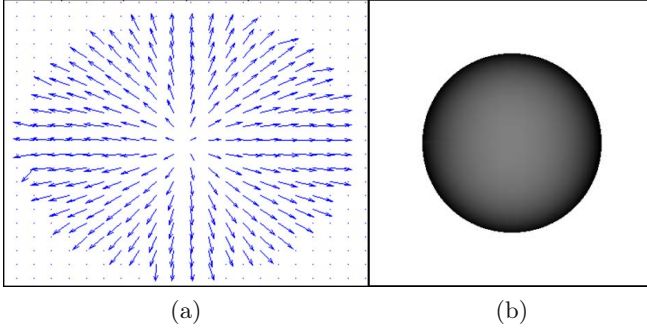
Fig. 5. Needle maps (a) and depth map (b)

3   Results and Conclusions

To examine the new 3D shape measurement methodology in real conditions, the measurement of static object were investigated. The implemented prototype and measure process is shown on Fig. 1. The sequence of images with polarization anlyzys proved to be very efficient for the analysis of 3D scenes and obtine of the depth map. The precision of depth values that can be computed is limited by efficiency of the filter dynamics and sensivity.
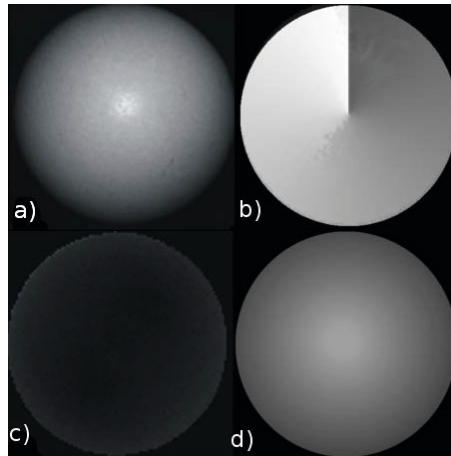
Fig. 6. Experimental results: (a) measurement object (b) azimuth (c) DOP, (d) depth map
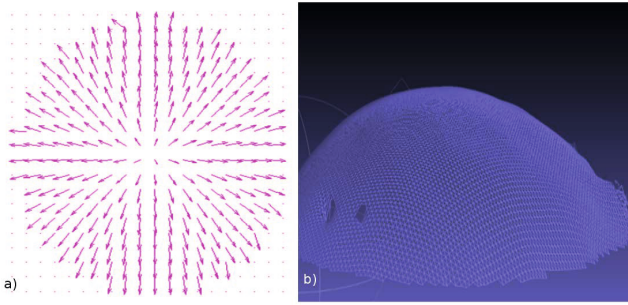
Fig. 7. Experimental results: (a)normal vectors in polar system (b) 3D shape

The result of experiment performed on real object is presented on Fig. 6. Pictures show captured images and obtained depth map. The experiment with polarization image analysis module confirmed improvement quality of gathered image and influence on RMS Error of depth reconstruction. Polarization supported methodology allow to shape reconstruction with error from 1,2 to 0,7 cm. In comparison to the methods based on standard polarization measurement setup, proposed solution is faster. However at the moment the accuracy is not very high, calculations are very simple so depth map may be obtained in nearly real-time (20 Hz) which is in most cases enough for multimedia applications.

References

1. Chen, F., Brown, G.M., Song, M.: Overview of three-dimensional shape measurement using optical methods. Opt. Eng. 39 (2000)
2. Lu, C., Cho, G.: Projection pattern intensity control technique for 3-d optical measurement. Opt. Express 13, 106–114 (2005)
3. Treibitz, T., Schechner, Y.Y.: Active polarization descattering. IEEE Trans. Pattern Anal. Mach. Intell., 385–399 (2009)
4. Tyo, J.S., Rowe, M.P., Pugh, J.E.N., Engheta, N.: Target detection in optically scattering media by polarization-difference imaging. Appl. Opt. 35, 1855–1870 (1996)
5. Narasimhan, S.G., Nayar, S.K., Sun, B., Koppal, S.J.: Structured light in scattering media. In: Proceedings of the Tenth IEEE International Conference on Computer Vision, ICCV 2005, vol. 1, pp. 420–427. IEEE Computer Society, Washington, DC (2005)
6. Wallace, A.M., Liang, B., Trucco, E., Clark, J.: Improving depth image acquisition using polarized light. Int. J. Comput. Vision 32, 87–109 (1999)

Background Subtraction and Movement Detection Algorithms in Dynamic Environments – An Evaluation for Automated Threat Recognition Systems

Adam Flizikowski, Mirosław Maszewski[1], Marcin Wachowiak[2], and Grzegorz Taberski[3]

[1] University of Technology and Life Sciences, Bydgoszcz, Poland
   `{adamfli,mmasz}@utp.edu.pl`
[2] ITTI Ltd., Poznan, Poland
   `marcin.wachowiak@gmail.com`
[3] Adam Mickiewicz University, Poznan, Poland
   `gtab@amu.edu.pl`

Summary. A background subtraction and movement detection is a very popular subject of investigation in the video processing domain. Despite number of already proposed algorithms and methods the question of suitability of such algorithms in dynamically changing, realistic environment holds (e.g. parking lots). In this paper authors compare three different implementations of the saliency-based algorithms and Gaussian Mixture Model algorithm for different cameras on a parking lot. Authors show that matching algorithms to the scene can be improved by managing semantic knowledge about the scene.

1 Introduction

In the recent years video streams analysis for automated content recognition became very popular subject of interest, mostly because of popularization of the surveillance, security and threat-detection systems. Currently the menace of the real life-threatening situations like terrorist attacks or hooligan riots determines governments or city municipalities to look forward for automated systems capable of detecting potential threats before they will grow and get out of control (e.g. the Total Information Awareness platform developed by the Information Awareness Office (IAO) [7], the SGR created by Samsung [8]). Other examples of typical situations, where surveillance systems may be useful, include big events like Olympic Games, football competitions or music concerts. Thus in the frame of the FP7 ARENA project authors have compared several available background subtraction algorithms to evaluate their usefulness in such surveillance systems that requires robustness and reliability. There are

numerous already developed algorithms, but most of them can be used only under some specific conditions e.g. they require constant luminance, static background or learning phase before they become fully operational. An interesting comparison of popular motion detection algorithms like Adjacent Frame Difference (AFD), Mean and Threshold (MaT) or Bayesian Decision can be found at [6]. Another group of algorithms, designed especially to deal with the dynamic backgrounds like Dynamic Texture Mixture (DTM) or Gaussian Mixture Model (GMM) were presented and compared in [3]. A comprehensive comparison showing, how changeable scene conditions affect various algorithms was provided in [6]. As it was presented, **most of the basic algorithms like AFD or MaT will start to generate a lot of false detections each time scene conditions will significantly change**. Most of the already developed algorithms aim to detect movement in strictly controlled environments - like closed indoor spaces - where scene background can be fully controlled and number of distractions like e.g. changeable weather conditions can be significantly minimized or even removed. We are focusing in this paper on the algorithms that were designed for environments with highly-dynamic scene background.

2   Background Detection Algorithms

The solutions in the domain of object recognition and tracking developed within the FP7 ARENA project are targeting the outdoor environments, where constant conditions (like luminescence or weather conditions) cannot be guaranteed. It is assumed, that despite weather conditions, ARENA system should be operational 365 days a year and should be autonomous to the level that enables dealing with various conditions with minimized intervention of the human operator. Algorithms used for evaluation include:

- Saliency algorithm: implementation proposed by Tian and Hampapur [1]
- Saliency algorithm: implementation proposed by Hou and Zhang [5]
- Saliency algorithm: implementation proposed Montabone and Soto [4]
- Gaussian Mixture Model: implementation proposed by Chan and Mahadevan [3]

The three implementations rely on the use of saliency feature. That's because saliency approach is very popular in the movement detection area and as it will be shown in our results one can achieve good results using these algorithms with operational parameters tuned for a single camera. In the subsequent sections we enumerate the algorithms and their main characteristics in order to provide a base/reference for eventual comparison of algorithms in the frame of ARENA scenarios in following chapters.

2.1 Simple Thresholding

The simple background thresholding (referred as SimpleDiff in this article) is one of the simplest and widely used algorithms in the video processing domain. In the basic version of the above mentioned algorithm a two consecutive frames are taken and then difference is calculated for each pair of corresponding pixels in both frames. If difference between pixels' values becomes greater than some arbitrarily defined threshold then a pixel will be classified as a part of the foreground. Thus the key performance indicator for this algorithm is the value of threshold parameter: too small value will cause raise in false detections visible in the output images. On the contrary too high value will cause that some of the pixels that are in fact part of the real moving object be classified as a background.

2.2 Saliency Detection Algorithm – Base Implementation (BaseSaliency)

Algorithms that fall into a saliency group (i.e. based on the image content) try to characterize movement in the image, and then classify it into one of the two classes: salient movements (points of interests) and non-salient ones (not interested objects, noise in the image). The first one presented in this paper was proposed by Tian and Hampapur [1]. For this approach, overall image processing can be easy divided into three separate parts: In the first one, foreground pixels are detected in the image. Then, in the second phase optical flow is calculated for detected areas to find if they meet requirements and constraints of the algorithm. Provided the answer is positive then in the third phase these pixels are added to the foreground map. In our approach phase one was implemented using enhanced version of the SimpleDiff - i.e. frame buffers were added to keep information about pixel history. Optical flow (phase two) was done using Lukas-Kanade algorithm. For phase three, custom algorithm was created to group adjacent objects into larger ones as well as to remove small blobs.

2.3 Saliency Detection Algorithm – Speed-Optimized Approach (FGS)

During the work in the ARENA system, authors decided to implement more than one saliency algorithm. The second Fine Grained Saliency (FGS) implementation uses a concept of an integral image proposed in [4]. For this algorithm an input image must be converted to grayscale and then smoothed two times using Gaussian filter. Then, for every pixel in the image, the system calculates on-center and off-center differences using a unique integral image with variable size filter windows. For example $\varsigma \in \{12, 24, 28, 48, 56, 112\}$

represents the surroundings, which were used in our system. In the next step both difference maps are summed: if calculated value will exceed some defined threshold then pixel will be classified as salient.

2.4 *Saliency Detection Algorithm – Experimental (Non-optimized) Approach (SlowSaliency)*

The salient regions in the image may contain various elements e.g.: foreground, parts of the background, interesting patterns and so on. A pixel is salient if its appearance is unique. In the more general approach, one should not look at an isolated pixel, but at its surrounding patch - so in this approach, first the image was divided into several 8×8 pixels patches. Also $L * a * b*$ color space was used to measure the color difference between two patches because the distance in $L * a * b*$ color space reflects the visual difference. To measure the difference of patterns, the discrete cosine transform (DCT) was taken on each patch. For each patch, distances were computed to all other patches and then saliency score was then computed using K most similar patches. The saliency map is a gray level image where light regions correspond to the salient areas, whereas the dark ones represent the non-salient part of the image. In the last step, a 7×7 Gaussian kernel was applied on the output saliency map to smooth it.

2.5 *Gaussian Mixture Model*

The Gaussian Mixture Model (referred as GMM in this article) was another type of algorithm to be implemented and evaluated against the needs of ARENA object detection system. As in the previous examples this algorithm according to its authors was designed to be used in environments containing significant stochastic motion - like the one specific to water or leafs' movements [3]. GMM is a probabilistic model which assumes that all the data points are generated from a mixture of a finite number of Gaussian distributions with unknown parameters. These component functions are combined to provide a multimodal density. They can be employed to model the colors of an object in order to perform tasks such as real-time color-based tracking and segmentation.

3 Background Subtraction Algorithms – Performance Evaluation

For evaluating the above mentioned algorithms' performance several video sequences of a threat behavior were recorded in the scope of ARENA project. The majority of video sequences were recorded in the closed parking area;

the remaining ones were recorded in the open sea. The latter videos were captured using low quality cameras that is why they will not be used for evaluation here.

3.1   Parking Sequence – "Camera 1"

Scenarios used for recording a sequence were chosen to mimic real life conditions and threat events. The target object detection and tracking within ARENA system is intended to be used in such environments to provide surveillance services with threat detection capabilities. Results obtained using the algorithms mentioned above are presented in the table below.

Table 1. Comparison of results for different cameras (Left - camera1; Right - camera2)

Original image	Ground Truth
BEST: FGS. Parameters: thr=20	BEST: GMM
WORSE: BaseSaliency. Parameters: bk=2, db=8	WORSE: Simple diff, thr=20

As one can observe, for the parking sequence captured with "Camera 1" the best results were obtained for the FGS algorithm. Moving silhouette of a person was correctly recognized and extracted from the background. Also, there were no false positives (random noise) in the output. Acceptable results were also provided using GMM algorithm, but in this case, human silhouette was not fully detected - only these elements of the blob were detected, which had different illumination than the corresponding background. Whenever a blob has the same color (luminance) as the original background model (area behind the blob) then GMM doesn't recognize it as a foreground. Nevertheless algorithm can be used in such situations, because, similarly as for the FGS, there were no false positives in the output binary matrix. GMM results can be further enhanced by different algorithms e.g. by adding surrounding pixels to the main detected object. Results obtained with the SlowSaliency for the "Camera 1" look slightly better than these obtained by GMM, but low performance and slow data processing are making this algorithm unusable in the online video processing as a threat detection should be. The computational complexity for this algorithm is quite large: O(n3) data processing of the standard camera frame (1024×800) took on the testing machine (Intel i3 CPU + 4 Gb of RAM) about 90 seconds. By scaling image down by factor of 2 the processing time was limited to about 10 seconds which is still far from acceptable (see Table 4). The two remaining algorithms: SimpleDiff and BaseSaliency have generated a lot of noise in the output image. There are enhancements available for the BaseSaliency algorithm - e.g. optical flow-based operations, which improves output results, but as a side-effect it would significantly decrease the algorithm's performance. The SimpleDiff was given here as an example of the algorithm, which was not designed to deal with dynamic background, so the results obtained here simply indicate its poor relevance in the dynamic environments like e.g. parking area with people walking around. In the Table 2 comparison results were collected for all analyzed algorithms to provide better overview, how they match the reference Ground Truth image.

Table 2. Comparison of processing results with the Ground Truth - Camera 1

	Findings	Matches	Invalid	Valid Ratio	Inv/Vld Ratio
GT	507	507	0	100,00%	0,00%
GMM	300	276	24	54,44%	8,00%
BaseSaliency	780	161	619	31,76%	**79,36%**
FGS	643	472	171	**93,10%**	26,59%
SlowSaliency	607	349	258	68,84%	42,50%
SimpleDiff-8	3975	369	3606	**72,78%**	**90,72%**
SimpleDiff-20	394	278	116	54,83%	29,44%

The Ground Truth (GT) value for the "Valid Ratio" is equal to 100%, which means that "all POIs were correctly detected in the image". Ground truth has been provided by manually marking the human silhouette and other objects on the scene (frame by frame). As it can be found in the table, the best "Valid Ratio" was obtained for FGS and SimpleDiff algorithms. Values achieved by GMM and SlowSaliency are also acceptable, especially for tracking purposes. Accuracy for other algorithms (e.g. BaseSaliency) is below an acceptable level, but can be easily increased: this algorithm has enabled detection of the shape of the moving object omitting its body. So some additional step may be added here, which will add pixels laying between blob boundaries to that blob. The worst "Inv/Vld Ratio" was obtained for BaseSaliency and SimpleDiff-8 algorithms: these algorithms generate a highest number of false positives (moving leafs in the video sequence). Value of this parameter also can be easily in-creased by introducing additional filters in the processing mechanism e.g. filter which will remove all small, randomly generated blobs in the image. Such fine tuning algorithms may be introduced to improve the processing results for the above algorithms.

3.2   Parking Sequence – "Camera 2"

In order to further evaluate the algorithms authors have used the video sequence collected using another camera (Camera2). This latter camera captures movements of exactly the same object on the scene, at the same time as "Camera 1" above. The only difference being the perspective from which the scene has been recorded.

Table 3. Algorithms performance comparison for parking scenario - Camera 2

	Findings	Matches	Invalid	Valid Ratio	Inv/Vld Ratio
GT	6274	6274	0	100,00%	0,00%
GMM	7388	5320	2068	**84,79%**	27,99%
BaseSaliency	20661	5471	15190	**87,20%**	73,52%
FGS	5430	1429	2257	22,78%	41,57%
SlowSaliency	4525	1797	2728	28,64%	60,29%
SimpleDiff-8	7743	1966	5777	31,34%	**74,61%**
SimpleDiff-20	4505	1113	3392	17,74%	**75,29%**

It should be noticed that the efficiency of the background subtraction algorithms in the case of the second camera significantly differs from the results recorded for Camera 1. The algorithms that have provided highest performance for the scene captured by "Camera 1" are no longer the best ones (FGS, SimpleDiff-8) when considering the "Valid Ratio" parameter for "Camera 2". Neither are these algorithms worse from the perspective of the

"Invalid/Valid" ratio. This stems from the fact that **composition of the areas of interest differs** for the two cameras - although they both overlook exactly the same objects of interest. The areas covered by the AOIs are different and so the coverage of the part of the frame where the background artifacts are seen differs. Namely the object moving in front of the "camera 1" can be discerned more easily from the background due to more static nature of the latter. Whereas the same object seen on the background of big trees (camera 2) is more challenging to be subtracted from the noise. The last table presents an algorithm's computational complexity for normal as well as scaled frame.

Table 4. Algorithms performance comparison for parking scenario

Algorithm	Normal frame		Scaled frame	
	FPT (s)	FPS	FPT (s)	FPS
SimpleDiff	0,019	**52,53**	0,008	**125,82**
BaseSaliency	0,022	**45,52**	0,007	**141,82**
FGS	0,085	11,70	0,029	34,91
SlowSaliency	17,80	**0,06**	1,017	**0,98**
GMM	0,05	19,41	0,014	69,53

It is clearly seen that for originally sized frames the FGS and GMM approaches are most complex as the frames per second parameter is only 25% of its simplest counter-parts. After scaling the frames down the average FPS grows at least 3 times (e.g. to the speed offered by simple algorithms at normal-sized frames). The ratio between the FPS of BaseSaliency and GMM has the highest value but the ratio FGS / BaseSaliency remains unchanged when one scale down the frames.

4   Discussion of Results

It needs to be highlighted is that scene processing results (namely background subtraction) have been generated using algorithms with default (thus scene independent) values of operational parameters. Each of the algorithms when properly integrated into target threat analysis system shall be adjusted by the external operator (or automated agent) to assure appropriate i.e. scene aware parameter setting.

4.1   *Main Challenges for Automated Surveillance Systems*

The type of surveillance systems that ARENA represents relies on a mobile ad-hoc infrastructure of the cameras. The latter will eventually be attached

to the truck according to a set of "configuration" directives. This approach although representing ultra-high portability of data collection and processing capabilities comes for the price of numerous challenges. The latter may result from the limited use (or the availability) of stationary audio-video recording infrastructure at parking facilities. However the existing CCTV cameras deployed at the particular parking lot facility according to authors should be used in tandem with the portable sensors in order to increase the overall system performance. It is important not forget the role of human operator (CCTV) who follows a preprocessed video feed (e.g. to mark threat zones). In addition an intelligent, reasoning component shall be available to improve adaptability of the system. The functionality of such module would e.g. focus on adjustment of selected parameters (of the cameras, image processing algorithms) based on the scene content that the particular camera is currently observing. A hybrid approach is necessary where the information observed by human operator (on-site) gets enhanced with the data captured by the cameras attached to the trucks (ad-hoc). It is recommended for the automated threat detection systems that human presence shall be limited, or fully replaced by the "intelligent" reasoning element. This can be for example neural-network-based algorithm or an expert system (e.g. ontology based) one.

4.2 Ontology Concept

The reliability of the target ARENA threat recognition capabilities should be parking area agnostic, i.e. independent of sensors position (e.g. camera mounted on a truck can have a different viewing angle/direction given the current truck position at the parking). Therefore automating the adjustment process and providing a common knowledge base becomes an important function of the future threat recognition system. Automating the adjustment process can be supported by dedicated knowledge base. Using ontology as a knowledge base the ARENA expert/operator/system will gain additional information about objects, relations and interactions between objects. Based on that knowledge, ARENA Expert will know factors which can affect a given algorithm and adjust it better to a given circumstances, making the algorithm more effective.

The following functions of the ontology supporting automated threat recognition and alerting are proposed (see Fig. 1):

- Algorithms calibration – algorithms adjustment based on data included in ontology, algorithms specifications and actual conditions at the parking area (e.g. weather conditions, time of the day etc.),
- Threats identification – data fusion of camera surveillance, image processing algorithms and domain specific knowledge contained in ontology (e.g. about parking zones or possible Modus Operandi; these knowledge should be derived from ARENA Expert as well as HMI Operator)
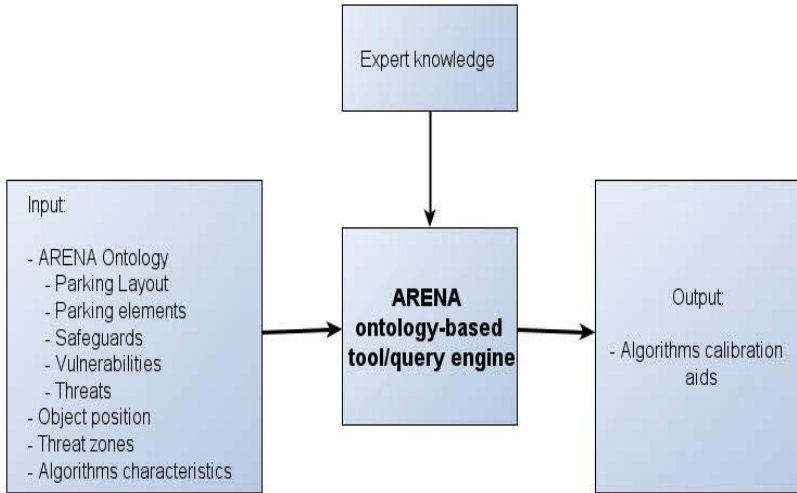
Fig. 1. ARENA ontology execution tool - inputs and outputs

- Rules management – knowledge included in ontology can be extended by additional rules, they should be defined by ARENA Expert and HMI Operator and provide knowledge which is specific for a particular parking or circumstances,
- Threats ranking – ontology is envisioned to be used as decision aid tool, which provides ranking capabilities of threats included in ontology.

The target ontology module is intended to work in the "closed loop" mode: e.g. results generated by the movement detection algorithms are analyzed by the reasoning component. Rules and conditions defined in the ontology will assist analysis of the results, and then undertaking most appropriate actions e.g. change foreground detection algorithm used by the movement-detection element. A simple rule may looks like the one below:

```
IF noiseRatio > 0.01 THEN threshold = threshold+2
```

The above sample rule simply checks, if the proportion between noise (false positives - small, random objects in the output image) and total number of pixels in the image is lower than 1%. If not, then value of the threshold parameter used by the foreground detection algorithm should be increased by two. **More sophisticated rules can be used** to change the data flow based on several factors, as well as short-term history (last N frames), similar patterns in the different video sequences and so on. Using ontology-based reasoning one may be able to create fully operational, autonomous system, which can successfully replace or actively support real operators.

5 Summary

In this paper authors presented and compared the application of saliency based background removal algorithms for the realm of automated threat detection. Results of the tests clearly reveal, that some algorithms can quite well deal with complicated, or low-quality videos however the question of *"which particular algorithm fits given scene?"* is not straightforward to answer especially for the surveillance system that is portable and adheres to the "ad-hoc" infrastructure composition by design. When using the above set of algorithms for processing the same scene but captured from distinct perspectives it is likely that different algorithms will be selected as "best choice" when default values of operational parameters are set. Moreover algorithms performance will come with a tradeoff in processing complexity of the different implementations. Authors thus propose to use a notion of ontology-in-the-loop to enable dealing with the challenges (mainly in the area of image processing and threat detection) that may decrease target usability and adjustability of the portable surveillance system like the one created by FP7 ARENA project.

References

1. Tian, Y.L., Hampapur, A.: Robust Salient Motion Detection with Complex Background for Real-time Video Surveillance. In: IEEE Workshop on Motion and Video Computing, vol. 1, pp. 30–35 (2005)
2. Mahadevan, V., Vasconcelos, N.: Background Subtraction in Highly Dynamic Scenes. In: Proceedings of IEEE Conference on Computer Vision and Pattern Recognition, vol. 1, pp. 1–6 (2008)
3. Chan, A.B., Mahadevan, V.: Generalized Stauffer-Grimson background subtraction for dynamic scenes. Machine Vision and Applications 22, 751–756 (2011)
4. Montabone, S., Soto, A.: Human Detection Using a Mobile Platform and Novel Features Derived From a Visual Saliency Mechanism. Image and Vision Computing 28(3), 391–402 (2010)
5. Hou, X., Zhang, L.: Saliency Detection: A Spectral Residual Approach. In: Proceedings of IEEE Conference on Computer Vision and Pattern Recognition, vol. 1, pp. 1–8 (2007)
6. Toyama, K., Krumm, J., Brumitt, B., Meyers, B.: Wallflower: Principles and Practice of Background Maintenance. In: Proceedings of International Conference on Computer Vision, vol. 1, pp. 255–261 (1999)
7. `http://web.archive.org/web/20020802012150/http://www.darpa.mil/iao/`
8. `https://www.samsung-security.com/en/products/`
   `Samsung_SecurityRobots/Surveillance-Robot/Thermal_Imaging/SGR-3.aspx`
9. Lucas, B.D., Kanade, T.: An Iterative Image Registration Technique with an Application to Stereo Vision. In: Proceedings of Imaging Understanding Workshop, vol. 1, pp. 121–130 (1981)

Layer Image Components Geometry Optimization

Adam Marchewka and Jarosław Zdrojewski

Institute of Telecommunication,
University of Technology and Life Sciences,
Kaliskiego 7, 85-791 Bydgoszcz
{adimar,jaz}@utp.edu.pl

Summary. Digital image representation can significantly limit a geometry of the layer components when converting it from its analog form (GERBER). In this case single pixel representation is fixed to the given gray level or state in the case of black and white format. This process can introduce dimensional deviation of the image components on the level up to 100% of the pixel size. Proposed method has a goal to maintain those limit and reduce it to minimal possible to reach level. Result of experimental research are presented.

1 Introduction

PCB printing process is being redefined. New technology takes new direction and is in general trying to free producers from the need to use films [1, 2, 5, 6]. Digital initial form of the board design can currently be sent directly to a printer and used in one of a few concurrent imaging technologies. Starting from laser direct imaging (LDI), through the units based on digital mirror device (DMD) and ending with the solutions similar to ink jet printers, a wide range of techniques is offered. All of them do eliminate films as a tool with a pattern image and all of them must turn input design into its digital form based on size limited pixels. A very good sample of digitalization can be DMD (Fig. 1). DMD [3] is an array of movable micro-mirror pixels controlled digitally. Each pixel is an electro-mechanical element with two stable mirror states defined by tilt angle of +12 degrees or -12 degrees determined by electric signal. The DMD pixel is basically an opto-mechanical element where mirror tilt determines the direction of deflected light. The positive (+) state, or the so-called the ON state, is tilted toward the illumination. The negative (-) state is tilted away from the illumination and represents OFF state. Figure 1 shows a pixel in the on and off states.

DMD are used in multimedia projectors and light deflection and control devices. One of the aforementioned applications of the DMD is the imaging process. Imaging fidelity has always been a crucial part of the production
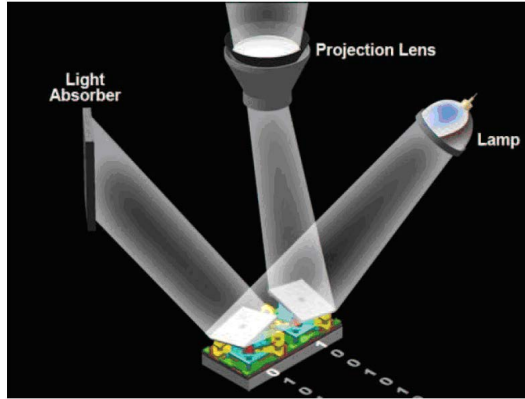
Fig. 1. DMD pixels in On and Off State [3]

process. Exposed pattern geometry in most cases must match panel and drilled holes. In the case of fine lines being exposed, keeping minimal track width and spacing is very important for getting proper results of development and etching process.

2   Motivations

Geometrical error appearing when converting Gerber file into its digital image representation is a fidelity limiting effect, and is strictly related to the change from a vector into its raster representation. Quantity of those limitations is dependent on the imaging device. One of the main parameters which have a significant impact on the conversion error is final resolution of the printer that is usually significantly lower than the one declared PCB designing process. In any case the most critical are the fine lines printed on the board and impact of the mentioned error on their geometry and, in the end, on the electrical conditions when board is ready, filled with components and powered up [4, 7, 8, 9].

3   Error Converting

A track is a key element of the PCB image. In the design stage, the track has a defined geometry which is strictly depending on the function, signals and power of the circuit it will belong to. When printing, the target is for the etched track to match the pattern, and should an error happen at any stage, the goal is to minimize its impact on the resulting board. When looking from the imaging side, the key parameters, which are also very crucial when we consider later exploitation, are as follows: track width - defining together

with copper thickness cross-section and its relation to current density, - and surface area potentially responsible for heat transfer in many applications. In any case of bigger deviations in tracks' geometry, in relation to the designed ones, can lead to improper behavior of the device where such PCB is included. Current limiting, overheating, improper or especially too small line and space distance can be an unwanted exploitation or production-issues-based side effect. Usually tracks are sets of lines with a desired thickness and shape which very often just run horizontally or vertically, and if not, then in any case both of them can well represent considered limitations.

Dimension of single pattern objects usually is significantly bigger than a single pixel and aliasing issue is not present. Picture transferred to the imaging unit is binary, therefore no matter what conversion algorithm is used the last operation will always be thresholding. In most cases, decision to set the pixel value is made on the base of the following test:

$$I_c[x, y] = \begin{cases} 1 & \text{if } \frac{1}{N \cdot N} \sum_{i=1}^{N} \sum_{j=1}^{N} I[x_i, y_j] \geq \tau \\ 0 & \text{for other} \end{cases} \tag{1}$$

where $N \times N$ is the area dimension approximated to one pixel, τ - threshold level.

If single pixel after conversion is represented by $N \times N$ μm area of the pattern image I, then in the case of threshold τ being set at the level above the value representing given analyzed area, then this area based on equation (1) will be included in the background part (in the case of the binary image), no matter how important part of track would disappear. Described case will take place only on the border of an object. This means for every width of the object we can notice three different cases:

- No error $e_N = 0$ only in the case if dimensions of the object are the N value multiplication and its edges match the conversion grid (see Fig. 2a),
- Single edge error $e_N = e_s$ or $e_N = e_e$ when object with a single edge goes beyond conversion grid because of its size being out of converting resolution N limit (see Fig. 2b);
- Double edge error $e_N = e_s + e_e$ - when object goes beyond converting resolution N limit with both edges because of its size and location in relation to conversion grid (see Fig. 2c).

Let thickness of the track be equal $d_c\mu$m and let resolution of the image being converted be $N\mu$m/pixel. During pattern image conversion into the raster we will get d div N directly pointing to the track area and single pixel out of d mod N % result. Resulting track thickness d_c described in pixels can be calculated using the following formula:

$$d_c = d \text{ div } N + \begin{cases} 1 & \text{if } d \text{ mod } N \geq \tau \\ -1 & \text{if } d \text{ mod } N < \tau \end{cases} \tag{2}$$

where: τ - threshold.
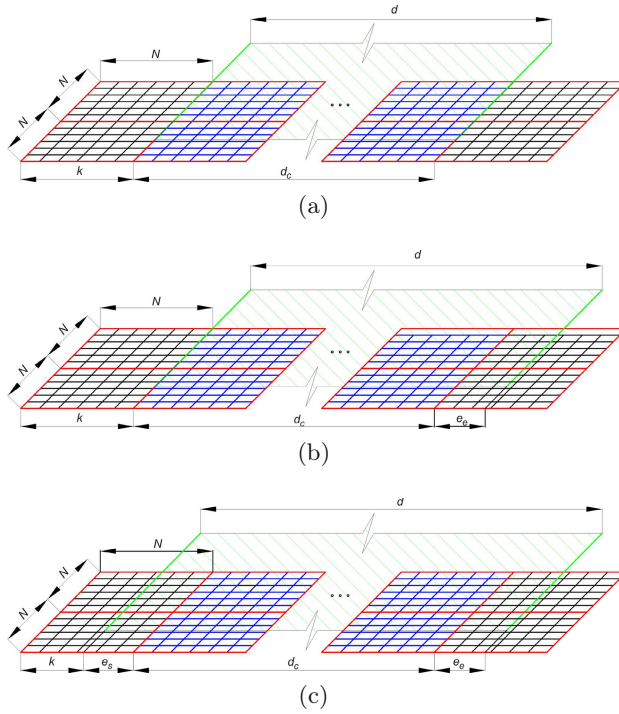
Fig. 2. Track placement errors

At the same time the error e_N will be equal:

$$e_N = d \bmod N \tag{3}$$

We find such error only in the case where the edge of the track starts from the first pixel. If the element is shifted by $k\mu$m in the pattern image, in relation to the edge of the picture, the resulting error will have a different value. In this case value describing the final width of the track will depend on two parameters, k and N, and can be expressed as:

$$d_{k,N} = d_c(k, N) + d_l(k, N) + d_r(k, N) \tag{4}$$

where:

$$d_c(k, N) = (d - N - (k \bmod N)) \operatorname{div} N \tag{5}$$

$$d_l(k, N) = \begin{cases} 1 & \text{for } N - (k \bmod N) \geq \tau \\ 0 & \text{otherwise} \end{cases} \quad \text{for } k \neq N \tag{6}$$

and

$$d_r(k, N) = \begin{cases} 1 & \text{for } (d - (k \bmod N)) \bmod N \geq \tau \\ 0 & \text{otherwise} \end{cases} \tag{7}$$

To get the smallest difference between desired track width d and its corresponding element matching conditions defined by imaging device, it is necessary to find such a k value which gives the function $e_d(k, N)$ the lowest value:

$$e_d(k, N) = |d - d_{k,N}(k, N) \cdot N| \tag{8}$$

where d is representing the width of the track, $d_{k,N}$ - track width in the position k, N - parameters of the imaging device.

The function $e_d(k, N)$ is periodic with a period equal N, and its minimum will appear for the variable $0 + n \cdot N$, where $n \in \{-\infty, \dots, -2, -1, 0, 1, 2, \dots, \infty\}$. It results from the single edge error being produced under those conditions and values range (Fig. 2b).

Probability of the error $e_d(k, N)$ for $d \in \Re$ ocurrence is shown in Fig. 3. Local minimum of the presented function is indicating a point in the image (in relation to its edge), where the edge of the track should be placed to minimize $e_d(k, N)$ error.
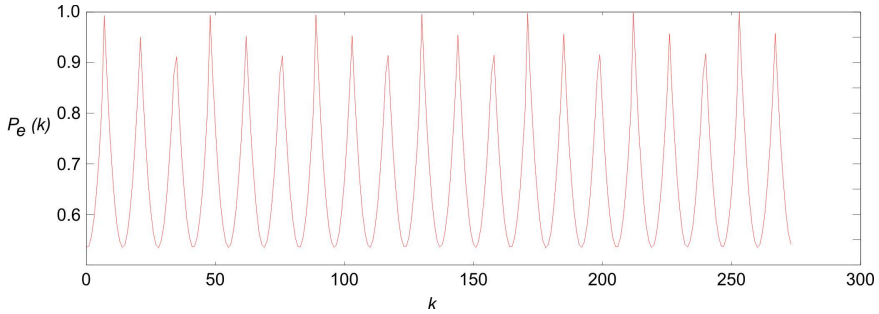
Fig. 3. Probability of the error $e_d(k, N)$ for any track width and $N = 13.67\mu m$

For small values of d such as $d < N$, it is important to remember that minimal value of $e_d(k, N)$ function is pointing to a k offset for which the track will not exist. In this case, the overall consequence is that the conversion will ignore a whole track because of its width being equal to d/N pixel.

4   Experimental Results

During experiments a limitation of the resolution and precision of considerations to 1 μm was assumed. Even in this case it is much more than what imaging system can supply and what current exposing technology expects. In such case pattern image I is an image where the sizes of all elements it contains are defined with 1 μm precision. Because of physical limitations of the exposure machine and imaging device, the vector image has to be converted into its digital representation I_c with a resolution of $N\mu$m per pixel.

Error $e_d(k, N)$ can be minimized already in the design stage by following some rules and placing all tracks in a well defined and limited position. Having assumed 4 different thicknesses of the tracks $d_n \in \{25\mu m, 50\mu m, 75\mu m, 100\mu m\}$, and limiting the resolution of the device to $13.67\mu m$/pixel, it is possible to set all potential points of insert for each particular track. Situation get more complex when board is already designed, transferred into the Gerber format, and our goal is to minimize discrepancies pattern - resulting layer layout. In this case we must determine how the track width can be expected to change especially in relation to its distance from the edge of the image. This kind of analysis must be performed for each width separately (Fig. 4).
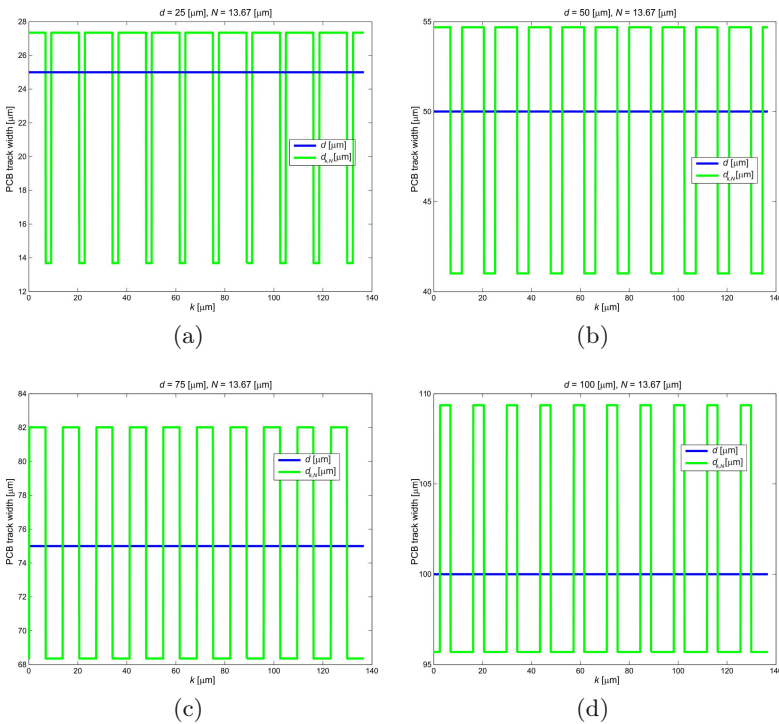
Fig. 4. Track width in relation to its distance from the image border for $N = 13.67\mu m$, $d_n \in \{25\mu m, 50\mu m, 75\mu m, 100\mu m\}$

In this case, the range for $k_{e,d}(N) = \min\{e_d(k, N)\}$ where the error is minimal (Fig. 5a) must be estimated on the basis of calculated error $e_{d_n}(k, N)$, separately for each track width. Knowing ranges of $k_{e,d_n}(N)$ for each width of the track, the point on the image with the most preferred inserting conditions can be calculated. Calculating $E(k, N) = \max\{k_{e,d_n}(N)\}$ we get distance ranges describing track relation to the image edge (excluding track width analysis) and maximal width error can be calculated (Fig. 5b). Applying obtained measure $E(k, N)$ to the overall image of the board, an error

distribution map can be generated. Error distribution map is shown in the Fig. 6.

As mentioned before, conversion error $e_d(k, N)$ must be evaluated separately for each individual film element, especially including all tracks, pads, and vias. For this purpose all mentioned parameters were estimated for the pattern image I, and segmentation for converted image I_c exposure unit parameters was performed (Fig. 7).

(a) (b)
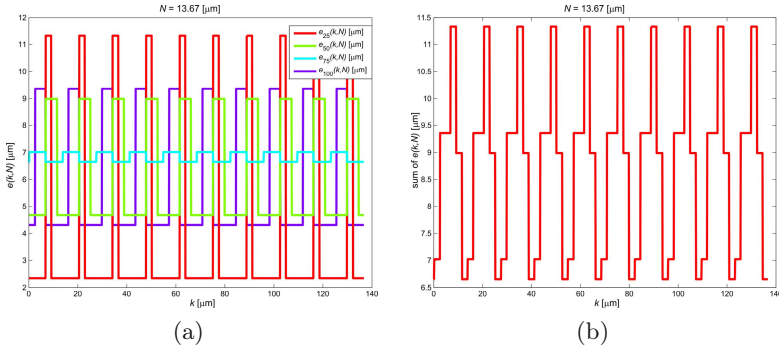
Fig. 5. Geometry error (a) for each track width, (b) total error

(a) (b)
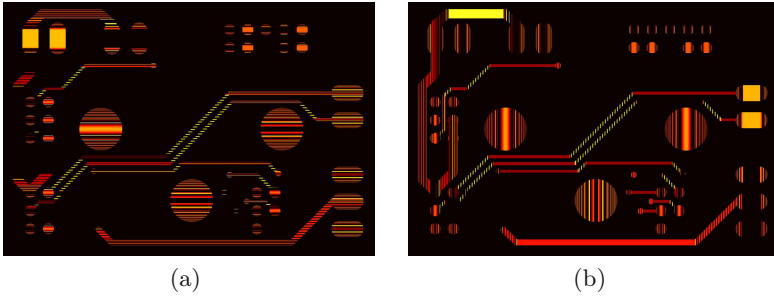
Fig. 6. Error distribution map - brighter image relates to the bigger error
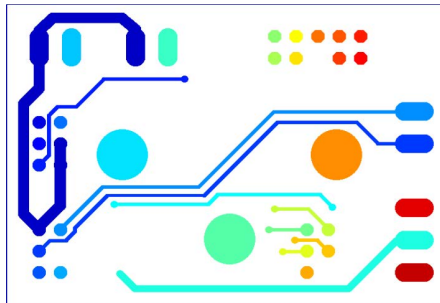
Fig. 7. Matrix containing labels for the connected objects

5   Conclusions

This article presents an approach to analyzing limitations of the Gerber data conversion process into its digital form. Resulting image is used in the exposure machine to lead its transfer to the panels covered with photopolymer. Any geometry error mistake will be copied during the exposure cycle over several or hundreds of panels. To avoid printing without detecting and resolving potential issues with an input data, very strict designing rules are necessary or an automatic sense of conversion errors must be realized. Placement and dimensional errors can be partially compensated and minimized. It is especially important in the case of fine lines on the panel. If line and spaces parameter is close to pixel size on digital mirror device, significant impact on geometry will be observed and finally, on resulting board, electrical power issues are very likely to occur. In this case, also panel development and etching can be limited as well. However, in future work, an analysis of border conditions for detecting and minimizing conversion errors and its limitations will be considered.

References

1. Coombs Jr., C.F.: Printed Circuit Handbook, 6th edn. McGraw-Hill (2007)
2. Holden, H.: Calculate Your Fabrication Capability Coefficient, Happy Thoughts, CircuiTree. BNP, 23.5 (February 15, 2006)
3. Introduction to Digital Micromirror Device (DMD) Technology, Application Report DLPA008-2008, Texas Instruments Incorporated (2008)
4. Marchewka, A., Zdrojewski, J.: Film Alignment Before Solder Mask Exposure. In: Choraś, R.S. (ed.) Image Processing and Communications Challenges 3. AISC, vol. 102, pp. 387–393. Springer, Heidelberg (2011)
5. Marchewka, A., Zdrojewski, J.: Data Matrix in the PCB production. Image Processing & Communications 16(2-3), 31–36 (2011)
6. Marchewka, A., Wocianiec, R., Zdrojewski, J.: PCB Exposure and Data Matrix Based Job Verification. Journal of POLISH CIMAC 7(3), 183–190 (2012)
7. Ohlig, B.: Registration and Knowledge Through and Across Your Panel, CircuiTree (April 1, 2002)
8. Wocianiec, R., Zdrojewski, J.: Film Position Optimization Before Exposure. Image Processing & Communication an International Journal 5(2), 35–46 (2010)
9. Zdrojewski, J., Marchewka, A.: Phototool geometry verification. In: Burduk, R., Jackowski, K., Kurzynski, M., Wozniak, M., Zolnierek, A. (eds.) CORES 2013. AISC, vol. 226, pp. 501–508. Springer, Heidelberg (2013)

A Hybrid Image Compression Technique Using Neural Network and Vector Quantization With DCT

Mohamed El Zorkany

Electronics Department,
National Telecommunication Institute (NTI), Cairo, Egypt
`M_zorkany@nti.sci.eg`

Summary. Image and video transmissions require particularly large bandwidth and storage space. Image compression technology is therefore essential to overcome these problems. Practically efficient compression systems based on hybrid coding which combines the advantages of different methods of image coding have also being developed over the years. In this paper, different hybrid approaches to image compression are discussed. Hybrid coding of images, in this research, deals with combining three approaches to enhance the individual methods and achieve better quality reconstructed images with higher compression ratio. In this paper A new Hybrid neural-network, vector quantization and discrete cosine transform compression method is presented. This scheme combines the high compression ratio of Neural network (NN) and Vector Quantization (VQ) with the good energy-compaction property of Discrete Cosine Transform (DCT). In order to increase the compression ratio while preserving decent reconstructed image quality, Image is compressed using Neural Network, then take the hidden layer outputs as input to re-compress it using vector quantization (VQ), while DCT was used the code books block. Simulation results show the effectiveness of the proposed method. The performance of this method is compared with the available jpeg compression technique over a large number of images, showing good performance.

1 Introduction

Day by day the use of multimedia, images and videos are rapidly increasing in a variety application. Type of technique that is used to store in multimedia data is an important although storage is bigger than ever, however it is not enough. Hence, the data compression particularly the image compression plays a vital role. Image compression is a technique for image data rate reduction to save storage space. In other words, the purpose of image compression is to reduce the amount of data and to achieve low bit rate digital representation without perceived loss of image quality. Since it was an area

of interest of many researchers, many techniques have been introduced. In the literature different approaches of image compression have been developed. Most image compression techniques are based on either statistical approaches or applied transforms such as DCT and wavelet transform. JPEG standard is based on DCT while JPEG2000 standard is based on wavelet transform [1, 2]. Most image compression methods divide image into number of non overlapping pixel blocks, and fed as patterns for network training. Image compression is achieved by encoding the pixel blocks into the trained weight set, which is transmitted to the receiving side for reconstruction of the image. But in such cases limited amount of compression is achieved since it exploited only the correlation between pixel within each of the training patterns [3].

There are also two well-known major approaches to implement image compression: Neural Network (NN), Vector Quantization (VQ) technique. A Neural Network is a powerful data modelling tool that is able to capture and represent complex input/output relationships. It can perform "intelligent" tasks similar to those performed by the human brain. Neural Networks seem to be well suited to image compression due to their massively parallel, noise suppression, learning capabilities and distributed architecture. NNs have the ability to pre-process input patterns to produce simpler patterns with fewer components. This compressed information preserves the full information obtained from the external environment. Neural Networks based techniques provide sufficient compression rates of the data fed to them, also security is easily maintained. Many different training algorithms have been used as back-propagation algorithm [4, 5].

Another well-known image compression method is vector quantization. VQ is a classical quantization technique from signal processing which allows the modeling of probability density functions by the distribution of prototype vectors. It was originally used for data compression. It works by dividing a large set of points (vectors) into groups having approximately the same number of points closest to them. Each group is represented by its centroid point, as in k-means and some other clustering algorithms. Vector quantization is used for lossy data compression, lossy data correction, pattern recognition and density estimation [6, 7].

Discrete Cosine Transform (DCT) is another well-known image compression method, in this method compression is accomplished by applying a linear transform to de-correlate the image data (source encoder), quantizing the resulting transform coefficients (quantizer), and entropy coding the quantized values (entropy encoder) [8, 9]. This paper proposes a new image compression scheme based on Combined NN and VQ with DCT to take advantages of them.

This paper is organized as follows. A brief review of NN and VQ scheme is presented in Section 2. DCT scheme is illustrated in Section 3. The proposed hybrid scheme for image compression is presented in Section 4. Simulation results and discussions are given in Section 5 and finally conclusions are drawn in Section 6.

2   Neural Network Structure

Neural Network models are specified by network topology and learning algorithms. Network topology describes the way in which the neurons (basic processing unit) are interconnected and the way in which they receive input and output. Learning algorithms specify an initial set of weights and indicate how to adapt them during learning in order to improve network performance. A Neural Network can be defined as a "massively parallel distributed processor that has a natural propensity for storing experiential knowledge and making it available for use". A number of simple computational units, called neurons are interconnected to form a network, which perform complex computational tasks. There are many different types from NNs, the most common type is MLP which employed for image compression.

For basic image compression using NN, the Neural Network structure can be illustrated in Fig. 1. Three layers, one input layer, one output layer and one hidden layer, are designed. Both input layer and output layer are fully connected to the hidden layer. Compression is achieved by designing the value of K, the number of neurones at the hidden layer, less than that of neurones at both input and output layers [10]. The input image is split up into blocks or vectors of 8×8, 4×4 or 16×16 pixels. When the input vector is referred to as N-dimensional which is equal to the number of pixels included in each block, all the coupling weights connected to each neurone at the hidden layer can be represented by $\{w_{ji}, j = 1, 2, ...K$ and $i = 1, 2, ...N\}$, which can also be described by a matrix of $K \times N$. From the hidden layer to the output layer, the connections can be represented by another weight matrix of $N \times K$.

Fig. 1. Basic structure of NN for image compression

Image compression is achieved by training the network in such a way that the coupling weights, $\{w_{ji}\}$, scale the input vector of N-dimension into a narrow channel of K-dimension ($K < N$) at the hidden layer and produce the optimum output value which makes the quadratic error between input and output minimum. In accordance with the Neural Network structure, the operation can be described as follows:

$$y_i^m = 1/\left(1 + e^{\lambda net_i}\right) \ \text{and} \ net_i = W_i^T X \tag{1}$$

Where $\lambda \ \varepsilon \ [0,1]$ is a weighting factor and W_i^T is the ith weight that links the ith neuron in layer m with its input X. Back propagation (BP) algorithm is employed to optimize the parameters of the network. Its goal is to reduce the mean square error (MSE),which can be expressed as:

$$\varepsilon = \frac{1}{2N_p} \sum_{p=1}^{N_p} \sum_{i=1}^{N_M} (d_i(p) - y_i^M(p))^2 \tag{2}$$

Where N_p is the number of input patterns considered, NM is the number of neurons in the output layer, and $d_i(p)$ and $y_i^M(p)$ are the desired and actual outputs of the ith neuron i of the output layer for the input pattern p, respectively.

For basic image compression using NN, the Neural Network structure can be illustrated in Fig. 1. Three layers, one input layer, one output layer and one hidden layer, are designed. Both input layer and output layer are fully connected to the hidden layer. Compression is achieved by designing the value of K, the number of neurones at the hidden layer, less than that of neurones at both input and output layers [10]. The input image is split up into blocks or vectors of 8×8, 4×4 or 16×16 pixels. When the input vector is referred to as N-dimensional which is equal to the number of pixels included in each block, all the coupling weights connected to each neurone at the hidden layer can be represented by $\{w_{ji}, j = 1, 2, ...K \ \text{and} \ i = 1, 2, ...N\}$, which can also be described by a matrix of $K \times N$. From the hidden layer to the output layer, the connections can be represented by another weight matrix of $N \times K$.

Image compression is achieved by training the network in such a way that the coupling weights, $\{w_{ji}\}$, scale the input vector of N-dimension into a narrow channel of K-dimension $(K < N)$ at the hidden layer and produce the optimum output value which makes the quadratic error between input and output minimum. In accordance with the Neural Network structure, the operation can be described as follows:

$$h_j = \sum_{i=1}^{N} w_{ji} \cdot x_i \ 1 \le j \le K \tag{3}$$

for encoding and

$$x_i = \sum_{j=1}^{k} w_{ji} \cdot h_j \ 1 \le i \le N \tag{4}$$

for decoding. where $x_i \in [0, 1]$ denotes the normalized pixel values for grey scale images with grey levels $[0, 255]$. The reason of using normalized pixel values is due to the fact that Neural Networks can operate more efficiently when both their inputs and outputs are limited to a range of $[0, 1]$.

3 Vector Quantization (VQ)

Vector quantization (VQ) is a lossy data compression method based on the principle of block coding. It is a fixed-to-fixed length algorithm. VQ compression is highly asymmetric in processing time: choosing an optimal codebook takes huge amounts of calculations, but decompression is lightning-fast-only one table lookup per vector. This makes VQ an excellent choice for data which once created will never change.

The principle of the VQ techniques is simple. A vector quantizer is composed of two operations encoder and decoder. The encoder takes an input vector and outputs the index of the codeword that offers the lowest distortion. In this case the lowest distortion is found by evaluating the Euclidean distance between the input vector and each codeword in the codebook. Once the closest codeword is found, the index of that codeword is sent through a channel (the channel could be computer storage, communications channel, and so on). When the encoder receives the index of the codeword, it replaces the index with the associated codeword. Fig. 2 shows a block diagram of the operation of VQ.

VQ coding procedure often needs several epochs of clustering to obtain a codebook; K-means is one of the simplest unsupervised learning algorithms that solve the well known clustering problem. K-means clustering generate codebooks from k-means models, and quantizing vectors by comparing them with centroids in a codebook.
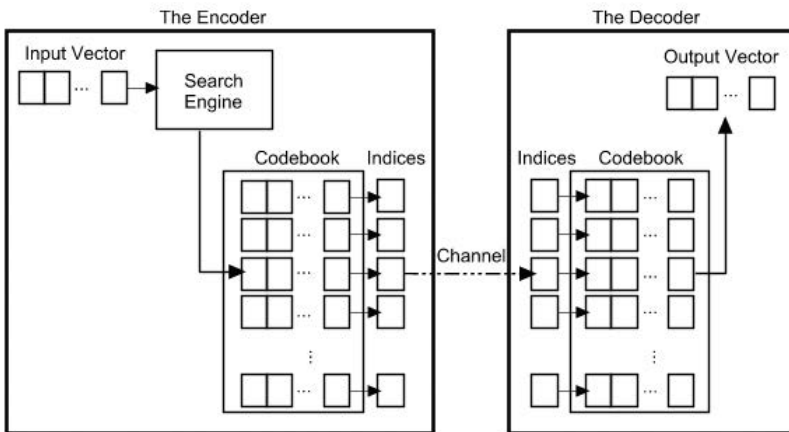
Fig. 2. Basic structure of vector quantization

4   Discrete Cosine Transform (DCT)

Transform coding became popular mainly due to the introduction of the Discrete Cosine transform-an efficient transform with high computational efficiency and compression performance. This fact has made the DCT favorable for still image and video coding.

The widest used commercial product that is used for the still image coding scheme is the JPEG baseline system, which has the advantage of simple computation, but suffers from blocking artifacts due to course quantization of coefficients at high compression ratios.

DCT is widely used for image compression because it provides a good energy-compaction property. DCT is actually a cut-down version of the fast Fourier transform (FFT) where only the real part of FFT is used. The DCT transformation generally results in the signal energy being distributed among a small set of transformed coefficients only. Given an image consisting of the N×N pixels $f(x, y)$, its two-dimensional DCT produces the $N \times N$ array of numbers $F(i, j)$ given by

$$F(i,j) = \sum_{x=0}^{N-1} \sum_{y=0}^{N-1} 4f(x,y) \cos\left(\frac{(2x+1)i\pi}{2N}\right) \cos\left(\frac{(2y+1)j\pi}{2N}\right) \qquad (5)$$

where $0 \leq i, j \leq N - 1$.

5   The Proposed Scheme

This paper proposes a new image compression scheme based on Combined NN and VQ with DCT to take advantages of them. In order to increase the compression ratio while preserving decent reconstructed image quality, Image is compressed using NN as a first stage of compression. Next, the output of first stage (compressed image) coded using vector quantization (VQ), then the codebooks are transformed from spatial domain to frequency domain using DCT. So in the proposed technique first image is compressed using NN as a first compression stage then VQ technique used to create codebooks by K-means clustering technique, then DCT compression technique is used to compress codebooks. Two different approaches were used to merge the DCT with VQ compression technique. First approach aggregates all codebooks in one big block and applies DCT on this block. The second approach applies DCT on each codebook alone. Fig. 3 shows the general block diagram of the proposed scheme where I can divide the proposed scheme into three stages: NN stage, VQ stage and DCT stage.

First Stage

in the proposed method, image is compressed using NN as a first stage of compression. For our purpose three layers feed forward Neural Network had
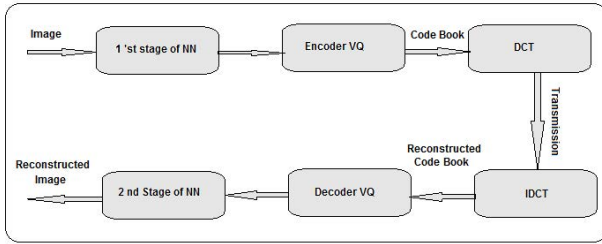
Fig. 3. Block diagram of the proposed scheme

been used. Input layer with 64 neurons, hidden layer with 16 neurons, and output layer with 64 neurons. Back propagation algorithms had been employed for the training processes. To do the training input prototypes and target values are necessary to be introduced to the network so that the suitable behaviour of the network could be learned. The idea behind supplying target values is that this will enable us to calculate the difference between the output and target values and then recognize the performance function which is the criteria of our training. For training the network, the 256×256 pixels "Standard" test images (a set of images found frequently in the literature: Lena, peppers, cameraman, lake, etc., all in uncompressed and of the same size) had been employed.

Also for scaling purposes, each pixel value should be divided by 255 to obtain numbers between 0 and 1. In image compression technique using NN, the compression is achieved by training a Neural Network with the image and then using the weights and the coefficients from the hidden layer as the data to recreate the image.

The following steps summarize the first stage of proposed scheme:

- Divide the original image into 8×8 pixel blocks and reshape each one into 64×1 column vector.
- Arrange the column vectors into a matrix of 64×1024.
- Let the target matrix equal to the matrix in step 2.
- Choose a suitable learning algorithm, and parameters to start training.
- Simulate the network with the input matrix and the target matrix.
- Obtain the output matrices of the hidden layer and the output layer.
- Post-process them (using VQ and DCT as will show in the following stages) to obtain the compressed image, and the reconstructed image respectively.

Second Stage

In the second stage of our proposed method depend on compress the compressed image which yield from first stage using VQ as in the following steps:

- The Neural Network image is splitted into square blocks of $T \times T$ pixels, for example 4×4 or 8×8; each block is considered as a vector in a 16- or 64-dimensional space, respectively to create code vectors.
- Optimize the number of required codebooks, according to the required compression ratio and quality of reconstructed image.
- Apply clustering technique to create codebooks. K-means clustering is used in our method.

Third Stage

After generating codebooks from second stage using VQ, the codebooks are then compressed using DCT. Two different approaches were studied for DCT code books compression.

1-Integrated Code Books

In this approach, I take all codebooks from first stage which generated using VQ and re-aggregate it to generate one big block, and then apply DCT on this big block as follows:

Apply DCT to a sequence of values of big codebook to construct new book X. Then, Drop a portion of high-order values from X to create X'. To drop a portion of this value, I rearrange the DCT coefficients beginning with the DC coefficient. This results in a column vector. Since the image information (energy) is usually concentrated in the low frequency region. The code books can be decreased by discarding some coefficients which represent high frequency. This is equivalent to a low pass filtering of the image. The cut off frequency of the filter affects on the compression ratio and reconstructed image quality. The code word index in the compressed code book is then transmitted.

2-Discrete Code Books Compression Approach

In this approach DCT is applied on each codebook separated, using the same technique in first approach. finally, applied any lossless line coding technique pefore transmit image as Huffman code or Run length encoding (RLE) which increase compression ratio about 1.5 to 2.

Decompress (Compressed-Image)

For decompression or decoding the compressed image:

- Read the compressed image.
- Decode RLE or Huffman coding data.

- Compute two dimension Inverse Fourier transform (2D IFFT) for this image to convert encode the results using inverse VQ to generate compressed image which represents output of hidden layer of NN.
- Result image is encoded using NN as the second part of NN.

The overall compression ratio equations of proposed technique are:

$$Compression\ ratio\ =\ compression\ using\ \text{NN}\ \times (original\ image\ size)/ \atop /(new\ codebooks\ size\ +\ no.\ of\ indexes) \tag{6}$$

$$New\ codebooks\ size = (codebooks\ size\ from\ \text{ VQ}) \times \atop \times (compression\ percentage\ from\ \text{ DCT}) \tag{7}$$

$$Codebooks\ size = (number\ of\ codebooks) \times (size\ of\ each\ codebook) \tag{8}$$

6 Simulation Results

Mean Square Error (MSE) measure and peak signal-to-noise ratio ($PSNR$) are used to determine the reconstructed image quality. MSE is using the following equation:

$$MSE = \frac{1}{N \cdot M} \sum_{x=0}^{N-1} \sum_{y=0}^{M-1} [f'(x,y) - f(x,y)]^2 \tag{9}$$

Where $f(x,y)$ and $f(x,y)$ represent the original and the reconstructed images, respectively; M and N represent the image size. And the peak signal-to-noise ratio ($PSNR$) in dB is calculated using the following equation:

$$PSNR = 10 \times \log_{10} \frac{255^2}{MSE} dB, \tag{10}$$

The size of the compressed image (SOCI) and the Compression Ratio (CR) are calculated as in equations (6) to (8).

The proposed scheme was tested by different standard test images, Lena, Pepper, cameraman, gray and color images with different sizes. Also I have tested text, medical, compressed and color images. It is obvious from PSNR results that, proposed technique works quite well for different types of images, and the images would be decompressed quite perfect.

For gray image, Fig. 4a shows the original Lena image with size [256×256] and Fig. 4b shows the reconstructed image after decompressed the image with compression ratio equal 8 and PSNR equal 38 dB and Fig. 4c compression ratio equal 32 and PSNR still more than 32 dB. Table 1 presents results of testing the new image compression procedure of standard Lena image at different compression ratios. From Table 1 it is evident that high compression ratio can be achieved in our scheme which reaches to 64 with PSNR near to 30 dB.

Table 1. Compression ratio of Lena image

Compression Ratio	PSNR in dB
8	36.40
16	36.00
32	34.50
48	32.20
64	30.00
96	29.60
128	27.50

(a) Original Lena image (b) Compressed image (CR=8 & PSNR=36.4 dB) (c) Compressed image (CR=64 & PSNR=30 dB)

Fig. 4. Gray Image Compression using proposed method

For color images, Fig. 5a shows the original pepper image with size $[256 \times 256 \times 3]$ and Fig. 5b shows the reconstructed image after decompressed the image with compression ratio equal 32 and PSNR still more than 30 dB. Comparing the performance of the proposed scheme with the result of standard JPEG compression for Lena image in Table 2 and Fig. 6, the compression ratio and PSNR obtained using proposed scheme is better than results of JPEG.

Table 2. Comparing the obtained results with JPEG For Lena image

CR	PSNR for proposed scheme	PSNR In JPEG
8	36.4	35.88
16	36	33.81
24	34.5	31.84
32	32.2	29.56
64	30	24.11

(a) Original color image (b) Compressed image (CR=32)
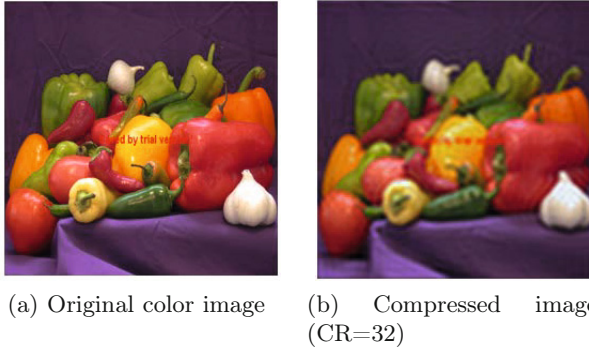
Fig. 5. Color Image Compression using proposed method
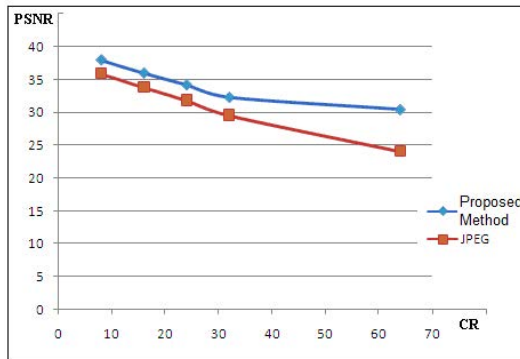
Fig. 6. Comparing the obtained results with JPEG

7 Conclusion

This paper has proposed a new scheme for image coding at very low bit rate. This scheme is a hybrid method that combines the high compression ratio of Neural network (NN) and Vector Quantization (VQ) with the good energy-compaction property of Discrete Cosine Transform (DCT). A Combined NN and VQ with DCT are utilized to take advantages provided by both of them. In order to increase the compression ratio while preserving decent reconstructed image quality, Image is compressed using NN, then take the hidden layer outputs as input to re-compress it using vector quantization (VQ), while DCT was used the code books block. The main aim of the proposed scheme is to achieve high compression ratio without much compromise in the image quality. I have compared the performance of the proposed scheme with image compression using traditional methods as JPEG, NN and some other schemes which depend on VQ and DCT. I have presented results

showing that the proposed method produce better compression ratio than these schemes. Moreover, I have presented results showing that the proposed algorithm produces better image quality than the JPEG.

References

1. Fiorucci, F., Baruffa, G., Frescura, F.: Objective and subjective quality assessment between JPEG XR with overlap and JPEG 2000. Journal of Visual Communication and Image Representation 23(6), 835–844 (2012)
2. Au, K.M., Law, N.F., Siu, W.C.: Unified feature analysis in JPEG and JPEG 2000-compressed domains. Journal of Pattern Recognition 40, 2049–2062 (2007)
3. Li, Drew: Fundamentals of Multimedia. In: Image Compression Standards, ch. 9. Prentice Hall (2003)
4. Jiang, J.: Image compression with neural networks - A survey. Signal Processing: Image Communication 14(9), 737–760 (1999)
5. Dokur, Z.: A unified framework for image compression and segmentation by using an incremental neural network. Expert Systems with Applications 34(1), 611–619 (2008)
6. Sasazaki, K., Saga, S., Maeda, J., Suzuki, Y.: Vector quantization of images with variable block size. Applied Soft Computing 8, 634–645 (2008)
7. Esakkirajan, S., Veerakumar, T., Murugan, V.S., Navaneethan, P.: Image Compression Using Hybrid Vector Quantization. International Journal of Signal Processing 4 (2008)
8. Tseng, H., Chang, C.: A Very Low Bit Rate Image Compressor Using Transformed Classified Vector Quantization. Informatica 29, 335–341 (2005)
9. Robinson, J., Kecman, V.: Combining Support Vector Machine Learning With the Discrete Cosine Transform in Image Compression. IEEE Transactions on Neural Network 14(4) (2003)
10. Jiang, J.: Image compression with neural networks - A survey. Signal Processing: Image Communication 14(9), 737–760 (1999)

Gabor Wavelet Recognition Approach for Off-Line Handwritten Arabic Using Explicit Segmentation

Moftah Elzobi[1], Ayoub Al-Hamadi[1], Zaher Al Aghbari[2],
Laslo Dings[1], and Anwar Saeed[1]

[1] Institute for Information Technology and Communications (IIKT),
Magdeburg, Germany
`{Moftah.Elzobi,Ayoub.Al-Hamadi}@ovgu.de`
[2] Computer Science Department, University of Sharjah, UAE
`zaher@sharjah.ac.ae`

Summary. This article proposes an un-constrained recognition approach for the handwritten Arabic script. The approach starts by explicitly segment each word image into its constituent letters, then a filter-bank of Gabor wavelet transform is used to extract feature vectors corresponding to different scales and orientation in the segmented image. Classification is carried out by employing a support vectors machine algorithm, where IESK-arDB and IFN/ENIT databases are used for testing and evaluation of the proposed approach respectively. A Leave-one-out estimation strategy is followed to assess performance, where results confirmed the approach efficiency.

1 Introduction

Given the importance of Arabic script, first, as the writing medium of many languages (e.g., Arabic, Farsi, Urdu, and etc.), and second, as being the script used in a huge amount of historical documents that cover the history of many nowadays countries throughout Middle East, North Africa, Central Asia, and Balkan over several centuries. Many research papers and articles have been appeared, suggesting various solutions for the problem of Arabic handwriting recognition over the past three decades, yet with minor advances.

Literature addressing the problem of handwriting recognition can be classified into two broad categories: (**i**) Segmentation-based recognition; this category includes all approaches that perform segmentation (into letters or primitives) prior to recognition. Advantage of such approaches is, their capability to cope with the high variability nature of the problem; the disadvantage however is the complexity and the error-prone characteristics of the segmentation process. One of the earliest segmentation-based approach, suggested for the recognition of Arabic handwritten text, is the one proposed by Almullim and Yamaguchi [4]. In this approach, words are

over-segmented into their basic strokes, where a stroke is the curve between any two structure points (End points or Branch points). Each stroke is then classified to one of five groups according to its shape. Two of these groups contain what is called secondary strokes, and the other three contains primary strokes. Furthermore, a set of heuristics proposed to assign secondaries to their primary strokes, in a try to construct the corresponding character. A recognition rate of 81.25% is reported. In [6], Bushofa and Spann propose a segmentation-based recognition methodology for off-line printed Arabic text. The segmentation algorithm stars by locating the text baseline. Having the baseline discovered, a fixed size window is used along the baseline to search for specific types of angles that are expected to be formed when letters joined together. Multiple heuristics rules are used to confirm the segmentation results. Finally, features are extracted and a decision tree based classifier is used for recognition, achieving 94.17% as a success rate. Abuhaiba et al. [1] presented a recognition system for off-line Arabic handwritten text. The system is segmentation-based one, thinned and smoothed images of the strokes (sub-word) are processed and converted into 1-D representations called direct straight-line approximation. The representation is processed further to produce a loop less graph called the reduced graph where loops replaced by vertices. Ultimately, the reduced graph representative is segmented into tokens that are fed to a fuzzy sequential machine for recognition. As a sub-word (no segmentation) recognizer, the proposed system achieved 55.4% recognition rate; when segmentation involved the recognition rate degraded to 51.1%. In [16], Xiu et al. proposed probabilistic segmentation-based recognition model, in which a tentative contour-based over-segmentation is first performed on the text image. As a result, a set of what they called graphemes is produced. The approach differentiates among three types of graphemes. The confidence of each character is calculated according to the probabilistic model, respecting other factors e.g., recognition output, geometric confidence and logical constraint. The authors experimented the proposed methodology on five different test sets, achieving 59.2% success rate.

(**ii**) Segmentation-free recognition, as its name implies, includes all approaches that are treating each word image as single entity upon which features is extracted. Even though such approaches proof successfulness in some application areas, they are completely Lexicon dependent and are incapable to serve in an unconstrained environment [12] [13]. One of the earliest works that is followed a holistic approach for the recognition of type-written and printed Arabic words is the approach proposed by Al-Bader and Haralick [2]. In their approach, they first start by detecting what they called "shape primitives", then matching the regions containing the shape primitives against a set of pre-defined symbol models. A spatial arrangement of the best fitted symbol models is regarded as a description of the recognized word. The system is experimented with various types of samples; a rate of 73% is achieved

on scanned words. Pechwitz and Maergner in [14], addressed the problem of handwritten Arabic words. They proposed a holistic HMM-based approach, which starts by normalizing word images and then extracting features using a sliding window approach. Ultimately, features are passed to a semi-continuous 1-D HMM for recognition. The system performance is tested on IFN/ENIT database, achieving a maximal recognition rate of 89%. Al-Hajj et al. in [3], proposed an approach for the recognition of handwritten Arabic city names. Two different types of features have been extracted, namely baseline-independent and baseline-dependent using a sliding window approach. For recognition, a right-left HMM classifier is developed, and experiments are conducted on IFN/ENIT database with recognition rates ranged from 85.45% to 87.20%.

The fact that, a Gabor function has the ability to imitate the functionality of simple kinds of cells in the human visual system, motivated its application in many image processing fields[11]. Several works proposing various Gabor-filter-based solutions for the problem of Latin, Chinese, and Numeral handwriting [11],[8]. In case of Arabic handwriting, Haboubi et. al.[10], conduct a comparative study on different kinds of features, e.g. structural, statistical, Gabor-filter-based, and pixel-based. With no detailed explanations, the Gabor-filter based features show the Worst-Case-Performance compared to the rest. In the contrary to [10], Chen et. al. [8], reported very good results, when they used Gabor-Filter based features to recognize Arabic PAWs. They tested their approach on the AMA-Arabic-Dataset, reporting 82.7% as recognition rate. Since the set of Arabic PAWs is a very huge one, putting such approach in service is unlikely.

In this work, we propose a segmentation-based, Gabor-filter-based approach for the recognition of the Arabic handwriting. Unlike [8], we include the segmentation as an integral part, since we believe it is an intuitively prerequisite operation to reduce the infinite domain of possible words and/or PAWs into a limited number of classes that can be accommodated and processed.

2   Methodology

2.1   Segmentation

Segmentation begins with pre-processing step, where morphological based procedures like closing, opening and reconstruction are, firstly performed on word images to tackle artifacts introduced during extraction and binarization processes. And in order to correct for the skew, a combination of Local Minima Regression (LMR) and Hough Transform (HT) is used. LMR is employed to reduce the search domain of HT parameters, resulting in efficient and accurate estimation of skew angle. To facilitate the process of letter segmentation further, PAWs overlap should be first resolved. We first identified the
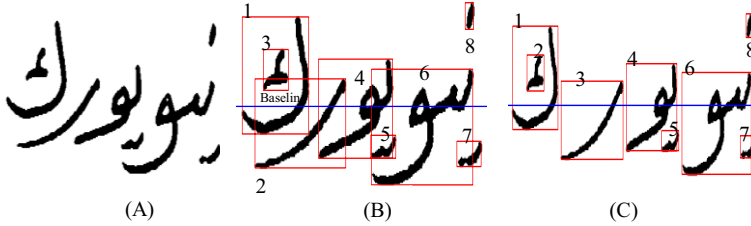
Fig. 1. PAWs' overlap resolving: (A) Original word image. (B) Word image with the Main CCs overlapping. (C) The Main CCs overlapping resolved.

word baseline. Along the baseline, we differentiate between two kinds of connected-components (CC). Namely, Main CCs (mostly are PAWs), which are all CCs that intersect the baseline and Auxiliary CCs (mostly are diacritics) that are not. To resolve the Main CCs overlapping, and to relate Auxiliary CCs to their correspondence Main CCs, we formulated a set of heuristics over the four corner coordinates of the connected component bounding-box. Fig.1, shows an example of PAWs overlap resolving. To segment the word image into letters representatives, we first extract a thinned version from the PAWs overlapping-free word images. Thinning is necessary operation in order to reduce the computation cost and also to ease the process of extracting features points (FP) (e.g. End-pont, Branch-point, ánd Loop-point), that we employ for segmentation. Our approach is inspired by the approach presented in [5], but instead of using only the set of contour local minima as a candidate for segmentation points (SP), we included in SP all one-pixel columns as candidates, since we observed that local minima occur very often inside many of the letters (ب, س, ص, ف, ك, ل, ن, ي) and etc.). Then a heuristic based election operation is performed, to exclude from SP unlikely candidates, as follow: (**i**) exclude from SP all candidates that are containing any FP, respecting the fact that any column contains FP, cannot be a SP in the same time; (**ii**) starting from the most right, whenever encountering two direct neighboring candidates, exclude the one on the right. To handle over-segmentation (SP inside a letter), we further apply three other heuristic as follow: (**a**) if there are two consecutive SP candidates and no FP in between, delete the one on the right; (**b**) if the direct neighboring on the left, a column contains pixels of a diacritic(Dots and Hamza -pixels), then delete the candidate from SP; (**c**) if a column containing Branch-point or Loop point pixel encountered before reaching another SP candidate then confirm the candidate as SP. Finally we insert SP candidates before and after every Main CC. Fig.2, shows samples taken from IESK-arDB as well as IFN/ENIT database [9] [15], segmented according to the aforementioned approach.

Binary	Thinned	Segmented	Binary	Thinned	Segmented
مؤقت		مؤ قت	ت طاوبنا 7 نوفمبر	طاوبنا 7 لوفس	تطاوبنا 7 نوفمبر
الليلة		الليلة	هثليـن	هلسـر	هثليـن
انتحارى		انتحارى	القصو ر	القصوا ر	القصو ر
الإنرنت		الإنرنت	ثبلا ط	ثبلا ط	ثبلا ط
صن		من	الصنزة	الصسـر	الصنـزة
	(A)			(B)	

Fig. 2. Results of the segmentation: (A) Samples taken from IESK-arDB. (B) samples taken from IFN/ENIT.

2.2 Features Extraction

As a result of segmentation, we get multiple images of letters constituting the word image. Before feature extraction taking place, images should be normalized into a fixed dimensionality to reduce the within-class variation of shape. While preserving the aspect ratio, we normalized letter images into a square of size 64×64, and then extracting Gabor-filter-based features.

Gabor Filter Based Features

Motivated by its similarities to the functionality of certain cells in the human primary visual cortex and its spatial frequency localization property, Gabor filter used extensively in the field of image processing (e.g, Face recognition, Segmentation, Edge detection, OCR, and image compression)[8]. In 2D, Gabor filter (as illustrated in Figure 3), is the result of a Gaussian kernel function (envelope) modulated by a complex plane sinusoidal function of frequency and orientation (carrier). It is defined in the spacial plane as follows:

$$g(x, y; \lambda, \theta, \sigma_x, \sigma_y) = \exp\left\{-\frac{1}{2}\left(\frac{\acute{x}^2}{\sigma_x^2} + \frac{\acute{y}^2}{\sigma_y^2}\right)\right\} \times \exp\left\{i(2\pi\frac{\acute{x}}{\lambda})\right\} \qquad (1)$$

where λ is the frequency (in pixel) and θ is the orientation of the sinusoidal function. σ_x and σ_y are the standard deviations along the x- and y-axis, and $\acute{x} = x\cos\theta + y\sin\theta$, $\acute{y} = -x\sin\theta + y\cos\theta$.

Intuitively, the real and/or the imaginary components of the filter can be derived from Eq. 1, and can be used instead. In our case, for feature's extraction, we convolve the normalized segmented letter images with a bank of Gabor kernels, generated by choosing different values for θ, namely $(0, \frac{\pi}{4}, \frac{\pi}{2}, \frac{3\pi}{4})$ and for λ 3 pixels and 5 pixels. The choose of λ values is inspired by a study conducted in[11]. Additionally, It is observed that σ_x and σ_y parameters are actually a function of λ, thus we calculate them both as $= 0.5\lambda$, which is empirically proven to be the optimal. The various Gabor kernels are later used
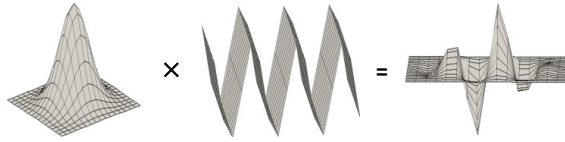
Fig. 3. Gabor filter: The result of sinusoidal plane modulated by a Gaussian Kernel

to generate eight different Gabor representations of the letter image, corresponding to the different orientation and frequency. Subsequently, we divide the 64×64 representation into 8×8 feature regions, resulting in 64 regions. From each, we extract one value as an element in 512 feature vector (8×64). Figure 4, illustrate the process. Before passing the features into a machine learning algorithm, the feature vector $\mathbf{f} = (f_1, f_2, \ldots, f_{512})$ is normalized to be $\tilde{\mathbf{f}} = (\tilde{f}_1, \tilde{f}_2, \ldots, \tilde{f}_{512})$ as follows.

$$\tilde{f}_i = \frac{f_i - \mu_i}{4\sigma_i} + 0.5, \qquad i = 1, ..., 512. \tag{2}$$

Where μ_i and σ_i are mean and standard deviation of the ith feature across the training data, respectively.
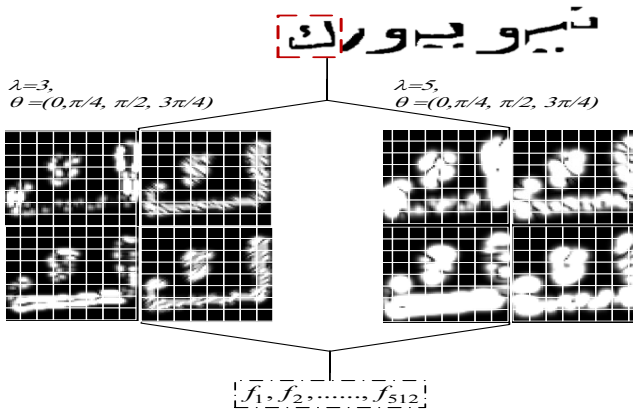
Fig. 4. Gabor filter: The result of sinusoidal plane modulated by a Gaussian Kernel

2.3 SVM Classification

We formulated the handwriting recognition problem as a supervised multi-class learning process, in which a class is created for each letter in each form. Due to its capability, to avoid the over-fitting problem, the local minima

problem, and the un-correlation between its computation complexity and the dimensionality of input vector, we choose support vector machines based classifier.

$$f(\mathbf{x}) = \text{sign}(\mathbf{w} \cdot \mathbf{x} + b),$$

Recalling that a hyperplane can be written as any set of $\mathbf{x}$, satisfying $\mathbf{w} \cdot \mathbf{x} - b = 0$, where $\mathbf{w}$ is a weight vector, normal to the hyperplane, and b is the offset separating the hyperplane from the origin of the space. Any two vectors $\mathbf{x}_1$, $\mathbf{x}_2$, satisfying $\mathbf{w} \cdot \mathbf{x}_1 - b = 1$, $\mathbf{w} \cdot \mathbf{x}_2 - b = -1$ respectively, are called support vectors, and the formed hyperplanes are called the standard hyperplanes, the distance separating them is found to be $\frac{2}{\|\mathbf{w}\|}$. Thus, the optimal hyperplane separating the two classes, can be found by minimizing $\|\mathbf{w}\|$ respecting the follwing condition

$$y_i(\mathbf{w} \cdot \mathbf{x}_i - b \geq 1) \quad \forall i$$

In this work, we formucreated a class for each letter shape (ranging from 2 to 4 classes a letter, according to the aforementioned shapes a letter may appear in). Several one-vs-all SVM classifiers are trained. For experiments, we used the LIBSVM library [7], choosing the Radial basic function (RBF) as a kernel.

3   Experimental Results

Firstly, given the crucial importance of the segmentation step, we conducted experiments to demonstrate the robustness of our segmentation approach (aside from recognition results). The used set of samples contains 600 word images, where 300 word images have been taken from IESK-arDB database and the other half taken from IFN/ENIT database. During experiments we reported two different types of errors; over-segmentation error which take place when segmentation occurs inside a letter (splitting it into multiple strokes). If however, multiple letters are segmented together as one letter representative, we call such error under-segmentation error. In literature, there are relatively very few works that are addressing the problem of off-line Arabic handwriting segmentation and in the same time reporting their results separately from the recognition results. In our experiments we implemented the most up to date work that is solely addressing the Arabic handwriting segmentation problem, and compared our segmentation results to their. Fig.5 , illustrates the achieved results of our approach against results of [16], which confirming the efficiency of ours. Interestingly, however, our approach achieved better results for samples taken from IESK-arDB compared to samples taken from IFN/ENIT. This can be justified by the fact that many samples of IFN/ENIT are violating the writing rules of Arabic, e.g. connected letters are often written un-connected, letters with loops written without, extensive use of diacritics that are not common in case of Arabic handwriting
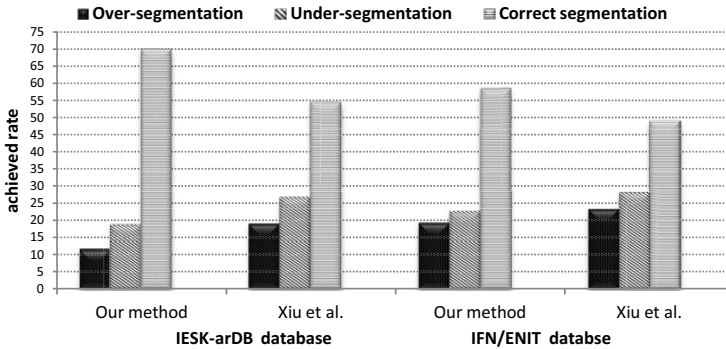
Fig. 5. The segmentation results: The results of our segmentation approach compared to results of [16] on two different databases

(e.g. SHADA). Roughly, our approach correctly segment 70% of word images taken from IESK-arDB and 59% of samples taken from IFN/ENIT, compared to 55% and 49% for [16] approach on samples taken from the aforementioned databases respectively.

The second types of experiments are carried out to demonstrate the system recognition performance. Around 1000 word images taken from IESK-arDB, resulted in 5436 letter images (after segmentation) that were used to train a SVM classifier. Leave-one-out estimation method is used to evaluate recognition accuracy of each letter, where the average rate reached 91.6%. As for recognition of word images, the system tested on 600 word images from IESK-arDB and validated it on 200 word images taken from sets (a, b, c) of FIN/ENIT database. Fig.6, illustrate the test and validation results of our system on IESK-arDB and FIN/ENIT databases respectively. Besides overall recognition results, deletion, substitution and insertion errors are as well drawn. The average recognition rate of word images reached 71%, which is a quite satisfactory result in such an un-constrained environment. In order to further demonstrate the proposed system capability, we validated it on never seen samples drawn from a different database (FIN/ENIT). Compared to testing results, validation rates were relatively humble. This can be refered to the extreme variability of writing styles that characterize most samples in this database, and also, to the fact that none of these database samples has been seen during the training. In general, the system achieved a complete recognition in 55% of the validation set samples. The first column in Fig.7 (A), shows samples taken from FIN/ENIT database, notice that letters printed in red (in the second column) indicate failed recognition (substitution error in this case). Likewise Fig. 7(B), demonstrates the recognition result on samples taken from IESK-arDB database.
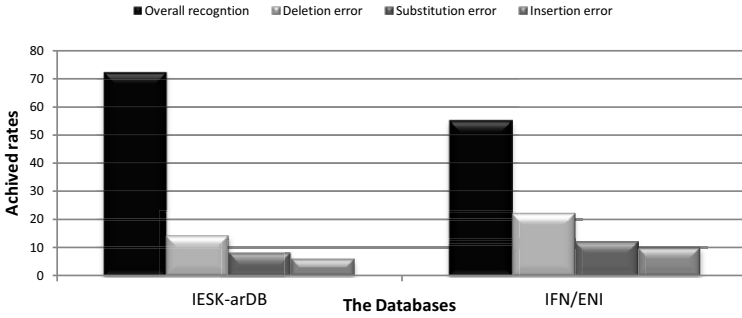
Fig. 6. Recogntion Results : The results of our recogntion approach compared to results of [16] on two different databases

Fig. 7. System output: (A) segmented samples taken from IFN/ENI and recognized Unicode, (B) segmented samples taken from IESK-arDB and recognized Unicode

The low rate of recognition of some other letters (e.g.,ح B, and ل M), is caused by, the similarity in shape with other multiple letters; and also, because of the fact, that those letters belong to a group (1CC) with high number of classes (25 classes), which in turn leads to a degradation in recognition rate, given the direct relationship between the number classes and the recognition error.

4 Conclusion and Future Works

In this paper, we proposed segmentation based, Gabor-filter based approach for an un-constrained recognition of the Arabic handwriting script. The approach is experimented on two different database achieving satisfactory results. Number of classes reduction through pre-classification step, optimization of classification model parameters, and post-processing step using spelling correction techniques, are all possible improvements on the system in the future.

References

1. Abuhaiba, I.S.I., Holt, M.J.J., Datta, S.: Recognition of off-line cursive hand-writing. Computer Vision and Image Understanding 71(1), 19–38 (1998)
2. Al-Badr, B.H.: A segmentation-free approach to text recognition with application to Arabic text. Ph.D. thesis, Seattle, WA, USA (1995)
3. Al-Hajj Mohamad, R., Likforman-Sulem, L., Mokbel, C.: Combining slanted-frame classifiers for improved hmm-based arabic handwriting recognition. IEEE Transactions on Pattern Analysis and Machine Intelligence 31(7), 1165–1177 (2009)
4. Almuallim, H., Yamaguchi, S.: A method of recognition of arabic cursive hand-writing. IEEE Trans. Pattern Anal. Mach. Intell. 9, 715–722 (1987)
5. Atici, A.A., Yarman-Vural, F.T.: A heuristic algorithm for optical character recognition of arabic script. Signal Processing 62(1), 87–99 (1997)
6. Bushofa, B.: Segmentation and recognition of arabic characters by structural classification. Image and Vision Computing 15(3), 167–179 (1997)
7. Chang, C.C., Lin, C.J.: LIBSVM: A library for support vector machines. ACM Transactions on Intelligent Systems and Technology 2, 27:1–27:27 (2011), software available at `http://www.csie.ntu.edu.tw/~cjlin/libsvm`
8. Chen, J., Cao, H., Prasad, R., Bhardwaj, A., Natarajan, P.: Gabor features for offline arabic handwriting recognition. In: Proceedings of the 9th IAPR International Workshop on Document Analysis Systems, DAS 2010, pp. 53–58. ACM, New York (2010)
9. Elzobi, M., Al-Hamadi, A., Al Aghbari, Z., Dings, L.: Iesk-ardb: a database for handwritten arabic and an optimized topological segmentation approach. International Journal on Document Analysis and Recognition (IJDAR), 1–14 (2012)
10. Haboubi, S., Maddouri, S., Ellouze, N., El-Abed, H.: Invariant primitives for handwritten arabic script: A contrastive study of four feature sets. In: 10th International Conference on Document Analysis and Recognition, ICDAR 2009, pp. 691–697 (2009)
11. Hamamoto, Y., Uchimura, S., Watanabe, M., Yasuda, T., Mitani, Y., Tomita, S.: A gabor filter-based method for recognizing handwritten numerals. Pattern Recognition 31(4), 395–400 (1998)
12. Lorigo, L., Govindaraju, V.: Offline arabic handwriting recognition: a survey. IEEE Transactions on Pattern Analysis and Machine Intelligence 28(5), 712–724 (2006)
13. Madhvanath, S., Govindaraju, V.: The role of holistic paradigms in handwritten word recognition. IEEE Trans. Pattern Anal. Mach. Intell. 23(2), 149–164 (2001)
14. Pechwitz, M., Maergner, V.: Hmm based approach for handwritten arabic word recognition using the ifn/enit - database. In: Proceedings. Seventh International Conference on Document Analysis and Recognition, pp. 890–894 (2003)
15. Pechwitz, M., Maddouri, S.S., Märgner, V., Ellouze, N., Amiri, H.: Ifn/enit - database of handwritten arabic words. In: Proc. of CIFED 2002, Tunis, pp. 129–136 (2002)
16. Xiu, P., Peng, L., Ding, X.-q., Wang, H.: Offline Handwritten Arabic Character Segmentation with Probabilistic Model. In: Bunke, H., Spitz, A.L. (eds.) DAS 2006. LNCS, vol. 3872, pp. 402–412. Springer, Heidelberg (2006)

Construction of Sequential Classifier Based on MacArthur's Overlapping Niches Model

Robert Burduk and Paweł Trajdos

Department of Systems and Computer Networks,
Wroclaw University of Technology,
Wybrzeze Wyspianskiego 27,
50-370 Wroclaw, Poland
`robert.burduk@pwr.wroc.pl`

Summary. This paper presents the problem of building the sequential model of the classification task. In our approach the structure of the model is built in the learning phase of classification. In this paper a split criterion based on the MacArthur's overlapping niches model is proposed. The MacArthur's overlapping niches distribution is created for each row of the confusion matrix. The split criterion is associated with the analysis of the received distributions. The obtained results were verified on ten data sets. Nine data sets come from UCI repository and one is a real-life data set.

1 Introduction

Finding the classification rules is becoming more and more difficult when the number of classes in data set increases. For some classifiers the increasing number of classes causes a significant decrease in the quality or loss of performance. One of the possible solutions to this problem is to use multistage classifiers. The general idea of the sequential methods is to break up classification into a number of simple decision [1, 2, 3]. So the built classifiers are usually more flexible than the single-stage classifiers, and their ability to class prediction is generally higher.

In particular, this paper discusses a way to design a decision tree structure. The split criterion is based on the confusion matrix. The potential division of the node is associated with the analysis of misclassification in the learning process. In the experiment decision rules are chosen arbitrarily in the entire tree.

The content of the work is as follows. Section 2 describes work related to sequential classification. Section 3 introduces the idea of the hierarchical (sequential) classifier. In Section 4 the proposed split criterion is described. In the next section the results of the experiments verified on data sets form UCI

repository and one real-life data set of the computer-aided medical diagnosis are presented. The last section concludes the paper.

2   Related Work

Generally, the synthesis of the multistage classifier is a complex problem. It involves a specification of the following components [4],:

- design of a decision tree structure [5],
- extraction and selection of features used at each non-terminal node of the decision tree [6, 7, 8, 9],
- the choice of decision rules for performing the classification.

A decision tree structure can be built in two main ways. The first method is to build a tree structure in the learning process [10]. This type of the tree structure induction does not need any additional information about the nature of the problem. However the obtained structure can vary significantly. In other approaches the decision tree structure is fixed before the learning process [11]. However this kind of structure induction needs some expert knowledge.

The choice of decision rules in nodes can be done in a local or global way. The local choice minimizes node error but does not guarantee minimization of global classifier error. On the other hand the global choice of decision rule guarantees minimum global error but these methods are more computationally demanding than the local ones.

The overlapping niches model was proposed in [12]. In mentioned paper the overlapping niches model was considered as one of three hypothesis.The remaining criteria were the broken stick model and the non continous particulate niches model. The overlaping niches hypothesis was rejected by MacArthur due to not fitting the data on relative aboundance of bird species. However paper [13] proved that certain abundance pattern data fits to the MacArthur's overlapping niches model. Another overlapping niches models were proposed in [14].

3   Hierarchical Classifier

The hierarchical classifier contains a sequence of actions [1, 15]. These actions are simple classification tasks executed in the individual nodes of the decision tree. Some specific features are measured on every nonleaf node of the decision tree. At the first nonleaf node features x_0 are measured, at the second features x_1 are considered and so on. Every set of features comes from the whole vector of features. In every node of the decision tree the classification is executed according to the specific rule. The decisions $i_0, i_1, ..., i_N$ are the results of recognition in the suitable node of the tree. The design of a decision tree structure is based on the split criterion.

In our task of classification the number of classes is equal to NC. The terminal nodes are labeled with the number of the classes from $M = 1, 2, ..., NC$, where M is the set of labels classes. The non-terminal nodes are labeled by the numbers of 0, NC+1, NC+2 reserving 0 for the root-node. The notation for the received model of the multistage recognition can be presented as follows [4]:

- $\overline{\mathcal{M}}$ – the set of internal (nonleaf) nodes,
- $\mathcal{M}_i$ – the set of class labels attainable from the i-th node ($i \in \overline{\mathcal{M}}$),
- $\mathcal{M}^i$ – the set of nodes of the immediate descendant node i ($i \in \overline{\mathcal{M}}$),
- m_i – the node of the direct predecessor of the i-th node ($i \neq 0$).

In each interior node the recognition algorithm is used. It maps observation subspace to the set of the immediate descendant nodes of the i-th node [16]:

$$\Psi_i : X_i \to \mathcal{M}^i, \quad i \in \overline{\mathcal{M}} . \tag{1}$$

This approach minimizes the misclassification rate for the particular nodes of a tree. The decision rules at each node are mutually independent. In the experiment the decision rules are chosen arbitrarily in the entire tree. Each of the classifiers used in the nodes of the tree takes a decision based on the full set of attributes available in the training set.

In our method of induction, the classification tree is a regular binary tree. This means that on each of the tree nodes there is a leaf or a node which has two children.

Induction of the decision tree is performed by the top-down method. This means that it is initiated by the classifier located in the root of the tree. Using the proposed criterion the decision is made whether to continue the division. The process is repeated for the subsequent child nodes of the tree, until the state wherein the nodes in the tree can no longer be divided.

4 Split Criteria

The overlapping niches model was proposed in [12]. This model describes the relative abundance of species by random segmentation of a line representing the resources of the environment. The abundance of species is determined by the distance between pair of points placed randomly onto a line. The model implicates that species shares some resources instead of competing for them. Assuming that the N pairs of points were placed on a stick. Distance between points in each pair is C_k, $k \in 0, 1, ..., N - 1$. Then the expected size of the $k - th$ largest distance is:

$$E(C_k) = \frac{\sqrt{N - k} - \sqrt{N - k - 1}}{\sqrt{N}}. \tag{2}$$

In the proposed method the division of the internal node is made on the basis of the overlapping niches distribution in the confusion matrix. Specifically,

Table 1. The confusion matrix for the nonleaf node i

	estimated			
	k_1	k_2	$\ldots$	k_L
k_1	$w_{1,1}$	$w_{1,2}$	$\ldots$	$w_{1,L}$
true k_2	$w_{2,1}$	$w_{2,2}$	$\ldots$	$w_{2,L}$
$\vdots$	$\vdots$	$\vdots$		$\vdots$
k_L	$w_{L,1}$	$w_{L,2}$	$\ldots$	$w_{L,L}$

the overlapping niches distribution is created for the rows of the confusion matrix. For all class labels from the internal node the $L \times L$ dimensional confusion matrix is created. The example of the confusion matrix is presented in Tab. 1.

The columns of the confusion matrix correspond to the predicted labels (decisions made by the classifier in the internal node). The rows correspond to the true class labels. The $w_{i,j}$ element is the number of $i-th$ class elements classified as the $j - th$ class. In this matrix the diagonal elements represent the overall performance of each label. The off-diagonal elements represent the errors related to each label.

Now the split criterion will be presented. For each class label l the number of misclassified objects is counted:

$$W(k_l) = \sum_{m=1, m \neq l}^{L} w_{l,m}. \tag{3}$$

Then all the values $W(k_l)$ are normalized:

$$W^*(k_l) = \frac{W(k_l)}{\sum_{i=1}^{L} W(k_i)} \tag{4}$$

The obtained $W^*(k_l)$ values apportion the total error made by the classifier in node. For these values can therefore use the overlapping niches model. The values $W^*(k_l)$ are not ascending sort, and compare with the expected values of the overlapping niches distribution. The values that are greater than the corresponding expected value of the overlapping niches distribution means that the classifier error is greater than the expected random error. Classes for these labels should be recognized by the next node of sequential classifier.

The division of node occurs when in the values $W^*(k_l)$ we can distinguish both the larger and smaller ones than the corresponding value of the expected overlapping niches. Otherwise, there is no division of the node. If there is no division at the beginning of the experiment, it indicates that the classification process is performed in the one-stage approach.

Example. Let Tab. 2 be the confusion matrix for nonleaf node i. Now the misclassification is counted for each row of confusion matrix: $W(k_1) = 20$, $W(k_2) = 30$, $W(k_3) = 10$. Next step is to normalize misclassification factors: $W^*(k_1) = \frac{20}{60}$, $W^*(k_2) = \frac{30}{60}$, $W^*(k_3) = \frac{10}{60}$. Another step is sorting $W^*(k_l)$ values and comparing them to the overlaping niches model(ONM) values Tab. 3. The mentioned table shows that the given node should be split. The k_1 and k_3 classes are classified in left child node, the k_2 class is classified in right child node.

Table 2. The sample confusion matrix for the nonleaf node i

	estimated		
	k_1	k_2	k_3
k_1	30	10	10
true k_2	10	20	20
k_3	5	5	40

Table 3. The comparison of sorted $W^*(k_l)$ values to the values obtained by the ONM

	estimated		
	k_2	k_1	k_3
sorted $W^*(k_l)$	0.5	0.(3)	0.1(6)
ONM values	0.58	0.24	0.18

5   Experiments

In the experiential research several data sets were tested. The first set refers to the acute abdominal pain diagnosis problem and comes from the Surgical Clinic Wroclaw Medical Academy. The other nine data sets come from UCI repository [17]. A set of all the available features was used for all data sets, however, for the acute abdominal pain data set the selection of features has been made in accordance with the suggestions from another work on the topic [18, 19]. The numbers of attributes, classes and available examples of the investigated data sets are presented in Tab. 4.

Tab. 5 presents the mean error and average ranks for one step classifier. In Tab. 6 we presented the mean error and the average ranks for sequential classifier. The average ranks are calculated on the basis of the Friedman test.

The value of achieved improvement is not significant from the statistical point of view. For the post-hoc Bonferroni-Dunn test [20] the critical difference (CD) for the 10 algorithms and 10 data sets is equal $CD = 3,76$. This CD is calculated at $\alpha = 0.05$.

Table 4. Description of data sets selected for the experiments

Data set	example	attribute	class
Acute Abdominal Pain	476	31	8
Breast Tissue	106	10	6
Ecoli	336	7	8
Glass Identification	214	10	6
Irys	150	4	3
Lung Cancer	31	52	3
Seeds	210	7	3
Vertebral Column	310	6	3
Wine	178	13	3
Yeast	1484	8	10

Table 5. Average error for the one-step classifier

Data set	$3-NN$	$5-NN$	$7-NN$	$9-NN$	SVM
Acute	0,164	0,164	0,176	0,195	0,175
Breast Tissue	0,400	0,398	0,528	0,572	0,493
Ecoli R	0,409	0,474	0,573	0,498	0,294
Glass R	0,174	0,180	0,178	0,147	0,149
Iris	0,304	0,342	0,325	0,359	0,338
Lung	0,303	0,290	0,322	0,267	0,047
Seeds	0,040	0,038	0,026	0,051	0,023
Vertebral Column	0,140	0,121	0,134	0,118	0,155
Wine	0,449	0,451	0,414	0,413	0,448
Yeast R	0,109	0,109	0,098	0,096	0,076
Aver. rank (group)	2,91	3,18	3,55	3,18	2,18
Aver. rank (all)	5,64	5,95	6,82	5,77	4,14

Table 6. Average error for the sequential classifier

Data set	$3-NN^{SBS}$	$5-NN^{SBS}$	$7-NN^{SBS}$	$9-NN^{SBS}$	SVM^{SBS}
Acute	0,161	0,161	0,172	0,194	0,175
Breast Tissue	0,333	0,415	0,488	0,562	0,493
Ecoli R	0,395	0,481	0,586	0,539	0,294
Glass R	0,174	0,183	0,176	0,15	0,149
Iris	0,323	0,339	0,331	0,348	0,338
Lung	0,298	0,284	0,3	0,29	0,047
Seeds	0,04	0,025	0,026	0,051	0,023
Vertebral Column	0,128	0,124	0,127	0,118	0,155
Wine	0,442	0,449	0,417	0,417	0,448
Yeast R	0,109	0,109	0,098	0,096	0,076
Aver. rank (group)	2,64	3,18	3,36	3,45	2,36
Aver. rank (all)	4,45	5,77	6,00	6,50	3,85

Experiments done in the work show that the promising results have been obtained. The proposed approach slightly improved the quality of classification for all except $9 - NN$ classifiers. However the differences are far from the critical difference.

6 Conclusions

In the paper a split criterion based on the analysis of the confusion matrix is proposed. Specifically, the division associated with an incorrect classification is introduced. This criterion is used in the design of a decision tree structure in the multistage classifier. With a fulfilled criteria a binary split of the analyzed decision node is carried out.

The idea of using the resource apportionment models in sequential classification needs to be carefully explored. In order to achieve better results using another statistical model of an error apportionment can be considered. A good starting point is to use other models proposed by MacArthur, Motomura [21, 22] or Dale. On the other hand some improvement can be done by using split criterion that considers the correctly classified objects. An approach that combines the correctly and incorrectly classification rate is worth considering. In another approach to the sequences classification, the separable linearization [23] can be used in the split criterium.

References

1. Burduk, R.: Classification error in Bayes multistage recognition task with fuzzy observations. Pattern Analysis and Applications 13(1), 85–91 (2010)
2. Kolakowska, A., Malina, W.: Fisher Sequential Classifiers. IEEE Transaction on Systems, Man, and Cybernecics – Part B Cybernecics 35(5), 988–998 (2005)
3. Podolak, I.T.: Hierarchical classifier with overlapping class groups. Expert Syst. Appl. 34(1), 673–682 (2008)
4. Kurzyński, M.: Decision Rules for a Hierarchical Classifier. Pat. Rec. Let. 1, 305–310 (1983)
5. Wozniak, M.: A hybrid decision tree training method using data streams. Knowledge and Information Systems 29(2), 335–347 (2010)
6. Choras, M.: Image feature extraction methods for ear biometrics–A survey. In: 6th International Conference on Computer Information Systems and Industrial Management Applications, CISIM 2007, pp. 61–265. IEEE (2007)
7. Choraś, R.S.: Content-based retrieval using color, texture, and shape information. In: Sanfeliu, A., Ruiz-Shulcloper, J. (eds.) CIARP 2003. LNCS, vol. 2905, pp. 619–626. Springer, Heidelberg (2003)

8. Guyon, I., Elisseeff, A.: An introduction to variable and feature selection. The Journal of Machine Learning Research 3, 1157–1182 (2003)
9. Rejer, I.: Genetic Algorithms in EEG Feature Selection for the Classification of Movements of the Left and Right Hand. In: Burduk, R., Jackowski, K., Kurzynski, M., Wozniak, M., Zolnierek, A. (eds.) CORES 2013. AISC, vol. 226, pp. 579–589. Springer, Heidelberg (2013)
10. Penar, W., Woźniak, M.: Experiments on classifiers obtained via decision tree induction methods with different attribute acquisition cost limit. In: Kurzynski, M., Puchala, E., Wozniak, M., Zolnierek, A. (eds.) Computer Recognition Systems 2. ASC, vol. 45, pp. 371–377. Springer, Heidelberg (2007)
11. Manwani, N., Sastry, P.S.: Geometric decision tree. IEEE Transactions on Systems, Man, and Cybernetics, Part B: Cybernetics 42(1), 181–192 (2012)
12. MacArthur, R.: On the relative abundance of bird species. Proc. Natl. Acad. Sci. USA 43, 293–295 (1957)
13. Jin-Tun, Z.: Species Abundance Patterns in Some Broad-leaved Deciduous Forests in New York, USA. Chinese Journal of Plant Ecology 23(6), 481–489 (1999)
14. MacArthur, R.: Niche Overlap as a Function of Environmental Variability. Proc. Natl. Acad. Sci. USA 43, 293–295 (1972)
15. Kurzyński, M.: On the Multistage Bayes Classifier. Pattern Recognition 21, 355–365 (1988)
16. Berger, J.: Statistical Decision Theory and Bayesian Analysis. Springer, New York (1993)
17. Asuncion, A., Newman, D.J.: UCI machine learning repository (2007)
18. Burduk, R., Woźniak, M.: Different decision tree induction strategies for a medical decision problem. Central European Journal of Medicine 7(2), 183–193 (2012)
19. Kurzyński, M.: Diagnosis of acute abdominal pain using three-stage classifier. Computers in Biology and Medicine 17(1), 19–27 (1987)
20. Trawiński, B., Smetek, M., Telec, Z., Lasota, T.: Nonparametric statistical analysis for multiple comparison of machine learning regression algorithms. International Journal of Applied Mathematics and Computer Science 22(4), 867–881
21. Motomura, I.: A statisticaltreatmen of associations. Jpn. J. Zool. 44, 379–383 (1932) (in Japanese)
22. Mutsunori, T.: Apportionment or Random Assortment: Species Abundance Patterns Revisited. Journal of Animal Ecology 59(3), 1129–1146 (1990)
23. Bobrowski, L., Topczewska, M.: Separable Linearization of Learning Sets by Ranked Layer of Radial Binary Classifiers. In: Burduk, R., Jackowski, K., Kurzynski, M., Wozniak, M., Zolnierek, A. (eds.) CORES 2013. AISC, vol. 226, pp. 131–140. Springer, Heidelberg (2013)

Extraction of Data from Limnigraf Chart Images

Adam Marchewka[1] and Rafał Pasela[2]

[1] Institute of Telecommunication,
University of Technology and Life Sciences,
Kaliskiego 7, 85-791 Bydgoszcz
adimar@utp.edu.pl

[2] Department of Sanitary and Water Engineering,
University of Technology and Life Sciences,
Kaliskiego 7, 85-796 Bydgoszcz

Summary. This article presents a system of data extraction from limnograph chart images. Proposed system will be composed of five main modules that are: extraction of axis and grid, text detection, graph vectorization, calibrations and read data using image content analysis algorithms. In the paper the fundamental characteristics of the system are presented including the simplified scheme of system modules.

1 Introduction

Entries made on paper are by far the most frequently found in archives of registered measurements from devices used for example on weather stations all over the world. Information gathered during such measurements are the main source of information for meteorologists and hydrologists. On their basis, weather forecasts and databases used for research and statistics are created. Data acquired in this way can be used for further proper and detailed development and preparation of output data for new generation hydrological models, simulating water circulation in the basin of a city. Accurate reading of chosen analog parameters is difficult, and requires a lot of time and energy [11, 12]

Frequent analysis of research material leads to its deterioration. Therefore, there is a need of converting classic records in the form of thermograms, higrograms, barograms, pluviograms or limnograms into digital form, which allows for saving such records from destruction. For the analysis in this paper data about water level and level changes was used, that is limnograms. Limnograms are paper strips depicting a graph of the continuous work of a limnograph.

Basing on conducted literary research we can notice that over the years numerous methods have been invented for image analysis in order to have
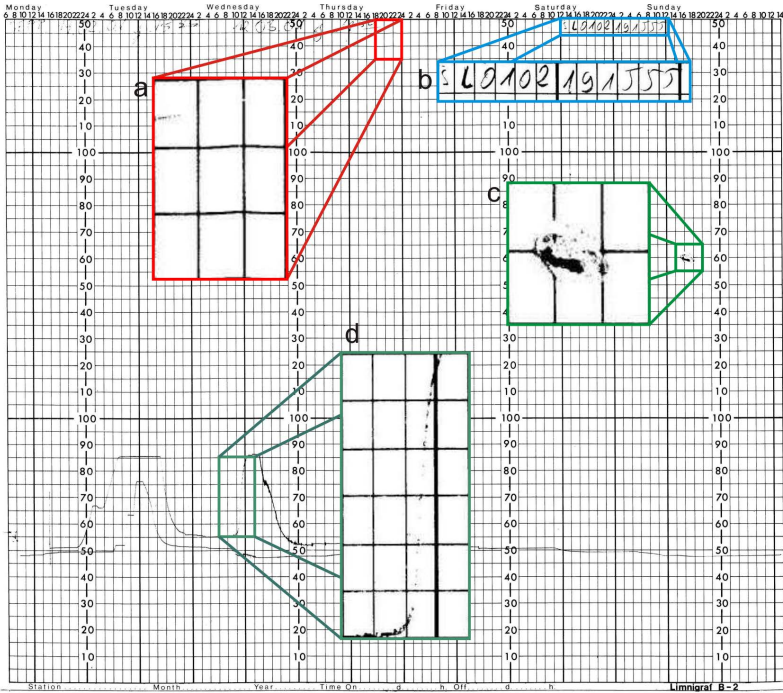
Fig. 1. Examples of usual defects of scanned pluviographic records. a - grid geometry errors, b - handwritten annotations, c - stains, mechanical damage, d - lack of graph continuity

Automated Classification [7, 8, 15, 16, 19], Analysis [1, 5, 6, 9, 10] and Redesign of Chart Images [3, 17]. First attempts at automated graph analysis were conducted in the last decade of the previous century. At first such attempts were focused on recognizing graph type and segmentation of separate elements, such as graph axes, labels, title etc. Over the years new suggestions for graph analysis algorithms and reading numeric data contained in those were developed. Up until this day new methods are being developed, but the authors are focusing rather on redesigning of raster Chart Images. In practice, it means that in these days algorithms are tested on images acquired from the Internet. What is characteristic for those raster images is that they are generated with the use of dedicated computer programs and thanks to this graph geometry depicted on them is unaltered.

Limnographic data record (Fig. 1) is generated using specialized analog device. The operating principle is similar to sand plotters, with the difference being that they are not controlled by computer, but by meteorological phenomenon effect. Entry made in such way is stored for years, which usually leads to mechanical damage, staining or discoloration. In the examined material there are many annotations made by hand. Also the size of examined

material can have adverse effect on data extraction since it deforms when stored, extracted and scanned. Conditions so specific call for developing a dedicated method of data extraction.

2 System Modules

The idea of a proposed system for data extraction from limnograph records is presented in Fig. 2. Proposed system will be composed of five main modules that are: extraction of axis and grid, text detection, graph vectorization, calibrations and read data.
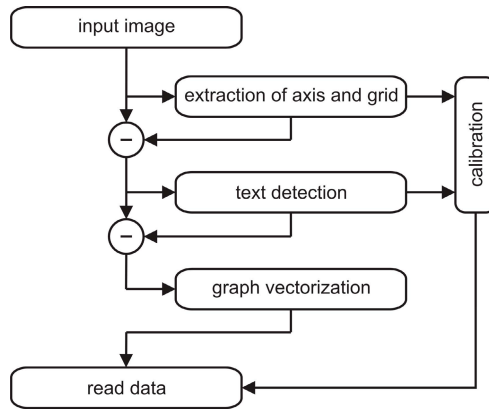
Fig. 2. Flowchart of proposed limnograph data extraction system

A scanned Limnographic record is entered into the system as a raster image $I[x, y]$. The functioning of the proposed method is based on image decomposition into base componets:

$$I[x, y] = I_G[x, y] + I_T[x, y] + I_D[x, y] + I_e[x, y] \qquad (1)$$

where $I_G[x, y]$ - grid image, $I_T[x, y]$ - image containing text, $I_D[x, y]$ - chart line, $I_e[x, y]$ - noise, defects, damage.

First, on the contrary to most methods, the graph grid is singled out. Such action limits significantly the amount of objects in the image subjected to the following steps in the analysis. Next, the algorithm for finding and recognition of text is performed Graph line is detected in image without previously detected objects. Basing on information about the grid and text labels image translation table is estimated.

3 Employed Methods and Algorithm

It was assumed that the proposed system will make use of already existing solutions. However, during the implementation process a need for certain changes became apparent. The next section describes each separate module with the necessary changes.

Axis and grid extraction algorithm is supposed to find and extract grid image $I_G[x, y]$. In order to achieve this, a simple and effective method is proposed in [9]. In this method, axis is detected by projection analysis. Maxima of projection in horizontal direction are candidates the elements of horizontal coordinates. Found local maxima are classified as grid lines according to threshold value. Next, classification of horizontal position is performed in the same way. (Fig. 3a).

(a)   (b)
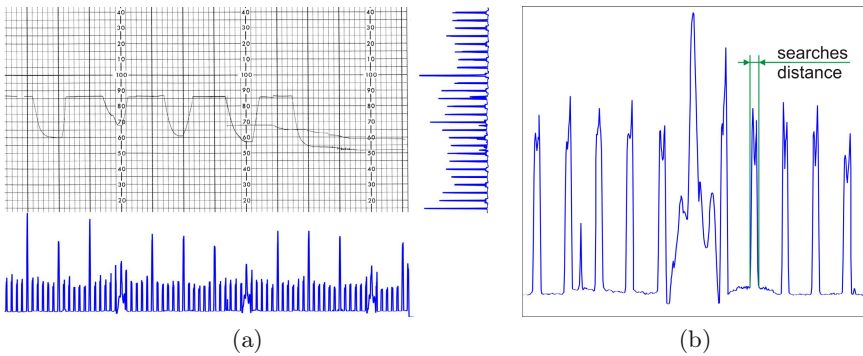
Fig. 3. Extraction axis and grid. (a) projection in horizontal and vertical direction, (b) ambiguity of local maxima.

Because of high nonlinearity of the grid and other defects occurrences in the examined image which influence unfavorably vertical and horizontal projection characteristics, (Fig. 3b) local maxima aren't unequivocal. This means that the width of individual maximum peaks is directly proportional to the occurring grid geometry errors. That is why the process of image grid lines segmentation should be performed locally for an area indicated by the width of individual peaks. For an area marked out in this way line segmentation is performed with the use of Radon transform [14, 20]. In this module characteristic points, that is lines intersections, are also designated and used later in the calibration process.

Text detection module is responsible for detecting and recognizing text in the examined image. For this purpose, for an image $I[x, y] - I_G[x, y]$ segmentation of connected pixels is performed [4]. Areas in which geometry does not point to text content (size, height to width ratio) anot subjected to further analysis in this step. For other areas a different method was used [18]. However, due to the occurrence of handwritten annotations, other OCR methods are still being tested.

Because of lack of continuity of the graph lines (see Fig. 1 case d) in Graph vectorization module the verification algorithm was used as presented in [13]. Another criterion of classification is the assumption, that graph line is a function of time. In practice it means that for a next image column only one pixel belongs to the graph line. In the case of several connected pixels which fulfill all other criteria, it points to the center of this pixel area as a point belonging to the graph [2].

Calibration process is finding the matrix of characteristic point projection indicated in the extraction grid module. The grid reference is created on the basis of detected labels. Using such reference matrix the value of separate graph points is defined in accordance with the reference. Next, the acquired data is saved and can be processed in any way.
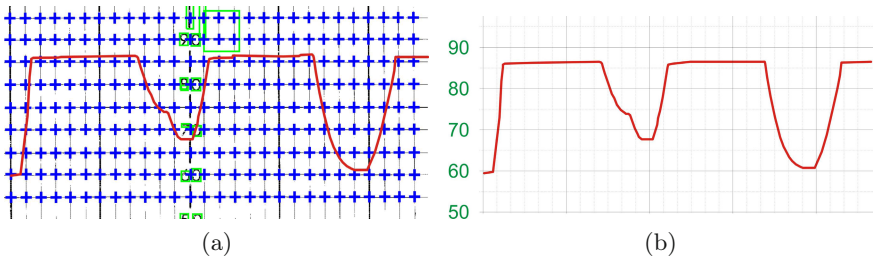
Fig. 4. Algorithm outcome (a) image components calibration: green color - $I_T[x, y]$, blue color - $I_G[x, y]$, red color - $I_D[x, y]$ (b) graph after calibration

4   Conclusion

In manual limnograms reading a big mistake is, because human perception and used measuring instruments are limited. Typically, the reading accuracy is limited to 0.5 mm. Knowing that 1mm is a positive growth of 1 cm and the size of the water is 10 000 m^2 is the error at the level of $\pm$ 50 m^3. By using the proposed system, the error reading can be reduced to a single pixel with a value of 0.05 mm - thus $\pm$ 5 m^3.

References

1. Cheng, B., Wang, R., Antani, S., Stanley, R.J., Thoma, G.R.: Graphical image classification combining an evolutionary algorithm and binary particle swarm optimization. In: IS&T/SPIE Electronic Imaging, p. 829703. International Society for Optics and Photonics (2012)
2. Dori, D., Liu, W.: Sparse pixel vectorization: An algorithm and its performance evaluation. IEEE Transactions on Pattern Analysis and Machine Intelligence 21(3), 202–215 (1999)

3. Gao, J., Zhou, Y., Barner, K.E.: View: Visual Information Extraction Widget for improving chart images accessibility. In: 2012 19th IEEE International Conference on Image Processing (ICIP), pp. 2865–2868. IEEE (September 2012)
4. Haralick, R.M., Shapiro, L.G.: Computer and Robot Vision, vol. 1, pp. 28–48. Addison-Wesley (1992)
5. Huang, W., Tan, C.L., Leow, W.K.: Model-based chart image recognition. In: Lladós, J., Kwon, Y.-B. (eds.) GREC 2003. LNCS, vol. 3088, pp. 87–99. Springer, Heidelberg (2004)
6. Huang, W., Tan, C.L., Leow, W.K.: Associating text and graphics for scientific chart understanding. In: Proceedings. Eighth International Conference on IEEE Document Analysis and Recognition, pp. 580–584 (2005)
7. Huang, W., Zong, S., Tan, C.L.: Chart image classification using multiple-instance learning. In: IEEE Workshop on Applications of Computer Vision, WACV 2007, p. 27. IEEE (February 2007)
8. Jayant, C., Renzelmann, M., Wen, D., Krisnandi, S., Ladner, R., Comden, D.: Automated tactile graphics translation: in the field. In: Proceedings of the 9th International ACM SIGACCESS Conference on Computers and Accessibility, pp. 75–82. ACM (2007)
9. Koga, M., Murakami, T., Shima, Y., Fujisawa, H.: An Extraction Method of Search Indexes for Graph Image Retrieval. In: Proc. of MVA, vol. 9, pp. 163–166 (1992)
10. Liu, R., Huang, W., Tan, C.L.: Extraction of vectorized graphical information from scientific chart images. In: Ninth International Conference on IEEE Document Analysis and Recognition, ICDAR 2007, vol. 1, pp. 521–525 (September 2007)
11. Licznar, P., Łomotowski, J., Rojek, M.: Pomiary i przetwarzanie danych opadowych dla potrzeb projektowania i eksploatacji systemów odwadnieniowych, Monografia, Wydawnictwo Futura, Poznań (2005)
12. Łomotowski, J.: Wody opadowe a zjawiska ekstremalne, Ed. Janusz Łomotowski, Wydawnictwo Seidel Przywecki (2011)
13. Marchewka, A.: Crack Detection on Asphalt Surface Image Using Local Minimum Analysis. Image Processing & Communications Challenges 2 84, 353–359 (2010)
14. Marchewka, A., Zdrojewski, J.: Data Matrix in the PCB production. Image Processing & Communications 16(2-3), 31–36 (2011)
15. Prasad, V.S.N., Siddiquie, B., Golbeck, J., Davis, L.: Classifying computer generated charts. In: International Workshop on Content-Based Multimedia Indexing, CBMI 2007, pp. 85–92. IEEE (June 2007)
16. Savva, M., Kong, N., Chhajta, A., Fei-Fei, L., Agrawala, M., Heer, J.: Revision: Automated classification, analysis and redesign of chart images. In: Proceedings of the 24th Annual ACM Symposium on User Interface Software and Technology, pp. 393–402. ACM (2011)
17. Wang, Z., Xu, X., Li, B.: Enabling seamless access to digital graphical contents for visually impaired individuals via semantic-aware processing. Journal on Image and Video Processing 2007(3), 3 (2007)

18. Wu, V., Manmatha, R., Riseman, E.M.: Textfinder: An automatic system to detect and recognize text in images. IEEE Transactions on Pattern Analysis and Machine Intelligence 21(11), 1224–1229 (1999)
19. Yang, L., Huang, W., Tan, C.L.: Semi-automatic ground truth generation for chart image recognition. In: Bunke, H., Spitz, A.L. (eds.) DAS 2006. LNCS, vol. 3872, pp. 324–335. Springer, Heidelberg (2006)
20. Zdrojewski, J., Marchewka, A.: Phototool geometry verification. In: Burduk, R., Jackowski, K., Kurzynski, M., Wozniak, M., Zolnierek, A. (eds.) CORES 2013. AISC, vol. 226, pp. 501–508. Springer, Heidelberg (2013)

A Simplified Visual Cortex Model for Efficient Image Codding and Object Recognition

Rafał Kozik

Institute of Telecommunications, UT&LS Bydgoszcz, Poland
`rkozik@utp.edu.pl`

Summary. In this article a simplified model of biologically inspired mechanisms for an object recognition is presented. The proposed approach is based on the HMAX hierarchical cortex model that was proposed by Riesenhuber and Poggio [1] and later extended by Serre et al [2]. The work described in this paper is an extension of a previous research [3, 4, 5, 6] focused on a computer vision software (named SMAS - Stereovision Mobility Aid System) dedicated for visually impaired persons. Therefore, the emphasis here is put on a one-class detection problem of dangerous objects with the possibility of a future deployment of the proposed solution on a mobile device. The conducted experiments show that the introduced modifications of the hierarchical HMAX model allows for an efficient feature extraction and a visual information coding without decreasing the effectiveness of an object detection process.

1 Introduction

This paper is a continuation of the author previous work on the SMAS system that proposes an efficient threat detection and an object recognition technique. The general architecture and discussion concerning system performance with demo cases were previously presented in [3, 4, 5, 6, 7]. Therefore, in this paper only the main aspects of SMAS system are explained.

The object recognition and the threat detection are two separate tasks that feed the SMAS system. The treat detection aims at detecting dangerous objects (or classes of objects) around the blind person. It engages algorithms that continuously scan the scene regions that are close to the camera. The SMAS system is a stereovision one, therefore such regions are extracted using depth map segmentation. The architecture of a system assumes that objects detectors have to be rapid, robust and invariant to a perspective, scale and rotation changes. Such assumptions usually require complicated and time

consuming learning phase. Detectors also have to be adapted to localization. In example, there is no need (and there is not enough computational power) to scan environment for a car in the kitchen.

On the other hand, the object recognition algorithm is using a database of objects. In order to perform the object recognition task the database has to be queried. Such approach allows different users to add new instances of objects to a centralized database. Unfortunately, such a method is less efficient in a context of the speed and the recognition.

Therefore, in order to maximise the situational awareness of a blind person, it is assumed that the detection task focuses only on objects that have to be detected (due to the danger they constitute to blind person), while recognition task is associated with object that knowledge about may by valuable but not crucial.

This paper is structured as follows. First, the overview of the HMAX Visual Cortex model proposed by Riesenhuber and Poggio [1] is explained. The modifications introduced to the HMAX model are given in section 3. The conducted experiments are described and discussed in section 4. Final conclusions and remarks are given afterwards.

2   HMAX Visual Cortex Model

The HMAX Visual Cortex model proposed by Riesenhuber and Poggio [1] exploits a hierarchical structure for the image processing and coding. It is arranged in several layers that process information in a bottom-up manner. The lowest layer is fed with a grayscale image. The higher layers of the model are either called "S" or "C". These names correspond to simple the (S) and complex (C) cells discovered by Hubel and Wiesel [8]. Both type of cells are located in the striate cortex (called V1), which is the part of visual cortex that lies in the most posterior area of the occipital lobe.
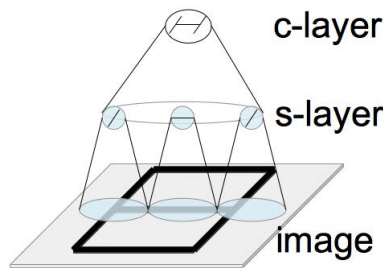
Fig. 1. The simple and complex cells. Each S-cell responses to edges in the image (typically there are four edges orientations: horizontal, vertical, and two diagonal). Each C-cell for a associated region of S-cells chooses the strongest responses of a given type (direction) using a strong max pooling filter.

The simple cells located in "S" layers apply local filters that responses form a vector of texture features. As noted by Hubel and Wiesel the individual cell in the cortex respond to the presence of edges. They also discovered that these cells are sensitive to edge orientation (some of cells fire only when a given orientation of an edge is observed).

The complex cells located in "C" layers calculate in a limited range of a previous layer the strongest responses of a given type (orientation). That way more complex combination of simple features are obtained (see the "H" letter in Fig.1 combined from three simple features).
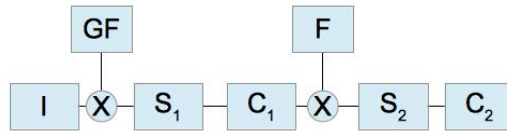
Fig. 2. The structure of a hierarchical model proposed by Mutch and Lowe [9]. (used symbols: I - image, S - simple cells, C - complex cells, GF - Gabor Filters, F - prototype features vectors, X - convolution operation)

The hierarchical HMAX model proposed by Mutch and Lowe [9] is a modification of the model presented by Serre et al in [2]. It introduces two layers of simple cells (S_1 and S_2) and two layers of complex cells (see Fig.2). It uses set of filters designed to emulate V1 simple cells. The layers are computed using a hard max filter. It means that the "C" cells responses are the maximum values of the associated "S" cells (Fig.1). As it is shown in the Fig.2 the images are processed by the subsequent simple and complex cells layers and reduced to feature vectors, which are further used in the classification process. The set of features (F) is shared across all images and object categories. Features are computed hierarchically in subsequent layers built from the previous one by alternating the template matching and the max pooling operations.

The S_1 layer in the Mutch and Lowe [9] model adapts the 2D Gabor filters computed for four orientations (horizontal, vertical, and two diagonal) at each possible position and scale. The Gabor filters are 11x11 in size, and are described by:

$$G(x, y) = \exp(-\frac{X^2 + \gamma Y^2}{2\sigma^2})cos(\frac{2\pi}{\lambda}X) \tag{1}$$

where $X = x \cos \phi - y \sin \phi$ and $Y = x \sin \phi + y \cos \phi$; x, y $\in < -5; 5 >$, and $\phi \in < 0; \pi >$. The aspect ration (γ), effective width (σ), and wavelength (λ) are set to 0.3, 4.5 and 5.6 respectively. The response of a patch of pixels X to a particular filter G is is computed using the formula 2.

$$R(X, G) = abs(\frac{\sum X_i G_i}{\sqrt{\sum X_i^2}}) \tag{2}$$

The complex cells located in C_1 layer pool associated units in the S_1 layer. For each orientation, the S_1 responses are convolved with a max filter, that is 10x10 of size in x, y dimension (position) and has 2 units of deep in scale.

As it is shown in the Fig. 2, the intermediate S_2 layer is formed by convolving the C_1 layer response with set of intermediate-level features (depicted as F in Fig. 2). The set of intermediate-level features is established during the learning phase. For a given set of learning images C_1 responses are computed. The most meaningful features are selected using SVM weighting. Mutch and Lowe [9] suggested to sub-sample the C_1 responses before feature selection. Therefore, authors select at random positions and scales of the C_1 layer patches of size 4x4, 8x8, 12x12, and 16x16. Selected and weighted features compose so called prototypes that are used in the Mutch and Lowe model as filters which responses create the S_2 layer. The C_2 layer composes a global features vector which particular element corresponds to the maximum response to a given prototype patch. In order to identify the visual object on the basis of features vector a classifier is learnt (e.g. SVM).

3   Proposed Modifications

The modifications introduced to model of the HMAX visual cortex proposed by Riesenhuber and Poggio [1] include:

- the different method for determining the direction of edges in the image,
- the number of direction encoded by simple cells in the S_1 layer,
- the number of prototype features vectors used to compute the S_2 layer response,
- the different method for features vector selection,
- the different classifiers used to recognize an object on the basis of the C_2 layer output.

3.1   Algorithm for Determining an Edge Direction

The algorithm engages local information about luminance gradients in the image in order to compute the direction of an edge. Firstly, the gradients in x and y directions are computed separately using the Sobel filter of length 7. Afterwards, for each image point the $atan()$ (inverse trigonometric tangent function) function value is computed. In order to reduce the computation time, the $atan()$ function is approximated as a line $y = x$ in (-1,1) range. Outside that range values of the $atan()$ function are evaluated using a look-up table. Once the value of $atan()$ in (x, y) point is computed the magnitude of a gradient in that point is measured and stored at a position (x, y) in one of 8 arrays (one array per direction). In order to evaluate the average magnitude of a gradient in a region bigger than one pixel, the integral images are used.

3.2   Simple Cells and Complex Cells Layers

In the S_1 layer there are 416 simple cells arranged in a rectangular block of size 20x16. For each cell a block of pixels of an image is assigned (a receptive field). For the associated regions of pixels each simple cell computes an edge direction. The processing is applied for three scales (an original image, and two images scaled by a factor of 0.7 and 1.5). Therefore, the S_1 layer output has dimensionality of a size 4 (x,y,scale and 8 direction units). The max-pooling filter applied to S_1 layer is a three dimensional filter of a size 6x6x3 (x, y, scale). Therefore, the C_2 layer output is two dimensional one.

3.3   Prototype Feature Selection and Classifier Selection

The output of the C_1 layer cells is used in order to select features that are meaningful for a given task of an object detection. Firstly, randomly selected images of an object are reduced to a features vectors by a consecutive layers of the proposed model. Afterwards, the PCA is applied to calculate the eigenvectors. Each eigenvector is used as a single feature in a features vector. The PCA is one the most popular and efficient approaches used in the literature (e.g. [6, 13, 12, 14, 15, 16]) for features selection and a dimensionality reduction.

In order to recognize the object using the output of C_2 layer a classifier is learnt. In this paper two types of classifiers were investigated (the similar ones were used in the previous work [6]), namely the PART classifier and the Naive Bayes classifier.

4   Results

The proposed method was evaluated against the effectiveness using two classes of so called dangerous (for a visually impaired person) objects, namely mug and kettle. In order to learn the proposed visual cortex model to detect a given class, images of the mentioned above objects were collected. The taken photos include objects seen from different angles, distances and rotations (see Fig.3).

The main purpose of the conducted experiments was to evaluate how the model parameters influence the average object detection effectiveness. For the evaluation purposes the 10-fold approach was adapted. Therefore, the database of images was divided into 10 subsets and during the evaluation one subset of the database was used for the model learning, while the remaining 9 for the testing. Such procedure was repeated 10 times and the results were averaged. As stated in the abstract and explained in the introduction, the paper addresses the one-class detection problem. Therefore, for different classes of objects the proposed model has to be learnt separately.

Fig. 3. Two classes of object used to evaluate the effectiveness of the proposed method

The first experiment aimed at evaluating the impact of a number of a simple cell direction units on effectiveness of the object detection process (Fig.4). The number of directions was changed from 1 to 8. When only one direction unit of a simple cell is used the effectiveness of the proposed solutions is rather poor (84% for the PART classifier and 82% for the Naive Bayes). When the number of directions is increased from 1 to 8 the model effectiveness increases significantly (about 20% for Naive Bayes classifier and 10% for PART classifier).

Fig. 4. The average effectiveness of two methods of classification (PART and Naive-Bayes - NB) for the varying number of directions that a simple cell is sensitive to

As it may be expected the model effectiveness is also impacted by the number of the prototype features used to compute the responses in the S_2 layer. Surprisingly, for such simple object like mug and kettle less than 10 prototype features were enough to achieve the effectiveness higher than 90%.

Moreover, only for the PART classifier it was noted that with a rising number of the prototype features the effectiveness of average object recognitions increases significantly (see Fig.5).
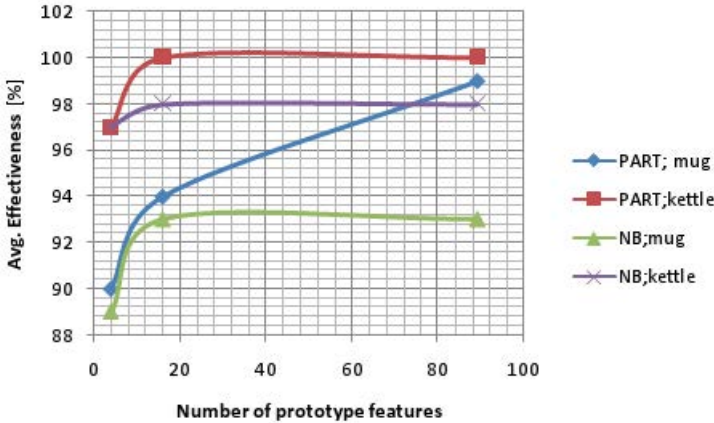
Fig. 5. Average Effectiveness of two methods of classification (PART and Naive-Bayes - NB) for two different object types: mug and kettle

5 Conclusions

In this article a simplified model of biologically inspired cortical mechanisms for object recognition was presented. The proposed approach was based on the HMAX hierarchical cortex model that was proposed by Riesenhuber and Poggio [1] and later extended by Serre et al [2]. The main contribution of this paper is a proposal of modifications introduced to HMX model. The changes include a different method for edges detection used by the V1 simple cell, the number of direction unit (8 direction), the number of prototype features and the method for prototype features selection. Te experiments show that the introduced modification of the hierarchical HMAX model allows for efficient feature extraction and an visual information coding without decreasing the effectiveness of an object detection process.

References

1. Riesenhuber, M., Poggio, T.: Hierarchical models of object recognition in cortex. Nat. Neurosci. 2, 1019–1025 (1999)
2. Serre, T., Kreiman, G., Kouh, M., Cadieu, C., Knoblich, U., Poggio, T.: A quantitative theory of immediate visual recognition. Progress in Brain Research, Computational Neuroscience: Theoretical Insights into Brain Function 165, 33–56 (2007)

3. Kozik, R.: Stereovision Based Obstacles Detection and Identification. Developments in Machinery Design and Control 11/2009 (2009)

4. Kozik, R.: SMAS - Stereovision Mobility Aid System for People with a vision impairment. In: Choraś, R.S. (ed.) Image Processing and Communications Challenges 2. AISC, vol. 84, pp. 315–322. Springer, Heidelberg (2010)

5. Kozik, R.: Ontology-based Reasoning for Stereovision Travel Aid System. In: II International Interdisciplinary Technical Conference of Young Scientists InterTech. (2010)

6. Kozik, R.: Rapid Threat Detection for Stereovision Mobility Aid System. In: Czachórski, T., Kozielski, S., Stańczyk, U. (eds.) Man-Machine Interactions 2. AISC, vol. 103, pp. 115–123. Springer, Heidelberg (2011)

7. Kozik, R.: Stereovision system for visually impaired. In: Burduk, R., Kurzyński, M., Woźniak, M., Żołnierek, A. (eds.) Computer Recognition Systems 4. AISC, vol. 95, pp. 459–468. Springer, Heidelberg (2011)

8. Hubel, D.H., Wiesel, T.N.: Receptive fields, binocular interaction and functional architecture in the cat's visual cortex. J. Physiol. 160, 106–154 (1962)

9. Mutch, J., Lowe, D.G.: Object class recognition and localization using sparse features with limited receptive fields. International Journal of Computer Vision (IJCV) 80(1), 45–57 (2008)

10. MAX pooling, `http://ufldl.stanford.edu/wiki/index.php/Pooling`

11. Forczmański, P.: Experimental Comparison of PCA/2DPCA and IPCA Performance in Image Recognition Task. In: Information Systems Architecture and Technology: System Analysis Approach to the Design, Control and Decision Support. Biblioteka Informatyki Szkol Wyzszych, pp. 163–176. Wroclaw University of Technology (2010)

12. Forczmański, P.: On the dimensionality of PCA method and color space in face recognition. In: Choraś, R.S. (ed.) Image Processing and Communications Challenges 4. AISC, vol. 184, pp. 55–62. Springer, Heidelberg (2013)

13. Forczmański, P.: Comparison of tensor unfolding variants for 2DPCA-based color facial portraits recognition. In: Bolc, L., Tadeusiewicz, R., Chmielewski, L.J., Wojciechowski, K. (eds.) ICCVG 2012. LNCS, vol. 7594, pp. 345–353. Springer, Heidelberg (2012)

14. Choraś, M., Kozik, R., Żelek, A.: A Novel Shape-Texture Approach to Palmprint Detection and Identification. In: Proc. Intelligent Systems Design and Applications, ISDA 2008, pp. 638–643. IEEE CS Press, Kaohsiung (2008)

15. Kozik, R., Żelek, A., Choraś, M.: Palmprint Segmentation and Feature Extraction Methods. In: Rutkowski, L., et al. (eds.) Computational Intelligence: Methods and Applications, pp. 377–388. Academic Publishing House EXIT (2008)

16. Kozik, R., Żelek, A., Choraś, M.: Palmprint Recognition Enhanced by the Shape Features. In: Proc. of 7th International Conference on Computer Information Systems and Industrial Management Applications (CISIM 2008), pp. 214–215. IEEE CS Press, Ostrava (2008)

Part II

Communications

Network Structures Constructed on Basis of Chordal Rings 4th Degree

Damian Ledziński[1], Sławomir Bujnowski[1], Tomasz Marciniak[1],
Jens Myrup Pedersen[2], and José Gutierrez Lopez[2]

[1] University of Technology and Life Sciences, Bydgoszcz, Poland
  {dledzinski,slawb,tomasz.marciniak}@utp.edu.pl
[2] Department of Electronic Systems, Aalborg University, Denmark
  {jens,jgl}@es.aau.dk

Summary. In this paper, on analysis of the properties of modified chordal ring 4th degree topologies has been presented. Two special types of these structures, namely optimal and ideal graphs, have been defined. The basic parameters (diameter and average path distance) were calculated and described by approximate formulas which makes possible to evaluate these parameters for any modified graph proposed by authors, and it gives possibility to model the properties of these networks without requiring any specific path calculation between pairs of nodes which may be time and resource consuming for large scale systems. In the last part of paper the comparison of the analyzing structures and reference graph has been carry out.

1   Introduction

Nowadays there is a tendency towards designing telecommunications systems as distributed ones. These systems contain several numbers of identical, intelligent modules that communicate with each other via the interconnection networks. One of the most interesting examples in current research are optical transmission systems. These allow building high-bandwidth, error-free communication networks, with capacities orders of magnitude higher than traditional networks. High data transmission rates are achieved by transmitting information through optical signals, and maintaining the signals in optical form, thus avoiding the need of temporarily converting them into electronic forms. An important issue on designing these systems is the choice of interconnection network topology as it has the biggest impact on transmission ability of entire system [1]. The systems which used fibers as transmissions medium can be modeled by symmetric digraphs. In relation to the study of network interconnections from a graph perspective the paper [2] presents a survey of the known topologies was presented. The author mainly focused on: connection costs expressed in the total number of links; communication

delay in terms of diameter of the graph and average distance of the path; fault tolerance characterized by connectivity and cohesion; regularity & symmetry; easy of routing; extensibility. Among the analyzed structures which would be used to construct distributed systems, it proposes to use the chordal rings cause their simplicity, extensibility and quite good transmission properties [2]. Authors in the prior publications analyzed properties of this type regular topologies different degree [3, 4, 5, 6, 7]. In this paper they concentrated on fourth degree chordal rings.

The structure of the paper is as follows. Section 2 presents the basic information concerning chordal rings and particularly commonly described rings fourth degree. In section 3 modification of chordal rings 4th degree, proposed by authors, is presented. Section 4 contains summary and conclusion following from the analysis of subject being the topic of paper.

2   Background

Analysis of regular network structures is an important issue in telecommunications and computer science. The application of chordal rings in computer systems, TDM networks (communication between distributed switching modules), core optical networks and optical access networks in many publications has been analyzed. Fourth degree chordal rings possess some properties that make them very suitable for construction of interconnection networks [8, 9, 10]. The basic feature of fourth degree chordal rings is their ability to physically realize some of them as the optimal graphs and the majority of them as the reference ones (exact definitions of these graphs will be given further in the paper). These graphs give the lower limits of basic parameters which can be obtained by analyzed type of structures. This allows evaluating the "quality" of examined chordal rings.

The general definition of the analyzed graphs in this work is as follows:

Definition 1

Chordal ring is a ring with additional chords It is defined by the pair (p, Q), where p means the number of nodes appearing in the ring and Q is the set of the chords q_i - additional connections where $q_i \in \{2, ..., p/2\}$. Each chord $q_i \in Q$ connects every pair of nodes of ring that are at distance q_i in the ring. This structure is denoted by $G(p; q_1, ..., q_i)$, $q_1 < q_2 < ... < p_i$. Degree of chordal rings is $2i$ in general whenever there is a chord of distance $p/2$, in this case p has to be even and ring's degree is $2_i - 1$ [11].

The most popular, standard fourth degree chordal ring is a special case of the structures mentioned above.

Definition 2

A chordal ring 4th degree denoted as CHR4 is a ring consisting of p nodes. Each node v_i is connected to four other nodes: $v_{i-1(mod\,p)}$, $v_{i+1(mod\,p)}$ and

additionally to two nodes $v_{i-q(modp)}$, $v_{i+q(modp)}$, where q means distance of additional connections (chords). The values p and q must be relatively primes and they define a graph as CHR4$(p; q)$.

An example of a chordal ring of fourth degree is shown in Fig. 1.
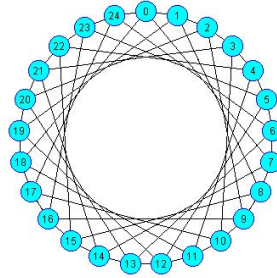
Fig. 1. Example of standard graph CHR4(25; 7)

The average distance and diameter were chosen in order to provide a general and simple indication of transmission properties of the analyzed topologies. For example: in a packet switched network, the average hop distance indicate how many routers and lines are on average involved in the transmission of each packet. So if the average distance is doubled, then the same traffic will on average double the load on routers and lines; in an optical network, a similar reasoning can be made - or: if a "route" is a light path, then it will (on average) need more colors to transmit the same amount of traffic.

These follow standard definitions as summarized below. Average distance and diameter are formally defined as follows [12]:

Definition 3

The diameter $D(G)$ is the largest distance among all of the shortest distances of the paths between any pair of nodes. It is defined as follows:

$$D(G) = \max_{v_i v_j}\{d_{\min}(v_i, v_j)\} \tag{1}$$

where v_i means the number of the node, $d_{\min}$ distance (number of edges) between i-th and j-th node.

Definition 4

The average path distance d_{av} between all pairs of nodes is defined by the formula:

$$d_{av} = \frac{1}{p(p-1)} \sum_{i=0}^{p-1} \sum_{j=0}^{p-1} d_{\min}(v_i, v_j) \tag{2}$$

where $d_{\min}(v_0, v_j)$ is the minimal number of edges between a source node v_0 and every other chosen node v_j, and p denotes the number of nodes.

For more basic definition of e.g. paths and path lengths, we refer to any basic graph theory book, such as [12].

In order to determine these parameters of the theoretically calculated reference topologies of chordal rings, two types of these structures were defined. The first one is called ideal graph and the second one optimal graph. In fact these graphs exist only in particular cases, but they are useful as reference models for evaluation of expected parameters of tested graphs [3, 8].

Definition 5

The ideal chordal ring degree $d(V)$ is the regular graph with total number of nodes pi described by the formula:

$$p_i = 1 + \sum_{d=1}^{D(G)-1} |p_d| + |p_{D(G)}| \qquad (3)$$

where p_d means the number of nodes that belong to the d-th layer (the layer is the subset of nodes that are at a distance d from the source node), while $p_{D(G)}$ denotes the number of the remaining nodes which appear in the last layer, $D(G)$ means diameter of analyzed graph. For ideal rings, for every n and $m < D(G) = \oslash$. If for certain $D(G)$ the subset $p_{D(G)}$ of chordal ring reaches the maximal possible value, then such a ring is called the optimal ring and the graph is optimal graph.

For ideal chordal ring the average path distance d_{avi} is expressed as:

$$d_{avi} = \frac{\sum_{d=1}^{d(G)-1} d\,|p_d| + D(G)\,|p_{d(G)}|}{p_i - 1} \qquad (4)$$

whereas for the optimal graph the average path distance d_{avo} is equal to:

$$d_{avo} = \frac{\sum_{d=1}^{d(G)} dp_d}{p_o - 1} \qquad (5)$$

where d - layer number, p_d - number of nodes in d-th layer, p_o - number of nodes in optimal graph.

Optimal graphs were used to calculate the formulas describing parameters of each type of analyzed chordal ring, whereas ideal rings were used to compare theoretically calculated values of parameters of analyzed structures.

In order to find optimal and ideal graphs it is necessary to first determine the maximal number of nodes which can be appear in successive layers of a graph respect to any source node (the layer is the set of nodes equally distant from this node).

Distribution of maximal number of nodes in the successive layers obtained in a theoretical way, and confirmed by experiments is shown in Table 1. Table 1. Maximal number of nodes in the successive layers

Table 1. Maximal number of nodes in the successive layers

d	1	2	3	4	5	6	7	8
p_{do}	4	8	12	16	20	24	28	32

The distribution of these numbers can be described by polynomial:

$$p_d = 4d \tag{6}$$

Using Table1 it was counted total number of nodes appearing in optimal structures, which is shown in Table 2.

Table 2. Total number of nodes in dependence of graph diameter

$D(G)$	1	2	3	4	5	6	7	8
p_o	5	13	25	41	61	85	113	145

In this case the total number of nodes is given by expression:

$$p_o = 2D(G)^2 + 2D(G) + 1 \tag{7}$$

Some optimal graphs exist in reality. They can be constructed when the distance of chord is described by formula:

$$q_o = 2D(G) + 1 \tag{8}$$

so the diameter of these graphs is equal to:

$$D(G)_o = \frac{\sqrt{(2p_o - 1)} - 1}{2} \tag{9}$$

In this case the average path distance is equal to:

$$d_{avo} = \frac{\left(\frac{4}{3}D(G)^3 + 2D(G)^2 + \frac{2}{3}D(G)\right)}{2\left(D(G)^2 + D(G)\right)} = \frac{2D(G) + 1}{3} = \frac{q_o}{3} \tag{10}$$

Among the chordal rings of this type consisting of $5 \div 1000$ nodes they counted 22 optimal graphs.

It was found many ideal graphs. In the above mentioned range the number of them is equal to 361. They found one group of ideal graphs which has even number of nodes. In dependence of its diameter the number of nodes which they consist of is described by expression:

$$\textbf{when } D(G) > 1 \textbf{ then } p_i = 2D(G)^2 \tag{11}$$

The length of chord is equal to:

$$q_i = 2D(G) - 1 \tag{12}$$

In this case the average path distance can be calculated using formula:

$$d_{avi} = \frac{D(G)\left(4D(G)^2 - 1\right)}{3\left(2D(G)^2 - 1\right)} \tag{13}$$

Each element of this group has two neighbours which are ideal graphs possessing the same length of chords described by expression:

The average path distances are equal to:

$$\textbf{when } D(G) > 1 \textbf{ then } p_i = 2D(G)^2 \pm 1 \tag{14}$$

The number of nodes creating another group of ideal graphs is described by following expression:

$$\textbf{when } D(G) > 1 \textbf{ and } p_i = 2D(G)^2 - 1$$
$$\textbf{then } d_{avi} = \frac{4D(G)\left(D(G)^2 - 1\right)}{6\left(D(G)^2 - 1\right)} = \frac{2}{3}D(G)$$
$$\textbf{when } D(G) > 1 \textbf{ and } p_i = 2D(G)^2 + 1$$
$$\textbf{then } d_{avi} = \frac{2D(G)\left(2D(G)^2 + 1\right)}{6D(G)^2} = \frac{2D(G)^2 + 1}{3D(G)} \tag{15}$$

Just as before the chord length is equal to:

$$p_i = 2D(G)^2 + 2D(G) - 1 \tag{16}$$

The average path distance is given by:

$$q_i = 2D(G) - 1 \tag{17}$$

The next groups of ideal graphs are described as follows:

$$\textbf{when } D(G) = 3 \textbf{ or } D(G) = 3i - 1 i = 2, 3, ...$$
$$p_i = 2D(G)^2 - 2D(G) + 3 q_i = \frac{2\left(D(G)^2 - 2D(G) + 3\right)}{3}$$
$$d_{avi} = \frac{2D(G)\left(2D(G)^2 - 3D(G) + 4\right)}{3\left(D(G)^2 - D(G) + 1\right)}$$
$$\textbf{when } D(G) = 3i + 1 \textbf{ or } D(G) = 3i + 3 i = 1, 2, 3, ...$$
$$p_i = 2D(G)^2 - 2D(G) + 5$$
$$d_{avi} = \frac{2D(G)\left(2D(G)^2 - 3D(G) + 14\right)}{3\left(D(G)^2 - D(G) + 4\right)} \tag{18}$$

In second case it was not possible to find the general formula to calculate length of ideal graph chords. For other cases they did not define expressions allowing determining how to find the ideal graphs.

The aim of authors of this publication was to find structures possessing better basic parameters, so it was proposed a few modifications of the regular fourth degree structures based on chordal rings.

3   Modification of Chordal Rings 4th Degree

In this part of the paper a review of basic parameters of structures proposed by the authors is given. In order to determine these parameters a program made by the authors was used to examine the modified, analyzed graphs. In this way it was possible to find the maximal number of nodes in the optimal graph successive layers, which was the base for calculating the other parameters: total number of nodes, diameter and average path distance.

3.1   CHR4a

Definition 6

A chordal ring CHR4a is a ring consisting of p nodes, where p must be even. Each node v_i is connected to nodes $v_{i-1(modp)}$ and $v_{i+1(modp)}$, where $i \in 0, 1, ..., p-1$. Additionally each even node v_{2i} is connected to nodes $v_{2i-q1(modp)}$ and $v_{2i+p/2(modp)}$ while each odd node $v_{2i+1(modp)}$ is connected to two adjacent nodes $v_{2i+1-q1(modp)}$ and $v_{2i+1+p/2(modp)}$. In this case the values q_1 and $p/2$ mean the lengths of chords. The value q_1 has to be odd. This structure is defined as CHR4a$(p; q_1)$.

An example of a CHR4a structure is shown in Fig. 2.
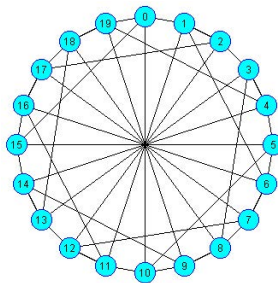
Fig. 2. Example of CHR4a(20; 5) structure

The distribution of nodes in the layers in virtual optimal graphs in dependence of number of nodes (is it divisible by 4 or not) looks as follows (Table 3):

Table 3. Distribution of nodes in the layers of optimal graphs

D	1	2	3	4	5	6	7	8	Number of nodes
p_{do}	4	9	15	21	27	33	39	45	p div by 4
	4	10	16	22	28	34	40	46	p not div by 4

These distributions can be described by polynomials:

> **for $d > 1$**
> **when p is divisible by 4 then $p_d = 6d - 3$**
> **when p is not divisible by 4 then $p_d = 6d - 2$** (19)

The total number of nodes in optimal graphs CHR4a is shown in Table 4.

Table 4. Number of nodes in virtual, optimal graphs CHR4a

D	1	2	3	4	5	6	7	8	Number of nodes
p_{do}	5	14	29	50	77	110	149	194	p div by 4
	5	15	31	53	81	115	155	201	p not div by 4

These numbers can be described by expressions:

for $D(G) > 1$
when p is divisible by 4 then $p_{oD(G)} = 3D(G)^2 + 2$
when p is not divisible by 4 then $p_{oD(G)} = 3D(G)^2 + D(G) + 1$ (20)

The theoretically counted average path distance is equal to:

> **for $D(G) > 1$**
> **when p is divisible by 4**
>
> $$\text{then } d_{avo} = d(G)\frac{3D(G)^3 + 6D(G)^2 + 5D(G) + 2}{4(3D(G)^2 + 1)}$$
>
> **when p is not divisible by 4**
>
> $$\text{then } d_{avo} = \frac{9D(G)^3 + 22D(G)^2 + 15D(G) + 2}{12(3D(G) + 1)} \tag{21}$$

It was not possible to find any optimal graph, but in range 5 1000 nodes they found the 14 ideal graphs shown in Table 5.

In Fig. 3 the differences between theoretical and real parameters of the analysed structures are shown.

Table 5. Ideal graphs CHR4a

p	q	$D(G)$	d_{av}
8	3	2	1,429
12	3	2	1,636
16	5	3	1,867
20	5	3	2,105
22	7	3	2,143
24	7	3	2,261
36	7	4	2,714
40	7	4	2,846
56	11	5	3,291
60	23	5	3,407
84	25	6	3,952
226	25	9	6,12
342	31	11	7,452
482	37	13	8,784
646	43	15	10,116

Fig. 3. Difference between basic parameters real and theoretical graphs CHR4a

3.2   CHR4b

Definition 7

A chordal ring CHR4b is a ring consisting of p nodes, where p must be even. Each node v_i is connected to nodes $v_{i-1(modp)}$ and $v_{i+1(modp)}$. Additionally each even node v_{2i} is connected to nodes $v_{2i-q1(modp)}$ and $v_{2i+q1(modp)}$ while each odd node $v_{2i+1(modp)}$ is connected to two adjacent nodes $v_{2i-q2(modp)}$ and $v_{2i+q2(modp)}$. The parameters q_1 and q_2 are even and they mean the

length of chords. The values $p/2$ and $q1/2$, $q2/2$ have to be relatively prime to each other. This structure is defined as CHR4b$(p; q1; q2)$.

An example of this structure is shown in Fig. 4.

Distribution of maximal number of nodes in the layers of virtual optimal graphs is shown in Table 6.

Table 6. Maximal number of nodes in successive layers

d	1	2	3	4	5	6	7	8
p_{do}	4	12	30	58	94	138	190	250
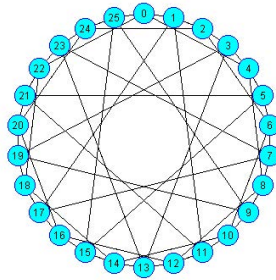
Fig. 4. Graph CHR4b(26; 4,10)

Table 7. Total number of nodes in optimal graphs

d	1	2	3	4	5	6	7	8
p_{do}	5	17	47	105	199	337	527	777

This distribution is described by the polynomial:

$$\textbf{when } d > 2 \textbf{ then } p_d = 4d^2 - 6 \tag{22}$$

The optimal graphs do not exist in reality (apart from the case of chordal ring constructed with 5 nodes) but the total number of nodes of them is given by expression:

$$p_o = \frac{4D(G)^3 + 6D(G)^2 - 16D(G) + 27}{3} \tag{23}$$

From the assumption it follows that the number of nodes in graphs CHRb must be even, so for this reason expression has to be odd. A simple transformation shows that it is always even, so it is not possible to construct optimal rings CHRb in reality.

The theoretical average path distance is equal to:

$$d_{avo} = \frac{3\left(D(G)^4 + 2D(G)^3 - 2D(G)^2 - 3D(G) + 10\right)}{4D(G)^3 + 6D(G)^2 - 16D(G) + 24} \tag{24}$$

It was found only six ideal graphs in the range 5 -1000 nodes, when total

number of nodes is equal to:

$$p = 10 \quad \text{when } q_1 = 2, q_2 = 4$$
$$p = 22 \quad \text{when } q_1 = 4, q_2 = 8$$
$$p = 26 \quad \text{when } q_1 = 4, q_2 = 10$$
$$p = 68 \quad \text{when } q_1 = 6, q_2 = 26$$
$$p = 70 \quad \text{when } q_1 = 22, q_2 = 32$$
$$p = 146 \text{ when } q_1 = 12, q_2 = 64.$$

In Fig. 5 comparison of diameter and average path distances of real and ideal graphs is shown.
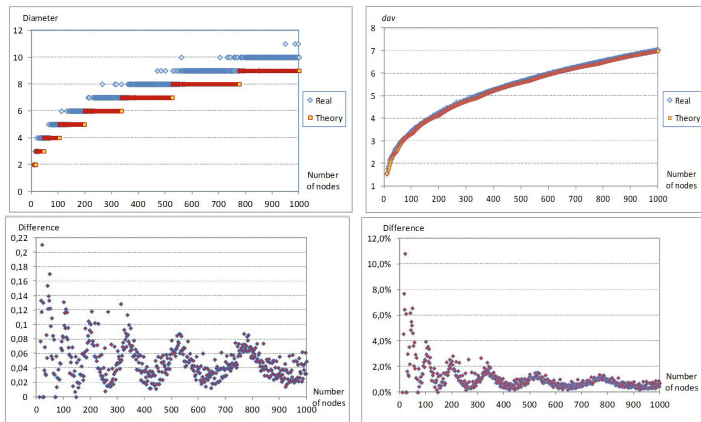
Fig. 5. Difference between basic parameters for real and theoretical graphs CHR4b

3.3 CHR4c

Definition 8

A chordal ring CHR4c is a ring consisting of p nodes, where p must be even. Each node v_i is connected to nodes $v_{i-1(modp)}$ and $v_{i+1(modp)}$. Additionally each even node v_{2i} is connected to nodes $v_{2i+q1(modp)}$ and $v_{2i+q2(modp)}$ while each odd node $v_{2i+1(modp)}$ is connected to two adjacent nodes $v_{2i-q1(modp)}$ and $v_{2i-q2(modp)}$. The values q_1 and q_2 mean the lengths of chords. The values q_1, q_2 have to be odd. This structure is defined as CHR4c$(p; q1; q2)$.

An example of CHR4c structures is shown in Fig. 6. Distribution of nodes in the layers in virtual optimal graphs is shown in Table 8.

Table 8. Maximal number of nodes in layers

d	1	2	3	4	5	6	7	8
p_{do}	4	12	24	42	64	92	124	162
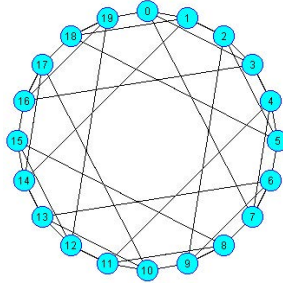
Fig. 6. Graph CHRc(20; 3,7)

Table 9. Total number of nodes in optimal graphs

$D(G)$	1	2	3	4	5	6	7	8
p_{do}	5	17	41	83	147	239	363	525

Polynomials which describe the number of nodes in layers have the shapes as follows:

$$\text{when } d \text{ is odd then } p_d = 2,5d^2 + 1,5$$
$$\text{when } d \text{ is even then } p_d = 2,5d^2 + 2 \tag{25}$$

The total number of nodes can be expressed by formulas:

$$\text{when } D(G) \text{ is odd then } p_o = \frac{10D(G)^3 + 15D(G)^2 + 26D(G) + 9}{12}$$
$$\text{when } D(G) \text{ is even then } p_o = \frac{10D(G)^3 + 15D(G)^2 + 26D(G) + 12}{12} \tag{26}$$

so it is not possible to construct optimal graphs.

The theoretical average path distance is equal to:

$$\text{when } D(G) \text{ is odd then}$$
$$d_{avo} = \frac{3}{2} \frac{5D(G)^4 + 10D(G)^3 + 12D(G)^2 + 9D(G) - 1}{10D(G)^3 + 15D(G)^2 + 26D(G) - 3}$$
$$\text{when } D(G) \text{ is even then}$$
$$d_{avo} = \frac{3}{2} \frac{5D(G)^3 + 10D(G)^2 + 12D(G) + 8}{10D(G)^2 + 15D(G) + 26} \tag{27}$$

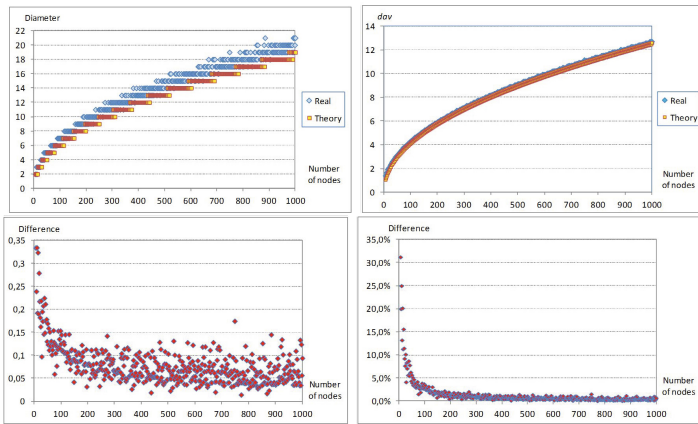In Fig. 7 the difference between real and theoretical structures is shown.
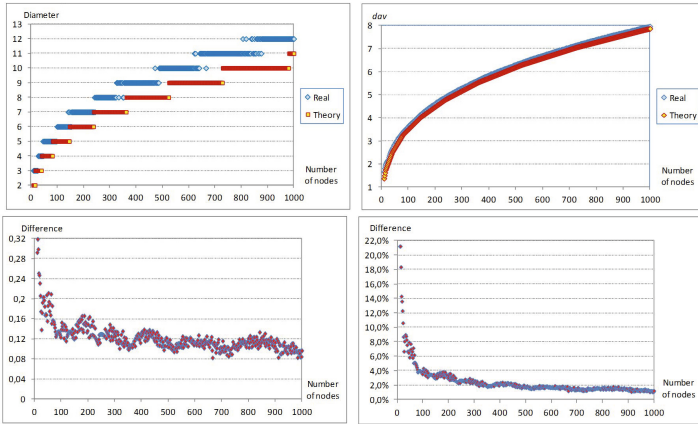
Fig. 7. Difference between basic parameters real and theoretical graphs CHR4c

3.4   CHR4d

Definition 9

A chordal ring CHR4d is a ring consisting of p nodes, where p must be divisible by 4. Each node vi is connected to nodes $vi-1(modp)$ and $vi+1(modp)$. Additionally each even node v_{2i} when $2i = 0(mod4)$ is connected to nodes $v_{2i+q1(modp)}$ and $v_{2i+q2(modp)}$, when $2i = 2(mod4)$ this node is connected to nodes $v_{2i+q1(modp)}$ and $v_{2i-q2(modp)}$; while each odd node $v_{2i+1(modp)}$ when $2i + 1 = 1(mod4)$ is connected to two adjacent nodes $v_{2i+1-q1(modp)}$ and $v_{2i+q3(modp)}$ and when $2i + 1 = 3(mod4)$ then this node is connected to nodes $v_{2i+1-q1(modp)}$ and $v_{2i+1-q3(modp)}$. The values $q_1, q_2, q_3 < p/2$ mean the lengths on chords. The values q_1 must be odd, q_2 and q_3 - even. This type of structures can be constructed on condition, that:

This structure is defined by CHR4d$(p; q_1, q_2, q_3)$.
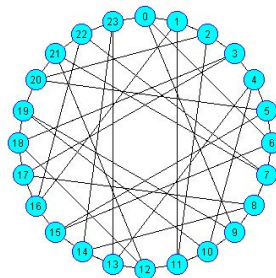
Fig. 8. Example of analysed structure - CHR4d(24; 9,6,10)

The distribution of nodes in the layers of virtual, optimal graphs is given in Table 10 and the total number of nodes in Table 11.

Table 10. Distribution of nodes in the layers

d	1	2	3	4	5	6	7	8
p_{do}	4	12	30	70	126	206	330	476

when d is equal to $0 \bmod (3)$ then $p_d = \dfrac{8d^3 + 8d - 2}{9}$

when d is equal to $1 \bmod (3)$ then $p_d = \dfrac{8d^3 + d^2 + 25d + 2}{9}$

when $d > 2$ and d is equal to $2 \bmod (3)$ then $p_d = \dfrac{8d^3 - d^2 + 31d + 4}{9}$

$$(28)$$

Table 11. Total number of nodes in optimal graphs

$G(D)$	1	2	3	4	5	6	7	8
$p_{D(G)o}$	5	17	47	117	243	449	779	1255

In this case it is not possible to construct optimal graphs as well. In dependence of $D(G)$ value the total number of nodes in an optimal graph can be calculated using expressions:

when $D(G) = 1$ then $p_o = 5$

when $D(G)$ is equal to $0 \bmod (3)$ then

$$p_o = \frac{2D(G)^4 + 4D(G)^3 + 15D(G)^2 + D(G) - 1}{9}$$

when $D(G)$ is equal to $1 \bmod (3)$ then

$$p_o = \frac{2D(G)^4 + 4D(G)^3 + 16D(G)^2 + 8D(G) - 3}{9}$$

when $D(G)$ is equal to $2 \bmod (3)$ then

$$p_o = \frac{2D(G)^4 + 4D(G)^3 + 15D(G)^2 + 11D(G) + 7}{9} \qquad (29)$$

and theoretical average path distance is equal to:

when $D(G) = 1$ then $d_{avo} = 1$

when $D(G)$ is equal to $0 \bmod (3)$ then

$$d_{avo} = 9 \frac{\frac{216}{5} \left\lfloor \frac{D(G)}{3} \right\rfloor^5 + 36 \left\lfloor \frac{D(G)}{3} \right\rfloor^4 + \frac{101}{3} \left\lfloor \frac{D(G)}{3} \right\rfloor^3 + 11 \left\lfloor \frac{D(G)}{3} \right\rfloor^2 - \frac{28}{15} \left\lfloor \frac{D(G)}{3} \right\rfloor - 4}{2D(G)^4 + 4D(G)^3 + 15D(G)^2 + D(G) - 10}$$

when $D(G)$ is equal to $1 \bmod (3)$ then

$$d_{avo} = 9 \frac{\left\lfloor \frac{D(G)}{3} \right\rfloor \left[\frac{216}{5} \left\lfloor \frac{D(G)}{3} \right\rfloor^4 - 108 \left\lfloor \frac{D(G)}{3} \right\rfloor^3 + \frac{398}{3} \left\lfloor \frac{D(G)}{3} \right\rfloor^2 - 87 \left\lfloor \frac{D(G)}{3} \right\rfloor + \frac{407}{15} \right]}{2D(G)^4 + 4D(G)^3 + 18D(G)^2 + 8D(G) - 12}$$

when $D(G)$ is equal to $2 \bmod (3)$ then

$$d_{avo} = 9 \frac{\frac{216}{5} \left\lfloor \frac{D(G)}{3} \right\rfloor^5 - 36 \left\lfloor \frac{D(G)}{3} \right\rfloor^4 + \frac{101}{3} \left\lfloor \frac{D(G)}{3} \right\rfloor^3 - 13 \left\lfloor \frac{D(G)}{3} \right\rfloor^2 + \frac{62}{15} \left\lfloor \frac{D(G)}{3} \right\rfloor - 4}{2D(G)^4 + 4D(G)^3 + 15D(G)^2 + 11D(G) - 2}$$

$$(30)$$

In Fig. 9 comparison of real and theoretical calculated parameters is shown.
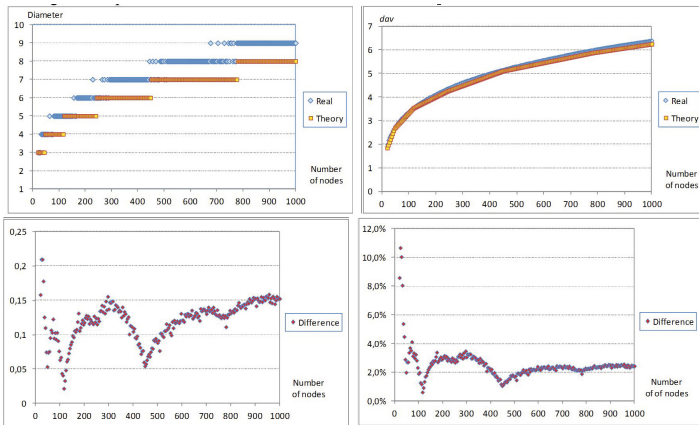
Fig. 9. Difference between real and theoretical calculated parameters of CHRd

3.5   Summing Up

Reviewing the proposed structures of fourth-degree based on ring topology we can conclude as follows:

- An advantage of the standard chordal ring topology CHR4 is the fact that there is a possibility of physical design for any number of nodes. In other cases, the proposed topology must have an even number of nodes, and in the case of CHR4d the number of nodes has to be divisible by 4.

- For all types of considered structures simpler or more complex formulas were found describing the distribution of the nodes in the layers, the total number of nodes and the average path distance depending on the diameter of the optimal graphs.

Figure 10 shows the comparison of the actual performance of the proposed structures for the number of nodes not exceeding 100.

For CHR4 structures it is important that in most cases for both the physical construction of optimal graph (described strictly with mathematical formulas) and ideal graphs is possible. In the case of the other proposed structures is not possible to obtain the optimal graph, which is due to a conflict between the assumption of parity number of constituent nodes and the theoretically calculated odd number of nodes characteristic for the optimal graph. However, it was found that for maximum 1000 node, there exists fourteen ideal CHR4a and six CHR4b, and in other cases no other graphs were found.
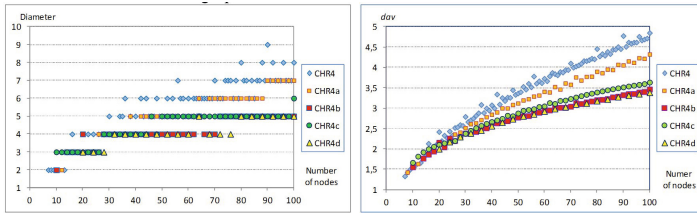
Fig. 10. Comparison of basic parameters of analyzed graphs

The presented diagrams show, that the worst transmission properties belong to a standard chordal ring, and the best to CHR4d and CHR4b structures. In the investigated range (of the number of nodes) forming these structures differences are quite small, so due to the fact that CHR4d is realized only for the number of nodes divisible by 4, the structure CHRb would be recommended for use in real networks.

For these two topologies parameters were compared extending the number of nodes to 1000 (Fig. 11). The comparison shows in the following graphs indicate that with the increase in the number of nodes the parameters of CHR4d structures are superior to the other.

In order to find real best reference parameters of fourth degree graphs it was defined the Reference Graph. It represents lower bounds for average distance and diameter for all these graphs, but since it is in many cases "virtual graph" these bounds may not always be achievable.

The Reference Graph parameters were calculated using as reference parameters of simple tree and they are described as follows:

1. The number of nodes p_{dRG} in d-th layer is determined by formula:

$$p_{dRG} = 4 \cdot 3^{(d-1)} \tag{31}$$
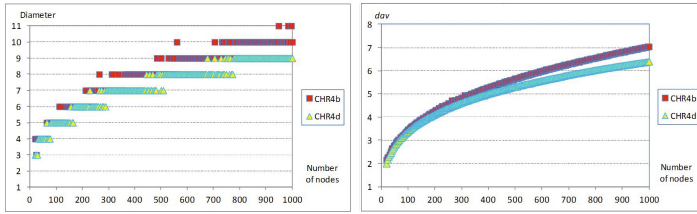
Fig. 11. Comparison of parameters of real CHR4b and CHR4d graphs

2. Total number of nodes $p_{D(G)RG}$ versus graph diameter is described by expression:

$$p_{D(G)RG} = \frac{4 \cdot 3^{D(G)RG} - 2}{2} = 2 \cdot 3^{D(G)RG} - 1 \tag{32}$$

3. Value of diameter versus total number of nodes is given can be calculated following formula:

$$D(G) = \left\lfloor \log_3 \frac{p_{D(G)RG} + 1}{2} \right\rfloor \tag{33}$$

4. Average path distance of optimal Reference Graph davRG in function of diameter is equal to:

$$d_{avRG} = \frac{(2D(G) - 1) \cdot 3^{D(G)RG} + 1}{2 \cdot \left(3^{D(G)RG} - 1\right)} \tag{34}$$

5. 5. This graph is symmetrical; it means that regardless from which node they are calculated its parameters have the same values.

In Fig. 12 the comparison of the best real analyzed structures CHR4 and Reference Graphs is shown.
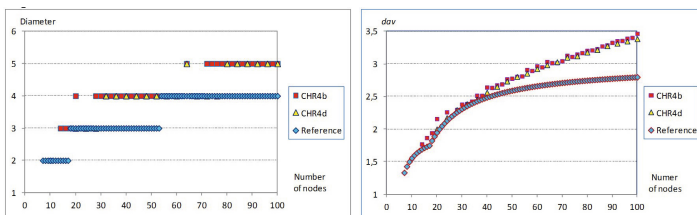
Fig. 12. Comparison of parameters of real CHR4b and CHR4d with Reference Graphs 4$^{\text{th}}$ degree

From these diagrams It follows that the parameters of Reference Graphs are considerably better than those of the proposed CHR4 structures.

Authors tried to find the answer to the question - is it possible to construct Reference Graphs 4th in reality. In this order to do it they used special program prepared by themselves. The examples of the founded graphs are shown in Figure 13.
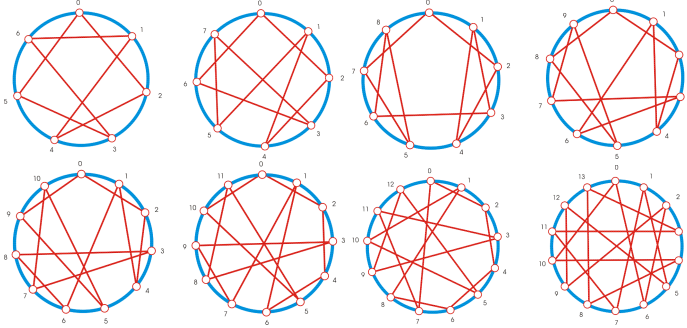
Fig. 13. Examples of founded Reference Graphs fourth degree

4 Conclusions

In this paper the authors presented an analysis of the modified 4th degree chordal rings. It was assumed that the average distance and diameter provide a general and simple indication of transmission properties of the considered structures. For each type of modified chordal rings it was defined optimal and ideal graphs which parameters determined the lower limits of the analyzed parameters. In order to make it they found the distribution of nodes appearing in successive layers and calculated total number in optimal graphs, and on this base, they defined formulas describing the average distance and diameter.

They proposed to introduce the concept of Reference Graph, which is the objective measure of 4th degree graphs. Unfortunately the process of finding these structures needs long time of calculations. The next step of author's researches will be the study how to shorten this time. It will make possible to find other Reference Graphs possessing more nodes what it can be useful to construct optimal networks basing on ring structures. New matter which appears in this case is problem of the simple description of analyzed topologies and them applications in real fiber networks. The topic of Reference Graphs will be the object of further of researches of authors.

References

1. Bhuyan, L.N.: Interconnection Networks for Parallel and Distributed Processing. IEEE Computer 20(6), 9–12 (1987)
2. Kotsis, G.: Interconnection Topologies and Routing for Parallel Processing Systems. ACPC, Technical Report Series, ACPC/TR92-19 (1992)

3. Bujnowski, S., Dubalski, B., Pedersen, J.M., Zabłudowski, A.J.: Analysis of Regular Structures Third Degree Based on Chordal Rings. Image Processing & Communications 14(1), 13–24 (2009)
4. Bujnowski, S., Dubalski, B.z., Zabłudowski, A., Ledźinski, D., Marciniak, T., Pedersen, J.M.: Comparison of Modified Degree 6 Chordal Rings. In: Choraś, R.S. (ed.) Image Processing and Communications Challenges 2. AISC, vol. 84, pp. 435–445. Springer, Heidelberg (2010)
5. Bujnowski, S., Dubalski, B.z., Zabłudowski, A., Pedersen, J.M., Riaz, T.: Analysis of Degree 5 Chordal Rings for Network Topologies. In: Choraś, R.S. (ed.) Image Processing and Communications Challenges 3. AISC, vol. 102, pp. 445–457. Springer, Heidelberg (2011)
6. Dubalski, B., Bujnowski, S., Ledziński, D., Zabłudowski, A., Kiedrowski, P.: Analysis of Modified Fifth Degree Chordal Rings. In: New Frontiers in Graph Theory, pp. 43–88. InTech (2012) ISBN 978-953-51-0115-4
7. Zabłudowski, Ł., Dubalski, B., Kiedrowski, P., Ledziński, D., Marciniak, T.: Modified NDR structures. Image Processing & Communications 17(3), 29–47 (2012) ISSN 1425-140X
8. Narayanan, L., Opatrny, J.: Compact Routing on Chordal Rings of Degree Four. Algorithmica 23, 72–96 (1999)
9. Comellas, F., Mitjana, M., Narayanan, L., Opatrny, J.: Optical routing of uniform instances in tori. In: Nielsen, M., Rovan, B. (eds.) MFCS 2000. LNCS, vol. 1893, pp. 285–294. Springer, Heidelberg (2000)
10. Narayanan, L., Opatrny, J., Sotteau, D.: All-To-All Optical Routing in Chordal Rings of Degree 4. Algorithmica 31, 155–178 (2001)
11. Bermond, J.C., Comellas, F., Hsu, D.: Distributed Loop Computer Networks: A Survey. Journal of Parallel and Distributed Computing 24, 2–10 (1995)
12. Diestel, R.: Graph Theory, 4th edn. Graduate Texts in Mathematics, vol. 173. Springer, Heidelberg (2001)

Fuzzy Rule-Based Systems
for Optimizing Power
Consumption in Data Centers

Moad Seddiki, Rocío Pérez de Prado, José Enrique Munoz-Expósito,
and Sebastián García-Galán

Telecommunication Engineering Dpt., University of Jaén,
Alfonso X El Sabio, 28, Linares, Spain
ramdyt@hotmail.com, {rperez,jemunoz,sgalan}@ujaen.es

Summary. One of the most important aspects in cloud computing is the infraestructure as a service (IaaS). In the basic cloud service model, providers offers virtual machines and solutions based on virtualization. An user pays for consumption of resources (disk space, virtual local area networks, etc.). A data center is a facility used to house computer systems to provide IaaS. Large data centers consume a lot of electricity (high power consumption) and are a source of environmental pollution and costs, so it is important to improve their performance. In this paper a fuzzy rule-based system is proposed to schedule virtual machines in a data center based on Green Computing concepts: minimum power consumption as performance index is considered. This approach is compared to classic scheduling algorithms in literature.

1 Introduction

Cloud computing is an emerging paradigm than provides computational capabilities for the solving of large-scale problems in science and engineering. A cloud is made up of a set of heterogeneous resources, interconnected through high speed networks that cooperate together. A major challenge is a efficient assignment of virtual machines and jobs (called cloudlets) to existing resources. This paper presents an algorithm based on fuzzy rule-based systems (FRBSs) to allocate virtual machines in different hosts housed in a datacenter. This system incorporates knowledge in the form of IF-THEN fuzzy rules and fuzzy sets [1]. The selected optimization criteria is minimum power consumption, for reducing ambiental pollution and electric consumption costs. Distributed power management principles and allocation of virtual machines on different hosts with better ratios in MIPS, CPU utilization, instant power host and maximun power and utilization after allocation new virtual machines are used.

This paper is organized as follows. Section 2 establishes some background. Section 3 formally introduces the proposed FRBS algorithm. In Section 4, simulations and results are shown and finally in Section 5 we conclude with final remarks and conclusions.

2 Background

Many static and dynamic scheduling heuristics have been proposed to scheduling a set of virtual machines and cloudlets on datacenters. Braun et al. [2] compare a wide range of static scheduling strategies extensively used in heterogeneous computing environments. FRBSs have proved a high accuracy in their decisions on the basis of the features describing the controlled system and their acquired knowledge. Many applications use FRBSs in diverse areas as modeling of traffic flow [3], connection admission in ATM networks [4], speech/music discrimination [5] and scheduling [6][7]. These systems are proposed in this work for improving the scheduling process in cloud computing datacenters.

The complex optimization problem of virtual machines and cloudlets scheduling on datacenters requires several criteria to be considered. The optimization of power consumption with FRBSs is considered in this work. A scheduler or broker that uses dynamic inputs for the fuzzy system, thus characterizing the system state, to schedule virtual machines in a data center based on Green Computing concepts is presented. This type of optimization has been studied in previous works [8] as:

- Beloglazov [9] proposes a scheduler that reduces operating costs and provides quality of service. It considers resource utilization, virtual network topologies established and temperature states of the nodes.
- Duy et al. [10] implement a scheduling algorithm based on neural networks to optimize the datacenter power consumption. It predicts future workload based on demand and turns off of servers, minimizing the number of running servers.
- Berl et al. [11] review the use of methods for reducing power consumption based on hardware (i.e., enery control centers) and infraestructure for large scale networks.

3 Proposed Algorithm

The algorithm proposed in this work uses a FRBS [1]. It handles computing clouds consisting of datacenters, assuming that all centers are in the same cloud and made up of heterogeneous machines. It dynamically checks the processing needs and optimizes energy consumption. Every datacenter has a dedicated server called broker wich allocates virtual machines in datacenter hosts using this algorithm.

We formulate the scheduling problem as the allocation of a set V of virual machines $\{V_{m1}, V_{m2}, \ldots, V_{mn}\}$ to a set of heterogeneous and distributed hosts within a data center DC following a scheduling criteria. We seek for scheduling strategies to optimize energy consuption (performance criteria). In addition, the features that allow the classification of all the possible scheduling conditions must be defined. Datacenter current utilization inputs can be summarized as follows:

1. *Available MIPS (mips)*. It represents the number of free MIPS in each host.
2. *Host Power (pow)*. It gets the instant host power.
3. *Utilization Of Cpu (cputil)*. It denotes free MIPS ratio of a host. It is defined as:

$$utilizationOfCpu = 1 - \frac{host.getAvailableMips()}{host.getTotalMips()} \qquad (1)$$

where getTotalMips() gets total MIPS and getAvailableMips() free MIPS.
4. *Max Utilization After Allocation (ualloc)*. It provides the power after allocation.
5. *Power after allocation (palloc)*. It is the host power after allocation.

3.1 Fuzzy Rule-Based Scheduler

In Fig. 1 the organization of the fuzzy rule-based scheduler is shown. It is made up of four entities, i.e., the Fuzzification Interface, the Knowledge Base, the Inference Engine and the Defuzzification Interface, following the general schema of FRBSs [1]. As shown, the fuzzy system is based on the Mamdani model [1] and the coding schemes are adjusted from the studies of Juang [12]. It is distinguished by a set of rules or knowledge representation and by the specification of some concepts associated to the reasoning strategy. A rule R_i is made up of antecedents and consequents and follows Mamdani definition of rules [13]:

$$R_i = if \ \omega_1 \ is \ A_{1n} \ and/or \ \ldots \ \omega_m \ is \ A_{mn} \ then \ y \ is \ B_n \qquad (2)$$

where ω_m is a system feature (mips,pow,cputil,ualloc,palloc), y is the output variable and A_{mn} and B_n represent fuzzy sets related to feature m and output, respectively, each considering n possible sets. The conditional component corresponds to the rule activation conditions whereas the consequent part reflects the associated broker response. A complete rule base must consider a set of rules capable to address every system situation. For the proposed model, every feature ω is designed by three Gaussian membership functions (GMFs):

$$g_i^{(\omega)}(x) = \frac{1}{\sigma_i^{(\omega)}\sqrt{2\pi}} \exp\left\{\frac{-(x-\mu_i^{(\omega)})^2}{2\sigma_i^{(\omega)2}}\right\} \left\{x \in \mathbb{R}^+ \mid x \le 1\right\} \qquad (3)$$
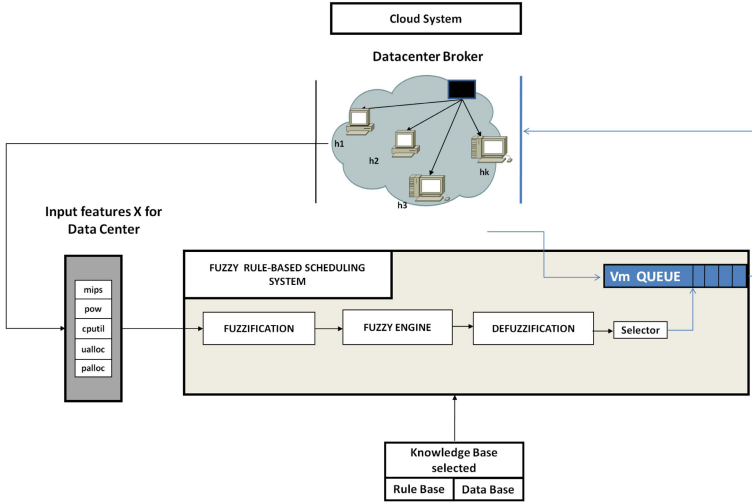
Fig. 1. Fuzzy rule-based system scheduler

Every feature ω for each rule R_i is described by means of two values, $\mu_i^{(\omega)}$ and $\sigma_i^{(\omega)}$. In this work we characterize the system state by five different inputs and so the number of features N_F is set to this value. Fig. 2 shows the normalized GMFs used for every feature. Every input feature is characterized by three membership functions, representing the low, medium and high fuzzy sets. The output of the fuzzy system is representd by five fuzzy sets: very low, low, medium, high and very high. The aggregation of the consequents of the activated rules let in the final output decision making. For a given system state the superposition of the output parts of all rules is calculated in order to obtain the general output decision. The degree of membership for all rules and all features is estimated. Centroid method is then applied in defuzzification in order to obtain the final controller output decision [14]. Two fuzzy rule set or rule bases are used in our approach, one for medium scale datacenters
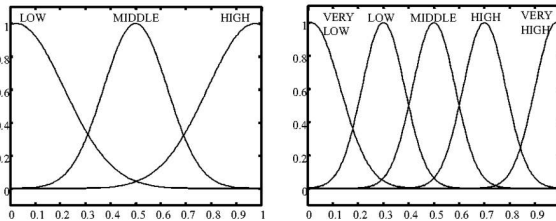
Fig. 2. Gaussian membership functions

and other for large scale. The expert systems are highly dependent on their knowledge, and it is important to adapt this knowledge for each situation, if it involves qualitative/quantitative changes (medium or large scale). They are shown in equations (4) (5) and they can be easily interpreted.

$$MEDIUM\ DATACENTERS$$

$$
\begin{aligned}
R_1 =& If\ (mips\ is\ not\ high)\ or\ (pow\ is\ not\ low)\ or\ (cputil\ is\ not\ middle) \\
& or\ (utilalloc\ is\ middle)\ then\ out\ is\ veryhigh \\
R_2 =& If\ (mips\ is\ low)\ or\ (pow\ is\ not\ middle)\ or\ (cputil\ is\ not\ low) \\
& or\ (utilalloc\ is\ low)\ or\ (powalloc\ is\ not\ middle)\ then\ out\ is\ high \\
R_3 =& If\ (pow\ is\ low)\ and\ (cputil\ is\ high)\ and\ (utilalloc\ is\ middle) \\
& and\ (powalloc\ is\ not\ low)\ then\ out\ is\ high \\
R_4 =& If\ (mips\ is\ not\ high)\ or\ (pow\ is\ low)\ or\ (cputil\ is\ not\ middle) \\
& or\ (utilalloc\ is\ not\ low)\ or\ (powalloc\ is\ not\ low)\ then\ out\ is\ not\ veryhigh \\
R_5 =& If\ (cputil\ is\ middle)\ or\ (utilalloc\ is\ middle)\ or\ (powalloc\ is\ low) \\
& then\ out\ is\ not\ verylow
\end{aligned}
\tag{4}
$$

$$LARGE\ DATACENTERS$$

$$
\begin{aligned}
R_1 =& If\ (mips\ is\ middle)\ or\ (cputil\ is\ middle)\ or\ (utilalloc\ is\ high) \\
& or\ (powalloc\ is\ high)\ then\ out\ is\ not\ middle \\
R_2 =& If\ (mips\ is\ middle)\ and\ (pow\ is\ not\ middle)\ and\ (cputil\ is\ middle) \\
& and\ (powalloc\ is\ low)\ then\ out\ is\ not\ middle \\
R_3 =& If\ (mips\ is\ not\ low)\ and\ (pow\ is\ high)\ and\ (utilalloc\ is\ not\ middle) \\
& and\ (powalloc\ is\ middle)\ then\ out\ is\ middle
\end{aligned}
\tag{5}
$$

4   Simulation Results

Several tests have been conducted to evaluate the proposed allocator algorithm. The algorithm performance have been evaluated with CloudSim [15] and RealCloudSim [16]. CloudSim is a a framework for modeling and simulation of cloud computing infrastructures and services. RealCloudSim is a simulator of allocations of virtual machines based on the main engine of the CloudSim project. RealCloudSim provides a interface to read network topologies based on the BRITE format [17].

The cloud scenario consists of both medium and large datacenters with heterogeneus hosts. The medium datacenter is made up of 100 hosts and 250 virtual machines. For the large one, 1000 hosts and 2500 virtual machines are considered. Datacenter integrates x86 architecture, Xen as virtual machine monitor and Linux as operating system. Each host has a single PE (processing entity) and available MIPS can be 1000, 1500, 2000, 2500 or 3000 (following a round robin distribution) as presented in Guimaraes et al. [8].

Table 1. Example of hosts configuration (Mips/watts)

Host	H_1	H_2	H_3	H_4	H_5
Mips	1000	1500	2000	2500	3000
Power	200	250	300	350	200

The power consumption for every host follows a round robin distribution with values 200, 250, 300 or 350 watts. An example is shown in Table 1. Virtual machines have a number of MIPS equal to: 1000, 750 and 500 (round robin). A number of instructions are needed to process each cloudlet in a virtual machine, the values follows a round robin distribution as: 150,000, 200,000, 100,000 and 25,000. An example is shown in Table 2.

Table 2. Example of virtual machines configuration

Vm	Vm_1	Vm_2	Vm_3	Vm_4	Vm_5
Mips	1000	750	500	1000	750
Instructions	150,000	200,000	100,000	25,000	150,000

For testing process, energy power consuption performance E_c is considered. The results of simulation are compared with other literature classic scheduling algorithms: *Round Robin* (RR), *Best resource selection* (BRS), *Minimum Power Diff* (MPD), *MinMin*, *Maxmin* and *Sufferage* [18][19]. In the Round Robin algorithm, each virtual machine is allocated in a different host, making a cycle. Hosts that cannot allocate virtual machines are skipped. In the Best Resource Selection algorithm, the host with the highest MIPS in use divide MIPS ratio is allocated. In Minimum Power Diff each incoming virtual machine is allocated to the host which will consume less energy. MinMin allocates virtual machine in the host with minimun power after allocation. MaxMin allocates virtual machine in the host with maximum power after allocation. The Sufferage heuristic is based on the idea that better mappings can be generated by assigning a virtual machine to a host that would *suffer* most in terms of expected power consuption if that particular virtual machine is not assigned to it. Table 3 presents an energy power consumption comparison between these algorithms, compared to the algorithm proposed in this work. Results suggest that FRBS performs better in large-scale environments. It is shown that FRBS scheduler achieves the best performance in terms of power consumption in comparison to the rest of strategies. It improves MPD (Minimum Power Difference) by 2.4% and outperforms BRS (Best Resource Selection) by 2.9% for medium datacenters.

Table 3. Scheduling strategies results (kWh) for FRBS, RR, BRS, MPD, MinMin, MaxMin and Sufferage

Datacenter	FRBS	RR	BRS	MPD	MinMin	MaxMin	Suffer
Medium	6.378	6.990	6.569	6.531	6.531	6.569	6.531
Large	67.350	69.132	70.660	67.986	67.986	68.368	67.986

For large datacenters and high virtual machines allocation, it improves MPD 1% and nearly 4% BRS. Thereby, the proposed strategy can be a competitive algorithm in heterogeneus datacenters.

5   Conclusions

Large data centers make use of a lot of electricity due to the required high power consumption for their performance. Since they are a source of air pollution and other eviromental problems and high companies costs, it is relevant to increase their efficiency in electricity management. In this work a scheduling algorithm for cloud computing has been presented. It uses a FRBS system for scheduling in homogeneus and heterogeneus datacenters and reduces power consumption. Results indicate that a FRBS scheduler achives better performance in terms of power consumption in comparasion to classic scheduling algorithms: it reduces consumption by 2.4% and 1% with respect to the best of its competitors in medium and large datacenters, respectively, and thus, it arises as a competitive green scheduling strategy for cloud computing.

References

1. Cordon, O., Herrera, F., Hoffmann, F., Magdalena, L.: Genetic fuzzy systems: Evolutionary tuning and learning of fuzzy knowledge bases. World Scientific Pub. Co. Inc. (2001)
2. Braun, T.D., Siegel, H.J., Beck, N., Bölöni, L.L., Maheswaran, M., Reuther, A.I., ... Freund, R.F.: A comparison of eleven static heuristics for mapping a class of independent tasks onto heterogeneous distributed computing systems. Journal of Parallel and Distributed Computing 61(6), 810–837 (2001)
3. Quek, C., Pasquier, M., Lim, B.: A novel self-organizing fuzzy rule-based system for modelling traffic flow behaviour. Expert Syst. Appl. 36(10), 12167–12178 (2009)

4. Cheong, F., Lai, R.: Connection admission control of mpeg streams in atm network using hierarchical fuzzy logic controller. Eng. Appl. Artif. Intell. 22(1), 117–128 (2009)

5. Munnoz-Exposito, J.E., García-Galán, S., Ruiz-Reyes, N., Vera-Candeas, P.: Adaptive network-based fuzzy inference system vs. other classification algorithms for warped lpc-based speech/music discrimination. Eng. Appl. Artif. Intell. 20(6), 783–793 (2007)

6. Franke, C., Hoffmann, F., Lepping, J., Schwiegelshohn, U.: Development of scheduling strategies with Genetic Fuzzy systems. Appl. Soft Comput. 8(1), 706–721 (2008)

7. Prado, R.P., García Galán, S., Yuste, A.J., Muñoz Expósito, J.E., Sánchez Santiago, A.J., Bruque, S.: Evolutionary Fuzzy Scheduler for Grid Computing. In: Cabestany, J., Sandoval, F., Prieto, A., Corchado, J.M. (eds.) IWANN 2009, Part I. LNCS, vol. 5517, pp. 286–293. Springer, Heidelberg (2009)

8. Guimaraes, D., Madeira, E., Bittencour, L.F.: Power-Aware Virtual Machine Scheduling on Clouds Using Active Cooling Control and DVFS. In: MGC 2011, Lisbon, Portugal (2011)

9. Beloglazov, A., Buyya, R.: Energy Efficient Resource Management in Virtualized Cloud Data Centers. In: 10th IEEE/ACM International Conference on Cluster, Cloud and Grid Computing (2010)

10. Duy, T., Inoguchi, Y.: Performance Evaluation of a Green Scheduling Algorithm for Energy Savings in Cloud Computing. In: 2010 IEEE International Symposium on Parallel and Distributed Processing, IPDPSW (2010)

11. Berl, A., et al.: Energy Efficient Cloud Computing. University of Passau (2009)

12. Juang, C.F., Lin, J.Y., Lin, C.T.: Genetic reinforcement learning through symbiotic evolution for fuzzy controller design. IEEE Transactions on Systems, Man, and Cybernetics, Part B: Cybernetics 30(2), 290–302 (2000)

13. Mamdani, E., et al.: Application of fuzzy algorithms for control of simple dynamic plant. Procdings of IEEE 121(12), 1585–1588 (1974)

14. Takagi, T., Sugeno, M.: Fuzzy identification of systems and its application to modeling and control. IEEE Transactions on Systems, Man, and Cybernetics 15(1), 116–132 (1985)

15. Buyya, R., Ranjan, R., Calheiros, R.N.: Modeling and simulation of scalable Cloud computing environments and the CloudSim toolkit: Challenges and opportunities. In: International Conference on High Performance Computing & Simulation, HPCS 2009, pp. 1–11. IEEE (June 2009)

16. Rocha, L.R.: REALcloudSim cloud cimulator (2013), http://sourceforge.net/projects/realcloudsim/

17. Medina, A., Lakhina, A., Matta, I., Byers, J.: BRITE: Universal Topology Generation from a User's Perspective (2001), http://www.cs.bu.edu/brite/user_manual/

18. Freund, R.F., et al.: Scheduling resources in multiuser, heterogeneous, computing environments with SmartNet. In: Proceedings of the Heterogeneous Computing Workshop, HCW 1998, pp. 184–199 (1998)

19. Maheswaran, M., Ali, S., Siegal, H.J., Hensgen, D., Freund, R.F.: Dynamic matching and scheduling of a class of independent tasks onto heterogeneous computing systems. In: Proceedings of the Heterogeneous Computing Workshop (HCW 1999), pp. 30–44 (1999)

A Scalable Distributed Architecture for Emulating Unreliable Networks for Testing Multimedia Systems

Marek Parfieniuk, Tomasz Łukaszuk, and Tomasz Grześ

Bialystok University of Technology,
Wiejska 45A, 15-351 Bialystok, Poland
`m.parfieniuk@pb.edu.pl`

Summary. This paper presents a software-based approach to emulating unreliable WAN networks in a LAN environment, without interfering in the configuration of the latter. A program must only be installed on all computers which host a multimedia system to be tested, which intercepts outgoing packets and forwards them to an emulation proxy, where, in accordance with a connection model, they are rejected or delayed before being submitted to the destination computer. The proxy collects packet header data, supplemented with timestamps, and sends them to a warehouse server which stores the report about the network traffic of the tested application. By analyzing such reports and observing how programs react to packet losses and delays, multimedia systems can be evaluated for correctness, performance, and tolerance to network failures. Using the Java and C programming languages, a prototype of such an emulation architecture has been implemented together with GUI-based tools for modeling connections, supervising experiments, and analyzing traffic reports.

1   Introduction

For about 15 years a significant research effort has been devoted to the development of algorithms for image and video coding that produce data representations that are not only compact but also are well suited to network transmission [1]. Such algorithms are multiple description coding (MDC), scalable coding, distributed coding, and forward error correction (FEC), which protect data against packet losses or allow for adjusting bitstreams to capabilities of networks and user terminals. On the other hand, architectures for image retrieval and video streaming have evolved from the straightforward client-server configuration to accelerated multitier schemes, peer-to-peer systems, and content delivery networks, in which data replication and caching,

load balancing, parallelism, and path diversity are used to achieve high performance and reliability.

Testing such advanced algorithms and architectures is difficult but is often necessary to prove their correctness, to measure their performance, and to evaluate their robustness to network failures. A widely accepted method of testing network applications is emulation [2], which is less abstract and less computationally demanding than simulation, and more flexible and more economical than building a test network. A variety of emulators have been developed over the years [3, 4, 5, 6, 7], as networks can be emulated in different ways, and there is no optimal solution.

Working on image coding for network applications, we need an emulation tool, but none of existing emulators satisfies our needs. Most of them were written for only one operating system, they do not scale easily to tests with a dozen or so clients and servers, and they are difficult to use. In particular, some solutions require network devices or LAN topology to be reconfigured, and no solution seamlessly combines emulation with traffic logging and analysis. Thus, we decided to develop our own solution, which would be tailored to our needs.

The aim of this paper is to present its architecture and properties. We managed to overcome all the aforementioned shortcomings, as our emulator works on both Windows and Linux, can be set up without changing the LAN infrastructure, is able to handle many end-hosts, provides graphical user interface (GUI), and supports network traffic reporting. Its drawbacks are that our network model is simple, and that packets cannot be delayed very accurately. Nevertheless, the system is pragmatic and allows for performing many practical tests of network applications, especially when a qualitative rather than quantitative approach to the quality-of-service (QoS) is satisfactory.

Our emulator has been developed as a part of the TEWI project, whose aim is to create a diverse software-hardware platform for scientific research. On the other hand, we plan to use the system to teach students advanced networking concepts and principles of multimedia communications.

2   Distributed Architecture for Network Emulation

Our approach to network emulation is explained in fig. 1. It is based on interception of Ethernet frames, which is essentially equivalent to intercepting IP packets. For this purpose, an agent software has been developed that must be installed on every computer that hosts a component of a multimedia system to be tested. The agent hooks into the network protocol stack and intercepts only outgoing frames whose destination is another application host. Every intercepted frame is encapsulated into a separate UDP packet, which is sent to an emulation proxy. The proxy rejects the frame or delays it before submitting it to the destination host. The decision is made, and the delay is determined, based on the IP header data and on the link model that has been

assigned to the virtual connection between the source and destination hosts. When agents are installed on all hosts, the entire network traffic related to a multimedia system can be passed through proxies, which emulate an unreliable WAN network.

Obviously, the accuracy of delay emulation is limited by the delays related to passing packets by the proxy and to frame processing by both agent and proxy. However, the unavoidable delay is not large, of order of dozen or so milliseconds, provided that the components of the emulator run on modern computers that reside in the same LAN network and are interconnected using a fast network switch, and no other systems burden the network. If a proxy is overloaded, then more proxies can be added, so our architecture is scalable.

Both agents and proxies are controlled using a supervisor program, which also provides a graphical user interface for modeling unreliable networks. The main window of the supervisor is shown in fig. 2(a).

Communication among emulator components is based on binary messages, which are transferred using the UDP protocol. We have defined about thirty types of messages, which can carry control commands, status information, or configuration data. Even though we assume that packets cannot be lost in LAN environments, we have developed a mechanism of sequential numbering of packets so as to make it possible to detect data losses.

3   Unreliable Network Modeling

In contrast to many existing emulators, our solution uses abstract network models, so that experiments can easily be repeated using different hardware. Network modeling begins with defining virtual hosts, and then for each pair of hosts the link between them needs to be characterized. By assigning descriptive identifiers to hosts and by consistently using some pre- or postfixes in the identifiers, emulator users can make identification of a host or a group of hosts easier than in the case of using IP addresses and subnet masks, which is often required by the existing emulators.

Before running emulation, the user must associate the identifiers with real computers on which the agent software works. He also must assign an emulation proxy to each of the computers. Knowing how the logical network is mapped onto physical devices, the supervisor is able to sent configuration data to agents and proxies. There is no need for changing physical connections among the devices.

The link model is shown in fig. 3 as a relational database schema. In our approach, both delay and loss probability, which characterize a link, can vary during emulation in accordance with a given schedule. The schedule comprises one or more time slots each of which determines how long a particular delay or loss pattern should be emulated by a proxy before switching to the next pattern. This allows users to naturally and easily model dynamic networks, in which connection links can fade, recover, or change their characteristics.

(a)

(b)
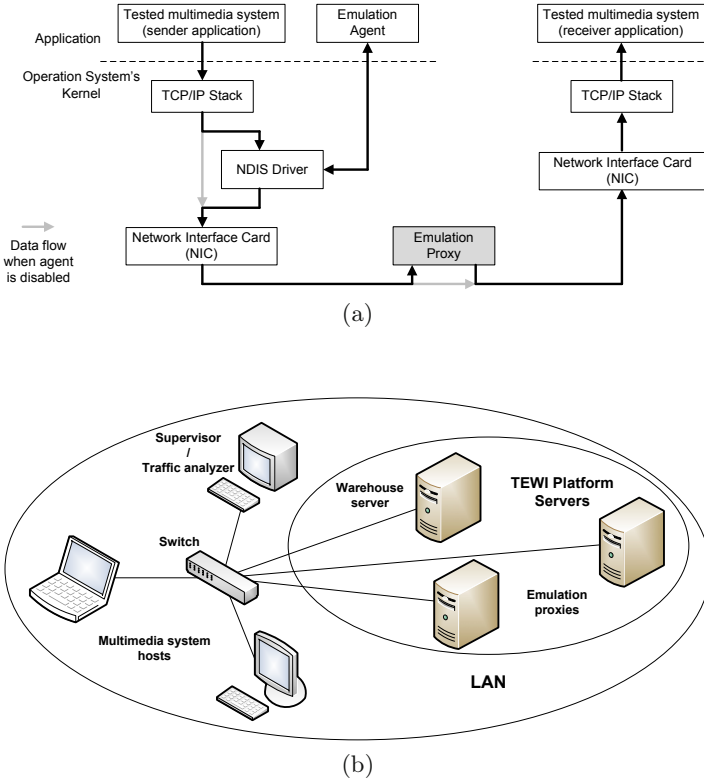
Fig. 1. The proposed architecture for network emulation: (a) the essential data flow and (b) system setup

In most of the existing emulators, this can be achieved by reconfiguring them during experiments. If there are many hosts, or many parameters must be changed, it may be too slow or too laborious to do this using GUI. Usually, a user needs to learn a mechanism for programmatically controlling an emulator, to write scripts, and to run them at the appropriate times. Even using programmatic control, it is usually impossible to reconfigure several links or parameters simultaneously, even approximately, as reconfiguration commands are sent and processed sequentially.

In our approach, the proxy knows in advance what it has to do during emulation and switches link models on its own in appropriate moments. This allows users to conveniently define many practical test scenarios, even though interactive experiments are impossible. Even more advanced tests could be performed after extending the agent software so as to allow it to run applications on hosts in accordance with a given schedule. This would allow
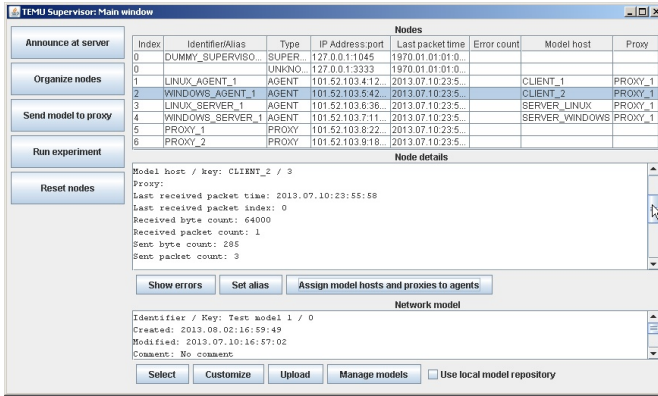
(a)
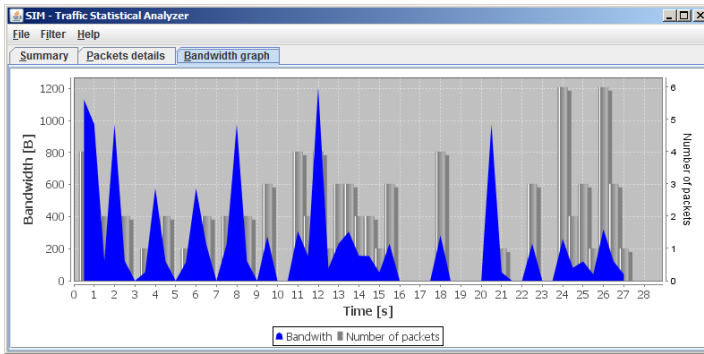
(b)

Fig. 2. The graphical user interface of (a) the supervisor and (b) traffic analyzer

users to easily compare how different configurations of a multimedia system behave.

Network models are stored using the SQLite engine for local databases. By incorporating database management into our programs, we have reduced the number of the servers that must be installed in order to set up an emulation environment. Similarly, a HTTP server has been built into the warehouse server, so as to have only one piece of software that hosts network models, traffic reports, and the website that supports emulator users by providing the documentation and executable files.

4 Traffic Logging and Analysis

The supervisor, agents, and proxies implement emulation clocks, which are synchronized up to milliseconds using mechanisms inspired by the Network
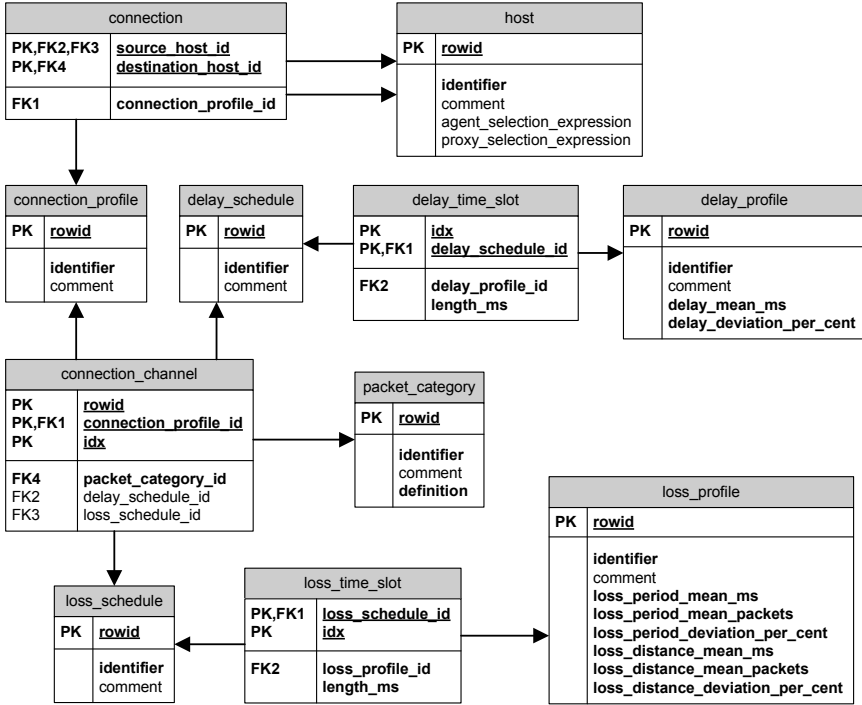
Fig. 3. The relational database schema used for modeling unreliable networks

Time Protocol (NTP) [8]. The clocks allow for attaching timestamps to a packet when it is intercepted by an agent, sent to a proxy, received by the proxy, and sent to the destination host. After processing every packet, the proxy constructs a log record from these timestamps and packet header data (size, protocol, source/destination hosts/ports) and puts the record into a buffer. When the buffer is full or an emulation task is finished, the buffer content is sent to the warehouse server which stores reports of experiments. A report comprises not only log records, but also the abstract network model, and the information how that model was mapped on real computers that were used in the experiment.

About 30 bytes of log data per Ethernet frame are transmitted and saved, so if the Maximum Transmission Unit (MTU) is about 1500 bytes, as in most LANs, then only one log frame must be sent for every 50 frames processed by a proxy. Thus, the related data flow does not much affect the network and emulation performance, and even for long lasting emulation experiments, reports do not take up much space on server disks.

For performance reasons, the traffic log can be analyzed only after finishing emulation. The application for this purpose provides rich GUI as demonstrated in fig. 2(b). It allows users to retrieve the data of interest from the warehouse server, and then to present traffic statistics in tables and plots.

5   Implementation Details

All our applications are multithreaded programs and use shared memory and queues to pass data among threads. The project source code comprises about 200 classes. The agent software have been developed using the C++ programming language, whereas the remaining components of our emulator have been implemented in Java. Some additional libraries have been used: JFreeChart to draw plots, JNetPCAP to inject packets that leave proxies, and SQLite4Java to manage network model databases.

For Windows, packet interception requires low-level network driver programming in accordance with the Network Driver Interface Specification (NDIS). We plan to write our own NDIS driver in the near future, but in order to speed up the development, the prototype agent has been implemented using WinpkFilter. This high-performance packet filtering framework for Windows allows developers to create applications that efficiently analyze and modify raw network packets without having to write low-level driver code.

It is much easier to intercept Ethernet frames on Linux, as this operating system provides the "'iptables"' command for filtering, redirecting, and queuing packets as necessary. This command controls the "'netfilter"' framework, which has been a part of the Linux kernel since version 2.4.

6   Conclusions

Several usage scenarios have been developed that are aimed at both testing and demonstrating the emulator as well as at teaching students some concepts related to multimedia communications. The most notable scenarios are related to TCP congestion control and to video streaming using the VLC/Videolan software.

Preliminary experiments showed that our architecture is practically useful, and that the emulation performance and accuracy of its prototype implementation are satisfactory if an application test to be performed is not very sophisticated. On the other hand, the built-in traffic logging and analysis make experiments easy. Finally, GUI tools we have developed allow users to conveniently model networks, configure emulation tasks, and analyze empirical results.

Subjects for future works are to implement the proxy using an FPGA device or a network processor, and to develop the agent software for mobile devices running the Android operating system.

References

1. Chou, P.A., van der Schaar, M.: Multimedia over IP and wireless networks: compression, networking, and systems. Elsevier/Academic Press, Amsterdam
2. Blum, R.: Network Performance Open Source Toolkit: Using Netperf, tcptrace, NIST Net, and SSFNet. Wiley, Indianapolis (2003)
3. Nussbaum, L., Richard, O.: A comparative study of network link emulators. In: Proc. 12th Communications and Networking Simulation Symp. (CNS)/Spring Simulation Multiconference (SpringSim), San Diego, CA (2009)
4. Landsiedel, O., Kunz, G., Götz, S., Wehrle, K.: A virtual platform for network experimentation. In: Proc. 1st ACM Workshop on Virtualized Infrastructure Systems and Architectures (VISA), New York, NY, pp. 45–52 (2009)
5. Kalita, H., Nambiar, M.: Designing WANEM: A wide area network emulator tool. In: Proc. 3rd Int. Conf. Communication Systems and Networks (COM-SNETS), Bangalore, India, pp. 1–4 (2011)
6. Zheng, P., Ni, L.: Experiences in building a scalable distributed network emulation system. In: Proc. 9th Int. Conf. Parallel and Distributed Systems (ICPADS), Taiwan, China, pp. 189–194 (2002)
7. Alsaeed, M., Speirs, N.: A wide area network emulator for CORBA applications. In: Proc. 10th IEEE Int. Symp. Object and Component-Oriented Real-Time Distributed Computing (ISORC), Santorini Island, Greece, pp. 359–364 (2007)
8. Mills, D.: Computer network time synchronization: the Network Time Protocol. CRC Press, Boca Raton (2006)

An Algorithm for Finding Shortest Path Tree Using Ant Colony Optimization Metaheuristic

Mariusz Głąbowski, Bartosz Musznicki,
Przemysław Nowak, and Piotr Zwierzykowski

Poznań University of Technology, Faculty of Electronics and Telecommunications
Chair of Communication and Computer Networks, Poznań, Poland
`bartosz@musznicki.com, przemyslaw.nowak@inbox.com`

Summary. This paper introduces the ShortestPathTreeACO algorithm designed for finding near-optimal and optimal solutions for the shortest path tree problem. The algorithm is based on Ant Colony Optimization metaheuristic, and therefore it is of significant importance to choose proper operation parameters that guarantee the results of required quality. The operation of the algorithm is explained in relation to the pseudocode introduced in the paper. An exemplary execution of the algorithm is depicted and discussed on a step-by-step basis. The experiments carried out within the custom-made framework of the experiment are the source of suggestions concerning the parameter values. The influence of the choice of the number of ants and the pheromone evaporation speed is investigated. The quality of generated solutions is addressed, as well as the issues of execution time.

1 Introduction

This article aims at presenting available possibilities of application of the Ant Colony Optimization (ACO) technique in finding the Shortest Path Tree (SPT) as a novel technique and alternative to the methods based on conventional algorithms for finding the shortest path such as the Dijkstra's or Bellman-Ford algorithm [1]. It should be stressed that the Ant Colony Optimization metaheuristic has been constructed to seek solutions of $\mathcal{NP}$-hard problems [2]. As such, there is thus no guarantee that the most optimum solution will be always found. Therefore, the obtained results may be both optimal (accurate) and approximations that depend on the degree of fitness of the algorithm itself for each individual problem to be solved. Therefore, it is crucial to first analyse a given task and to properly select the operations running parameters to be executed and to perform their optimization. Having carried out many research studies and tests, the authors have eventually

established and chosen appropriate parameters, methods and ways that prove to be the most effective in solving a given specific problem.

The two following subsections of the article present the base algorithm and define the problem of the shortest path tree. Section 2 provides a presentation of the proposed algorithm, discusses its pseudocode, as well as discusses its operation based on an example of a selected graph. Then, in Section 3, the authors present the results of the simulation study of the operation of the algorithm. The first subsection is focused at the percentage of correct solutions, while the second subsection discusses the duration of operation of the algorithm. Final remarks and conclusions are presented in the summary.

1.1 *ShortestPathACO Algorithm*

The *ShortestPathACO* algorithm is a method and a set of recommendations to ensure that the Ant Colony Optimization metaheuristic for solving the shortest path problem is properly applied. A detailed introduction to the methodology, discussion on the context and methods for finding paths, as well as a discussion on the classes of parameters and the methods for updating pheromones, are introduced by the authors in [3]. The subsequent paper [4] presents a thorough analysis of the *ShortestPathACO* based strategy to find the shortest path between two nodes.

1.2 *Shortest Path Tree Problem*

It can be proved [5, 6] that the shortest paths from one vertex of a graph to all of the remaining vertices create a shortest paths tree. A characteristic feature of this tree is the fact that its root is formed from the initial (source) vertex, all of its edges are directed in the direction opposite to the vertex, and each path that can be created from the initial vertex to any other vertex is the shortest path to this vertex. By having the vector $d = \{d_i : i \in \mathcal{N}\}$, whose each element d_i is called *vertex label* and takes on numerical values or is equal to infinity and denotes the shortest distance between a given vertex and the initial vertex, we are in position to create this tree. All labels, however, have to satisfy the following conditions called *Bellman's Equation* [7]:

$$d_s = 0 \tag{1a}$$

and

$$d_j = \min_{(i,j)\in\mathcal{A}} \{d_i + a_{ij}\}, \qquad \forall \, j \neq s \tag{1b}$$

The solution for the problem of finding the shortest path tree in a graph finds most of its recent applications in different demanding applications that are based upon multicast routing in communication networks [8, 9, 10, 11].

2 The Application of the ShortestPathACO Algorithm for Finding the Shortest Path Tree

Using the *ShortestPathACO* algorithm, the *ShortestPathTreeACO* algorithm has been developed – an algorithm that aims at constructing the shortest path tree. In this way, the Single-Source Shortest Paths problem (SSSP), related to finding the shortest paths from a single initial node to all other nodes in a weighted graph [5], is solved at the same time. Thanks to a construction of the shortest path tree it is not necessary to find the shortest paths from the source to all of the nodes one by one, but only to such nodes that have not yet been included in the tree. By taking this kind of approach to a solution of the single-source problem, we obtain full and extensive information on the shortest paths but with a lower number of operational counts and initiations of the *ShortestPathACO* algorithm.

Data: $\mathcal{G} = (\mathcal{N}, \mathcal{A})$ – graph, a – edge cost vector, s – initial node, t – end node, m – the number of ants, α – the parameter that defines the influence of pheromones on the choice of the next node, β – parameter that determines the influence of remaining data on the choice of the next node, ρ – parameter that determines the speed at which evaporation of the pheromone trail occurs; takes on values from the interval $\langle 0, 1 \rangle$, τ_0 – initial level of pheromones on the edges, τ_{min} – the minimum acceptable level of pheromones on edges, τ_{max} – maximum acceptable level of pheromones on edges, $iteration\_limit$ – the limit of ShortestPathACO iterations

Result: d – vector of labels, $pred$ – vector of predecessors

foreach $i \in \mathcal{N}$ **do**
> $d_i \leftarrow +\infty$;
> $pred_i \leftarrow 0$;

end
$d_s \leftarrow 0$;
$remaining \leftarrow N - 1$;
$t \leftarrow N$;
while $remaining > 0$ **do**
>   **while** $d_t \neq +\infty$ **and** $t > 1$ **do**
>> $t \leftarrow t - 1$;
>
>   **end**
>   **if** $t > 1$ **then**
>> $path, length \leftarrow$
>> $\texttt{ShortestPathACO}(\mathcal{G}, a, s, t, m, \alpha, \beta, \rho, \tau_0, \tau_{min}, \tau_{max}, iteration\_limit)$;
>> $current\_length \leftarrow 0$;
>>   **foreach** $(i, j) \in path$ **do**
>>> $current\_length \leftarrow current\_length + a_{ij}$;
>>>   **if** $d_j > current\_length$ **then**
>>>>   **if** $d_j = +\infty$ **then**
>>>>> $remaining \leftarrow remaining - 1$;
>>>>
>>>>   **end**
>>>> $d_j \leftarrow current\_length$;
>>>> $pred_j \leftarrow i$;
>>>
>>>   **end**
>>
>>   **end**
>
>   **end**

end

Algorithm 1. ShortestPathTreeACO Algorithm

2.1 Pseudo-code and a Discussion on the Algorithm

The operation of the *ShortestPathTreeACO* algorithm is based on the iterative implementation of the *ShortestPathACO* algorithm with a variable value of the parameter t. At the beginning, the variables d and *pred* are initiated. The variables are responsible for respectively storing the vector for the labels of vertices (the length of the shortest path from the initial node to a given node) and for memorization of the vector of vertices that have been previously in the path to the initial node. Then, the label of the initial vertex d_s is set to 0, the variable *remaining* to $N - 1$ (this is the number of labels of vertices that are still to be calculated), whereas the variable t is set to the last vertex in the graph.

The remaining operations are performed in the loop for as long as there are any vertices whose labels have not yet been ultimately calculated (the variable *remaining* is greater than 0) available. Initially, the label d_t of vertex t is checked whether it is already set and whether t is greater than 1. Then, the variable t is decreased by 1 until both of the conditions are satisfied. If t is still greater than 1, the next action the algorithm has to perform is to initiate the *ShortestPathACO* algorithm for the current value of the variable t, which results in obtaining a calculated *path* between nodes s and t, as well as its *length*.

The next step is to set an auxiliary variable *current_length* for a given path to 0 and to follow thus obtained path to update the variables d and *pred*. For each edge of the path *path*, the length of this edge is added to the variable *current_length*. Later, only when the label of a vertex in which this edge terminates is greater than the variable mentioned earlier further action is performed. If the label of the vertex in which the current edge terminates has not been set earlier, the variable *remaining* is decreased by 1. Then, this label is set to the current value of the variable *current_length*, while the variable *pred* for this vertex is being set to the vertex from which the considered edge starts.

2.2 Illustration of the Operation of the Algorithm

Fig. 1 shows subsequent steps in an exemplary process of building up the shortest path tree with the help of the *ShortestPathTreeACO* algorithm in the hand-made graph constructed from 10 vertices that were joined together by 19 edges. At each of the stages a partial tree is shown, as well as it is shown what values are taken on by particular parameters before the *ShortestPathACO* algorithm for the operative value t is activated. The edges marked with broken line indicate the elements that belong to SPT.

Fig. 1a shows the state of the graph after the initial stage, i.e., after all actions from the line 1-7 of the 1 algorithm have been executed. All labels of the vertices except the initial vertex *1* are not set, which means that there are 9 vertices to be calculated left. The first vertex to be considered is the

$$d = \begin{bmatrix} 0 & \infty & \infty & \infty & \infty & \infty & \infty & \infty & \infty & \infty \end{bmatrix}$$
$$pred = \begin{bmatrix} 0 & 0 & 0 & 0 & 0 & 0 & 0 & 0 & 0 & 0 \end{bmatrix}$$
$$remaining = 9$$
$$t = 10$$

(a) Step 1

$$d = \begin{bmatrix} 0 & 2 & \infty & 4 & \infty & \infty & 7 & \infty & \infty & 9 \end{bmatrix}$$
$$pred = \begin{bmatrix} 0 & 1 & 0 & 2 & 0 & 0 & 4 & 0 & 0 & 7 \end{bmatrix}$$
$$remaining = 5$$
$$t = 9$$

(b) Step 2

$$d = \begin{bmatrix} 0 & 2 & \infty & 4 & \infty & 7 & 7 & \infty & 8 & 9 \end{bmatrix}$$
$$pred = \begin{bmatrix} 0 & 1 & 0 & 2 & 0 & 4 & 4 & 0 & 6 & 7 \end{bmatrix}$$
$$remaining = 3$$
$$t = 8$$

(c) Step 3

$$d = \begin{bmatrix} 0 & 2 & \infty & 4 & \infty & 7 & 7 & 8 & 8 & 9 \end{bmatrix}$$
$$pred = \begin{bmatrix} 0 & 1 & 0 & 2 & 0 & 4 & 4 & 7 & 6 & 7 \end{bmatrix}$$
$$remaining = 2$$
$$t = 5$$

(d) Step 4

$$d = \begin{bmatrix} 0 & 2 & \infty & 4 & 7 & 7 & 7 & 8 & 8 & 9 \end{bmatrix}$$
$$pred = \begin{bmatrix} 0 & 1 & 0 & 2 & 2 & 4 & 4 & 7 & 6 & 7 \end{bmatrix}$$
$$remaining = 1$$
$$t = 3$$

(e) Step 5

$$d = \begin{bmatrix} 0 & 2 & 4 & 4 & 7 & 7 & 7 & 8 & 8 & 9 \end{bmatrix}$$
$$pred = \begin{bmatrix} 0 & 1 & 1 & 2 & 2 & 4 & 4 & 7 & 6 & 7 \end{bmatrix}$$
$$remaining = 0$$
$$t = 0$$
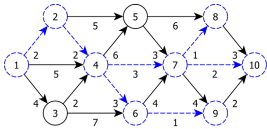
(f) Step 6

Fig. 1. Consecutive steps in the operation of the *ShortestPathTreeACO* algorithm

vertex *10*. After the execution of the first iteration of the main loop of the algorithm, its state is presented in Fig. 1b. The shortest path to vertex *10* has been found and thus to all vertices that are included in it, i.e., vertices *2*, *4* and *7*. There are now 5 vertices without labels left, while the next end vertex will be vertex *9*. The next iteration complements the list of labels *d*

by the next 2 values related to the end vertex *9* and vertex *6*, which is shown in Fig. 1c. Now there are only 3 vertices left that still have to have their labels established. The next end vertex is vertex *8*. In the next 3 iterations the paths to vertices *8*, *5* and *3* are found and the elements of the vector of labels *d* are complemented, while the value of the variable *remaining* is being decreased to 0, which terminates the operation of the algorithm.

In the discussed example, to construct the shortest path tree, and in this way to solve the single-pair shortest path problem, the *ShortestPathACO* algorithm had to be activated 5 times.

3 Study on the Operation of the Algorithm

Exactly as in the study on the general application of the *ShortestPathACO* [3] algorithm, a number of tests was performed to find out whether the solutions given by the *ShortestPathTreeACO* algorithm are correct, as well as to check how the selection of parameters influences the operation of the method in different kinds of graphs. For the discussion in this paper, the hand-constructed graph that is presented in Fig. 1 has been chosen. All the experiments were conducted in a simulation environment prepared using programming language C#. To obtain reliable results, each test was performed 100 times. To diminish the influence of the simulation environment, extreme results were rejected, and then the average values for the remaining results were calculated.

The values of the parameters of the algorithm were the same as during the conducted simulation tests of the *ShortestPathACO* algorithm to find the shortest path between two nodes [4]. Therefore, the values of the parameter α was determined as 1. The value β was adopted here as the one equal to 0.6, since for lower values the algorithm was not capable of finding accurately an optimum solution to the SPT. The parameters τ_0, τ_{min} and τ_{max} were set to 0, 0 and 200, respectively, while the parameter *iteration_limit* was set to 25000. It should be reminded that due to the heuristic nature of ACO-based methods, the values of these parameters are extremely important and in the case of different types of graphs these values should be verified.

In the following subsections we discuss the experiments aimed at verifying the influence of the choice of the number of ants m and of the parameter ρ on the quality of generated solutions and on the execution time of the algorithm. The methodology for the calculation of the quality of a solution was modified. In the case of the *ShortestPathACO* algorithm it was equal to the number of optimal lengths of paths divided by the number of tests performed. This time, taking into consideration the fact that a greater number of paths included in a tree was to be analysed, the quality of solution takes additionally into account the number of properly constructed labels of vertices in relation to the number of vertices. This value, taken from all the tests, was then added up and divided by the number of tests, which means that it is the average of

the results of one test. For example, if the algorithm properly calculates the shortest path for 9 out of 10 vertices, then the quality of solution will amount to 90%. If in the second attempt the number of correct paths decreases to 7, then for the two tests the average of the quality of solution will be 80%, with the standard deviation equal to 10%.

3.1 Percentage of Correct Solutions

The percentage of optimal solutions in relation to the parameters m and ρ can be retraced in Graph 2. In the case of the considered graph, it is already with a small number of ants that the percentage of correct solutions ranges within the boundaries of 70%, while the results for different values of ρ are similar. It should not be forgotten, however, that this value means that for 9 of sought-after paths, for nearly 7 of them the found path was the shortest. In addition, the result is also influenced by the fact that the resulting value is the average for 100 measurements. By watching closely the standard deviation we can observe that with a small number of ants it exceeds even 15% for $\rho = 0.001$. This results from a large differentiation in the obtained results between individual measurements and is tantamount to the fact that during some of the tests the quality of solution dropped below 50%, while on other occasions was well above 90%. Along with the increase in the number of ants the percentage number of correct solutions increases, while the standard deviation decreases, which translates into a decrease in the width of confidence intervals in the obtained results. With 14 ants, or more, all paths that have been found are the shortest paths, whereas the standard deviation is equal to 0, which means that in all attempts the results were the same.
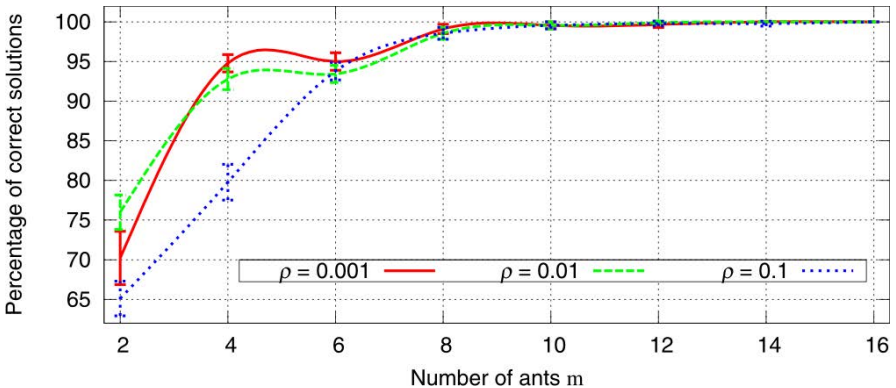
Fig. 2. The quality of generated solutions provided by the *ShortestPathTreeACO* algorithm for the graph from Figure 1 depending on the parameters m and ρ

By analysing the influence of the parameter ρ we can observe that for its higher values, with a small number of ants, the standard deviation takes on higher values, whereas from the number of at least 6 ants the obtained results are remarkably similar for different values of ρ. It is clearly visible that despite the worse results for $\rho = 0.1$ with a small number of ants, after an increase in the number of ants to 6, all three graphs are very similar. With 8 ants, the algorithm approaches 99%, and from the number of 14 ants all found paths are optimal regardless of the number of tests. The data presented in the graph are non-decreasing functions, whereas from a certain threshold, in fact, solid functions.

3.2 Duration of Operation

While analysing the operation times of the algorithm in relation to the parameters m and ρ shown in Graph 3 some interesting dependencies are clearly observable. With a small number of ants, the operation time of the algorithm is very long — considerably longer than that with a substantially higher number of ants. The reason for the above might be the fact that with a small number of ants the time necessary to check as large number of edges as possible prolongs. A colony composed of just 2 ants is not capable of effectively checking available paths, hence the convergence is reached very late. Starting from 4 ants and with $\rho = 0.001$ and $\rho = 0.01$, the operating time of the algorithm stabilizes and increases proportionally to the number of ants. For $\rho = 0.1$, the situation looks quite differently. Despite very similar results for different ρ with 2 ants, from the number of 4 ants, the operation time of the algorithm doubles and drops to an acceptable level with as many as 10 ants. Such results are derived from the fact that the exploration features of
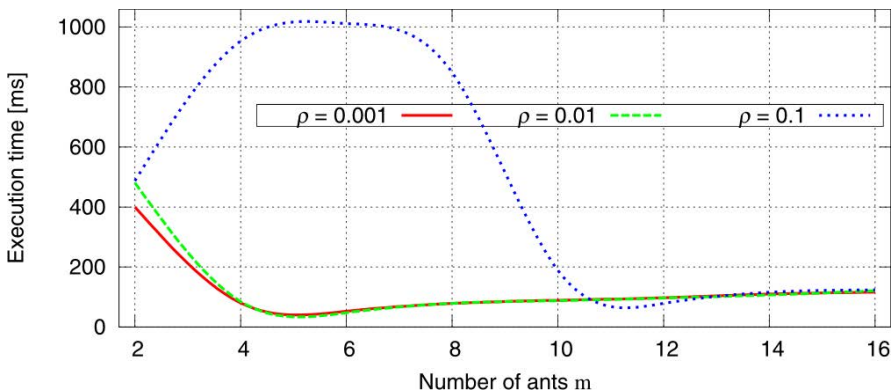
Fig. 3. Execution time of the *ShortestPathTreeACO* algorithm for the graph from Figure 1 depending on the parameters m and ρ

ants become too high. This in turn causes pheromones to be deposited on a great number of edges, while the paths obtained in successive iterations do not repeat, which makes it difficult for the algorithm to reach convergence. From the number of 10 ants, regardless of the value of the parameter ρ, the operation time of the algorithm improves gradually along with the increase in the number of ants.

One can conclude unequivocally from graph 3 that an excessive increase in the value of the value of the parameter ρ may lead to a prolongation of the operation time of the algorithm that ultimately does not improve at all obtained results — as referred to Graph 2.

Taking into consideration both the analysis of the obtained results and the operation time of the algorithm, it is possible to determine that for $\rho = 0.001$ and $\rho = 0.01$ and from the number of about 8 ants, the algorithm performs very well and generates good quality solutions with relatively short time of its operation.

4   Conclusion

The study described in the present article proves that the proposed *Shortest-PathTreeACO* algorithm can be successfully used for constructing the shortest path tree based on the method that has been derived from Ant Colony Optimization metaheuristic. It results from the the simulation tests that, for the graph under consideration, it is possible to establish the minimum value of the number of ants that makes the most optimum solutions obtainable. Any further increase would make no sense because it would only translate into an increase in the operation time of the algorithm and a further demand for calculation resources. The number of ants used cannot though be too small because this leads to an increase in time required for the solution to be found. A similar dependence is observable in the case of the parameter that defines the speed of the evaporation of pheromones.

There is a clear need for a careful selection of appropriate parameters for the operation of the algorithm to a specific application, in this particular case to the type of the structure of the graph. This necessity can have its detrimental effect on the possibility of a wide application of the algorithm for any graphs in practice. The initial analysis of the performance of the algorithm in other types of graphs carried out by the authors clearly indicates that in order to obtain acceptable results in more complex and complicated structures, for example in multi-stage graphs, it may be necessary to carry on with additional studies aimed at developing methods for even better improvement in obtainable results.

References

1. Wu, B.Y., Chao, K.-M.: Spanning Trees and Optimization Problems. Chapman & Hall/CRC Press, USA (2004)
2. Dorigo, M., Stützle, T.: Ant Colony Optimization. The MIT Press, Cambridge (2004)
3. Głąbowski, M., Musznicki, B., Nowak, P., Zwierzykowski, P.: Shortest Path Problem Solving Based on Ant Colony Optimization Metaheuristic. International Journal of Image Processing & Communications 17(1-2), 7–17 (2012)
4. Głąbowski, M., Musznicki, B., Nowak, P., Zwierzykowski, P.: ShortestPathACO based strategy to find the Shortest Path between two nodes. In: Proceedings of 2013 IEICE Information and Communication Technology Forum (ICTF), Sarajevo, Bosnia and Herzegovina, pp. 29–31 (May 2013)
5. Cormen, T.H., Leiserson, C.E., Rivest, R.L., Stein, C.: Introduction to Algorithms. The MIT Press, Cambridge (2009)
6. Ahuja, R.K., Magnanti, T.L., Orlin, J.B.: Network Flows: Theory, Algorithms, and Applications. Prentice Hall, Englewood Cliffs (1993)
7. Bertsekas, D.P.: Network Optimization: Continuos and Discrete Models. Athena Scientific, Belmont (1998)
8. Maxemchuk, N.F., Shur, D.H.: An Internet multicast system for the stock market. ACM Transactions on Computer Systems 19(3), 384–412 (2001)
9. Pragyansmita, P., Raghavan, S.V.: Survey of Multicast Routing Algorithms and Protocols. In: Proceedings of ICCC 2002, the Fifteenth International Conference on Computer Communication, Washington, DC, USA, pp. 902–926 (2002)
10. Piechowiak, M., Zwierzykowski, P.: The Evaluation of Unconstrained Multicast Routing Algorithms in Ad-Hoc Networks. In: Kwiecień, A., Gaj, P., Stera, P. (eds.) CN 2012. CCIS, vol. 291, pp. 344–351. Springer, Heidelberg (2012)
11. Musznicki, B., Tomczak, M., Zwierzykowski, P.: Dijkstra-based Localized Multicast Routing in Wireless Sensor Networks. In: Proceedings of CSNDSP 2012, 8th IEEE, IET International Symposium on Communication Systems, Networks and Digital Signal Processing, Poznań, Poland, pp. 18–20 (July 2012)

A Sensor Network Gateway for IP Network and SQL Database

Piotr Lech

West Pomeranian University of Technology, Szczecin
Department of Signal Processing and Multimedia Engineering
26. Kwietnia 10, 71-126 Szczecin, Poland
piotr.lech@zut.edu.pl

Summary. This article presents the concept of building the access gate between a sensor network and Internet. A sensor network can be built in any standard, through wire or wireless (ZigBee, Bluetooth or Wi-Fi). Data transmission was made by higher layers of ISO/OSI web model, with local caching and data saving on the SQL server. The developed gateway has to ensure proper data transfer in different conditions concerning the bitrate and latency. The developed solution includes a variety of operating systems.

1 Introduction

Web technologies enable creating the applications which gather and process data obtained from local area sensor networks as well as from wide areas. One of the problems in data transferring is changing of delays over time which originate from local or wide area network disturbances. The main priority in developed solution is ensuring the proper data registration from sensors, regardless of any external factors. Affordable modules – working in IEEE 802.11b/g or Ethernet standards – extending the capabilities of microprocessor systems, enable building the sensor network couplers with Internet, becoming a cheaper alternative for industrial systems. Implementation of wireless sensor network projects, encounters problems related to radio disturbances from coexisting networks working in the same frequency range or technology limited range Wi-Fi devices. Using the wide area network introduces additional disturbances linked to irregularity of the network bandwidth. Microprocessor systems can handle hardware (or software) TCP/IP stack, enabling the data transfer to the higher layers of the ISO/OSI model [1].

In the next section the concept of using a gateway will be presented, which enables implementation of data transmission services from sensor network to the IP network and data registration in the SQL server with ability of caching data in the local SQL database [2]. It is assumed that the processes are not time critical.

2 Gateway Project

The gateway should enable data travelling from the sensor network with different wired or wireless standards. It was assumed that the data from each sensor is acquired at a defined time interval. It should provide caching to eliminate irregular transfers within local and wide area network. The proposed system solution is presented on a block diagram (Fig. 1).
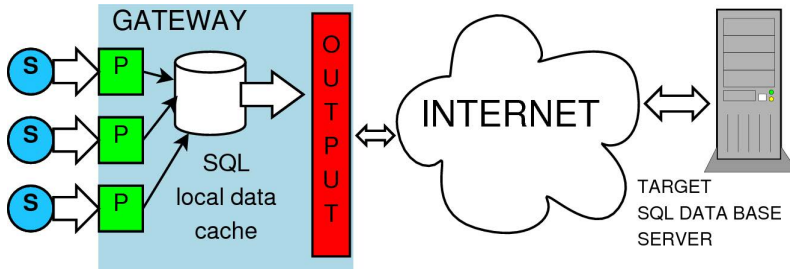
Fig. 1. Block diagram of the proposed solution (S-sensor, P-acquisition process)

The gateway consists of:

- Coupler to sensor network ensuring data transfer in frames of used technology.
- Interface for the access to local database, which provides saving and storing, for limited time, the data gathered from sensor network, indirectly determined by the number of entries stored in a local database.
- SQL database client (assuming the server is available for the specified IP address), which has to provide data transfer from the local to the target database while deleting transferred data from the local one.

3 Simulation

The virtual network environment (Oracle VM VirtualBox) was created using the configuration of virtual machines [3] shown on Fig. 2.
The virtual network environment configuration:

- Gateway (192.168.56.103) (OS: ArchLinux 32 bit, RAM: 512 MB, network settings : two network cards (Host-only Adapter and NAT)),
- Gateway (192.168.56.133) (OS: ArchLinux 32 bit, RAM: 512 MB, network settings : two network cards (Host-only Adapter and NAT)),
- Server MySQL (192.168.56.102) (OS: Windows 7 32 bit, RAM: 1024 MB, network settings : two network cards (Host-only Adapter and NAT)).
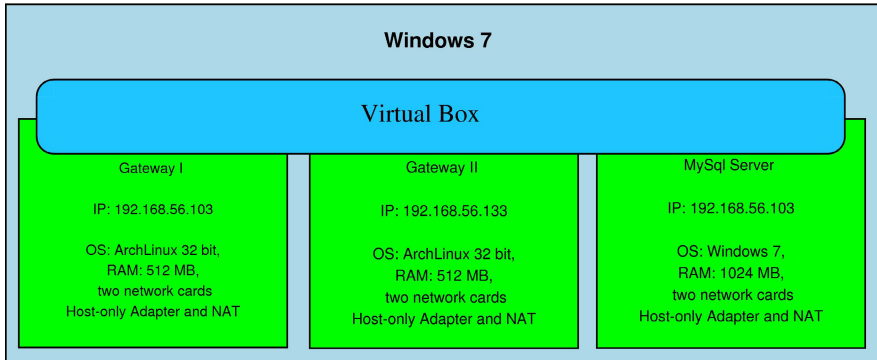
Fig. 2. The Oracle VM VirtualBox configuration

Each machine was provided with Internet and the direct communication interfaces between each of them. The Oracle VM VirtualBox settings require configuration of NAT (Network Address Translation) process to ensure automatic access to Internet and configuration of Only Host Adapter service, which creates internal local network, whereby all virtual machines communicate. For easier communication between machines the static addressing is used. Transfers of data from the sensor network were emulated as individual processes – a single process for each sensor network. The main task of the emulator was a delivery in the sequential times of the sample data to the local database. The variable n was defined as the length of the FIFO data buffer [4].

The model of a single queue can be represented in Kendall's notation as D/G/1 with limited number of customers [5]. The gateway with multiple sensors is represented by the D/G/c queue model.

In this test the cache size in the local database was set to ten ($n = 10$) entries from a single sensor. The gateway application was transferring the stored data to the target MySQL server. Each sensor had its own SQL table for caching data (Fig. 3). The local field of table was cleaned when the data was transferred by output process to the target database.

Test program was written in Java. Presented configuration requires advanced computer devices in order to work properly: at least 3-core processor with at least 2 GHz clock speed and at least 4 GB RAM. The correctness of entries to databases and CPU usage was checked experimentally and data transfer was measured using NetBalancer software [6].

Conducted tests showed no irregularities. It was not requirement of change of the buffer in this case.
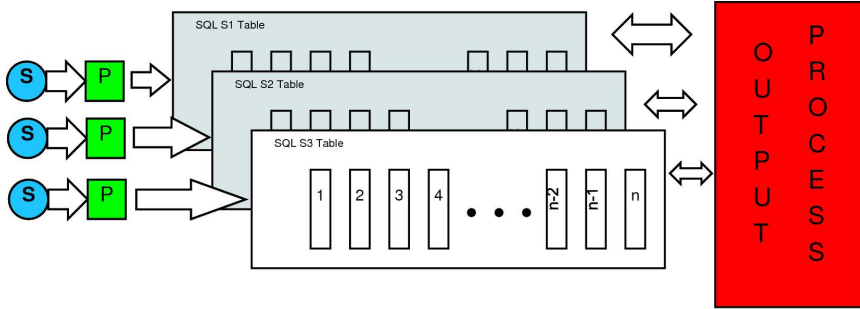
Fig. 3. The FIFO SQL table based buffer

4   Real Environment

The real environment was powered by two gateways and one MySQL server
(Fig. 4). The gateways were connected by two different internet access tech-
nologies. The GPRS connection was used for a slow data transfer. Two sensor
networks were handled by the gateway with slow connection. In this case four
SQL tables (one for each sensor) for buffers were used. The second gateway
was used for fast transfer data (WiMax technology) from one sensor network
to the SQL server with one local buffer. The MySQL server was connected by
ADSL technology. The sensors were read every 10 ms and this time interval
can be changed by the user separately for each sensor.

The gateway 1 – Raspberry Pi with Linux – configuration:

- Wi-Fi interface,
- Bluetooth interface,
- Java server application to acquisition data,
- local MySQL database server,
- modem GPRS,
- output application for transfer data from local buffer to target database.

The Sensor network 1 – the tablet with Android 2.3.2 system – configuration:

- build-in – angle and accelerometer sensor,
- Java client application,
- Wi-Fi interface.

The Sensor network 2 – the tablet with Android 4.0.2 system – configuration:

- build-in – angle and accelerometer sensor,
- Java client application,
- Bluetooth interface.
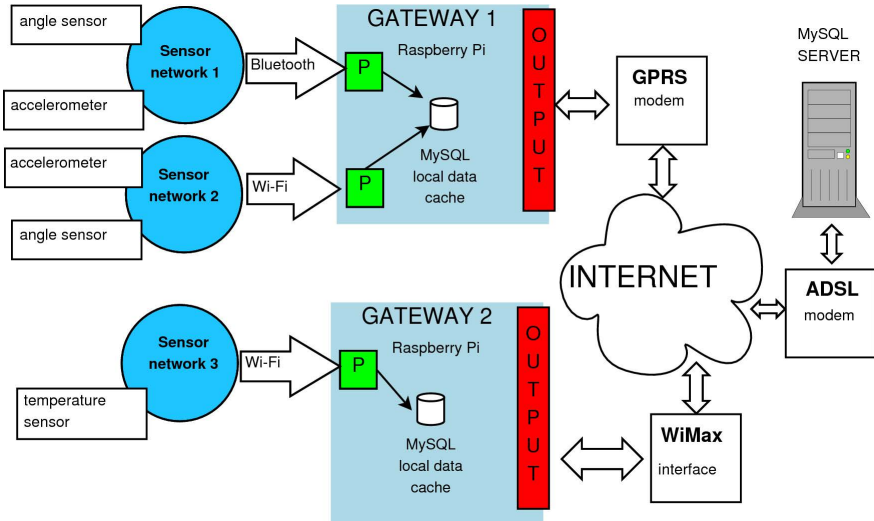
Fig. 4. The real network configuration (P-acquisition process)

The gateway 2 – Raspberry Pi with Linux – configuration:

- Wi-Fi interface,
- Java server application for acquisition data,
- local MySQL database server,
- Ethernet to WiMax Gateway connection,
- out-put application for transfer data from local buffer to target database.

The Sensor network 3 – FriendlyArm Tiny 210 (SDK-Board) module with embedded Linux system – configuration:

- I2C temperature measurement sensor,
- Java client application,
- Wi-Fi interface.

The SQL Server – PC with Windows 7 – configuration:

- AMD Phenom(tm) II P840 Triple-Core 1.9 GHz processor, 4 GB RAM
- MySQL Database Server,
- USB - ADSL modem.

Table 1. The 10 minutes average bitrate

Gateway 1, n=10	Gateway 1, n=1000	Gateway 2
buffer overflow	38,8 kb/s	12,5 kb/s
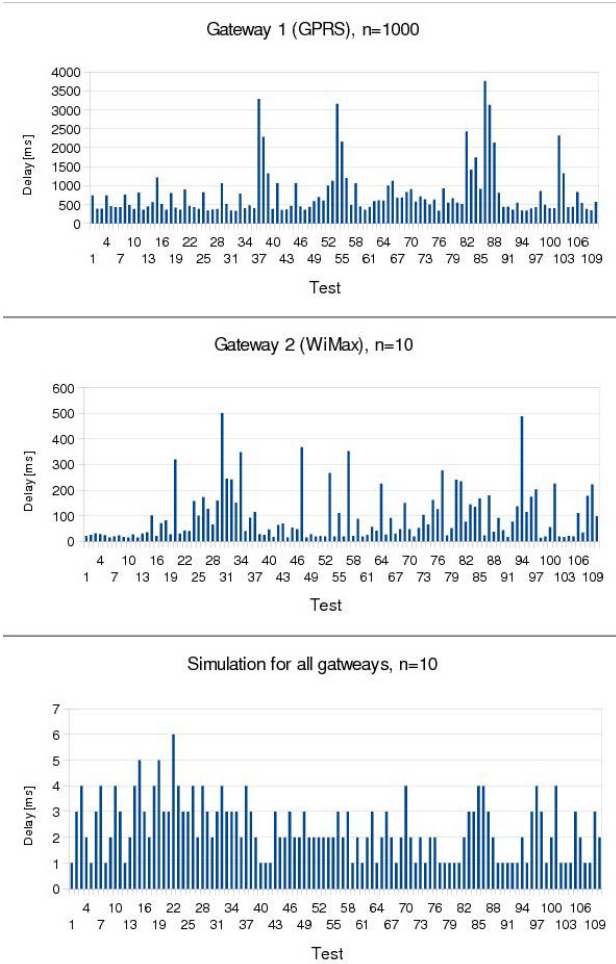
Fig. 5. The data transfer delay

Buffering Problem

Sometimes, some buffering problems occur when the bitrate of the WAN net-
work connection is dramatically reduced. In this case we can observe the over-
run buffer process (Table. 1). This problem with the GPRS connection was
observed in the proposed experiment. The size (n) was manually corrected
for a proper data caching without buffer overrun [7]. The measurement delay
writing to MySQL database was carried out by comparing the timestamps
entries. One of them was generated by the sensor network acquisition process,
and the second by a user-defined function performed by SQL Server (Fig. 5).
It is possible to choose the optimal value defining the length of the buffer

for different data rates and delays on the analysis of the obtained results of research.

In this case it is possible to build the procedure for auto-resizing the buffer [8]. The single queue model for real networks can be represented in Kendall's notation as G/G/1 (or G/G/c for the gateway with multiple sensors) with limited number of customers in the queue and the possible loss of customers [9].

5 Conclusion

The error-free delivery of data using a variety of network technologies and different operating systems is a big challenge for application developers. Implementation issues of data transfers to the upper layer of the ISO/OSI model and providing correct buffering facilitates the task of building this type of application. Finding the optimal values which define the length of the buffer for different data rates and delays are possible on the basis of observation of data delivery delays and the bitrate. In the future work an adaptive algorithm for the estimation of the optimal value of the buffer size will be needed for the observed network parameters.

References

1. Ding, H., Zhang, B., Ding, Y., Tao, B.: On a novel low-cost webbased power sensor via the Internet. Sensors and Actuators A136, 456–466 (2006)
2. Govindan, R., Hellerstein, J., Hong, W., Madden, S., Franklin, M., Shenker, S.: The sensor network as a database. Technical Report 02-771, Computer Science Department, University of Southern California, pp. 02–771 (2002)
3. Muller, R., Alonso, G., Kossmann, D.: BA virtual machine for sensor networks. In: Proc. EuroSys Conf., Lisbon, Portugal, pp. 145–158 (2007)
4. Chen, S., Yang, N.: Congestion avoidance based on lightweight buffer management in sensor networks. IEEE Transactions on Parallel and Distributed System 17(9), 934–946 (2006)
5. Servi, L.D.: D/G/1 queues with vacations. Operations Research 34, 619–629 (1986)
6. Arlos, P., Fiedler, M., Nilsson, A.A.: A distributed passive measurement infrastructure. In: Dovrolis, C. (ed.) PAM 2005. LNCS, vol. 3431, pp. 215–227. Springer, Heidelberg (2005)
7. Schmidt, K., Bchle, S.: Low-overhead decision support for dynamic buffer reallocation. Computer Science - Research and Development 27(1), 29–43 (2012)
8. Jiang, S., Zhang, X., Chen, F.: CLOCK-Pro: An Effective Improvement of the CLOCK Replacement. In: Proc. Anuual Technical Conf. USENIX, ATEC 2005, p. 35 (2005)
9. Ackroyd, M.: Computing the waiting time distribution for the G/G/1 queue by signal processing methods. IEEE Transactions on Communications 28(1), 52–58 (1980)

Multi-stage Switching Networks with Overflow Links for a Single Call Class

Mariusz Głąbowski and Michał Dominik Stasiak

Chair of Communication and Computer Networks,
Poznan University of Technology, Poznań, Poland
{mariusz.glabowski,michal.stasiak}@doctorate.put.poznan.pl

Summary. This article proposes a new analytical model of a multi-stage switching network with a system of overflow links in the first stage of the network. The initial assumption in the study was that the system of overflow links would be used by one class of calls. The article presents the dependencies between the internal blocking probability and the capacity of the overflow link. The results of the analytical calculations are then compared with the results of the simulations of multi-stage switching networks. The present study has confirmed fair accuracy of the proposed method and proved the validity of the implementation of overflow links in switching networks.

1 Introduction

One of the most effective ways of decreasing the internal blocking probability in single-service [3, 15, 21, 16, 2] and multi-service switching networks [25, 13, 12, 14, 8] is an application of overflow links between the switches of the first stages. Single-service, two-stage switching networks with overflow links were initially used in switching nodes of the Pentaconta system [3]. At the time, the application of overflow links made it possible to significantly reduce the phenomenon of the internal blocking in switching networks. However, works on modelling of multi-service switching networks with overflow links have been initiated fairly recently. In [25] the authors prove that the introduction of overflow inter-stage links to the first stage of the switching network is the most effective. The works [13, 12, 14] propose analytical models for switching networks with overflow links and point-to-point selection [13] as well as with point-to-group selection [12, 14]. The basic idea behind the considerations in the present article is included in [10] in which a modification to the PGBMT method (Point-to-Group Blocking with Multi-rate Traffic [23]) for modelling multi-service networks with overflow links and point-to-group selection is proposed. The method [10] assumes that the capacity of the overflow links is so big that the losses in these links can be omitted. Such an approach has been proved and validated by simulation experiments [25]. The present

article attempts to determine the point-to-group blocking probability in a multi-service switching network with overflow links. The model assumes that the capacity of the overflow link can be finite. A further assumption is that the system of overflow links will be offered only one class of calls that can be selected according to, for example, the maximum loss criterion in a switching network without overflow links. The article is structured as follows: Section 2 provides a description of the structure and operation of a three-stage Clos network [1] with overflow links. Section 3 presents the methods for modelling the switching networks with overflow links. Section 4 includes a comparison of the analytical results of the modelling with the simulations carried out for a number of selected switching networks. Section 5 sums up the article.

2 Switching Network with Overflow Links

Fig. 1 shows the structure of a Clos switching network with overflow links in the first stage. The network is composed of k symmetrical switches with $k \times k$ links in each of the stages. The initial assumption was that each inter-stage link had the capacity of f BBUs (Basic bandwidth Unit [20, 24, 11]), whereas the overflow link had the capacity of f_o BBUs. The network was offered a mixture of a number of classes of call streams with different demands. The outputs of the switching network were grouped into directions in such a way that each i-th output of each switch of the last stage belonged to the i-th output direction. The assumption of the article was that the overflow links would be used in the first stage of the network and would connect an additional output of a given switch with an additional input of the adjacent switch of the first stage (Fig. 1). In point-to-group selection, following the arrival of a new call, the controlling algorithm chooses a switch of the last stage that has a free link in a given direction. Then, the algorithm attempts to set up a connection with a selected switch of the last stage. If this is not possible, the algorithm tries to set up a connection through an overflow link, i.e., the call is being redirected to a neighbouring switch of the first stage and an attempt to set up a connection between this "new" switch of the first stage and a selected switch of the last stage will follow. If setting up of such a connection fails to succeed, the algorithm will choose another switch of the last stage that has a free output link in the demanded direction and will repeat the above sequence of attempts to set up a connection. In the case where a connection to free switches of the last stage still cannot be set up, the call will be lost due to internal blocking. If all output links in a given direction are busy, the controlling algorithm will reject the call due to external blocking.

3 Modelling of a Network with Overflow Links

Let us consider now the three-stage switching network presented in Fig. 1 and assume that s output links in a given direction can service a call of class i. Our further assumption is that for a given switch of the first stage there are $d(i)$ switches of the last stage available. This means that the system is capable of setting up a connection of class i between a switch of the first stage and one of the available switches of the last stage. For a call of class i, internal blocking in the network occurs when $d(i)$ output links in a given direction do not have a sufficient number of free BBUs to service the call of class i. The internal blocking probability $E_{\text{int}}(i)$ for calls of class i in the PGBMT method is expressed with Formula [23, 6]:

$$E_{\text{int}}(i) = \sum_{s=1}^{d(i)} \frac{P(i,s)}{1 - P(i,0)} \left[\binom{k-s}{d_e(i)} \bigg/ \binom{k}{d_e(i)} \right], \tag{1}$$

where k denotes the number of all outgoing (output) links in a given direction (Fig. 1), whereas $P(i,s)$ is the distribution of free links of the output group for a call of class i. The internal blocking probability is determined with the assumption of at least one free output link, hence in Formula (1) the distribution $P(i,s)$ has been replaced by the truncated distribution $P(i,s)/[1 - P(i,0)]$. The distribution $P(i,s)$ in the PGBMT method is approximated by a model of a limited availability group (LAG)[22, 9]. The external blocking probability $E_{\text{ext}}(i)$ is approximated in turn by the blocking probability in LAG, which is equal to the probability $P(i,0)$:

$$E_{\text{ext}}(i) = P(i,0). \tag{2}$$
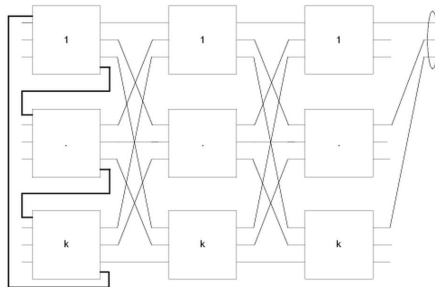
Fig. 1. Three-stage Clos network with overflow links

The total blocking probability $E(i)$ for calls of class i in the switching network is the sum of the internal and the external blocking probabilities. Assuming independence of events of the internal and the external blocking, we get:

$$E = E_{\text{ext}}(i) + E_{\text{int}}(i)[1 - E_{\text{ext}}(i)]. \tag{3}$$

To calculate the blocking probability $E(i)$, it is necessary to know the effective availability $d(i)$ and the distribution of available links of the output group $P(i, s)$.

3.1 Limited-Availability Group (LAG)

The distribution $P(i, s)$ in Formulas (1), (2) is approximated by the distribution of free links in LAG [23]. LAG is a model of separated links with the same capacity of f BBU. The distribution $P(i, s)$ determines the probability of an event in which s LAG output links (from among k of all links) can service a call of class i:

$$P(i, s) = \sum_{n=0}^{V} [P_n]_V P(i, s|V - n),\qquad(4)$$

where $[P_n]_V$ is the occupancy distribution in a LAG with the total capacity $V = kf$:

$$nP[n]_V = \sum_{i=1}^{M} A_i t_i \zeta_i(n - t_i) P[n - t_i]_V,\qquad(5)$$

where A_i represents traffic of class i offered to a given direction, M is the number of classes of offered traffic, whereas t_i is the number of BBUs demanded by a call of class i. The parameter is the so-called conditional stage-passage probability which in the LAG model can be determined by the following formula:

$$\zeta_i(n) = \frac{F(V - n, k, f, 0) - F(V - n, k, t_i - 1, 0)}{F(V - n, k, f, 0)}.\qquad(6)$$

The parameter $F(x, k, f, t)$ defines the number of arrangements of x free BBUs in k links, each with the capacity of f BBU. Additionally, each link has been given t_i free BBU. According to [23], we get:

$$F(x, k, f, t) = \sum_{j=1}^{\left\lfloor \frac{x - kt_i}{f - t_i + 1} \right\rfloor} (-1)^j \binom{k}{j} \binom{x - k(t_i - 1) - 1 - j(f - t_i + 1)}{k - 1}.\qquad(7)$$

The probability $P(i, s|x)$ in Formula (4) is the conditional distribution of free links in LAG, determined with the assumption that x BBUs in the group are free:

$$P(i, s|x) = \frac{\binom{k}{s} \sum_{w=st_i}^{\Psi} F(w, s, f, t_i) F(x - w, k - s, t_i - 1, 0)}{F(k, x, f, 0)},\qquad(8)$$

where: $\Psi = sf$, if $x >= sf$, $\Psi = x$, if $x < sf$. In the PGBMT method, the LAG model, defined by Formulas (4)–(8), makes it possible to evaluate the blocking probability.

3.2 Effective Availability of the Switching Network

The basic idea behind the determination of effective availability for a traffic stream of class i is the concept of the so-called equivalent network [23] that services single-service traffic. Each link of such a network is given a fictitious load $b(i)$ that is equal to the blocking probability of a stream of class i in the inter-stage link of a real switching network. Conventionally, it is adopted that the effective availability in the equivalent network is equal to the effective availability of a real network. To determine the probability $b(i)$ in the PGBMT method, the occupancy distribution in the multi-service full-availability group (FAG) is used [17, 19]:

$$n[P_n]_f = \sum_{i=1}^{M} a_i t_i [P_{n-t_i}]_f, \tag{9}$$

$$b(i) = \sum_{n=f-t_i+1}^{f} P[n]_f, \tag{10}$$

where a_i is the class i traffic offered to a single inter-stage link.

Effective availability for calls of class i in a three-stage Clos network is determined on the basis of Formula [23]:

$$d(i) = [1 - \pi(i)]k + \pi(i)b(i) + \pi(i)[k - b(i)][1 - b(i)]b(i), \tag{11}$$

where $\pi(i)$ is the probability of direct unavailability of a switch of the last stage for calls of class i. This probability results from an analysis of the channel graph of the switching network with the application of Lee method [18]. For the considered network without overflow links, the probability can be determined on the basis of the graph from Fig. 2a:

$$\pi(i) = \{1 - [1 - b(i)]^2\}^k. \tag{12}$$

3.3 Effective Availability of the Switching Network for Overflow Class of Calls

The proposed model assumes that only one class of calls can be overflowed. This means that the graph for the equivalent network for this class of calls will have the structure presented in Fig. 2b (the graphs for the remaining classes of calls have the structure presented in Fig. 2a). On the basis of Fig. 2b we can determine the probability of direct unavailability for a class of calls that undergoes the overflow process:

$$\pi(i) = \{1 - \{1 - [1 - (1 - \pi(j))(1 - b(j))][b(j)]\}\{1 - b(j)\}\}^k. \tag{13}$$

The probability $\pi(j)$ in Equation (13) is a fictitious load of the overflow link. This parameter can be evaluated on the basis the analysis of overflows
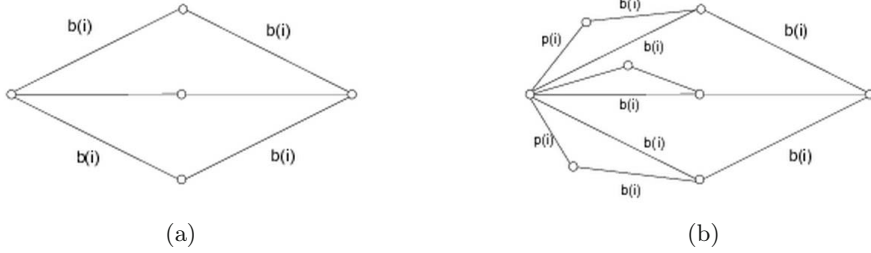
Fig. 2. Probability graph (a)without overflow links (b)with overflow links

in the considered switching network. One can adopt that overflow traffic will be equal (equivalent) to traffic of class j that is lost due to internal blocking in the switching network without overflow links:

$$R_j = A_j E_{\text{int}}^0(j), \tag{14}$$

where the superscript 0 in the symbol that determines the internal blocking probability is meant to indicate the switching network without overflow links. Due to the complex structure of overflows in the network, we assume that traffic R_j is traffic that overflows from a given fictitious group with the capacity of V^*. Hence, we get:

$$E_{\text{int}}^0(j) = E_{(V^*)}A_j. \tag{15}$$

Formula (15) makes it possible to determine the capacity of a fictitious group on the basis of the Erlang's model. The knowledge of the capacity of the fictitious group enables us in turn to apply the Riordan's formula [26] to determine variance and the peakedness factor of overflow traffic:

$$\sigma_j^2 = R_j \left[\frac{A_j}{V^* + 1 - A_j + R_j} + 1 - R_j \right], \tag{16}$$

$$Z_j = \frac{\sigma_j^2}{R_j}. \tag{17}$$

Then, on the basis of the Hayward formula [4, 7, 5], we are in position to evaluate the blocking probability that approximates the fictitious load of the overflow link:

$$p(i) = E_{\frac{f_o}{Z_j}} \left(\frac{R_j}{Z_j} \right). \tag{18}$$

The parameter f_o (Equation (18)) determines the capacity of a single overflow link. Having determined the value $p(i)$ it is possible to determine, on the basis of (13), the probability $\pi(j)$ and then, using (11), the value of the effective availability for the same class of calls of overflow traffic.

3.4   Algorithm for Modelling the Network with Overflow Links for a Single Class of Calls

The process of the determination of the internal blocking probability in multi-service switching networks with point-to-group selection can be presented in the following three steps:

- A determination, on the basis of the PGBMT method, of the blocking probability in the switching network without overflow links (Formulas (1)–(12)).
- A determination of the effective availability for a specific traffic class of overflow traffic (Formulas (11), (13)–(18)) and for the classes that do not undergo overflow (Formulas (11), (9)–(12)).
- A determination, on the basis of the PGBMT method, of the blocking probability in the switching network with overflow links (Formulas (1)–(3), (4)–(8)).

4   Sample Results of Modelling

The analytical method for modelling of multi-service switching networks with overflow traffic presented in Section 3 is an approximated method. Therefore, in order to corroborate the adopted theoretical assumptions, the results of the calculations were compared with the available simulation data of a 3-stage switching network (Fig. 1) composed of switches with $k \times k$ links, each with the capacity f BBUs. The adoption was that $k = 4$, and $f = 30$. The network was offered three classes of traffic in the following proportions: $A_1 t_1 : A_2 t_2 : A_3 t_3 = 1 : 1 : 1$, where the demands of particular classes were as follows: $t_1 = 1, t_2 = 2, t_3 = 6$. Figures 3-5 show the results of the calculations of the blocking probability in the studied switching network. The analytical results were then compared with the results of the simulations of the switching network. These results are indicated in the figures with appropriate points with 95 per cent confidence intervals, calculated after the t-Student distribution for five series, with 100,000 calls of each class. The results of the modelling are presented in relation to the value of traffic a offered to one BBU in input links to the switching network: $a = \sum_{i=1}^{M} (\frac{A_i t_i}{k^2 f})$.

Fig. 3 shows the results of the simulations and calculations for the point-to-group internal blocking probability with the assumption that there are no overflow links in the network. Fig. 4 presents the results concerning the network in which overflow links with the capacity of $f_0 = 30$ for traffic that required $t = 6$ BBUs were used. Fig. 5 in turn shows the values of the internal blocking probability in relation to the changes in the capacity of overflow links for the average traffic offered to a unit of the input link, equal to $a = 1$ Erl. The results clearly indicate a significant reduction of the internal blocking probability following the introduction of overflow links. The calculation error mainly results from the adopted linear interpolation of the results of the
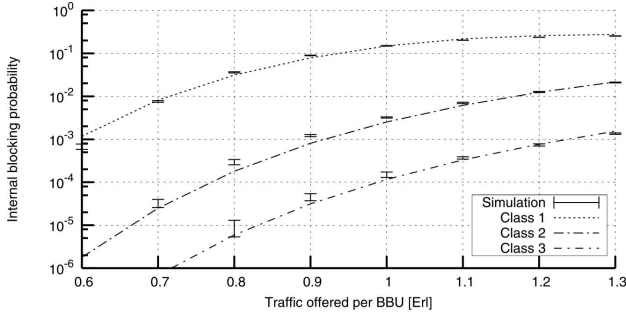
Fig. 3. Internal blocking in the network without overflow links
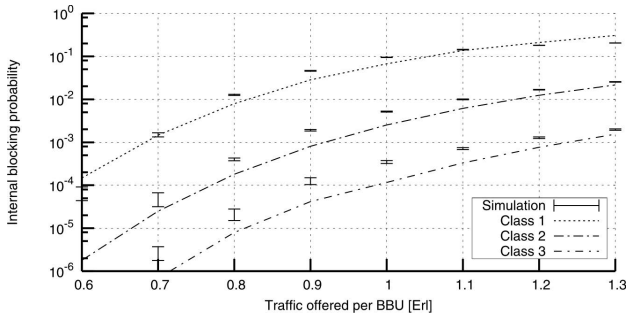
Fig. 4. Internal blocking in the network with overflow link with the capacity of 30 BBU
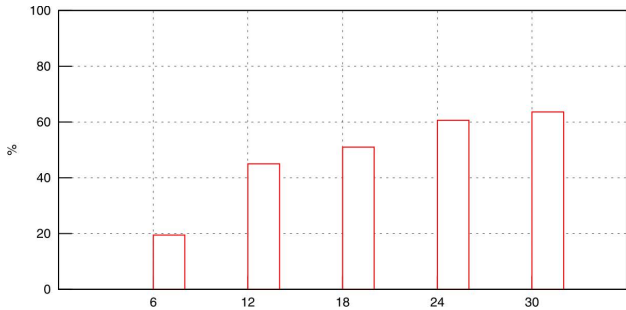
Fig. 5. Percentage decrease in the internal blocking in relation to the capacity of overflow links

calculations for non-integral values for effective availability (Formula (1)). The proposed method can be successfully applied for solving engineering issues, i.e. for the analysis of multi-service switching networks with overflow links.

5 Conclusions

This article proposes a generalization of the PGBMT method to be applied for modelling of multi-service switching networks with point-to-group selection and overflow links in the first stage. The results of the simulations confirm fair accurateness of the method that has an advantage of providing a possibility of determining the optimum capacity of overflow links. Consequently, the method makes it possible to determine dependencies between the blocking probability and the capacity of overflow links. The study findings also indicate substantial effectiveness of the introduction of overflow links in multi-service switching networks with point-to-group selection [12, 14].

References

1. Clos, C.: A study of non-blocking switching networks. Bell System Technical Journal, 406–424 (1953)
2. Ershova, E., Ershov, V.: Digital Systems for Information Distribution. Radio and Communications, Moscow (1983) (in Russian)
3. Fortet, R.: Systeme Pentaconta Calcul d'orange. LMT, Paris (1961)
4. Fredericks, A.: Congestion in blocking systems – a simple approximation technique. Bell System Technical Journal 59(6), 805–827 (1980)
5. Głąbowski, M., Kaliszan, A., Stasiak, M.: Convolution algorithm for state-passage probabilities calculation in limited-availability group. In: Proceedings of Fourth Advanced International Conference on Telecommunications 2008, Athens, pp. 215–220 (2008)
6. Głąbowski, M., Kaliszan, A., Stasiak, M.: Modeling product-form state-dependent systems with bpp traffic. Journal of Performance Evaluation 67, 174–197 (2010)
7. Głąbowski, M., Kubasik, K., Stasiak, M.: Modeling of systems with overflow multi-rate traffic. Telecommunication Systems 37(1-3), 85–96 (2008)
8. Głąbowski, M., Stasiak, M.: Point-to-point blocking probability in switching networks with reservation. Annales des Télécommunications 57(7-8), 798–831 (2002)
9. Głąbowski, M., Stasiak, M.: Multi-rate Model of the Group of Separated Transmission Links of Various Capacities. In: de Souza, J.N., Dini, P., Lorenz, P. (eds.) ICT 2004. LNCS, vol. 3124, pp. 1101–1106. Springer, Heidelberg (2004)
10. Głąbowski, M., Stasiak, M.: Internal blocking probability calculation in switching networks with additional inter-stage links. In: Grzech, A., Borzemski, L., Świątek, J., Wilimowska, Z. (eds.) Information Systems Architecture and Technology, A. Service Oriented Networked Systems, pp. 279–288. Oficyna Wydawnicza Politechniki Wrocławskiej (2011)
11. Głąbowski, M., Stasiak, M., Wiśniewski, A., Zwierzykowski, P.: Uplink blocking probability calculation for cellular systems with WCDMA radio interface, finite source population and differently loaded neighbouring cells. In: Proceedings of Asia-Pacific Conference on Communications, Perth, Australia, pp. 138–142 (2005)

12. Głąbowski, M., Stasiak, M.D.: Internal blocking probability calculation in switching networks with additional inter-stage links and Engset traffic. In: Proceedings of the 8th IEEE, IET International Symposium on Communication Systems, Networks and Digital Signal Processing, CSNDSP 2012, Poznań, Poland (July 2012)

13. Głąbowski, M., Stasiak, M.D.: Switching networks with overflow links and point-to-point selection. In: Grzech, A., Borzemski, L., Świątek, J., Wilimowska, Z. (eds.) Information Systems Architecture and Technology, Networks Design and Analysis, pp. 149–159. Oficyna Wydawnicza Politechniki Wrocławskiej (2012)

14. Głąbowski, M., Stasiak, M.D.: Recurrent method for blocking probability calculation in switching networks with overflow links. Journal of Telecommunications and Information Technology 1, 56–64 (2013)

15. Inose, H., Saito, T., Kato, M.: Three-stage time-division switching junctor as alternate route. Electronics Letters 2(5), 78–84 (1966)

16. Katzschner, L., Lorcher, W., Weisschuh, H.: On a experimental local PCM switching network. In: International Seminar o Integrated System for Speech, Video and Data Communication, Zurich, pp. 61–68 (1972)

17. Kaufman, J.: Blocking in a shared resource environment. IEEE Transactions on Communications 29(10), 1474–1481 (1981)

18. Lee, C.: Analysis of switching networks. Bell System Technical Journal 34(6) (1955)

19. Roberts, J.: A service system with heterogeneous user requirements – application to multi-service telecommunications systems. In: Pujolle, G. (ed.) Proceedings of Performance of Data Communications Systems and their Applications, pp. 423–431. North-Holland, Amsterdam (1981)

20. Roberts, J., Mocci, V., Virtamo, I. (eds.): Broadband Network Teletraffic, Final Report of Action COST 242. Commission of the European Communities. Springer, Berlin (1996)

21. Stasiak, M.: Computation of the probability of losses in switching systems with mutual aid selectors. Rozprawy Elekrotechniczne, Journal of the Polish Academy of Science XXXII(3), 961–977 (1986) (in Polish)

22. Stasiak, M.: Blocking probability in a limited-availability group carrying mixture of different multichannel traffic streams. Annales des Télécommunications 48(1-2), 71–76 (1993)

23. Stasiak, M.: Combinatorial considerations for switching systems carrying multichannel traffic streams. Annales des Télécommunications 51(11-12), 611–625 (1996)

24. Stasiak, M., Głąbowski, M., Wiśniewski, A., Zwierzykowski, P.: Modeling and Dimensioning of Mobile Networks. Wiley (2011)

25. Stasiak, M., Zwierzykowski, P.: Performance study in multi-rate switching networks with additional inter-stage links. In: Głąbowski, M., Mynbaev, D.K. (eds.) Proceedings of the Seventh Advanced International Conference on Telecommunications, AICT 2011, St. Maarten, The Netherlands Antilles, pp. 77–82. IARIA (2011)

26. Wilkinson, R.: Theories of toll traffic engineering in the USA. Bell System Technical Journal 40, 421–514 (1956)

Comparison of Different Path Composition Approaches to Multicast Optimization

Krzysztof Stachowiak and Piotr Zwierzykowski

Chair of Telecommunications and Computer Networks
Faculty of Electronics and Telecommunications
Poznan University of Technology, Poznań, Poland
`krzysiek.stachowiak@gmail.com`

Summary. In this paper the different algorithms that are based on the different interpretations of the path composition have been evaluated and compared. A new technique – the Aggregated MLARAC has been proposed and described. Two different ways of the algorithm performance evaluation have been utilized in order to present the different aspects of the considered algorithms.

1 Introduction

The multicast is, besides the unicast, one of the major ways of the Internet data transfer. Although it is used less, performing it efficiently is a greater algorithmic challenge, because of the increased computational complexity of the routing procedure. Note that in this article the static approach to the mutlicast is taken, i.e. the routing algorithms are considered. The alternative is the dynamic point of view that focuses on the routing protocols [10].

The modern routing complexity includes the problem of providing the transmission quality, which has been formulated as the Quality of Service (QoS) requirements. QoS introduces precise description of the transmission path properties to enable the efficient transfer of the data of different types. The particular traffic types are assigned the according QoS classes that define multiple requirements with the regard to the network path [1, 2].

The mathematical reflection of the mutlicast transmission is the Steiner Tree problem, which in the general form is an $\mathcal{NP}$-complete problem. The introduction of the QoS requirements adds extra criteria to the mathematical optimization which for both, the unicast as well as the multicast transmission, is an $\mathcal{NP}$-complete problem as well [2].

One of the types of the multi-criteria multicast optimization is the Multi Constrained Minimum Steiner Tree (MCMST) problem in which we define a single minimized criterion and a set of the constrained criteria. The two

aforementioned independent complexity factors render the MCMST optimization hard to solve. It is worth noting that in the real life scenarios, this procedure is bound to be performed in real-time, which sanctions the use of the heuristic approaches in the most cases. More complex approaches are still valid for the academic use as long as they provide high quality results. Finding better results at longer, but reasonable times, may serve as a ground for the reliable algorithm's performance comparison.

In this article a novel path composition based algorithm has been presented. The proposed technique has been classified as one of the path composition schemes. The algorithm's performance has been verified in a simulation in comparison to a selection of similar algorithms, and the simulation results have been presented and discussed.

The article is divided into the following parts. Section 2 describes some of the existing algorithms as the instances of the path composition approach. In Section 3 the mathematical model for the telecommunication networks and for the considered problems is defined. Section 4 introduces the new algorithm in the context of the other mentioned solutions. In Section 5 the simulation technique is explained thoroughly, and its results are presented in Section 6. Section 7 concludes the article.

2 Previous Work

A class of the MCMST algorithms can be isolated, that consists in the composition of the multiple unicast algorithm results into to the multicast result. This approach is founded on the lower complexity of the unicast algorithms which is only increased by a scalar factor in such case. Several algorithms which take this kind of route will be briefly presented in the following subsections.

2.1 *Precomputation Based Algorithms*

One of the ways of the path composition is to perform a precomputation algorithm in order to obtain some information about the analyzed topology. For example running the Dijkstra's algorithm [3] returns a map of labels assigned to the individual graph nodes, that determine the distances of the nodes from the assumed source as well as the back tracking information about the routes towards the nodes.

An interesting unicast representative of the precomputation based approach is the LBPSA algorithm presented in [6]. The authors propose a single pass of the Dijkstra's algorithm enhanced with a multi-criteria length metric is performed from the end node, that produces the aforementioned map of the cost labels. In the second pass a branch and bound procedure [7] is utlized to find the path from the source node, with the omission of the paths that

are likely to break the constraints based on the previously stored distance information.

The RDP algorithm presented in [9] is the example of the multicast pre-computation based algorithm. The precomputation generates distance maps for all the mutlicast participants concurrently, and the attempts are made at building the result tree by backtracking from one of the graph nodes for which the constraints are the least likely to be broken. In the practical realization the actual result building is performed simultaneously with the precomputation, it is however merely an optimization detail, and the general preprocessing idea is maintained.

2.2 *Optional Path Aggregation*

The Dijkstra's algorithm may result in the list of the shortest paths to all the graph's nodes, which may be directly adopted to the mutlicast optimization.

The HMCMC algorithm [4] utilizes this concept by attempting at the creation of the multicast tree at the first pass. If it fails to connect any of the multicast receivers with a feasible path (i.e. one that doesn't break the constraints), another pass, dedicated to the specific participant is performed in the attempt at optimizing the particular path. Such an approach produces results of satisfactory quality, however it consists of two different algorithms, which in the practical case may present an additional implementation cost.

2.3 *Simple Path Aggregation*

The optional path aggregation technique may be simplified at the cost of the running time performance by the assumption that all the multicast pairs shall be connected individually. At the end of such a procedure the obtained paths are merged into the mutlicast tree, with an optional pruning for the sake of the topological optimality.

Another solution of this nature has been proposed – the MLRA algorithm [8]. This kind of the approach results in an increased average running time compared to the optional aggregation. This is due to the possibility of the obtaining of the satisfactory result in the first algorithm's pass. However from the theoretical point of view, in the worst cases the complexities of the simple aggregations are always smaller because of the lack of the first pass.

3   Mathematical Model

The network is modeled by an undirected graph $G(E, V)$, where V is a finite set of nodes and $E \subseteq (u, v) : u, v \in V$ is a set of edges that represent point-to-point links. Each of the edges is assigned M metrics, given by the functions:

$(m_i : E \to \mathbb{R}^+, i = 0, 1, \ldots, M-1)$, that reflect additive costs of the according edges.

A path $p(s, d)$, from the node s to the node d, where $s, d \in V$, is defined as a sequence of non-repeated nodes $v_1, v_2, \ldots, v_k \in V$, such that for each $1 \leq i < k$ an edge $(v_i, v_{i+1}) \in E$ and $v_1 \equiv s, v_k \equiv d$. We define the accumulated metrics for the paths, so that the cost of a path p, based on the edges that form it $e \in p \subseteq E$, the $i-th$ is defined : $m_i(p) = \sum\limits_{e \in p} m_i(e)$.

A rooted multicast tree $t(s, d_1, d_2, \ldots)$, connecting the source node $s \in V$ with the multiple destinations $d_1, d_2, \cdots \in D \subseteq V$, is defined as a tree in G, of which the only leaf nodes are the ones from the set $\{s\} \cup D$, with one of them, the node s, arbitrarily selected as the root. We define the accumulated cost of a tree t analogously to the accumulated path's cost as: $m_i(t) = \sum\limits_{e \in t} m_i(e)$.

Let $T(s, d_1, d_2, \ldots)$ define the set of all the trees spanning the nodes from the set $\{s\} \cup D$.

For a tree t we define a path $p_t(s, d_i)$ which is a path connecting the nodes s and d_i within the given tree.

We define the constraints set C as : $(c_i \in \mathbb{R}^+, i = 1, 2, \ldots M - 1)$. The constrains are associated with the metrics of the same indices.

The MCMST problem is defined as finding the tree t^* spanning the source node s and the destination nodes D that fulfills the following conditions:

(1) $\forall\ t \in T(s, d_1, d_2, \ldots) : m_0(t^*) \leq m_0(t)$,
(2) $\forall\ d_i \in D, c_j \in C : m_j(p_t(s, d_i)) \leq c_j$.

4   The Proposed Algorithm

The new algorithm presented in the article belongs to the the simple path aggregation family and has been named the Aggregated MLARAC, as it is based on the MLARAC unicast algorithm [11].

The procedure consists in finding the paths that connect the multicast source with each of the multicast receivers individually. The underlying MLARAC algorithm guarantees that the paths don't break the constraints. The paths are then merged into a single subgraph, which is in turn pruned in order to remove cycles. The cycles removal is optional, because if the structure is directed, it may still be used for the multicast transmission. However the pruning maximizes the gain of the utilization of the network resources as in such case the information is transmitted via as few point-to-point links as possible.

5   Simulation Methodology

The proposed experiment consists in solving numerous routing problems that are given by the set of different parameters. Part of the parameters set has

been arbitrarily chosen to give the best exposition of the considered algorithms' properties. Other parameters have been used as the multidimensional result space for the presented charts.

The algorithms, that have been selected for this comparison are HMCMC [4], RDP in the heuristic variant [9] and the solution proposed in this article, the aggregated variant of the MLARAC algorithm [11].

The results have been analysed in two different ways. One of them is to measure the costs of the obtained mutlicast trees. This technique enables comparison of the quality of the results produced by each of the algorithms. In general there are two categories of the metrics to be compared. These are the base metric, which is the one that is to be minimized, and the set of the constrained metrics which are not to exceed the given constraints.

Another space of the results comparison is the technique described in [10] which consists in the simulation of the network resources depletion. In the experiment scenarios multiple routing problems are solved for a given graph, and after each of the algorithm passes the resources acquired by the resulting tree are subtracted from the topology. Once a given edge is drained of all the resources that are associated with it (e.g. all the bandwidth has been utilized) the edge is removed from the graph. This procedure continues as long as the graph remains connected. This kind of the comparison is an extension to the measurement of the algorithm's success rate as it not only provides a binary answer (whether the algorithm was able of setting up a tree or not), but gives the number of the trees that could be set up by the given algorithm.

5.1 Fixed Parameters

The analyzed topologies have been generated with the Waxman's algorithm [12] with the parameters $\alpha = 0.15$ and $\beta = 0.2$. For each of the graphs a number of the randomly generated routing problems were solved in order to guarantee the good statistical quality of the results – the confidence intervals being two orders of magnitude smaller than the measured mean values. For the costs comaprison 300 problems have been solved and the result trees costs were recorded. For the drainage scenario 600 problems were performed and the numbers of the trees that could be set up were stored. The edge weights have been randomly generated by an uniform generator from the interval $\langle 1, 1000 \rangle$. The MCMST problems have been given the constraints generated by the technique proposed earlier in [5] with the coefficient of 0.9.

5.2 Variable Parameters

The networks of 50, 100 and 150 nodes have been generated. The edges have been given 2, 3 or 4 metrics, which reflects 1, 2 or 3 constrained metrics respectively. Each topology was analyzed for the groups of $4, 8, \ldots, 24$ multicast members.
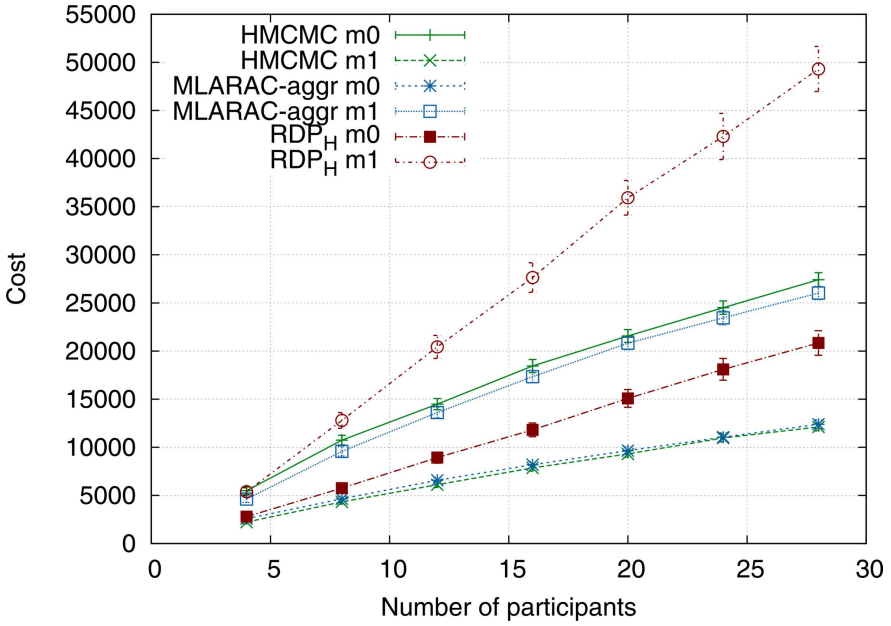
(a) Cost comparison
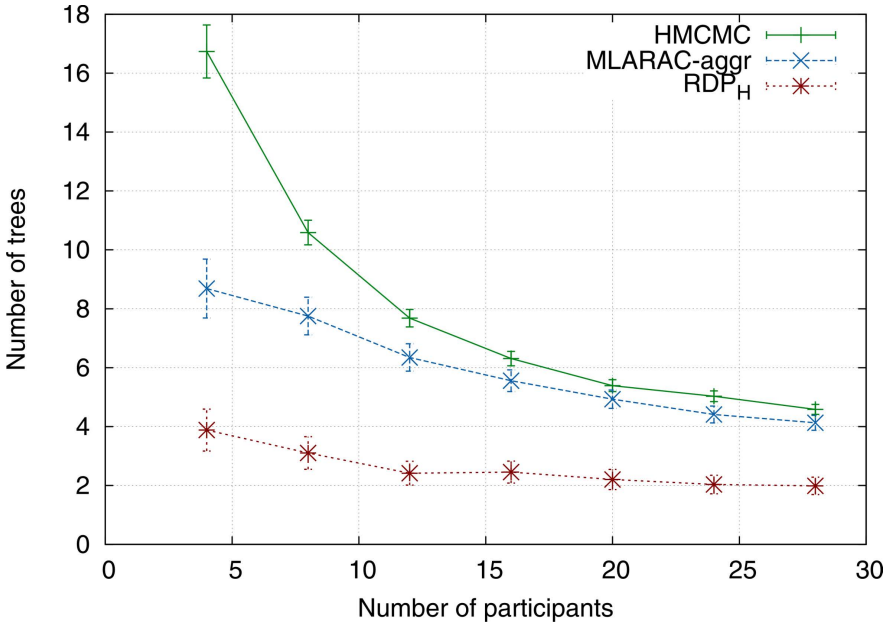
(b) Resource drainage comparison

Fig. 1. The experiment results for 2 metrics and 150 nodes

6 Simulation Results

The results of the experiment have been gathered and divided into two main parts. In the following subsection the mean costs of the obtained multicast trees have been presented. Subsequently the resource drainage analysis results are described. Due to the space limits only two charts have been chosen for the presentation. The case of two metrics was selected because in the case of all the presented algorithms the results only differed between the optimized metric and the constrained metrics. Also the charts are clearer in such case. The results didn't differ significantly in the function of the topology sizes therefore only the charts for the networks of 150 nodes have been presented.

6.1 Cost Results

In the Fig. 1a it may be observed that the RDP algorithm presents different cost trends than the other algorithms. A favorable property emerges that the minimized metric is relatively small whereas the constrained metric is higher than for the other algorithms. The aggregated MLARAC and the HMCMC algorithm present similar trends, however it may be noticed that the results for the constrained and for the optimized metrics are reversed.

6.2 Drainage Results

The Fig. 1b presents easily distinguishable curves for the three presented algorithms. The RDP algorithm performs the worst in this regard, however its performance depends steadily on the number of the multicast participants. The aggregated MLARAC and the HMCMC algorithms' results differ significantly for the lower numbers of the multicast members, however they assume similar values with the increase of the number of the participants.

6.3 Results Discussion

The aggregated MLARAC algorithm performs similarly to the HMCMC algorithm. This may have been expected as the two algorithms are based on the similar foundation. The very different in nature RDP algorithm generated different results. In case of the cost comparison they may be viewed as advantageous, however the resource drainage comparison yields acceptable but the worst results.

7 Conclusions

In the article the path composition based approaches to the multi-criteria multicast algorithms have been presented. The proposed new aggregation

scheme with the use of the MLARAC algorithm was presented in comparison with two other algorithms. The experimental simulations present the aggregated MLARAC as a viable solution to the multi-criteria multicast routing.

The utilization of the path aggregation scheme may be an interesting solution as it is relatively simple in the implementation. In any environment that is already equipped with the means of the multi-criteria unicast routing, the path aggregation technique may be introduced with a small amount of the implementation overhead.

References

1. Ahuja, R.K., Magnanti, T.L., Orlin, J.B.: Network flows: theory, algorithms, and applications. Prentice-Hall, Inc., Upper Saddle River (1993)
2. Chen, S., Nahrstedt, K.: An overview of quality of service routing for next-generation high-speed networks: problems and solutions. IEEE Network 12, 64–79 (1998)
3. Dijkstra, E.W.: A note on two problems in connexion with graphs. Numerische Mathematik 1, 269–271 (1959)
4. Feng, G.: A multi-constrained multicast QoS routing algorithm. Computer Communications 29(10), 1811–1822 (2006)
5. Feng, G.: The revisit of QoS routing based on non-linear Lagrange relaxation: Research Articles. Int. J. Commun. Syst. 20, 9–22 (2007)
6. Jiang, H., Yan, P.-L., Zhou, J.-G., Chen, L.-J., Wu, M.: Multi-constrained least cost qoS routing algorithm. In: de Souza, J.N., Dini, P., Lorenz, P. (eds.) ICT 2004. LNCS, vol. 3124, pp. 704–710. Springer, Heidelberg (2004)
7. Land, A.H., Doig, A.G.: An Automatic Method of Solving Discrete Programming Problems. Econometrica 28(3), 497–520 (1960)
8. Piechowiak, M., Zwierzykowski, P., Stasiak, M.: Multicast routing algorithm for packet networks with the application of the lagrange relaxation. In: NETWORKS 2010, 14th International Telecommunications Network Strategy and Planning Symposium, Warsaw, Poland, pp. 197–202 (September 2010)
9. Stachowiak, K., Zwierzykowski, P.: Architektura i Implementacja Wielokryterialnego Algorytmu Routingu Dla Ruchu Rozgałęźnego. In: The International Science Conference: Computer Networks – CN 2013, Lwówek Śląski, Poland (accepted, June 2013)
10. Stachowiak, K., Zwierzykowski, P.: Innovative Method of the Evaluation of Multicriterial Multicast Routing Algorithms. Journal of Telecommunications and Information Technology 1, 49–55 (2013)
11. Stachowiak, K., Zwierzykowski, P.: Lagrangian Relaxation and Linear Intersection Based QoS Routing Algorithm. International Journal of Electronics and Telecommunications 58(4), 307–314 (2013)
12. Waxman, B.M.: Routing of multipoint connections. IEEE Journal on Selected Areas in Communications 6(9), 1617–1622 (1988)

A New Testing Method of Routing Protocols for Wireless Mesh Networks

Adam Kaliszan, Mariusz Głąbowski, and Sławomir Hanczewski

Chair of Communication and Computer Networks,
Polanka 3, 60-965 Poznan
adam.kaliszan@et.put.poznan.pl

Summary. The paper presents a new testing method of routing protocols for wireless MESH networks. This method combines the advantages of tests carried out on physical devices and in simulation environment. The presented solution uses open source software. An important advantage of the proposed method is its scalability and lack of necessity of developing two dedicated implementations for the experiments in testbeds and for the simulation experiment. It is enough to implement only one universal solution for performing both types of tests. This advantage makes the presented solution worth using while testing the new systems.

1 Introduction

Keeping abreast of the current developmental trend on the market, called the Post PC era [1], largely depends on efficient operation of MESH (wireless) networks. In line with the main assumptions of this trend, the traditional PC computer is being replaced by a number of other devices that operate in the network, which in consequence leads to a significant increase in the number of its nodes. These devices are supposed to communicate with one another regardless of their type. Most of them are mobile and work in changeable conditions creating the so-called ad-hoc networks. As a result, intense work has been going on recently aimed at creating effective protocols for networks of this type [2, 3], routing protocols in particular. Similar works have been also conducted within the CARMNET project [4], among others.

One of the most important stages in designing any new or modified protocol, for example a routing protocol, is the testing process. This involves the evaluation of the usefulness of the protocol to the needs of particular types of networks as well as the comparison of its effectiveness with other protocols and other existing solutions.The testing stage for a protocol is usually very time-consuming and requires time consumption comparable to the time needed for a new protocol to be developed. This is particularly important

in the case of routing protocols in which, due to their particular purpose, the testing process is complicated and long-lasting, as well as requires an appropriate testing environment to be constructed.

Currently, in studies on routing protocols, two approaches are used. The one involves an implementation of the tested protocol in a network constructed from hardware routers, whereas the other is based on carrying out appropriate experiments in a simulation model. Testing of a protocol in a testing network may not be sufficient to obtain reliable results because of frequently limited number of nodes. The solution using simulation experiments lacks this limitation though in turn the latter approach does not provide a possibility to evaluate the influence of a routing protocol on the efficiency of real network nodes. Regardless of a chosen approach to the testing method for routing protocols, obtaining reliable results requires changeable conditions of the operation of a network to be taken into consideration while performing tests. They include both mobility of the network devices themselves and the capability of them of working in immediate proximity to other devices that generate interference.

The limitations imposed by the presented testing methods for networks make them being often used in parallel, independently of each other. However, this leads to a situation in which a double implementation of a protocol under study is necessary and has to be effected, the first being the implementation in a test network that makes use of hardware routers, and the other implementation in a simulation environment. Such an approach nearly doubles the necessary volume of time required for the implementation of a routing protocol in both test environments. The presented limitations in the testing methods for networks used so far have prompted the authors of the article to propose a new testing method that would make a simplification of the method and a significant shortening of the testing process of new or modified routing protocols for ad-hoc networks possible. The proposed method is basically based on the assumption that the same software (source) code can be used for both the needs of a simulation experiment and a test network composed of hardware routers.

The remaining part of the paper is structured as follows: Section 2 presents the methods for conducting tests of routing protocols. Section 3 provides a description of the proposed testing method for new or modified routing protocols. Section 4 includes a description of a plan for an implementation of the method. Section 5 sums up the article.

2 Methodology of Testing

In order to verify the accuracy of operation of a new (or modified) routing protocol, either of the two following commonly used methods is applied: simulation experiment or test implementation of the *proof of concept* type approach. Either of the methods requires a dedicated implementation of the

protocol, while the differences between them exclude an instance of co-sharing of a single code.

The simulation experiment makes it possible for a network to be quickly constructed and to make it easily configured, since any instance of adding successive nodes will not require thus any installation or reconfiguration of new devices. An addition of nodes makes the duration of a simulation experiments only longer. A simulation in which a given network under consideration does not have any connection with physical nodes needs not be at the same time an experiment performed in real time. Thanks to this, it is possible to analyse the behaviour of a network within a given requested time span in a considerably much shorter time. Oftentimes, a simulation experiment is conducted to verify whether the protocol specifications are correct. Additionally, the stability of state automates can be also evaluated in this way.

It should not be forgotten, however, that a simulation experiment often adopts certain simplifications that may omit certain phenomena that normally occur in a real network. This is of particular importance in the case of wireless networks, for which in order to map the operation of the radio interface approximated models are used for the purpose. In addition, tests conducted in a simulation environment do not make it possible to obtain reliable evaluation of the efficiency of nodes. Because a construction of a simulation environment is a complex and time-consuming process, to test routing protocols one of the available existing simulation environments such as NS-2, NS-3 [5, 6] can be used.

The other approach in testing routing protocols involves a preparation of an implementation of the protocol to be used in a test (*proof of concept*) network. The code developed for the purposes of such an implementation often becomes later the reference code. However, tests carried in networks constructed with hardware routers are labour-intensive. They require a test network to be developed, which, in consequence, is related to a necessity to buy (usually a great) number of devices. Moreover, it is important to remember about as best mapping of the real conditions of the operation of the network (e.g., the level of interference) as possible. A significant advantage of tests using physical devices is that it is possible to carry out performance tests. It is thanks to such tests that we are in position to examine the increase in the efficiency of nodes after the introduction of a new (modified) routing protocol and, additionally, to compare it with other protocols.

An alternative solution in testing routing protocols is the application of the so-called software routers activated in a virtual environment. Each such software router is activated on a separate virtual machine, while the latter operates on a single server. The application of virtualization of devices solves the problem of a separate implementation of a routing protocol for the purposes of a simulation experiment. As a result, it is possible to significantly speed up the process of the implementation of a new protocol.

Such a simplification of the existing software router architectures brings in, however, certain disadvantages such as limitations in obtaining reliable and

complete results in tests. Available tools for virtualization prevent virtual links in which errors in transmission or loss of a signal occur from being created, which is of particular importance for wireless networks.

3   New Hybrid Approach

3.1   A Reference Architecture of the Software Router

In order to present the proposed new method for testing routing protocols let us first consider a reference architecture of the software router.

In terms of functional coverage the architecture of the software router can be divided into planes (in the right side of Fig. 1), whereas in terms of implementation into layers (in the left side of Fig. 1). Within the functional context we can distinguish 2 planes: Data Plane (DP) and Control Plane (CP). The Control Plane includes the routing layer, among others. The remaining layers of the Control Plane are meant for communication with the core layer of the operating system that works in DP. There are many modules operating in the routing layer. Each of them is responsible for a different routing protocol.

Data Plane is responsible for switching and modification of headers of packets. These packets are transmitted according to the routing table. Packet switching can be accomplished either in hardware [7] or software. Hardware switching eliminates the necessity of sending packets across the bus to memory, their modification by the processor and resending across the bus to an appropriate network interface.

In the software router, packet switching is executed by the kernel (core) layer and, from the point of view of a programmer, is serviced in exactly the same way, regardless of the hardware or software implementation. Moreover, Data Plane makes information on states of interfaces available. Between the core layer and the routing layer, the following layers have been added – in the software router architecture – the adapter layer and API layer within the operating system. The introduction of these additional layers is necessary, since the API layer within the operating system is furnished by the operating system, while the adapter layer is included in the software of the software router.

The interface between the adapter layer and the API layer within the operating system cannot be standarized because it depends on the operating system of the machine on which the software runs. The adapter layer depends on the operating system, whereas the layer of routing protocols is independent of the operating system within which it runs (the modules of the layers included in the original software are indicated in Fig. 1 in grey colour).

The layer model used in the reference architecture of software routers in which a given layer interacts only with the layers in immediate adjacency (i.e., upper and lower), makes a simple extension of the functionality of the router feasible. For example, any new addition of a new routing protocol does not

require the knowledge of the API of the operating system nor the knowledge of handling network interfaces and routing tables.At the same time, in order to transfer software into another operating system the only thing necessary is to modify the adapter layer. In addition, the layer-like architecture of software routers makes it possible to effectively introduce certain modifications in the router that will be required for the application of the new method for testing routing protocols proposed in the article.
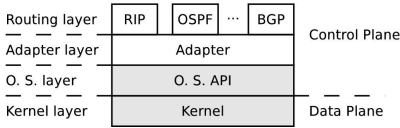
Fig. 1. Software router architecture
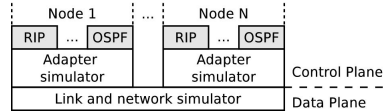
Fig. 2. A new method for examining network protocols

3.2 Hybrid Tests

The main idea behind the new testing method for routing protocols developed in the article, the so-called hybrid method, is to replace Data Plane of the software router with an appropriate simulator. This solution enables Control Plane for a number of nodes on the same machine, without a necessity to apply virtualization, to be activated. The general idea of the proposed method is presented in Fig. 2. In the figure, the vertical lines separate the nodes of the simulated network. The simulator of the adapter of the Data Plane emulates the Data Plane of the nodes that constitute a fragment or the whole of a network. Additionally, the presented approach assumes a possibility of a simulation of a packet transfer. This in turn makes it possible to introduce errors to transmissions and to simulate how connections react in the process. The elements with grey background colour shown in the figure do not require to be re-written anew for the purpose of any new simulation. Thus, only one-time work is needed that basically involves a preparation of the simulator of the adapter layer that communicates with the routing layer.

4 Plan of the Implementation of the New Method

The first step in the implementation of the new testing method is to choose a software router whose code is to be appropriately modified. The most common projects of the software router are nowadays Quagga [8] and XORP [9]. Other projects include BIRD [10], though the latter is still in its early stage of development. In addition, there is a number of implementations of a single protocol such as, for example, OLSRd [11]. The Quagga and XORP projects share similar assumptions that are compatible with the architecture of the software router. They include a special module that mediates communication between Data Plane and Control Plane. This module is located in the adapter

layer. As a result, modules responsible for routing protocols have limited access to the API within the operating system and, in consequence, such an approach increases the portability of the code to other platforms.

The most commonly used software router is the router developed with the Quagga project [8]. Quagga is so popular because of its stable operation and the GPLv2 licence [12]. Fig. 3 shows the architecture of the Quagga software router. In this project, communication between Data Plane and Control Plane is handled by the Zebra module. The module is responsible for sending information on the state of interfaces from Data Plane to Control Plane and for forwarding the assigned routing table in the opposite direction. In Fig. 3, communication between CP and DP with the application of the Zebra module is represented by bidirectional arrows (solid line). For the modules responsible for the proper operation of routing protocols (determining the routing table and forwarding it with the help of the Zebra module to DP), it is necessary to make transfer of messages of routing protocols between nodes possible (e.g., updating of routing tables in the case of distance-vector protocols or the Hello message in the case of link-state protocols). This communication is executed directly between the routing module and the OS API layer. In Fig. 3, it is indicated by bidirectional arrows in dotted line.
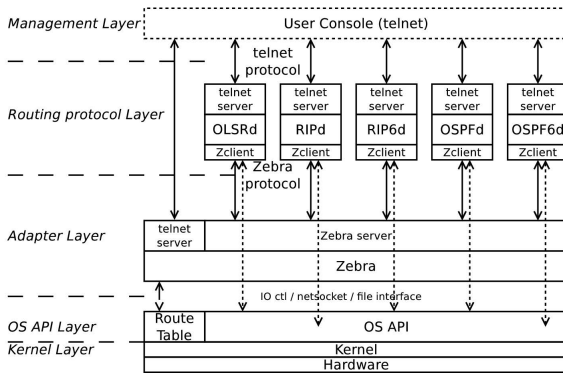
Fig. 3. Architecture of the Quagga project   **Fig. 4.** Modified architecture of the Quagga project
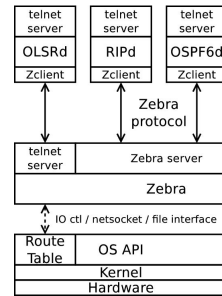
Fig. 3 additionally shows the management layer. This layer can be optionally added to the project and in this article will be omitted. Note that in the presented architecture the principle of inter-layer communication has not been entirely retained (communication of a given layer with the layer immediately superior or subordinate). Here, the modules operating in the routing layer also communicate directly with the API layer within the operating system. Such an approach is validated by the fact that the method for sending and receiving packets is similar in most of the available operating systems, i.e. compatible with Barkley API [13]. Such a simplification, however, introduces a number of shortcomings: impediment in transferring a router to

another operating system, and prohibits modules from being transferred on to another machine [15]. In addition, the method for testing routing protocols proposed in the article cannot be directly applied because there is no possibility of creating a full and extensive simulator for Data Plane. The simulator that can be prepared for the presented architecture will lack the functionality of sending and receiving packets with messages exchanged between routing protocols.

In the Quagga project, the modules of the routing layer communicate with the Zebra module that operates in the adapter layer via the Zebra protocol. The Zebra protocol is a network protocol. At the stage of the compilation of a project it is possible to determine whether it is a local connection for the servicing inter-processor communication or whether it is a TCP connection. The appropriate format of a message of the Zebra protocol is shown in Fig. 5.

Bits 0-15	Bits 16-23	Bits 24-31	Bits 32-47	Bits 48 - ...
Message len	Marker	Version	Command	Message data

Fig. 5. The format of a message of the Zebra protocol

The first 16-bit field *Message length* defines the length of the whole of a message. This field has been introduced because in a single TCP datagram it is possible to send a great number of messages of the Zebra protocol. The next 8-bit field *Marker* should have the value of 255. In the earlier version of the Zebra protocol, this field defined a command. 16-bit field *Command* defines the code of a command. The codes of commands are presented in Table 1. The last field *Message Data* includes additional data that are forwarded along with a command. Its length depends on the type of command.

The Zebra module operates as it were a server. In the case of the choice of communication with the help of the TCP protocol, it listens to new connections on port 2600. Modules from the routing layer set up a connection with the Zebra module.

Communication between layers with the application of the API within the operating system prevents the adapter layer and the API layer from being replaced with a simulator of these layers. What would be needed here is a replacement of system call service routine (O.S. API) with an emulator of this service. Hence, prior to the implementation of the simulator, it is necessary to appropriately modify the Quagga project. Such a modification introduces a possibility of separating Control Plane from Data Plane [14]. Fig. 4 shows the modified architecture of the Quagga project.

The presented modification requires new commands to be added to the Zebra module. Table 1 presents the messages of the Zebra protocol. The existing Quagga commands with the numbers from 1 to 23 should be expanded by new commands that will be responsible for sending and receiving packets, creating a new network socket and for modifying its settings. These commands are commands with the number 24-26, and are presented in Table 1.

Table 1. Zebra protocol messages

code	command	code	command
1	ZEBRA_INTERFACE_ADD	14	ZEBRA_REDISTRIBUTE_DEFAULT_DELETE
2	ZEBRA_INTERFACE_DELETE	15	ZEBRA_IPV4_NEXTHOP_LOOKUP
3	ZEBRA_INTERFACE_ADDRESS_ADD	16	ZEBRA_IPV6_NEXTHOP_LOOKUP
4	ZEBRA_INTERFACE_ADDRESS_DELETE	17	ZEBRA_IPV4_IMPORT_LOOKUP
5	ZEBRA_INTERFACE_UP	18	ZEBRA_IPV6_IMPORT_LOOKUP
6	ZEBRA_INTERFACE_DOWN	19	ZEBRA_INTERFACE_RENAME
7	ZEBRA_IPV4_ROUTE_ADD	20	ZEBRA_ROUTER_ID_ADD
8	ZEBRA_IPV4_ROUTE_DELETE	21	ZEBRA_ROUTER_ID_DELETE
9	ZEBRA_IPV6_ROUTE_ADD	22	ZEBRA_ROUTER_ID_UPDATE
10	ZEBRA_IPV6_ROUTE_DELETE	23	ZEBRA_HELLO
11	ZEBRA_REDISTRIBUTE_ADD	24	ZEBRA_SEND
12	ZEBRA_REDISTRIBUTE_DELETE	25	ZEBRA_CREATE_SOCKET
13	ZEBRA_REDISTRIBUTE_DEFAULT_ADD	26	ZEBRA_SET_SOCKET_OPTIONS

In addition, it is important to unequivocally assign the process servicing the routing algorithm to an appropriate simulated node. To achieve this, it is necessary to modify the Zebra protocol in such a way that the routing process will show the node identifier or, alternatively, to add a mechanism in which the simulator will be capable of activating routing processes. The former approach requires additional changes in the modules of the routing layer to be introduced, hence the latter approach seems to be more adequate. This approach involves the process responsible for the simulation of the adapter layer to automatically activate for its own needs (individually for each of its nodes) processes that service routing algorithms. For each of the algorithms involved, an appropriate configuration needs to be given, as well as a specific port on which the server with the interpreter of commands listens should be specified. It is thanks to the interpreter of commands that any analysis of the behaviour of the protocol will be possible.

The next step in the implementation is to create a simulator of the adapter layer of the virtual network. The software of the simulator will be a multi-threaded software. Each TCP connection that mediates between the routing layer and the adapter layer will be serviced in a separate thread. Threads will communicate via the module that simulates the behaviour of the links of the network. This will make possible to investigate the influence of interference on the operation of the routing protocol. Additionally, the module simulating the network makes it possible to perform statistics calculations related to traffic and packet forwarding of packets with messages of the routing protocol.

5   Conclusions

This article proposes a new methodology for testing routing protocols in wireless mobile mesh ad-hoc networks. The proposed methodology makes it possible to eliminate the necessity of a double implementation of software for the routing protocol: the same reference code of the protocol can be used for tests carried out with both hardware routers and software routers. Furthermore, due to the proposed solution it is possible: (1) to connect (add) physical devices to the test network, (2) to dynamically change the topology of the test network,

and (3) to collect statistical data. In addition, the proposed solution makes its possible to eliminate the necessity of using virtual machines, which can be followed by a significant increase in the number of serviced software nodes. A significant advantage of the solution is also a possibility to introduce interference to links between nodes.

References

1. Ross, S.J., et al.: A composable framework for secure multi-modal access to Internet services from post-PC devices. In: Proc. of the Third IEEE Workshop on Mobile Computing Systems and Applications, Los Alamitos, pp. 171–182 (2000)
2. Perkins, C.E., Royer, E.M.: Ad-hoc on-demand distance vector routing. In: Proc. of the Second IEEE Workshop on Mobile Computing Systems and Applications, New Orleans, pp. 90–100 (1999)
3. Xu, B., Hischke, S., Walke, B.: The role of ad hoc networking in future wireless communications. In: Proc. of the International Conference on Communication Technology, vol. 2, pp. 1353–1358 (2003)
4. Kaliszan, A., Glabowski, M.: An Environment for Implementing and Testing Routing Protocols in CARMNET Architecture. Accepted for presentation on AICT 2013, Rome (2013)
5. NS-3 homepage, `http://www.nsnam.org`
6. Ikeda, M., Kulla, E., Barolli, L., Takizawa, M., Miho, R.: Performance Evaluation of Wireless Mobile Ad-Hoc Network via NS-3 Simulator. In: Proc. of the 14th International Conference on Network-Based Information Systems, Tirana, pp. 135–141 (2011)
7. Chydzinski, A., et al.: Virtualization Devices for Prototyping of Future Internet. In: Proc. of the 13th ACIS International Conference on Software Engineering, Artificial Intelligence, Networking and Parallel/Distributed Computing, Kyoto, pp. 672–678 (2012)
8. Quagga homepage, `http://www.nongnu.org/quagga`
9. XORP homepage, `http://www.xorp.org`
10. BIRD homepage, `http://bird.network.cz`
11. OLSR homepage, `http://www.olsr.org`
12. GNU homepage, `http://www.gnu.org/licenses/gpl-2.0.html`
13. Hall, B.: Beej's guide to network programming using internet sockets (2012), `http://beej.us/guide/bgnet/`
14. Kaliszan, A., Glabowski, M., Hanczewski, S.: A didactic platform for testing and developing routing protocols. In: Proc. of the Eighth Advanced International Conference on Telecommunications, pp. 197–202 (2012)
15. Kaliszan, A., Hanczewski, S., Glabowski, M., Stasiak, M., Zwierzykowski, P.: Routing and control plane in the Parallel Internet IPv6 QoS. In: Proc. of the 8th CSNDSP, Poznan (2012)

Performance Evaluation of Multicast Routing Algorithms with Fuzzy Sets

Maciej Piechowiak and Piotr Prokopowicz

Kazimierz Wielki University,
Bydgoszcz, Poland
`{mpiech,piotrekp}@ukw.edu.pl`

Summary. The paper presents a proposal of a new methodology that evaluates multicast routing algorithms in packet-switched networks with an application of fuzzy sets. Proposed multicriteria mechanism evaluate representative multicast routing algorithms: KPP, CSPT and MLRA (*Multicast Routing Algorithm with Lagrange Relaxation*) that minimize cost of paths between source and each destination node using Lagrange relaxation, and finally, minimize the total cost of multicast tree. A wide range of simulation research carried out by the authors, confirmed both the accuracy of new methodology and the effectiveness of the proposed algorithm.

1 Introduction

In common real-life problems often both parameters and data used in mathematical modelling are vague. In mathematical modelling vagueness can be described by a fuzzy sets and numbers. Idea of the fuzzy sets was started in 1965 by Zadeh [19]. Fuzzy set theory has its well-known achievements in many branches of science and technology. Fuzzy concept have been introduced in order to model such vague terms, as observed values of some physical or economical terms, like pressure values or stock market rates, that can be inaccurate, can be noisy or can be difficult to measure with an appropriate precision because of technical reasons. In our daily life there are many cases that observations of objects in a population are fuzzy. Thus, the idea to implement fuzzy sets in evaluation of multicast routing algorithms were adopted.

Multicasting is a transmission method used in packet-switched networks for delivering mainly voice and multimedia data at the same time from one to many receivers. This technique require effective methods of scalable realtime data compression [10] and efficient routing algorithms defining a tree with a minimum cost between the source node and the particular nodes representing the users. Such a solution prevents from duplication of the same packets in

the links of the network. Routing of the sent data occurs only in those nodes of the network that lead directly to destination nodes.

The article discusses the effectiveness of the *Multicast Lagrange Relaxation Algorithm* (MLRA) and its comparison with most commonly used constrained heuristic algorithms: KPP (Kompella et all [7]) and CSPT (Crawford et all [2]). Authors are describing preliminary analysis and the beginning of the research on applying fuzzy systems to the problem of multicriterial assessment of the multicast trees. It expand authors previous work [13] increasing granularity of linguistic variables.

The paper is divided into five sections. Section 2 describes the implemented network model. Section 3 presents the overview of multicast routing algorithms. Section 4 describe linguistic and fuzzy sets assumptions. Section 5 contain results of evaluations.

2 Network Model

The network is represented by an undirected, connected graph $G = (V, E)$, where V is a set of nodes, and E is a set of links. With each link $e_{ij} \in E$ between nodes i and j two parameters are coupled: cost c_{ij} and delay d_{ij}. The cost of a connection represents the usage of the link resources; c_{ij} is then a function of the traffic volume in a given link and the capacity of the buffer needed for the traffic. A delay in the link is in turn the sum of the delays introduced by the propagation in a link, queuing and switching in the nodes of the network. The multicast group is a set of nodes that are receivers of the group traffic (identification is carried out according to a unique i address), $M = \{m_1, ..., m_m\} \subseteq V$. The node $s \in V$ is the source for the multicast group M. Multicast tree $T(s, M) \subseteq E$ is a tree rooted in the source node s that includes all members of the group M and is called *Steiner tree*.

The total cost of the Steiner tree $T(s, M)$ can be defined as $\sum_{t \in T(s,M)} c(t)$. The path $p(s, m_i) \subseteq T(s, M)$ is a set of links between s and $m_i \in M$. The cost of path $p(s, m_i)$ can be expressed as: $\sum_{p \in P(s,m_i)} c(p)$, where $P(s, m_i)$ is a set of possible paths between s and $m_i \in M$. The delay is measured between the beginning and the end of the path as: $\sum_{p \in P(s,m_i)} d(p)$. Thus, the maximum delay in the tree can be determined as: $\max_{m \in M}[\sum_{p \in P(s,M)} d(p)]$.

Because of time complexity (the problem is proven to be $\mathcal{NP}$-hard) heuristic algorithms are most preferable for solving this problem.

3 Multicast Routing Algorithms

The implementation of multicasting requires solutions of many combinatorial problems accompanying the building of optimal transmission trees. In the optimization process it can be distinguished: MST – *Minimum Steiner Tree*, and the tree with the shortest paths between the source node and each of the

destination nodes – SPT (*Shortest Path Tree*). Finding the MST, which is a $\mathcal{NP}$-complete problem, results in a structure with a minimum total cost [18]. The relevant literature provides a wide range of heuristics solving this (one and multicriterial) problem in polynomial time [8, 12, 15, 16, 20]. From the point of view of the application in data transmission, the most commonly used is the KMB algorithm [8] and its modification – KPP algorithm [7] that reflect additional link parameter – delay.

During the first phase of the KPP, a complete graph is constructed whose all vertices are the source node s and the destination nodes $m_x \in M$, while the edges represent the least cost paths connecting any two nodes a and b in the original graph $G = (V, E)$, where $a, b \in \{M \cup s\}$. Then, the minimal spanning tree is determined in this graph taking the delay constraint Δ into consideration, and then the edges of the obtained tree are converted into the paths of the original graph G. Any loops that appeared in this formed structure are removed with the help of the shortest path algorithm, for instance, by Dijkstra algorithm [3]. The computational complexity of the algorithm is $O(\Delta |V|^3)$.

Other methods minimize the cost of each of the paths between the sender and each of the members of the multicast group by forming a tree from the paths having the least costs. In general, at first either the Dijkstra algorithm [3] or the Bellman-Ford algorithm [1] is used, then the branches of the tree that do not have destination nodes are pruned. Several routing algorithms have been proposed in the literature for this problem [2, 17, 11, 14].

In research studies the Constrained Shortest Path Tree (CSPT) is commonly used. It contains constrained shortest paths between the source and each destination node. The CSP problem (*Constrained Shortest Path*), also known as DCLC (*Delay Constrained Least Cost*), can be stated as the problem of minimizing: $z^* = \min \sum_{e_{ij} \in E} c_{ij} e_{ij}$, subject to: $\sum_{(i,j) \in E} d_{ij} e_{ij} \leq \Delta$, where: $e_{ij} \in \{0, 1\}$ [6].

Lagrange relaxation is a popular technique for calculating lower bounds and finding better solutions than popular CSP heuristics offer [6]. Held and Karp used this first to solve the *traveling salesman problem* [4]. It bases on modified cost function c_λ which is aggregated metric. Problem can be stated as follows:

$$L(\lambda) = \min \sum_{(i,j) \in E} (c_{ij} + \lambda d_{ij}) e_{ij} - \lambda \Delta, \tag{1}$$

for certain λ: $L(\lambda) = z^*$.

The proposed *Path Lagrange Relaxation Algorithm* (PLRA) refers to Jüttner et all idea [5]. Proposed algorithm relay on minimizing aggregated (modified) cost function: $c_\lambda = c + \lambda d$. In each iteration of PLRA, the current value of λ is calculated, in order to increase the dominance of delay in the aggregated cost function, if the optimum solution of c_λ suits the delay requirements (Δ).
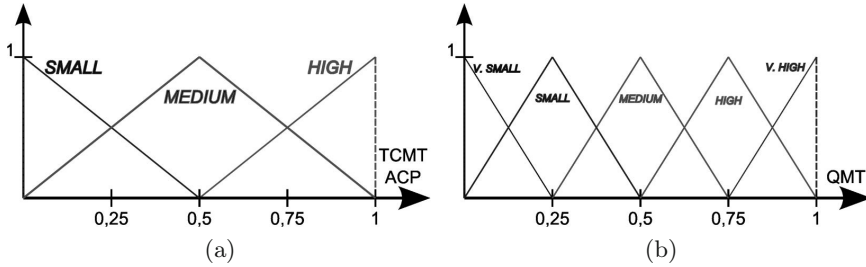
Fig. 1. Linguistic model variables: total cost and average path's cost in multicast tree (a), quality of multicast tree (b)

The operation performed by the proposed *Multicast Lagrange Relaxation Algorithm* (MLRA) consists in determining the shortest path tree between source node s and each destination node m_i, along which the maximum delay value (Δ) cannot be exceeded. The paths determined one by one are added to the multicast tree. If there is at least one path that does not meet the requirements multicast tree cannot be constructed. Since the network structure created in that way may contain cycles, in order to avoid them Prim's algorithm has been used.

In the last phase it removes leaves nodes with outdegree 1 that are not multicast nodes. On the basis of links entering the tree and their metrics (cost and delay) the total cost of the constrained tree is calculated.

4   Linguistic and Fuzzy Model

Authors describe preliminary analysis and the beginning of the research on applying fuzzy systems to the problem of multicrterial assessment of the multicast algorithms. Therefore the proposed linguistic model is exceptionally simple. Its relying on vital statistics of individual features concerning the assessment of the multicast network, so its complexity is minimized.

Linguistic model assumptions:

- two input variables:
    - total cost of multicast tree (TCMT) – Fig. 1a,
    - average cost of paths between source and each destination node (ACP) – Fig. 1a,
- one output variable: quality of multicast tree (QMT) – Fig. 1b,
- input variables have three values: $SMALL$, $AVERAGE$, $HIGH$,
- output variable have five values: $VERY SMALL$, $SMALL$, $AVERAGE$, $HIGH$, $VERY HIGH$,
- the domain of variables is normalized to interval $[0, 1]$.

Table 1. Results of Multicriteria Fuzzy Evaluation for Multicast Algorithms

	$\Delta = 2000$			$\Delta = 2500$			$\Delta = 3000$		
	KPP	MLRA	CSPT	KPP	MLRA	CSPT	KPP	MLRA	CSPT
Avg. val.	0,6665	0,6440	0,6169	0,6621	0,6496	0,6265	0,6653	0,6636	0,6466
Max. val.	0,8125	0,7938	0,7839	0,8668	0,7963	0,7945	0,8501	0,8525	0,8525
Min. val.	0,4267	0,3778	0,3152	0,2802	0,3174	0,3241	0,4172	0,4408	0,2816

Parameters of fuzzy system:

- type of system: Mamdani,
- fuzzyfication method: singleton,
- aggregation operator for premise parts of fuzzy rules: min,
- implication operator in approximate reasoning: min,
- aggregation method for fuzzy conclusions from rules: max,
- defuzzyfication method: center of gravity.

Basics assumptions used to determine base of linguistic rules:

- total cost of multicast tree – the smaller, the better,
- average cost of paths between source and each destination node – the smaller, the better.

The principles presented earlier lets constitute a set of eight rules used in the fuzzy system:

- IF $TCMT$ is $SMALL$ AND ACP is $SMALL$ THEN QMT is $HIGH$,
- IF $TCMT$ is $SMALL$ AND ACP is $HIGH$ THEN QMT is $MEDIUM$,
- IF $TCMT$ is $HIGH$ AND ACP is $SMALL$ THEN QMT is $MEDIUM$,
- IF $TCMT$ is $HIGH$ AND ACP is $HIGH$ THEN QMT is $SMALL$,
- IF $TCMT$ is $SMALL$ AND ACP is $SMALL$ THEN QMT is $HIGH$,
- IF $TCMT$ is $SMALL$ AND ACP is $HIGH$ THEN QMT is $MEDIUM$,
- IF $TCMT$ is $HIGH$ AND ACP is $SMALL$ THEN QMT is $MEDIUM$,
- IF $TCMT$ is $HIGH$ AND ACP is $HIGH$ THEN QMT is $SMALL$.

In the further part of this article such fuzzy system will be named Multi-criteria Fuzzy Evaluator (MFE).

5   Results of Evaluations

In order to reliable comparison of multicast algorithms into network topologies with different properties, a flat random graph constructed graphs according to the Waxman method was used [18].

Due to a wide range of solutions presented in the literature of the subject, the following representative algorithms were chosen: KPP [7] and CSPT [2] algorithms and MLRA algorithm proposed in [9]. Such a set of algorithms
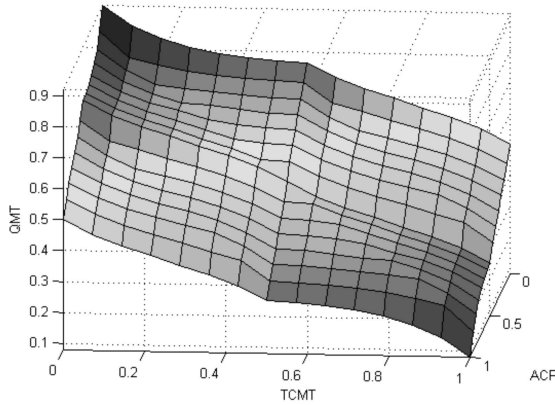
Fig. 2. Fuzzy model surface plot between total cost of multicast tree (TCMT) and average cost path (ACP) with quality of multicast tree (QMT)

includes solutions potentially most and least effective in terms of costs of constructed trees. The results were evaluated for three values of maximum delay (Δ: 2000, 2500 and 3000).

Earlier results show that KPP algorithm constructs multicast trees with the minimum total cost among all results [9, 13]. CSPT algorithm creates multicast trees with highest costs on average. Analyzing average path's cost, it is observable that proposed MLRA algorithm construct trees with paths costs 40% lower on average in relation to the KPP algorithm. MLRA algorithm achieve best results constructing trees when maximum delay along path Δ is 2500.

Multicriteria Fuzzy Evaluator (MFE) let for evaluation of multicast trees combining total cost of tree and average cost of each path in tree. It was used in order to conduct independent evaluation for three algorithms and three Δ values. Results were normalized to a range between 0 and 1. It is observable that average value of QMT parameter for MLRA and KPP algorithm are comparable for ($\Delta = 3000$).

Fig. 2 show a plot of the surface of a model of fuzzy system with two inputs (TCMT, ACP) and one output (QMT). The surface of the fuzzy model has monotonic character what confirms that the system properly realize the intuition from the linguistic model. Any reduction of the ACP and/or the TCMT leads to increase the quality (QMT) of algorithm.

6   Conclusions

The article presents a new technique for evaluation multicast algorithms. Research works were conducted for representative algorithms and shows that

proposed MLRA algorithm with Lagrange relaxation is more effective than popular CSPT algorithms. It was compared with representative routing algorithms for multicast connections emphasizing the quality of the network model.

It is difficult to find precise method for an evaluation of the multicast trees for large number of essential parameters. The method proposed in the article based on a simplified linguistic model which combine different estimations and join them into one estimation. This method allow for the effective implementation of muticriteria evaluations. Moreover, the results are fulfilling expectations and covers with previous (individual criterion) estimations for certain algorithms [9].

The proposed algorithm can be also successfully applied in large, dense networks with a high average node degree D_{av} [9]. The MLRA compared with CSPT and KPP, achieves a good compromise between reasonable costs of trees and low time complexity.

References

1. Bellman, R.: On a Routing Problem. Quarterly of Applied Mathematics 16(1), 87–90 (1958)
2. Crawford, J.S., Waters, A.G.: Heuristics for ATM Multicast Routing. In: Proceedings of 6th IFIP Workshop on Performance Modeling and Evaluation of ATM Networks, pp. 5/1–5/18 (1998)
3. Dijkstra, E.: A note on two problems in connexion with graphs. Numerische Mathematik 1, 269–271 (1959)
4. Held, M., Karp, R.: The Traveling Salesman Problem and Minimum Spanning Trees. Operation Research (18), 1138–1162 (1970)
5. Juttner, A., Szviatovszki, B., Mecs, I., Rajko, Z.: Lagrange Relaxation Based Method for the QoS Routing Problem. In: IEEE INFOCOM (2001)
6. Magnanti, L., Ahuja, K.: Network Flows: Theory, Algorithms and Applications. Prentice Hall, Upper Saddle River (1993)
7. Kompella, V.P., Pasquale, J., Polyzos, G.C.: Multicasting for Multimedia Applications. In: INFOCOM 1992, pp. 2078–2085 (1992)
8. Kou, L., Markowsky, G., Berman, L.: A fast algorithm for Steiner trees. Acta Informatica (15), 141–145 (1981)
9. Stasiak, M., Piechowiak, M., Zwierzykowski, P.: Multicast Routing Algorithm for Packet Networks with the Application of the Lagrange Relaxation. In: Proceedings of NETWORKS 2010 – 14th International Telecommunications Network Strategy and Planning Symposium, pp. 197–202 (2010)
10. Marchewka, A.: Segmentation of Motion Field for Scalable Video Compression. An International Journal Image Processing and Communications 14(1), 1–8 (2009)
11. Mokbel, M.F., El-Haweet, W.A., El-Derini, M.N.: A Delay Constrained Shortest Path Algorithm for Multicast Routing in Multimedia Applications. In: Proceedings of IEEE Middle East Workshop on Networking. IEEE Computer Society (1999)

12. Musznicki, B., Tomczak, M., Zwierzykowski, P.: Dijkstra-based Localized Multicast Routing in Wireless Sensor Networks. In: Proceedings of CSNDSP 2012, 8th IEEE, IET International Symposium on Communication Systems, Networks and Digital Signal Processing, Poznań, Poland, pp. 18–20 (2012)
13. Piechowiak, M., Prokopowicz, P.: Evaluation of Multicast Routing Algorithms with Fuzzy Sets. In: Advances in Electronics and Telecommunications. Poznan University of Technology (2013)
14. Piechowiak, M., Zwierzykowski, P.: Heuristic Algorithm for Multicast Connections in Packet Networks. In: Proceedings of EUROCON 2007 the International Conference on: Computer as a Tool, Warsaw, Poland, pp. 948–955. IEEE (September 2007)
15. Shaikh, A., Shin, K.G.: Destination-Driven Routing for Low-Cost Multicast. IEEE Journal on Selected Areas in Communications 15(3), 373–381 (1997)
16. Stachowiak, K., Weissenberg, J., Zwierzykowski, P.: Lagrangian Relaxation in the Multicriterial Routing. In: AFRICON 2011, pp. 1–6 (2011)
17. Sun, Q., Langendoerfer, H.: Efficient Multicast Routing for Delay-Sensitive Applications. In: Proceedings of the 2nd Workshop on Protocols for Multimedia Systems (PROMS 1995), pp. 452–458 (1995)
18. Waxmann, B.: Routing of multipoint connections. IEEE Journal on Selected Area in Communications 6, 1617–1622 (1988)
19. Zadeh, L.A.: Fuzzy Sets. Information and Control, 338–353 (1965)
20. Zhu, Q., Parsa, M., Garcia-Luna-Aceves, J.J.: A Source-based Algorithm for Delay-constrained Minimum-cost multicasting. In: INFOCOM 1995: Proceedings of the Fourteenth Annual Joint Conference of the IEEE Computer and Communication Societies, vol. 1, pp. 377–385 (1995)

Performance of IGMP Protocol on Embedded Systems with OpenWRT

Maciej Piechowiak, Michał Chmielewski, and Paweł Szyszkowski

Kazimierz Wielki University, Bydgoszcz, Poland
`mpiech@ukw.edu.pl`

Summary. Effective use of multicast technology can significantly reduce network load, especially in networks that support multimedia transmission. This technique has reported number of implementations due to increasing interest in audiovisual technology and the capabilities of modern networks. However, multicast is still mystery for many programmers, network administrators and ordinary users who could make it more popular, and utilize this promising technique of transmission [1, 2, 11]. The article discusses the IP Multicast technology and focuses on the study of IGMP on different hardware platforms – the Cisco 2611 router and the ASUS WL500g Premium (installed with OpenWRT Linux operating system).

1 Introduction

The continual development of the Internet, networks and multimedia forced operators to develop measurement methods. These methods allow the measurement of transmission parameters such as the efficiency of manifold routing protocols and performance of network devices. The implementation of the measurement procedures allows the assessment of work of a single unit and assessment of the measuring unit (multiple devices) among each other [18]. Performance testing shows how a network behaves under the circumstances.

IETF Benchmarking Methodology (BMWG) [8] is a working group on basis of which the following documents were developed: RFC 1242 [3], RFC 2285 [4], RFC 2544 [5], RFC 2432 [6], RFC 3918 [7], which describe the methods of measurement, their execution and presentation of results. The basic scope of research is divided into two groups: the first group consists of measuring the performance of packet forwarding between equipment's interfaces, while the second group is a measure of the delay of different multicast routing protocols. In the first case, the measurement depends on the performance and configuration of the device itself. In the latter case, the measurement depends only on signaling protocols.

Multicast differs from unicast on the principle of operation and hence efficiency. Service providers increasingly implement this technology into the core of their networks, but it still poses a problem for an end user when it comes to functionality. Cheap and easy to use home routers are not equiped with network address translation (NAT), compatible with multicast.

This paper discusses the implementation of multicasting on SOHO (Small Office Home Office) devices running on OpenWRT. Chapter 2 define measurement procedures used in multicast traffic. Chapter 3 show exemplary network topology while Chapter 4 presents the research on joining and leaving groups in IGMP protocol and ASUS WL500g Premium router. Chapter 5 discuss CPU performance of embeded system. The final chapter presents the conclusions of the study.

2   Measurement Procedures Used in Multicast Traffic

Presentation of the measurement procedures described in RFC 3918 requires prior definition of several terms [21]. The basic concepts are the System Under Test (SUT) and the Device Under Test (DUT), which are defined in RFC 2285 [4]:

- Device Under Test (DUT) is a network device which is the subject of the study;
- System Under Test (SUT) is a team of network devices, considered as a whole, also the subject of the study.

In the presented system, measuring packets are sent from a source to a single interface, one of the devices included in the SUT, then sent to the next device included in the SUT, until they reach the appropriate output interfaces. Before the start of the appropriate tests it is required to validate the DUT or SUT action. This check should be made by sending, from the test equipment, *IGMP Group Report* messages, in the direction of SUT/DUT output interfaces. Then, from the test data source a stream of data should be sent directed to a group which IGMP message concerns, and it should be verified if it has been received on all output interfaces.

2.1   *Group Join Delay Measurement*

The purpose of *Group Join Delay Measurement* (GJD) measurement is to determine what the values of this parameter are in the course of the study. GJD measurement methods are dependent on the current status of *Multicast Forwarding Database* (MFDB). There are two states MFDB:

- State 0, which does not address MFDB groups used in the measurements,
- State 1, in where MFDB contains the address of the group used during the measurements.
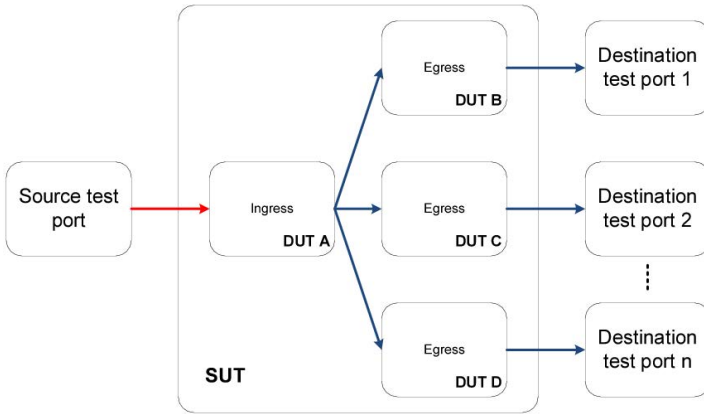
Fig. 1. Idea of SUT and DUT measurements procedures

In the first case, the measurement takes into account the time that is needed to create the appropriate entries in MFDB and start forwarding to the appropriate interfaces. This measurement allows you to specify how long you need to add a new multicast group to the MFDB base. In the latter case, the measure takes into account the time required to modify the database by adding new MFDB output interfaces and start forwarding multicast for the group.

After the completion of testing procedures, sending data from the source should begin. Then, a request must be sent to join the group (*IGMP Group Membership Report*) in the direction of the appropriate output interface. Group Join Delay is set as the time interval between sending a request to join group t_a, and the time when the first frame to group tb on the right interface is received:

$$t_{gjd} = t_b - t_a \tag{1}$$

where t_a is the time when the last bit of *IGMP Group Membership Report* message is sent, while t_b is the time of receiving the first bit of the first frame addressed to the multicast group. The measurement results must take into account the following parameters: frame size, the number of output interfaces, the IGMP version, the number of multicast groups, and the rate at which data is sent from the source, and the measurement method used.

2.2 Group Leave Delay Measurement

The purpose of *Group Leave Delay Measurement* (GLD) measurement is to determine what the values of this parameter are during the DUT or SUT study. Measurements should be carried out with the use of one multicast group. Before beginning, ensure that all output interfaces are attached to

the multicast group by sending a stream of data from a source sent to the multicast group used during the measurements, and verify that packets will be received on the appropriate output interfaces.

Once the verification process is completed, start generating a stream of data from the source. Then, send *IGMP Leave Group* messages in the direction of each target port. Group Leave Delay is set as the time interval between sending a disconnect request to group t_a, and the time when the last frame to group tb on the right interface is received:

$$t_{gld} = t_b - t_a \qquad (2)$$

3   Exemplary Network Topology

Network topology have been created in order to conduct test multicast transmission with an application of video streaming server, ISP router (represented by Cisco 2611 router), embedded system – access network device providing IGMP Proxy (ASUS WL-500g Premium) and computers represents end users – members of multicast group (Fig. 2).
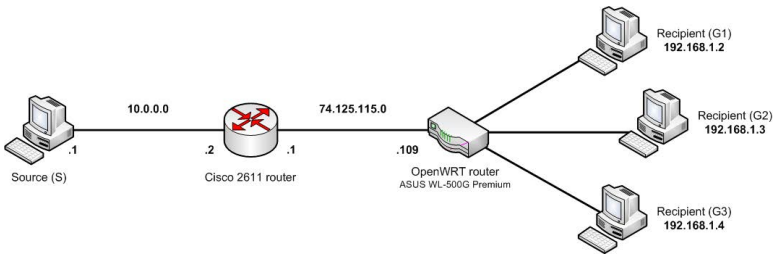
Fig. 2. Exemplary network topology

ASUS WL500G Premium v1 is equipped in MIPS CPU based on Broadcom BCM4704 architecture with clock rate at 264MHz. It also featured 8MB flash memory, 32MB of RAM, two USB 2.0 ports and miniPCI slot that allow to change the wireless card.

For this research two computer programs have been used to track communication networks. The first is the popular *Wireshark* program, which was launched on one of the computers that was set to receive the multicast transmission. The second program is *tcpdump* – used on the ASUS router.

4   Time Measurement of GJD and GLD

Before any streaming was commenced on the recipient's computer, Wireshark was up and running to capture IGMP packets from the interface on which the receiver is connected to the ASUS router. Then a command was executed

on the ASUS router. It launched a program with the option of *tcpdump* to capture IGMP packets from the interface `br-lan` in ASUS router. Debugging of IP IGMP packets was enabled on the Cisco 2611 router (via command `debug ip igmp`).

Then the source began transmitting a data stream using VLC program to the address 239.1.1.1. Packet capture software running on the devices collected dozens of IGMP packets, from which GJD time and GLD time were read. The data obtained and the time measurements were analyzed, which were averaged and are presented in the Table 1.

Table 1. Time measurement results [s]

	S – router – G1		S – 2611 – ASUS – G1	
Router	**GJD**	**GLD**	**GJD**	**GLD**
Cisco 2611	0.3023	0.3068	0.6903	0.7001
ASUS WL500G Premium	1.7911	1.7744	1.7911	1.7744

This study aimed to compare the measurements of the time needed for connecting and disconnecting multicast groups using IGMP. The study was conducted on the Cisco 2611 router and the SOHO device ASUS WL500g Premium. For the Cisco 2611 router, the time for getting to and leaving the groups fluctuates within 0.3 seconds. For comparison, the ASUS router entered and left the multicast group oscillating in the range 1.79 seconds. This is a significant difference in favor of a Cisco router. It means that the Cisco 2611 router is a professional tool that is well suited for multicast techniques.

Next test was to see how the timing changes when connecting two devices. Time to join the group on the Cisco router in this case increased to about 0.7 seconds. However, the time on the ASUS remained unchanged at 1.79 seconds.

5   Performance Analysis

Figure 2 shows the whole testing network. The computer on the left starts by sending a video sequence to the address 239.0.0.1 using RTP protocol. In order to test lab topology VideoLAN Media Player application [29] have been used and configured for multicast purposes. OpenWRT router starts sending data to the recipients G1, G2 and G3. The application on the receiving computers generates an IGMP Report message. On receiving the message, OpenWRT sends the multicast transmission in the direction of this receiver, plus any other receivers in the group that will receive the multicast data.

The study involved two video streams that were sent from the source to the ASUS router's WAN port, forwarded on the router's LAN ports, and then received by the recipient. Streams used: Stream A with 652×278 image
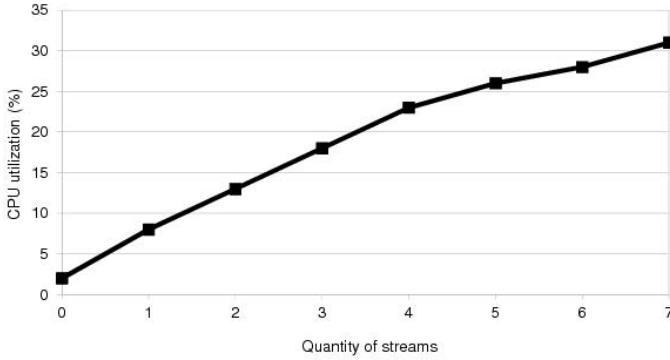
Fig. 3. CPU utilization versus the number of streams (stream A)

resolution and average bitrate 892kbps and stream B with a resolution of 1280×536 image and the average bitrate 6260kbps. To obtain the CPU load measurement a `top` program was used. ASUS router CPU load in idle state was 2%. CPU load was studied with an increasing number of streams of the same type (stream A and stream B). When increasing the number of transmitted streams, SIRQ value, responsible for software processes interrupt requests (*Software Interrupt Request*) was also increasing. With the increase of the number of broadcasted streams, the router memory usage was constant. It can be seen in the presented graphs how the router's processor was behaving when increasing the amounts of broadcasted streams.

In the case of stream A maximum value of the average CPU utilization was 31% at 7 transmitted streams at the same time (Fig. 3). The received image was smooth and had no artifacts. In the case of stream B maximum average CPU utilization was 97% at 7 transmitted streams at the same time (Fig. 4). The received image was *jamming* and had artifacts which prevented
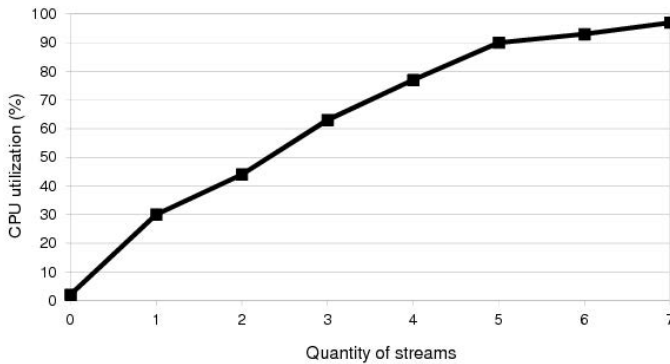
Fig. 4. CPU utilization versus the number of streams (stream B)

watching. At 7 transmitted streams, the top program which was running on the router got jammed.

Increased use of the CPU by the stream B (6260kbps) is due to a greater amount of data in one second, which increased more than 7 times in comparison with stream A (892kbps).

6 Conclusions

The results show the efficacy of using popular SOHO network devices for streaming transmissions with an application of IP Multicasting. It is appropriate solution to provide many high quality streams that is especially important in IPTV.

Multicasting is a complex issue, and here we present only the most basic concepts. Nevertheless, this brief introduction should give a head start in determining how best to implement multicasting in end-user environment.

Implementation of OpenWRT system on popular network devices that reflect IP Multicasting is not widely described in the literature.

References

1. Pasquale, J., Polyzos, G., Xylomenos, G.: The Multimedia Multicasting Problem. ACM Multimedia Systems Journal 6, 43–59 (1998)
2. Musznicki, B., Tomczak, M., Zwierzykowski, P.: Dijkstra-based Localized Multicast Routing in Wireless Sensor Networks. In: Proceedings of CSNDSP 2012, 8th IEEE, IET International Symposium on Communication Systems, Networks and Digital Signal Processing, Poznań, Poland (2012)
3. Brander, S.: Benchmarking Terminology for Network Interconnection Devices. RFC 1242 (Proposed Standard) (1991)
4. Mandeville, R.: Benchmarking Terminology for LAN Switching Devices. RFC 2285 (Proposed Standard) (1998)
5. Brander, S., McQuaid, J.: Benchmarking Methodology for Network Interconnect Devices. RFC 2544 (Proposed Standard) (1999)
6. Dubray, K.: Terminology for IP Multicast Benchmarking. RFC 2432 (Proposed Standard) (1998)
7. Stopp, D., Hickman, B.: Methodology for IP Multicast Benchmarking. RFC 3918 (Proposed Standard) (2004)
8. IETF Benchmarking Methodology (2011),
   http://datatracker.ietf.org/wg/bmwg/charter/
9. Cisco Visual Networking Index,
   http://www.cisco.com/en/US/netsol/ns827/
   networking_solutions_sub_solution.html
10. Ballardie, A., Francis, P., Crowcroft, J.: Core-based Trees (CBT) – an Architecture for Scalable Inter-domain Multicast Routing. Computer Communication Review 23, 85–95 (1993)
11. Wei, L., Estrin, D.: The Trade-offs of Multicast Trees and Algorithms. In: Proceedings of ICCCN 1994, pp. 55–64. IEEE (1994)

12. Piechowiak, M., Bartczak, T., Szewczyk, T., Zwierzykowski, P.: Między-domenowe protokoły routingu rozgałęźnego. In: XI Poznańskie Warsztaty Telekomunikacyjne, Poznań, Grudzień. Politechnika Poznańska, pp. 91–96 (2006) (in Polish)
13. Minoli, D.: IP Multicast with Applications to IPTV and Mobile DVB-H. Wiley-IEEE Press (2008)
14. O'Driscoll, G.: Next Generation IPTV Services and Technologies. Wiley (2008)
15. Hallinan, C.: Embedded Linux Primer. Prentice Hall (2010)
16. XORP Documentation, http://www.xorp.org
17. OpenWRT Documentation, http://www.openwrt.org
18. Yuzo, I., Pereira, M.: How to architect an IPTV system. Image Analysis for Multimedia Interactive Services 53 (2007)
19. Hersent, O., Petit, J., Gurle, D.: IP Telephony: Deploying Voice-over-IP Protocols. Wiley (2005)
20. Bartczak, T., Piechowiak, M., Szewczyk, T., Zwierzykowski, P.: Exploring multicast IP in Linux. Linux Magazine 201, 55–59 (2009)
21. Szewczyk, T., Zwierzykowski, P.: Testy wydajności protokołów routingu rozgałęźnego. In: XI Poznańskie Warsztaty Telekomunikacyjne, Poznań, Grudzień. Politechnika Poznańska (2006) (in Polish)
22. Deering, S.: Host Extensions for IP Multicasting. RFC 1112 (Proposed Standard) (1989)
23. Fenner, B., Handley, M., Holbrook, H., Kouvelas, I.: Protocol Independent Multicast – Sparse Mode (PIM-SM): Protocol Specification. RFC 4601 (Proposed Standard) (2006)
24. Christensen, M., Kimball, K., Solensky, F.: Considerations for Internet Group Management Protocol (IGMP) and Multicast Listener Discovery (MLD) Snooping Switches. RFC 4541 (Informational) (2006)
25. Fenner, B., He, H., Haberman, B., Sandick, H.: IGMP/MLD-based Multicast Forwarding (IGMP/MLD Proxying) (Internet Draft) (2004)
26. Cain, B., Deering, S., Fenner, B., Thyagarajan, A.: Internet Group Management Protocol, Version 3. RFC 3376 (Proposed Standard) (2002)
27. Vida, R., Costa, L.: Multicast Listener Discovery Version 2 (MLDv2) for IPv6. RFC 3810 (Proposed Standard) (2004)
28. Wing, D., Eckert, T.: IP Multicast Requirements for a Network Address Translator (NAT) and a Network Address Port Translator (NAPT). RFC 5135 (Proposed Standard) (2008)
29. VideoLAN Media Player, http://www.videolan.org

The Threat of Digital Hacker Sabotage to Critical Infrastructures

Sara Ligaard Norgaard Hald and Jens Myrup Pedersen

Department of Electronic Systems, Aalborg University, Denmark
{slh,jens}@es.aau.dk

Summary. In this paper, we analyze the threat of digital sabotage, specifically Denial of Service (DoS) attacks, to critical infrastructures such as power plants, Intelligent Transportation Systems, airports, and similar. We compare the profile of critical infrastructure installations to known attacker profiles to establish which attackers are most likely to be a threat, thereby creating a more precise threat picture to help prioritize digital defence efforts in critical infrastructure. The main contribution of the paper is the identification of which hacker categories are most probably to attack critical infrastructures. Together with the profiles of the hacker categories this can be used for identifying appropriate countermeasures against potential attacks.

1 Introduction

"It is said that if you know your enemies and know yourself, you will not be imperiled in a hundred battles; if you do not know your enemies but do know yourself, you will win one and lose one; if you do not know your enemies nor yourself, you will be imperiled in every single battle."- [Sun Tzu, 500 B.C.]

As the digital aspect of society and our lives in general becomes ever more important, the defence hereof becomes an increasingly higher priority. Billions of dollars are spent each year to protect the systems that form the basis for our everyday lives against malicious attackers who would steal our data or sabotage our critical infrastructure. It is an uneven battle - attackers need only be successful once, while the defenders must be successful every time. Therefore it is imperative that we know as much as possible about the would-be attackers and their methods to be able to prioritize the defence efforts. If we know the potential attackers, we are better able to predict, detect and manage possible attacks.

To do this, it is necessary to make a threat assessment for the systems in question (see e.g. [11]). Threats can be divided into three categories: Natural disasters, accidents, and attacks. Traditionally, attackers are considered to be the same attackers who would attack the installation/system in the physical

world (e.g. criminals and terrorists), with an added category of "hackers" (see e.g. [5] and [17]). However, "hackers" is such a loose term that by grouping all attackers into this category, it is very difficult to say anything specific about important threat properties.

For an assessment of the hacker threat to critical infrastructures to be useful, it should have a greater granularity with respect to the attacker identification. By dividing the "hacker" category into a number of subcategories, for which we can determine specific threat properties, it is possible to give a much more precise picture of the threat.

In this paper, we use the hacker categories developed by [7] to analyze the hacker threat by comparing their known profiles against the profiles of critical infrastructures to determine which subcategories pose an actual threat. The most important contribution is a precise picture of the threat of digital hacker sabotage to critical infrastructure. It forms a valuable input for further research, for example in providing inputs as to which kind of attacks are relevant to consider in more specific scenarios. Another contribution is the demonstration of how the systematic way of analysing threats of digital hacker sabotage is used.

1.1 Reader's Guide

This paper is organized as follows: In section 2 we describe the method used to assess the hacker threat, specifically the categories of hackers. Section 3 describes how their threat properties correspond with the profile of critical infra-structure at large and the detailed threat picture, including triggers and attack methods favoured by the relevant hacker categories. Finally, we put our work into perspective in section 4 and conclude in section 5.

2 Methods

In [7] hackers are divided into eight different categories, each with their own distinctive profile with regards to threat properties:

1. Script Kiddies
2. Cyper-Punks
3. Insiders
4. Petty Thieves
5. Gray Hats
6. Professional Criminals
7. Hacktivists
8. Nation States

Each of these categories will be evaluated separately, whether or not they represent a sabotage threat against critical infrastructures. Sabotage is in this context considered as reducing or removing the availability of the service

provided by the critical infrastructure. In terms of cyberattacks, this can be achieved e.g. by a malicious use of controls, (Distributed) Denial of Service (DDOS) attacks, or worms[18], and for this paper these are the vectors that will be considered.

The threat assessment is performed by comparing hacker motives (intent) and capabilities (competencies and resources available)[11], with the profile of the critical infrastructure. This profile is described widely in literature, e.g. [14] and [10], and will be summarized in the following section.

2.1   Threat Profile for Critial Infrastructure

Critical infrastructure is generally well protected, or at least should be. While the rapid amount of infrastructure relying on network- and Internetbased systems do form a challenge, we generally assume that appropriate action has been taken to make critical infrastructure well protected - otherwise this would be a first step to do. Thus we assume that security (including cybersecurity) is a priority, and that critical infrastructure is not vulnerable to exploits of common security holes. The following provides a description of the profile of critical infrastructure as a target as described by threat properties[7].

Intent: Critical Infrastructure is a high-profile target that provides critical services to the area it is located in, indicating that attackers with Notoriety or Revenge motives would find critical infrastructure tempting targets. The return on investment on sabotaging critical infrastructure for money is very low because of the high security and the lack of monetary gain, so Financial motives are not likely to drive a hacker to this type of attack. And while Curiosity might cause an attacker to try and break into critical infrastructure, it is unlikely that it would spur the hacker to perform sabotage[12].

Triggers: Critical infrastructures, being high-profile targets, do not need any special triggers to be attacked. However, since critical infrastructures are often state-run and a necessity for a state to run, attackers with revenge motives could be triggered to attack at a perceived threat or insult from the government of the state in question.

Capabilities - Skills: Critical infrastructures should be and usually are protected against common vulnerabilities; the systems are updated and protected by security solutions. Therefore it takes either a significant amount of very specialized skills to break the defences and/or considerable resources[13].

Capabilities - Resources: For sabotage of critical infrastructures to be really effective, several facilities need to be hit for prolonged periods. This requires either huge amounts of resources to be able to hit several systems in parallel and sustain attacks, or very specialized skills and insider knowledge to create cascading effects between networked systems.

Methods: While critical infrastructures are generally well protected, no system is completely secure. Critical infrastructures are vulnerable to all considered attack vectors (malicious use of controls, DDoS attacks, and worms) if the attackers utilize them with enough resources and/or skills.

Trends: The increased focus on cybersecurity in the society in general also has a positive effect on the security awareness of critical infrastructure. One example is that industrial control systems are generally better protected after the Stuxnet incident made everyone aware that they are a potential target[8].

2.2   Threat Assessment

For each hacker profile it is assessed if the group has *the will* (intent, triggers) to attack, and *the capabilities* (skills, resources) to execute a successful attack, and a hacker category is only considered a threat if both these parameters are present[5]. The result will be an assessment of which categories of hackers presently should be considered a digital sabotage threat to critical infrastructures. This assessment is further refined by looking at the preferred vectors of attack.

3   Results

In this section, we compare the threat properties for each of the hacker categories with the target profile of critical infrastructures to determine whether or not each category is a threat. The threat properties of the hacker categories below are found in [7].

3.1   Script Kiddies

Attackers of the Script Kiddies category are novices with low hacking skills and limited understanding of technical consequences, who use tools or scripts downloaded from the Internet.

Intent: Primary motivations for Script Kiddies are notoriety and curiosity, and as such critical infrastructure being a high-profile target would be attractive, but the tools used by script kiddies often choose targets at random, see for example [16].

Triggers: The only trigger Script Kiddies need to attack is the opportunity. If they find a vulnerability in their random, automated search, they will exploit it.

Capabilities - Skills: Low technical competencies makes it highly improbable that a Script Kiddie could execute a successful attack against a target

with a minimum of up-to-date defences. This is expected to exclude critical infrastructures from their targets.

Capabilities - Resources: Having very little resources available and operating solo further decreases the probability of a successful attack.

Threat Assessment: Have the will but lack the capabilities.

3.2 Cyper-Punks

Members of the Cyber-Punks category are medium-skilled but mostly solitary hackers and virus writers.

Intent: Primary motivations for Cyber-Punks are notoriety and curiosity. They might target critical infrastructure.

Triggers: Cyber-punks need no trigger to attack.

Capabilities - Skills: Cyber-Punks have some technical skills and understanding, and they will be able to use and even improve tools available on the Internet. A Cyber-Punk might write their own malware exploiting well-known vulnerabilities, but they are not likely to develop their own zero-days or perform very advanced attacks.

However, some virus writers also fall under this category, and a novel virus might compromise one or more critical infrastructure systems[6]. It is not likely that systems could be compromised in such a manner as to cause cascading failures without being specifically designed to do so, but if a worm spreads aggressively enough to infect a large number of critical infrastructure systems, then it could cause widespread denial of service.

Capabilities - Resources: Cyber-punks have limited resources since they are mostly solitary, or in small groups. They are likely to able to perpetrate simple, isolated attacks, although nothing sustained or large-scale.

Threat Assessment: Have the will and the capabilities.

3.3 Insiders

Insiders are malicious but trusted people with privileged access and knowledge of the systems in question.

Intent: Insiders are motivated by revenge and to some degree notoriety, and the former part makes them likely to try to conduct sabotage.

Triggers: A malicious Insider mostly needs to be triggered to attack, however since the trigger can be any perceived insult or slight at the workplace, it can be very hard to determine whether or not a potential attacker has been triggered - especially considering that the potential attacker is typically a trusted employee.

Capabilities - Skills: An Insider can have extensive knowledge of the system, including vulnerabilities, as well as privileged access to controls. An Insider might even have the skills to perpetrate an effective cascading attack.

Capabilities - Resources: While Insiders very often work alone, they usually have the resources needed to make an effective attack, namely privileged access to controls, and physical access to the systems.

Threat Assessment: Have the will and the capabilities.

3.4   Petty Thieves

Members of the Petty Thieves category commit low-level fraud and theft, usually by using existing tools and scripts.

Intent: Petty Thieves are primarily motivated by financial gain, and as such, critical infrastructures do not constitute an attractive target to members of this category.

Triggers: This group needs no other trigger than opportunity and a viable business case to attack.

Capabilities - Skills: Petty Thieves use a standard portfolio of tools and techniques primarily focused around phishing, scamming, and credit card fraud. They are not likely to possess the skill set nor the tools needed to attack critical infrastructures.

Capabilities - Resources: Members of this group work alone or in small groups, and considering their focus on low-level crime, it is not likely they will have the resources needed to commit a successful attack.

Threat Assessment: Lack the will and the capabilities.

3.5   Grey Hats

Grey Hats are often skilful hackers with limited criminal intent but a lack of respect for limitation on information flow and a large curiosity.

Intent: This category of attackers is primarily motivated by curiosity, and they are very unlikely to perpetrate any form of sabotage. Triggers: Rumours of secret information or "impenetrable" defences might increase the risk of attack.

Capabilities - Skills: Grey Hat hackers have very specialized technical skill sets and an extensive exchange of information, and as such it is likely they would be able to execute an attack successfully.

Capabilities - Resources: While there is a high degree of knowledge exchange in this group, most work alone and as such do not have the manpower

to make widespread and persistent attacks. They do have the skills and equipment however, to gain insider access to the systems in question, which could enable them to execute a cascading attack.

Threat Assessment: Lack the will but have the capabilities.

3.6   Professional Criminals

Professional Criminals are organised groups of hackers with a strict business approach to attacks.

Intent: Professional Criminals are purely financially motivated. There is currently no business model that makes the reward of an infrastructure attack worth the risk, since most governments do no negotiate with terrorists, so they are unlikely to attack.

Triggers: Like Petty Thieves, the Professional Criminals need no specific trigger apart from a viable business case.

Capabilities - Skills: Members of this group of attackers possesses a wide variety of technical skills and knowledge, and they are willing to recruit or hire people with the necessary competencies to complete an operation.

Capabilities - Resources: This group has many resources in the form of money, equipment, and manpower - enough to perpetrate a successful attack against critical infrastructures.

Threat Assessment: Lack the will but have the capabilities.

3.7   Hacktivists

Hacktivists are groups of ideologically motivated hackers with varying technical skills, but many and geographically distributed members.

Intent: Since Hacktivists are motivated by ideological agendas and notoriety and known for a lack of regard for consequences, they are likely to target critical infrastructures. The US Department of Defense warns that it believes one of the biggest hacktivist groups, Anonymous, have both the will and the capability to attack[4]. However, Anonymous have publicly declared[1] that they are not interested in attacking the power grid because they realize the adverse effect it would have on the general population, and as such the intent in this regard is not completely clear. There are many groups, though, and not all of them have the same moral scruples as Anonymous claims to have. On the other hand, they do not alone have the necessary resources available.

Triggers: Hacktivists are triggered by perceived threats or insults to their ideology.

Capabilities - Skills: While the levels of technical skills are diverse within the Hacktivist groupings, they usually have members with high technical competencies, although they might not have the highly specialized skills needed for a cascading attack.

Capabilities - Resources: Hacktivists have a large geographical spread and sometimes vast amounts of manpower. They may also have the attack resources in the form of botnets available to execute a widespread and sustained attack. However, only Anonymous is big enough at this point in time to conduct a sustained attack, and they have declared a lack of interest in doing so. This is subject to change though.

Threat Assessment: Have the will or the capabilities, but not both.

3.8 Nation States

Nation States or representatives hereof have been known to perpetrate everything from industrial espionage over acts of terrorism to devastating nationwide attacks in the cyber arena.

Intent: In case of a conflict, any disruption of the enemy's infrastructure is desirable, and as such, critical infrastructures represent an extremely attractive target to a hostile Nation State.

Triggers: Nation States are almost exclusively triggered by disputes in the physical arena, most often geopolitical in nature.

Capabilities - Skills: Many Nation States have substantial presence in cyberspace and commands many highly skilled experts in the critical infrastructure field.

Capabilities - Resources: They have vast resources in the form of money, manpower, specialized knowledge and intelligence, and equipment. They are very likely to be able to conduct a successful attack.

Threat Assessment: Have the will and the capabilities.

3.9 Threat Picture

Three of the hacker categories - Insiders, Hacktivists, and Nation States, see Table 1 - can be considered a substantial sabotage threat to critical infrastructure at this time, but this is subject to change. Currently, only these three categories have both the will and the capabilities to execute a successful attack on critical infrastructure.

Table 1. Threat matrix indicating will and capabilities of attackers

Categories	Will	Capability	Threat
Script Kiddies	Yes	No	No
Cyber-Punks	Yes	Yes	Yes
Insiders	Yes	Yes	Yes
Petty Thieves	No	No	No
Gray Hats	No	Yes	No
Professional Criminals	No	Yes	No
Hacktivists	Yes/No	Yes/No	No
Nation States	Yes	Yes	Yes

3.10   Defence Priorities

Working to defend critical infrastructure in a resource-constrained environment means that limited budget funds must be applied to achieve the best effect. While the thorough "basic" security is assumed in place, there are many areas in which a security officer could focus his or her attention.

By looking deeper into the threat property "methods"[7], it is possible to refine the threat picture even further, and suggest which defence measures to priotitize.

Cyber-Punks Methods

While most of the attacks performed by this category of attackers are limited in scope and sophistication, the Cyber-Punks do have one weapon that is a legitimate sabotage threat to critical infrastructures, namely viruses. A worm exploiting an unanticipated attack vector might plausibly infect several of critical infrastructure systems and causing widespread denial of service. Viruses such as Melissa (1999), ILOVEYOU (2000), Nimda (2001), Slammer (2003), and Conficker (2008) (most contributable to Cyber-Punks) show that it is certainly possible to reach a critical amount of infection in a very short while. To defend against such a worm may prove difficult[19]. An Intrusion Detection and Prevention System (IDPS) that uses statistical anomaly-based detection and/or stateful protocol analysis detection would have a good of chance of catching such a threat, and there are different ways of hardening the network, depending on how fast the worm propagates[2][15].

Insider Methods

Attacks by Insiders will likely take the form of malicious use of controls. In a survey, 43% of Insider attacks were executed while the attacker still had legitimate access to the systems. The majority of the attacks were executed while the attacker should no longer have this access[9]. The defence mechanisms that would help defend against such attacks would implement the

principle of least privilege to limit the amount of damage that can be done with malicious use of legitimate access. Also, having tight management of personnel access would limit the amount of damage previous employees could cause, since they would lose access as soon as they were no longer employed. More detailed advice on how to mitigate the threat of Insider attacks can be seen in [3].

Nation State Methods

The methods employed by Nation States vary, but there seems to be a prevalence towards spear-phishing and zero-day exploits combined with worms (e.g. Night Dragon and Stuxnet attacks) as well as devastating DDoS attacks (e.g. Georgia, 66, and 10 Days of Rain). Defence priorities include educating staff and increasing awareness to avoid anyone falling victim to spear-fishing or similar social engineering attacks. It is quite difficult to detect the use of zero-day exploits, but good intrusion detection systems might be able to pick up the change in network behaviour. DDoS prevention should also be a priority, and the volume of the attacks can be expected to be severe, so cooperation with e.g. large ISPs might be an option to consider.

4   Discussion

By dividing the "hacker" category into subcategories with distinctive threat properties for the assessment of the hacker sabotage threat to critical infrastructure, it is possible to give a more precise threat picture than what is known today. Compared to other threat assessments, e.g. as presented in [5] and [17], it is possible to give more details on the expected attack methods and triggers for attack.

Based on the threat picture in this paper, defence efforts against digital sabotage of critical infrastructures should focus on dealing with malicious Insiders as well as Cyber-Punks, and hostile Nation States. This could be done by prioritizing access management, including implementing the principle of Least Privilege, as well as installing an Intrusion Detection and Prevention System, educating staff to be wary of spear-phishing and similar social engineering attacks, and protecting systems from DDoS attacks.

Defence efforts should be particularly focused in times of geopolitical conflict, where the risk of a Nation State attack is high. Furthermore, an eye should be kept on the development in the Hacktivist category, since there is a risk that this group will develop into a threat in the near future.

The analysis presented can also be used when designing and deploying new infrastructures such as Smart Grid, Intelligent Transportation Systems, and infrastructures supporting Tele-Health in larger scales. Knowing which groups are the most probable attackers, and knowing their capabilities in terms of skills and resources, can help identify which kinds of attacks are

important to prepare for. There is a big difference between being attacked by Insiders, Nation States, or Script Kiddies. For researchers in the domain of cyber security this knowledge can be used to indicate where further research and development is needed, e.g. when developing technologies for intrusion detection systems for general or specific critical infrastructures.

The authors would like to stress that the analysis presents a current picture of threats, and that the hacker groups and threat properties can and probably will change over time. However, we believe that the method provided in this paper is useful for future updates.

Finally, threat assessment of digital hacker sabotage is no exact science, and what we have presented does not provide any quantitative measures for what attacks will be done by who in the near and far future, nor any analysis of what counter measurements to take. We will leave such more specific threat assessment to relevant authorities. However, we believe and hope that our more general results are useful for researchers and developers working with critical infrastructure.

5   Conclusion

In this paper we analysed the threat of digital sabotage to critical infrastructure systems. Based on hacker categories and their attacker profiles, we have drawn a picture of the most important threats to critical infrastructure, which can help prioritize defence efforts, and provide valuable inputs to researchers and developers. Our analysis shows that Cyber-punks, Insiders and Nation States are the hacker categories, which possess the wills and capabilities to perform such attacks.

The main contribution of the paper is the actual results obtained, e.g. an identification of which hacker categories are most probably to attack critical infrastructures, as well as descriptions of their profiles, which can be used for taking appropriate countermeasures for prediction, prevention and management of attacks.

Another contribution is the methodology demonstrated which is useful for updating the threat assessment presented, and which can be used for other analyses of threats of digital hackers.

We would like to encourage further research in the domain of systematically assessing threats to both critical infrastructures and other large-scale IT-systems. There is a specific need for validation of models and categories used, based on e.g. previous attacks and identification of actual threats.

References

1. Anonymous, @YourAnonNews (2012),
   `https://twitter.com/youranonnews/status/171941104860672000`
2. Antonatos, S., Akriditis, P., et al.: Defending against Hitlist Worms using Network Address Space Randomization. In: WORM 2005. ACM, USA (2005), 1-59593-229-1/05/0011

3. Capelli, D., Moore, A., et al.: Common Sense Guide to Prevention and Detection of Insider Threats, 3rd edn., Version 3.1. Software Engineering Institute, Carnegie Mellon University (2009)
4. Department of Homeland Security, National Cybersecurity and Communications Integration Center Bulletin: Assessment of Anonymous Threat to Control Systems, Department of Homeland Security, USA (2011)
5. Devost, M.G.: Current and Emerging Threats to Information Technology Systems and Critical Infra-structures. Global Business Briefing (2000)
6. Eronen, J., Karjalainen, K., et al.: Software Vulnerability vs. Critical Infrastructure - a Case Study of Antivirus Software. International Journal on Advances in Security 2(1) (2009) ISSN 1942-2636
7. Hald, S.L.N., Pedersen, J.M.: An Updated Taxonomy for Characterizing Hackers According to Their Threat Properties. In: 14th International Conference on Advanced Communication Technology (ICACT) 2012. IEEE (2012) ISBN 978-8955191639
8. Hunt, J.: Stuxnet, Security, and Taking Charge, Industrial Ethernet Book Issue 62/53, IEB Media GbR, Germany (2011) ISSN 1470-5745
9. Keeney, M., Cappelli, D., et al.: Insider Threat Study: Computer System Sabotage in Critical Infrastructure Sectors. United States Secret Service and Carnegie Mellon Software Engineering Institute, USA (2005)
10. Lewis, J.A.: Cybersecurity and Critical Infrastructure Protection. Center for Strategic and International Studies, USA (2006)
11. Moteff, J.: Risk Management and Critical Infra-structure Protection: Assessing, Integrating, and Managing Threats, Vulnerabilities and Consequences. Congressional Research Service, USA (2005)
12. Rogers, M.: A two-dimensional circumplex approach to the development of a hacker taxonomy. Digital Investigation 3, 97–102 (2006)
13. Rollins, J., Wilson, C.: Terrorist Capabilities for Cyberattack: Overview and Policy Issues. Congressional Research Service, USA (2007)
14. Shea, D.A.: Critical Infrastructure: Control Systems and the Terrorist Threat. Congressional Research Service, USA (2004)
15. Shou-Chuan, L., Wen-Chu, K., et al.: Defending against Internet Worm-like Infestations. In: Proceedings of the 18th International Conference on Advanced Information Networking and Application (AINA 2004). IEEE (2004) ISSN 0-7695-2051-0/04
16. The Honeynet Project. Know Your Enemy: Learning about Security Threats, 2nd edn. The Honeynet Project, USA (2004) ISBN 978-0321166463
17. The White House. The National Strategy to Secure Cyberspace, p. 5. The White House, USA (2003)
18. Vatis, M.A.: Cyber Attacks During the War on Terrorism: A Predictive Analysis. Institute for Security, Dartmouth College (2001)
19. Wiley, B.: Curious Yellow: The First Coordinated Worm Design (2002), http://blanu.net/curious_yellow.html

Machine Learning Techniques for Cyber Attacks Detection

Rafał Kozik[1] and Michał Choraś[1,2]

[1] Institute of Telecommunications, UT&LS Bydgoszcz, Poland
  chorasm@utp.edu.pl
[2] ITTI Ltd., Poznań, Poland
  mchoras@itti.com.pl

Summary. The increased usage of cloud services, growing number of users, changes in network infrastructure that connect devices running mobile operating systems, and constantly evolving network technology cause novel challenges for cyber security that have never been foreseen before. As a result, to counter arising threats, network security mechanisms, sensors and protection schemes have also to evolve in order to address the needs and problems of nowadays users.

1 Introduction

Recently there is an increasing number of security incidents reported all over the world. This situation is strongly related to the fact that recently there is also an increasing number of mobile devices users that form the population of connect-from-anywhere terminals that regularly test the traditional boundaries of network security.

In our previous work [2], we have introduced an innovative evolutionary algorithm for modeling genuine SQL queries generated by web-application. In this paper we have extended our algorithm with Bayes inference in order to incorporate advantages of signature-based and anomaly-based methods. The proposed approach allows for extracting patterns (in form of a PCRE regular expression) of a genuine SQL queries that can be easily incorporated in any rule processing engine (e.g. Snort). Moreover, the results showed that combining that kind of attack detector with character distribution allows for additional effectiveness improvements.

The paper is structured as follows. In Section 2 we present an overview of existing machine learning techniques for cyber attack detection. In Section 3 we present our own solution for SQL Injection attempts detection based on Bayes inference. The experimental setup and results are provided in consecutive sections. Conclusions are given thereafter.

2   Overview of Methods for Cyber Attack Detection

2.1   Signature-Based Methods

The Signature-based category of cyber attacks detection methods typically include Intrusion Prevention and Detection Systems (IDS and IPS) which use predefined set of patters (or rules) in order to identify an attack. The patterns (or rules) are typically matched against a content of a packet (e.g. TCP/UDP packet header or payload). Commonly IPS and IDS are designed to increase the security level of a computer network trough detection (in case of IDS) and detection and blocking (in case of IPS) of network attacks.

One of the most popular IDS/IPS software, widely deployed worldwide, is Snort [7]. Since it is an open source project, its users are allowed to freely modify it as well as feed the Snort engine with rules obtained from different sources (e.g. not only form Snort homepage).

Commonly the signatures (in form of reactive rules) of an attack for a software like Snort are provided by experts form a cyber community. Typically, for deterministic attacks it is fairly easy to develop patterns that will clearly identify particular attack. It often happens when given malicious software (e.g. worm) uses the same protocol and algorithm to communicate trough network with command and control center or other instance of such software. However, the problem of developing new signatures becomes more complicated when it comes to polymorphic worms or viruses. Such software commonly modifies and obfuscates its code (without changing the internal algorithms) in order to be less predictive and hard to detect.

Therefore, recently a machine learning based algorithms have been adapted for developing signatures that will be efficiently identify both code and behaviour of malicious code. The Network-based Signature Generation (NSG) [3], Length-based Signature Generation (LSEG) [4], and F-Sign [5] are examples of algorithms designed for automated and fast extraction of signatures of polymorphic worms. The LESG algorithm targets those worms that use buffer overflow attack to infect victims, while the F-Sign extracts the signature on a basis of code of a worm (such signature can be use to detect and stop worm from spreading). In literature there are also algorithms such as SA (Semantic Aware [6]) that are designed to generate signatures of malicious software on a basis of network traffic they generate. Such solutions like [6] can even properly identify malicious behaviour when the traffic is noise-like.

2.2   Anomaly-Based Methods

The anomaly-based methods for a cyber attacks detection typically build a model that is intended to describe normal and abnormal behaviour of network traffic. Commonly such methods use two types of algorithms borrowed from machine learning theory, namely unsupervised and supervised approach.

For unsupervised learning commonly [8, 9, 10, 11, 12, 13, 14] clustering approaches are used that usually adapt algorithms like k-means, fuzzy c-means, QT, and SVM. The clustered network traffic established using mentioned approaches commonly requires decision whenever given cluster should be indicated as a malicious or not. Pure unsupervised algorithms use a majority rule telling that only the biggest clusters are considered normal. That means that network events that happen frequently have no symptoms of an attack. In practice, it is a human role to tell which cluster should be considered as an abnormal one.

The supervised machine learning techniques require at least one phase of learning in order to establish the traffic model. The learning is typically off-line one and is conducted on specially prepared (cleaned) traffic traces. One of the exemplar approaches to supervised machine learning for cyber attack detection uses auto regression stochastic process (AR) [15, 16, 17]. In literature there are also methods using Kalman filters [21]. Recently, more gaining in popularity are solutions adapting SVM [20], neural networks [19], and ID3-established decision trees [18].

3   Proposed Approach to Injection Attack Detection

The proposed approach engages a Bayesian inference theory for cyber attacks detection. For that purpose a directed acyclic network (graph) is built, which is a graphic representation of the joint probability distribution function over a set of variables. In such graph each node represents random variable while the edge indicates a dependant relationship.
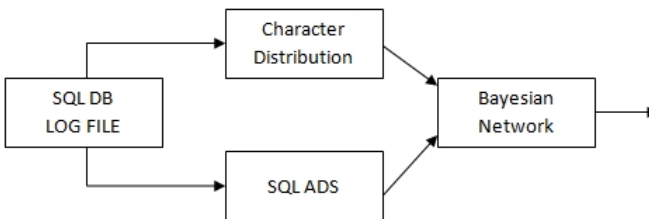
Fig. 1. Diagram of proposed algorithm

As it is shown in Fig.1, two types of observations are used in order to evaluate a probability of an attack. One of the observations is obtained from SQL-ADS, while the other comes from character distribution model. Both of the methods of injection attack detection are detailed in following sections. The fact that particular query (Q) is an injection attack (A) given the observation (O_{ads}, O_{chisq}), is evaluated using formula 1.

$$\dot{A} = \arg\max_A p_Q(A|O_{ads}, O_{chisq}) \tag{1}$$

The probability $p_Q(A|O_{ads}, O_{chisq})$ is represented as a joint probability distribution function over a set of variables A, O_{ads}, O_{chisq} incorporated into equation 2.

$$p_Q(A|O_{ads}, O_{chisq}) = \frac{p_Q(A, O_{ads}, O_{chisq})}{p_Q(O_{ads}, O_{chisq})} \tag{2}$$

After applying Bayes's formula the joint probability in the nominator can be substituted with conditional probability as it is shown in equation 3.

$$p_Q(A|O_{ads}, O_{chisq}) = \frac{p_Q(O_{ads}|O_{chisq}, A)p_Q(O_{chisq}|O_{ads}, A)p_Q(A)}{p_Q(O_{ads}, O_{chisq})} \tag{3}$$

The denominator in formula is a constant value that does not depend on variable A. Moreover, we also have assumed both observations O_{ads} and O_{chisq} are statistically independent. Therefore, the probability $p_Q(A|O_{ads}, O_{chisq})$ can be rewritten as equation 4

$$p_Q(A|O_{ads}, O_{chisq}) \propto p_Q(O_{ads}|A)p_Q(O_{chisq}|A)P_Q(A) \tag{4}$$

The methods for evaluating value of O_{ads} and O_{chisq} for a given SQL query Q were described in section 3.1 and section 3.2 respectively.

3.1   Extracting Signatures from SQL Queries

The details about the algorithm can be found in our previous work [2]. Therefore, to keep this paper self-contained here we only introduce the most important aspects.

The proposed method exploits genetic algorithm, where the individuals in the population explore the log file that is generated by the SQL database. Each individual aims at delivering an generic rule (which is a regular expression in form "SELECT [a-z,]+ FROM patient WHERE name like [a-zA-z]+") that will describe visited log line. It is important for the algorithm to have an set of genuine SQL queries during the learning phase. The algorithm is divided into the following steps:

- Initialization. Each individual and line from log file is assigned. Each newly selected individual is compared to the previously selected in order to avoid duplicates.
- Adaptation phase. Each individual explores the fixed number of lines in the log file (the number is predefined and adjusted to obtain reasonable processing time of this phase).
- Fitness evaluation. Each individual fitness is evaluated. The global population fitness as well as rule level of specificity are taken into consideration, because we want to obtain set of rules that describe the lines in the log file.

- Cross over. Randomly selected two individuals are crossed over using algorithm for string alignment. If the newly created rule is too specific or too general it is dropped in order to keep low false positives and false negatives.

The fitness function, that is used to evaluate each individual, takes into account the particular regular expression effectiveness (number of times it matches to a given SQL query string), the level of specificity of such rule and the overall effectiveness of the whole population. The fitness function is described by equation 5, where I indicates the particular individual regular expression, $E_{population}$ indicates the fitness of the whole population, E_f effectiveness of regular expression (number of times the rule fires), and E_s indicates the level of specificity (in order to avoid too short regular expressions like ".*"). The α, β, and γ are constants that normalize the overall score and weight each coefficient importance.

$$E(I) = \alpha * E_{population} + \beta * E_f(I) + \gamma * E_s(I) \qquad (5)$$

$$E_{population} = \sum_{I \in Population} E_f(I) \qquad (6)$$

3.2 Estimating Character Distribution for SQL Queries

The method is similar to the one proposed by C.Kruegel in [1]. The proposed character distribution model for describing the genuine traffic generated to web application. The Idealized Character Distribution (ICD) is obtained during the training phase from "clean" requests sent to web application. The IDC is calculated as mean value of all character distributions. During the detection phase the probability that the character distribution of a query is an actual sample drawn from its ICD is evaluated. For that purpose Chi-Square metric is used. The equation used for evaluating the value of variable $O_{chisq}(Q)$ for a query Q is described by formula 7, where N indicates the length of a query Q, ICD the character distribution of all genuine SQL queries, σ the standard deviation form the ICD, and $h()$ the character distribution of a tested query Q.

$$O_{chisq}(Q) = \sum_{n=0}^{N} \frac{1}{\sigma^2}[ICD_n - h(Q_n)]^2 \qquad (7)$$

4 Experiments and Results

In this section our evaluation methodology is described. The SQL Injection Attacks are conducted on php-based web service with state of the art tools for services penetration and SQL injection. The traffic generated by attacking

tools are combined together with normal traffic (genuine queries) in order to estimate the effectiveness of the proposed methods. The genuine queries are both man-made and generated by web crawlers as well.

The web service used for penetration test is so called LAMP (Apache + MySQL + PHP) server with MySQL back-end. It is one of the most common worldwide used servers and therefore it was used for validation purposes. The server was deployed on Linux Ubuntu operation system. For penetration tests examples services developed in PHP scripts and shipped by default with the server are validated.

Attack injection methodology is based on the known SQL injection methods, namely: boolean-based blind, time-based blind, error-based, UNION query and stacked queries. For that purpose sqlmap tool is used. It is an open source penetration and testing tool that allows the user to automate the process of validating the tested services against the SQL injection flaws.

In order to avoid double-counting the same attack patterns during the evaluation process, we decided to gather first the malicious SQL queries generated by sqlmap (several hundreds of different injection trials). After that genuine traffic (generated by crawlers and during the normal web service usage) is gathered.

The proposed method for injection attack detection has been compared with known in the literature solutions, namely Apache SCALP, SNORT, and ICD. Apache SCALP is an analyzer of Apache server access log file. It is able to detect several types of attacks targeted on web application. The detection is a signature-based one. The signatures have form of regular expressions that are borrowed from PHP-IDS project.

The results show that SCALP and Snort are not efficient solutions for SQL attack detection. The advantage is that they can be easily fed with new signatures. However, most of the available rules are intended to detect very specific type of attacks that usually exploit very specific web-based application vulnerabilities.

Table 1. Effectiveness of injection attack detection

	SNORT	ICD	SCALP	Proposed Methods
Effectiveness	78,3%	95,0%	89,0%	97,0%

5 Conclusions

In this paper we have extended our previous work presented in [2]. We have compared our method with known in the literature solutions for injection attack detection. Our experiments showed that available signatures-based solutions for SQL injection attacks are not efficient. Most of the available rules are intended to detect very specific type of attacks that usually exploit very specific web-based application vulnerabilities. The proposed algorithm

combines advantages of ADS and signature-based methods. It allows the algorithm to achieve detection effectiveness that is significantly better when compared to signature-based methods only.

References

1. Kruegel, C., Toth, T., Kirda, E.: Service specific anomaly detection for network intrusion detection. In: Proc. of ACM Symposium on Applied Computing, pp. 201–208 (2002)
2. Choraś, M., Kozik, R., Puchalski, D., Hołubowicz, W.: Correlation Approach for SQL Injection Attacks Detection. In: Herrero, Á., et al. (eds.) Int. Joint Conf. CISIS'12-ICEUTE'12-SOCO'12. AISC, vol. 189, pp. 177–185. Springer, Heidelberg (2013)
3. NSG, `http://www.ijcst.com/vol31/4/sridevi.pdf`
4. LESG, `http://www.cs.northwestern.edu/~ychen/Papers/LESG-ICNP07.pdf`
5. Shabtai, A., Menahem, E., Elovici, Y.: F-Sign: Automatic, Function-Based Signature Generation for Malware. IEEE Transactions on Systems, Man, and Cybernetics, Part C: Applications and Reviews 41(4), 494–508 (2011)
6. Kong, D., Jhi, Y.-C., Gong, T., Zhu, S., Liu, P., Xi, H.: SAS: Semantics aware signature generation for polymorphic worm detection. In: Jajodia, S., Zhou, J. (eds.) SecureComm 2010. LNICST, vol. 50, pp. 1–19. Springer, Heidelberg (2010)
7. SNORT. Project homepage, `http://www.snort.org/`
8. Sharma, M., Toshniwal, D.: Pre-clustering algorithm for anomaly detection and clustering that uses variable size buckets. In: 2012 1st International Conference on RecentAdvances in Information Technology (RAIT), pp. 515–519 (2012)
9. Adaniya, M.H.A.C., Lima, M.F., Rodrigues, J.J.P.C., Abrao, T., Proenca, M.L.: Anomaly detection using DSNS and Firefly Harmonic Clustering Algorithm. In: 2012 IEEE International Conference on Communications (ICC), pp. 1183–1187 (2012)
10. Mazel, J., Casas, P., Labit, Y., Owezarski, P.: Sub-Space clustering, Inter-Clustering Results Association and anomaly correlation for unsupervised network anomaly detection. In: 2011 7th International Conference on Network and Service Management (CNSM), pp. 1–8 (2011)
11. Yang, C., Deng, F., Yang, H.: An Unsupervised Anomaly Detection Approach using Subtractive Clustering and Hidden Markov Model. In: Second International Conference on Communications and Networking in China, CHINACOM 2007, pp. 313–316 (2007)
12. Liang, H., Wei-wu, R., Fei, R.: An Adaptive Anomaly Detection Based on Hierarchical Clustering. In: 2009 1st International Conference on Information Science and Engineering (ICISE), pp. 1626–1629 (2009)
13. Pons, P., Latapy, M.: Computing Communities in Large Networks Using Random Walks. Journal of Graph Algorithms and Applications 10(2), 191–218 (2006)

14. Liao, Q., Blaich, A., Van Bruggen, D., Striegel, A.: Managing networks through context: Graph visualization and exploration. Computer Networks 54, 2809–2824 (2010)
15. Ricciato, F., Fleischer, W.: Bottleneck Detection via Aggregate Rate Analysis: A Real Casein a 3G Network. In: Proc. IEEE/IFIP NOMS (2004)
16. Thottan, M., Ji, C.: Anomaly Detectionin IP Networks. IEEE Trans. Signal Processing, Special Issue of Signal Processing in Networking 51(8), 2191–2204 (2003)
17. Rish, I., Brodie, M., Sheng, M., Odintsova, N., Beygelzimer, A., Grabarnik, G., Hernandez, K.: Adaptive Diagnosis in Distributed Systems. IEEE Tran. Neural Networks 16(5), 1088–1109 (2005)
18. Gaddam, S.R., Phoha, V.V., Balagani, K.S.: K-Means+ID3: A Novel Method for Supervised Anomaly Detection by Cascading K-Means Clustering and ID3 DecisionTree Learning Methods. IEEE Transactions on Knowledge and Data Engineering 19(3), 345–354 (2007)
19. Ma, R., Liu, Y., Lin, X., Wang, Z.: Network Anomaly Detection Using RBF Neural Network with Hybrid QPSO. In: IEEE International Conference on Networking, Sensing and Control, ICNSC 2008, pp. 1284–1287 (2008)
20. Ma, J., Dai, G., Xu, Z.: Network Anomaly Detection Using Dissimilarity-Based One-Class SVM Classifier. In: International Conference on Parallel Processing Workshops, ICPPW 2009, pp. 409–414 (2009)
21. Soule, A., Salamatian, K., Taft, N.: CombiningFiltering and Statistical Methods for AnomalyDetection. In: Proc. of IMC Workshop (2005)

Genetic Algorithm for Scheduling Routes in Public Transport

Maria de los Angeles Sáez Blázquez, Sebastián García-Galán,
José Enrique Munoz-Expósito, and Rocío Pérez de Prado

Telecommunication Engineering Dpt., University of Jaén,
Alfonso X El Sabio 28, Linares, Spain
`masb0001@red.ujaen.es`, `{sgalan,jemunoz,rperez}@ujaen.es`

Summary. In this paper a genetic algorithm for scheduling routes in public transport is presented. It combines bus, light rail and metro, with access to other sea and air communication nodes. Results are compared with the shortest path routing algorithm Dijkstra, optimizing the distance and generation of a greenhouse gas as CO_2. The proposed algorithm has a computational cost advantage compared to shortest path algorithms.

1 Introduction

This paper presents a strategy to find optimal paths in passenger transport lines using genetic algorithms. For planning an urban public transport system, the efficiency of each route must be considered in a way that it allows a minimun number of paths or the shortest distance to users. Also, the solutions need to be economically viable and furthermore, it is desirable to offer green solutions. In large cities the generation of greenhouse gases is a relevant problem, and public transport helps combat this effect, reducing emissions compared to private vehicles. In this work less polluting path in terms of CO_2 emissions is used as an optimization critera. It has been shown in the literature [1] that there is a proportional relationship between fuel consumption, distance and CO_2 emissions.

This paper is organized as follows. Section 2 establishes some basic notation and background. Section 3 formally introduces the proposed genetic algorithm including the preprocessing. In Section 4, simulations and results are shown and finally in Section 5 we conclude with final remarks and conclusions.

2 Background

For scheduling routes in public transport, we define the different paths between stops as set of vertices connected by edges. This set is represented as a

graph. A graph is a representation of a set of objects where some pairs of the objects are connected by links. The interconnected objects are represented by mathematical abstractions called vertices and the links that connect some pairs of vertices are called edges: an ordered pair $G = (V, E)$ comprising a set V of vertices or nodes together with a set E of edges or lines, which are 2-element subsets of V [2]. The vertices belonging to an edge are called endpoints. A vertice is also called node or vertex. The degree of a vertice in a graph is the number of edges incident to it. The order of a graph is the number of vertices and the size is the number of edges. These values are represented by $|V|$ and $|E|$ respectively. Let $P(u, v)$ denote the shortest path from u to v, and $|P(u, v)|$ the sum of its edge lengths (length). We assume that every edge e is the shortest path between its endpoints. For a r let $C_{u,r} = \{v \in V, P(u, v) \leq r\}$ is the circle of radius r centered at u, $D = \max |P(u, v)|$ is the diameter of the network, and Δ the maximum degree of a verttice in G. Fig. 1 shows a graph example.
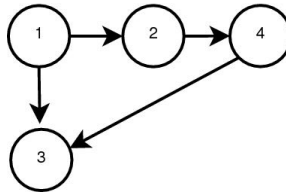

Fig. 1. A graph example with 4 vertices and edges. There are 2 paths from node 1 to node 3.

2.1 Dijkstra's Algorithm

Dijkstra's Algorithm is a short path algorithm developed Edsger Dijkstra [3]. It is a graph search algorithm that solves the single source shortest path problem for a graph with non negative edge path costs, producing a shortest path tree [4]. This algorithm maintains the length $d(v)$ of the shortest path from the source s to v found and the predecessor $p(v)$ of v on the path for every vertice. Initially $d(s) = 0$, $d(v) = \infty$ for all other vertices and $p(v) = null$ for all v. A queue of unscanned vertices with finite d values is maintained. In different steps it extracts the minimum valued vertice from the queue and scans it. If v is the vertex in queue with smallest distance, and $d_e(v, u)$ the distance from v to a neighbour u, for each neighbor u of v the algorithm looks at all edges $(v, u) \in E$ and if $d(u) > d(v) + d_e(v, u)$, sets $d(u) = d(v) + d_e(v, u)$ and $p(v) = u$. The algorithm terminates when the target t is extracted. The bidirectional version of Dijkstra's algorithm is similar running a forward search from s and a reverse search from t. If an edge (v, u) is scanned by the forward search and u has already been scanned by the reverse search, the concatenation of paths $s - v$ and $u - t$ is a new path P from s to t. The algorithm updates and saves the shortest path rised

in the steps execution. Dijkstra's original algorithm has high computational cost and runs in $O(|V|^2)$. Dijkstra's algorithm is usually the working principle behind link-state routing protocols.

2.2 *Genetic Algorithms*

Genetic Altorithms (GAs) are general purpose algorithms that use principles inspired by genetics to evolve solutions to problems [5]. They were proposed by Holland [6, 7, 8, 9] and provide a robust search in complex spaces. A GAs operates on a population (set of individuals) of randomly generated solutions. Every individual has chromosomes often represented by binary strings. The population advances toward better solutions by applying genetic operators, such as crossover and mutation. In each generation, favourable solutions generate new individuals that replace the inferior individuals in a selection process. Crossover cross the genes of two parent chromosomes in order to exploit the search space and constitutes the main genetic operator. The purpose of mutation is to maintain the diversity of the gene pool. A fitness function plays the role of the environment to distinguish between good and bad solutions.

3 Proposed Algorithm

The proposed algorithm is a genetic algorithm and deals with a large number of nodes and paths and reduces the calculation of routes. We supose that a public transport network node can belong to different bus,metro or train lines. In our approach, it will be considered the source and destination nodes and important junctions nodes (belongs to different lines) called *transit nodes.* That allows to reduce complexity of paths. All nodes and edges data are stored in a database. Database contains node name and location, edge information, its vertices, vertices location, geometry, distance cost, CO_2 cost and lines to which it belongs.

The algorithm consists of several steps. The first step reduces the graph size, as it shown the Fig. 2. The right side shows a graph with 10 nodes and 3 lines, and is reduced to 4 nodes and 3 lines (left side). We can appreciate that there exists one transit node ($v5$) and three source/destination nodes ($v1,v7,v10$). In a second step, a population is randomly generated. Every individual represents a feasible path from source node to destination node. An invidivual has a number N of cromosomes and every cromosome is made up of two values: the first is a transit node value and the second represents a transport line. Thus, a path is represented by transit nodes and lines that should choose to get from source to destination. In the following steps, favourable solutions generate new individuals that replace worst in a selection process. Three genetic operators are applied: selection, crossover and mutation.
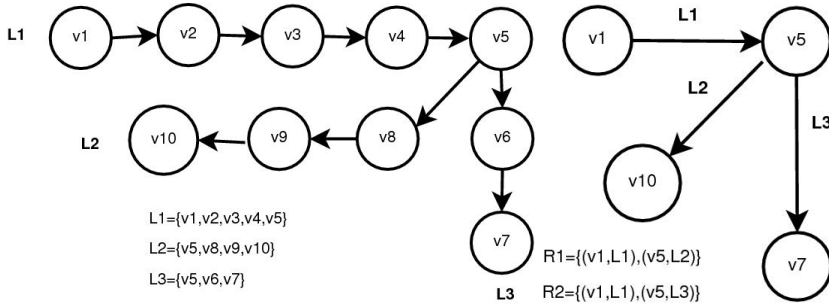
Fig. 2. First step: reducing graph

3.1 Selection

For the selection a roulete algorithm is chosen [8]. The population is mapped onto a roulette wheel such a slot size correspond to its selection probability: each chromosome is assigned a slot of the total area and cromosomes with higher area will be selected.

3.2 Crossover

We consider that all nodes are not connected and that the routes must be feasible. One-point crossover is selected in *Parent A* for generating new individuals, this point becomes the tentative cutoff. We discover the neighbor nodes to cutoff and select a random one. If connection exists in *Parent B*, then *offspring A* inherits from the beginning to cutoff (Parent A) and from connection rnadomly selected to end in Parent B, as shown in Fig. 3. Then the process is reapeted from *Parent B* to find the second *offspring B*. If the connection selected is not present in the other Parent, other neighbor node will be tested. If none of the nodes connected to the cutting point is present, other crossover point will be selected and proceed in the same way.
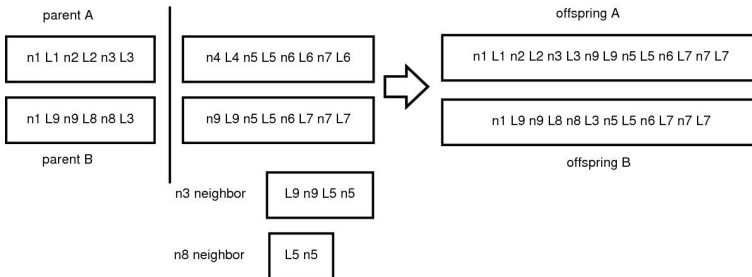

Fig. 3. Crossover

3.3   Mutation

Every individual represents a feasible path for mutation, a new individual is generated according to a probability (mutation rate). It provides a means to explore new genetic material.

4   Simulation and Results

Several tests have been conducted to evaluate the proposed scheduling routing scheme. Concretely, the scheduler is tested through simulations scenarios and traces from real world. In our tests, the environment is based on city public transport of Malaga in the south of Spain. In our simulations, 1043 different nodes (total 1780) made up the public transport system. It is observed that the system integrates 89 unidirectional routes of heterogeneous types: 81 uniderectional bus lines (39 double lines and 3 circular), 2 double metro lines and 2 double train lines. Further, data from nodes (locations, names, code) and lines (location, source and target nodes, parameters) are obtained from Malaga bus transport company (EMT) [10], Malaga train timetables [11] and metro lines [12], collected from January 2013 that are available at [10, 11, 12].

Node locations are designated using a specific pairing of latitude and longitude, using Google Maps style. It uses the SRS (Spatial Reference System) called as 900913 or EPSG 3857 (European Petroleum Survey Group) [13]. This reference system corresponds to the WGS 84 geodetic system (World Geodetic System) [14] using a spherical Mercator projection [14, 15] with distance coordinates in meters. This SRS indicates that WGS 84 coordinates are spherical and x/y values are expressed in meters. WGS 84 is a standard for use in cartography, geodesy, and navigation. It comprises a standard coordinate frame for the Earth, a standard spheroidal reference surface for raw altitude data, and a gravitational equipotential surface that defines the nominal sea level.

In order to test the efficiency of genetic system, a comparison to short path Dijkstra's Algorithm is made. The evolution of learning during the training can be compared at every iteration in terms of computational effort. Computational effort in this work is measured in number of individuals evaluations. GA strategy evaluates the whole population in the first generation and then it evaluates a number of individuals in consideration of selection rate λ. This way, computational effort for GA approach can be formulated as follows:

$$CE_{GA} = GA + GA * \lambda * (num_{iter} - 1) \tag{1}$$

where GA denotes the number of individuals or population size, λ represents the selection factor and num_{iter} is the number of iterations or stopping condition. On the other hand, in Dijkstra every node cost (vertice) is evaluated and thus computational effort can be expressed as

$$O(|V|^2) \tag{2}$$

with V denoting the number of nodes. Genetic algorithm computational effort is lower than short path Dijkstra's algorithm. Table 1 summarizes the setting for GA learning strategies respectively. Global search are favored at first iterations and a deepest exploration of the reached locations is allowed at the end of the iterations. As it is shown in Table 1, is configured with elitist selection operator, one-point crossover and decreasing mutation rate. Training is done for 100 iterations where the algorithm has to address the allocation of routes scenario. A stopping condition has been determined by the analysis of the learning strategy. For testing process, two performance

Table 1. Parameters configuration for GA approach

Parameters configuration		
Selection rate (elitism) λ=0.9	Mutation rate=$0.1e^{(-iter/Num_{iter})}$	Population size (PS)=20

indexes are considered: *distance cost* and CO_2 *cost*. If $P_i(u,v)$ is the i path from node u to node v, the distance cost $d_i(u,v)$ is defined as de sum of its edge lenghts, $|P_i(u,v)|$

$$d_i(u,v) = |P_i(u,v)| = \sum_{k=u}^{v} d_e \tag{3}$$

where d_e is the distance of every edge e between node u and node v. For calculating CO_2 cost, Table 2 of CO_2 emissions is considered [16]. We calculate the CO_2 cost value for i path from node u to node v as

$$CO2_i(u,v) = \sum_{k=u}^{v} (d_e * E_F) \tag{4}$$

where E_F is an emission factor value from the the table 2. Table 3 shows an example of Dijkstra distance cost from node 152 to 253. This result is compared to the best achieved best individual (whole test) obtained by GA. The results for CO_2 cost are shown in table 4. The average for all the best individual in every GA test are shown in Table 5.

Table 2. CO_2 emissions

Public transport	Emission Factor (g/passenger x km)
Bus (urban)	82.81
Train	35.97
Metro	39.53

Table 3. Dijkstra distance cost and GA Best individual distance cost (Km) from node 152 to 253

	Dijkstra				GA		
From	To	Line	Cost	From	To	Line	Cost
152	153	1	0.1372	152	153	1	0.1372
153	2671	26r	0.3887	153	2671	26r	0.3887
2671	259	26r	0.6142	2671	259	26r	0.6142
259	260	2r	1.1783	259	260	2r	1.1783
260	261	2r	1.8108	260	261	2r	1.8108
261	262	2r	2.1378	261	262	2r	2.1378
262	253	2r	2.3937	262	253	2r	2.3937

Table 4. Dijkstra and GA Best individual CO_2 cost (g/passenger x km) from node 152 to 253

	Dijkstra				GA		
From	To	Line	Cost	From	To	Line	Cost
152	153	1	11.3615	152	153	1	11.3615
153	2671	26r	32.1882	153	2671	26r	32.1882
2671	259	26r	50.8619	2671	259	26r	50.8619
259	260	2r	97.5750	259	260	2r	97.5750
260	261	2r	149.9523	260	261	2r	149.9523
261	262	2r	177.0312	261	262	2r	177.0312
262	253	2r	198.2222	262	253	2r	198.2222

Table 5. Mean Population individuals costs from node 152 to 253 for distance and CO_2 algorithms

Algorithm (dist)	μ	Algorithm (CO_2)	μ
Dijkstra	2.39	Dijkstra	198.2222
GA	2.43	GA	201.6337

5   Conclusions

In spite of the existence of a large diversity in literature related to scheduling routes in public transport, there are only a few efficiently dealing with a large number of nodes and paths. The proposed algorithm reduces the calculation of routes using the source and destination nodes and important junctions nodes (exists a line change). An algorithm based on transit node that allows to reduce paths in public transport networks to a small number has been proposed here. The genetic algorithm is compared with a classical short path

distance algorithm. Further, performance indexes as *distance cost* and CO_2 *cost* have been used to test the system. It has been shown that this strategy reduces the computational effort. Results also show that genetic algorithm outperforms the best of classical strategies in discovering the short path between two nodes.

References

1. Lopez Martínez, J.M., Sanchez, A.J.: Energy consumption and emissions associated with transportation by car and truck. U.P.M Madrid, Spain (2009)
2. Trudeau, R.J.: Introduction to Graph Theory, p. 19. Dover Pub., New York, ISBN 978-0-486-67870-2; Information technology encyclopedia and acronyms. Springer, Heidelberg (1993)
3. Dijkstra, E.W.: A Note on Two Problems in Connexion with Graphs. Numerische Mathematik 1, 269–271 (1959)
4. Tarjan, R.E.: Data Structures and Network Algorithms. Society for Industrial and Applied Mathematics, Philadelphia (1983)
5. Cordon, O., Herrera, F., Hoffmann, F., Magdalena, L.: Genetic Fuzzy Systems: Evolutionary Tuning and Learning of Fuzzy Knowledge Bases. World Scientific Publishing Co. Pte. Ltd., Singapore (2001)
6. Holland, J.H.: Adaptation in Natural and Artificial Systems. University of Michigan Press, Ann Arbor (1975)
7. Back, T.: Evolutionary Algorithms in Theory and Practice. Oxford University Press (1996)
8. Goldberg, D.E.: Genetic Algorithms in search, optimization and machine learning. Addison Wesley (1989)
9. Mitchell, M.: An Introduction to Genetic Algorithms. MIT Press, Cambridge (1996)
10. EMT SAM EMT Bus lines and timetables (2013),
    `http://webnet.emtsam.net:7083/RedEMT/faces/pages/redweb.jspx`
11. RENFE Malaga train lines and timetables (2013),
    `http://www.renfe.com/viajeros/cercanias/malaga/index.html`
12. METRO Malaga metro lines and timetables (2013),
    `http://www.metrodemalaga.info/`
13. EPSG OGP Geomatics Committee (2013), `http://www.epsg.org/`
14. Osborne, P.: The Mercator Projections, Edinburgh (2013)
15. Maling, D.H.: Coordinate Systems and Map Projections. Pergamon Press (1992) ISBN 0080372333
16. Catalonian office for climatic change, Practical guide for calculating greenhouse gas emissions. Generalitat de Catalunya. Comision Interdepartamental del Cambio Climatico (2012)

Routing and Spectrum Assignment in Spectrum Flexible Transparent Optical Networks

Ireneusz Olszewski

Faculty of Telecommunications,
Computer Science and Electrical Engineering,
University of Technology and Life Sciences,
Al. Prof.S.Kaliskiego 7 85-796 Bydgoszcz, Poland
`ireneusz.olszewski@utp.edu.pl`

Summary. In this paper the heuristic algorithm for the selection lightpaths in flexible transparent optical networks has been presented. The considered problem of routing and spectrum assignment (RSA) takes into consideration minimizing the length of the transmission distance under spectrum continuity constraints and relationship between the traffic bitrates and the spectrum bandwidth. The proposed algorithm constitutes modification the well-known Dijkstra's algorithm. The obtained results show that a significant reduction in the number of rejected requests can be achieved by an appropriate selection of the scheme spectrum segments in the aggregated spectrum of the path.

1 Introduction

A spectrum-sliced elastic optical path network (SLICE) has been proposed as an efficient solution for a flexible bandwidth allocation in optical networks. The used optical orthogonal frequency-division multiplexing (OFDM) supports the transport of multi-granularity Internet traffic, however, requires a grid-flexible (sliced or mini-grid) or a fully gridless network. In SLICE, spectrums of OFDM signals are flexible and sliced to utilize arbitrary contiguous spectrum slots transfering traffic with arbitrary bitrates. Similarly to Routing and Wavelength Assignment in DWDM optical networks, Routing and Spectrum Assignment (RSA) problem appears in the SLICE networks. In [1] a dynamic RSA problem, which takes into account the relationship between the spectrum bandwidth, signal format and traffic bitrates has been formulated. The objective function includes minimizing the path length, and spectrum continuity constraints and spectrums of OFDM signals non-overlap constraints play the role of constraints in the formulated optimization problem. In addition, two different algorithms for solving the formulated problem have been proposed, based on the spectrum segment representation, which

supports both mini-grid and fully gridless networks. On the other hand, in [2] dynamic routing algorithm with distance adaptive modulation in SLICE networks has been proposed. In [3] k-path Signaling-based RSA scheme was proposed and simulation results show that it works better than other RSA schemes in Bandwidth Flexible Optical Networks. In [4] the problem of optical network planning based on OFDM in which the connections are protected by spectrum non-overlap rule has been formulated. To solve this RSA problem, several of algorithms from optimal and decomposition ILP algorithms to a sequential heuristic algorithm combined with appropriate ordering policies and simulated annealing meta-heuristic, have been proposed. In [5] the problem of serving dynamic traffic in a spectrum flexible optical network is considered, where the spectrum allocated to an end-to-end connection varies dynamically with time so as to follow the required source transmission rate. In [6] a novel lightpath fragmentation mechanism for dynamic scenarios in flexible spectrum networks has been proposed. The proposed mechanism helps in avoiding potential blocking by permitting a demand to be split in multiple parts and served as multiple connections.

It should be noted that further studies of the RSA problem are needed to propose new routing algorithms minimizing the blocking probability of requests with possibly a small function of computational complexity. In this paper, the algorithm for solving the basic RSA problem, that is based on the well-known Dijkstra's algorithm, has been proposed. The proposed scheme selection of the segments from the available spectrum of the path provides significant reduction in the number of the rejected requests as compared to other known algorithms.

The remaining part of paper is organized as follows. The first part describes the formulation of the optimization problem. The second part gives an overview of the compared algorithms and proposes a heuristic algorithm solving this problem. The third part contains the results of simulation, obtained after the application of the presented algorithms. The last section presents the final conclusions.

2   Formulation of Optimization Problem

Let $G(V, E, D)$ be the network, where V is the set of nodes, E is the set of unidirectional links and D is the set of lengths of links. R is the symbol rate for each subcarrier (in baud), while G (Hz) is a guard band between adjacent OFDM signals. In this paper, as in [1], segment representation of the spectrum is assumed that supports coarse WDM grid networks, mini - grid (slot based) networks and fully gridless networks. Therefore, the spectrum S_{ij} of link (i, j) can be defined as [1]:

$$S_{i,j} = \bigcup_{k=1}^{K_{ij}} S_{ij}^k = \bigcup_{k=1}^{K_{ij}} (a_{ij}^k, b_{ij}^k) \subseteq (f^{start}, f^{end}) \tag{1}$$

where: $S_{ij}^k = (a_{ij}^k, b_{ij}^k)$ is k segment of contiguous spectrum available (blank) of link (i,j), such that $a_{ij}^k \prec b_{ij}^k \leqslant a_{ij}^{k+1} \prec b_{ij}^{k+1}, k \in (1,2,...,K_{ij})$ and K_{ij} is the number of available segments of this link. $B = (f^{start}, f^{end})$ is the spectral window bandwidth of each link (i,j). Furthermore, let the current request between a pair of nodes $s, d \in N$ be for C units of bandwidth [in bps]. The relationship between the traffic bitrate C and the spectrum of the signal B when using OFDM modulation can be defined as follows [1]: $B = (\lceil C/2mR \rceil + 1) R$, where m is the number of bits per symbol and R is the symbol rate (in baud) for each subcarriers. The above dependence was obtained basing on the assumption that all the subcarriers have the same signal format and use PDM and AMF [1]. Before presenting the optimization problem the variables used in this formulation need to be defined: A^{sd} - binary variable equals 1 if the request is accepted and 0 otherwise, r_{ij} - binary variable equals 1 if the OFDM lightpath passes through link (i,j) and 0 otherwise, r_{ij}^k - binary variable equals 1 if the OFDM signal passes through link (i,j) and the spectrum of the signal is included in the k-th segment $S_{ij}^k = (a_{ij}^k, b_{ij}^k)$. Variables f_a, f_b define a contiguous range of signal spectrum for the incoming request, i.e. $(f_b - f_a) = B + G$. Generally speaking, the considered problem is to find the shortest path P_{sd} between pair of nodes (s,d), for which aggregated spectrum S_{sd} enables the realization of the incoming request. Aggregated spectrum of the path S_{sd} should be understood as spectrum intersection of links belonging to the path, i.e. $S_{s,d} = \bigcap\limits_{(i,j) \in P_{s,d}} S_{ij}$, where S_{ij} is the spectrum of link (i,j). A formulation of the basic RSA problem with the constraints of the spectrum continuity and the constraint of the format transmitted signal constraint has been shown below [1]:

$$\max \left[\alpha A^{sd} - \sum_{(i,j) \in E} (r_{ij} D_{ij}) \right] ; \alpha > \sum_{(i,j) \in E} D_{ij} \qquad (2)$$

The objective function (2) minimizes the length of the path being selected.

$$\sum_j r_{ij} \leqslant A^{sd} \forall_{i \in N} \qquad (3)$$

Constraint (3) ensures that the selected path does not contain cycles, which means that for each node i on the path being chosen between a pair of nodes (s,d), $(A_{sd} = 1)$, only one arc (i,j) belongs to the path $(r_{ij} = 1)$.

$$\sum_i r_{ij} - \sum_i r_{ji} = \begin{cases} -A^{sd}, & j = s \\ A^{sd}, & j = d \quad \forall_{i \in N} \\ 0, & j \neq s, d \end{cases} \qquad (4)$$

Equations (4) give the flow balance for the path.

$$\sum_{k=1}^{K_{ij}} \pi_{ij}^k = r_{ij} \forall_{ij \in N} \qquad (5)$$

Equations (5) ensure that only one available segment S_{ij}^k is selected on link (i, j) of the path being chosen between a pair of nodes (s, d).

$$f_b - f_a - G = B = (\lceil C/2mR \rceil + 1) R \qquad (6)$$

Equation (6) defines the relationship between the spectrum bandwidth B and bitrate C for the incoming request.

$$\begin{cases} f_b - b_{ij}^k \leqslant B^{total} \left(2 - r_{ij} - \pi_{ij}^k\right) \\ a_{ij}^k - f_a \leqslant B^{total} \left(2 - r_{ij} - \pi_{ij}^k\right) \end{cases} \forall ij \in E, \forall k \qquad (7)$$

Equations (7) ensures the spectrum non-overlap rule. $B^{total} = f^{end} - f^{start}$ is the total spectrum bandwidth of each link (i, j). If the OFDM signal path of the current request passes through link (i, j) and is implemented within the k-th segment $S_{ij}^k (r_{ij} = 1, r_{ij}^k = 1)$, then the system of inequalities (7) becomes: $a_{ij}^k \leqslant f_a, f_b \leqslant b_{ij}^k$ which means that the signal spectrum is located in the segment. However, for the other segments $S_{ij}^{\overline{k}}, \overline{k} \in \{1, 2, ..., k-1, k+1, K_{ij}\}$, that have not been changed, $(r_{ij} = 1, r_{ij}^k = 0)$ the system of inequality becomes: $f_b - b_{ij}^{\overline{k}} \leqslant B^{total}, a_{ij}^{\overline{k}} - f_a \leqslant B^{total}$ which means that the spectrum of the signal does not exceed total bandwidth of the link.

Because of the non-linear constraint (6) presented basic RSA problem is an integer non-linear programming problem.

3   Heuristic Algorithms-Sub-Optimal Solution

In [1] three different algorithms have been proposed to solve the basic RSA problem. The first of these, marked as SPV (Spectrum - Vector Constraint Path Searching Algorithm), generates a vector path searching tree (PVST), which is similar to the trees generated by algorithms based on the branch-and-bound method. In this tree, the candidate paths are stored together with the aggregated spectrum and tested at each level of the tree. The computational complexity of the algorithm (determined for the worst case) is an exponential function, and is $O(N) = q_m^{|N|-1}$, where q_m is the maximum out-degree of the network. Due to the very limited scalability of the algorithm, a solution generated by the algorithm may be used only to verify the solutions generated by other algorithms for the networks with small number of nodes.

The second of the proposed algorithms denoted as KSP (k Shortest Paths) is based on a set - k shortest paths, sequenced by the transmission distance (TD), which are calculated off-line for each pair of nodes. For an incoming request between a given pair of nodes the aggregated spectrum is determined for each of k designated paths between them. It should be noted that the constant k-element set of paths, determined statically, can provide only a sub-optimal solution.

The third algorithm, MSP (Modified Shortest Path Algorithm) is a modification of the well-known Dijkstra's algorithm. Modification of this algorithm

is based on the introduction of the spectrum intersection of the links belonging to the paths being chosen and checking if there is bandwidth available for the incoming request. The computational complexity of this algorithm is polynomial and is $O(K|N|^2)$, where K is equal to the average number of segments in the aggregate spectrum of the path. It should be noted that this algorithm can not find a solution, even if there are the bandwidth resources available for the incoming requests. The reason of this is the trap that is based on the fact that the algorithm, after reaching the node on the shortest path, can not find the link outgoing to the next node or the end node with spectrum bandwidth to allow admission request.

It should be emphasized that in all of these algorithms it is the first feasible segment from aggregated spectrum of the path, which enables the realization of the bandwidth $(B+G)$ that is selected. Assuming that the average number of segments in the aggregated spectrum of the path is K, the computational complexity of the function detecting the first feasible segment is $O(K)$.

In this paper, the algorithm for solving the basic RSA problem, based on Dijkstra's algorithm has been proposed. This algorithm is marked as the MSP2.

3.1   MSP2 Algorithm

For a given matrix D whose elements D_{ij} determine the length of links (i,j) and available spectrum S_{ij} on these links, the shortest path is determined basing on modified Dijkstra's algorithm. Modification of this algorithm is based on the introduction of the spectrum intersection of the links belonging to the path being chosen and detects whether the aggregated spectrum enables realization of the request. The general idea of Dijkstra's algorithm [8] is based on the movement on the network arcs, in the subsequent iterations, from source node s to destination node d and marking the intermediate nodes by their current distances from node s. The feature of node u is fixed when it is equal to the length of the shortest path from node s to u. During the initialization of the algorithm source node s receives a fixed feature. Then, in the first iteration, a temporary feature of each successor v of node s is changed from infinity to the feature equal to weight of arc D_{sv}. The node with the smallest feature of a temporary node, for example node u, is replaced by a fixed feature, which does not change until the end of the work of the algorithm. In the next iteration the successors of node u are featured. Then, as before, the node with the smallest temporary feature of all, receives a fixed feature. The algorithm terminates when the destination node d receives a fixed feature. In each iteration of the algorithm the value of the temporary features is reduced. Let $dist$ be an n-element vector, where element $dist(v)$ is the distance from the source node s to node v and $pred$ is a vector of the predecessors on the shortest path from node s to node d. Furthermore, let the variable $newlabel$ be the value of feature of temporary node v,

determined from node u for which the feature has recently been established, i.e. $newlabel \rightarrow dist(u) + D_{u,v}$. If the value of feature of node v, i.e. the distance from node s to node v through node u is reduced, then $dist(v) \leftarrow newlabel$ and $pred(v) \leftarrow u$. At this point, the algorithm should be modified. Let S_{su} be the aggregated spectrum of the links belonging to the path from node s to node u and let S_{uv} be the spectrum of the link from node u to node v. Let the value of the variable $S_{sv} = S_{su} \bigcap S_{uv}$ be determined together with the value of the variable $newlabel$. If the feature node v is reduced, i.e. the path from node s to node v by node u is reduced and spectrum S_{sv} enables the realization of the bandwidth $B + G$ then the process is continued until the node d. Otherwise, the request is blocked. The key of the proposed algorithm is to select the smallest feasible segment (a_d^k, b_d^k) $k \in \{1, 2, ..., k, ..., K_d\}$ from the aggregated spectrum of the path, which enables the realization of the bandwidth $(B+G)$. In order to explain the validity of the proposed scheme, let be assume that the spectrum of links S_{ij} between pair of nodes i and j, which limits the aggregated spectrum of the path S_{sd}, has two segments of the available spectrum $S_{ij} = (0-100) \cup (150-200)$ GHz. If between the pair of nodes $s - d$, or other, the request of bandwidth realization $B+G = 50$ GHz appears and link (i, j) will be belong to the shortest path, the second segment will be occupied. Then, if the link (i, j) will be belong to the shortest path between the same or another pair of nodes between which a connection with the bandwidth $B + G = 80$ GHz should be set the first segment will be occupied. Otherwise, i.e., if the first segment would be occupied for the first request the second request would be rejected. In the SPV, KSP and MSP [1] the first feasible segment (first-fit selection scheme) that allows the implementation of bandwidth $(B + G)$ is always occupied. The algorithm MSP2 minimizing the length of path between a pair of nodes (s, d), which enables the realization of bandwidth $B + G$ is shown below. Let $F(S_{sv}, B + D)$ be a boolean function which that is true if the aggregated spectrum S_{sv} enables the realization of bandwidth $B+G$ and false otherwise. Let $final$ be an n-element vector of boolean, where $final(i)$ changes its state from false to true when feature node i is changed from temporary to fixed.

The length of the shortest path is in variable $dist(t)$, (if $dist(t) = \infty$ then the request of path choice is rejected) and the course of the path can be obtained on the basis of pred. Computational complexity of the algorithm, without function $F()$, is $O(|N|^2)$. Assuming that the computational complexity of the $F()$, equal to the average number of segments in the aggregated spectrum S_{sv} is equel to $O(K)$, the computational complexity of the MSP2 can be defined as $O(K|N|^2)$.

4 Obtained Results

Verification of the algorithms was made for two different networks. The first one, for which the topological structure is shown in Fig. 1a. [1] contains 14

Input: request between a pair of nodes s, d with bandwidth $(B + G)$
Output: the shortest path with aggregated spectrum S_{sd} which enables
     realization of bandwidth $(f_a - f_b) = B + G$
 1: **for** $v \in V$ **do**
 2:    $dist(v) \leftarrow \infty$,
 3:    $finaly(v) \leftarrow false$
 4: **end for**
 5: $dist(s) \leftarrow 0$, $final(s) \leftarrow true$, $u \leftarrow s$, $S_{ss} \leftarrow (f^{start}, f^{end})$,
 6: **while** $final(d) = false$ **do**
 7:    **for** each direct successor v of node u if not $final(v)$ **do**
 8:       $newlabel \leftarrow dist(u) + D_{u,v}$;
 9:       $S_{sv} \leftarrow S_{su} \cap S_{u,v}$; {bandwidth aggregation}
10:       **if** $(newlabel < dist(v))$ **and** $F(Ssv, B + D)$ **then**
11:          $dist(v) \leftarrow newlabel$; {change the shortest path to node v}
12:          $pred(v) \leftarrow u$;
13:       **end if**
14:    **end for**
15:    find a node y with the smallest temporary feature $dist(y)$, different from
      ∞;
16:    **if** $dist(y) < \infty$ **then**
17:      $final(y) \leftarrow true$; { y receives a fixed feature }
18:      $u \leftarrow y$;
19:      **if** $u = d$ **then**
20:         select the smallest segment S_{sd}^k, such that $B + G \subseteq (a_{sd}^k, b_{sd}^k)$, from the
21:         aggregated spectrum S_{sd}; $f^a \leftarrow a_{sd}^k$, $f^b \leftarrow f^a + (B + G)$
22:      **end if**
23:    **else**
24:      Rejection of the request;
25:    **end if**
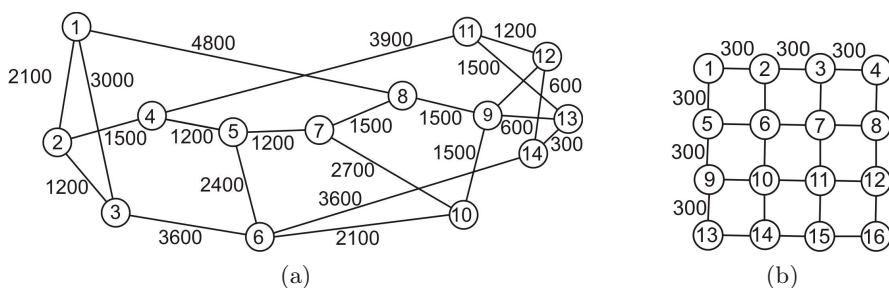26: **end while**

Algorithm 2. MSP2 Algoritm

Fig. 1. Topological structure of the network: (a) the NSFNET (b) the GRID

nodes connected by links with the continuous spectrum equal to $B^{total} = 400$GHz. The second [1], for which the topological structure is shown in Fig. 1b. contains 16 nodes connected by the links with the same continuous spectrum.

Each edge of the graph is a pair of the unidirectional links. In this work, it was assumed that each node can be input and the output node. Thus, in the first network 196 pairs of nodes can be distinguished, while in the second 256 pairs of nodes. On the edges of the graph the length of the links of the network are presented. It is assumed that the stream of requests between each pair of nodes (s, d) is the Poisson with intensity λ, and holding time of the call has an exponential distribution with an average value equal to $1/\mu = 1$. The bandwidth of request is uniformly distributed from 10 Gbps to 200 Gbps with an average value equal to $\bar{C} = 105$ Gbps. The volume of traffic (in bps) between each pair of nodes is $\rho\bar{C}$, where ρ is the volume of traffic in the erl. Network simulation was carried out in dynamic conditions. In dynamic conditions connections are set up and disconnected (short-lived connections) and the results are recorded after obtaining an equilibrium state of the system. For each load of the network T=10 simulation trials have been done. The number of requests in the network is a condition for the end of the simulation. Each trial included 25000 requests. In addition, it was assumed that the systems have the same OFDM modulation rate equal to $R = 1$ Gbaud. The Tables $1 \div 4$ show the number of rejected requests, blocking probability, spectrum utilization ratio and processing time of the algorithms, depending on the amount of traffic offered to the network for the different of modulation level $m = 2, 4$. Blocking probability is defined as the capacity blocking probability equal to $\sum C_i A_i / \sum C_i$ where C_i is the capacity of the i-th request while A_i is a binary variable equal to 1 if the request is accepted and 0 otherwise. Spectrum efficiency ratio is defined as the ratio of the occupied bandwidth to the total spectrum bandwidth of the network. The proposed MSP2 algorithm has been compared with the MSP algorithm [1], which is an algorithm of polynomial computational complexity and provides lower blocking probability than KSP [1].

Table 1. Number of rejected requests for network consisting of $n = 14$ nodes

| Total Load | $m = 2$ | | $m = 4$ | |
In Gbps	MSP	MSP2	MSP	MSP2
1200	128.4	104.3	0.0	0.0
1600	809.4	793.4	1.4	1.5
2000	2154.0	2073.7	11.6	10.6
2400	3414.6	3424.3	50.0	51.0
2800	4572.4	4465.7	161.6	140.0
3200	6057.2	5823.4	632.8	592.9
3600	6797.5	6683.9	1225.2	1189.8
4000	7577.4	7381.5	1894.9	1752.5

From Table 1 it can be shown that for $m = 2$, 4 a smaller number of requests rejects MSP2, which differs from MSP algorithm [1] the selection scheme of the spectrum feasible segments only from the aggregated spectrum of the path for the incoming request. Therefore, the obvious conclusion is that the reduction in the number of rejected requests can be obtained by using the proper selection scheme of the spectrum feasible segments in an aggregated spectrum of the path and an algorithm of polynomial complexity.

Table 2. Capacity blocking probability for network consisting of $n=14$ nodes

Total Load In Gbps	$m = 2$		$m = 4$	
	MSP	MSP2	MSP	MSP2
1200	0.0067	104.3	0.0000	0.0000
1600	0.0511	793.4	0.0000	0.0000
2000	0.1309	2073.7	0.0007	0.0006
2400	0.2032	3424.3	0.0031	0.0032
2800	0.2687	4465.7	0.0101	0.0090
3200	0.3427	5823.4	0.0407	0.0382
3600	0.3853	6683.9	0.0785	0.0761
4000	0.4197	7381.5	0.1194	0.1110

Table 2 shows the blocking probability obtained after using the examined algorithms. The smallest blocking probability is obtained after the using the MSP2 algorithm.

Table 3. Spectrum utilization ratio for network consisting of $n=14$ nodes

Total Load In Gbps	$m = 2$		$m = 4$	
	MSP	MSP2	MSP	MSP2
1200	0.4613	0.4672	0.2646	0.2639
1600	0.5684	0.5601	0.3334	0.3337
2000	0.6080	0.6063	0.4050	0.4002
2400	0.6332	0.6287	0.4655	0.4719
2800	0.6506	0.6544	0.5187	0.5335
3200	0.6726	0.6760	0.6009	0.5908
3600	0.6845	0.6894	0.6265	0.6225
4000	0.6905	0.6956	0.6473	0.6436

Table 3 shows the spectrum utilization ratio after using the examined algorithms. As can be seen, the values of spectrum utilization ratio are similar for both examined algorithms.

In turn, Table 4 shows the processing time (in ms) after using of examined algorithms. The shortest times were obtained after using the MSP2 algorithm.

A similar relationships, not shown here, were obtained for a network with 16 nodes (the GRID) for which the topological structure is shown on Fig. 1b.

Table 4. Processing time for network consisting of $n=14$ nodes (in ms)

Total Load	$m = 2$		$m = 4$	
In Gbps	MSP	MSP2	MSP	MSP2
1200	26807.6	23411.0	33523.2	28244.5
1600	32113.1	27901.0	43854.1	33599.1
2000	35947.6	30951.4	53192.6	39397.6
2400	39173.4	33235.5	51674.7	46219.4
2800	41446.6	34865.1	15791.0	56150.3
3200	44151.4	37426.8	25700.5	14639.3
3600	45265.3	37954.5	23332.3	12459.4
4000	46735.0	38609.6	26720.5	20433.1

5   Conclusions

In this work the shortest lightpath selection algorithm that allows realization of the request with given bandwidth in flexible transparent optical networks has been proposed. The considered problem covers minimizing the length of the laightpath (transmission distance) being chosen with the constraints imposed on the spectrum continuity and the format of the transmitted signal.

The obtained results showed that the proposed algorithm MSP2, which is based on Dijkstra's algorithm, rejects a smaller number of requests then MSP. Reducing the number of rejected requests is achieved by using a proper selection scheme of the spectrum feasible segments in an aggregated spectrum of the path, which occupies the minimal segment enabling realization of the incoming request.

References

1. Wan, X., Hua, N., Zheng, X.: Dynamic Routing and Spectrum Assignment in Spectrum-Flexible Transparent Optical Networks. Opt. Commun. Netw. 4(8), 603–613 (2012)
2. Jnno, M., Kozicki, B., Takara, H., Watanabe, A., Sone, Y., Tanaka, T., Hirano, A.: Distance adaptive spectrum resource allocation in spectrum-sliced elastic optical path network. IEEE Communication Magazine 48(8), 138–145 (2010)
3. Jin, Q., Wang, L., Wan, X., Zheng, X., Zhou, B., Liu, Z.: Study of Dynamic Routing and Spectrum Assignment Schems in Bandwidth Flexible Optical Networks. In: Communicationa and Photonics Conference (2011), Asia (2007)
4. Christodoulopoulos, K., Tomkos, I., Varvarigos, A.E.: Routing and Spectrum Allocation in OFDM-based Optical Networks with Elastic Bandwidth Allocation. In: 2010 IEEE Telecommunications Conference (GLOBECOM 2010), December 6-10 (2010)
5. Christodoulopoulos, K., Varvarigos, E.: Routing and Spectrum Allocation Policies for Time Varying Traffic in Flexible Optical Networks. In: 16th International Conference on Optical Network Design and Modeling (ONDM), April 17-20 (2012)

6. Pagés, A., Perello, J., Spadaro, S.: Lightpath Fragmentation for Efficient Spectrum Utilization in Dynamic Elastic Optical Networks. In: Proceedings of ONDM, pp. 1–6 (2012)
7. Christodoulopoulos, K., Tomkos, I., Varvarigos, A.E.: Elastic Bandwidth Allocation in Flexible OFDM-based Optical Networks. J. Lightwave Technology 29(9) (2011)
8. Sysło, M.M., Deo, N., Kowalik, J.: Discrete Optimization Algorithms: With Pascal Programs. Dover Publications, Mineola (2006)

Index